Understanding radical chemistry in Beijing through observations and modelling

Eloise Jane Slater

Submitted in accordance with the requirements for the degree of Doctor of Philosophy

The University of Leeds

School of Chemistry

April, 2020

The candidate confirms that the work submitted is his/her own and that appropriate credit has been given where reference has been made to the work of others.

Acknowledgements

First of all, I would like to thank all the members of the FAGE group for support and guidance during my PhD making it an enjoyable experience, especially my supervisor Dwayne, Lisa and Dom. Especially to Lisa. She helped me get to grips with both the instrument and the MCM and was always happy to help with problems. Thanks to everybody involved in the APHH campaign, especially my fellow first-year PhD students: Archit, Jess, Joshi and Freya - you guys have been amazing. Thanks to everybody in the B36 office (Grace, Joanna, Graham and Lauren), both for the help with work and the much-needed distractions/laughter.

Of course, none of this would be possible without my family. Mum, Dad, Annice, Ollie and Brie thanks for the support even though I am sure none of you have a clue what my PhD is about. I would also like to thank my Aunt Jackie and Uncle Pete, for giving me a place to stay and your unwavering support. Thanks to my partner Mark who has supported me through the ups and downs of my PhD, so thanks for bearing with me and helping me through. Thanks to all the people I made to proofread my chapters, and I am sorry for putting you through that. Finally, I would like to thank COVID-19 for removing all the distractions so I could focus on writing up.

Abstract

In Beijing, poor urban air quality has a demonstrable effect on human health; with high aerosol loadings during winter and high ozone episodes during summer. The hydroxyl radical (OH) mediates virtually all the oxidative chemistry in the atmosphere, being responsible for the transformation of primary emissions into secondary pollutants such as NO_2, O_3 and SOA (secondary organic aerosol). Comparison of measured radicals with results from detailed chemical box models serves as a vital tool to assess our understanding of the underlying chemical mechanisms involved in tropospheric oxidation. A recent comparison of radical measurements with those predicted by box models highlight missing understanding at both high and low NO mixing ratios.

The Leeds FAGE (fluorescence assay by gas expansion) instrument was deployed in Beijing for two field campaigns, one in the winter in November/December 2016 and the other in summer in May/ June 2017. The chemical conditions varied vastly between the two campaigns, with NO concentrations exceeding 250 ppb in the winter, while O_3 levels over 100 ppbv were frequently observed during the summer. The average OH concentration during the winter campaign was high (~ 2.5×10^6 cm^{-3}) even during haze events, and during the summer elevated levels of OH were observed, reaching up to 2.5×10^7 cm^{-3}.

The OH measurements were compared with the OH calculated using a photostationary steady-state (PSS) calculation and showed that in winter the experimental budget could be closed, but in the summer the PSS calculation underpredicts OH by a factor of ~2 and highlights a missing source of OH. The measured radicals have been compared to results from a box model incorporating the Master Chemical Mechanism (MCM, v3.3.1). The model underpredicts OH, HO_2 and RO_2 in winter, and the underprediction increases with increasing NO. By contrast, in summer the model can replicate OH very well, but overpredicts HO_2 and underpredicts RO_2. Several model scenarios have been performed to investigate the differences between the measured radical values and the model results. In winter, the model can reproduce the measured OH reactivity. When the model is constrained to measured HO_2, the model can reproduce OH, which suggests the missing understanding is linked to RO_2 radical chemistry. In summer the model can reproduce the OH, HO_2 and RO_2 radical

concentration when the RO_2 + NO rate constant is reduced by a factor of ~10, and may suggest that the RO_2 species are undergoing autoxidation forming HOMs (highly oxidised molecules) which is competing with RO_2 + NO reaction. HOMs species were also observed during the summer campaign in both the gas-phase and aerosol phase by a CIMS (chemical ionisation mass spectroscopy) instrument. The impact of HO_2 uptake onto aerosols on both modelled HO_2 and calculated O_3 production was assessed for both the winter and summer campaign. It shows that HO_2 uptake decreases O_3 by up to ~6 ppbv hr^{-1} in summer; while there is a much smaller impact in winter as the reaction of HO_2 + NO outcompetes HO_2 uptake.

Table of Contents

List of Figures

List of Tables

Abbreviations

A/C	air conditioner
AAQS	Ambient Air Quality Standards
AIRLESS	Effects of air pollution on cardiopulmonary disease in urban & peri-urban residents in Beijing
AIRPOLL-Beijing	Sources and emissions of air pollutants in Beijing
AIRPRO	AIR PROcesses
APHH	Air Pollution and Human Health in Chinese megacities
APIC-ESTEE	Air pollution impacts on cardiopulmonary disease in Beijing: An integrated study of exposure science, toxicogenomics & environmental epidemiology
ARTCAS	Arctic Research of the Composition of the Troposphere from Aircraft and Satellites
ASOA	anthropogenic secondary organic aerosol
ATHOS	Airborne Tropospheric Hydrogen Oxides Sensor
AVOC	Anthropogenic Volatile Organic Compound
BBO	β-barium borate
BC	black carbon
BEARPEX-09	Biosphere Effects on Aerosols and Photochemistry Experiment II
BEST-ONE	Beijing winter finE particle Study – Oxidation Nucleation and light Extinctions
BVOC	biogenic volatile organic compounds
CalNex-LA	California Research at the Nexus of Air Quality and Climate Change measurement
CAREBeijing	Campaigns of Air Quality Research in Beijing and Surrounding Regions
CI	criegee intermediate
CIMS	chemical ionisation mass spectroscopy
ClearfLo	Clean air for London
CNN	cloud condensation nuclei
CPM	Channel Photomultiplier
CRDS	Cavity Ring Down Spectroscopy
CRM	comparative rate method
DNA	Deoxyribonucleic acid
DOAS	direct optical absorption spectroscopy
DOMINO	Diel Oxidants Mechanisms In relation to Nitrogen Oxides
DWP	dual wavelength plate
FAGE	fluorescence assay by gas expansion
FZJ	Forschungszentrum Julich

GB	gating box
GC-FID	measured using filtered radiometer
GEOS-CHEM	Gooddard Earth Observing System (Chemical transport model)
GHG	Green House Gases
GTHOS	Ground-based Tropospheric Hydrogen Oxides Sensor
HOPE	HOhenpeibenberg Photochemistry Experiment
HORUS	HydrOxyl Radical measurement Unit based on fluorescence Spectroscopy
HUMPPA-COPEC	Hyytiala United Measurements of Photochemistry and Particle Air – Comprehensive Organic Precursor Emissions and Concentration study
IAP	Institute of Atmospheric Physics
IC	ice nuclei
ICOZA	Integrated Chemistry of Ozone in the Atmosphere
ID	in-diameter
IMPACT	Integrated Measurement Program for Aerosol and oxidant Chemistry in Tokyo
INHANCE	Integrated assessment of the emission-health-socioeconomics nexus & air pollution mitigation solutions & interventions in Beijing
IPCC	Intergovernmental Panel on Climate Change
IPI	Inlet pre-Injector
IR	Infra-red Radiation
IU-FAGE	Indianna University FAGE
k(OH)	OH reactivity
LBO	lithium triborate
LIF	Laser Induced Fluorescence
LIM	Leuven isoprene Mechanism
LOD	limit of detection
LP	laser power
LP-LIF	laser photolysis – laser induced fluorescence
MACR	Methacrolein
MADE	modal aerosol dynamics model for europe
MCM	Master Chemical Mechanism
MCMA	Mexico City Metropolitan Area
MCP	micro-channel plate
MEGAPOLI	Megacities: Emissions, urban, regional and Global Atmospheric POLlution and
MFC	mass flow controller
MIM	Mainz Isoprene Mechanism

MOSIAC	Model for simulating aerosol interactions and chemistry
MPIC	Max Planck Institute for Chemistry
MVK	Methyl Vinyl Ketone
NACHTT	Nitrogen, Aerosol Composition, and Halogens on a Tall Tower
NCP	North China Plain
OC	organic carbon
ODR	Orthogonal Distance Regression
OHwave	Offline OH background signal
OHchem	Online chemical modulation system.
OPR	Ozone production rate
OVOC	oxygenated volatile organic compounds
PAN	Peroxyacetyl nitrate
PBL	planetary boundary layer
PD	photodiode
PERCA	PEroxy Radical Chemical Amplification
perCIMS	peroxy radical chemical ionisation mass spectroscopy
PeRCIMS	Peroxy Radical Chemical Ionisation Mass Spectrometry
PKU	Peking University
PM	Particulate Matter
PM_{10}	Particulate matter less than 10 nm in size.
$PM_{2.5}$	Particulate matter less than 2.5 nm in size.
PMT	photomultiplier tube
PMTACS-NY	$PM_{2.5}$ Technology Assessment and Characterization Study New York
PRD	Pearl River Delta
prf	pulse repetition frequency
PRIDE-PRD	Program of regional Integrated Experiments of Air Quality over the Pearl River
PROPHET	Programme for Research on Oxidants: Photochemistry, Emissions and Transport
PSS	a photostationary steady-state
PSU	Pennsylvania State University
PSU	power supply unit
PTR-MS	Proton-transfer-reaction Mass Spectrometry
PUMA	Pollution of Urban Midland Environments
RACM	Regional Atmospheric Chemical Mechanism
RH	relative humidity
SAPHIR	Simulation of Atmospheric PHotochemistry In a large Reaction Chamber

SARs	Structure Activity Relationships
sCI	stabilised criegee intermediate
SD	standard deviation
SE	standard error
SHARP	Study of Houston Atmospheric Radical Precursors
SHARP	Study of Houston Atmospheric Radical Precursors/Surface-Induced Oxidation of
SNR	signal-to-noise
SOA	secondary organic aerosol
SZA	solar zenith angle
THG	third harmonic generation
TMB	trimethyl benzene
TOR	turnover rates
TOR	turnover rate
TRAMP	Texas-II Radical and Aerosol Measurement Project
UPS	Uninterruptable Power Supply
UV	ultraviolet
VOC	volatile organic compounds
WRF-CHEM	Weather Research and Forecasting (WRF) model coupled with Chemistry
$\gamma(HO_2)$	reactive uptake coefficient for HO2

1. Introduction

1.1 Air Quality and Important Atmospheric Pollutants

Atmospheric chemistry research can be divided into three mains areas: field measurements, laboratory experiments and modelling studies. Field measurements can give an insight into emissions and their trends, and how these link to the formation and losses of different trace gases and aerosols. On the other hand, laboratory experiments can give more details into the processes that occur and their physical parameters including rate constants and how these change as a function of temperature and pressure. Numerical models are used for future predictions, and to test theoretical understanding of processes occurring in the atmosphere, including climate change and urban air pollution.

Inhabitants of megacities, a metropolitan area with a population over 10 million (Sekovski et al., 2012), are vulnerable to health effects caused by air pollution (Gurjar et al., 2010), important air pollutants include SO_2, NO_2, O_3 and particulate matter (PM). Air pollution is linked to over 40,000 (Roberts, 2016) early deaths per year in the UK alone (Gurjar et al., 2010). This thesis shall focus on air pollution in Chinese megacities, where in 2012 air pollution was related to more than 1 million (Vaugham, 2016) premature deaths, with data from two field campaigns during winter and a summer in central Beijing.

NO_2 is formed from reactions of NO with radicals (RO_2 and HO_2) or ozone. NO_2 can also be generated directly from combustion processes with higher emissions coming from diesel vehicles (Finlayson-Pitts and Pitts, 1997). NO_2 can cause health problems including airway inflammation and can cause various health problems for people affected by asthma (Dab et al., 1996). NO_2 can also cause a net change in ozone from the oxidation of NO_x in the presence of light and volatile organic compounds (VOCs) (Finlayson-Pitts and Pitts, 1997). Ozone is a radiatively active gas interacting with short (downwelling radiation) and long wavelengths (upwards IR). Changes in ozone have been estimated to contribute ~10% to the positive radiative forcing of climate change (Ramaswamy et al., 2001). O_3 is an air pollutant in the troposphere and can cause difficulty breathing (Lamarque et al., 2013). Ozone is also attributed to plants and crop death

(Agency, 2017a). The long-term effects of exposure to ozone can lead to permanent lung damage and abnormal lung development in children (Agency, 2017a). Ozone is also a source of the OH radical (R1.1 – R1.2) hence an increase in ozone leads to a higher tropospheric OH concentration and a decreased lifetime of methane (Finlayson-Pitts and Pitts, 1997). Both methane and ozone are greenhouse gases meaning HO_x chemistry has an impact on global climate change.

$$O_3 + h\nu(\lambda \leq 336\ \mathrm{nm}) \rightarrow O(^1D) + O_2 \qquad \text{R1.1}$$

$$O(^1D) + H_2O \rightarrow 2OH \qquad \text{R1.2}$$

Most SO_2 comes from: burning fossil fuels; power plants; industrial facilities and is also emitted from volcanoes (Agency, 2017b). SO_2 can cause short-term effects on the respiratory system. Large concentrations of SO_2 also leads to the formation of SO_x which contributes to PM (particulate matter) (Agency, 2017b). SO_2 can also contribute to acid rain which can damage the ecosystems of fish and wildlife. Table 1.1 shows the EU and Chinese set limits for concentrations of $PM_{2.5}$ (particulate matter less than 2.5 nm), SO_2, NO_2, PM_{10} (particulate matter less than 10 nm) and O_3 (Comission, 2017, China, 2012).

Pollutant	European Concentration (μg m^{-3})	Chinese Concentration (μg m^{-3})		Averaging Period
		Grade-I	Grade-II	
$PM_{2.5}$	25	15	75	1 year
SO_2	350	150	500	1 hour
	125	50	150	24 hours
NO_2	200	200	200	1 hour
	40	40	40	1 year
PM_{10}	50	50	150	24 hours
	40	40	70	1 year
O_3	120	100	160	8 hour mean

Table 1.1 European Union (Comission, 2017) and Chinese (Comission, 2017, China, 2012) limits for Grade-I and Grade-II on exposure to $PM_{2.5}$, SO_2, NO_2, PM_{10} and O_3. Grade-II is for urban or industrial areas; whilst Grade-I is for everywhere else in China.

The role of ambient airborne PM has been highlighted as an important pollutant for cardiopulmonary diseases and lung cancer (Valavanidis et al., 2008). It has been shown that different sizes and different surface areas of PM determines the

potential to cause inflammatory injury, oxidative damage and other biological effects (Valavanidis et al., 2008). The effects are stronger for fine and ultrafine particles as they can penetrate deeper into the airway, and effect the alveoli (Valavanidis et al., 2008). PM can be made up of transition metals, sulfate, nitrate, organic compounds, stable radicals of carbonaceous material, minerals and reactive gases (Valavanidis et al., 2008). Particulate matter can cause adverse effects through several mechanisms including oxidative stress; oxygen-free radical generating; DNA oxidative damage and mutagenicity (Valavanidis et al., 2008). It is estimated that a decrease of 10 μg m^{-3} $PM_{2.5}$ is related to ~0.6-year mean life expectancy increase (Gao et al., 2016b). In general, studies have shown that smaller particles ($PM_{2.5}$), which are generally produced from vehicular emissions in urban areas, have higher toxicity by causing oxidative stress and inflammation than larger particles (PM_{10}) (Valavanidis et al., 2008).

It has also been shown that aerosol, natural or anthropogenic, can impact global climate (Gao et al., 2016b). Atmospheric aerosol can directly affect the Earth's radiation budget by scattering and absorbing solar radiation, and indirectly by disturbing clouds acting as a cloud condensation nuclei (CCN) and ice nuclei (IC) (Gao et al., 2016b). It is difficult to distinguish between anthropogenic PM and PM from biogenic sources and to identify the pollution source, as this requires *in-situ* chemical measurements which are restricted to time and location. In January 2013 in Beijing, a haze event occurred and the daily $PM_{2.5}$ reached over 500 μg m^{-3} (Wang et al., 2014). From 1960 to 2010 dramatic changes in emissions led to +260% increases in sulfate, +320% increases in nitrate, +300% increases in ammonium, +160% increases in black carbon (BC), and +50% increases in organic carbon (OC)(Gao et al., 2016b). Also, it has been observed that the winters in China, especially in the northern regions, are warming up (Gao et al., 2016b). Additionally, the average wind speed in China has lowered along with the decrease of RH (relative humidity) throughout China (Gao et al., 2016b).

The PM in the atmosphere can be directly emitted from wildfires, combustion, windblown dust and sea salt: or formed from gases *via* secondary organic aerosol mechanisms. Meteorology affects PM levels by chemical reactions, transport, deposition processes and changing chemical emissions (Dawson et al., 2007). An example of this is shown by increased temperatures leading to higher biogenic emissions, which in turn are important SOA precursors (Dawson et al., 2014).

Increasing temperatures can also increase sulfate concentration due to SO_2 oxidation *via* the OH into H_2SO_4 which is a temperature dependant reaction (Dawson et al., 2007). At higher temperatures semi-volatile aerosols may also decrease due to evaporation (Dawson et al., 2007). High RH favours the formation of nitrate and increasing precipitation decreases PM species because wet scavenging occurs (Dawson et al., 2007).

Generally in China organic material contributes 20-50% of $PM_{2.5}$, and organic aerosols can be produced by either primary emissions or secondary formation (secondary organic aerosol), estimated using the WRF-CHEM (Weather Research and Forecasting (WRF) model coupled with Chemistry) regional model over China. SOA is formed from semi-volatile organic gases and may account for 20-80% of the total aerosol in organic aerosol (Jiang et al., 2012). For SOA simulation it is important to understand oxidation reactions of organic species in the gas-phase and the associated heterogeneous reactions which generate the low volatility organic compounds. These processes are very complex and not completely understood, and SOA concentrations are generally underestimated by the models (Jiang et al., 2012). Emission sources for SOA include anthropogenic (alkane, alkene, aromatic and isoprene), biomass burning (alkane, alkene, aromatic) and biogenic sources (isoprene and monoterpene) (Jiang et al., 2012). Summary of Chinese air pollution and models can be found in section.1.3.

1.2 Photochemistry in the Troposphere

Anthropogenic and biogenic emissions including CH_4, CO, SO_2, NO_x and VOCs are processed in the troposphere through photochemical oxidation reactions mainly with short-lived radical species such as OH. Tropospheric oxidation is dominated by reaction of hydroxyl radical (OH), but other radicals are important including Cl, NO_3 and halogen oxides (XO, X=Br, I). A non-radical oxidant is O_3. Tropospheric oxidation controls the lifetime of primary emitted species and their formation into secondary pollutants, which can have implications on climate change and air quality. Photochemical reactions involving NO_x and VOCs can lead to the formation of ground-level O_3 (a component of photochemical smog) and can also lead to the formation of secondary organic aerosols.

1.2.1 Hydrogen Oxides

OH, HO_2 and RO_2 play an important role in the chemistry of the atmosphere (Stone et al., 2012). The OH radical initiates the oxidation of VOCs, converting the OH into either HO_2 or RO_2 (organic peroxy radicals). As shown in Figure 1.1, the radical chain following this leads to the production of ozone (in the presence of NO_x) and SOA in the troposphere (Stone et al., 2012, Lu et al., 2012). The understanding of the chemistry underpinning OH, HO_2 and RO_2 is important in developing air quality control strategies (Griffith et al., 2016). Oxidation proceeds through a series of partially oxidized intermediates; the primary emitted compounds and the intermediates have a wide range of atmospheric lifetimes that mostly depend on their rate of reaction with OH and the OH concentration (Stone et al., 2012). OH clearly plays a pivotal role in the tropospheric chemistry; this is why a large emphasis has been placed on *in-situ* measurements, but the short lifetime and low concentration makes measuring these radicals difficult (Stone et al., 2012). There are several instruments in use to measure OH including the following: fluorescence assay by gas expansion (FAGE); differential optical absorption spectroscopy (DOAS) and chemical ionisation mass spectrometry (CIMS) (Heard and Pilling, 2003). These instruments are described further later in section.1.4.

In remote areas the major sources of OH is from the photolysis of O_3 at short wavelengths to form atomic oxygen in either its electronically excited state (O^1D) (R1.3) or its electronic ground state (O_3P) (R1.5):

$$O_3 + h\nu \rightarrow O(^1D) + O_2 \qquad \text{R1.3}$$

$$O_3 + h\nu \rightarrow O(^3P) + O_2 \qquad \text{R1.4}$$

Conversion of spin dictates that the dioxygen formed from R1.3 must also be in a singlet state:

$$O_3 + h\nu(\leq 310\ nm) \rightarrow O(^1D) + O_2(^1\Delta_g) \qquad \text{R1.5}$$

However, at longer wavelengths photolysis can also occur through the spin-forbidden channel:

$$O_3 + h\nu(310 < \lambda < 340\ nm) \rightarrow O(^1D) + O_2(^3\Sigma\ ) \qquad \text{R1.6}$$

$j(O^1D)$ the photolysis rate of O_3 to form $O(^1D)$, is given by:

$$j(O^1D) = \int \sigma_{O3}(\lambda,T)\phi_{O1D}(\lambda,T)F(\lambda)d\lambda \qquad \text{R1.7}$$

where $\sigma_{O3}(\lambda,T)\ and\ \phi_{O1D}(\lambda,T)$ are the O_3 absorption cross-section and $O(^1D)$ quantum yield, respectively, and $F(\lambda)$ is the spectral actinic flux. The actinic flux increases rapidly at longer wavelengths and between 310 nm and 320 nm, there is more than a factor of ten increase in the flux. The increase of actinic flux at longer wavelengths means that the spin-forbidden channel (R1.6) is significant despite both the O_3 absorption cross-section and quantum yield decreasing dramatically above 310 nm (Finlayson-Pitts and Pitts Jr, 1999). The spin-forbidden process is especially important at dawn and dusk when the solar zenith angle is high (SZA), as the spectral actinic flux is red-shifted as the scattering efficiency through the atmospheric column is proportional to 1/ λ.

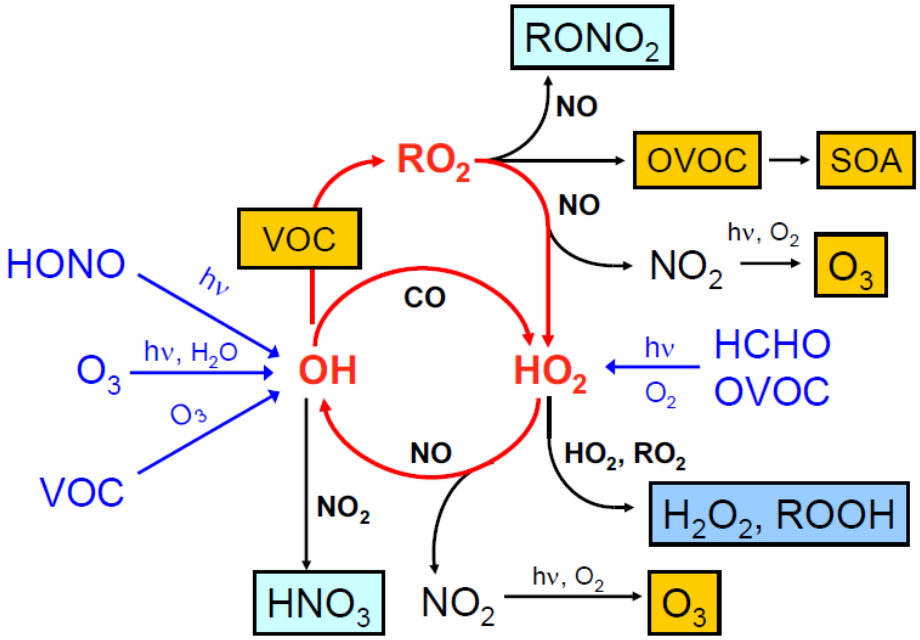

Figure 1.1 Schematic of the HO_x chemistry and the major pathways in the troposphere. The blue arrows represent the initiation of radical chemistry. Radical chain reactions are represented by the red arrows. The termination reactions include radical recombination reactions forming nitric acid (HNO_3), hydroperoxides (H_2O_2, ROOH) and organic nitrates ($RONO_2$). The reaction of RO_2 and HO_2 with NO leads to the photochemical production of ozone, OVOCs and SOA and secondary OH production. Figure taken from Lu et al. (2013).

The $O(^1D)$ formed, proceeds to react with water vapour to form OH (Finlayson-Pitts and Pitts Jr, 1999) (R1.8):

$$O(^1D) + H_2O \rightarrow 2OH \qquad \text{R1.8}$$

The importance of R1.8 decreases with increasing altitude due to decreasing water vapour concentration (Finlayson-Pitts and Pitts Jr, 1999). Only a small fraction (~10%) of $O(^1D)$ reacts with water to form OH (R1.8) at the surface, as collisional quenching by collisions with N_2 and O_2 to form $O(^3P)$ is favoured (Finlayson-Pitts and Pitts Jr, 1999). OH can also be formed from alkene ozonolysis and hydrogen peroxide (H_2O_2, R.10) photolysis; in polluted areas there are additional sources of OH from nitrous acid (HONO, R1.9) (Finlayson-Pitts and Pitts Jr, 1999). Also when the NO concentration becomes larger then HO_2 becomes a secondary source of OH (R1.11) (Stone et al., 2012):

$$\mathrm{HONO} + h\nu(\lambda < 400\ \mathrm{nm}) \rightarrow \mathrm{OH} + \mathrm{NO} \quad \text{R1.9}$$

$$\mathrm{H_2O_2} + h\nu(\lambda < 370\ \mathrm{nm}) \rightarrow 2\mathrm{OH} \quad \text{R1.10}$$

$$\mathrm{HO_2} + \mathrm{NO} \rightarrow \mathrm{OH} + \mathrm{NO_2} \quad \text{R1.11}$$

OH can be removed in the troposphere by the reaction with CH_4 and other volatile organic compounds (VOCs), to form peroxy radicals (RO_2, R1.12 – R.13) (Stone et al., 2012). The chemically activated RO_2 is stabilised from the reaction with M, which is usually N_2 or O_2, *via* collisional quenching (R1.13) (Stone et al., 2012). These RO_2 can either undergo a self-reaction (R1.14) or a cross-reaction, this eventually leads to the formation of formaldehyde and HO_2 (R1.15) (Stone et al., 2012).

$$\mathrm{OH} + \mathrm{RH} \rightarrow \mathrm{R} + \mathrm{H_2O} \quad \text{R1.12}$$

$$\mathrm{R} + \mathrm{O_2} + \mathrm{M} \rightarrow \mathrm{RO_2} + \mathrm{M} \quad \text{R1.13}$$

$$\mathrm{RO_2} + \mathrm{RO_2} \rightarrow \mathrm{RO} + \text{other products} \quad \text{R1.14}$$

$$\mathrm{RO} + \mathrm{O_2} \rightarrow \mathrm{HO_2} + \mathrm{HCHO} \quad \text{R1.15}$$

In environments with high NO concentrations, the following reactions become important (R1.11, R1.16 –R1.18), and form hydroperoxy radical (HO_2) and carbonyl species (R1.20) (Stone et al., 2012).

$$\mathrm{HO_2} + \mathrm{NO} \rightarrow \mathrm{OH} + \mathrm{NO_2} \quad \text{R1.11}$$

$$\mathrm{RO_2} + \mathrm{NO} \rightarrow \mathrm{RO} + \mathrm{NO_2} \quad \text{R1.16}$$

$$\mathrm{RO_2} + \mathrm{NO} + \mathrm{M} \rightarrow \mathrm{RNO_3} + \mathrm{M} \quad \text{R1.17}$$

$$\mathrm{RO_2} + \mathrm{NO_2} + \mathrm{M} \rightleftharpoons \mathrm{RO_2NO_2} + \mathrm{M} \quad \text{R1.18}$$

$$\mathrm{RCO_3} + \mathrm{NO_2} + \mathrm{M} \rightleftharpoons \mathrm{PAN} + \mathrm{M} \quad \text{R1.19}$$

$$\mathrm{RO} + \mathrm{O_2} \rightarrow \mathrm{R'CHO} + \mathrm{HO_2} \quad \text{R1.20}$$

$$\mathrm{NO_2} + \mathrm{hv} \xrightarrow{\mathrm{O_2}} \mathrm{O_3} + \mathrm{NO} \quad \text{R1.21}$$

HO_2 has a typical lifetime that ranges from 5 to 100 s and a concentration of $\sim 10^8$ molecule cm^{-3}. HO_2 can also be formed from the reaction of OH with CO and O_3 (R1.22 - R1.23) (Stone et al., 2012).

$$OH + CO + O_2 \rightarrow HO_2 + CO_2 + H_2O \quad \text{R1.22}$$

$$OH + O_3 \rightarrow HO_2 + O_2 \quad \text{R1.23}$$

HO_2 can also be formed from the photolysis of formaldehyde (HCHO, R1.24 - R1.27) (Stone et al., 2012).

$$HCHO + h\nu(\lambda < 361\ \text{nm}) \rightarrow H_2 + CO \quad \text{R1.24}$$

$$HCHO + h\nu(\lambda < 330\ \text{nm}) \rightarrow H + HCO \quad \text{R1.25}$$

$$H + O_2 + M \rightarrow HO_2 + M \quad \text{R1.26}$$

$$HCO + O_2 \rightarrow HO_2 + CO \quad \text{R1.27}$$

OH can be reformed from the reaction of HO_2 by reacting with O_3 (R1.28) and NO (R1.11) (Stone et al., 2012).

$$HO_2 + O_3 \rightarrow OH + 2O_2 \quad \text{R1.28}$$

HO_2 can be lost through termination with itself and peroxy radicals in low NO_x environments (R1.29 - R1.30) (Stone et al., 2012).

$$HO_2 + HO_2 \rightarrow H_2O_2 + O_2 \quad \text{R1.29}$$

$$HO_2 + RO_2 \rightarrow ROOH + O_2 \quad \text{R1.30}$$

Whilst both H_2O_2 and ROOH can photolyse to form OH, these species have a short lifetime in respect to deposition and so results in a net loss of radicals. Other important HO_x loss processes include uptake on aerosol surfaces, and the reaction of OH with SO_2 and NO_2 (Stone et al., 2012).

1.2.2 NO_3

Most of the OH sources are photolytic and this makes OH the major primary oxidant during daylight hours in the removal of trace gases in the troposphere. NO_3 can act as an oxidant during the night-time. NO_3 is formed by the reaction of NO_2 with O_3 (R1.31) (Stone et al., 2012). The NO_3 formed can react with NO_2 to form N_2O_5 in a reversible process (R1.32).

$$NO_2 + O_3 \rightarrow NO_3 + O_2 \quad \text{R1.31}$$

$$NO_3(g) + NO_2 + M \leftrightarrows N_2O_5 + M \quad \text{R1.32}$$

The dissociation of N_2O_5 is favoured at higher temperatures. Unlike OH, the hydrogen abstraction reactions of NO_3 with saturated hydrocarbons are relatively slow. However, the addition of NO_3 to unsaturated hydrocarbons is relatively fast, especially for a biogenic compound (e.g. isoprene). NO_3 can also react with aldehydes, dimethyl sulphide and phenolic compounds *via* a hydrogen abstraction. The typical NO_3 mixing ratio is 10 pptv at night (Brown and Stutz, 2012), although the NO_3 concentration is generally lower at ground level as it can be lost onto surfaces. NO_3 also reacts with NO to form NO_2, and the NO_3 concentration is very low during the day as it is lost through rapid photolysis (Brown and Stutz, 2012).

1.2.3. Cl Chemistry

Chlorine atoms are highly reactive and, especially in marine environments, may contribute significantly to the oxidation of VOCs. While the Cl atom concentration is generally very low (between ~10^3 – 10^4 molecule cm^{-3}) (Saiz-Lopez and von Glasow, 2012), Cl reactivity towards VOCs is much higher compared to OH. For example, the hydrogen abstraction of CH_4 is 14 times faster for Cl than OH and the overall CH_4 loss through Cl is 3 – 15% (Platt et al., 2004). In polluted air $ClNO_2$ may be formed when N_2O_5 reacts with chloride on aerosol particles:

$$N_2O_5(g) + Cl^-(aq) \rightarrow ClNO_2(g) + NO_3^- \quad \text{R1.33}$$

$ClNO_2$ accumulates overnight and then photolyses rapidly in the morning:

$$ClNO_2 + hv\ (\lambda < 400\ nm) \rightarrow Cl + NO_2 \quad \text{R1.34}$$

The photolysis of $ClNO_2$ in the morning represents the major course of Cl radicals in polluted environments (high NO_x) in both marine and continental regions (Thornton et al., 2010). Therefore, Cl chemistry can be important for the formation of peroxy radicals in the morning and contribute to the net formation of O_3.

1.2.4 Ozone

O_3 reacts with alkenes in a reaction termed ozonolysis, which can form Criegee biradicals. The rate of ozonolysis is usually an order of magnitude slower than OH radical oxidation, but at high O_3 concentrations these reactions can contribute to a significant loss of VOCs. An example is shown below of propene ozonolysis (R1.35a – R1.36c) (Beebe and Barnet, 1987).

$$O_3 + CH_2 = CHCH_3 \rightarrow CH_3CHOO + HCHO \quad \text{R1.35a}$$

$$\rightarrow CH_2OO + CH_3CHOO \quad \text{R1.35b}$$

$$CH_3CHOO \rightarrow CH_3 + CO + OH \quad \text{R1.36a}$$

$$\rightarrow CH_3 + CO_2 + H \quad \text{R1.36b}$$

$$\rightarrow CH_4 + CO_2 \quad \text{R1.36c}$$

CH_2OO and $CH_{3CH}OO$ are Criegee biradicals and are often denoted as C1 and C2 Criegee intermediates (CIs). Decomposition of the CI (Criegee Intermediates) are an important source for night-time HO_x as primary production of OH through photolytic routes are not available (as discussed above). OH production has been observed after IR (infrared radiation) excitation of CIs (Liu et al., 2014, Newland et al., 2015). Criegee Intermediates (CIs) can be collisionally stabilised (sCI) and these have been suggested as important oxidants for SO_2 (Mauldin et al., 2012, Novelli et al., 2015, Welz et al., 2012). The only net source of O_3 in the troposphere is through the reaction of peroxy radicals (RO_2/HO_2) with NO (R1.11 and R1.16) to form NO_2. NO_2 can be photolysed to form $O(^3P)$ which reacts with O_2 to form O_3 (R2.21). Furthermore, even though ozone is formed through photochemistry it is long-lived enough to be present during the night-time, hence it affects both day and night-time chemistry in the troposphere.

1.2.3 Secondary Organic Aerosol Production

SOA is formed from the low volatility products from the oxidation of VOCs (Lim and Ziemann, 2005). SOA formation is dominated mostly by monoterpenes and aromatic compounds that form low volatility organic compounds that can partition to the condensed phase (Kroll and Seinfeld, 2008a). VOCs can be oxidised in the gas phase with species such as OH, NO_3, Cl and O_3. A generic reaction mechanism is shown in Figure 1.2. The reaction of RO_2 and HO_2 with each other can lead to low volatility products and is predicted to be a major component of SOA (Kroll and Seinfeld, 2008a). At high NO_x either an organic nitrate formation dominates or an alkoxy radical can be formed *via* RO_2 + NO (dominant reaction). Hence under high NO_x conditions the reaction of alkoxy (RO) radicals are important (Kroll and Seinfeld, 2008a). The alkoxy radicals have three primary reactions available, shown in Figure 1.3 (Kroll and Seinfeld, 2008a), with the rates of these reactions strongly dependent on the structures. The rate of dissociation increases with increasing substitution on the centre where the radical is formed. Isomerisation only occurs when there is a hydrogen four carbons away from the

radical centre. Isomerisation rate increases with the substitution of the carbon where the hydrogen is abstracted.

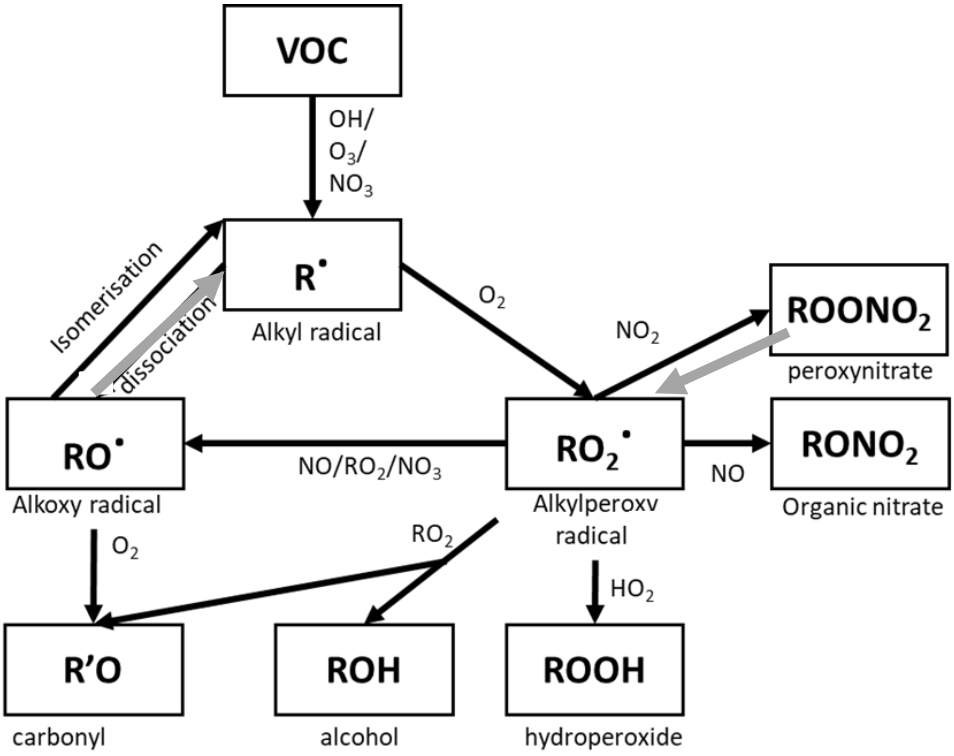

Figure 1.2 Simplified mechanism of the atmospheric oxidation of VOCs. The thick black arrows represent reactions that can lead to a significant decrease in volatility; grey arrows represent reactions that lead to an increase in volatility. Figure reproduced from (Kroll and Seinfeld, 2008).

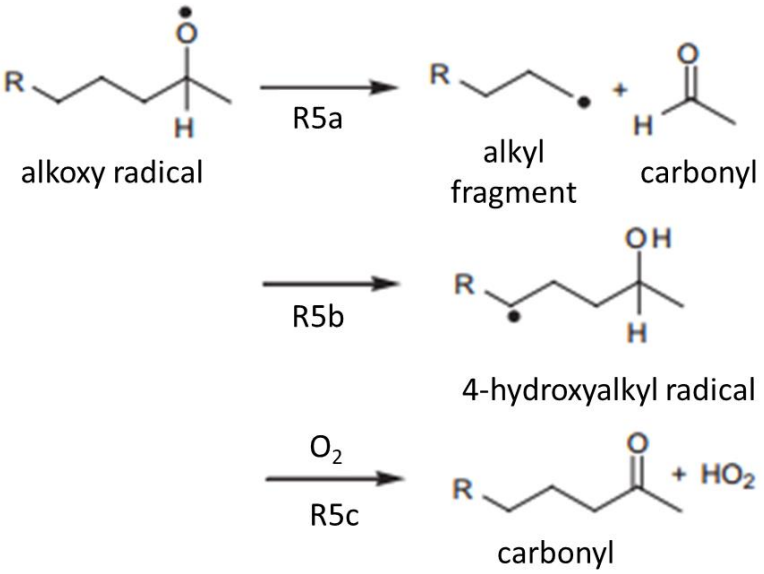

Figure 1.3 Reaction of alkoxy radicals: Dissociation (R5a), isomerization (R5b) and reaction with O_2 (R5c). Figure reproduced from (Kroll and Seinfeld, 2008).

1.2.4 Autoxidation of RO_2 species

Autoxidation is when an RO_2 radical can undergo an inter- or intramolecular H-abstraction, for unsaturated RO_2 radicals autoxidation can also proceed via endocyclization (Jokinen et al., 2014). Functionalised and complex RO_2 groups have weaker C-H bonds compared to pure hydrocarbons, making these molecules more prone to intramolecular H-abstraction.

The fate of the peroxy radicals formed is a competition between uni- and bimolecular reactions. The bimolecular reactions partners are NO, HO_2 and other RO_2 species, and since the concentration of the reaction partners can vary significantly the RO_2 lifetime is highly variable. For the unimolecular reactions to occur in this case, the H-shift represented by arrow A1 in Figure 1.4, it needs to be competitive with the bimolecular reaction (A3 and A4). The rate of the H-shift reactions depends on the strength of the C-H bond and the steric restraint for the RO_2 to reach the active site (Jokinen et al., 2014). Normally the optimum configuration for H-shifts is by the 1,6 or 1,5(Jokinen et al., 2014). The strength of the C-H bonds depends strongly on: branching; structure of the carbon backbone and types of adjacent functional groups.

Following the H-shift a carbon-centered radical is formed whose lifetime is very short, as the addition of O_2 takes place with a rate of ~2.5 x 10^7 s^{-1} (Jokinen et al., 2014) (A2 in Figure 1.4). The addition of O_2 to the $R^{\cdot}$ forms a new peroxy radical but this time with two added oxygens. The combination of route A1 and A2 in Figure 1.4 is what constitutes autoxidation and it can proceed multiple times, each time the molecule gets more oxidised, until the reaction is terminated via some other channel. There are some cases when unimolecular termination reactions can outcompete the O_2 addition. For example, if the radical formed was on a carbon with a hydroperoxide functional group a carbonyl would immediately be formed whilst releasing OH.

The alkoxy radicals can also undergo H-shifts (Jokinen et al., 2014) (A6 and A7) to form a new RO_2 that has one more oxygen than the previous RO_2 radical. This can take place by either: H-abstraction from a C-H bond (A6) followed by the addition of oxygen or by directly abstracting a H-atom from a hydroperoxide group (A7). Ultimately the termination reaction of A4, A5 and A8 will form closed-shell products that may be classified as HOMs if enough steps of autoxidation have occurred (Jokinen et al., 2014). The resulting HOM can either have a similar

composition to the precursor VOC with a higher degree of oxygenation, but organic nitrates ($RONO_2$) or dimer species (ROOR) can also be formed.

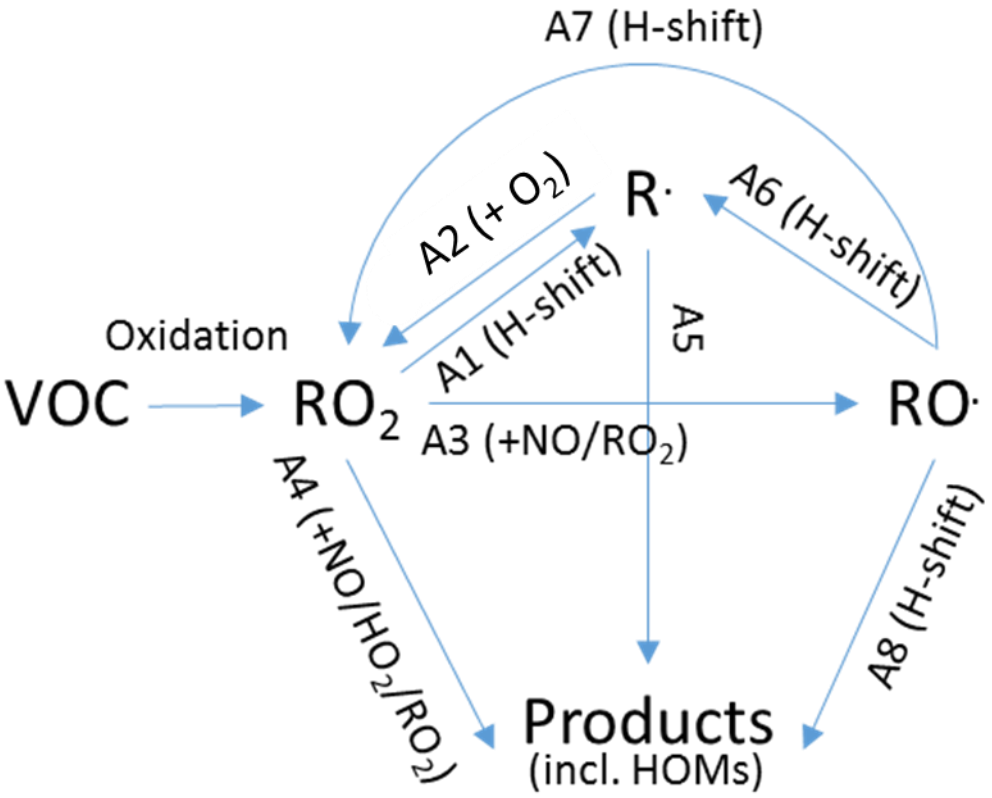

Figure 1.4 Schematic overview of typical radical reaction pathways forming HOMs, starting from an initial RO_2 from VOC oxidation (see the text for details).

1.2.5 HONO

HONO was first detected in the atmosphere in 1979 by Perner and Patt (Perner and Platt, 1979), who detected a concentration of ~0.8 ppbv just before sunrise in Juelich. HONO is a major source of OH in urban areas as it builds up overnight and photolyses in the morning (Ma et al., 2013). The main loss pathway for HONO is photolysis and reaction with OH. HONO can be produced overnight from the conversion of NO_2 on humid ground surfaces (Harrison et al., 1996). Compared to O_3, HONO photolyses at longer wavelengths, which means HONO is photolysed earlier than ozone at higher solar zenith angles (SZA) and can act as the dominant source of OH (Colussi et al., 2013, Jarvis et al., 2005). Also, HONO is damaging to human health as it causes damage to the lungs and mucous membranes (Jarvis et al., 2005).

During the daytime, the lifetime of HONO is ~10 minutes. The daytime concentration in urban and rural environments is between 100-330 pptv and 100 - 200 pptv (Leong et al., 2016), respectively. Observable concentrations of HONO during the day suggests there must be additional sources to counterbalance photolysis (Alicke et al., 2003). In urban environments, high concentrations of HONO have been observed during the day. Model simulations are often unable to predict these elevated concentrations (Lee et al., 2015a, Acker et al., 2006, Kleffmann, 2007, Li et al., 2012). In Lee et al. (2015a) the Master Chemical Mechanism (v3.2) was used to assess the different source of HONO. The base model only included the gas-phase source of HONO through the reaction of OH + NO. Additional heterogeneous sources were incorporated into the model (discussed below) and improved the measurement:model agreement.

There have been various studies for different sources for HONO involving both homogeneous and heterogeneous reactions. The well understood homogeneous source of HONO involves the reaction:

$$\mathrm{OH + NO + M \rightarrow HONO + M} \qquad \text{R1.37}$$

R1.37 is primarily a daytime source as the OH radical is generally generated through photolysis. The rate of R1.37 at 298 K is approximately 9.7 x 10^{-12} cm^3 $molecule^{-1}$ s^{-1} (1 bar, Stone et al., 2014). Also, there can be an additional source of HONO during the night-time in environments where OH can be generated through ozonolysis. HONO has also been found to be directly formed through several combustion processes and emitted by cars and power plants (Alicke et al., 2003).

Other than homogeneous reactions and direct emission sources of HONO there has been a larger focus on HONO production through heterogeneous reactions (surfaces and aerosol). R1.38 shows HONO produced from the reaction of NO_2 with water on different surfaces which, it has been suggested, is why during field campaigns a build-up of HONO is observed throughout the night (Alicke et al., 2003). In R1.380 HONO is released into the gas-phase, whilst the HNO_3 that is produced stays absorbed onto the surface.

$$\mathrm{2NO_2 + H_2O \xrightarrow{surface} HONO(g) + HNO_3(ads)} \qquad \text{R1.38}$$

Other sources of HONO have also been suggested that included the production from humic acid (Stemmler et al., 2006) and titanium dioxide particles (Dupart et al., 2014). Also, other studies have shown that snow (Michoud et al., 2015) and soot surfaces (Kalberer et al., 1999) enhance the production of HONO under illuminated conditions.

1.2.6 HO_2 Uptake

In many previous studies, models have overpredicted the HO_2 concentration compared to the observed concentration measured in campaigns. The overprediction of HO_2 has reached up to 95% and has been attributed to the heterogeneous uptake of HO_2 onto aerosols (Mao et al., 2013). The uptake of HO_2 is commonly measured by the reactive uptake coefficient ($\gamma(HO_2)$), which is defined as the fraction of HO_2 collisions with aerosol surfaces resulting in reactions (George et al., 2013). A summary of previous campaigns where $\gamma(HO_2)$ has been inferred from the comparison of measurements of HO_2 with modelled HO_2 is shown in Table 1.2. Table 1.2 shows that the estimated $\gamma(HO_2)$ for all the campaigns was between 0.5 – 1, with the majority campaigns using an uptake coefficient of 1 (1 being the maximum effect HO_2 uptake can have, rather than the experimentally determined value).

The global impact of heterogeneous loss of HO_2 onto aerosol has been assessed and shows that uptake can significantly reduce the tropospheric HO_2 concentration. In most global studies the value of $\gamma(HO_2) = 0.2$ has been used, as recommended by Jacob (2000). However, experimental work has shown that the value of HO_2 uptake coefficient varies widely depending upon the type of aerosol, Table 1.3 shows a summary for the experimental determination of HO_2 uptake onto different salt composition aerosols. Table 1.3 shows there is a large difference between dry and aqueous aerosol; with aqueous aerosol having a higher $\gamma(HO_2)$ value as HO_2 is soluble and is a weak acid. Also, very high $\gamma(HO_2)$ have been measured with aerosols containing transition metals ions like copper.

This work highlights that HO_2 uptake coefficients will vary in different areas depending on the type of aerosol composition. Recent work by Li et al. (2019) has suggested the upwards trend in O_3 observed in China is caused by a decrease in PM, which in turn is decreasing HO_2 uptake onto aerosols. Less HO_2 uptake will results in an increased HO_2 concentration in the gas-phase which will lead to an increase in net ozone formation from the oxidation of NO.

Location	Type	HO_2 Conc (pptv)[a]	Estimated γ(HO2)	Comments	Reference
Mauna Loa, Hawaii	Remote	15[b]	0.5 – 1		Cantrell et al. (1996)
Southern Ontario, Canada	Rural	10	~1	HO_x reduced by a factor of 2	McConnell et al. (1996)
Oki Island, Japan,	Remote	10	~1	To reduce HO_2 by 50%	Kanaya et al. (2000)
Remote marine boundary layer near Australia	Remote	5	1		Sommariva et al. (2004); Haggerstone et al. (2005)
Saharan dust plume	Plume	8	1	No H_2O_2 formed from HO_2 uptake. Also needs uptake for H_2O_2.	De Reus et al. (2005)
Mace Head, Ireland	Remote	15[b]	1		Sommariva et al. (2006)
Rishiri Island, Japan	Remote	6	1		Kanaya et al. (2007b)
Jungfraujoch research station[c]	Remote	6	1		Parker et al. (2009)
Arctic spring	Remote	5	~1		Mao et al. (2010); Olson et al. (2012)
Arctic summer	Remote	10	~1		Olson et al. (2012)

Table 1.2 Evidence for HO_2 uptake from the comparison of field measurement with modelled values. All uptake coefficients are inferred from photochemical modelling. [a] noon mean or median value. [b] estimated from the measured total peroxy radicals (HO2 + RO2).[c] estimated for the uptake on the snow surface. This table has been modified from Mao et al. (2013)

Salt Composition	Substrate type and phase	RH/%	$[HO_2]/cm^{-3}$	$\gamma(HO_2)$	Reference
$(NH_4)_2SO_4$	Dry aerosol	20	$\sim10^8$	0.04 ± 0.02	Taketani et al. (2008)
	Dry aerosol	45	$\sim10^8$	0.05 ± 0.02	Taketani et al. (2008)
	Dry aerosol	32 – 54	1.5×10^8 - 1.5×10^9	<0.004	George et al. (2013)
NaCl	Dry film	0	$4 \times 10^9 – 3 \times 10^{11}$	0.016	Remorov et al. (2002)
	Dry film	0	$4 \times 10^9 – 5 \times 10^{11}$	0.0117 ± 0.0008	Remorov et al. (2002)
	Dry film	28	$4 \times 10^9 – 5 \times 10^{11}$	0.0102 ± 0.0008	Remorov et al. (2002)
	Dry aerosol	20	$\sim10^8$	<0.01	Taketani et al. (2008)
	Dry aerosol	45	$\sim10^8$	0.02 ± 0.01	Taketani et al. (2008)
	Dry aerosol	0	5×10^{11}	0.0018	Loukhovitskaya et al. (2009)
	Dry aerosol	33 – 54	1.5×10^8 - 1.5×10^9	<0.004	George et al. (2013)
$(NH_4)_2SO_4$	Aqueous aerosol	42	5×10^{10}	~0.1	Thornton and Abbatt (2005)
	Aqueous aerosol	45	$\sim10^8$	0.11 ± 0.03	Taketani et al. (2008)
	Aqueous aerosol	55	$\sim10^8$	0.15 ± 0.03	Taketani et al. (2008)
	Aqueous aerosol	65	$\sim10^8$	0.17 ± 0.04	Taketani et al. (2008)
	Aqueous aerosol	75	$\sim10^8$	0.19 ± 0.04	Taketani et al. (2008)
	Aqueous aerosol	65 – 75	1.5×10^8 - 1.5×10^9	0.01 ± 0.01	George et al. (2013)
	Aqueous aerosol	55	1.5×10^8 - 1.5×10^9	0.003 ± 0.005	George et al. (2013)
NaCl	Aqueous aerosol	53	$\sim10^8$	0.11 ± 0.03	Taketani et al. (2008)
	Aqueous aerosol	63	$\sim10^8$	0.09 ± 0.02	Taketani et al. (2008)
	Aqueous aerosol	75	$\sim10^8$	0.10 ± 0.02	Taketani et al. (2008)
	Aqueous aerosol	54	1.5×10^8 - 1.5×10^9	0.016 ± 0.008	George et al. (2013)
	Aqueous aerosol	67 - 76	1.5×10^8 - 1.5×10^9	0.01 ± 0.02	George et al. (2013)
Cu(II)-doped $(NH_4)_2SO_2$	Aqueous aerosol	42	5×10^{10}	0.5 ± 0.1	Thornton and Abbatt (2005)
	Aqueous aerosol	45	$\sim10^8$	0.53 ± 0.13	Taketani et al. (2008)
Cu(II)-doped NaCl	Aqueous aerosol	53	$\sim10^8$	0.65 ± 0.17	Taketani et al. (2008)
Cu(II)-doped NH_4HSO_4	Aqueous aerosol	75	$10^8 – 10^9$	0.40 ± 0.08	Mozurkewich et al. (1987)
	Aqueous aerosol	53 – 65	1.5×10^8 - 1.5×10^9	0.4 ± 0.3	George et al. (2013)
TiO_2	Dry aerosol	11	1.6×10^9	0.021 ± 0.001	Moon et al. (2018)
	Dry aerosol	66	1.6×10^9	0.036 ± 0.007	Moon et al. (2018)

Table 1.3 Uptake coefficients for HO_2 onto inorganic salts from previous studies. This table has been updated from George et al. (2013).

1.3 Air Pollution in China

China has one of the fastest expanding economies and industrial developments in the world, which has rapidly grown its urban area population to form many megacities (Chan and Yao, 2008). The rapid expansion has caused an increase in industrial areas and energy consumption (Zhang et al., 2007) thus an increase in the emission of air pollutants (Chan and Yao, 2008). Beijing, Shanghai, Pearl River Delta (PRD), Shenzhen and Hong Kong are the most densely populated areas in China, with of changes from 19.6 to 40.5% of the Chinese population living in urban areas from the years 1980 to 2005 (Chan and Yao, 2008). The population in Beijing increased by 250% between 1989 to 2012 (Li et al., 2017). Figure 1.5 shows a map of China. Beijing is the capital city of China and is located on the northwest border of the Great North China Plain and is surrounded by the Yanshan Mountains in the west, north and northeast (Chan and Yao, 2008).

Figure 1.5 Map of China and the locations of the major megacities, including a larger diagram of the Pearl River Delta region. Figure copied from Chen et al (2007).

1.3.1 Annual Variation

Figure 1.6 shows the annual variation of $PM_{2.5}$, PM_{10}, O_3, SO_2, NO_2 and CO in Beijing between May 2014 to April 2015. The PM concentration is lowest during May, June and August with less than 100 µg/m^3 and 130 µg/m^3 for PM_{10} and $PM_{2.5}$, respectively (Chen et al., 2015). PM concentration increases sharply from October to February, this correlates with heating time in Beijing, most of which comes from coal. SO_2 follows a similar trend as PM; highest in winter and lowest in summer (Chen et al., 2015). The SO_2 trend also correlates to the heating period in Beijing. O_3 is highest during summertime with the highest daily maxima between June and August, with minimum concentration during the winter. NO_2 follows the same trend as PM and SO_2, although not as noticeably (Chen et al., 2015). In the summer NO_2 is higher at the traffic sampling station compared to the suburban, urban and background stations. Although in summer all the stations are comparable, this could indicate a different source of NO_2 in summer and winter. CO concentrations are much higher in the winter compared to the summer (Chen et al., 2015).

$PM_{2.5}$, SO_2, NO_2 and CO concentrations increase in Beijing with southwest, northwest and easterly winds with a wind speed less than 3 m s^{-1}, and very slow wind speeds (2 m s^{-1}) are associated with very high concentrations of $PM_{2.5}$ and NO_2. PM_{10} generally comes from high speed northwest winds, and high concentrations of ozone from southerly wind. In general, the northwest winds have a positive impact on air pollutants concentration, except PM_{10}, while southwest and easterly winds increase the concentration of pollutants.

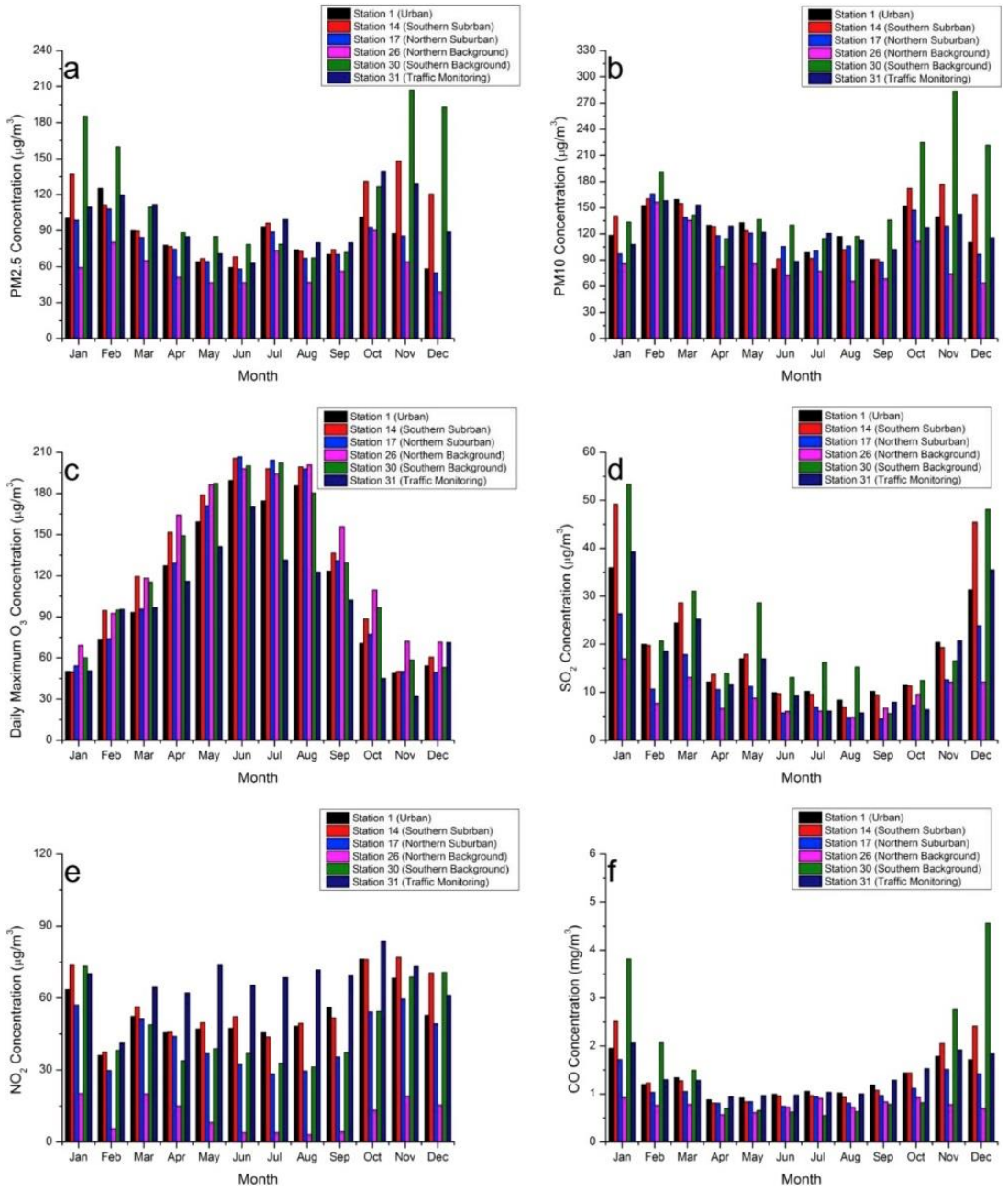

Figure 1.6 Monthly variation of a) $PM_{2.5}$, b) PM_{10}, c) O_3, d) SO_2, e) NO_2 and f) CO between May 2014 to April 2015. Figure copied from Chen et al. (2015).

1.3.2 Pollutant changes over time in Beijing

1.3.2.1 Ozone

Ground ozone has become a major airborne pollutant and the frequency of ozone pollution episodes has increased rapidly in China (Chen et al., 2019). The ozone trend in Beijing from 2006 to 2016 is shown in Figure 1.7 and shows that the O_3 concentration is on the rise. It shows that the levels of O_3 is in the order summer>spring>auntumn>winter. The influence of meteorological factors was assessed by Chen et al. (2019) for each season, with meteorological factors

influencing ozone production being the strongest in spring and autumn. The main factor contributing to ozone production was the temperature, except in winter when wind and humidity was key. The rise in O_3 in China, whilst other pollutants (PM, SO_2 NO and NO_2) have been decreasing, has been suggested to be from the increase in HO_2; the HO_2 concentration is suggested to be increasing due to the decrease in PM which is, in turn, is decreasing the loss of HO_2 onto aerosols (Li et al., 2019).

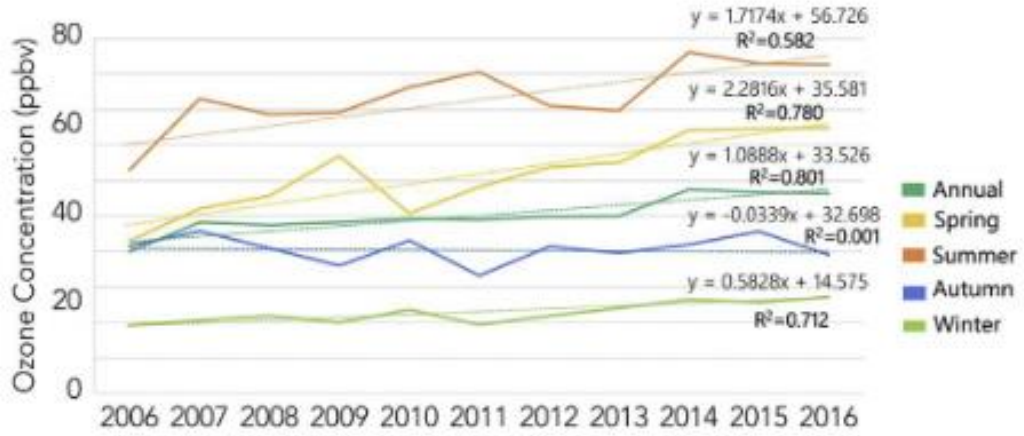

Figure 1.7 Inter-annual and seasonal variations of ozone concentrations in Beijing during 2006 – 2016. The figure has been taken from Chen et al. (2019).

1.3.2.2 PM, NO_2 and SO_2

The inter-annual trend of PM, NO_2 and SO_2 is shown in Figure 1.8. The annual average concentration of PM_{10} in Beijing has steadily decreased from 188 μg m^{-3} in 1998 to 108 μg m^{-3}, although the values are still higher than the limit value of 70 μg m^{-3} of China's AAQS (Ambient Air Quality Standards) for PM_{10} (Zhang et al., 2016). Also, the ratio of $PM_{2.5}/PM_{10}$ has increased from 0.61 in 2008 to 0.82 in 2013 which indicates the particulate pollution is mainly from $PM_{2.5}$ in Beijing. The SO_2 and NO_2 concentration in Beijing dropped from 121 μg m^{-3} in 1998 to 27 μg m^{-3} in 2013 and from 74 μg m^{-3} in 1998 to 56 μg m^{-3} in 2013, respectively. In 2013 the SO_2 concentration was much lower than the guideline value of 60 μg m^{-3} of China's AAQS Grade-II (urban and industrial areas) and only slightly higher than 20 μg m^{-3} for Grade-1 (not urban and industrial areas) standard, which indicates the SO_2 emission control has been successful (Zhao et al., 2013). NO_2 concentration has not shown a large decrease from 1998 to 2013, and there has been no noticeable decrease from 2008 (Zhang et al., 2016). It has been

suggested that no reduction in NO_2 has been observed from 2008 as the reduction in coal-burning has been counteracted by the increase in vehicle emissions (Zhang et al., 2016).

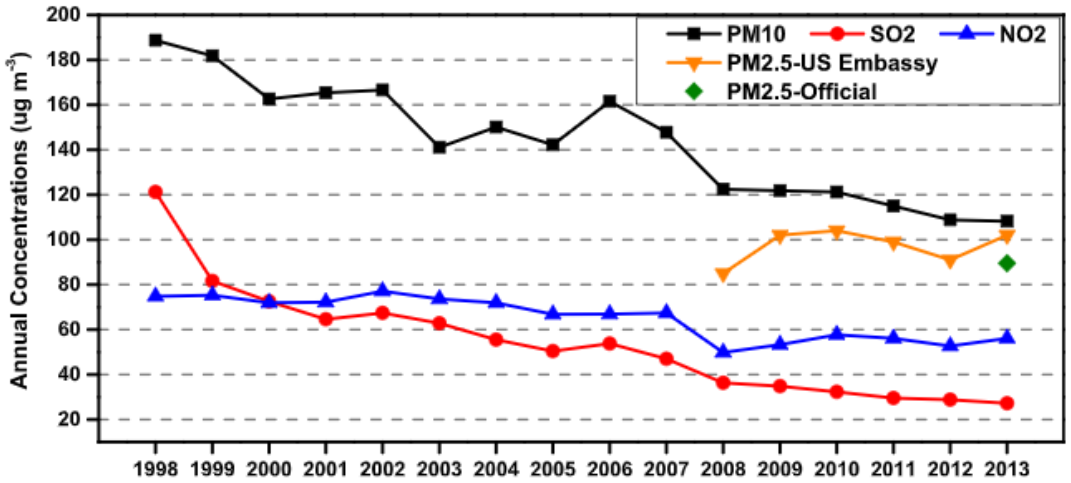

Figure 1.8 Trend of PM_{10}, $PM_{2.5}$, SO_2 and NO_2 in Beijing. PM_{10}, SO_2 and NO_2 data presented from 1998 to 2013; whilst $PM_{2.5}$ is presented from 2008 to 2013. , $PM_{2.5}$ SO_2 and NO_2 are from Beijing Municipal Environmental Protection Bureau (http://www.bjepb.gov.cn/). $PM_{2.5}$-U S Embassy is from the Embassy of the United States (http://beijing.usembassy-china.org.cn/070109 air.html). This figure has been taken from Zhang et al. (2016).

1.3.3 SOA Formation in Beijing

The WRF-CHEM model was coupled with a secondary organic aerosol model (SORGAM) to investigate the spatial and temporal characteristics of SOA and the contribution from anthropogenic and biogenic sources in the formation of SOA over China in 2006 (Jiang et al., 2012). In a previous study, SOA was found to contribute 30-77% and 44-71% of $PM_{2.5}$ and organic aerosol, respectively, across Beijing, Shanghai, Guangzhou and Xi'an (Huang et al., 2014). The high SOA concentrations are in central China during the summer (8 μg m^{-3}), but in winter this moves down to the Pearl River Delta region with a concentration of 2 μg m^{-3} (Jiang et al., 2012). Across the whole country average ground level SOA concentrations was 0.94, 2.54, 1.41, 0.43, and 1.34 μg m^{-3} in spring, summer, autumn, winter, and year, respectively (Figure 1.9) (Jiang et al., 2012). SOA concentrations are dominated by biogenic emissions in the summer and most regions anthropogenic sources dominated during winter. Across China, anthropogenic sources contribute 35% to total SOA, with 41%, 26%, 39%, and

59% in spring, summer, autumn and winter, respectively. SOA formation from isoprene oxidation accounts for 29% of total SOA in 2006. The estimated annual production of SOA is 3.05 Tg yr^{-1} in China which accounts for 4-25% of the global SOA formation (Jiang et al., 2012). SOA formation was described further in section.1.2.3.

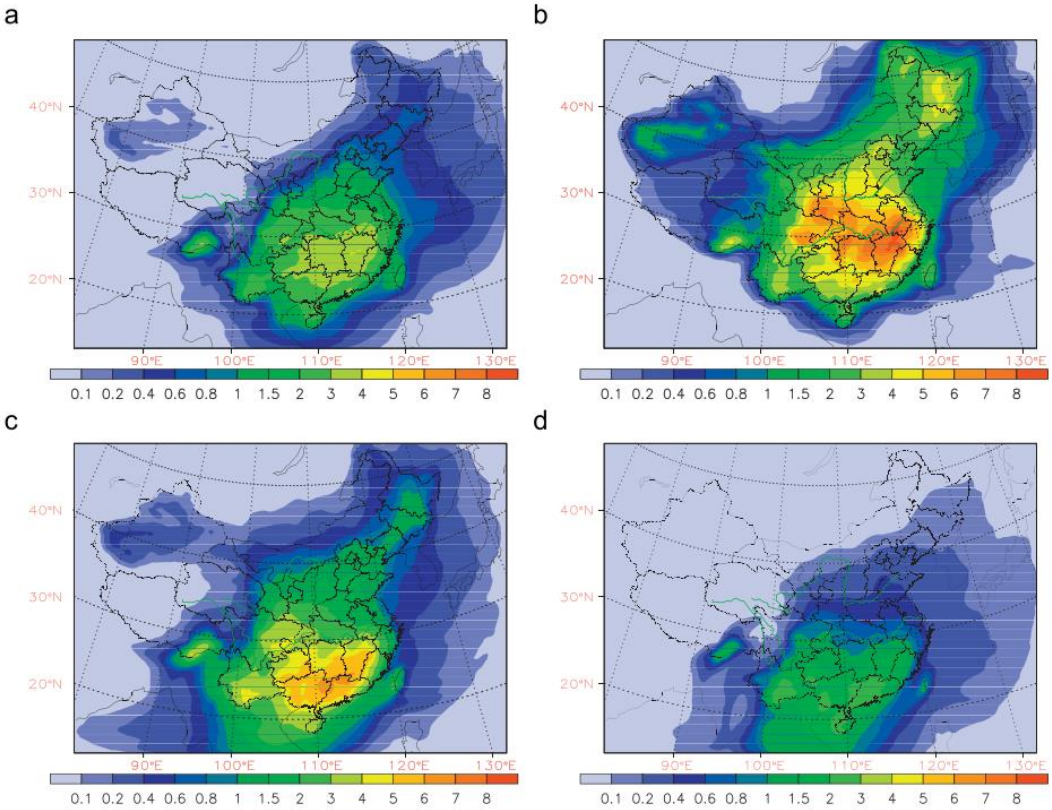

Figure 1.9 The seasonal mean surface concentration of SOA (μg m^{-3}) a) spring, b)summer, c) autumn and d) winter. Figure copied from Jiang et al. (2015).

The high SOA in the summer is related to strong solar radiation and high air temperature which leads to high BVOCs (biogenic volatile organic compounds) emission and intensive photochemical reactions which favour SOA formation (Jiang et al., 2012). Even though south China has larger biogenic emissions and stronger solar radiation than Central China, the level of SOA is lower, due to transport of clean marine air which suppresses air pollution formation (Jiang et al., 2012).

The comparison of anthropogenic sources (ASOA) and total SOA (Figure 1.10) shows that the North China Plain has a high anthropogenic contribution (>60%), and in the west and southern China ASOA contributes less than 40% and biogenic emissions are the dominant source of SOA (Jiang et al., 2012). There is

a large difference between summer and winter with most areas, other than the North China Plain, showing less than a 30% contribution from ASOA (Jiang et al., 2012).

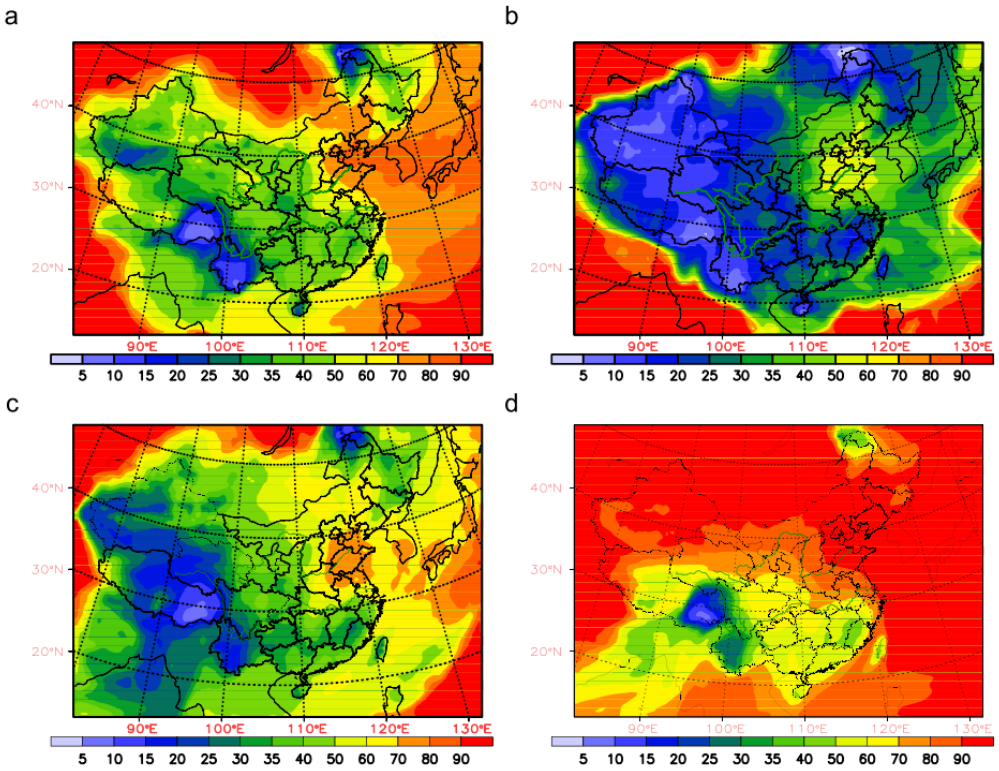

Figure 1.10 Seasonal mean percentage contribution from ASOA to total SOA a) spring, b) summer, c) autumn and d) winter. Figure copied from Jiang et al. (2015).

1.3.4 Haze Dependence on Meteorological Conditions and Emissions

The WRF-CHEM model was applied to simulate haze event conditions that occurred in January 2010 in the North China Plain (NCP) (Gao et al., 2016a). The haze event was caused by high emission of air pollutants and anticyclonic weather conditions. Air pollutants transported from outside of Beijing contributed to 64.5% of the $PM_{2.5}$ level in Beijing, the aerosol was mainly transported from south Hebei, Tianjin, Shandong and Henan provinces. The aerosol feedback affects the RH and wind speeds, which can affect the aerosol formation (Gao et al., 2016a).

Another haze event occurred in Beijing with $PM_{2.5}$ concentrations peaking at 450 μg m^{-3} (He et al., 2015) on 18th January 2013 and rapidly decreased on January 19 2013 to 100 μg m^{-3} (He et al., 2015). The variability gave a good

opportunity to study the causes of haze formation. *In-situ* measurements (surface meteorological data and vertical structures of the winds, temperature, humidity, and planetary boundary layer (PBL) and use of the WRF-CHEM model were used to analyse the strong variability in $PM_{2.5}$ concentrations (He et al., 2015).

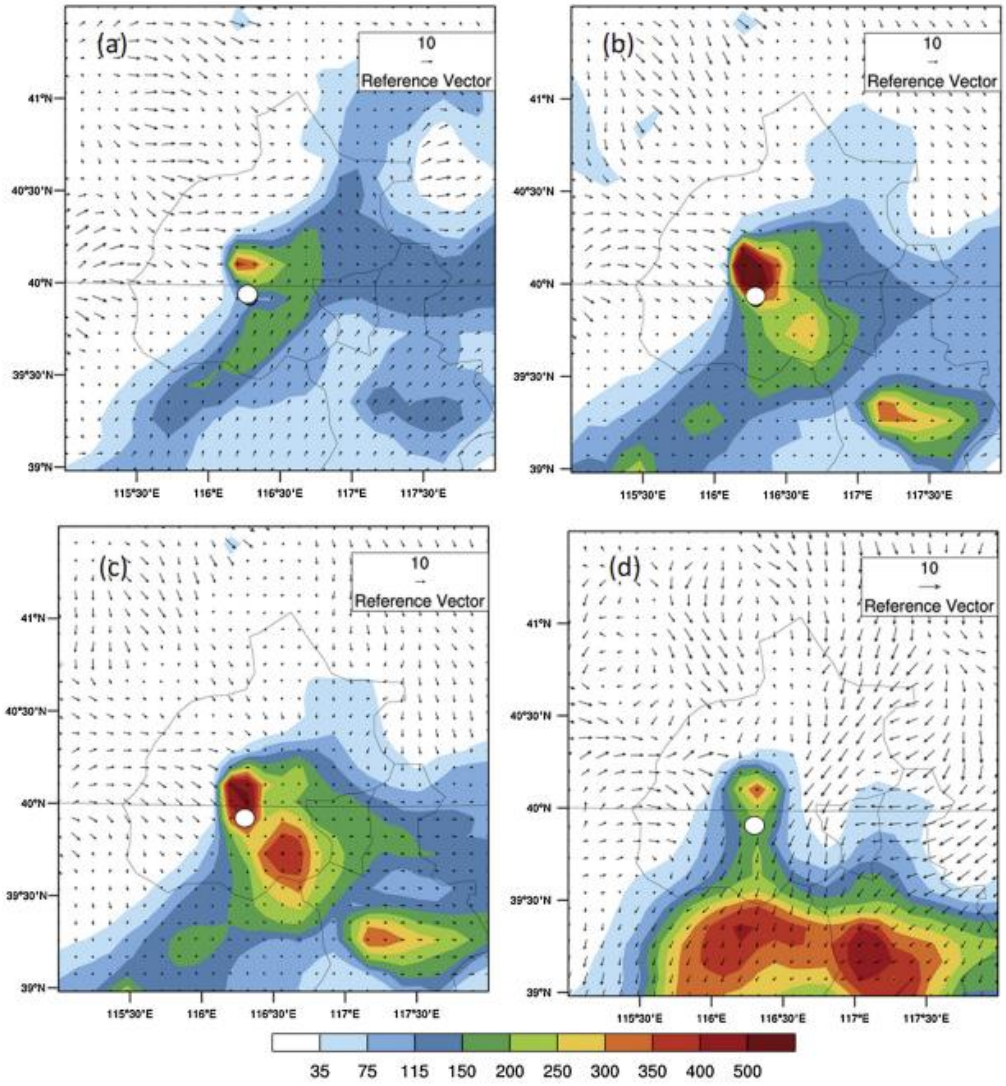

Figure 1.11 Calculated $PM_{2.5}$ surface concentration (μg m^{-3}) and wind at a) 06:00, b) 18:00, c) 20:00 on 18th of January and d) on 19th of January 2013. Figure copied from He et al.(2015).

The effect on horizontal transport was studied and the regional $PM_{2.5}$ concentration distribution in the Beijing region was calculated. Figure 1.11 shows the results of the model, which showed that at 06:00 on 18th of January the wind was from the southwest with speeds of 4 m s^{-1} (He et al., 2015). This resulted in dispersed air pollution. At 18:00 on January the wind speed calmed (1 m s^{-1}) and the pollution accumulated near the large emission areas, the winds were continuously calm leading to the build-up of pollution and the measurement of

450 μg m^{-3} of $PM_{2.5}$ (He et al., 2015). The wind speed increased to 3 m s^{-1} and transported from the pollution from Beijing to the southern part of the city. These results suggest that regional transport plays an important role in haze events as the highest $PM_{2.5}$ concentration was when northwestern winds dominated (He et al., 2015).

An experiment was performed to determine the contribution from regional and local emissions for January 18 at 20:00 when the $PM_{2.5}$ concentration was at a peak value (450 μg m^{-3}) (He et al., 2015). It was shown that without local emission, the calculated $PM_{2.5}$ concentration would be 100 μg m^{-3}, and that local emissions contributed to 350 μg m^{-3}. This suggests that local emissions (78%) dominated the contribution to the heavy haze, and regional emissions only contributed about 22% (He et al., 2015).

These two haze events discussed here show that there is a large variability between whether the haze is formed from regional (January 2010) or from local emissions (January 2013).

1.4 Methods for detection of HO_x and RO_x

1.4.1 Chemical Ionisation Mass Spectrometry (CIMS)

CIMS detects OH by first converting it into H_2SO_4 (R1.39 - R1.41) followed by conversion into $H_2SO_4^-$ by the reaction with NO_3^- ions, which can then be detected via mass spectrometry (Stone et al., 2012). The instrument injects $^{34}SO_2$ (isotopically labelled) into a flow tube which initiates the conversion, $^{34}SO_2$ is used to distinguish from ambient H_2SO_4.

$$OH + {}^{34}SO_2 + M \rightarrow H{}^{34}SO_3 + M \quad \text{R1.39}$$

$$H{}^{34}SO_3 + O_2 \rightarrow {}^{34}SO_3 + HO_2 \quad \text{R1.40}$$

$$^{34}SO_3 + H_2O + M \rightarrow H_2{}^{34}SO_4 \quad \text{R1.41}$$

Little sensitivity is lost in the conversion stage of this instrument as conversion occurs on a time scale of 10-20 ms, which is small compared to the 0.1-1 s lifetime of OH (Stone et al., 2012). Twice as much $^{34}SO_2$ is injected as required and this leads to a 99% conversion of OH to H_2SO_4. An OH scavenger propane is used further downstream to remove any OH generated within the flow tube from the

reaction of HO_2 or RO_2 with NO and O_3. Conversion into ions is achieved by adding $NO_3.HNO_3$ (R1.42) (Stone et al., 2012):

$$NO_3^- \cdot HNO_3 + H_2^{34}SO_4 \rightarrow H^{34}SO_4^- \cdot HNO_3 + HNO_3 \qquad \text{R1.42}$$

The $H^{34}SO_4^- \cdot HNO_3$ is moved out of the sampling stream and into an N_2 flow, and then into a collisional dissociation chamber where the fragments form HNO_3 and $H_2^{34}SO_4$ (Stone et al., 2012). The ratio between the NO_3^- (initial reactant ion) and $H_2^{34}SO_4$ (derived from OH), allowing for the OH concentration to be calculated. Propane can be injected at the same time as $^{34}SO_2$ to remove 98% of the sample OH, which allows for the background OH to be measured, this is like the IPI method described later (Stone et al., 2012).

CIMS has a detection limit of (1 - 4 x 10^5 molecule cm^{-3}, 5 - 10 minutes) (Stone et al., 2012). CIMS can also be used to measure HO_2 radicals by adding NO into the SO_2 injection stream and converting HO_2 into OH. The peroxy radical CIMS (PerCIMS) leads to the recycling of HO_2 in the system so amplification of SO_3 occurs (Stone et al., 2012). The ratio of SO_2/NO at the injection, and the parameters of the experiments allows for the HO_2 concentration to be determined. The use of different buffer gases ratio (N_2/O_2) allows for the measurement of $HO_2 + RO_2$ or just HO_2. At low levels of O_2, the conversion of RO into HO_2 is not favoured except for those derived from alkenes, on the other hand, high levels of O_2 total peroxy concentrations can be measured (Stone et al., 2012). PerCIMS has a lower detection level than OH (1 - 4 x 10^7 molecule cm^{-3}, 15 seconds), but the more abundant peroxy radicals do not require such high sensitivity as OH (Stone et al., 2012).

1.4.2 Differential Optical Absorption Spectroscopy (DOAS)

The DOAS techniques uses the Beer-Lambert law. By using 308 nm light to excite the $A^2\Sigma^+ (v'=0) \leftarrow X^2\Pi (v''=0)$ transition (the same used for FAGE) the OH radical concentration can be calculated using the transmittance (E1.1 - E1.2) (Heard and Pilling, 2003):

$$I = I_0 \exp(-\sigma_{OH}[OH]\,l) \qquad \text{E1.1}$$

$$[OH] = \ln(I_0/I) \,/\, (\sigma_{OH}\,l) \qquad \text{E1.2}$$

where I_0 and I are the intensity of light before and after absorption respectively, σ_{OH} is the absorption cross-section at 308 nm and l is the path length (Heard and

Pilling, 2003). The rovibrational transition lines for OH are very narrow, and lasers must be used to achieve the high intensity required over a narrow line. Also, a longer path length allows for a lower detection limit, but to be used in ambient conditions a path length of 1 km is required to reach high enough sensitivity (~1 x 10^6 molecule cm^{-3}) (Heard and Pilling, 2003). The long path length required is now achieved using a multipass setup, which uses two mirrors to reflect light back and forth over short distances (Heard and Pilling, 2003). The multipass system is better than the use of a single pass system where the light is reflected off mirrors kilometres away (the single-pass systems suffers from averaging of the airmass being sampled where the concentration of OH is variable across the airmass). The multipass does not suffer from this, but maintains the sensitivity (Heard and Pilling, 2003).

DOAS also suffers from a much more complex data analysis compared to FAGE, as species other than OH absorb at 308 nm (Heard and Pilling, 2003). This means these species must be subtracted from the differential spectrum, the largest interference comes from trace gases (e.g. SO_2 and HCHO). Also, signal from unknown species must be accounted for which leads to an uncertainty in the measurements. This makes DOAS less sensitive (1-4 x 10^6 molecules cm^{-3}, 3-6 minutes) than FAGE and CIMS. DOAS is also difficult to transport because of the complex laser system and optical setup (Heard and Pilling, 2003). DOAS now is just used in the SAPHIR (Simulation of Atmospheric PHotochemistry In a large Reaction Chamber) chamber at Juelich and retired from the field.

1.4.3 Fluorescence Assay by Gas Expansion (FAGE)

FAGE was pioneered by Hard and O'Brien in 1979, and has overcome the O_3 interference suffered by earlier LIF measurements, and is one of the most common instruments in the measurement of HO_x radicals.

In FAGE, ambient air is expanded through a pinhole (~1 mm diameter) into a cell that is operated at low pressure (0.7-4 Torr) to reduce the water vapour and to allow temporal gating of the laser scattered light (Heard and Pilling, 2003). Earlier instruments of FAGE used 282 nm light to excite the (v' = 1) ← (v'' = 0) transition, however, this experienced significant interference from the generation of OH from the photolysis of ozone (R1.43) (Heard and Pilling, 2003).

$$O_3 + h\nu(282\ \mathrm{nm}) \rightarrow O(^1D) + O_2 \qquad \text{R1.43}$$

$$O(^1D) + H_2O \rightarrow OH + OH$$ R1.44

All current FAGE setups now use 308 nm light to excite the (v' = 0) ← (v'' = 0) transition, with fluorescence also collected at 308 nm (on-resonance fluorescence). The use of 308 nm compared to 282 nm means the O_3 interference is reduced by a factor of ~30, this is due to a combination of the lower O_3 absorption cross-section and lower quantum yield of $O(^1D)$ at this wavelength (Heard and Pilling, 2003). Using the transition at 308 nm also increases the sensitivity as the OH absorption cross-section is ~6 times higher than at 282 nm (Heard and Pilling, 2003). The sensitivity of FAGE is 2 - 5 x 10^5 (1-5 minutes) and 1-4 x 10^6 (30 seconds - 5 minutes) for OH and HO_2 respectively.

In all current FAGE instruments the laser pulse is short (~30 – 40 ns) to allow distinction between OH fluorescence and the laser pulse (Heard and Pilling, 2003). The solar light is minimised *via* the sampling nozzle, and the low pressures reduce the Rayleigh scattering. The rate of collisional quenching of OH the $(A^2\ \Sigma^+)$ excited state is decreased because of the decrease in the number density of air, extending the fluorescence lifetime (Heard and Pilling, 2003). This extends the fluorescence lifetime to several hundred nanoseconds, and longer than the laser pulse. The OH fluorescence and scattered light are measured by a gated photon counter during a 500 ns integration period (Gate A), commencing 50 ns after the end of the laser pulse (Whalley et al., 2010) A small amount of the laser and solar scattered light, along with detector dark counts, constitutes a background signal to the OH fluorescence in gate A (Whalley et al., 2010). The contribution to the fluorescence made by solar is determined by a second photon counting gate (Gate B), which is delayed by ~50 μs to allow the laser pulse and OH fluorescence to subside (Whalley et al., 2010). The laser scatter in the signal (background) is measured by tuning the wavelength on and off, the off-line signal gives the background.

HO_2 is measured indirectly by conversion to OH using NO, and detection is performed using the method stated above (R1.45). (Heard and Pilling, 2003).

$$HO_2 + NO \rightarrow OH + NO_2$$ R1.45

1.4.3.1 Calibration

In principle, if detailed instrumental parameters were known it is possible to calculate the instrument response to [HO_x] (Holland et al., 1995), but in practice,

this is quite difficult. Instead, FAGE instruments are calibrated by adding a known concentration of OH and HO_2 into the inlet (Stevens et al., 1994). The signal that is observed is proportional to the radical concentration:

$$S_{HO_x} = C_{HO_x} \text{ x } [HO_x] \quad \text{E1.3}$$

where C_{HOx} represents the calibration factor for either OH or HO_2. The most common form of calibration uses the photolysis of water vapour in a flow of humidified zero air that is delivered to the inlet. A 184.9 nm mercury lamp is used to general equal concentrations of OH and HO_2 (concentration produced between ~10^6 – 10^9 molecule cm^{-3}):

$$H_2O + h\nu\ (\lambda=184.9\text{ nm}) \rightarrow H + OH \quad \text{R1.46}$$

$$H + O_2 + M \rightarrow HO_2 + M \quad \text{R1.47}$$

The concentration of OH and HO_2 can be calculated by:

$$[OH] = [HO_2] = [H_2O]\ \sigma_{H_2O,184.9nm}\ \phi_{OH}\ F_{184.9\,nm}\ t \quad \text{E1.4}$$

where $\sigma_{H_2O,184.9nm}$ = 7.14 x 10^{-20} cm^2 $molecule^{-1}$, φ_{OH} = 1 and $[H_2O]$ is measured during the calibration (stated above). The product $F_{184.9}$ *t* is determined by chemical actinometry which relies on either the photolysis of O_2 (laminar flow method) to produce O_3 (Aschmutat et al., 1994) or N_2O (turbulent flow method) to produce NO (Faloona et al., 2004), the O_3 and NO can then be measured. The uncertainty in FAGE measurements largely stems from the accuracy of the product of the flux and photolysis time measurements (~15 - 50%) deriving from chemical actinometry (Heard and Pilling, 2003).

1.4.2.2 Interferences

1.4.2.2.1 OH Interferences

As discussed earlier significant interference from O_3 photolysis was observed in a FAGE instrument using 282 nm for detection; whilst the effect has been reduced changing to detection at 308 nm but may still be significant. For the 308 nm FAGE set-up Griffith et al. (2016) measured an interference up to ~4 x 10^6 molecule cm^{-3}. For the Penn State, instrument laboratory experiments showed negligible interference in the OH detection range from H_2O_2, HONO, HCHO, HNO_3, acetone and various RO_2 radical species (Ren et al., 2004).

Measurements of OH and HO_2 radicals are sometimes higher than those predicted by the models for instruments measuring in certain environments,

especially those affected by high levels of biogenic emissions such as isoprene (Lelieveld et al., 2008, Whalley et al., 2011, Wolfe et al., 2011). The traditional background method ("OHwave") where the laser wavelength is scanned to off resonance does not discriminate between ambient OH and OH generated within the cell (interference). However, an alternative chemical method for determining the background is called OHchem, where a chemical scavenger for OH (C_3F_6 and propane) is injected into the ambient OH stream. The scavenger removes the ambient OH so anything detected within this period must be an interference generated within the cells.

The chemical background method has been used in several previous campaigns. The PROPHET (Programme for Research on Oxidants: Photochemistry, Emissions and Transport) campaign measured high night-time OH concentrations of ~ 1 x10^6 molecule cm^{-3}. One night during the PROPHET campaign the scavenger C_3F_6 was injected upstream of the OH detection axis for ~1 h, during this period the average OH concentration measured was ~1.1 x 10^5 molecule cm^{-3} (effectively zero) suggesting the high night-time OH measured was due to an interfering species.

During the BEARPEX-09 (Biosphere Effects on Aerosols and Photochemistry Experiment II) the Penn State FAGE instrument took measurements using a scavenger system (Mao et al., 2012). The comparison between OHwave and OHchem showed that only 40-60% of the OH signal was real. Mao et al. (2012) also concluded that the interference was not laser generated as the OH signal scaled linearly with the laser power suggesting it is a one-photon process. Also, the difference between OHwave and OHchem correlated well with temperature (R^2 = 0.94), suggesting the interference was related to BVOC oxidation.

A scavenger system was used in the SHARP (Study of Houston Atmospheric Radical Precursors) campaign (Ren et al., 2013). The results showed that ~30% (~ 2 x 10^6 molecule cm^{-3}) of the daytime signal and ~50% (~6 x 10^5 molecule cm^{-3}) of the night-time signal was from an interference. The Penn State scavenger system was also used during the SOAS (Southern Oxidant and Aerosol Study) that took place in a forest in Alabama (Feiner et al., 2016). During the day 75% (~ 3 x 10^6 molecule cm^{-3}) of the signal was from an interference; whilst at night the ~5 x 10^5 molecule cm^{-3} was measured through OHwave whilst OHchem measurement was below the LOD for the instrument

(2 – 3 x 10^5 molecule cm^{-3}). During the SOAS campaign, the background signal observed to decrease with increasing NO. The background and OHchem signal also increased linearly with isoprene.

The MPIC (Max Planck Institute for Chemistry) FAGE instrument (HORUS, HydrOxyl Radical measurement Unit based on fluorescence Spectroscopy) has been equipped with an “Inlet Pre-Injector” (IPI) system. The instrument made OH measurements in three separate field campaigns: measurements in a forested region of Finland made during the HUMPPA-COPEC 2010 (Hyytiala United Measurements of Photochemistry and Particle Air – Comprehensive Organic Precursor Emissions and Concentration study); measurements in Spain (DOMINO HO_x 2010: Diel Oxidants Mechanisms In relation to Nitrogen Oxides) and in Germany during the HOPE 2011 (HOhenpeibenberg Photochemistry Experiment) (Novelli et al., 2014). It was found that during the HUMPPA-COPEC, DOMINO HO_x and HOPE campaign that between 60 – 80%, 50% and 20 – 40% of the daytime signal was from an interference, respectively. In respect of all three of the campaigns, 100% of the night-time signal was from interference. For the HUMPPA-COPEC campaign, a strong correlation between OH background signal and: temperature (R^2 = 0.64); ozone (R^2 = 0.49) and a lesser extent OH reactivity (R^2 = 0.25) (Novelli et al., 2017), was observed. These results further support that the interference is caused by sCIs formed from ozonolysis of BVOCs. For the HOPE campaign the correlation was much weaker (R^2 < 0.26), but the addition of SO_2 which reacts rapidly with sCIs, reduces the background signal to zero, suggesting sCIs were the source of the interference.

Several interference tests have been conducted for different FAGE instruments. Fuchs et al. (2016) mixed ozone and various alkenes, along with a propane as a scavenger (up to 1000 ppmv) in a flow tube that was interfaced with the FAGE cell nozzle. Interferences were observed, and they were highly correlated with the ozonolysis turnover rates (TOR). However, once the concentrations used in the experiment were scaled back to ambient values the interference was negligible ~3 x 10^4 molecule cm^{-3} of OH at the highest TORs observed in the boreal forest (Hakola et al., 2012). The interference increased with a longer inlet, higher cell pressure and had no dependence on laser power. The concentration of H_2O vapour and SO_2, which react rapidly with sCIs, was increased and there was no dependence suggesting that the interference is not from sCIs which is

contrary to other studies (Novelli et al., 2014, Novelli et al., 2017). Similar to results from Fuchs et al. (2016), Rickly (2018) found an interference signal was observed at high O_3 and alkene concentration although the interference was negligible when scaled back to ambient concentrations. The interference was also not laser generated and increased with longer inlet, although unlike Fuchs et al. (2016) an addition of sCI scavenger (CH_3COOH) eliminated the interference.

The Peking University (PKU) LIF instrument used an IPI system to test for interferences. During the Wangdu campaign that took place in the North China Plain (NCP) revealed a small but significant interference of $0.5 – 1.2 \times 10^6$ molecule cm^{-3} that contributed to between 9 – 35% of the OH signal (Tan et al., 2017). The highest interference was observed during the afternoon/early evening and no trend was observed with kOH, temperature, NO, isoprene or ozone (including the product of isoprene and ozone). More extensive interference testing was conducted during the BEST-ONE (Beijing winter finE particle Study – Oxidation Nucleation and light Extinctions) campaign that took place Jan – March 2016 (Tan et al., 2018). During the BEST-ONE no significant interference was detected.

Fuchs et al. (2016) also explored an interference caused by NO_3 radicals. To generate the NO_3, NO_2 and O_3 were injected into the SAPHIR chamber. A NO_3 interference signal was observed for all the radical species, and despite the absence of a hydrogen atom a NO_3 interference was still seen for OH and was equivalent to 1.1×10^5 molecule cm^{-3} per 10 pptv of NO_3. The OH interference signal observed in the Juelich instrument showed a linear dependence with NO_3, and no dependence on inlet length, cell pressure, laser power or humidity. It was postulated that a heterogeneous process involving NO_3 and H_2O absorbed onto the cell walls was the source of the interference.

These results show that, especially in forested environments, significant interferences have been observed for some instruments and considering the interference for those instruments can improve the measurement-model agreement. It also suggests that chemistry in forested environments is better understood than previously thought (Feiner et al., 2016, Mao et al., 2012). Also, there has been the identification of two potential interferences, from ozonolysis and alkenes (Novelli et al., 2014, Rickly, 2018) and NO_3 (Fuchs et al., 2016).

However, the detected interferences under laboratory conditions are not able to explain OH background signal observed under ambient conditions. Also, it should be noted that the FAGE instruments are highly variable in design, and this will contribute to different interferences observed in different set-ups.

1.4.2.2.2 HO_2 Interferences

To measure HO_2 the addition of NO to the ambient airflow is required, which could convert any of the RO_2 radicals present into HO_2 and then into OH (Stone et al., 2012). Until recently it was assumed that while this is efficient at low pressures, R1.49 is too slow and is a negligible interference (Stone et al., 2012).

$$RO_2 + NO \rightarrow RO + NO_2 \qquad \text{R1.48}$$

$$RO + O_2 \rightarrow R'CHO + HO_2 \qquad \text{R1.49}$$

$$HO_2 + NO \rightarrow OH + NO_2 \qquad \text{R1.50}$$

More recently it has been shown that certain RO_2 radicals can interfere with the detecting of HO_2, especially β-hydroxy RO_2 radicals (Fuchs et al., 2011). Conversion efficiencies of RO_2 to OH were reported to be >80% relative to HO_2 for alkene and aromatic derived RO_2 radicals (Fuchs et al., 2011). For the isoprene oxidation products methyl vinly ketone (MKV) and methacrolein (MACR), the relative sensitivity ~60%. Interference for smaller chain RO_2 (methane and ethane), were found to be <10% (Fuchs et al., 2011). This work showed that previous measurements for some groups suffered from significant interferences, and was estimated to be >30% of the daytime observation for the PRIDE-PRD2006 field campaign (Lu et al., 2012). This interference can be corrected for using E1.5 (Whalley et al., 2013) All FAGE designs are different between groups, and each have their own level of interference. E1.5 can be used to correct for biases from RO_2 to calculate the true HO_2 concentration by using the total HO_2 concentration measured (HO_2^*).

$$[HO_2{}^*] = [HO_2] + \Sigma_i(\alpha^i_{RO_2} \text{ x } [RO_2]_i) \qquad \text{E1.5}$$

where $[HO_2]$ is the true concentration of HO_2 and $\alpha^i_{RO_2}$is the detection sensitivity of each RO_2 radical. However, to measure the detection sensitivity requires a laboratory determination in conjunction with a detailed box model to calculate the RO_2 mixture. The interference of the instrument can be lowered by decreasing either the NO concentration or the reaction time for the conversion of HO_2 to OH

(Whalley et al., 2013, Fuchs et al., 2011). Decreasing either the NO concentration or reaction time also decreased the sensitivity towards HO_2 but would still be acceptable for atmospheric measurements with the detection limit being on the order of 10^6 molecule cm^{-3}. The total RO_x (OH + HO_2 + RO + RO_2) can be measured by converting RO_2 into OH in a method called RO_xLIF. The RO_xLIF method works by drawing ambient air into a flow tube held at ~19 Torr with NO (~0.7 ppmv) added downstream to convert RO_x into OH (R1.48- R1.50) and then CO is added in excess which partitions almost all HO_x into HO_2 which reduces wall losses of OH (R1.51) (Whalley et al., 2013, Fuchs et al., 2008).

$$OH + CO + O_2 \rightarrow HO_2 + CO_2 + H_2O \qquad \text{R1.51}$$

The outlet of the flow tube is sampled by FAGE and measures OH by the reaction of HO_2 with NO (R1.50) (Stone et al., 2012). The long residence time in the flow tube ensures a high conversion of RO_2 to HO_2, with similar sensitivities for C_1-C_3 linear alkanes, ethane and isoprene which is limited by wall losses. Interferences suffered by FAGE instruments are highly dependent on cell design and operating conditions (Whalley et al., 2013). Previously it has also been shown that by varying the NO flow rate a partial speciation in RO_2 methods could be achieved between small (C_1-C_3) alkane RO_2 and larger alkane derived RO_2 (aromatic and alkene) (Whalley et al., 2013).

1.4.4 HO_x Instrument Intercomparisons

Radical (OH, HO_2 and RO_2) species are difficult to measure in the troposphere due to their short lifetime and low/highly variable concentration. Instrument comparison is important for quality assurance in ambient measurements. The most recent formal intercomparison campaign, HO_xComp, took place in Juelich in summer 2005 (Schlosser et al., 2009, Kanaya et al., 2012, Fuchs et al., 2010). HO_xComp was a blind intercomparison, and during HO_xComp there were 3 days of ambient measurements and 6 days of measurements within the SAPHIR chamber. During the HO_xComp campaign 4 LIF, 1 CIMS (ambient only) and 1 DOAS (chamber only) participated in the campaign. A wide range of NO and isoprene mixing ratio were sampled during the campaign. For OH (Schlosser et al., 2009) pairwise comparison between each instrument correlated well (R^2 = 0.75 – 0.96) yielding slopes between 1.01 – 1.13 (chamber) and 1.06 – 1.69 (ambient). The ambient OH comparison showed more variability

between instruments and the suggested differences were caused by inhomogeneous sampling and calibration issues. For HO_2 good correlations (R^2 = 0.82 – 0.98) were reported, although compared to OH the level of agreement varied, with slopes of 0.69 – 1.26 (chamber) and 0.46 - 2.95 (ambient). The variability in the HO_2 data was associated with H_2O vapour. Since the HO_xComp campaign, additional interferences, especially in the HO_2 measurement, from RO_2 (Fuchs et al., 2011) and NO_3 (Fuchs et al., 2016) have been reported.

An intercomparison between the Juelich RO_xLIF and MIESR technique was conducted in the SAPHIR chamber. In two separate experiments the oxidation of CH_4 and 1-butene to form CH_3O_2 and $C_2H_5O_2$, respectively, was studied. The results showed an excellent agreement between the RO_2LIF and MIESR technique, yielding slopes of 1.02 ± 0.13 (R^2 = 0.97).

During the ARCTAS (Arctic Research of the Composition of the Troposphere from Aircraft and Satellites) campaign a HO_x intercomparison between LIF and (PeR)CIMS was performed in the spring of 2008 (Ren et al., 2012). In general, there was a good agreement with slopes of 0.89 (R^2 = 0.72) and 0.86 (R^2 = 0.72) for OH and HO_2 respectively. Although the CIMS:LIF OH and HO_2 ratio decreased and increased, respectively, with increasing altitude, reaching ~0.4 and ~2 above 9 km. The discrepancies at high altitude were associated with water vapour, as the most severe discrepancies were observed at low water vapour (<3000 ppmv) that is characteristic of the upper troposphere.

During the SOAS (Southern Oxidant and Aerosol Study) campaign, an intercomparison between a LIF (with chemical background technique, see section.2.1.2) and CIMS was performed for OH. Intercomparison slope (LIF vs CIMS) was 0.65 (R^2 = 0.80). On a diurnal basis, the discrepancies between the instrument were highest in the morning and afternoon, which corresponds to the time when the OH concentration was below 1 x 10^6 molecule cm^{-3}. The differences were also associated with low NO and OH concentration, but high OH reactivities.

1.4.4 OH reactivity Measurements

OH reactivity (*k*OH) is an important measurement as it is difficult to measure all the species that contribute to OH loss, it has been estimated that 10^4 – 10^5

organic compounds have been measured in the atmosphere (Goldstein and Galbally, 2007). Measurements of OH reactivity can be compared with calculated and modelled OH reactivity, and this gives an insight into the unmeasured VOCs. The contribution to missing reactivity can be substantial, missing reactivity observed during the CLearFLo (Whalley et al., 2016) (15%), TOKYO2003 (Yoshino et al., 2006) (14%), TOKYO2007 (Chatani et al., 2009) (30%) and MEGAPOLI (Dolgorouky et al., 2012) (56%).

Three main methods are used to measure OH reactivity. The first measurement of OH reactivity was using a flow tube with a sliding injector technique (Kovacs et al., 2003, Kovacs and Brune, 2001, Ingham et al., 2009, Edwards et al., 2013). The flow tube methods use LIF to detect OH following injection of high OH concentrations into the flow tube whilst sampling ambient air. OH reactivity can be determined using a pseudo first-order decay of OH as a function of the residence time. The residence time can be changed by moving the injector position. The second technique is the laser flash photolysis pump and technique (see section.2.3) which also uses LIF detection of OH. The OH is generated by photolysis of O_3 followed by the reaction of $O(^1D)$ with H_2O vapour (R1.3, R1.8). The OH signal decay is observed in real-time (Jeanneret et al., 2001).The last technique is the comparative rate method (CRM) where OH reactivity is measured indirectly by monitoring the change in concentration of a reference compound (pyrrole) in ambient and synthetic air exposed to a high concentration of OH (Sinha et al., 2008).

1.4.5.1 OH Reactivity Intercomparison

Two intercomparison campaigns of different OH reactivity instruments were performed at Juelich in the SAPHIR chamber in October 2015 and April 2016 (Fuchs et al., 2017). The chemical conditions were chosen to be either representative of the atmosphere or to test the limitations of the instruments. Four different methods for measuring OH reactivity was used in the campaign including: CRM (comparative rate method), flow-tube LIF from PSU (Pennsylvania State University), CIMS and LP-LIF (laser photolysis – laser induced fluorescence). The CRM instruments during the campaign were called MDOUAI, LSCE and MPI (Max Plank Institute). The LP-LIF instruments used during this campaign were called Lille LP-LIF, Leeds LP-LIF, FZJM LP-LIF and

FZJS LP-LIF. The CIMS instrument used during this campaign was called DWD CIMS.

During several experiments only CO and CH_4 were present under dark conditions (no photochemistry), the tested range of *k*(OH) was up to 150 s^{-1}. The comparison between measured *k*(OH) and calculated showed a good agreement, the slopes varied between 0.98 – 1.17 (R^2 > 0.8) for most instruments. The mean of the relative absolute difference between measured and calculated OH reactivity was: 32 – 48% for CRM; 19% PSU LIF; 8 – 11% for the LP-LIF and CIMS.

The second set of experiments included VOCs (isoprene, 1 -pentane, *o*-xylene and toluene), NO_2 and CO. For most instruments, the agreement between the measured and calculated was as good as for experiments with CO/CH_4 only, yielding slope between 0.94 – 1.07 (R^2 > 0.8). However, the CIMS gave larger deviations from calculated OH reactivity in these experiments, yielding a slope of 0.73 (R^2 = 0.91), and the deviation between calculated and measured OH reactivity increased at higher reactivity. The deviation was attributed to instrumental instability from the CIMS reactant ion counts (NO_3^-). In another experimental alongside the isoprene, 1-pentane, *o*-xylene, toluene, NO_2 and CO; MVK, MACR and acetaldehyde (all oxidation products of VOCs in the previous mixture) was also injected. The LP-LIF instruments were not affected by these species. Also, the flow tube LIF instrument and the CRM by MPI gave similar values within 10 – 20%. The LSCE and MDOUAI CRM instruments were affected significantly, especially for the experiments with acetaldehyde, and Fuchs et al., (2017) suggested that the presence of oxygenated VOCs may cause additional complications in the CRM reaction system.

In a third test, the chamber either had a mixture of monoterpenes/sesquiterpenes injected or real plant emission flushed into the chamber. This experiment also included the ozonolysis reactions of terpenes. A high linear correlation between LP-LIF instruments yielding slope between 0.96 – 1.08 (R^2 > 0.96), and no systematic difference was observed when O_3 was present, hence no difference when ozonolysis products were present. The measurements by the flow-tube PSU instrument were 10 – 15% lower than the reference instrument when monoterpenes/sesquiterpene were not present but 20% higher when emission was flushed into the chamber. The differences observed for the flow tube PSU instrument did not depend on whether O_3 was present. Fuchs et al., (2017)

suggested the differences for the flow-tube PSU instrument may be caused by instrumental problems (laser and electronics driving the movable OH source). The agreement between the CRM and LP-LIF instrument is worse during these experiments, the R^2 for different CRM instrument varied between 0.48 – 0.72. The agreement for the CRM instruments is even worse during the ozonolysis experiments when the CRM measured 5 times lower than the LP-LIF instruments. Although the difference does vary between CRM instruments, all instruments measured lower than LP-LIF instruments. Fuchs et al., (2017) suggested that since the CRM instruments have longer residence time (5 to 6 s) compared to the LP-LIF (0.5 – 4 s) the monoterpenes/sesquiterpenes may stick to the walls, leading to a lower measured reactivity.

Finally, the OH reactivity in the presence of NO was tested as NO can affect measurements of OH reactivity due to recycling of OH by the reaction of HO_2 + NO. The NO concentration was increased stepwise up to 120 ppbv. OH reactivity from the Leeds LP-LIF agrees well with calculated OH reactivity below 20 ppbv. However, the Leeds LP-LIF values are increasingly lower with increasing NO. The lower measured OH reactivity measured by the Leeds LP-LIF instrument was, unlike other LP-LIF groups, fitted with a single exponential rather than a bi-exponential hence not considering NO recycling. The PSU LIF instrument tended to underestimate the reactivity values with increasing NO, with a maximum relative difference of 20%. The relative difference between measured OH reactivity for DWD CIMS and the reference (FZJS LP-LIF) increase with increasing NO, up to a factor of 1.3 for 10 to 20 ppbv. The difference between MWM CIMS and FZJS LP-LIF demonstrates the limitation of the CIMS instrument in its current configuration under high NO conditions.

1.5 RO_x measurements and Model Comparisons

Comparison of model simulation with observations allow us to assess our current understanding of the atmosphere. Models can vary in complexity for their treatment of different atmospheric processes, from detailed chemistry zero-dimensional box models that neglect physical processes to 3-D global chemistry-climate models that simulate transport and mixing effects and incorporate simplified chemistry.

1.5.1 Box model mechanisms

The short lifetimes of OH and HO_2 mean that their concentrations are controlled by local *in-situ* chemistry, and not *via* transport processes and makes them ideal for testing the mechanism of chemical models (Stone et al., 2012). Zero-dimensional models can be used to describe the chemistry of OH and HO_2 without having to include transport (Stone et al., 2012). Models can be used to compare with the results from various field campaigns. The models are highly constrained to the field data for long-lived species and photolysis rates, these models can require thousands of reactions and chemical species to adequately describe the photo-oxidative degradation of VOCs (Stone et al., 2012).

1.5.2 HO_x Measurement-Model comparisons

This section will summarise the comparisons of modelled HO_x to field measurements in urban environments.

1.5.2.1 Wintertime Urban Environments

1.5.2.1.3 PUMA

OH and HO_2 measurements were made during the winter PUMA (Pollution of Urban Midland Environments) campaign in Birmingham using FAGE. The average midday maximum of the OH and HO_2 measurements was 2×10^6 cm^{-3} and 3×10^8 cm^{-3} respectively (Heard et al., 2004). A zero-dimensional box-model based on the MCM (Master Chemical Mechanism) was used to calculate OH and HO_2 concentration and compared to the measurements, and in both cases the model underpredicted the concentrations of the radicals (Heard et al., 2004).

The important initiation, termination and propagation reactions are shown in Figure 1.12, and shows that O_3 + alkenes are the main contributor for OH initiation in winter, which is generally not considered a large source of radicals in winter (Heard et al., 2004). HONO was not measured during the PUMA campaign so the contribution from HONO photolysis should be considered a lower limit.

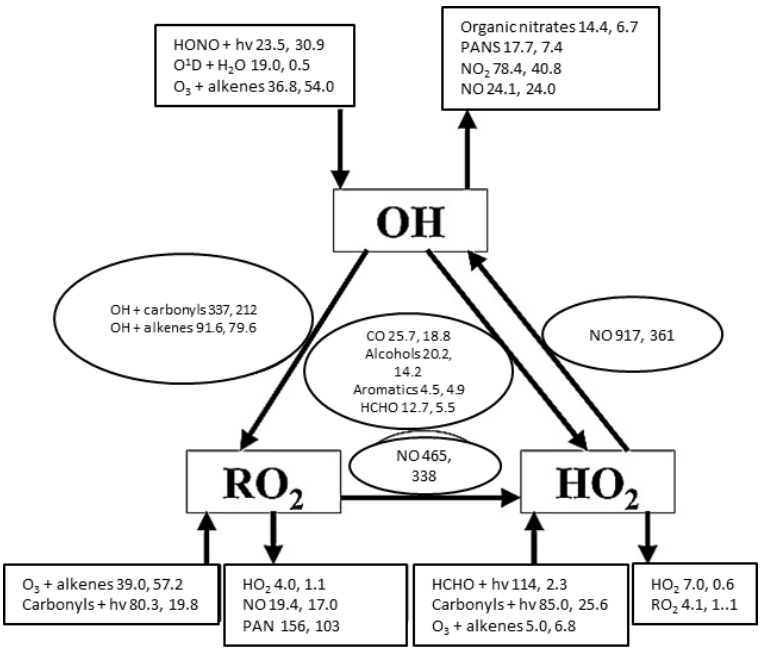

Figure 1.12 Reaction cycle showing the main initiation, propagation and termination steps for OH, HO_2 and RO_2 radicals for the PUMA campaign in Birmingham. The first number in italics is an average for summer (1999) and the second is the average for winter (2000). The values are given in units of 10^5 molecules cm^{-3} s^{-1}. Diagram copied from Heard et al. (2004).

1.5.2.1.4 NACHTT

Measurements of OH were made in Boulder, Colorado in February 2011 (Kim et al., 2014). The average midday maxima was 2.7 x 10^6 molecule cm^{-3}. HONO was the dominant primary source of radicals contributing 80.4%, with ozonolysis (4.9%) and ozone photolysis (14.7%) contributing the rest. The UWCM (University of Washington Chemical Mechanism) underpredicted the OH concentration by 1.3 in the morning (09:00 – 11:00). The impact of Cl atom chemistry was also assessed by constraining the model to measured $ClNO_2$, the Cl atom concentration produced in the model ~10^3 molecule cm^{-3} and the Cl concentration was too low to perturb the OH concentration (Kim et al., 2014).

1.5.2.1.5 IMPACT

OH and HO_2 radicals were measured using FAGE in Tokyo during January and February 2004. The average maximum concentration of OH and HO_2 measured during the campaign was 1.5 x 10^6 cm^{-3} and 0.27 x 10^8 cm^{-3}, respectively (Kanaya et al., 2007a). The RACM (Regional Atmospheric Chemistry Model) box model was used to compare to the measured radical values, to see how well the tropospheric chemistry is understood in urban environments. In general, the observed daytime OH was reproduced well by the model, but the model tends to

underestimate daytime HO_2 (Kanaya et al., 2007a). The budget for the radical species was assessed ($OH + HO_2 + RO_2$) for a smog event on the 29th of January. This budget showed that the reaction of O_3 + olefin was the dominant reaction during night and daytime (Kanaya et al., 2007a). During the day photolysis of carbonyls (e.g. HCHO and CH_3CHO) was more important than the photolysis of O_3 which only contributed 3% at noontime. The importance of carbonyl photolysis was highlighted during the PUMA campaign in Birmingham (see section.1.5.2.1.3). HONO photolysis made no impact on the net production of radicals as it was compensated by OH + NO (Kanaya et al., 2007a).

1.5.2.1.6 PMTACS-NY2001

OH and HO_2 was measured in New York City during wintertime (Jan – Feb) using FAGE. The mean OH and HO_2 concentrations that were measured during the PMTACS-NY (PM2.5 Technology Assessment and Characterization Study New York) was 1.4 x 10^6 cm^{-3} and 0.17 x 10^8 cm^{-3} respectively (Ren et al., 2003b). The RACM zero-dimensional box model was used to compare the model results with the measurements. The model generally reproduced daytime OH well, however, HO_2 was significantly underestimated especially at high NO concentrations (Ren et al., 2003b). The photolysis of HONO is the major daytime source, whilst O_3 alkenes reactions were the major night-time source. The discrepancy between the measured and modelled results could arise from a missing HO_x production source that is either an unknown new HO_x source or unknown HO_2 recycling that does not proceed *via* OH (Ren et al., 2003b). The PUMA, IMPACT IV and PMTACS show an underprediction of HO_2 especially at high NO_x, although these measurements were made before the discovery that significant interference in the HO_2 values may be present, this may reduce the measured values and bring them closer to the values predicted the models (Ren et al., 2003b).

1.5.2.1.1 BEST-ONE

Measurements of OH, HO_2 and RO_2 were made in Huairou (60 km Northeast of Beijing) in January to March 2016 as a part of the BEST-ONE campaign (Tan et al., 2018). The average midday OH concentration in clean and polluted air (k(OH) > 27 s^{-1}) was 3.6 x 10^6 molecule cm^{-3} and 2.4 x 10^6 molecule cm^{-3}, respectively. The RACM2 was used to simulate the radical concentration under polluted periods the model underpredicted the OH concentration by 1.6 and the HO_2 and

RO_2 by up to a factor of 5. During clean periods the RACM2 model could reproduce OH, HO_2 and RO_2 within a ratio of 1.5. The photolysis of HONO, ozonolysis and photolysis of carbonyls produced 46%, 28% and 24% of the primary radical production.

1.5.2.1.7 PKU

OH and HO_2 measurement were made during winter, November/December 2017, at the Peking University campus (Ma et al., 2019). The daily maxima of OH for clean and polluted ([CO] > 1 ppmv) periods was 2.0 x 10^6 molecule cm^{-3} and 1.5 x 10^6 molecule cm^{-3}. The daily maxima of HO_2 for clean and polluted periods was 0.4 x 10^8 molecule cm^{-3} and 0.3 x 10^8 molecule cm^{-3}, respectively. The RACM2-LIM1 mechanism during clean periods could reproduce the OH concentration but underpredicted HO_2 by 50%. During polluted periods, OH and HO_2 concentrations were underestimated by 50% and 12-fold, respectively. The underprediction of OH and HO_2 has a strong dependence on NO, with a higher underprediction with increasing NO. The major primary source of radicals during clean and polluted periods is HONO contributing 84% and 94%. The major termination pathway is through the reaction of OH with NO_x.

1.5.2.2 Summertime Urban Environment

1.5.2.2.1 PRIDE-PDR2006

OH and HO_2 measurements were made during the PRIDE-PRD2006 campaign in 2006 (Program of regional Integrated Experiments of Air Quality over the Pearl River Delta) in a rural site that is downwind of the megacity Guangzhou (Lu et al., 2012), the - is shown in Figure 1.13. The daily maximum of OH concentration observed reached (15 - 26) x 10^6 cm^{-3} and HO_2^* (3 - 25) x 10^8 cm^{-3}.

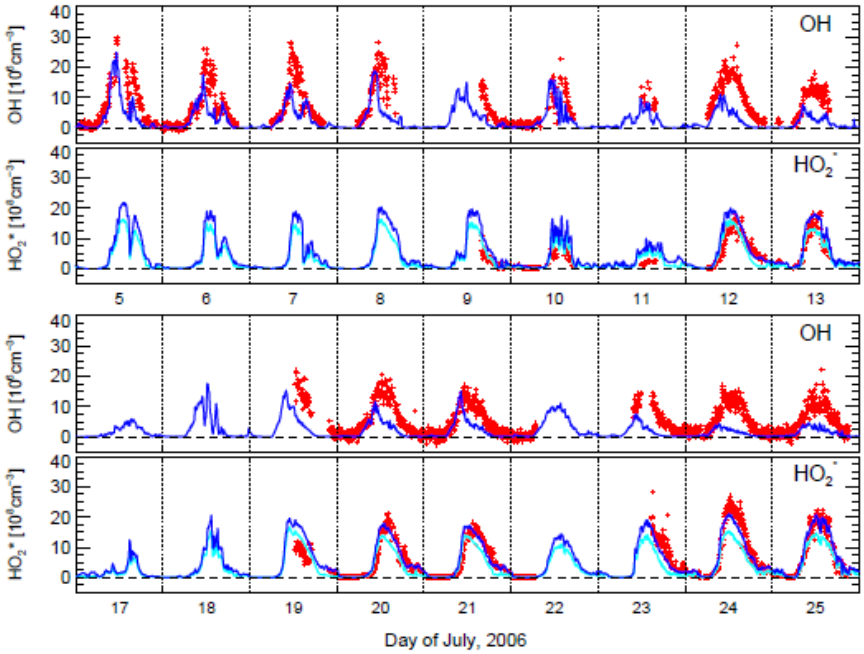

Figure 1.13 Time series of 5 min-average measured (red) and simulated concentration (blue) of OH and HO_2^* for the PRIDE-PRD2006 campaign. Figure copied from Lu et al. (2010).

The RACM-MIM-GK chemical model was applied, coupled with the Leuven Isoprene Mechanism (LIM) (Lu et al., 2012). The Leuven isoprene mechanism recycles HO_x with high efficiency at low NO. The mechanism proposes a fast interconversion of isoprene hydroxyperoxy radical isomers, some of which undergo fast 1,6-H shift, followed by reaction with O_2 (Lu et al., 2013). This favoured reaction is expected to form HO_2 and hydroperoxyaldehydes (HPALDs) (Lu et al., 2013). The HPALDs are assumed to undergo decomposition that leads to the formation of one HO_2 and up to three OH radicals. The mechanism is more important in forested environments when comparing to field data as levels of isoprene are higher (Lu et al., 2013). The measurement of *k*(OH) is reproduced well (within 20%) which shows that the model simulates total OH sinks well. The agreement between measured and modelled *k*(OH), but underprediction of observed OH, indicates that at low NO_x (afternoon) there is a missing OH production source (Lu et al., 2012). The model has been able to simulate HO_2^* (HO_2 + complex RO_2) well, the model indicates that interference from RO_2 is small in the morning and becomes large contributions in the afternoon with a daily average of 30% (Lu et al., 2012).

Table 1.4 shows various model scenarios used in (Lu et al., 2013).

Simulation	Chemical Mechanism
M0	RACM-MIM-GK (base case) mechanism
M1	as M0, with generic recycling reactions added: $RO_2 + X \rightarrow HO_2$ R1.52 $HO_2 + X \rightarrow OH$ R1.53
M2	as M0, with a single generic recycling reaction added: $HO_2 + Y \rightarrow OH$ R1.54
M3	as M0, with additional OH-forming channels in reactions of acyl peroxy + HO_2 and β-keto peroxy + HO_2 reactions.
M4	as M3, with the OH-reforming mechanism in which reactions of OH with isoprene hydroxyhydroperoxides produce epoxides and prompt OH
M5	as M4, with the LIM0 scheme incorporated, in which isoprene hydroxyperoxy radicals produce prompt HO_2 and HPALDs, followed by HPALDs photolysis. Two variants are tested: a) $HPALDs + h\nu \rightarrow OH + HO_2 + products$ R1.55 b) $HPALDs + h\nu \rightarrow 3OH + HO_2 + products$ R1.56
M6	as M3, with OH-formation from the reaction of isoprene hydroxyperoxy radicals with HO_2. Two variants are tested: a) $ISOP + HO_2 \rightarrow 2OH + products$ R1.57 b) $ISOP + HO_2 \rightarrow 4OH + products$ R1.58
M7	MCMv3.1

Table 1.4 Chemical mechanism used in box models simulation of HO_x for PRIDE-PRD2006. Reproduced from Lu et al.(2012).

The results from the different model scenarios are shown in Figure 1.14. M1 is the simplest solution to the additional recycling of OH in low NO_x and the concentration of X to bring the model and measured results to unity is 0.8 ppb of X. M2 with additional recycling using species Y (R1.54) can also explain the discrepancies between model and results, and both using additional recycling from X and Y (Lu et al., 2012). The MCM (M7) agrees well with the base model (M1), and this demonstrates that the underprediction of OH is not from RACM-MIM-GK model lumped VOC chemistry (Lu et al., 2012). The addition of acyl peroxy and β-keto peroxy made little difference to the model result. Also, for

model runs M3 and M4 are almost indistinguishable from M0. M5 and M6 calculate significantly larger OH concentration than M0, although none of these reactions can reproduce OH over a range of NO_x conditions (Lu et al., 2012).

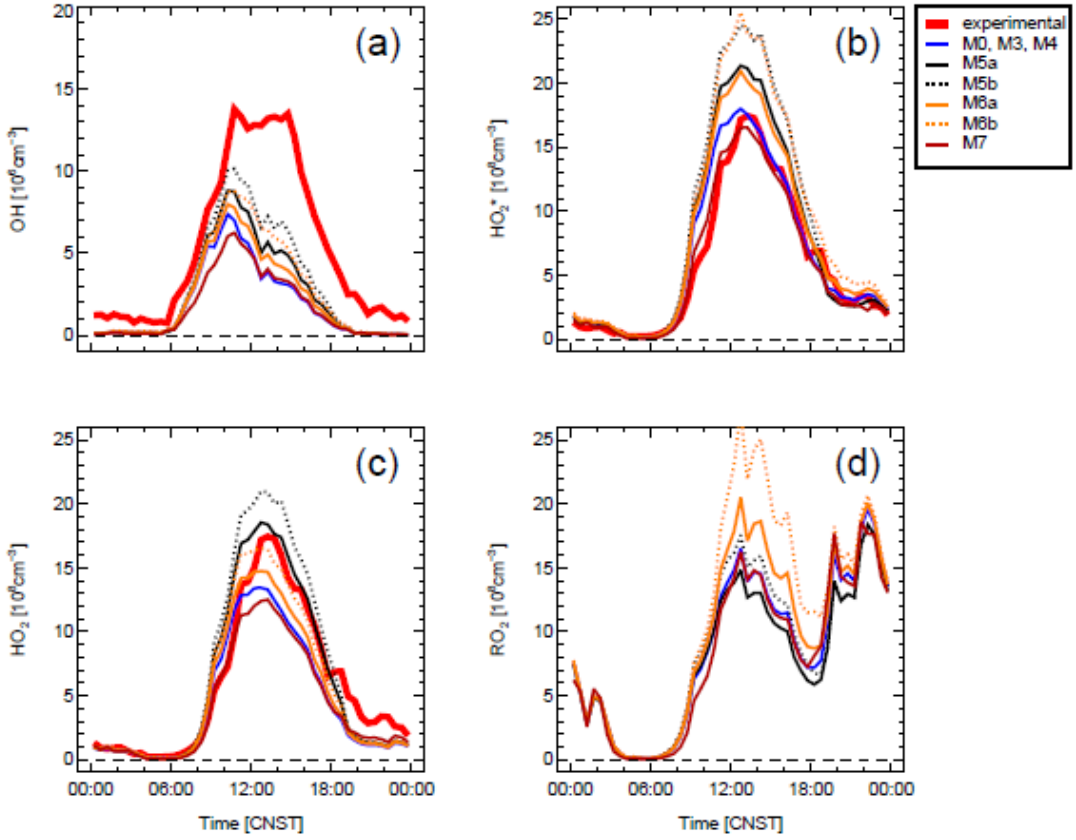

Figure 1.14 Comparison of measured and modelled concentrations of a) OH, b) HO_2^*, c) HO_2 and d) RO_2 with six different scenarios described above. The results for M0, M3 and M4 and indistinguishable. Figure copied from Lu et al. (2012).

1.5.2.2.2 CAREBeiijing

The CAREBeijing2006 campaign measured at the suburban site Yufa in the south of Beijing in summer 2006. The concentration of OH and HO_2 were measured using FAGE, no RO_2 measurements were taken during this campaign and the HO_2 interference from RO_2 was estimated (Lu et al., 2013). The concentration maximum was (4 - 17) × 10^6 cm^{-3} for OH and (2-24) × 10^8 cm^{-3} for HO_2 (including a model estimated interference of 25% from RO_2). The OH reactivity during the day were generally high, 10–30 s^{-1}, with contributions from VOCs and their oxidation products. The air chemistry was mostly influenced by aged air pollution in slow winds from the south. The modelled and measured HO_x concentrations reveal a systematic overprediction of OH as a function of NO. The largest

discrepancy of a factor of 2.6 is found at the lowest NO concentration encountered (0.1 ppb), whereas the discrepancy became insignificant above 1 ppb NO (Lu et al., 2013). The discrepancy at low NO concentrations is similar to the observations found during the Wangdu campaign (discussed in section.1.5.2.2.8). The OH discrepancy can be resolved if NO-independent recycling is assumed, also the inclusion of the postulated Leuven isoprene Mechanism (LIM) can explain the gap.

The model used in this campaign was RACM-MIM-GK which is derived from Regional Atmospheric Chemical Mechanism (RACM), with the addition of a condensed version MIM (Mainz Isoprene Mechanism). It also included reactions that recycles OH without NO including; carbonyl peroxy radicals with HO_2 and isoprene epoxide chemistry. Although these changes made little impact on the results of the model. An additional model was run that included species X and Y (R1.52 - R1.54) for recycling to OH without NO, which has been proposed previously as sources of missing OH (Lu et al., 2012).

$$RO_2 + X \rightarrow HO_2 \qquad \text{R1.52}$$

$$HO_2 + X \rightarrow OH \qquad \text{R1.53}$$

$$HO_2 + Y \rightarrow OH \qquad \text{R1.54}$$

The MCMv3.2 was used as a bench test for the models that were run earlier. A good agreement is achieved with the inclusion of additional OH recycling reactions. The RACM-MIM-GK and the MCMv3.2 agree well, which shows that higher levels of chemistry detail available in the MCM does not influence the discrepancies between modelled and measured results.

1.5.2.2.3 PUMA

The OH and HO_2 concentration was measured in June/July 1999 in Birmingham as a part of the PUMA campaign (Emmerson et al., 2005). The daily maxima in OH concentration varied between 2 – 9 x 10^6 molecule cm^{-3}; and the HO_2 daily maxima varied between 1.5 – 10 x 10^8 molecule cm^{-3}. The Master Chemical Mechanism (v3.1) was used to compare with the measurements and showed that the measured:modelled ratio was 0.58 and 0.56 for OH and HO_2 respectively. The primary radical formation from HONO, $O^1D + H_2O$ and ozonolysis contributed 39%, 24% and 46%, respectively, to the total primary OH formation.

1.5.2.2.4 ClearfLo

OH, HO_2 and RO_2 were measured during the ClearfLo project in London 2012 (Whalley et al., 2018). the HO_2 measurement was made using a low flow of NO (7.5 sccm) which laboratory studies have shown minimalizes the interferences from alkene and aromatic-derived RO_2 species (Whalley et al., 2013). During this campaign, a detailed budget analysis of HONO was made and it revealed a missing daytime source (Lee et al., 2015b). The missing HONO sources correlates with the product of $j(NO_2)$ with other species, in particular $j(NO_2)$ and the product of NO_2 with OH reactivity. This suggests this missing source is linked to NO_2 and sunlight is involved in the mechanism. When the photosensitized surface conversion of NO_2 is increased by a factor of 10 but varies as a function of $j(NO_2)$ this closes the daytime budget for HONO apart from in the late afternoon (Lee et al., 2015b). This suggests that urban surfaces may increase the production of HONO by enhancing the photosensitized (source from a surface exposed to light) source (Lee et al., 2015b).

$$\mathrm{HONO} + h\nu(\lambda < 400\ \mathrm{nm}) \rightarrow \mathrm{OH} + \mathrm{NO} \qquad \text{R1.9}$$

As shown by R1.9, HONO is an important source of OH during the day. Rate of production analysis (ROPA) was used for OH radicals to assess the importance of HONO and the missing HONO source (Figure 1.15) (Lee et al., 2015b). It shows that HONO is an important source in the early morning contributing 30-40% and is second to NO + HO_2. This is due to the build-up of HONO in the night when sunlight is absent. At solar noon HONO unconstrained accounts for 40% of the OH radical sources and 57% of the HO_x initiation sources (Lee et al., 2015b). The photolysis of O_3 is only a minor source throughout the day peaking at a contribution of 10%. The model can be constrained to the measured HONO and the OH production rate increases by ~20% compared with the modelled HONO, which shows that missing radical sources are important to HO_x production at ground level. This can be shown in Figure 1.16 when the model PSS-calculated HONO (OH + NO source only) OH is underpredicted by ~40% when known and postulated sources of HONO was added the predicted OH was increased by 1.4 - 1.6 during the day (Lee et al., 2015b). Although in the late afternoon there is still an underprediction of OH by ~20-30% suggesting further missing OH source (Lee et al., 2015b).

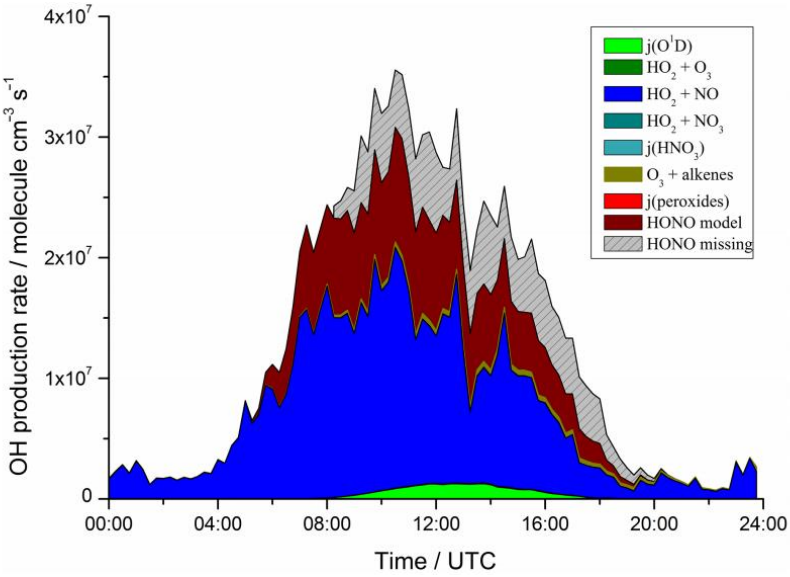

Figure 1.15 Average diurnal profile of gross OH production rates from different initiation and propagation sources calculated by the model. Figure copied from Lee et al. (2015).

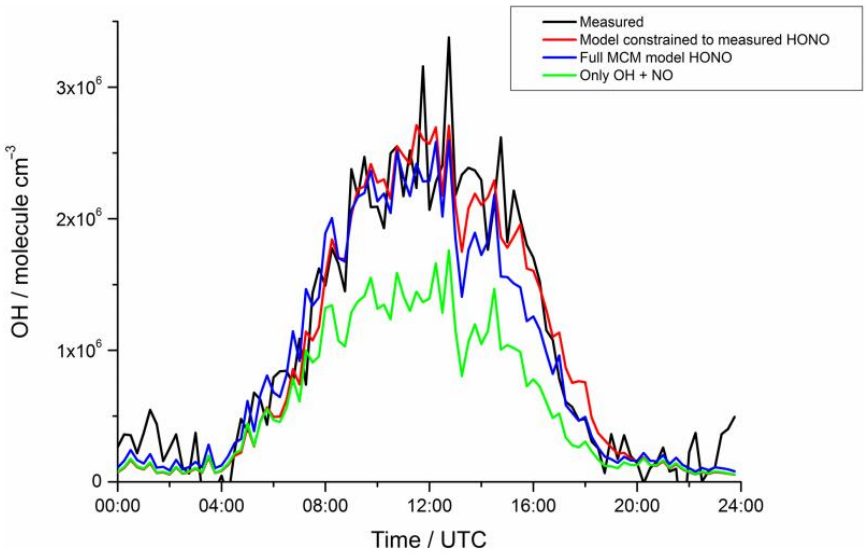

Figure 1.16 Average diurnal profile of OH showing measured (black), modelled with unconstrained HONO (green), modelled unconstrained with additional HONO sources (blue) and modelled constrained to measures HONO (red). Figure copied from Lee et al. (2015).

1.5.2.2.5 PMTACS-NY2001

OH and HO_2 were measured as a part of the PMTACS-NY2001 campaign in New York in 2001 (Ren et al., 2003a). The daytime maxima of OH and HO_2 varied between 5 – 20 x 10^6 molecule cm^{-3} and 0.4 – 6 x 10^8, respectively. Relatively

high OH was measured during the night-time (~0.8 x 10^6 molecule cm^{-3}). and was consistently above the LOD for OH and HO_2 of 3.0 x 10^5 molecule cm^{-3} and 2.5 x 10^6 molecule cm^{-3}. The RACM model was able to reproduce OH well during the day with a measured:model ratio of 1.1; whilst at night the model underpredicted the radical concentration. The HO_2 could be reproduced well by the model with a measured:model ratio of 1.24 for both day and night. The production of radical was from: photolysis of HONO (34%); ozonolysis (27%); photolysis of HCHO (9%) and $O^1D + H_2O$ (30%) (Ren et al., 2003a).

1.5.2.2.6 MCMA

Measurements of OH and HO_2 were made during the Mexico City Metropolitan Area (MCMA) field campaign in March 2006. Maximum OH concentrations observed varied between 2.0 × 10^6 and 1.5 × 10^7 molecule cm^{-3}, and the maximum daily HO_2 concentration ranged from 5.6 × 10^7 to 4.5 × 10^8 molecule cm^{-3} (Dusanter et al., 2009). The RACM model highlighted that measured concentrations of OH and HO_2 were underpredicted during the morning hours and HO_2/OH ratios underestimated when the NO mixing ratios were above 5 ppbv (Dusanter et al., 2009). These observations suggest missing sources of radicals in polluted environments and that under high NO_x concentrations a process converting OH into HO_2 is missing from the model. The elevated levels of HO_x during the morning coincided with high measurements of benzene and toluene, and is suggesting that the elevated HO_2 may be linked to oxidation capacity of aromatics under high NO_x (Dusanter et al., 2009) because OH is overestimated in the afternoon by ~1.7. The model predicts that HONO (35%), photolysis of HCHO (24%), O_3-alkene reactions (19%) and photolysis of dicarbonyls (8%) are the main sources of radicals (Dusanter et al., 2009).

1.5.2.2.7 IMPACT-L

The OH and HO_2 concentration was measured in Tokyo in July/August 2004 as a part of the IMPACT-L campaign (Kanaya et al., 2007a). The average daily maxima OH and HO_2 concentration was 6.3 x 10^6 molecule cm^{-3} and 2.31 x 10^8 molecule cm^{-3}. The RACM was used to simulate the radical concentrations and the modelled:observed ratio for OH and HO_2 was 0.86 and 1.29, respectively, showing an underprediction for OH and an overprediction for HO_2. The average production channels were not assessed for this campaign, but on the 8th August, the major primary production channels were $O^1D + H_2O$ (30%),

photolysis of HONO (9%), ozonolysis (3%), photolysis of carbonyls (18%) and photolysis of HCHO (22%) (Kanaya et al., 2007a).

1.5.2.2.8 Wangdu

The most recent published summer campaign in China took place in Wangdu 2014, using FAGE to measure OH, HO_2 and RO_2. Daily maximum concentrations between (5-15) × 10^6 cm^{-3}, (3-14) × 10^8 cm^{-3} and (3-15) × 10^8 cm^{-3} for OH, HO_2 and RO_2 respectively (Tan et al., 2016). The Regional Atmospheric Chemical Mechanism version 2 (RACM) box model is used to compare measured and modelled results. Figure 1.17 shows that modelled and measured OH concentrations agree for NO mixing ratios higher than 1 ppbv, but discrepancies occur in the afternoon for NO mixing ratios of less than 300 pptv (Tan et al., 2016). If additional OH recycling equivalent to 100 pptv NO is assumed, the model is also capable of reproducing the observed OH concentrations for high VOC and low NO_x concentrations with a good agreement for HO_2 and RO_2 (Tan et al., 2016).

Observed RO_2 are underestimated in the morning by a factor of 3 to 5, the underprediction occurs when there is high NO concentration ([NO] > 1 ppbv) (Tan et al., 2016). The underprediction of RO_2 suggests there is a missing source of peroxy radicals in the model and increasing the VOC concentration decreases the discrepancy between measured and modelled results (Tan et al., 2016). The underestimation of RO_2 leads to the underestimation of O_3 at high NO_x. OHchem was used during this campaign, the differences between OHwave and OHchem (see section 2.4.4) varied between 0.5 × 10^6 and 1 × 10^6 cm^{-3} (average: (0.85 ± 0.3) × 10^6 cm^{-3}), which is in the order of 10% of the total OH signal during daytime when no scavenger is present (Tan et al., 2016). The differences are with 2σ systematic error of S_{OH} (OH signal) and are at the limit of detection for the instrument. These differences can either be from error in the determination of S_{OH} or an unknown OH interference. Like the CAREBeijing and PRIDE-PRD2006, the model starts to underpredict HO_2 above ~ 3 ppbv of NO.

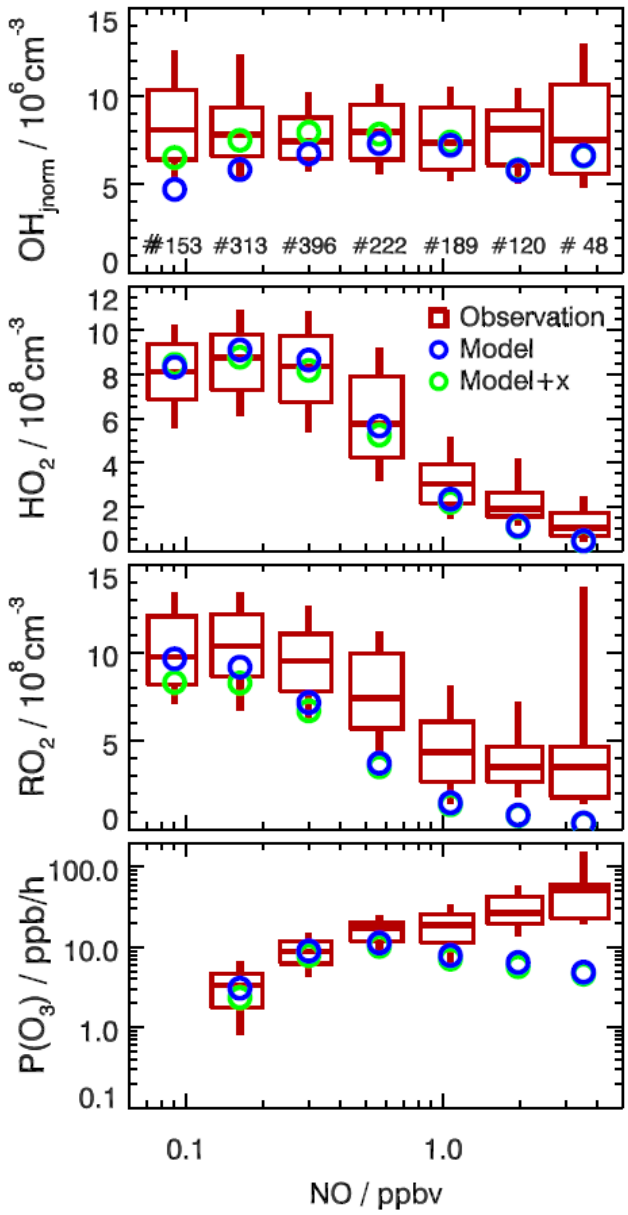

Figure 1.17 NO dependence of OH, HO_2 and the RO_2 concentrations and instantaneous ozone production rate for daytime conditions. OH is normalised to average $j(O^1D)$ value (1.5×10^{-5} s^{-1}). Figure copied from Tan et al. (2016).

1.5.2.2.9 CalNex

Measurements of HO_x were made at a Pasadena ground site during the CalNex-LA 2010 campaign using LIF (Griffith et al., 2016). The OH and HO_2^* concentrations exhibited a distinct weekend effect with higher radical concentrations being measured during the weekend corresponding with low NO_x (Griffith et al., 2016). The RACM-2 model was used to simulate the radical concentrations and the model overpredicted OH concentrations during the weekends by a factor of ~1.4 ± 0.3 but agreed better during weekdays

(~1.0 ± 0.2) when NO mixing ratio greater than 4 ppbv (Griffith et al., 2016). The model underpredicted HO_2^* by a factor of ~1.3 ± 0.2 on the weekends and weekday concentration was underpredicted by ~3.0 ± 0.5 (Griffith et al., 2016).

Increasing the modelled OH reactivity to match the measured OH reactivity during the campaign improved the general overall agreement between modelled and measured results. Due to this difference in measured and model OH reactivity, it suggests that the discrepancies may be related to incomplete characterisation of reactive trace gases (Griffith et al., 2016). Even with constraining the model to observed OH reactivity, HO_2^* on weekdays are still underpredicted by 2.0 ± 0.5. The underprediction of HO_2^* on weekdays leads to an underprediction of HO_2^*/OH at a higher mixing ratio of NO, this suggests that the propagation chemistry of RO_2 is not being understood well by the model. This could be due to simplified propagation chemistry that is used in the RACM-2 model or segregation of peroxy radicals and NO in these airmasses (Griffith et al., 2016). HONO photolysis accounted for 26-30% of radical initiation; photolysis of formaldehyde and carbonyl accounted for 40% and O_3 only accounted for 15% of the radical initiation (Griffith et al., 2016).

1.5.2.2.10 MEGAPOLI

OH and the sum of (HO_2 + RO_2) radical measurements were made during the summer MEGAPOLI campaign in Paris using a CIMS (Michoud et al., 2012). OH and (HO_2 + RO_2) showed an average daytime maxima of 5×10^6 and 1.2×10^8 molecule cm^{-3}, respectively (Michoud et al., 2012). The MCMv3.1 was used to calculate the radical concentrations and this lead to an overestimation of 12% and 5% for OH and (HO_2 and RO_2) respectively (Michoud et al., 2012). This shows that modelled and measured results agree well within error. A radical budget analysis was also conducted and indicates that HONO photolysis (~35%), O_3 photolysis (~23%), and aldehydes and ketones photolysis (~16% for HCHO and 18% for others) are the main pathways for radical initiation (Michoud et al., 2012).

A comparison between measured and modelled HONO using the PhotoStationary State (PSS) approach was made during both the winter and summer campaign (Michoud et al., 2014). The comparison of these results showed that the model underestimated the amount of HONO, and made evident

there was a missing HONO source (Michoud et al., 2014). This missing source shows a correlation with $j(NO_2)$ and the product of $j(NO_2)$ and soil moisture, this implies that the missing source is photolytic and occurring at the ground surface (Michoud et al., 2014).

1.5.2.2.11 SHARP

The OH and HO_2 concentration was measured in April/May 2009 as a part of the SHARP campaign (Ren et al., 2013). The average daily maxima OH concentration of OH and HO_2 measured was 9.3×10^6 molecule cm^{-3} and 4.9×10^8 molecule cm^{-3}. The OH and HO_2 concentration was replicated very well by the RACM with a modelled:measured ratio of 0.95 and 0.98. The OH and HO_2 concentration is underpredicted by the model at higher NO concentration. The major primary sources of radical during the SHARP campaign was: $O^1D + H_2O$ (30%), photolysis of HONO (22%), ozonolysis (13%), photolysis of carbonyls (15%) and photolysis of HCHO (14%).

1.5.2.2.12 TRAMP

The TRAMP campaign measured OH and HO_2 in Aug/Oct in 2006, the campaign took place in Texas. The average daily maxima of OH and HO_2 was 1.5×10^7 molecule cm^{-3} and 1.2×10^8 molecule cm^{-3}, respectively. The RACM model was used to simulate the radical concentration and the modelled:measured ratio was 1.6 and 1.37 for OH and HO_2, respectively, highlighting an overprediction of both radical species by the model. The model tended to overpredict the radical concentration below 0.4 ppbv of NO and underpredict the radical concentration above 0.4 ppbv. The major primary source of radical during the campaign was: $O^1D + H_2O$ (24%); photolysis of HONO (25%); ozonolysis (10%) and the photolysis of carbonyls (37%, including HCHO).

1.6 Summary

This introduction has highlighted the important air quality pollutants include SO_2, NO_2, O_3 and particulate matter (PM) and the effect/damage they can have on health. The fundamental reactions controlling oxidation chemistry and formation of secondary pollutants including O_3 and SOA. The trend in air pollutants in China/Beijing has shown that PM, SO_2 and NO_x have decreased; whilst O_3 has been increasing. The different techniques for measuring OH, HO_2 and RO_2 has

been outlined with a focus of the FAGE method. A summary of different RO_x measurements and comparison with box models for urban environments in the summer and winter has been explored. The comparison between measured and modelled values highlights missing understanding in high NO (above 3 ppbv) and low NO (below 1 ppbv). The radicals (OH, HO_2 and RO_2) under high NO environments tend to be underestimated; whilst under low NO conditions, the model tends to overpredict the HO_2 (except during the PRIDE-PRD2006 campaign) concentration and suggests that under low NO there is a missing source of OH.

1.7 Structure of Thesis

In the next chapter details of the experimental procedure conducted as part of this work are given, with a large focus on the description of the Leeds University of ground-based FAGE instrument. This section will include details of calibration, general running conditions, measurement uncertainties and the data workup procedure. Chapter 3 will explore instrument developments including: characterisation of the losses of OH and HO_2 on the inlet pre-injector (IPI); O_3 interference experiment; NO_3 interference experiment and theoretical calculation for the IPI internal losses. Chapter 4 will compare measurements of OH, HO_2, RO_2 and OH reactivity made in central Beijing during winter-time with several model scenarios and simple photostationary steady-state. The chapter will explore the measured and modelled radical concentration dependence on NO and also a comparison of radical measurements in and outside haze events. The impact of unconstraining the model to HONO and also the contribution of OH + NO to HONO formation. Finally, we compare calculated *in-situ* production rates of O_3 using measured and modelled radical values.

Chapter 5 will compare measurements of OH, HO_2, RO_2 and OH reactivity made in central Beijing during summer-time with several model scenarios and a simple photostationary steady-state calculation. The chapter will explore the possible source of OH interference observed sometimes during the campaign. Also, the measured and modelled radical concentration dependence on NO will be explored, with different model scenarios used to try and reconcile measurements with model, including a representation autoxidation. The impact of unconstraining the model to HONO and the contribution to HONO formation from OH + NO will

be discussed. The impact of including Cl atom chemistry in the model will also be explored. The missing OH reactivity observed during the campaign will be explored and will also show the impact of filling the missing reactivity with different species. And finally, we compare calculated *in-situ* O_3 production rates using measured and modelled radical values.

Chapter 6 will be a comparison between measurements of radical species in both summer and wintertime, and how well the model performs under different NO_x/O_3 regimes. It will compare the impact of similar model scenarios including: constraining the model to HO_2; changing the RO_2 + NO rate constant; the impact of unconstraining the model to HONO and the contribution to HONO formation from OH + NO. Chapter 6 will also compare the calculated *in-situ* ozone production rates during summer and winter using measured and modelled radical values. Finally, Chapter 6 will explore the impact of HO_2 uptake in summer and winter and show the effect on *in-situ* O_3 production. Chapter 7 will compare OH and HO_2 measurements made from two different FAGE instruments: the Leeds University ground-based instrument and Peking University FAGE instrument. This chapter will include time-series, diurnal and correlation comparison between the two instruments. Chapter 7 will also explore the reason for differences between the two-instrument including: NO segregation; chemical conditions and calibration differences. Finally, the overall conclusion of this thesis and suggestions for future work will be presented in Chapter 8.

1.8 References

Acker, K., Möller, D., Wieprecht, W., Meixner, F. X., Bohn, B., Gilge, S., Plass-Dülmer, C. and Berresheim, H. (2006) 'Strong daytime production of OH from HNO_2 at a rural mountain site', *Journal of Geophysical Research,* 33(2).

United States Environmental Protection Agency. (2017a) *Health Effects of Ozone Pollution*. Available at: https://www.epa.gov/ozone-pollution/health-effects-ozone-pollution (Accessed: 12/01/2017 2017).

United States Environmental Protection Agency. (2017b) *Sulfur Dioxide Basic*. Available at: https://www.epa.gov/so2-pollution/sulfur-dioxide-basics#what (Accessed: 12/01/2017 2017).

Alicke, B., Geyer, A., Hofzumahaus, A., Holland, F., Konrad, S., Pätz, H., Schäfer, J., Stutz, J., Volz-Thomas, A. and Platt, U (2003) 'OH formation by HONO

photolysis during the BERLIOZ experiment', *Journal of Geophysical Research: Atmospheres,* 108(D4), pp. PHO 3-1-PHO 3-17.

Aschmutat, U., Hessling, M., Holland, F. and Hofzumahaus, A. (1994) 'A tunable source of hydroxyl (OH) and hydroperoxy (HO_2) radicals: in the range between 10^6 and 10^9 cm^{-3}', *Physicochemical behaviour of atmospheric pollutants, European Commission, Brussels*.

Beebe, R. and Barnet, C. (1987) 'Chemistry of Atmospheres: An Introduction to the Chemistry of the Atmospheres of Earth, the Planets and Their Satellites', *Eos, Transactions American Geophysical Union,* 68(37), pp. 747-747.

Brown, S. S. and Stutz, J, (2012) 'Nighttime radical observations and chemistry', *Journal Chemical Society Reviews*, 41(19), pp. 6405-6447.

Cantrell, C., Shetter, R., Gilpin, T., Calvert, J., Eisele, F. and Tanner, D. J. J. o. G. R. A. (1996) 'Peroxy radical concentrations measured and calculated from trace gas measurements in the Mauna Loa Observatory Photochemistry Experiment 2', *Journal of Geophysical Research: Atmospheres*, 101(D9), pp. 14653-14664.

Chan, C. K. and Yao, X. (2008) 'Air pollution in mega cities in China', *Atmospheric environment,* 42(1), pp. 1-42.

Chatani, S., Shimo, N., Matsunaga, S., Kajii, Y., Kato, S., Nakashima, Y., Miyazaki, K., Ishii, K. and Ueno, H. (2009) 'Sensitivity analyses of OH missing sinks over Tokyo metropolitan area in the summer of 2007', *Atmospheric Chemistry and Physics,* 9(22), pp. 8975-8986.

Chen, W., Tang, H. and Zhao, H. (2015) 'Diurnal, weekly and monthly spatial variations of air pollutants and air quality of Beijing', *Atmospheric Environment,* 119, pp. 21-34.

Chen, Z., Zhuang, Y., Xie, X., Chen, D., Cheng, N., Yang, L. and Li, R. (2019) 'Understanding long-term variations of meteorological influences on ground ozone concentrations in Beijing During 2006–2016', *Environmental pollution,* 245, pp. 29-37.

Ministry of Environmental Protection of the People's Republic of China (2012) *Ambient air quality standards*. Available at: http://kjs.mep.gov.cn/hjbhbz/bzwb/dqhjbh/dqhjzlbz/201203/t20120302_224165.htm (Accessed: 08/08/2017 2017).

Colussi, A. J., Enami, S., Yabushita, A., Hoffmann, M. R., Liu, W.-G., Mishra, H. and Goddard III, W. A (2013) 'Tropospheric aerosol as a reactive intermediate', *Faraday discussions*, 165, pp. 407-420.

Comission, E. (2017) *Air Quality Standards*. Available at: http://ec.europa.eu/environment/air/quality/standards.htm (Accessed: 31/01/2017 2017).

Dab, W., Medina, S., Quenel, P., Le Moullec, Y., Le Tertre, A., Thelot, B., Monteil, C., Lameloise, P., Pirard, P. and Momas, I. (1996) 'Short term respiratory health effects of ambient air pollution: results of the APHEA project in Paris', *Journal of epidemiology and community health,* 50(Suppl 1), pp. s42-s46.

Dawson, J., Adams, P. and Pandis, S. (2007) 'Sensitivity of $PM_{2.5}$ to climate in the Eastern US: a modelling case study', *Atmospheric chemistry and physics,* 7(16), pp. 4295-4309.

Dawson, J. P., Bloomer, B. J., Winner, D. A. and Weaver, C. P. (2014) 'Understanding the meteorological drivers of US particulate matter concentrations in a changing climate', *Bulletin of the American Meteorological Society,* 95(4), pp. 521-532.

De Reus, M., Fischer, H., Sander, R., Gros, V., Kormann, R., Salisbury, G., Van Dingenen, R., Williams, J., Zöllner, M. and Lelieveld, J. (2005) 'Observations and model calculations of trace gas scavenging in a dense Saharan dust plume during MINATROC'. *Atmospheric Chemistry and Physics Discussions, European Geosciences Union*, 2005, 5 (1), pp.655-702.

Dolgorouky, C., Gros, V., Sarda-Esteve, R., Sinha, V., Williams, J., Marchand, N., Sauvage, S., Poulain, L., Sciare, J. and Bonsang, B. (2012) 'Total OH reactivity measurements in Paris during the 2010 MEGAPOLI winter campaign', *Atmospheric Chemistry and Physics,* 12(20), pp. 9593-9612.

Dupart, Y., Fine, L., D'Anna, B. and George, C. J. A. R. (2014) 'Heterogeneous uptake of NO2 on Arizona Test Dust under UV-A irradiation: An aerosol flow tube study', *Aeolian Research*, 15, pp. 45-51.

Dusanter, S., Vimal, D., Stevens, P., Volkamer, R. and Molina, L. (2009) 'Measurements of OH and HO 2 concentrations during the MCMA-2006 field campaign–Part 1: Deployment of the Indiana University laser-induced fluorescence instrument', *Atmospheric Chemistry and Physics,* 9(5), pp. 1665-1685.

Edwards, P., Evans, M., Furneaux, K., Hopkins, J., Ingham, T., Jones, C., Lee, J., Lewis, A., Moller, S., Stone, D. (2013) 'OH reactivity in a South East Asian tropical rainforest during the Oxidant and Particle Photochemical Processes (OP3) project', *Atmospheric Chemistry Physics Discussions*, 13(2), pp. 5233-5278.

Emmerson, K., Carslaw, N., Carpenter, L., Heard, D., Lee, J. and Pilling, M. J. (2005) 'Urban atmospheric chemistry during the PUMA campaign 1: Comparison of modelled OH and HO_2 concentrations with measurements', *Journal of Atmospheric Chemistry* , 52(2), pp. 143-164.

Faloona, I. C., Tan, D., Lesher, R. L., Hazen, N. L., Frame, C. L., Simpas, J. B., Harder, H., Martinez, M., Di Carlo, P. and Ren, X. (2004) 'A laser-induced fluorescence instrument for detecting tropospheric OH and HO_2: Characteristics and calibration', *Journal of Atmospheric Chemistry,* 47(2), pp. 139-167.

Feiner, P. A., Brune, W. H., Miller, D. O., Zhang, L., Cohen, R. C., Romer, P. S., Goldstein, A. H., Keutsch, F. N., Skog, K. M. and Wennberg, P.O (2016) 'Testing atmospheric oxidation in an Alabama forest', *Journal of the Atmospheric Sciences*, 73(12), pp. 4699-4710.

Finlayson-Pitts, B. J. and Pitts, J. N. (1997) 'Tropospheric air pollution: ozone, airborne toxics, polycyclic aromatic hydrocarbons, and particles', *Science,* 276(5315), pp. 1045-1051.

Finlayson-Pitts, B. J. and Pitts Jr, J. N. (1999) 'Chemistry of the upper and lower atmosphere: theory, experiments, and applications'*. Academic press*.

Fuchs, H., Bohn, B., Hofzumahaus, A., Holland, F., Lu, K., Nehr, S., Rohrer, F. and Wahner, A. (2011) 'Detection of HO_2 by laser-induced fluorescence: calibration and interferences from RO_2 radicals', *Atmospheric Measurement Techniques,* 4(6), pp. 1209-1225.

Fuchs, H., Brauers, T., Dorn, H.-P., Harder, H., Haseler, R., Hofzumahaus, A., Holland, F., Kanaya, Y., Kajii, Y. and Kubistin, D. (2010) 'Formal blind intercomparison of HO_2 measurements in the atmosphere simulation chamber SAPHIR during the HO_xComp campaign'*, Atmospheric Chemistry and Physics*, 10(24), pp. 1233 – 1250.

Fuchs, H., Holland, F. and Hofzumahaus, A. J. R. o. S. I. (2008) 'Measurement of tropospheric RO_2 and HO_2 radicals by a laser-induced fluorescence instrument', *Review of Scientific Instruments*, 79(8), pp. 084104.

Fuchs, H., Novelli, A., Rolletter, M., Hofzumahaus, A., Pfannerstill, E. Y., Kessel, S., Edtbauer, A., Williams, J., Michoud, V. and Dusanter, S. (2017) 'Comparison of OH reactivity measurements in the atmospheric simulation chamber SAPHIR'*, Atmospheric Measurement Techniques*, 10(10), pp. 4023-4053.

Fuchs, H., Tan, Z., Hofzumahaus, A., Broch, S., Dorn, H.-P., Holland, F., Künstler, C., Gomm, S., Rohrer, F. and Schrade, S. (2016) 'Investigation of potential interferences in the detection of atmospheric RO_x radicals by laser-induced fluorescence under dark conditions', *Atmospheric measurement techniques,* 9(4), pp. 1431-1447.

Gao, M., Carmichael, G., Wang, Y., Saide, P., Yu, M., Xin, J., Liu, Z. and Wang, Z. (2016a) 'Modeling study of the 2010 regional haze event in the North China Plain', *Atmospheric Chemistry & Physics,* 16(3).

Gao, M., Carmichael, G. R., Saide, P. E., Lu, Z., Yu, M., Streets, D. G. and Wang, Z. (2016b) 'Response of winter fine particulate matter concentrations to emission and meteorology changes in North China', *Atmospheric Chemistry and Physics,* 16(18), pp. 11837.

George, I., Matthews, P., Whalley, L., Brooks, B., Goddard, A., Baeza-Romero, M. and Heard, D. (2013) 'Measurements of uptake coefficients for

heterogeneous loss of HO_2 onto submicron inorganic salt aerosols', 15(31), *Physical Chemistry Chemical Physics*, 15, pp. 12829-12845.

Goldstein, A. H. and Galbally, I. E. 2007. 'Known and unexplored organic constituents in the earth's atmosphere'. *ACS Publications*.

Griffith, S., Hansen, R., Dusanter, S., Michoud, V., Gilman, J., Kuster, W., Veres, P., Graus, M., Gouw, J. and Roberts, J. (2016) 'Measurements of hydroxyl and hydroperoxy radicals during CalNex-LA: Model comparisons and radical budgets', *Journal of Geophysical Research: Atmospheres,* 121(8), pp. 4211-4232.

Gurjar, B., Jain, A., Sharma, A., Agarwal, A., Gupta, P., Nagpure, A. and Lelieveld, J. (2010) 'Human health risks in megacities due to air pollution', *Atmospheric Environment,* 44(36), pp. 4606-4613.

Haggerstone, A. L., Carpenter, L., Carslaw, N. and McFiggans, G. (2005) 'Improved model predictions of HO_2 with gas to particle mass transfer rates calculated using aerosol number size distributions', *Journal of Geophysical Research: Atmospheres*, 110(D4).

Hakola, H., Hellén, H., Henriksson, M., Rinne, J., Kulmala, M. (2012) 'In situ measurements of volatile organic compounds in a boreal forest', *Atmospheric Chemistry Physics Discussions*, 12(6).

Harrison, R. M., Peak, J. D. and Collins, G. M.(1996) 'Tropospheric cycle of nitrous acid', *Journal of Geophysical Research: Atmospheres*, 101(D9), pp. 14429-14439.

He, H., Tie, X., Zhang, Q., Liu, X., Gao, Q., Li, X. and Gao, Y. (2015) 'Analysis of the causes of heavy aerosol pollution in Beijing, China: a case study with the WRF-Chem model', *Particuology,* 20, pp. 32-40.

Heard, D., Carpenter, L., Creasey, D., Hopkins, J., Lee, J., Lewis, A., Pilling, M., Seakins, P., Carslaw, N. and Emmerson, K. (2004) 'High levels of the hydroxyl radical in the winter urban troposphere', *Geophysical research letters,* 31(18).

Heard, D. E. and Pilling, M. J. (2003) 'Measurement of OH and HO_2 in the troposphere', *Chemical Reviews,* 103(12), pp. 5163-5198.

Holland, F., Hessling, M. and Hofzumahaus, A. (1995) 'In situ measurement of tropospheric OH radicals by laser-induced fluorescence—a description of the KFA instrument', *Journal of the atmospheric sciences*, 52(19), pp. 3393-3401.

Huang, R.-J., Zhang, Y., Bozzetti, C., Ho, K.-F., Cao, J.-J., Han, Y., Daellenbach, K. R., Slowik, J. G., Platt, S. M. and Canonaco, F. (2014) 'High secondary aerosol contribution to particulate pollution during haze events in China', *Nature,* 514(7521), pp. 218-222.

Ingham, T., Goddard, A., Whalley, L., Furneaux, K., Edwards, P., Seal, C., Self, D., Johnson, G., Read, K. and Lee, J. J. A. M. T. (2009) 'A flow-tube based laser-induced fluorescence instrument to measure OH reactivity in the troposphere', *Atmospheric Measurement Techniques*, 2(2), pp. 465-477.

Jacob, D. J. (2000) 'Heterogeneous chemistry and tropospheric ozone', *Atmospheric Environment,* 34(12-14), pp. 2131-2159.

Jarvis, D., Leaderer, B., Chinn, S. and Burney, P. J. T. (2005) 'Indoor nitrous acid and respiratory symptoms and lung function in adults', *Thorax*, 60(6), pp. 474-479.

Jeanneret, F., Kirchner, F., Clappier, A., Van Den Bergh, H. and Calpini, B. (2001) 'Total VOC reactivity in the planetary boundary layer: 1. Estimation by a pump and probe OH experiment', *Journal of Geophysical Research: Atmospheres*, 106(D3), pp. 3083-3093.

Jiang, F., Liu, Q., Huang, X., Wang, T., Zhuang, B. and Xie, M. (2012) 'Regional modelling of secondary organic aerosol over China using WRF/Chem', *Journal of aerosol science,* 43(1), pp. 57-73.

Jokinen, T., Sipilä, M., Richters, S., Kerminen, V. M., Paasonen, P., Stratmann, F., Worsnop, D., Kulmala, M., Ehn, M. and Herrmann, H. (2014) 'Rapid autoxidation forms highly oxidized RO_2 radicals in the atmosphere', *Angewandte Chemie International Edition,* 53(52), pp. 14596-14600.

Kalberer, M., Ammann, M., Arens, F., Gäggeler, H. and Baltensperger, U. (1999) 'Heterogeneous formation of nitrous acid (HONO) on soot aerosol particles'*, Journal of Geophysical Research: Atmospheres,* 104(D11), pp. 13825-13832.

Kanaya, Y., Cao, R., Akimoto, H., Fukuda, M., Komazaki, Y., Yokouchi, Y., Koike, M., Tanimoto, H., Takegawa, N. and Kondo, Y. (2007a) 'Urban photochemistry in central Tokyo: 1. Observed and modeled OH and HO_2 radical concentrations during the winter and summer of 2004', *Journal of Geophysical Research: Atmospheres,* 112(D21).

Kanaya, Y., Cao, R., Kato, S., Miyakawa, Y., Kajii, Y., Tanimoto, H., Yokouchi, Y., Mochida, M., Kawamura, K. and Akimoto, H. J. (2007b) 'Chemistry of OH and HO_2 radicals observed at Rishiri Island, Japan, in September 2003: Missing daytime sink of HO2 and positive nighttime correlations with monoterpenes', *Journal of Geophysical Research: Atmospheres,* 112(D11).

Kanaya, Y., Hofzumahaus, A., Dorn, H., Brauers, T., Fuchs, H., Holland, F., Rohrer, F., Bohn, B., Tillmann, R. and Wegener, R. (2012) 'Comparisons of observed and modelled OH and HO_2 concentrations during the ambient measurement period of the HOxComp field campaign', *Atmospheric Chemistry and Physics*, 12(5), pp. 2567 – 2585.

Kanaya, Y., Sadanaga, Y., Matsumoto, J., Sharma, U. K., Hirokawa, J., Kajii, Y. and Akimoto, H. J. J. o. G. R. A. (2000) 'Daytime HO_2 concentrations at

Oki Island, Japan, in summer 1998: Comparison between measurement and theory', *Journal of Geophysical Research: Atmospheres,* 105(D19), pp. 24205-24222.

Kim, S., VandenBoer, T. C., Young, C. J., Riedel, T. P., Thornton, J. A., Swarthout, B., Sive, B., Lerner, B., Gilman, J. B. and Warneke, C. J. J. o. G. R. A. (2014) 'The primary and recycling sources of OH during the NACHTT-2011 campaign: HONO as an important OH primary source in the wintertime', *Journal of Geophysical Research: Atmospheres*, 119(11), pp. 6886-6896.

Kleffmann, J. J. C. (2007) 'Daytime sources of nitrous acid (HONO) in the atmospheric boundary layer', *ChemPhysChem*, 8(8), pp. 1137-1144.

Kovacs, T., Brune, W. H., Harder, H., Martinez, M., Simpas, J., Frost, G., Williams, E., Jobson, T., Stroud, C. and Young, V.. (2003) 'Direct measurements of urban OH reactivity during Nashville SOS in summer 1999', *Journal of Environmental Monitoring*, 5(1), pp. 68-74.

Kovacs, T. A. and Brune, W.(2001) 'Total OH loss rate measurement', *Journal of Atmospheric Chemistry*, 39(2), pp. 105-122.

Kroll, J. H. and Seinfeld, J. H. (2008a) 'Chemistry of secondary organic aerosol: Formation and evolution of low-volatility organics in the atmosphere', *Atmospheric Environment,* 42(16), pp. 3593-3624.

Lamarque, J., Shindell, D. T., Josse, B., Young, P., Cionni, I., Eyring, V., Bergmann, D., Cameron-Smith, P., Collins, W. J. and Doherty, R. (2013) 'The Atmospheric Chemistry and Climate Model Intercomparison Project (ACCMIP): overview and description of models, simulations and climate diagnostics', *Geoscientific Model Development,* 6(1), pp. 179-206.

Lee, J., Whalley, L., Heard, D., Stone, D., Dunmore, R., Hamilton, J., Young, D., Allan, J., Laufs, S. and Kleffmann, J. (2015a) 'Detailed budget analysis of HONO in central London reveals a missing daytime source', *Atmospheric Chemistry and Physics Discussions,* 15(16), pp. 22097-22139.

Lee, J., Whalley, L., Heard, D., Stone, D., Dunmore, R., Hamilton, J., Young, D., Allan, J., Laufs, S. and Kleffmann, J. (2015b) 'Detailed budget analysis of HONO in central London reveals a missing daytime source', *Atmospheric Chemistry & Physics Discussions,* 15, pp. 22097-22139.

Lelieveld, J., Butler, T., Crowley, J., Dillon, T., Fischer, H., Ganzeveld, L., Harder, H., Lawrence, M., Martinez, M. and Taraborrelli, D. (2008) 'Atmospheric oxidation capacity sustained by a tropical forest', *Nature,* 452(7188), pp. 737-740.

Leong, Y., Rutter, A., Wong, H., Gutierrez, C., Junaid, M., Scheuer, E., Gong, L., Lewicki, R., Dibb, J. E. and Tittel, F (2016) 'Impact of environmental variables on the reduction of nitric acid by proxies for volatile organic compounds emitted by motor vehicles', *Atmospheric Pollution Research*, 7(2), pp. 221-227.

Li, K., Jacob, D. J., Liao, H., Shen, L., Zhang, Q. and Bates, K. H. (2019) 'Anthropogenic drivers of 2013–2017 trends in summer surface ozone in China', *Proceedings of the National Academy of Sciences,* 116(2), pp. 422-427.

Li, S., Feng, K. and Li, M. J. J. o. C. P. (2017) 'Identifying the main contributors of air pollution in Beijing', *Journal of Cleaner Production,* 163, pp. S359-S365.

Li, X., Brauers, T., Häseler, R., Bohn, B., Fuchs, H., Hofzumahaus, A., Holland, F., Lou, S., Lu, K. and Rohrer, F. (2012) 'Exploring the atmospheric chemistry of nitrous acid (HONO) at a rural site in Southern China', *Atmospheric Chemistry and Physics,* 12(3), pp. 1497-1513.

Lim, Y. B. and Ziemann, P. J. (2005) 'Products and mechanism of secondary organic aerosol formation from reactions of n-alkanes with OH radicals in the presence of NO_x', *Environmental science & technology,* 39(23), pp. 9229-9236.

Liu, F., Beames, J. M., Petit, A. S., McCoy, A. B. and Lester, M. I. (2014) 'Infrared-driven unimolecular reaction of CH_3CHOO Criegee intermediates to OH radical products', *Science,* 345(6204), pp. 1596-1598.

Loukhovitskaya, E., Bedjanian, Y., Morozov, I. and Le Bras, G. (2009) 'Laboratory study of the interaction of HO_2 radicals with the NaCl, NaBr, $MgCl_2 \cdot 6H_2O$ and sea salt surfaces', *Physical Chemistry Chemical Physics*, 11(36), pp. 7896-7905.

Lu, K., Hofzumahaus, A., Holland, F., Bohn, B., Brauers, T., Fuchs, H., Hu, M., Häseler, R., Kita, K. and Kondo, Y. (2013) 'Missing OH source in a suburban environment near Beijing: observed and modelled OH and HO_2 concentrations in summer 2006', *Atmospheric Chemistry and Physics,* 13(2), pp. 1057-1080.

Lu, K., Rohrer, F., Holland, F., Fuchs, H., Bohn, B., Brauers, T., Chang, C., Häseler, R., Hu, M. and Kita, K. (2012) 'Observation and modelling of OH and HO_2 concentrations in the Pearl River Delta 2006: a missing OH source in a VOC rich atmosphere', *Atmospheric chemistry and physics,* 12(3), pp. 1541-1569.

Ma, J., Liu, Y., Han, C., Ma, Q., Liu, C. and He, H. (2013) 'Review of heterogeneous photochemical reactions of NOy on aerosol—A possible daytime source of nitrous acid (HONO) in the atmosphere', *Journal of Environmental Sciences,* 25(2), pp. 326-334.

Ma, X., Tan, Z., Lu, K., Yang, X., Liu, Y., Li, S., Li, X., Chen, S., Novelli, A. and Cho, C. (2019) 'Winter photochemistry in Beijing: Observation and model simulation of OH and HO_2 radicals at an urban site', *Science of The Total Environment,* 685, pp. 85-95.

Mao, J., Fan, S., Jacob, D. J. and Travis, K. (2013) 'Radical loss in the atmosphere from Cu-Fe redox coupling in aerosols', *Atmos. Chem. Phys*, 13(2), pp. 509 - 519

Mao, J., Jacob, D. J., Evans, M., Olson, J., Ren, X., Brune, W. H., St Clair, T., Crounse, J., Spencer, K. and Beaver, M. (2010) 'Chemistry of hydrogen oxide radicals (HO_x) in the Arctic troposphere in spring', *Atmospheric Chemistry and Physics*, 10(13), pp. 5823 – 5838.

Mao, J., Ren, X., Zhang, L., Van Duin, D., Cohen, R., Park, J.-H., Goldstein, A., Paulot, F., Beaver, M. and Crounse, J. (2012) 'Insights into hydroxyl measurements and atmospheric oxidation in a California forest', *Atmospheric Chemistry and Physics,* 12(17), pp. 8009-8020.

Mauldin Iii, R., Berndt, T., Sipilä, M., Paasonen, P., Petäjä, T., Kim, S., Kurten, T., Stratmann, F., Kerminen, V.-M. and Kulmala, M. (2012) 'A new atmospherically relevant oxidant of sulphur dioxide', *Nature,* 488(7410), pp. 193-196.

McConnell, J., Plummer, D., Shepson, P., Hastie, D. and Niki, H. (1996) 'Modelling of ozone formation at a rural site in southern Ontario', *Atmospheric Environment*, 30, pp. 2195 – 2217.

Michoud, V., Colomb, A., Borbon, A., Miet, K., Beekmann, M., Camredon, M., Aumont, B., Perrier, S., Zapf, P. and Siour, G. (2014) 'Study of the unknown HONO daytime source at a European suburban site during the MEGAPOLI summer and winter field campaigns', *Atmospheric Chemistry and Physics,* 14(6), pp. 2805-2822.

Michoud, V., Doussin, J.-F., Colomb, A., Afif, C., Borbon, A., Camredon, M., Aumont, B., Legrand, M. and Beekmann, M. (2015) 'Strong HONO formation in a suburban site during snowy days', *Atmospheric Environment,* 116, pp. 155-158.

Michoud, V., Kukui, A., Camredon, M., Colomb, A., Borbon, A., Miet, K., Aumont, B., Beekmann, M., Durand-Jolibois, R. and Perrier, S. (2012) 'Radical budget analysis in a suburban European site during the MEGAPOLI summer field campaign', *Atmospheric Chemistry and Physics,* 12(24), pp. 11951-11974.

Moon, D. R., Taverna, G. S., Anduix Canto, C., Ingham, T., Chipperfield, M. P., Seakins, P. W., Baeza-Romero, M.-T., Heard, D.E (2018) 'Heterogeneous reaction of HO_2 with airborne TiO_2 particles and its implication for climate change mitigation strategies'*, Atmospheric Chemistry Physics,* 18(1), pp. 327-338.

Mozurkewich, M., McMurry, P. H., Gupta, A. and Calvert, J. G. (1987) 'Mass accommodation coefficient for HO_2 radicals on aqueous particles', *Journal of Geophysical Research: Atmospheres*, 92(D4), pp. 4163-4170.

Newland, M. J., Rickard, A. R., Vereecken, L., Muñoz, A., Ródenas, M. and Bloss, W. J. (2015) 'Atmospheric isoprene ozonolysis: impacts of stabilised

Criegee intermediate reactions with SO_2, H_2O and dimethyl sulfide', *Atmospheric Chemistry and Physics,* 15(16), pp. 9521-9536.

Novelli, A., Hens, K., Ernest, C. T., Kubistin, D., Regelin, E., Elste, T., Plass-Dulmer, C., Martinez, M., Lelieveld, J. and Harder, H. (2014) 'Characterisation of an inlet pre-injector laser-induced fluorescence instrument for the measurement of atmospheric hydroxyl radicals'.

Novelli, A., Hens, K., Ernest, C. T., Martinez, M., Nölscher, A., Sinha, V., Paasonen, P., Petaja, T., Sipila, M. and Elste, T. (2017) 'Estimating the atmospheric concentration of Criegee intermediates and their possible interference in a FAGE-LIF instrument', *Atmospheric Measurement Techniques*, 7(10), pp. 3413-3430.

Novelli, A., Hens, K., Tatum-Ernest, C., Martinez, M., Noelscher, A., Sinha, V., Paasonen, P., Petaja, T., Sipila, M. and Elste, T. (2015) 'Identifying Criegee intermediates as potential oxidants in the troposphere', *Atmospheric Chemistry and* Physics, 17, pp. 7807 – 7823.

Olson, J., Crawford, J., Brune, W., Mao, J., Ren, X., Fried, A., Anderson, B., Apel, E., Beaver, M., Blake, D. J. A. C. and Physics (2012) 'An analysis of fast photochemistry over high northern latitudes during spring and summer using in-situ observations from ARCTAS and TOPSE', *Atmospheric Chemistry Physics*, 12(15), pp. 6799-6825.

Parker, A., Monks, P. S., Wyche, K. P., Balzani Lööv, J. M. (2009) 'Peroxy radicals in the summer free troposphere: seasonality and potential for heterogeneous loss', *Atmospheric Chemistry Physics*, 9(6), pp. 1989-2006.

Perner, D. and Platt, U. 1979) 'Detection of nitrous acid in the atmosphere by differential optical absorption', *Geophysical Research Letters*, 6(12), pp. 917-920.

Platt, U., Allen, W. and Lowe, D. (2004) 'Hemispheric average Cl atom concentration from 13 C/12 C ratios in atmospheric methane'.

Ramaswamy, V., Boucher, O., Haigh, J., Hauglustaine, D., Haywood, J., Myhre, G., Nakajima, T., Shi, G., Solomon, S. and Betts, R. E. (2001) *Radiative forcing of climate change*: Pacific Northwest National Laboratory (PNNL), Richland, WA (US).

Remorov, R., Gershenzon, Y. M., Molina, L. and Molina, M. J. (2002) 'Kinetics and mechanism of HO_2 uptake on solid NaCl', *The Journal of Physical Chemistry*, 106(18), pp. 4558-4565.

Ren, X., Harder, H., Martinez, M., Faloona, I. C., Tan, D., Lesher, R. L., Di Carlo, P., Simpas, J. B. and Brune, W. H. (2004) 'Interference testing for atmospheric HOx measurements by laser-induced fluorescence', *Journal of atmospheric chemistry,* 47(2), pp. 169-190.

Ren, X., Harder, H., Martinez, M., Lesher, R. L., Oliger, A., Shirley, T., Adams, J., Simpas, J. B. and Brune, W. H. J. A. E. (2003a) 'HO_x concentrations and OH reactivity observations in New York City during PMTACS-NY2001', *Atmospheric Environment,* 37(26), pp. 3627-3637.

Ren, X., Harder, H., Martinez, M., Lesher, R. L., Oliger, A., Simpas, J. B., Brune, W. H., Schwab, J. J., Demerjian, K. L. and He, Y. (2003b) 'OH and HO_2 chemistry in the urban atmosphere of New York City', *Atmospheric Environment,* 37(26), pp. 3639-3651.

Ren, X., Mao, J., Brune, W. H., Cantrell, C., Mauldin Iii, R., Hornbrook, R., Kosciuch, E., Olson, J., Crawford, J. and Chen, G.(2012) 'Airborne intercomparison of HO x measurements using laser-induced fluorescence and chemical ionization mass spectrometry during ARCTAS'*, Atmospheric Measurement Techniques,* 5(8), pp. 2025-2037.

Ren, X., Van Duin, D., Cazorla, M., Chen, S., Mao, J., Zhang, L., Brune, W. H., Flynn, J. H., Grossberg, N. and Lefer, B. L. (2013) 'Atmospheric oxidation chemistry and ozone production: Results from SHARP 2009 in Houston, Texas', *Journal of Geophysical Research: Atmospheres,* 118(11), pp. 5770-5780.

Rickly, P. J. A. M. T. (2018) 'Measurements of a potential interference with laser-induced fluorescence measurements of ambient OH from the ozonolysis of biogenic alkenes', *Atmospheric Measurement Techniques,* 11(1), pp. 1-16.

Roberts, M. (2016) *UK air pollution 'linked to 40,000 early deaths a year'*: BBC News Online. Available at: http://www.bbc.co.uk/news/health-35629034 (Accessed: 08/08/2016 2017).

Saiz-Lopez, A. and von Glasow, R. (2012) 'Reactive halogen chemistry in the troposphere', *Chemical Society Reviews,* 41(19), pp. 6448-6472.

Schlosser, E., Brauers, T., Dorn, H.-P., Fuchs, H., Haseler, R., Hofzumahaus, A., Holland, F., Wahner, A., Kanaya, Y. and Kajii, Y. (2009) 'Formal blind intercomparison of OH measurements: results from the international campaign HO_xComp', *Atmospheric Chemistry and Physics*, 9(20), pp. 7923 – 7948.

Sekovski, I., Newton, A. and Dennison, W. C. (2012) 'Megacities in the coastal zone: Using a driver-pressure-state-impact-response framework to address complex environmental problems', *Estuarine, Coastal and Shelf Science,* 96, pp. 48-59.

Sinha, V., Williams, J., Crowley, J. and Lelieveld, J. (2008) 'The Comparative Reactivity Method - a new tool to measure total OH Reactivity in ambient air', *Atmospheric Chemistry and Physics*, 8, pp. 2213 – 2227.

Sommariva, R., Bloss, W. J., Brough, N., Carslaw, N., Flynn, M., Haggerstone, A.-L., Heard, D. E., Hopkins, J. R., Lee, J. D. and Lewis, A. C. (2006) 'OH and HO_2 chemistry during NAMBLEX: roles of oxygenates, halogen oxides

and heterogeneous uptake', *Atmospheric Chemistry and Physics*, 6(4), pp. 1135 – 1153.

Sommariva, R., Haggerstone, A.-L., Carpenter, L., Carslaw, N., Creasey, D., Heard, D., Lee, J., Lewis, A., Pilling, M. and Zádor, J. (2004) 'OH and HO_2 chemistry in clean marine air during SOAPEX-2', *Atmospheric Chemistry and Physics*, 4(1), pp. 419 – 470.

Stemmler, K., Ammann, M., Donders, C., Kleffmann, J. and George, C.. (2006) 'Photosensitized reduction of nitrogen dioxide on humic acid as a source of nitrous acid', *Nature*, 440(7081), pp. 195-198.

Stevens, P., Mather, J. and Brune, W. H (1994) 'Measurement of tropospheric OH and HO_2 by laser-induced fluorescence at low pressure', *Geophysical Research: Atmospheres,* 99(D2), pp. 3543-3557.

Stone, D., Evans, M., Walker, H., Ingham, T., Vaughan, S., Ouyang, B., Kennedy, O., McLeod, M., Jones, R. and Hopkins, J. (2014) 'Radical chemistry at night: comparisons between observed and modelled HOx, NO_3 and N_2O_5 during the RONOCO project', *Atmos. Chem. Phys*, 14, pp. 1299-1321.

Stone, D., Whalley, L. K. and Heard, D. E. (2012) 'Tropospheric OH and HO_2 radicals: field measurements and model comparisons', *Chemical Society Reviews,* 41(19), pp. 6348-6404.

Taketani, F., Kanaya, Y. and Akimoto, H.(2008) 'Kinetics of heterogeneous reactions of HO_2 radical at ambient concentration levels with $(NH_4)\ 2SO_4$ and NaCl aerosol particles', *The Journal of Physical Chemistry*, 112(11), pp. 2370-2377.

Tan, Z., Fuchs, H., Lu, K., Hofzumahaus, A., Bohn, B., Broch, S., Dong, H., Gomm, S., Häseler, R. and He, L. (2017) 'Radical chemistry at a rural site (Wangdu) in the North China Plain: observation and model calculations of OH, HO_2 and RO_2 radicals', *Atmospheric Chemistry and Physics,* 17(1), pp. 663-690.

Tan, Z., Rohrer, F., Lu, K., Ma, X., Bohn, B., Broch, S., Dong, H., Fuchs, H., Gkatzelis, G. I. and Hofzumahaus, A. (2018) 'Wintertime photochemistry in Beijing: observations of ROx radical concentrations in the North China Plain during the BEST-ONE campaign', *Atmospheric Chemistry and Physics,* 18(16), pp. 12391-12411.

Thornton, J. and Abbatt, J. (2005) 'Measurements of HO_2 uptake to aqueous aerosol: Mass accommodation coefficients and net reactive loss', *Journal of Geophysical Research: Atmospheres,* 110(D8).

Thornton, J. A., Kercher, J. P., Riedel, T. P., Wagner, N. L., Cozic, J., Holloway, J. S., Dubé, W. P., Wolfe, G. M., Quinn, P. K. and Middlebrook, A. M. (2010) 'A large atomic chlorine source inferred from mid-continental reactive nitrogen chemistry', *Nature,* 464(7286), pp. 271.

Valavanidis, A., Fiotakis, K. and Vlachogianni, T. (2008) 'Airborne particulate matter and human health: toxicological assessment and importance of size and composition of particles for oxidative damage and carcinogenic mechanisms', *Journal of Environmental Science and Health, Part C,* 26(4), pp. 339-362.

China tops WHO list for deadly outdoor air pollution: Guardian. Available at: https://www.theguardian.com/environment/2016/sep/27/more-than-million-died-due-air-pollution-china-one-year (Accessed: 08/08/2017 2017).

Wang, J., Wang, S., Jiang, J., Ding, A., Zheng, M., Zhao, B., Wong, D. C., Zhou, W., Zheng, G. and Wang, L. (2014) 'Impact of aerosol–meteorology interactions on fine particle pollution during China's severe haze episode in January 2013', *Environmental Research Letters,* 9(9), pp. 094002.

Welz, O., Savee, J. D., Osborn, D. L., Vasu, S. S., Percival, C. J., Shallcross, D. E. and Taatjes, C. A. (2012) 'Direct kinetic measurements of Criegee intermediate (CH_2OO) formed by reaction of CH_2I with O_2', *Science,* 335(6065), pp. 204-207.

Whalley, L., Blitz, M., Desservettaz, M., Seakins, P. and Heard, D. (2013) 'Reporting the sensitivity of laser-induced fluorescence instruments used for HO_2 detection to an interference from RO_2 radicals and introducing a novel approach that enables HO_2 and certain RO_2 types to be selectively measured', *Atmospheric Measurement Techniques,* 6(12), pp. 3425-3440.

Whalley, L., Edwards, P., Furneaux, K., Goddard, A., Ingham, T., Evans, M., Stone, D., Hopkins, J., Jones, C. E. and Karunaharan, A. (2011) 'Quantifying the magnitude of a missing hydroxyl radical source in a tropical rainforest', *Atmospheric Chemistry and Physics,* 11(14), pp. 7223-7233.

Whalley, L., Furneaux, K., Goddard, A., Lee, J. D., Mahajan, A., Oetjen, H., Read, K. A., Kaaden, N., Carpenter, L. J. and Lewis, A. (2010) 'The chemistry of OH and HO_2 radicals in the boundary layer over the tropical Atlantic Ocean', *Atmospheric Chemistry and Physics,* 10(4), pp. 1555-1576.

Whalley, L. K., Stone, D., Bandy, B., Dunmore, R., Hamilton, J. F., Hopkins, J., Lee, J. D., Lewis, A. C. and Heard, D. E. (2016) 'Atmospheric OH reactivity in central London: observations, model predictions and estimates of in situ ozone production', *Atmospheric Chemistry and Physics,* 16, pp. 2109-2122.

Whalley, L. K., Stone, D., Dunmore, R. E., Hamilton, J. F., Hopkins, J. R., Lee, J. D., Lewis, A., Williams, P., Klefmann, J., Laufs, S.(2018) 'Understanding in situ ozone production in the summertime through radical observations and modelling studies during the Clean air for London project (ClearfLo)', *Atmospheric Chemistry Physics,* pp. 2547-2571.

Wolfe, G., Thornton, J., Bouvier-Brown, N., Goldstein, A., Park, J.-H., McKay, M., Matross, D., Mao, J., Brune, W. and LaFranchi, B. (2011) 'The Chemistry

of Atmosphere-Forest Exchange (CAFE) model–part 2: application to BEARPEX-2007 observations', *Atmospheric Chemistry and Physics,* 11(3), pp. 1269-1294.

Yoshino, A., Sadanaga, Y., Watanabe, K., Kato, S., Miyakawa, Y., Matsumoto, J. and Kajii, Y. (2006) 'Measurement of total OH reactivity by laser-induced pump and probe technique—comprehensive observations in the urban atmosphere of Tokyo', *Atmospheric Environment,* 40(40), pp. 7869-7881.

Zhang, H., Wang, S., Hao, J., Wang, X., Wang, S., Chai, F. and Li, M. (2016) 'Air pollution and control action in Beijing', *Journal of Cleaner Production,* 112, pp. 1519-1527.

Zhang, Q., Streets, D. G., He, K., Wang, Y., Richter, A., Burrows, J. P., Uno, I., Jang, C. J., Chen, D. and Yao, Z. (2007) 'NOx emission trends for China, 1995–2004: The view from the ground and the view from space', *Journal of Geophysical Research: Atmospheres,* 112(D22).

Zhao, B., Wang, S., Wang, J., Fu, J. S., Liu, T., Xu, J., Fu, X. and Hao, J.(2013) 'Impact of national NOx and SO_2 control policies on particulate matter pollution in China'*, Atmospheric Environment,* 77, pp. 453-463.

2. Experimental

All the data presented in this work has been obtained using instruments housed inside the University of Leeds Atmospheric Research shipping container, which acts as a mobile laboratory and normally resides at the School of Chemistry except during fieldwork periods. The container houses several instruments for ambient measurements of OH, HO_2, RO_2 and other species including O_3, NO_x and photolysis rates. A schematic for the Leeds shipping container is shown in Figure 2.1. The majority of the container, including the roof box, is used to house the Leeds ground-based FAGE instrument. OH reactivity instrument is not shown in Figure 2.1, but was housed in the Leeds shipping container for the APHH (winter and summer) and Tibet field campaigns.

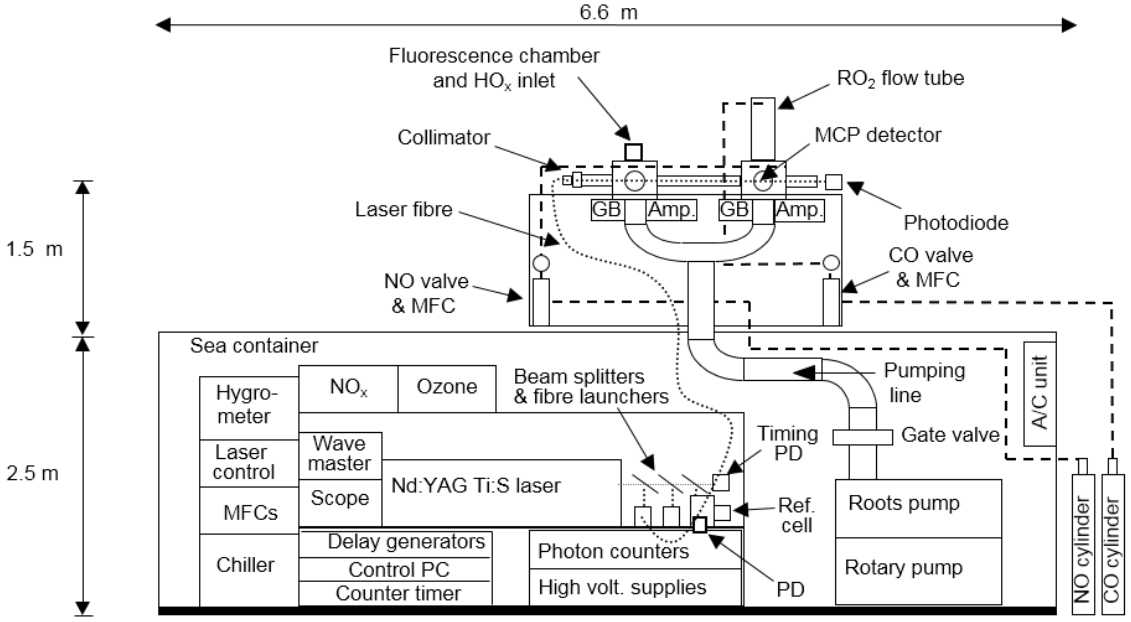

Figure 2.1 Schematic of the Leeds Atmospheric Research shipping container (not to scale), showing all key features. MFC = mass flow controller, PD = photodiode, MCP = micro-channel plate, GB = MCP gating box, Amp. = MCP signal amplifier, A/C = air conditioning.

2.1 Overview of the Leeds Ground-Based FAGE instrument

The FAGE technique was outlined in Chapter.1, the section below will describe the main principles behind the Leeds ground-based FAGE instrument. The Leeds ground-based FAGE (Whalley et al., 2010, Creasey et al., 1997) instrument has been involved in over 25 field campaigns after initially being deployed in 1996. Measurements of OH, HO_2 and more recently RO_2 have been made in various

locations including; pristine open oceans (Creasey et al., 2003, Whalley et al., 2010); rainforests (Whalley et al., 2011); Antarctica (Bloss et al., 2007) and urban environments including highly polluted megacities (Lee et al., 2016, Whalley et al., 2018).

2.1.1 Laser System

The Leeds FAGE setup uses 308 nm light to excite (v' = 0) ← (v'' = 0) transition, with fluorescence also being collected at 308 nm (on-resonance fluorescence); the schematic for the laser system is shown in Figure 2.2. The 308 nm laser light is provided by a wavelength tuneable Nd:YAG pumped Ti:Sapphire laser (Photonics Industries DS 20-532). The Nd:YAG produces ~10 W of 532 nm radiation at a pulse repetition of 5 kHz, which is used to pump a Ti:Sapphire laser which generates ~1.6 W of broadband (690 – 1000 nm) near-IR radiation. The wavelength of 924 nm is selected by changing the incident angle of an intra-cavity diffraction grating. The IR radiation is refocused into temperature-controlled (~50 ˚C) lithium triborate (LBO) and β-barium borate (BBO) non-linear optical crystals to generate 462 nm light *via* frequency doubling and finally the required 308 nm UV radiation required for OH excitation is produced *via* sum frequency 'mixing' of 462 and 924 nm light.

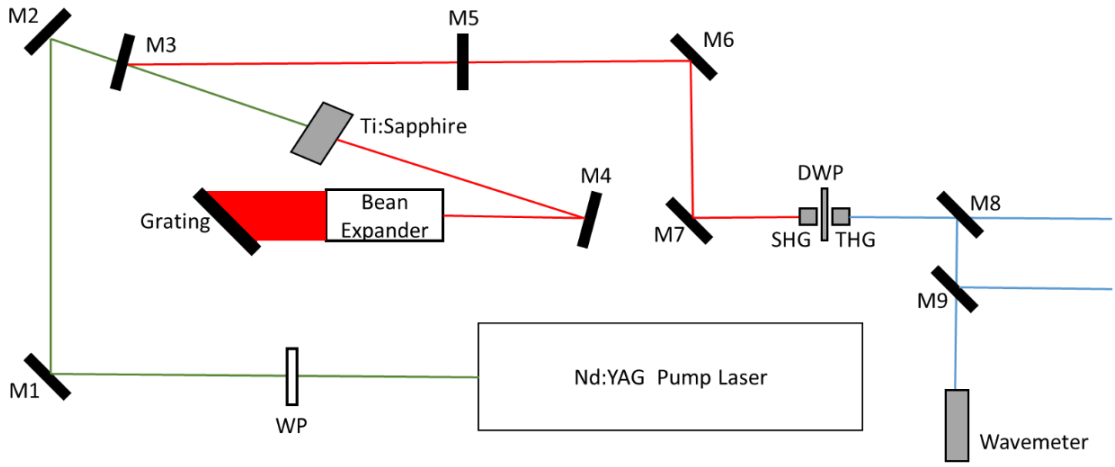

Figure 2.2 Schematic of the laser system used in the Leeds ground-based FAGE instrument. WP = half-wave plate, M = mirror, L =lens, SHG = second harmonic generation (LBO), THG = third-harmonic generation (BBO), DWP = dual-wavelength half/full-wave plate. Green represent λ = 532 nm, red presents broadband IR and λ = 924 nm and blue represents λ = 308 nm.

Typical UV power is in the range of 50 – 100 mW which is split between detection cells (HO_x, RO_x and OH reactivity) and the reference cell *via* beamsplitters and

coupled to optical fibres (Oz Optic QMMJ-55-UVVIS-200/240-3-5). Using optical fibre launchers (Elliot Gold) the laser power is split into 73.25:25:3.75 (HOx/ROx cells, OH reactivity instrument and reference cell respectively). The reference cell is used to produce a large concentration of OH *via* pyrolysis by flowing humidified air over a heated Nichrome filament into a low pressure (~2 Torr) fluorescence chamber. The wavelength is monitored from the back reflection at mirror M9 (Figure 2.2) using a wavemeter (Coherent Wavemaster 33-2650, 1 pm precision). The laser light is directed into the HO_x cell using a collimator attached to the entrance arm, the light passes through the HO_x cell into the RO_x cell via an anti-UV coated window, this results in a beam that is ~ 10 mm in the fluorescence imaging region inside the cells. The power of the laser light exiting the HO_x/RO_x is measured using UV sensitive filtered photodiodes (New Focus 2032) and a further photodiode is used to measure the position of the laser pulse in time (Timing Corr. PD).

2.1.2 Fluorescence Cells

The fluorescence cells are located on the roof of the shipping container within the aluminium roof box (Figure 2.1). The cells are held at low pressure (~1.2 – 2 Torr) which is provided by a Roots blower (Leybold RUVAC WAU 1001) backed by a rotary pump (Leybold SOGEVAC SV200), connected *via* 10 cm ID stainless steel flexible hose (length 5m). The pressure in the cells is measured using a capacitance manometer (Barotron, MKS instruments). The two cells are identical apart from the dimensions of the two inlets, the cells are 22 cm ID (in-diameter) stainless steel cylinder. The RO_x cell has been sandblasted and coated with black Teflon to reduce contributions to detector signal from scattered light.

Figure 2.3 shows a schematic of the cells. The optical rail is perpendicular to the laser axis and gas flow, the optical rail houses a spherical concave mirror and a biconvex lens. This focuses the light produced from LIF into a detection axis that passes through a bandpass filter (Barr Associates, >50% transmission at 308 nm), then is imaged using a planoconvex lenses on to the detector in this case a micro-channel plate (MCP) detectors are used (Photek OMT325).

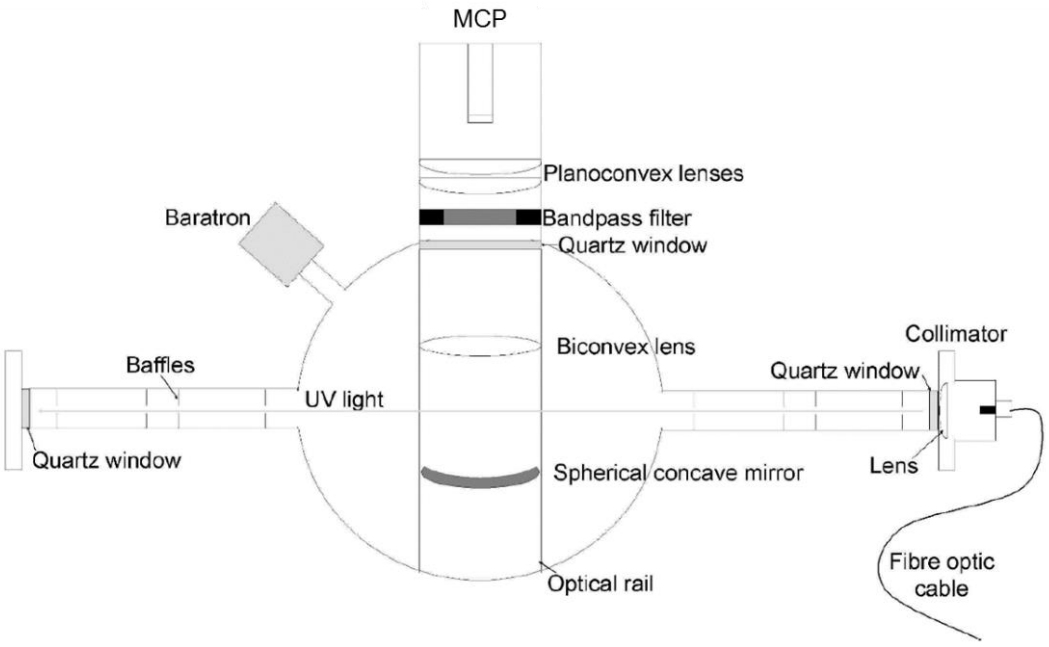

Figure 2.3 Schematic of the fluorescence cells, MCP = Micro-channel plate.

2.1.2.1 HO_x Cell

The HO_x cell (Figure 2.4) (Whalley et al., 2013) is used to make sequential measurements of OH and HO_2, with RO_2 interferences minimised (using a small flow of NO) in the HO_2 measurements. Ambient air is drawn in the fluorescence cell through a 1 mm ID pinhole on a flat stainless steel plate at ~8 slm, the plate sits on a 5 cm tall and 2.54 cm wide turret (Figure 2.4). The supersonic gas expansion results in a molecular beam which intersects the laser axis in the fluorescence imaging region.

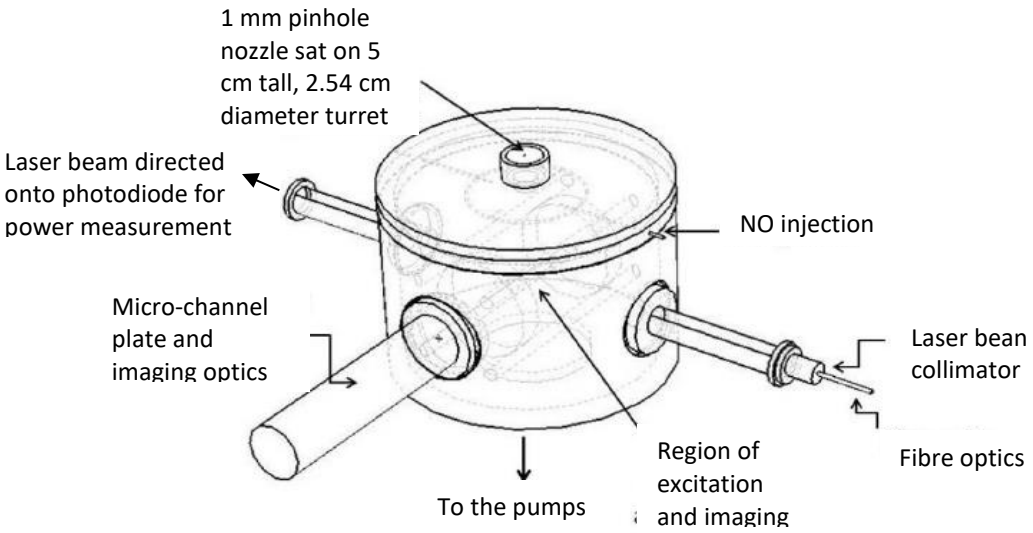

Figure 2.4 Schematic of then HOx cell design. Modified from Whalley et al.(2013).

To measure HO_2, NO (BOC, 99.95%) is injected into the centre of the cell, 7.5 cm below the pinhole, *via* a single 1.6 mm ID stainless steel injector using a solenoid valve (Metron Semiconductors). Normally 5 sccm is injected, which results in an ~8% conversion efficient from HO_2 to OH. The residence time between NO injection and OH detection is ~0.9 ms (Creasey et al., 1997)

2.1.2.2 RO_xLIF Cell

The RO_xLIF cell is used to measure HO_x (OH + HO_2^*) and RO_x (=OH + HO_2 + RO + RO_2) sequentially. The RO_xLIF cell and HO_x cell only differ by the addition of a differentially-pumped flow tube above the cell. The flow tube is 83 cm in length and 6.4 cm ID, it is constructed from aluminium and the internal walls are coated with halocarbon wax to reduce radical losses. Ambient air is drawn into the flow tube at ~7.5 slm through a 1 mm diameter pinhole, the flow tube itself is held at 30 Torr. The FAGE cells samples air at ~5 slm *via* a 4 mm diameter pinhole on a 5 cm turret from the base of the flow tube. This results in a cell pressure of ~1.5 Torr.

To measure HO_x 250 sccm of CO (BOC, 5% in N_2) enters the centre of the flow tube 2 cm below the pinhole, through a 6.4 mm ID stainless steel tubing. This results in the HO_x being partitioned into HO_2 (R2.1).

$$OH + CO + O_2 \rightarrow HO_2 + CO_2 + H_2O \qquad \text{R2.1}$$

To measure RO_x NO (BOC, 500 ppmv in N_2) is added at 30 sccm together with CO and converts the peroxy radicals into HO_2 (R2.2 - R2.3), the residence time in the flow tube of ~0.8 s ensure high conversion of OH back to HO_2.

$$RO_2 + NO \rightarrow RO + NO_2 \qquad \text{R2.2}$$

$$RO + O_2 \rightarrow R'CHO + HO_2 \qquad \text{R2.3}$$

$$HO_2 + NO \rightarrow OH + NO_2 \qquad \text{R2.4}$$

Some of the HO_2 reacts with NO to form OH (R2.4), but the OH is quickly converted back to HO_2 *via* R2.1. NO (BOC 99.95%) is continuously injected (100 sccm) into the fluorescence cell 7.5 cm below the pinhole *via* a 1.6 mm ID stainless steel injector. The NO converts the HO_2, produced from RO_2 conversion (R2.4) into OH for detection *via* LIF.

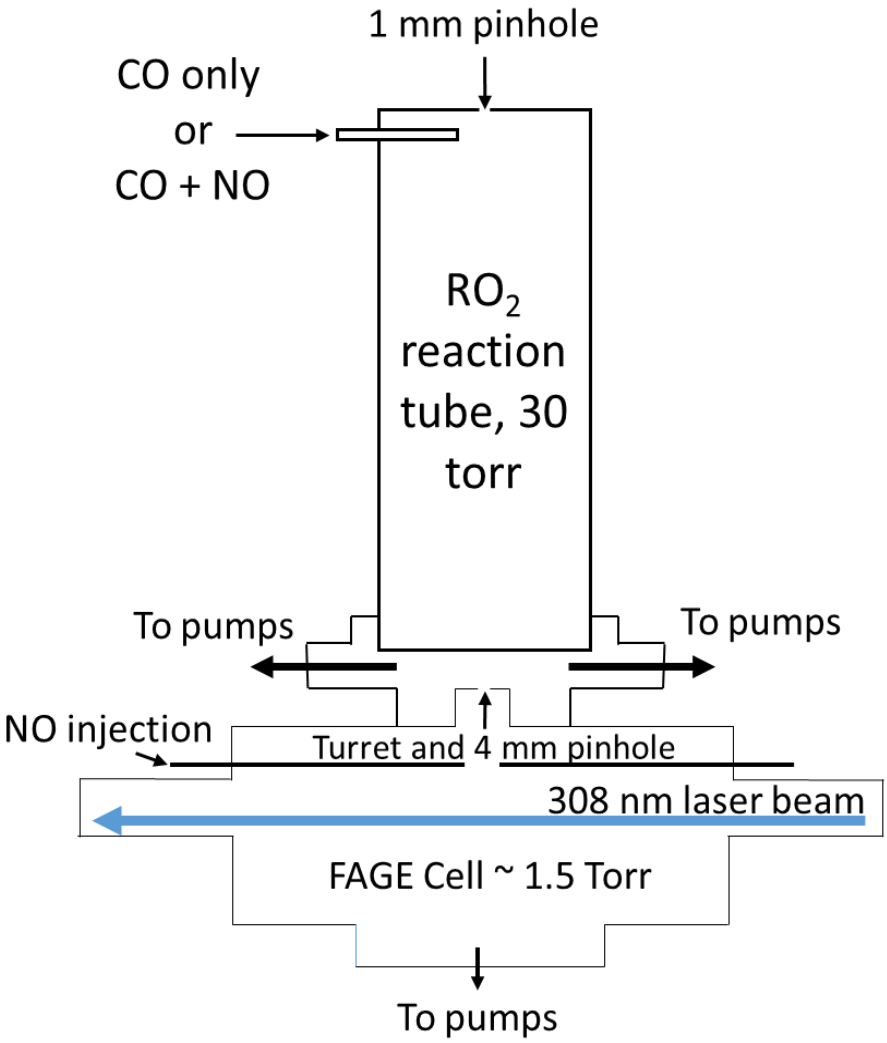

Figure 2.5 Schematic of the RO_xLIF cell design. Modified from Whalley et al (2013)

2.1.3 Photon Counting and Timing Control

Gating is used to discriminate between fluorescence and scattered light, the Leeds ground-based FAGE uses two delay generators (Stanford Research Systems SRS-DG535). See Figure 2.6 for a schematic of the photon counting and gating. The first delay generator is used to define t_0 and triggers the laser at t_0 + 5 µs, the actual temporal position of the laser pulse relative to t_0 is measured using a photodiode (Hamamatsu, S668 series) coupled with a counter timer (Agilent Technologies, 225 MHz). The temporal position of the laser is dependent upon laser power and alignment. This time (t_1 ~ 5.8-5.9 µs) measured is used to correct the temporal positions of the gating and photon counting processes to ensure the time between the laser pulse and fluorescence collection remains constant and thus ensures there is no change in the instrument sensitivity. The

second delay generator is used to control whether the MCP detectors are in low or high gain by sending signals to the gating units that control this process. The MCP is normally in a low gain state for 180 µs of the 200 µs cycle. The MCP is switched to high gain state after ~ 20 ns after the laser pulse ($\Delta t_{MCP} = t_1 + 20$ ns) for 20 µs. For the MCP detectors that were used in the APHH campaign compact gating units were used (Photek GM10-50B) and the potential held at 3900 V in the high gain state. The signal was amplified for part of the campaign using Photek PA200-10S preamplifier, 20 dB gain. The power for the MCP gating boxes (+5 V DC) and amplifiers (+12 V DC) is supplied by a home-built low noise power supply unit (PSU).

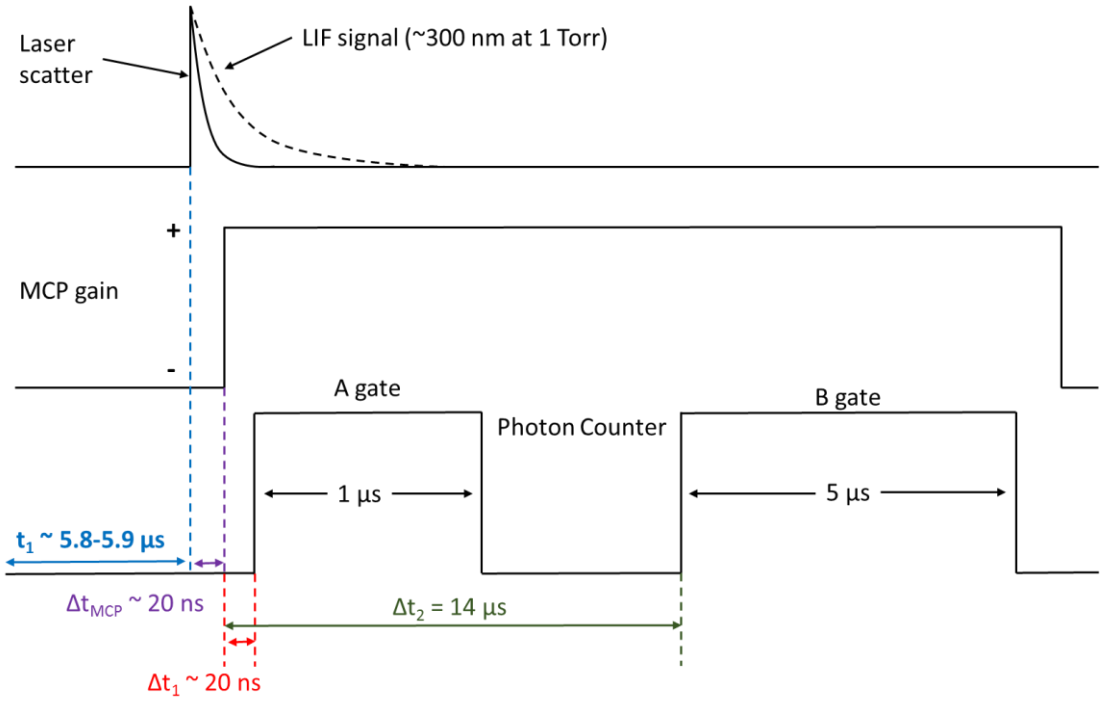

Figure 2.6 Diagram of the timings of the MCP detector gain state (middle trace) and photon counting windows (bottom) relative to t_0 and the temporal position of the laser pulse (top) during one 200 µs duty cycle. For details see text, diagram not to scale.

Following the fast decay of the scattered laser light, the photon counter (SRS SR400) measures photons (as electrical pulses) from LIF, solar, remaining laser light and dark counts from the detector for 1 µs collection window (A gate). The A gate starts 20 ns (Δt_1) after the MCP detector switches to high gain state, after 14 µs relative to MCP gain switch a 5 µs collection window (B gate) measures the solar light and dark count, by which time the fluorescence and scatter light has decayed to zero. The OH signal from fluorescence (OH_{sig}) is given by E2.1,

where A and B are the counts measured in the A and B gates, respectively and X is the ratio of the two gates (~5). This measurement is integrated over 5000 laser pulses to give the signal in count s^{-1}. A discriminator level is applied to the photon counter, so only pulses with amplitude greater than -25 mV and -5 mV are counted as photons to distinguish from electrical noise for amplified and non-amplified signal respectively.

$$OH_{sig} = A - B/X \qquad E2.1$$

2.1.4 Reference Cell and Data Acquisition Cycle

Inside the reference cell a large concentration of OH radicals is produced *via* pyrolysis by flowing humidified air over a Nichrome filament (V ~ 2-8 V, I ~ 4-8 A) into a small low pressure (~ 2 Torr) fluorescence chamber. The fluorescence is collected perpendicular to the laser axis using a CPM (Perkin Elmer 993P) in conjunction with a 308 nm bandpass filter (Barr Associates). The reference cell is used in data acquisition process to find the line and tune the laser wavelength to the peak of the Q1(2) branch of the (v' = 0) ← (v'' = 0) transition at 308 nm.

Figure 2.7 shows the overview for the acquisition cycle for the HO_x and RO_x measurements in OHwave mode. In step one (blue) the laser is scanned over 307.995 – 308.005 nm to find the peak position. The laser is then scanned back to the peak position and held constant (step 2, green) and OH and HO_2* is measured at 1 Hz for ~60 s in the HO_x and RO_x cells respectively. In step 3 (red) NO is injected and the sum of OH + HO_2 and RO_2 + HO_2^* is measured for ~ 60 s in the HO_x and RO_x cells, respectively. The wavelength is then changed to offline (~308.005 nm) and held constant to measure the offline background signal for OHwave mode (step 4, yellow). The background is typically measured for 30 s, with 15 s for OH background (NO off) and HO_2 background (NO on). The background with NO injection is sometimes higher, this is suspected to be from impurities in the NO cylinder (HONO and HNO_3) that photolyse to form excited OH.

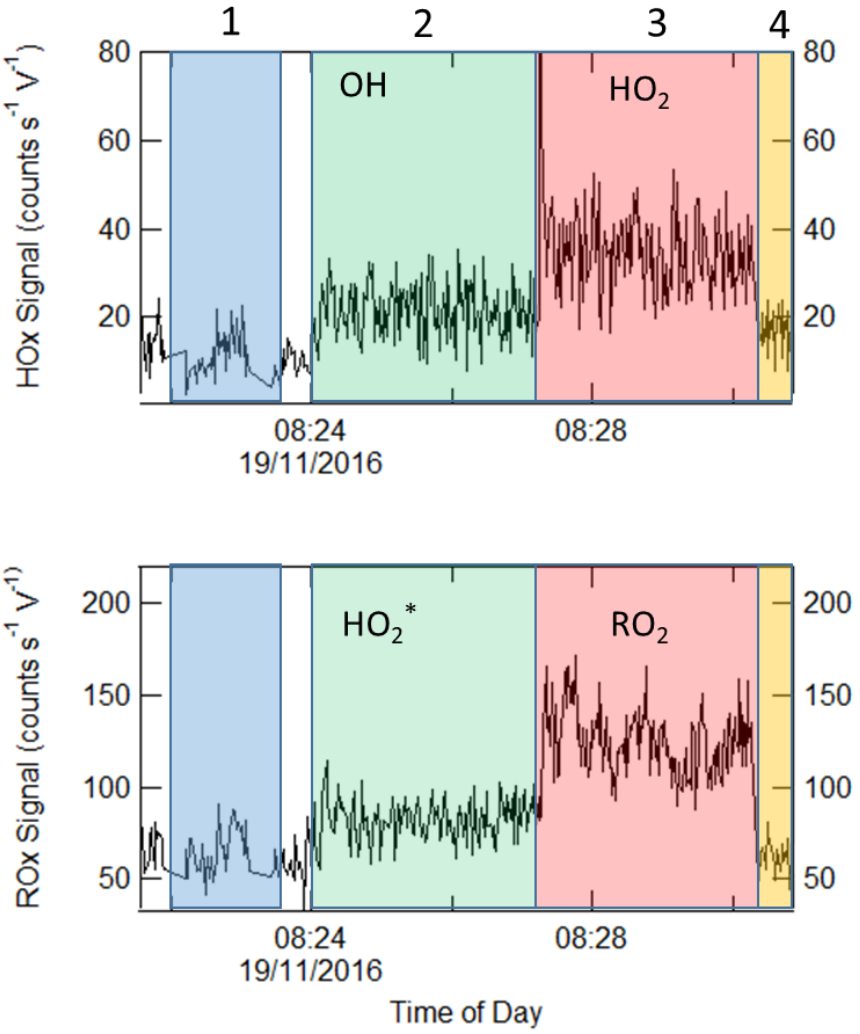

Figure 2.7 Figure showing the ambient data scan for FAGE measurement when in OHwave mode for the HO_x and RO_x cell. See text for me details.

The signal differential for OH, HO_2, HO_2^* and RO_2 (S_{OH}, S_{HO2}, S_{HO2*} and S_{RO2}) are shown in E2.2, E2.3, E2.6 and E2.7, respectively, where A and B are the counts measured in the A and B gates and X is the ratio of the two gates (~5) and I_x (X = HO_2, HO_2^* and RO_2) term accounts for the non-zero intercept for HO_2, HO_2^* and RO_2 calibrations.

$$S_{OH} = \left(A - \frac{B}{X}\right)_{online,\ NO\ off} - \left(A - \frac{B}{X}\right)_{offline,\ NO\ off} \quad \text{E2.2}$$

$$S_{HO_2} = \left(A - \frac{B}{X}\right)_{online,\ NO\ on} - \left(A - \frac{B}{X}\right)_{offline,\ NO\ on} - I_{HO_2} \quad \text{E2.3}$$

$$S_{HO2*} = \left(A - \frac{B}{X}\right)_{online,\ NO\ off} - \left(A - \frac{B}{X}\right)_{offline,\ NO\ off} - I_{HO_2^*} \quad \text{E2.4}$$

$$S_{RO2} = \left(A - \frac{B}{X}\right)_{online,\ NO\ on} - \left(A - \frac{B}{X}\right)_{offline,\ NO\ on} - I_{RO_2} \quad \text{E2.5}$$

In Figure 2.7 there is a spike in the signal after the injection of NO (step 3) which is caused by a pressure spike that increases the rate of reaction of R2.4, these points are not included in the data processing stage.

The use of the Inlet pre-injector (IPI) changes the data acquisition cycle, as shown in Figure 2.8, with the introduction of chemical modulation using propane as a scavenger to measure the OH background (step 3, purple area).

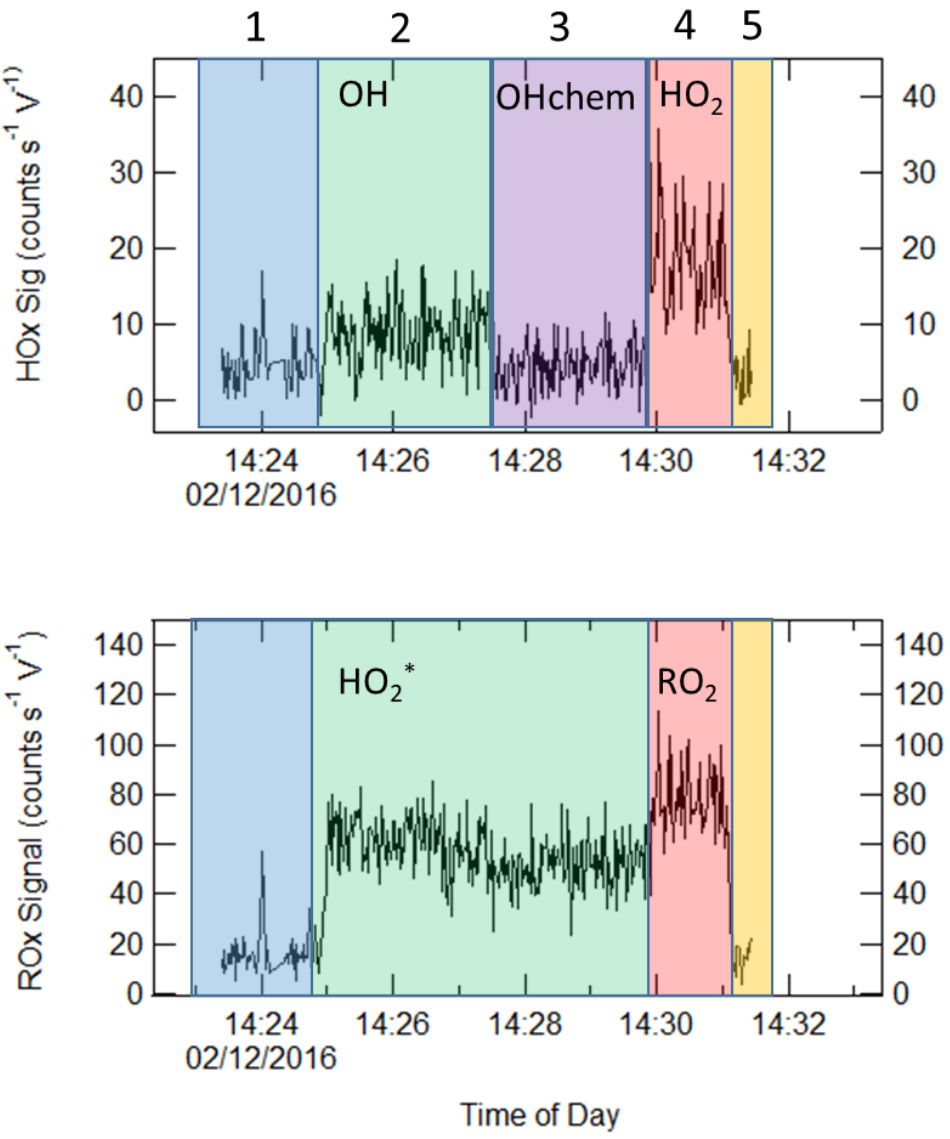

Figure 2.8 Figure showing the ambient data scan for FAGE measurement when in OHchem mode for the HO_x and RO_x cell. See text for me details.

During the OHchem period the RO_x cell continues to measure HO_2^* (green). The simultaneous measurements of the OHwave and OHchem backgrounds allow for a direct comparison between the two, and highlights whether the environment being measured introduces interferences into the FAGE measurement system.

The calculation for the signal differential for OH, HO_2, HO_2^* and RO_2 (E2.2- E2.5) is the same for both IPI and non-IPI periods (E2.2 - E2.4), except for the offline measurement is taken from the OHchem period (step 2). OHwave and OHchem can be measured simultaneously as the OHchem background is taken at the end of the data acquisition cycle (step 4).

The design for the Leeds inlet pre-injector is shown in Figure 2.9 and consists of a 4 cm, 1.9 cm ID perfluoroalkoxy (PFA) cylinder inside an aluminium housing. The scavenger was injected into the centre of the PFA flow tube, 4 cm above the FAGE inlet, *via* four 0.25 mm ID needles.

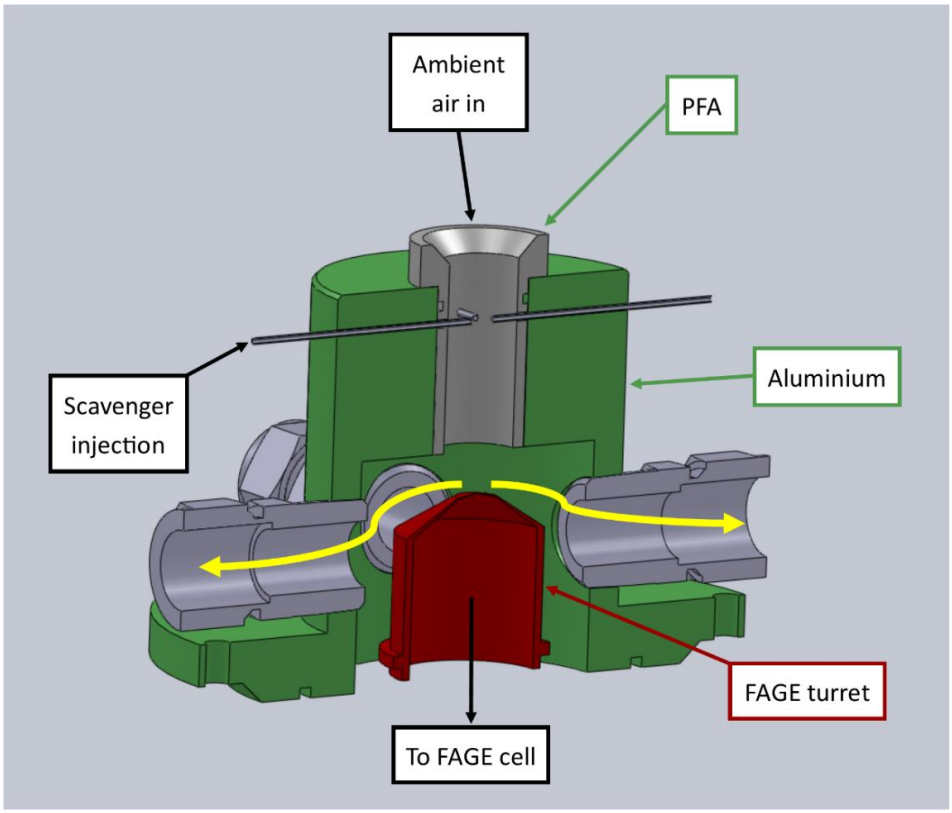

Figure 2.9 Labelled SolidWorks model of the Leeds IPI (provided by Dr Trevor Ingham). The scavenger is injected into the centre of the PFA flow tube via four 0.25 mm ID needles. The yellow arrows indicate the direction of the sheath flow. Taken from (Woodward-Massey, 2018)

Propane (BOC, research grade 99.95%, ~1100 ppmv) was used as the scavenger in this work, 5 sccm of propane was diluted in a flow of 500 sccm N_2 (BOC, 99.998%). Experimental work has shown that using the conditions stated above the inlet pre-injector has a removal efficiency for OH of ~100% and does not suffer from any internal removal of OH (OH generated within the cell)

(Woodward-Massey, 2018). Although further experimental work, see section.3.3, has shown that ~2020 ppmv results in ~38% internal removal. Experimental work has also shown that the Leeds inlet pre-injector does not suffer losses of OH on the wall of the IPI, thus no decrease in sensitivity for OH is observed when the HO_x cell is run with the inlet pre-injector.

2.1.5 FAGE Calibration

FAGE instruments can be calibrated by the addition of known concentrations of OH, HO_2 and RO_2 radicals into the inlet. The signal response to species X (X = OH, HO_2 or RO_2) is directly proportional to the concentration (E2.6).

$$S_x = C_x[X] \quad \text{E2.6}$$

C_x is the calibration factor (sensitivity of the instrument) for species X.

2.1.5.1 Radical Generation and Actinometry

2.1.5.1.1 HO_x Calibration

The radicals in the Leeds ground-based FAGE calibration are generated in a turbulent flow tube, with equal concentrations of OH and HO_2 (Fuchs et al., 2011) being made by vacuum UV photolysis of water vapour in the presence of oxygen (R2.5 and R2.6) (Stevens et al., 1994).

$$H_2O + h\nu\ (\lambda=184.9\ nm) \rightarrow H + OH \quad \text{R2.5}$$

$$H + O_2 + M \rightarrow HO_2 + M \quad \text{R2.6}$$

The flow tube is 30 cm in length, containing a square cross-section (1.27 x 1.27 cm) of black anodised aluminium tube with a Hg (Ar) pen-ray lamp (LOI LSPO35) mounted *via* a Suprasil window. The lamp is maintained a heat of ~30-40 ^oC using a resistance heater, the output of the lamp is λ = 184.9 nm.

The turbulent flow method for calibration ensures a constant radical distribution across the flow tube. This is achieved by using a fast flow (38 slm) of zero air (BOC, BTCA 178) which has been humidified using a bubbler and delivered to the wand using ¼'' perflouroalkoxy (PFA) tubing. A small portion of this flow (2 slm) is sampled by a chilled mirror dew point hygrometer (General Eastern 1311DR sensor and 4x4 Optica, range -65-20 ^oC) to measure the water concentration. The flow tube is held at 45^o to the FAGE inlet, with the inlet sampling air at the centre of the flow tube. The high flow rate (38 slm) relative to

the inlet flow ensures that no ambient air is sampled by the pinhole being "over-flowed". The HO_x concentration is varied by changing the lamp current (0 – 5 mA), which provides concentrations in the range of 5 x 10^7 to 1 x 10^9 molecule cm^{-3}. The concentrations of OH and HO_2 can be calculated using (E2.7):

$$[OH] = [HO_2] = [H_2O]\ \sigma_{H_2O,\ 184.9nm}\ \varphi_{OH}\ F_{184.9\ nm}\ t \qquad \text{E2.7}$$

where $\sigma_{H_2O,184.9nm}$ = 7.14 x 10^{-20} cm^2 $molecule^{-1}$, φ_{OH} = 1 and $[H_2O]$ is measured during the calibration (stated above). The product $F_{184.9}$ *t* is determined by chemical actinometry which relies on either the photolysis of O_2 (laminar flow method) to produce O_3 or N_2O (turbulent flow method) to produce NO, the O_3 and NO can then be measured.

The calibration constant (C_x) is determined from the plot of S_x against [X] which is shown in Figure 2.10 and Figure 2.11 for OH and HO_2, respectively. S_x has been normalised to laser power (mW) using the value of 2.1.5. f* is the relationship between the photodiode reading and laser power (E2.8).

$$f^*\left(V\ mW^{-1}\right) = \frac{PD_{cell}(V)}{P\ (mW)} \qquad \text{E2.8}$$

The calibration is shown in Figure 2.10 and Figure 2.11 was performed on the HO_x cell with the amplified MCP detector. NO is injected at ~5 sccm for the measurement of HO_2 with a conversion efficiency of ~8%.

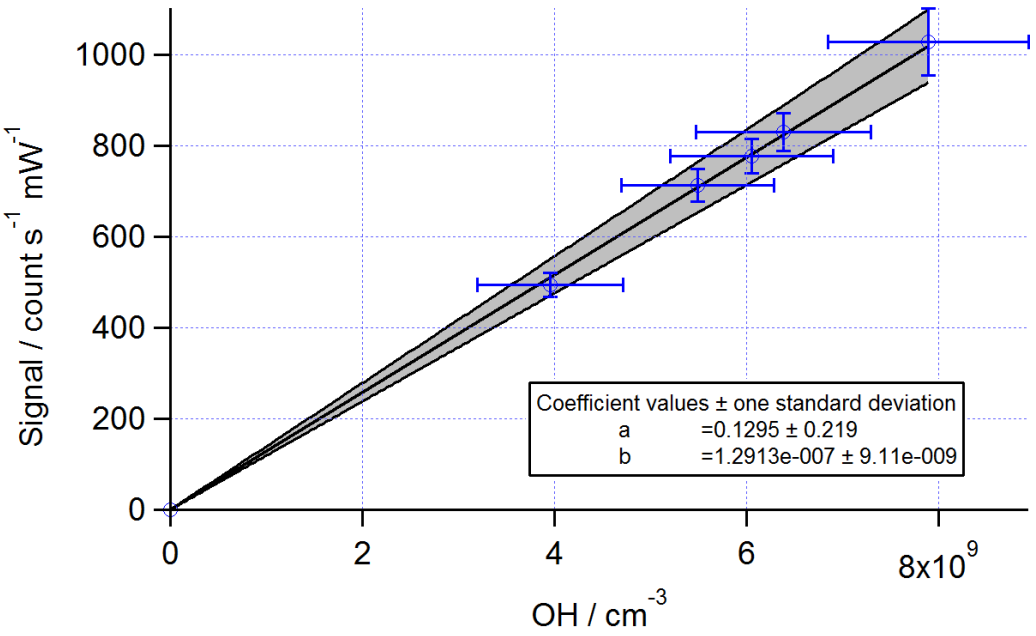

Figure 2.10 Example of OH calibration, the error bars are 1σ. The black line represents the line of best fit obtained from orthogonal distance regression (ODR), and the grey shaded area represents the 68.3% confidence interval bands. The intercept (a) and gradient (b) are in units of counts s^{-1} mW^{-1} and counts s^{-1} mW^{-1} $molecule^{-1}$ cm^3. Calibration taken during the winter AIRPRO campaign.

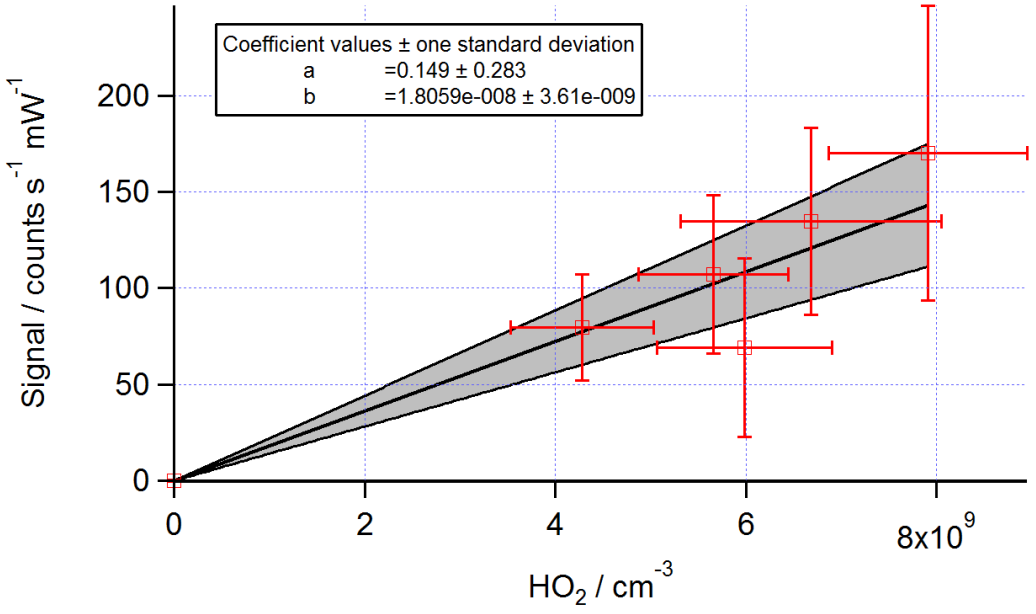

Figure 2.11 Example of HO_2 calibration, the error bars are 1σ. The black line represents the line of best fit obtained from orthogonal distance regression (ODR), and the grey shaded area represents the 68.3% confidence interval bands. The intercept (a) and gradient (b) are in units of counts s^{-1} mW^{-1} and counts s^{-1} mW^{-1} $molecule^{-1}$ cm^3. Calibration taken during the winter AIRPRO campaign.

2.1.5.1.2 RO_x Calibration

The calibration method for the RO_xLIF cell is slightly different than the HO_x calibration, an important step in the RO_xLIF calibration is quantifying the reduction in sensitivity after the addition of NO into the system which causes increased partitioning of RO_x to OH via R2.2 - R2.4, which causes increased wall losses. Equal concentrations of OH and HO_2 radicals are generated analogously to the HO_x calibrations. The flow rate is the same as that used in the HO_x calibration (38 slm) to ensure that the RO_xLIF flow tube inlet is over-flowed, the wand is also held at a ~45° angle. The radical concentration generated within the wand is calculated using E2.7, inside the flowtube the OH radicals are converted immediately into HO_2 *via* R2.1 (τ < 3 ms, compared to a residence time of ~0.8 s), making the HO_2 concentration double that calculated using E2.7. For the RO_2 calibration, a hydrocarbon is added to the flow to generate RO_2 radical (R2.7), in a typical calibration the hydrocarbon used is methane to produce CH_3O_2.

$$RH + OH + O_2 \longrightarrow RO_2 + H_2O \qquad \text{R2.7}$$

High hydrocarbon concentration used in the calibration ensures quantitative conversation of OH to RO_2, producing an RO_2 concentration equal to HO_2 concentration calculated through using equation E2.7. The typical RO_2 calibration data cycle is shown in Figure 2.12 during the APHH campaign. In the first part of the experiment no hydrocarbon is added to quantify with the addition of dilute NO (500 ppmv, 2ppmv in flow tube). During the first 30 seconds of the calibration only CO is added (250 sccm, 10% standard cylinder, 0.3% in the flow tube). The HO_2 signal (S_{HO2*}) is calculated by R2.9:

$$S_{HO2*} = S_{online,\ NO\ off} - S_{offline} \qquad \text{E2.9}$$

The subscript for the signal is HO_2* as this part of the data acquisition is used to calculated HO_2* for ambient HO_2* data. After 30 seconds dilute NO (500 ppmv, 30 sccm) is added alongside the CO for another 30 second period. The reduced signal when dilute NO is added to the flowtube is represented by S_{HO2*}(NO) and is given by R2.10:

$$S_{HO2*}(NO) = S_{online,\ NOinjected} - S_{offline} \qquad \text{E2.10}$$

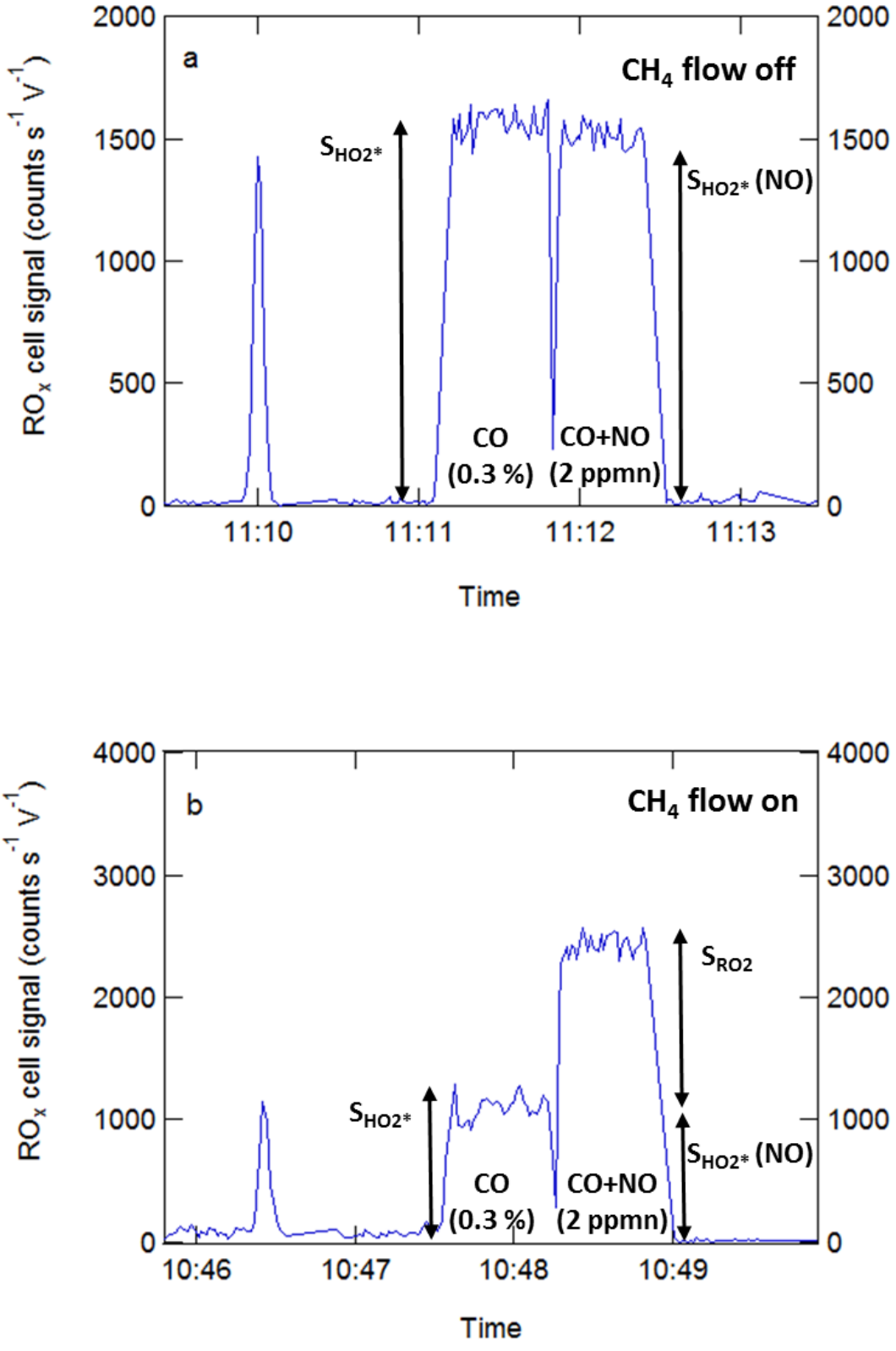

Figure 2.12 a) Shows the RO_x calibration without CH_4 showing the reduction in sensitivity from the introduction of NO. b) Shows the RO_x calibration with CH_4 and the relative signals of S_{HO2*} and S_{RO2}.

And the reduction in sensitivity is represented as the ratio, A in E2.11:

$$A = S_{HO2^*}/S_{HO2^*}(NO) \quad \text{E2.11}$$

The ratio is typically greater than 0.9, and in the example above the A factor calculated was 0.988. The average A factor for the APHH campaign was 0.98 and 0.94 for winter 2016 and summer 2017, respectively.

The second part of the RO_x calibration is shown in Figure 2.12, CH_4 (500 sccm) is added to the calibration wand flow (1.2%, τ_{OH+CH4} ~ 0.5 ms, compared to a residence time of ~7 ms in the photolysis region) to generate CH_3O_2 radicals *via* reaction R2.7. During the first 30 seconds of the calibration only CO is added, these points represented as $S_{HO2^*}(CH_4)$. Using the S_{HO2^*} and $S_{HO2^*}(CH_4)$ can be used to calculate the RO_xLIF cell sensitivity towards HO_2* (C_{HO2^*}, using E2.6). The CH_3O_2 do not undergo reaction during this time period hence not contribute to $S_{HO2^*}(CH_4)$. In the final 30 seconds of the calibration dilute NO is added into the RO_xLIF flowtube and CH_3O_2 is converted to HO_2 *via* (R2.2 - R2.3), and the presence of CO partitions HO_x into HO_2 R2.1. The signal from CH_3O_2 (S_{RO2}) is given by E2.12:

$$S_{RO2} = S_{\text{online, dNO injected}} - A \times S_{HO2^*}(CH_4) - S_{\text{offline}} \quad \text{E2.12}$$

A plot of $S_{RO2,}$ normalised to laser power, versus the calculated RO_2 concentration using E2.6, gives the calibration factor for the RO_2 (C_{RO2}). A calibration for RO_2 and HO_2^* is shown in Figure 2.13.

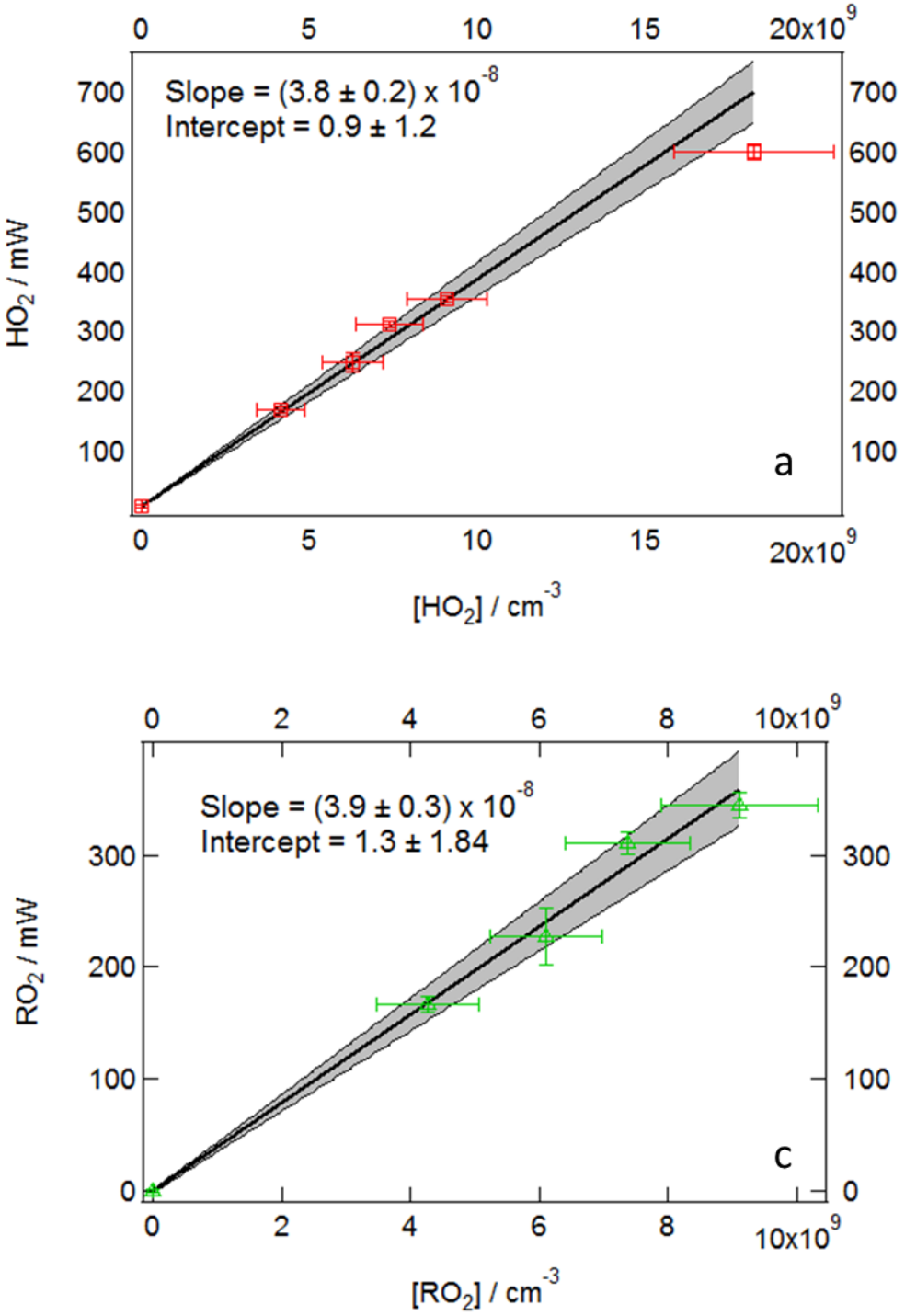

Figure 2.13 a) Example of HO_2^* calibration, the error bars are 1σ. b) Example of RO_2 calibration, the error bars are 1σ. For both, the black line represents the line of best fit obtained from orthogonal distance regression (ODR), and the grey shaded area represents the 68.3% confidence interval bands. The intercept and gradient are in units of counts s^{-1} mW^{-1} and counts s^{-1} mW^{-1} molecule^{-1} cm^3. Calibration taken during the winter AIRPRO campaign.

2.1.6 Actinometry

N_2O chemical actinometry is used to determine $F_{184.9\,nm}$, this involves measuring the NO produced from the photolysis of N_2O at different Hg lamp currents. NO is measured using a NO_x chemiluminescence instrument (Thermo Environemt Instruments Inc. 42C). Three steps are involved in chemical actinometry: (a) the MFCs must be calibrated; (b) the NO_x instrument must be calibrated as a function of N_2O concentration. This is because the NO_x instrument relies on the measurement of fluorescence from NO_2^* formed from the reaction of NO and O_3, but N_2O can collisionally quench by NO_2^* to the ground state which would lead to the underprediction of the NO concentration and (c) the NO produced from the N_2O photolysis is measured as a function of the lamp current.

Following the calibration of the NO_x box, a turbulent flow of air (40 slm) and N_2O (3.6 slm, 8.9%) is delivered to the calibration wand. The NO_x instrument samples from the centre of the wand exit. During the experiment, the lamp current is varied between ~0-7 mA. The chemistry within the flow tube is described by R2.8 - R2.13.

$$N_2O + h\nu\ (\lambda = 184.9\ nm) \rightarrow N_2 + O(^1D) \quad \text{R2.8}$$

$$O(^1D) + O_2 \xrightarrow{k_1} O(^3P) + O_2 \quad \text{R2.9}$$

$$O(^1D) + N_2 \xrightarrow{k_2} O(^3P) + N_2 \quad \text{R2.10}$$

$$O(^1D) + N_2O \xrightarrow{k_3} O(^3P) + N_2O \quad \text{R2.11}$$

$$O(^1D) + N_2O \xrightarrow{k_4} N_2 + N_2 \quad \text{R2.12}$$

$$O(^1D) + N_2O \xrightarrow{k_5} 2NO \quad \text{R2.13}$$

The rate constants for R2.9 - R2.13 is shown in Table 2.1. The quenching of O^1D by N_2O (R2.11) has a yield of less than 1% at 298 K and therefore is neglected when calculating the production of NO (Commane, 2009, Vranckx et al., 2008). The quenching of $O(^1D)$ (R2.9 and R2.10) and reaction with N_2O (R2.12) is fast enough to compete with the formation NO (R2.13), therefore the rate of production of $O(^1D)$ is given by E2.13:

$$\frac{d[O(^1D)]}{dt} = [N_2O]\ \sigma_{N_2O}^{184.9\,nm}\ \phi_{O(^1D)}\ F_{184.9\,nm} \quad \text{E2.13}$$

where $\sigma_{N_2O}^{184.9\,nm}$ = 1.43 x 10^{-19} cm^2 $molecule^{-1}$ (Sander et al., 2006) and the quantum yield of O(^{1}D), $\phi_{O(\,^1D)}$= 1 and $F_{184.9\,nm}$ is the lamp flux. E2.14 shows the expression for the lamp flux after applying the steady-state approximation for O(^{1}D), where t (~ 7.4 ms) is the photolysis exposure time, therefore $F_{184.9\,nm}$ can be calculated as a function of lamp current from the measurement of NO concentrations.

$$F_{184.9\,nm} = \frac{[NO](k_1[O_2] + k_2[N_2] + (k_4 + k_5)[N_2O]}{2tk_5\sigma_{N_2O}^{184.9\,nm}\,\phi_{O(\,^1D)}\,[N_2O]} \qquad \text{E2.14}$$

Rate Constant	Value/ cm^3 $molecule^{-1}$ s^{-1}	Value at 298 K/ cm^3 $molecule^{-1}$ s^{-1}	Reference
k_1	3.3 x $10^{-11}e^{(55/T)}$	3.95 x 10^{-11}	Sander et al.(2011)
k_2	2.15 x $10^{-11}e^{(110/T)}$	3.1 x 10^{-11}	Sander et al.(2011)
k_3	Not available	2.0 x 10^{-11}	Vranckx et al.(2008)
k_4	4.63 x $10^{-11}e^{(20/T)}$	4.95 x 10^{-11}	Sander et al.(2011)
k_5	7.25 x $10^{-11}e^{(20/T)}$	7.7 5 x 10^{-11}	Sander et al.(2011)

Table 2.1 Rate constants for quenching and reaction of O(^{1}D) in N_2O actinometry

To complete actinometry first the NO_x analyser is calibrated. The NO_x analyser uses chemiluminescence that is produced from the reaction NO and O_3 (R2.14 - R2.15):

$$NO + O_3 \rightarrow NO_2^* + O_2 \qquad \text{R2.14}$$

$$NO_2^* \rightarrow NO_2 + h\nu \qquad \text{R2.15}$$

The electronically excited NO_2* emits visible and IR light upon the relaxation to a lower state. The intensity of the light emitted is directly proportional to the concentration of NO. Although the N_2O that is used during actinometry can collisionally quench NO_2^* and reduce the intensity of emitted light for a given NO concentration. Therefore the NO_x analyser must be calibrated for sensitivity to NO and the reduction in sensitivity from the effect of N_2O. To calibrate the NO_x box variable flows of NO (BOC, 450 ± 5 ppbv in N_2) and N_2O (BOC, medical grade 98%) is mixed in 2 SLM of N_2 (BOC, 99.998%), and is flown through the calibration wand with the lamp off. For the NO_x analyser calibration shown in Figure 2.14, the NO flow was varied between 0 - 100 sccm and performed at three different concentrations of N_2O (0, 5.2 and 11%). The N_2O concentration

was achieved using flows of 0 sccm, 112 sccm and 262 sccm for 0%, 5.2% and 11%, respectively. Figure 2.14 also shows the reduction in sensitivity from the effect of N_2O.

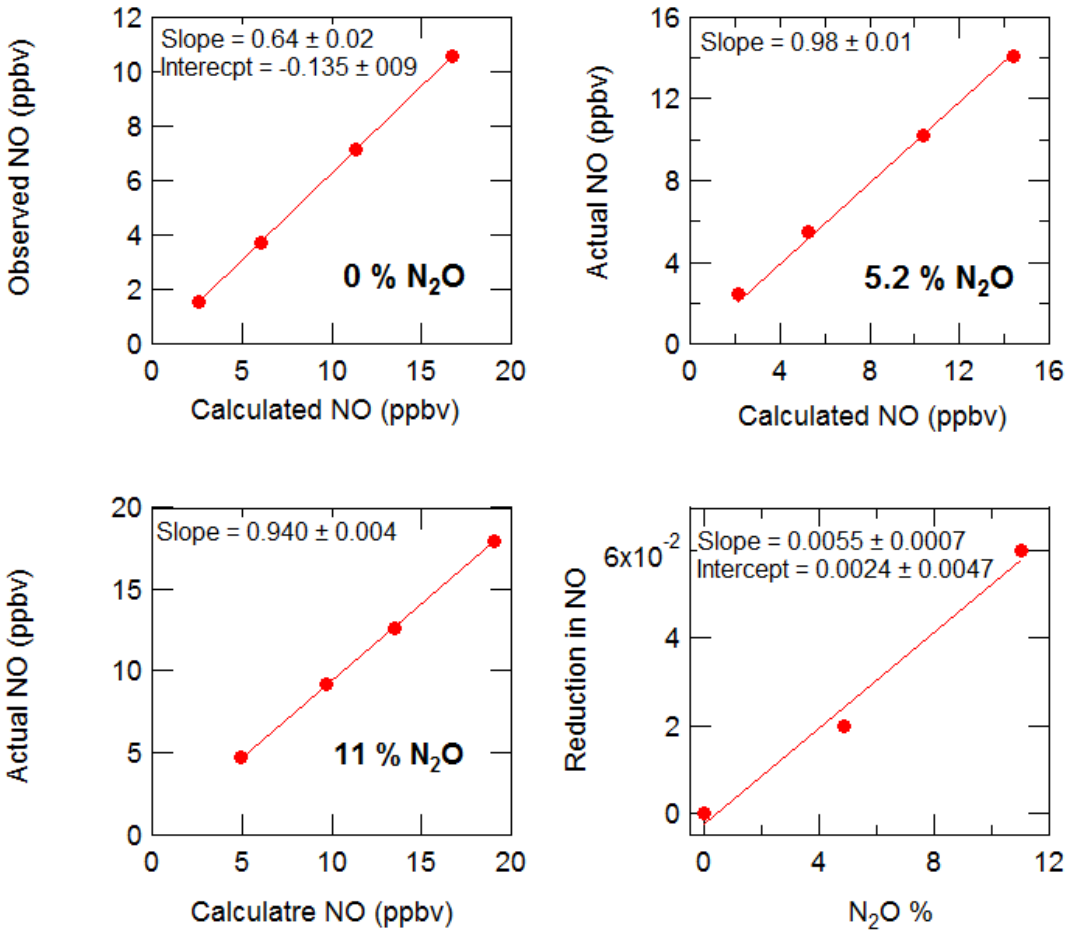

Figure 2.14 a) NO_x instrument calibrations, b) NO_x instrument calibration at 5.2% N_2O, c) NO_x instrument calibration at 11% N_2O, d) Thermo 42C instrument sensitivity to NO as a function of N_2O mixing ratio

The experimental details for N_2O actinometry are now described. A flow of 5 SLM N_2O (BOC, medical grade 98%) in 40 SLM of zero air (BOC, BTCA 178) gives a total flow rate of ~45 SLM. The flow is passed through the calibration wand where the N_2O is photolyzed using λ = 184.9 nm produce from the mercury lamp. The NO that is produced from R2.8 - R2.13 is sampled by the commercial NO_x analyser (Thermo environmental 42C) that measures the NO concentration every 5 seconds. During the actinometry experiment the lamp current is varied between 0 – 10 mW.

When calculating the lamp flux it is important to take in account the absorption of light by N_2O, O_3 and O_2. The photolysis of N_2O and O_2 leads to the production of O_3 (R2.16-R2.18):

$$N_2O + hv\ (\lambda = 184.9\ nm) \rightarrow N_2 + O(^3P) \quad \text{R2.16}$$

$$O_2 + hv \rightarrow O(^3P) + O(^3P) \quad \text{R2.17}$$

$$O(^3P) + O_2 \rightarrow O_2 + M \quad \text{R2.18}$$

N_2O, O_3 and O_2 can absorb light at λ = 184.9 nm and lead to an exponential decay of light intensity across the width of the photolysis region, therefore the lamp flux ($F_{184.9\ nm}$) that is calculated in E2.14 must be corrected to account for this absorption as N_2O is not present during the HO_x and RO_x calibration. Although it has been shown that the absorption of light by O_2 and O_3 is negligible at the concentration used in the actinometry (~10% N_2O) (Floquet, 2006). Therefore the transmittance of radiation across the tube, T, is calculated using the Beer-Lambert law (R2.13):

$$T = \frac{I}{I_O} = e^{(-\sigma_{N2O}[N_2O]l)} \quad \text{E2.15}$$

Where l is the distance across the calibration wand. The total transmittance, T_{total}, across the calibration wand (w = 1.27 cm) is found by integrating T with respect to w:

$$T_{total} = \int_0^w e^{(-\sigma_{N2O}[N_2O]l)}\, dw \quad \text{E2.16}$$

The mean transmittance, T, can be found by dividing results by w:

$$T = \frac{T_{total}}{w} = \frac{1}{w}\left(\frac{1}{\sigma_{N2O}[N_2O]} - \frac{e^{(-\sigma_{N2O}[N_2O])}}{\sigma_{N2O}[N_2O]}\right) \quad \text{E2.17}$$

The lamp flux can be corrected for the absorbance of light by N_2O dividing E2.14 by the mean transmittance (E2.18):

$$F = \frac{1}{T}\left(\frac{[NO](k_1[O_2] + k_2[N_2] + (k_4 + k_5)[N_2O]}{2tk_5\sigma_{N_2O}^{184.9\ nm}\,\phi_{O(^1D)}\,[N_2O]}\right) \quad \text{E2.18}$$

With the N_2O equal to 10% of the total flow T is calculated to be 0.8. The results for an actinometry experiment that took place in December 2018 is shown in Figure 2.15. The y error bars are calculated by propagating uncertainties in E2.18, and is summarised in Table 2.2. The error in the calculated lamp flux ~ 18% and is a reflection of the uncertainties in k_1 – k_5 (Table 2.2). The error is

the slope for Figure 2.15 is consistent with the previous estimate of the lamp flux derived using N_2O actinometry method (Commane, 2009, Walker, 2013, Furneaux, 2009, Woodward-Massey, 2018).

Parameter	Uncertainty calculation	Typical Uncertainty	Reference
Temperature		1%	
Pressure		1%	
K_1	$1.1\ x\ exp\left\|10\frac{1}{T}-\frac{1}{298}\right\|$	10%	Sander et al. (2011)
K_2	$1.1\ x\ exp\left\|20\frac{1}{T}-\frac{1}{298}\right\|$	10%	Sander et al. (2011)
K_4	$1.1\ x\ exp\left\|25\frac{1}{T}-\frac{1}{298}\right\|$	10%	Sander et al. (2011)
K_5	$1.1\ x\ exp\left\|25\frac{1}{T}-\frac{1}{298}\right\|$	10%	Sander et al. (2011)

Table 2.2 Parameters contributing to the uncertainty in the lamp flux.

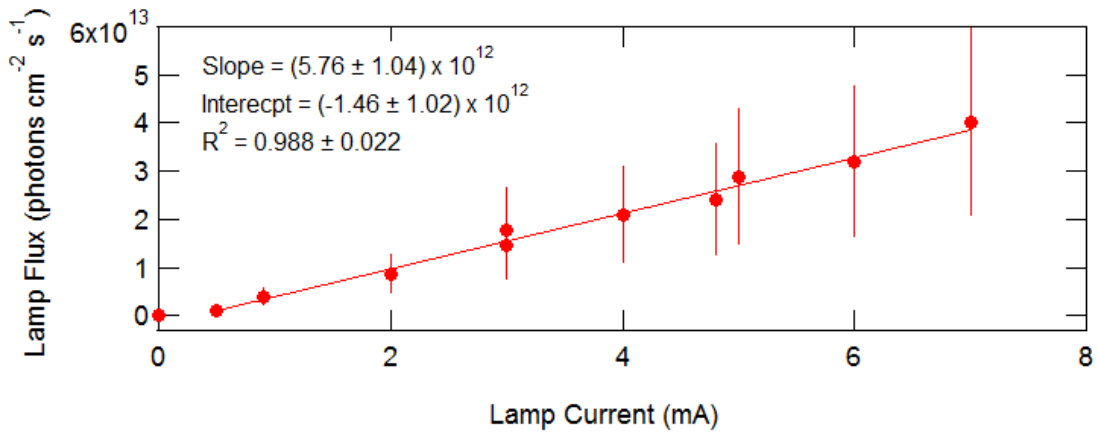

Figure 2.15 Lamp flux as a function of lamp current. The best fit line (black) for a-e obtained using a least-squares fit and (errors at 1σ).

2.1.7 Accuracy and Precision

The error in the precision of the OH (σOH) measurements is obtained by propagating the uncertainties in both the on and offline measurements (E2.19):

$$\sigma OH = \sqrt{\sigma^2_{\text{online,NO off}} + \sigma^2_{\text{offline,NO off}}} \qquad \text{E2.19}$$

The σ term in the E2.19 represents the 1σ standard deviation of the 1 s online OH data, and if Poisson statistics are assumed then $\sigma^2_{\text{offline,NO off}} = \sqrt{S_{\text{offline}}}$ and E2.19 equates E2.20:

$$\sigma\text{OH} = \sqrt{\sigma^2_{\text{online,NO off}} + S_{\text{offline}}} \quad \text{E2.20}$$

The precision error in HO_2 (σHO2) measurements are derived similarly to OH:

$$\sigma_{HO2} = \sqrt{(\sigma^2_{\text{online, NO off}} + \sigma^2_{\text{online, NO injected}} + S_{\text{offline, NO off}} + S_{\text{offline, NO injected}})} \quad \text{E2.21}$$

If there is no change in the signal when NO is injected then E2.21 equates:

$$\sigma_{HO2} = \sqrt{(\sigma^2_{\text{online, NO off}} + \sigma^2_{\text{online, NO injected}})} \quad \text{E2.22}$$

and finally, the precision in the HO_2^* and RO_2 are given by E2.23 and E2.24, respectively:

$$\sigma_{HO2*} = \sqrt{(\sigma^2_{\text{online, dNO off}} + S_{\text{offline}})} \quad \text{E2.23}$$

$$\sigma_{RO2} = \sqrt{(\sigma^2_{\text{online, dNO off}} + \sigma^2_{\text{online, dNO injected}})} \quad \text{E2.24}$$

For errors in calibration, the signal errors (y-error bars) are calculated just from the precision uncertainty at a 1σ, using E2.21, E2.22, E2.23, E2.24 for OH, HO_2, HO_2^* and RO_2, respectively. The errors in the radical concentration (x-axis error bars) are obtained from both the variability in the lamp and the uncertainty in the actinometry (18%), an example calculation for the OH radical concentration is shown in E2.25:

$$\text{OH} = \text{OH x} \sqrt{0.18^2 + (\frac{\sigma_{\text{lamp}}}{\text{lamp}})^2} \quad \text{E2.25}$$

The OH represents the OH radical concentration produced during the calibration, and the σ_{lamp} shows the 1σ standard deviation of the lamp current (mW). The error in the HO_2 and RO_2 radicals are derived in the same manner as the OH calculation. The calibration factors for OH, HO_2, HO_2^* and RO_2 are derived from the slopes of linear orthogonal distance regression (ODR), which takes into account the error in both the x and y-axis. The derived errors in the calibration

factors are not used during the ambient data work-up, but aids in comparison with previous calibrations.

2.1.8 Limit of Detection

The limit of detection (LOD) for the measurement of radical X (X = OH, HO_2, HO_2^* and RO_2), is given by E2.26:

$$[X]_{LOD} = \frac{SNR}{C_x LP}\sqrt{\frac{S_{offline}}{t}\left(\frac{1}{m}+\frac{1}{n}\right)} \qquad \text{E2.26}$$

Where SNR represent the signal-to-noise ratio, C_x is the instrument sensitivity to species X, LP is the laser power(mW), t(= 1 s) is the measurement periods, and m and n are the number of on- and offline points (duration of t), respectively. According to Poisson statistics, $S_{offline}$ is equivalent to the square of the standard deviation of the background signal ($\sigma^2_{offline}$), and is given by:

$$S_{offline} = S_{lb} + S_{sb} + S_{dc} = \sigma^2_{offline} \qquad \text{E2.27}$$

where S_{lb}, S_{sb} and S_{dc} are the contributions to the total background signal ($S_{offline}$, counts s^{-1}) from laser scatter, solar scatter and detector dark counts, respectively.

The median campaign LOD and sensitivities for OH, HO_2 and RO_2 for ClearfLo, APHH and ICOZA is shown in Table 2.3. In general the LOD between APHH, ICOZA and ClearfLo for OH and HO_2 is consistent despite the low ICOZA calibration factors. The low calibration factors during ICOZA is offset by higher laser power compared to AIRPRO and ClearfLo. The improvement in LOD for OH and HO_2 between the ClearfLo campaign and ICOZA is attributed to the use of MCPs rather than CPM detectors during ICOZA. MCPs have faster electronic switching and reduced after-pulsing effects that leads to lower background and increased sensitivities. The APHH winter campaign has a lower RO_2 calibration factor compared with the summer campaign, this is caused by changing to a better MCP on the RO_x cell in between the two campaigns. The ICOZA campaign has a much higher LOD for RO_2 and this comes from a combination of low RO_2 sensitivity but also changing between CPMs and MCPs frequently during the ICOZA campaign (Woodward-Massey, 2018).

Field Campaign	LP (mW)	C_{OH} (10^{-7})	$[OH]_{LOD}$ (10^5 cm^{-3})	C_{HO2} (10^{-8})	$[HO_2]_{LOD}$ (10^6 cm^3)	C_{RO2} (10^{-8})	$[RO_2]_{LOD}$ (10^6 cm^3)
APHH Winter	11	1.38	7.7	1.96	5.6	1.16	5.0
APHH Summer	11	1.37	6.9	3.61	2.8	3.2	8.4
ICOZA (Woodward-Massey, 2018)	16	0.53	6.1	0.89	4.0	0.51	50
ClearfLo (Whalley et al., 2018)	13		9.0		4.2		14

Table 2.3 A table showing the average laser power, calibration factor for OH, HO_2 and RO_2 (C_{OH}, C_{HO2} and C_{RO2}, respectively) and the LOD for OH, HO_2 and RO_2 ($[OH]_{LOD}$, $[HO_2]_{LOD}$ and $[RO_2]_{LOD}$, respectively) for the ClearfLo, ICOZA and APHH (winter and summer). LP = laser power, units for C_x is counts s^{-1} mW^{-1}.

2.1.8 RO_2 Speciation and Ambient Data Workup

The Leeds ground-based FAGE instrument can make measurements of OH, HO_2 and total organic peroxy radical concentration (RO_2). The RO_2 measurement can be speciated into different simple and complex RO_2 species, simple referring to small (C1-C3) alkane–derived RO_2 and the complex refers to alkene-, aromatic- and large (≥C_4) alkane derived RO_2 species. Simple RO_2 species are converted to alkoxy radicals through the addition of NO (R2.19)

$$RO_2 + NO \rightarrow RO + NO_2 \quad \text{R2.19}$$

$$RO + O_2 \rightarrow R' = O + HO_2 \quad \text{R2.20}$$

$$HO_2 + NO \rightarrow OH + NO_2 \quad \text{R2.21}$$

However, the reaction of the alkoxy radical and oxygen (R2.20) to is too slow at the lower pressure (~1.5 Torr) inside the FAGE on the timescale between the injection of the NO and the LIF detection to proceed efficiently. For complex RO_2 species, the propagation of RO_2 to HO_2 to OH is fast enough to allow for OH formation on the timescale of the NO injection. The mechanism for the fast formation of HO_2 from complex RO_2 species is shown in Figure 2.16 for ethene and butane derived RO_2 species. The key step is the formation of β- and δ-hydroxyalkoxy radicals, which undergo fast unimolecular decomposition and/or reaction with O_2 to generate HO_2.

Speciation of RO_2 radicals is achieved through the use of different NO flows in the HO_x and RO_x cell, as reported by Whalley et al. (2013). In the HO_x cell a low flow of NO (5 sccm, ~3×10^{13} molecule cm^{-3} at 1.5 Torr) is used to convert HO_2 into OH, suppressing the interference in the HO_2 measurement from complex RO_2 species. Whilst in the RO_x cell the interference from complex RO_2 species is maximised from an injection of a high concentration of NO (100 sccm, ~1×10^{15} molecule cm^{-3}). Determining the ambient concentrations of OH and HO_2 is relatively straightforward using E2.2 and E2.3, and then the signal calculated can be converted into concentration using calibrations factors (on field campaigns calibrations occur every 3-4 days). The determination of total organic peroxy radical concentration ($\sum RO_2$), and ($\sum RO_2$) speciation in simple and complex RO_2 involves more steps. The S_{HO2*} now includes the measurement of complex RO_2 and HO_2. S_{HO2*} can be converted into $[HO_2^*]$ using C_{HO2*}. The difference between $[HO_2]$ and $[HO_2^*]$ is proportional to the concentration of interfering RO_2 species, $[RO_2]_i$:

$$[HO_2^*] = [HO_2] + \Sigma_i \left(\alpha^i_{RO2} \times [RO_2]_i\right) \qquad \text{E2.28}$$

Where α^i_{RO2} is the conversion efficiency of different complex RO_2 species into OH, the conversion efficiency is dependent on different experimental conditions (i.e. residency time between NO injection and OH detection, [NO] and temperature). The α^i_{RO2} for various RO_2 species was explored by Whalley et al. (2013), α^i_{RO2} varied from 0.947 to 0.606 for ethane- and cyclohexane- derived RO_2, respectively. The conditions used by Whalley et al. (2013) are similar to the ones used in this work. The experimental OH yields for different RO_2 species are in good agreement with those that are predicted by the MCM (v3.2), which suggests that α^i_{RO2} can be modelled instead of being determined in the laboratory. Since further speciation of complex RO_2 species in ROxLIF cannot be achieved the RO_2 concentration determined here is the total concentration of complex RO_2 species, $[cRO_2]$ can be derived using the equation below:

$$[HO_2^*] = [HO_2] + \alpha^{avg}_{RO2} \times [cRO_2] \qquad \text{E2.29}$$

In Figure 2.17, S_{RO2} represents the signal from simple RO_2 species (alkanes C1 - C3), but first must be correct for the decrease in sensitivity (A_{NO}) when NO added, A_{NO} is determined during calibrations (see Section.2.4.1.2). The total

concentration of simple RO_2 species, [sRO_2], can be determined from C_{RO2}, [$\sum RO_2$] and [cRO_2]:

$$\Sigma[RO_2] = [sRO_2] + [cRO_2] \qquad \text{E2.30}$$

The uncertainty in complex RO_2 measurement is calculated by summing in quadrature the error of HO_2 and HO_2^*, and similarly the uncertainty in total RO_2 from the errors in both simple and complex RO_2 species.

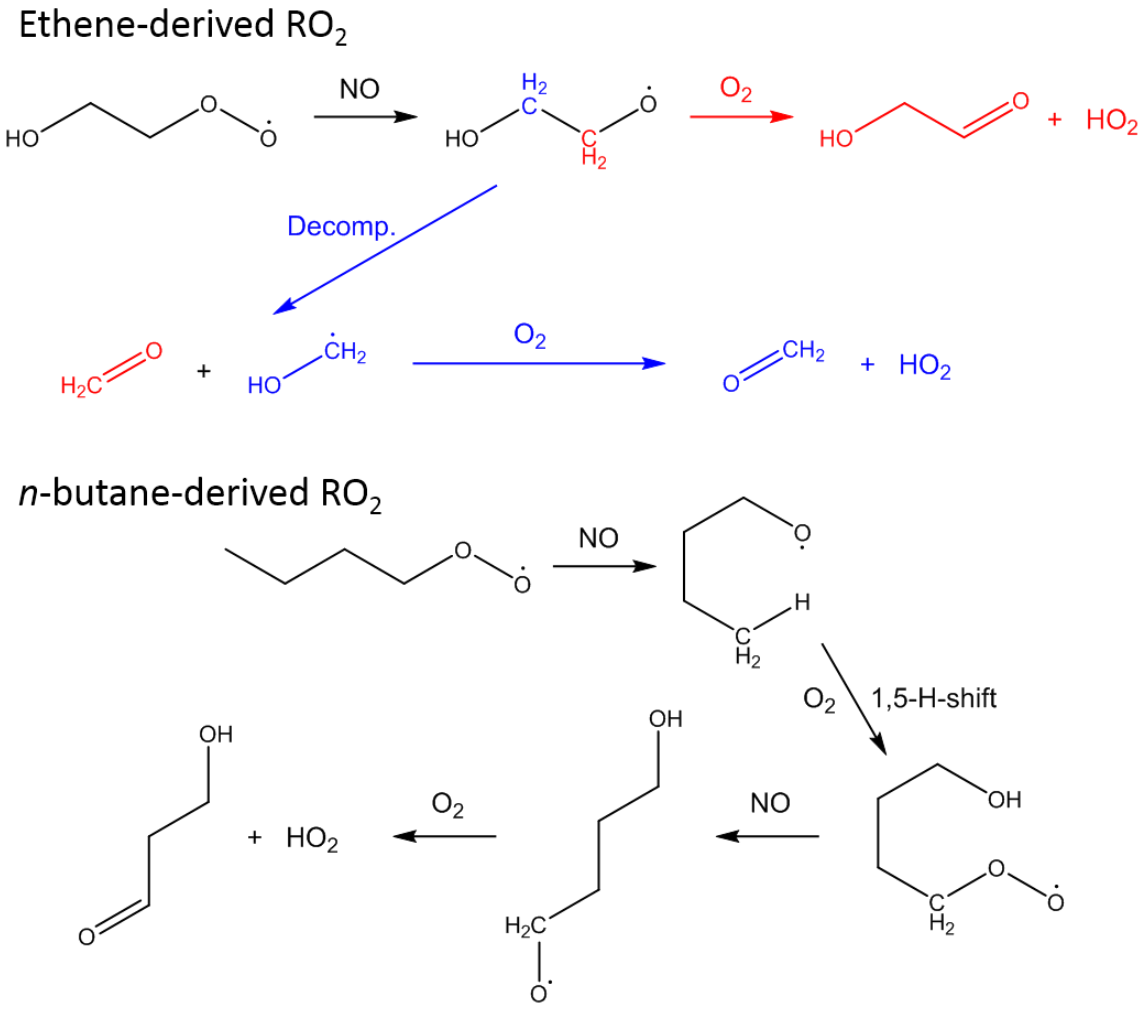

Figure 2.16 Top – Reaction of a ethane derived RO_2 with NO for the fast formation of HO_2. Bottom - Reaction of a n-butane derived RO_2 with NO for the fast formation of HO_2. Taken from (Woodward-Massey, 2018).

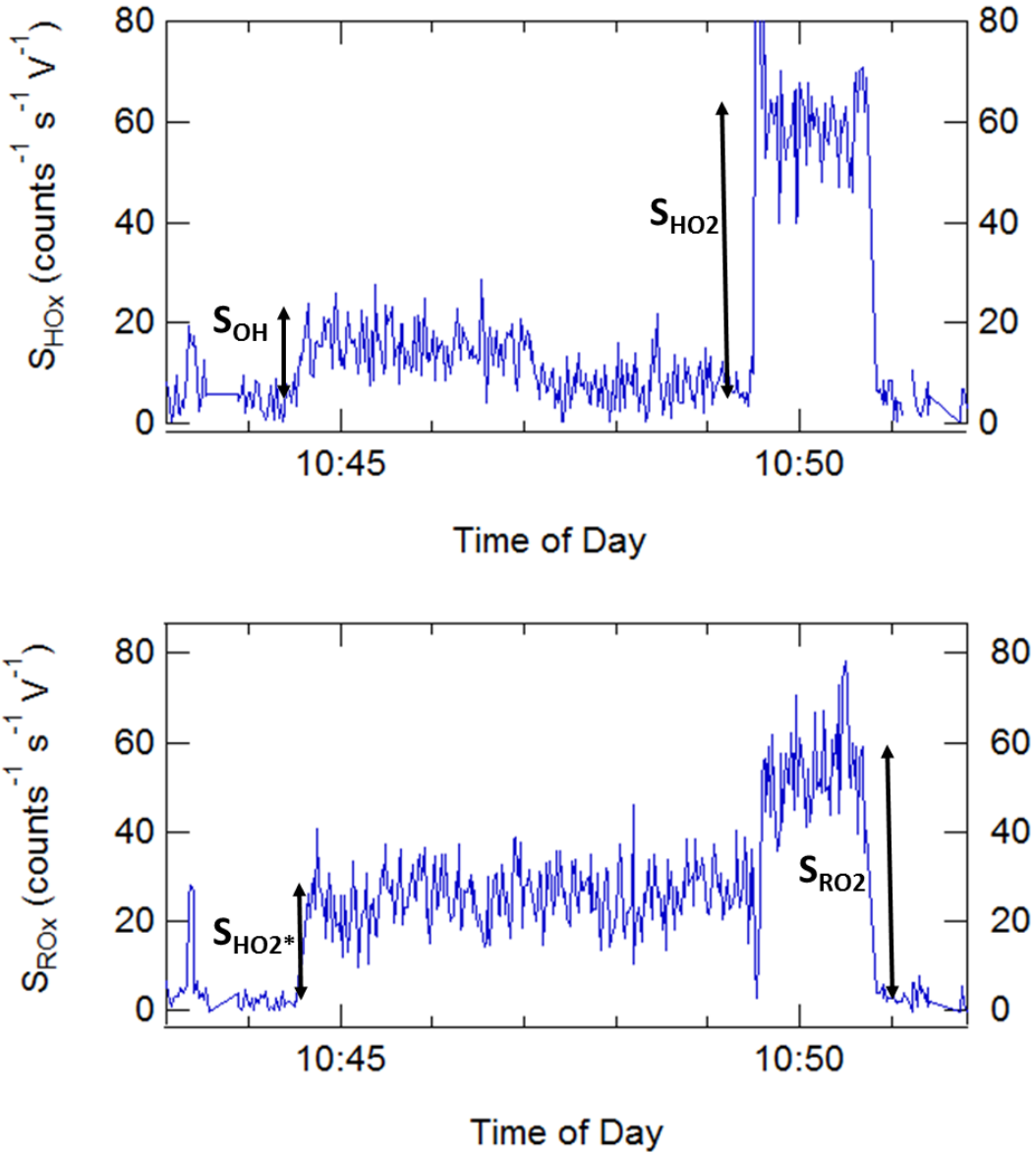

Figure 2.17 Ambient cycle for the HO_x and RO_x cells showing the signal contribution from OH, HO_2, HO_2^* and RO_2.

2.2 Laser Flash Photolysis-LIF Total OH Reactivity

The Leeds shipping container also houses an instrument that can measure total OH reactivity (*k*(OH)). It is difficult to measure the concentration of all species that account for OH loss in the atmosphere. But total OH reactivity, *k*(OH), can be measured instead. The measured *k*(OH) can be compared to the model OH loss to give an insight into the missing reactivity. The missing reactivity comes from unmeasured VOCs that contribute to OH reactivity. The Leeds instrument uses the laser flash photolysis pump and probe technique (Jeanneret et al., 2001,

Sadanaga et al., 2004) which also relies on LIF, but here the OH is produced from the 266 nm laser photolysis pump of O_3 (R2.22 - R2.23).

$$O_3 + hv(\lambda \leq 336\ nm) \rightarrow O(^1D) + O_2 \qquad \text{R2.22}$$

$$O(^1D) + H_2O \rightarrow 2OH \qquad \text{R2.23}$$

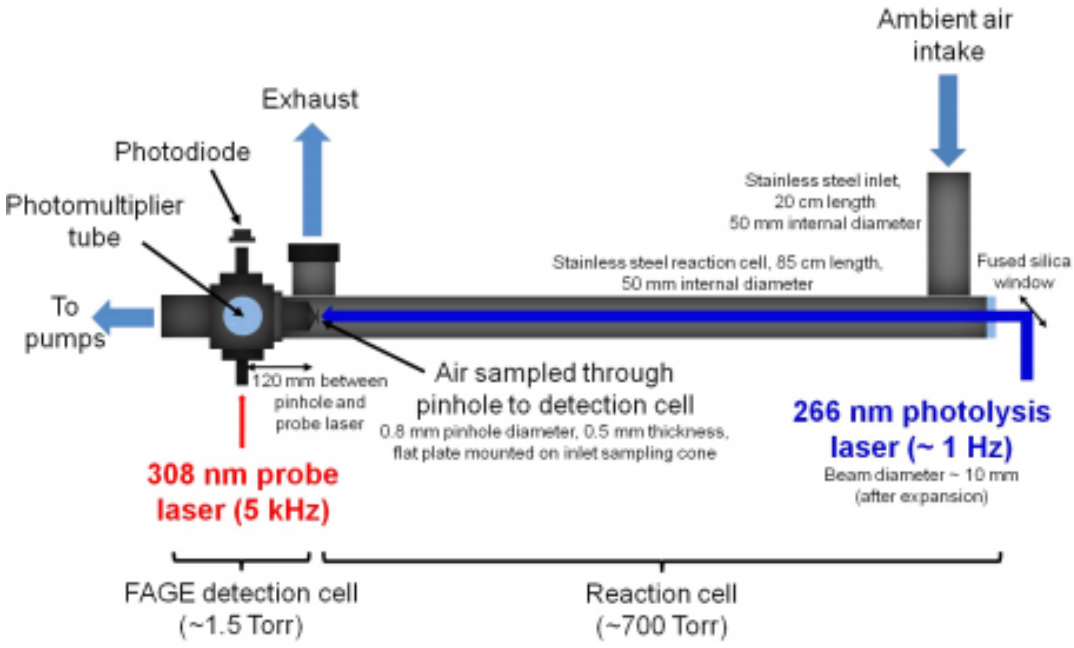

Figure 2. 18 Schematic of the laser flash photolysis laser-induced fluorescence OH reactivity. Figure copied from Stone et al.(2016).

The instrument consists of a reaction cell of cylindrical stainless steel that is 50 mm internal diameter and 85 cm in length. During the APHH the OH reactivity instrument was positioned on the roof of the laser rack (see Figure 2.1). The reaction cell is coupled to a low-pressure fluorescence cell that is held at 2 Torr, the pressure is achieved using the same pump as the FAGE instrument. The reaction cell samples ~16 slm of ambient air through ½" PFA using a vacuum pump (Agilent Technologies IDP-3 Dry Scroll Pump). The sample line for the OH reactivity instrument is positioned close to the FAGE inlets. OH radicals are produced in the reaction cell by the photolysis of O_3 (R2.22-R2.23) at 266 nm (Big Sky Laser CFR 200, Quantel USA) in the presence of H_2O vapour. The OH decay is observed in real-time by laser induced fluorescence using a probe light at 308 nm. The 308 nm probe light is generated using the same laser system as the FAGE instrument (see section.2.1.1) The first-order exponential decay of OH can be fitted to calculated the OH reactivity. Due to the OH reactivity instrument using the same laser system as the FAGE instrument, *k*(OH) can only be

measured when the FAGE instrument is online (308 nm). Full details on the OH reactivity instrument can be found at (Cryer, 2016, Stone et al., 2016)

2.3 HCHO LIF Instrument

HCHO was also measured during both of the APHH campaign using a LIF instrument developed in Leeds. During the APHH the HCHO was housed in a different shipping container to the FAGE and OH reactivity instrument. The instrument uses a pulsed (300 kHz) tuneable fibre laser (TFL2000, NOvawave) to generate UV radiation at 353.370 nm to excite HCHO $5_{0,5} \leftarrow 5_{1,4}$ rotational transition of the 4 $A^1A_2 \leftarrow X^1A_1$ vibronic band. The gas is sampled at low pressure (110 – 120 Torr) and the broadband fluorescence is collected at red-shifted wavelengths (λ ~ 390 – 550 nm). The fluorescence produced is detected using a PMT (Sens-Tech P25PC photodetector module) and the signal is recorded by a gated photon counter (PMS40A). Similar to the FAGE method the background is collected by moving the laser wavelength to an offline position (λ = 353.360 nm). Full details of the Leeds HCHO instrument can be found in Cryer (2016).

2.4 Auxiliary Measurements

A spectral radiometer (Bohn et al., 2016) was used to measure the photolysis rates of several species including $O(^1D)$, NO_2, H_2O_2, HONO and $ClNO_2$. $j(O^1D)$ was also measured using a filter radiometer (Bohn et al., 2016). A wireless weather station (Davis Vantage Vue) is used to collect meteorological data: temperature, humidity, wind speed and direction, pressure and rainfall. The met station is normally situated on the roof of the container.

2.5 References

Bloss, W., Lee, J., Heard, D., Salmon, R. A., Bauguitte, S.-B., Roscoe, H. and Jones, A. (2007) 'Observations of OH and HO_2 radicals in coastal Antarctica', *Atmospheric Chemistry and Physics,* 7(16), pp. 4171-4185.

Bohn, B., Heard, D. E., Mihalopoulos, N., Plass-Dülmer, C., Schmitt, R. and Whalley, L. K. (2016) 'Characterisation and improvement of $j(O^1D)$ filter radiometers', *Atmospheric Measurement Techniques,* 9(7), pp. 3455-3466.

Commane, R. (2009) 'Understanding radical chemistry throughout the troposphere using laser-induced fluoresence spectroscopy', *PhD Thesis,* University of Leeds.

Creasey, D., Evans, G., Heard, D. and Lee, J. (2003) 'Measurements of OH and HO_2 concentrations in the Southern Ocean marine boundary layer', *Journal of Geophysical Research: Atmospheres,* 108(D15).

Creasey, D. J., Halford-Maw, P. A., Heard, D. E., Pilling, M. J. and Whitaker, B. J. (1997) 'Implementation and initial deployment of a field instrument for measurement of OH and HO_2 in the troposphere by laser-induced fluorescence', *Journal of the Chemical Society, Faraday Transactions,* 93(16), pp. 2907-2913.

Cryer, D. (2016) Measurements of hydroxyl radical reactivity and formaldehyde in the atmosphere*. PhD Thesis,* University of Leeds.

Floquet, C. (2006), '*Airborne Measurements of Hydroxyl Radical by Fluorescence assay by Gas Expansion'. PhD Thesis,* University of Leeds.

Fuchs, H., Bohn, B., Hofzumahaus, A., Holland, F., Lu, K., Nehr, S., Rohrer, F. and Wahner, A. (2011) 'Detection of HO_2 by laser-induced fluorescence: calibration and interferences from RO_2 radicals', *Atmospheric Measurement Techniques,* 4(6), pp. 1209-1225.

Furneaux, K. (2009),' Field studies of the Chemistry of Free-Radicals in the troposphere using Laser Induced Fluorescence Spectroscopy'*.PhD Thesis*, University of Leeds.

Jeanneret, F., Kirchner, F., Clappier, A., Van Den Bergh, H. and Calpini, B. (2001) 'Total VOC reactivity in the planetary boundary layer: 1. Estimation by a pump and probe OH experiment', *Journal of Geophysical Research: Atmospheres,* 106(D3), pp. 3083-3093.

Lee, J., Whalley, L., Heard, D., Stone, D., Dunmore, R., Hamilton, J., Young, D., Allan, J., Laufs, S. and Kleffmann, J. (2016) 'Detailed budget analysis of HONO in central London reveals a missing daytime source', *Atmospheric Chemistry and Physics,* 16(5), pp. 2747-2764.

Sadanaga, Y., Yoshino, A., Watanabe, K., Yoshioka, A., Wakazono, Y., Kanaya, Y. and Kajii, Y. (2004) 'Development of a measurement system of OH reactivity in the atmosphere by using a laser-induced pump and probe technique', *Review of Scientific Instruments,* 75(8), pp. 2648-2655.

Sander, S., Friedl, R., Barker, J., Golden, D., Kurylo, M., Wine, P., Abbatt, J., Burkholder, J., Kolb, C. and Moortgat, G. (2011) 'Chemical kinetics and photochemical data for use in atmospheric studies, evaluation number 14', *JPL publication*, pp. 10-6.

Sander, S., Golden, D., Kurylo, M., Moortgat, G., Wine, P., Ravishankara, A., Kolb, C., Molina, M., Finlayson-Pitts, B. and Huie, R. (2006) *Chemical kinetics and photochemical data for use in atmospheric studies evaluation*

number 15: Pasadena, CA: Jet Propulsion Laboratory, National Aeronautics and Space.

Stevens, P., Mather, J. and Brune, W. H. (1994) 'Measurement of tropospheric OH and HO2 by laser-induced fluorescence at low pressure', *Journal of Geophysical Research: Atmospheres,* 99(D2), pp. 3543-3557.

Stone, D., Whalley, L. K., Ingham, T., Edwards, P., Cryer, D. R., Brumby, C. A., Seakins, P. W. and Heard, D. E. (2016) 'Measurement of OH reactivity by laser flash photolysis coupled with laser-induced fluorescence spectroscopy', *Atmospheric Measurement Techniques*, pp. 2827-2844.

Vranckx, S., Peeters, J. and Carl, S. (2008) 'Absolute rate constant and $O(^3P)$ yield for the $O(^1D)+ N_2O$ reaction in the temperature range 227 K to 719 K', *Atmospheric Chemistry and Physics,* 8(20), pp. 6261-6272.

Walker, H. (2013) 'Fields Measurements and Analysis of Reactive Tropospheric Species Using FAGE technique'*, PhD Thesis,* University of Leeds.

Whalley, L., Blitz, M., Desservettaz, M., Seakins, P. and Heard, D. (2013) 'Reporting the sensitivity of laser-induced fluorescence instruments used for HO_2 detection to an interference from RO_2 radicals and introducing a novel approach that enables HO_2 and certain RO_2 types to be selectively measured', *Atmospheric Measurement Techniques,* 6(12), pp. 3425-3440.

Whalley, L., Edwards, P., Furneaux, K., Goddard, A., Ingham, T., Evans, M., Stone, D., Hopkins, J., Jones, C. E. and Karunaharan, A. (2011) 'Quantifying the magnitude of a missing hydroxyl radical source in a tropical rainforest', *Atmospheric Chemistry and Physics,* 11(14), pp. 7223-7233.

Whalley, L., Furneaux, K., Goddard, A., Lee, J., Mahajan, A., Oetjen, H., Read, K., Kaaden, N., Carpenter, L. and Lewis, A. (2010) 'The chemistry of OH and HO_2 radicals in the boundary layer over the tropical Atlantic Ocean', *Atmospheric Chemistry and Physics,* 10(4), pp. 1555-1576.

Whalley, L. K., Stone, D., Dunmore, R., Hamilton, J., Hopkins, J. R., Lee, J. D., Lewis, A. C., Williams, P., Kleffmann, J. and Laufs, S. (2018) 'Understanding in situ ozone production in the summertime through radical observations and modelling studies during the Clean air for London project (ClearfLo)', *Atmospheric Chemistry and Physics,* 18(4), pp. 2547-2571.

Woodward-Massey, R. (2018) *Observations of radicals in the atmopshere: measurements and model comparisions.* University of Leeds.

3. Inlet Pre-Injector and FAGE Instrument Characterisation

3.1 Introduction

Previous observations of radicals in low-NO_x (below 1 ppbv NO) environments are much higher than models can predict when high levels of BVOCs are present (Lelieveld et al., 2008, Whalley et al., 2011, Wolfe et al., 2011) and has led FAGE groups to validate OH measurements through developing an alternative chemical background method called OHchem. The alternative background method, OHchem, was first deployed by Stevens et al. (1994). The conventional method to determine the background is called OHwave, where the laser wavelength is moved to an offline position where OH is not excited by the laser and so does not fluoresce. The OHwave method can lead to an overestimation of the ambient OH concentration as it is prone to interference from species that generate OH within the FAGE cell. The OHchem background method utilises an OH scavenger that reacts quickly with OH. The use of the OHchem background method has been shown to improve measurement-to-model agreement (Mao et al., 2012), suggesting previous measurements in low-NO_x/biogenic environments for that particular instrument could have been influenced by OH artefacts generated within the FAGE cells.

There have been several studies investigating potential interferences (see section.1.4.3) within the FAGE instrument including O_3, NO_3, VOCs (butane, isoprene etc.) (Fuchs et al., 2016, Novelli et al., 2014b, Rickly, 2018, Faloona et al., 2001). However, FAGE instruments can vary largely between different groups down to the home-built nature of the instruments. The main differences between instruments include: inlet size, inlet shape, residence time between the pinhole and laser axis and whether the laser crosses the detection axis once (single-pass) or multiple times (multi-pass). The difference in the FAGE designs may result in the magnitude of the interference investigated between instruments to vary significantly, and because of this, it is recommended that every FAGE group should develop their own chemical scavenger system and test for interferences within the laboratory (Hofzumahaus and Heard, 2015).

The Leeds ground-based FAGE instrument has been modified to incorporate a scavenger system called the Inlet pre-injector (IPI). The design of the IPI and

previous characterisation has been discussed in section.2.1.2. This chapter will focus on the characterisation of any sensitivity loss through the introduction of the IPI using both ambient measurements and laboratory experiments in section.3.1.1. This chapter will also cover the investigation O_3 and NO_3 interferences within the FAGE cell in section.3.4 and section.3.5, respectively.

3.2 Inlet pre-Injector Sensitivity Loss

The inlet pre-injector design and previous characterisation has been described in Chapter.2 and Woodward-Massey et al. (2020). The IPI was designed to minimise the reduction in sensitivity caused by additional surfaces which may remove radicals from ambient air sampled (Novelli et al., 2014a). Reducing OH loss is very important since the ambient OH concentration is generally very low, typically less than 1 pptv during the daytime. The IPI uses a sheath flow to minimise the FAGE instrument sampling air from near the walls of the IPI, housing and turret.

Previously experiments have been performed to determine the loss in sensitivity from the introduction of the IPI for the Leeds ground-based FAGE instrument. These experiments were performed by supplying a known concentration of OH and HO_2 to the instrument using the Leeds calibration system, this method is described in section.2.1.5. Although, unlike the calibration method described in section.2.1.5, in the IPI characterisation experiments the wand is held at 90° relative to the pinhole rather than 45°. The wand was held at 90° to minimise perturbation in the flow profile compared with sampling inside the IPI, if the wand was held at 45° like the standard calibration procedure (see section.2.1.5) the gas flow would have been directed at the walls of the IPI. The distance between the wand and the pinhole was ~3 cm. The results from older experiments performed at Leeds using the wand (using the 90° wand angle) to supply radicals to the instrument showed a ~40% and 10% loss of OH and HO_2, respectively, onto the walls of the IPI (Woodward-Massey, 2018).

Measurements of OH, HO_2 and RO_2 were made using the Leeds ground-based FAGE instrument during the summer 2017 for the Air Pollution and Human Health in Chinese megacities project (APHH). The APHH campaign took place in central Beijing at the Institute of Atmospheric Physics (IAP), and the OH concentrations

exceeded 2 x 10^7 (molecule cm^{-3}). Ambient measurements using both the OHwave and OHchem technique were made, and initially, the OH concentration was derived using a sensitivity loss of 40% which had been determined in older experiments (Woodward-Massey, 2018)). The levels calculated using the 40% loss showed very large OH concentrations (some days > 3.5 x 10^7 molecule cm^{-3}), and the steady-state calculation for OH showed a factor of 4 underprediction of OH at midday. Therefore, it was suspected that the discrepancy between the steady-state calculation and the measured OH could have been due to inaccurate parameterisation of the wall losses caused by the use of the IPI, and hence characterisation experiments were performed both in the field in Beijing and also at the University of Leeds and these experiments are described below.

The APHH summer campaign (see Chapter 5 for more details) provided ideal conditions to assess IPI losses, as the OH radical concentration was very high with OH peaking above 1 x 10^7 molecule cm^{-3} almost every day yielding a high signal-to-noise ratio. For the ambient experiment to determine the IPI losses that took place during the summer APHH campaign the instrument running conditions are the same as those described in Chapter.5. Sequential measurements of OHwave were made, where the IPI was taken on and off repeatedly after ~4 data acquisition cycles (7 mins per cycle). During the ambient experiment, only OHwave was measured using the OHwave data acquisition cycle (see section.2.1.4 for details) to see if the presence of the IPI assembly reduced the sensitivity of the instrument towards OH. The results from the ambient experiment are shown in Figure 3.1 and shows that the application of a 40% reduction in sensitivity (determined previously in older experiments performed at Leeds) results in significantly higher concentrations than those for the adjacent IPI-off sampling periods (with the IPI assembly taken off), and results in discontinuities in the OHwave time-series. Figure 3.1 also shows the comparison between IPI off and IPI-on sampling periods when no sensitivity reduction was applied, and shows a good qualitative agreement between the two OHwave data sets with no discontinuities in the OHwave time series, implying the sensitivity loss ~ 0%.

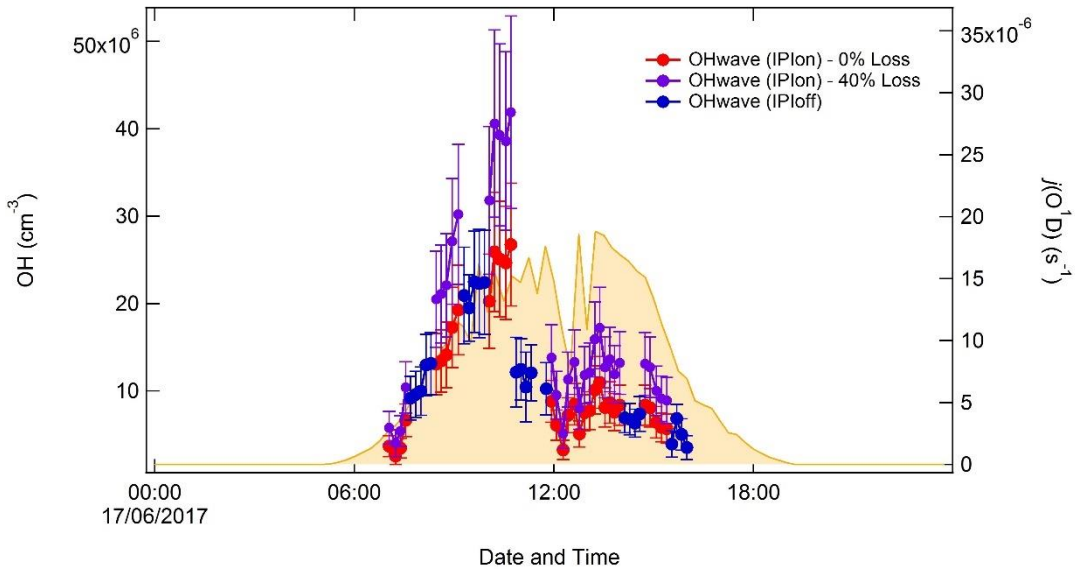

Figure 3.1 Time series of OH concentration for a day of sequential IPIon/IPIoff sampling during the summer APHH 2017 campaign. The IPI off periods in the blue, whilst if 40% or 0% reduction in sensitivity is applied to C_{OH} for the IPI-on sampling periods is shown in purple and red, respectively.

The above test which was performed during the APHH summer campaign to determine the loss of sensitivity towards OH was only qualitative as it is based off interpolation of ambient radical concentrations that may exhibit strong variability, especially during the day. To quantify the sensitivity loss further, calibration experiments were performed at the University of Leeds. The calibration experiments used a laminar flow (R_e < 2100) rather than a turbulent flow (R_e > 4000) that is normally used in the standard calibration experiments using the wand (see section.2.1.5 for details). Laminar flow was used as it was hypothesised that the difference between previous calibrations performed at Leeds (which indicated a 40% loss in sensitivity when the IPI was present) using the turbulent wand method and the ambient measurements performed in Beijing (which showed no decrease in sensitivity towards OH), was due to inappropriate sampling methodology (i.e. the turbulent flow method is not representative of how the IPI sampled ambiently) in the wand calibration case. For the turbulent wand method, it was thought that positioning the wand ~3 cm above the IPI would minimise flow perturbation inside the IPI, however, this may not have been sufficient to replicate the conditions inside the IPI during ambient sampling due to the fast wand gas velocity (~10 m s^{-1}) impinging on the sampling pinhole and may have resulted in the elevated radical wall loss of ~40% that was previously measured. To generate radicals by a method which provides conditions

analogous to ambient sampling, a 184.9 nm mercury lamp was placed ~ 19 cm above the IPI inside a tent which was placed around the fluorescence cell assembly on the roof of the container, which was outdoors next to the Chemistry department. The use of the Hg lamp, which photolysed ambient water vapour to form OH, allowed for the FAGE instrument to sample elevated radicals formed within the tent (~2 – 7 x 10^7 molecule cm^{-3}) in an ambient sampling set-up, and the loss of sensitivity could be determined under realistic conditions. The experiment was performed in a tent to minimise the effects of meteorological conditions (i.e. wind) and allowed the OH concentration to build up to a steady-state value and become homogeneous within the tent.

The experiment was performed with sequential measurements of IPIon and then IPIoff, and for each measurement, the online time-period was 60 seconds measuring OH only, then with 30 seconds offline. The experiment was repeated three times as the generated OH concentration can be affected by ambient variability (e.g. in NO_x levels, wind speeds impacting the environment within the tent). The results from the experiment are shown in Figure 3.2, based on the average for each set of repeated measurements the experiment yielded a mean IPIon/IPIoff signal ratio of 0.95 ± 0.12 (95% confidence errors, 2 σ) representing a ~5% sensitivity reduction due to the presence of the IPI. The reduction of HO_2 sensitivity from losses onto the wall of the IPI was not determined as it is less reactive than OH and is assumed to have no wall losses. For OH the reduction in sensitivity is smaller than the total instrumental uncertainty (~26% at 2σ, see section.2.1.7), and as such, no corrections have been applied to OH or HO_2 calibration factors for the work-up of ambient data. Also, the experiments performed in the tent in Leeds and the ambient experiment in Beijing are consistent with one another. The result for OH is consistent with previous studies by Mao et al. (2012) and Tan et al. (2017), where the introduction of a chemical modulation system (analogous to the Leeds IPI) caused no changes in the instrument sensitivity for OH. On the other hand, Novelli et al. (2014a) observed a ~34% reduction in sensitivity based on ambient measurements with sequential IPIon/IPIoff measurements.

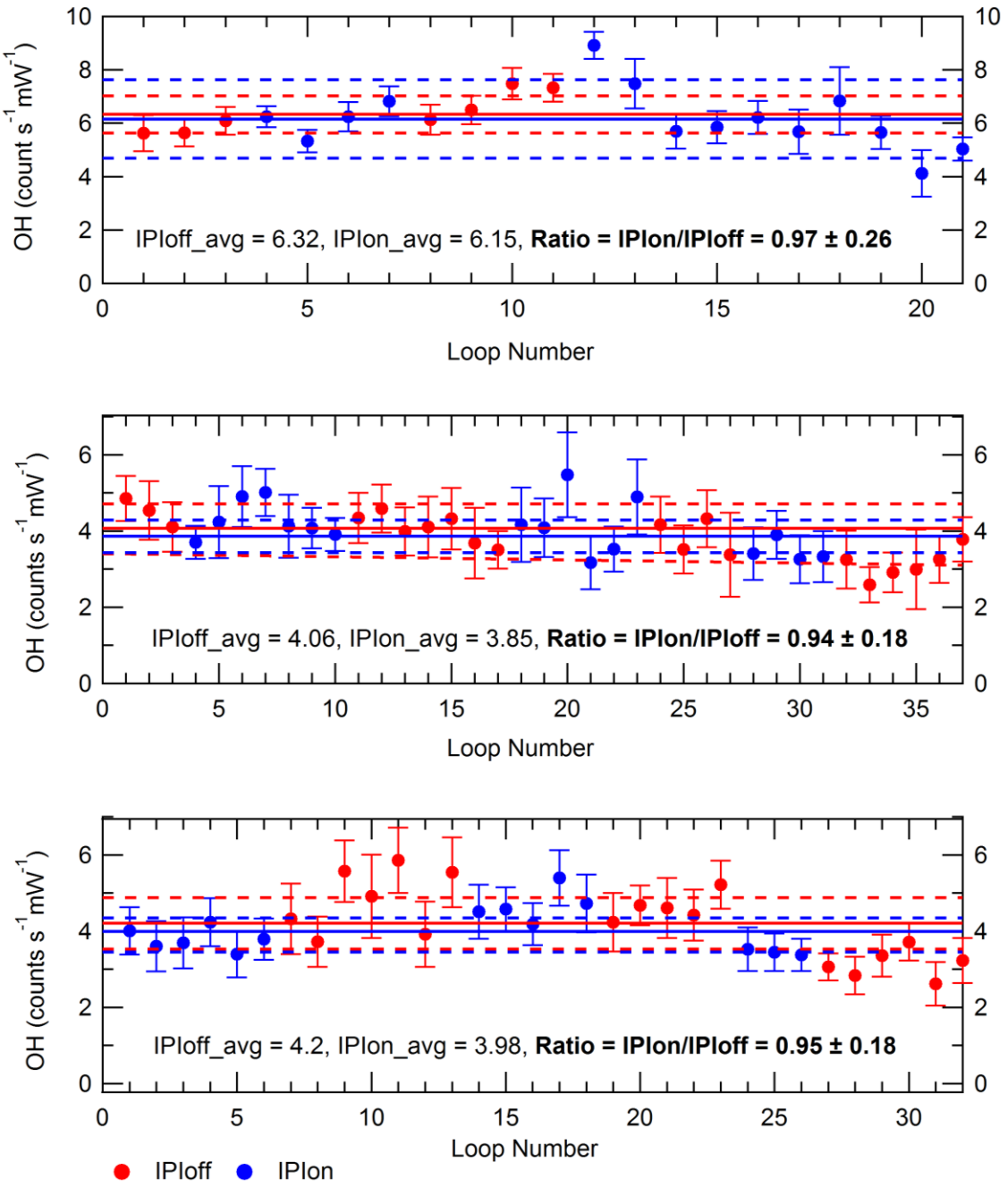

Figure 3.2 Testing of OH losses in the IPI system. Each panel shows repeat measurements of OH signals (±2σ) over the course of one day, where high OH concentrations were generated using a 184.9 nm Hg lamp placed ~19 cm above the instrument inlet. Blue and red markers denote individual measurements (one measurement "loop", i.e., one wavelength online-offline cycle) performed with ("IPIon") and without ("IPIoff") the IPI system, respectively. Solid lines correspond to the average signals for each day, with 2σ standard deviations (SD) shown by the dashed lines.

3.3 Inlet pre-Injector – Internal Removal

3.3.1 Introduction

Previous experiments have been performed to assess whether the scavenger (in this work propane) that removes external OH could also remove internally generated OH and cause the OHchem measurement to be underestimated. These experiments showed that, at the propane (110 – 1110 ppmv) concentration used for fieldwork, the internal removal was close to zero (Woodward-Massey et al., 2020) although a theoretical calculation showed that at 1110 ppmv of propane 12% of internally generated OH may be removed. Previous experiments used the calibration wand to generate equal concentrations of OH and HO_2, sufficient CO (75 sccm, 95 ppmv) was added to the calibration wand to quantitatively convert the OH formed into HO_2 (98.0 ± 0.4%). Then a high flow of NO (50 sccm) was injected inside the FAGE cell (injection point was immediately beneath the pinhole) to reconvert HO_2 back to OH inside the cell. The concentration of OH was tracked whilst the flow of propane was on and off. It should be noted that Tibet field data is only discussed within this chapter and no work-up data will be discussed later.

Although recent work during the Tibet field campaign highlighted there was internal removal of OH when 2020 ppmv of propane was used as a scavenger, the same flow and set-up were used in Tibet as the APHH summer campaign but due to the propane flowing into 0.55 Bar (atmospheric pressure of Namco measuring site, ~4800 m), the mixing ratio of propane was increased by a factor of ~1.82. For two days of the Tibet field campaign, the FAGE instrument was turned off, including the pumps (Roots blower (Leybold RUVAC WAU 1001) backed by a rotary pump (Leybold SOGEVAC SV200)) attached to the HO_x and RO_x cell, due to power supply issues. Another instrument (PERCA) shared the same exhaust line as the FAGE instrument, and whilst the FAGE instrument pumps were off it was suspected that the NO exhausted from the PERCA was able to enter the FAGE cells and damage the seal between the HO_x and RO_x cells. Damage to the seal meant that NO (injected into the ROx cell) could leak into the HO_x cell during the OH measurement period, and internally convert HO_2 into OH. However, the damage to the seal between the cells is currently only theoretical as the instrument has not been able to be assessed since the

campaign, and other reasons, such as a leak on the HO_x FAGE cell NO valve could also lead to HO_2 internally converting to OH during the OH measurement period. As shown in Figure 3.3, after the instrument was turned back on (14/05/2019 – 20/05/2019) a large spike in both OHwave and OHchem concentration was observed, compared to the previous period (30/04/2019 – 10/05/2019). The OHwave and OHchem values were ~3.7 and ~3 times larger during the 14/05/2019 – 20/05/2019 compared with the 30/04/2019 – 10/05/2019, respectively.

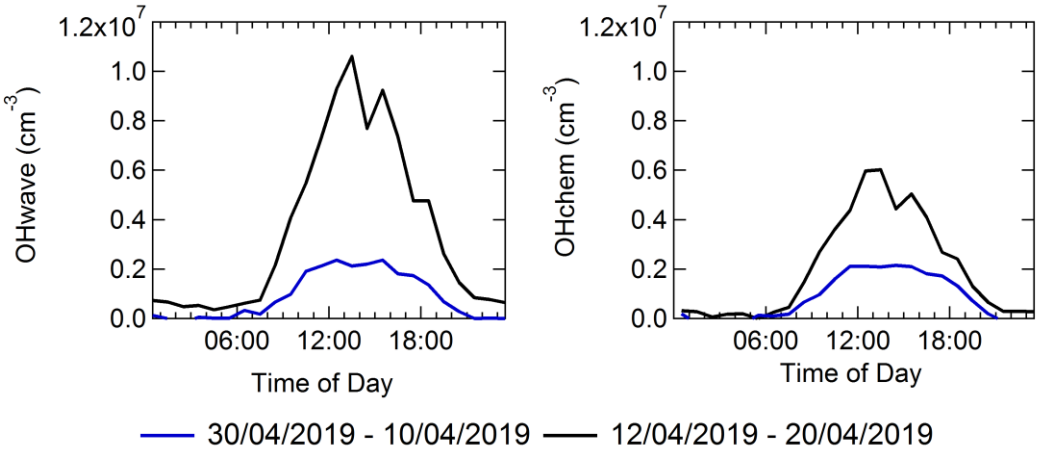

Figure 3.3 Measurements of OHwave(left) and OHchem(right) for the two different measurements periods with the 30/04/2019 – 10/05/2019 represented by blue, and the 12/04/2019 – 20/04/2019 represented by the black.

If there were no removal of internally generated OH, then only the OHwave value would be expected to increase as both ambient OH and the small % of ambient HO_2 converted to OH using the leaked NO would be measured, whilst the OHchem value should have stayed a similar order of magnitude. The OHchem value changing between the two measurement periods suggests that some of the OHchem signal is removed by propane entering the cell, and means that at 2020 ppmv of propane does internally remove OH which is not what the previous laboratory experiment showed.

The previous internal removal laboratory experiments may have shown no internal removal at 1100 ppmv as it used the turbulent calibration wand method to generate the radicals, which was shown in section.2.1.5 to give the incorrect sensitivity loss with the IPI in place. The turbulent wand method, in this case, may have prevented propane entering the cell by disrupting the flows, whilst when the FAGE instrument samples ambiently there is no turbulent air being directed at

the pinhole and propane may enter the cell and remove any internally generated OH. Unfortunately, no internal removal experiments using a laminar flow were made as a part of this work due to the time-frame, but a theoretical calculations based of the Tibet data and the step-change observed is shown in section.3.2.2.

3.3.2 Internal Removal Correction

As discussed in section.3.3 a removal of internally generated OH was noticed during the Tibet campaign. The major sources of radical (O_3, $j(O^1D)$ and H_2O) had very little day-to-day variability which means the measurement of OHchem between 30/04/2019 – 10/05/2019 and 14/05/2019 – 20/05/2019 should be similar once corrected for the internal removal. To calculate the theoretical internal removal the expected similar OHchem concentrations between the two different measurement periods has been exploited. The theoretical OHchem values for the 14/05/2019 – 20/05/2019 can be calculated by using the linear relationship of OHchem (30/04/2019 – 10/05/2019) vs j(HONO), which is shown in Figure 3.4, yields a slope of (9.48 ± 0.31) x 10^8 molecule cm^{-3} s. j(HONO) was used as it generated a linear relationship with OHchem.

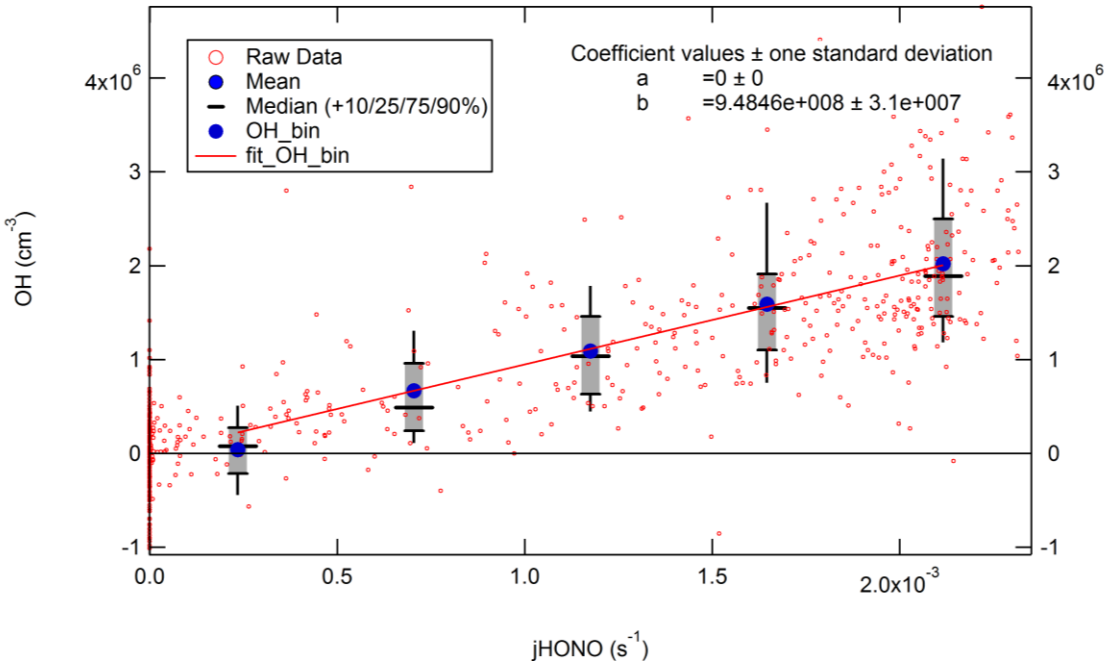

Figure 3.4 Relationship between OHchem measured from the 30/04/2019 – 10/05/2019 vs j(HONO). a represents the intercept that has been forced through zero, and b is the slope.

The slope can be used to calculate the OH between 14/05/2019 – 20/05/2019, as shown in E3.1:

$$\mathrm{OH_{cal}(molecule\ cm^{-3}) = } j\mathrm{HONO\ (s^{-1}) * 9.48\ x\ 10^{8}(molecule\ cm^{-3}\ s)} \quad \text{E3.1}$$

where the OH_{cal} is then converted in Counts (s^{-1}) by dividing through by the calibration factor and the measured f* (f* is the relationship between the laser power and the PDI, see section.2.1.5 for more details). Then the OH_{cal} can be compared to OHchem that has been adjusted at several values for internal removal (called OHchem(adjusted) from now on), and when OH_{cal} and OHchem(adjusted) are roughly the same the internal removal value is correct. The process to adjust the OHchem value is shown below, first, the online counts measured during the OHchem need to be increased, as shown in E3.2 using α:

$$\mathrm{OHchem(\alpha)\ (s^{-1}) = OHchem(observed)\ (s^{-1}) * \alpha} \quad \text{E3.2}$$

where OHchem(α) represents the signal that should have been observed if there was no internal removal. Next OHchem(adjusted) is calculated using E3.3:

$$\mathrm{OHchem(adjusted)(s^{-1}) = OHwave\ (s^{-1}) - OHchem(\alpha)(s^{-1})} \quad \text{E3.3}$$

where OHwave is the online counts measured during the OHwave period. The internal removal factor can be calculated using E3.4:

$$\mathrm{Internal\ Removal} = \left(1 - \frac{\mathrm{OHchem(observed)}}{\mathrm{OHchem(\alpha)}}\right) * 100 \quad \text{E3.4}$$

Figure 3.5a shows the comparison of OHcal and OHchem(adjusted) using 0.4 as the value for α, which yields an internal removal of 38 ± 26%. The error has been calculated by varying the internal removal such that all the points in Figure 3.5b are either above or below zero. The ~38% removal is higher than the theoretical value calculated ~12%, but the propane mixing ratio in Tibet was 2020 ppmv due to the ambient pressure of 0.55 bar and so at 1110 ppmv the calculated internal removal would be ~20 ± 14% which is similar to the 12% theoretical value calculated by Woodward-Massey et al. (2020). The difference between OHcal and OHchem is shown in Figure 3.5b and shows the value hovers around zero demonstrating that the internal removal value is bringing OHcal and OHchem close to unity. The deviation away from zero is expected as these measurements were taken under ambient conditions and would not expect to fall exactly on the line OH vs *j*(HONO) that was used to calculated OHcal, as there would be other

ambient factors to include (i.e change in air-mass, O_3, NO). A controlled laboratory experiment would yield better results, but as discussed earlier due to the time-frame no laboratory experiments have been completed.

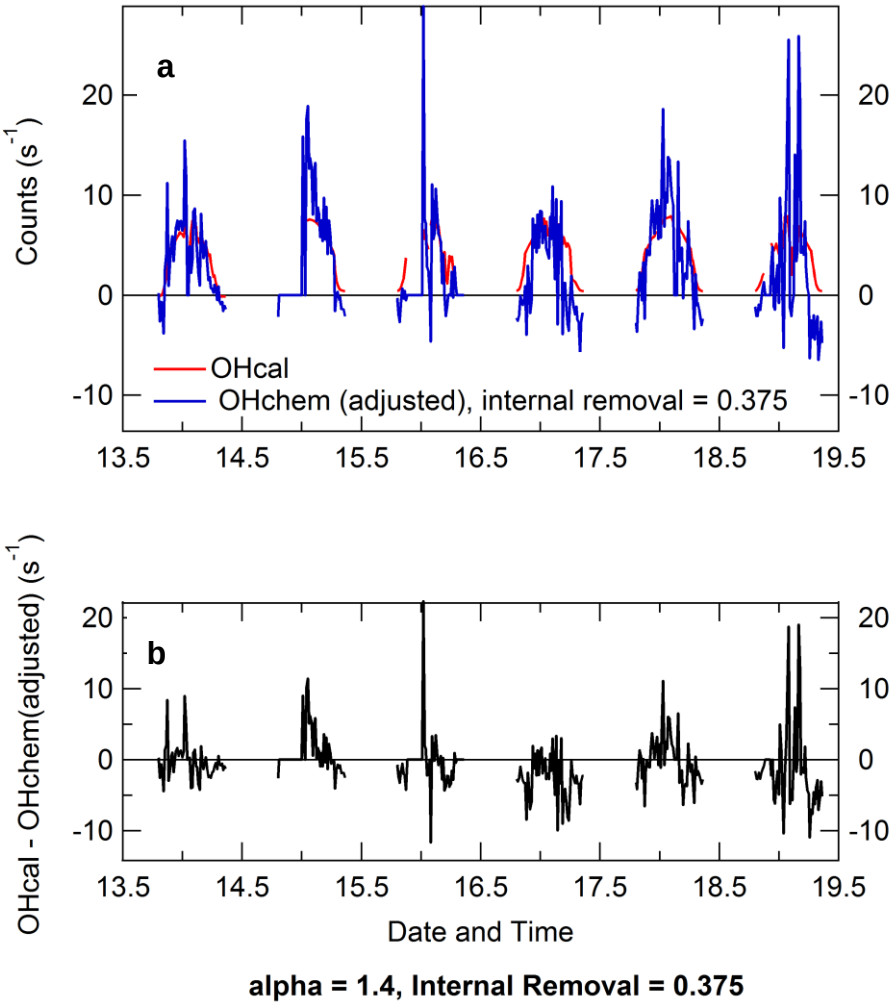

Figure 3.5 a) Comparison of OHcal and OHchem(adjusted), where OHchem(adjusted) was calculated using E3.2- E3.3 with a value of α = 0.4 yielding an internal removal of 38% using E3.4. b) Difference between OHcal – Ohchem(adjusted) yielding the results closest to zero for different internal removal.

To correct the ambient data from both the APHH summer campaign and the Tibet campaign for internal removal, several steps have to be taken into account. First the measured OHchem(observed) signal must have the OHwave(offline) subtracted as the internal removal of the OHchem does not affect the OHwave background signal(from laser scatter), but does make up a part of the OHchem(observed) signal. Then this is corrected for the internal removal by dividing through with 1 – internal removal value, and finally the OHwave is added

back on. The steps used to correct the online OHchem signal in counts is summarised E3.5:

$$\mathrm{OHchem(corr)} = \left(\frac{(\mathrm{OHchem(observed)} - \mathrm{OHwave(offline)})}{(1 - \text{internal removal})}\right) + \mathrm{OHwave(offline)} \quad \text{E3.5}$$

To calculate the ambient concentration of OH the corrected OHchem(corrected) value must be subtracted from the online OHwave, which is shown in E3.6:

$$\mathrm{OHchem(ambient)} = \frac{(\mathrm{OHwave(online)} - \mathrm{OHchem(corr)}}{\mathrm{C_{OH}}} \quad \text{E3.6}$$

The corrected summer APHH and Tibet data is shown in section.3.3.3.1 and section.3.3.3.2, respectively. The Penn. State University (PSU) internal removal of OH was quantified by Mao et al. (2012). PSU used a mercury lamp to generate OH inside the cell and compared the OH signal with and without the presence of the scavenger (C_3F_6), added externally using the IPI system. PSU found the internal removal loss was ~ 20% and that most losses occurred at the instrument inlet, rather than at the OH detection axis. The Max Planck Institute for Chemistry (MPIC) internal removal was not tested in the laboratory by Novelli et al. (2014a) but instead, they limited the scavenger (propene and propane) concentration such that the OH removal efficiency was <95%, to minimise possible reactions of the scavenger with OH inside the fluorescence cell. However, during ambient, night-time tests (constant atmospheric OH concentration assumed), no change in the OH background signal was observed after increasing the scavenger concentration by a factor of seven, providing evidence for a lack of internal removal (Novelli et al., 2014a). The Leeds ground-based FAGE instrument has a much higher internal removal than PSU and MPIC, although currently internal removal has only been tested qualitatively via the Tibet incident at the higher end of the propane concentrations. The internal removal in the Leeds ground-based FAGE instrument needs to be determined quantitively in the laboratory that is analogous to measuring ambiently, and lower propane mixing ratios should be used in future campaigns.

3.3.3 Corrected Data

3.3.3.1 APHH Summer

The APHH summer data reported in Chapter 5 has been corrected using the steps shown in section.3.3.2, using an internal removal value of 20%. The time-series comparison between OHwave, OHchem and OHchem(corrected) is shown in Figure 3.6. Figure 3.6 shows that in general, no correction needs to be applied to the APHH summer data as there are no observed differences between OHwave and OHchem (see section.5.4.2 for details). Although on 24/05/2017, 30/052017, 09/06/2017, 15/06/2017 and 16/06/2017 differences between OHwave and OHchem was observed, hence a correction for internal removal of OH is required for those days.

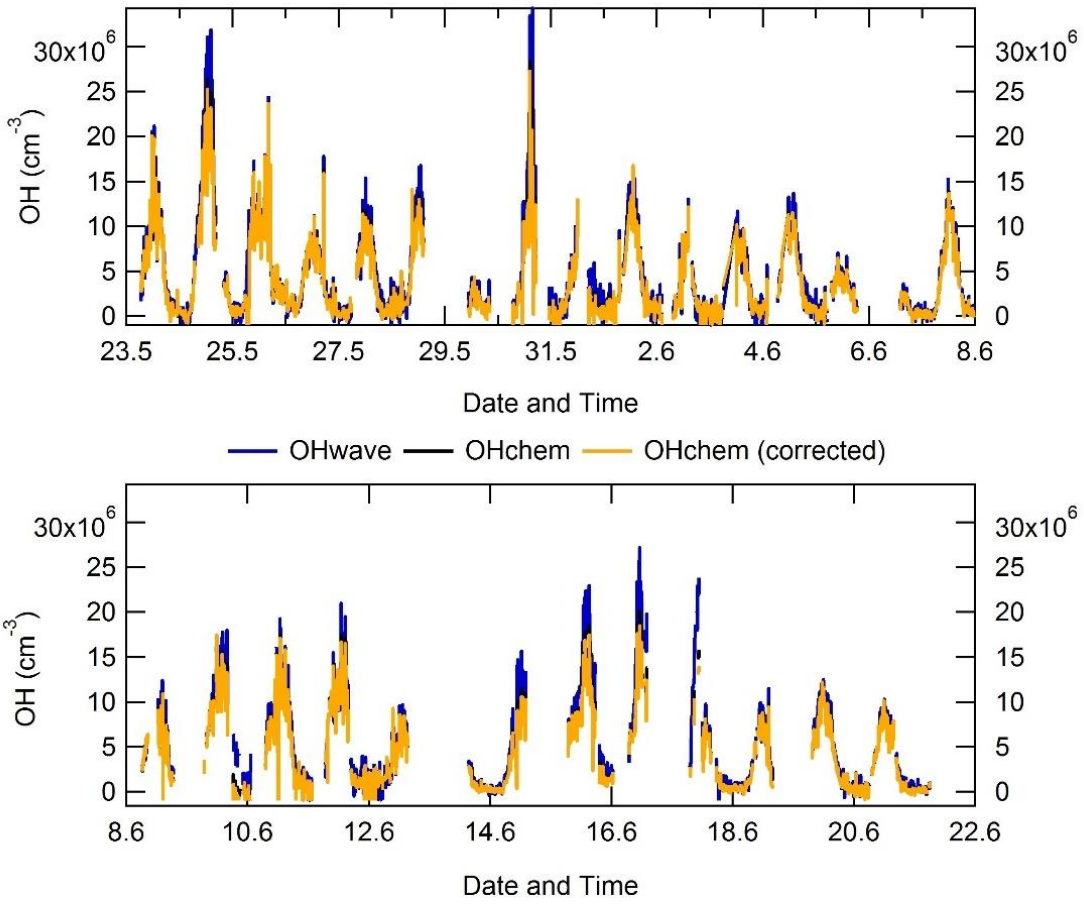

Figure 3.6 Time-series comparison of OHwave, OHchem and OHchem(corrected). OHchem(corrected) has the correction applied for internal removal. Top – represents the time-series comparison between 22/05/2017 to 08/06/2017. Bottom – represents the time-series comparison between 08/06/2017 – 22/06/2017.

The largest differences between OHwave and OHchem was observed on the 24/05/2017 and 15/06/2017, Figure 3.7 shows a case-study comparison between OHwave, OHchem and OHchem(corrected) for these days. The comparison shown in Figure 3.7 for both 24/05/2017 and 15/06/2017 shows that OHchem, within 2σ error, agrees with the OHchem(corrected) data.

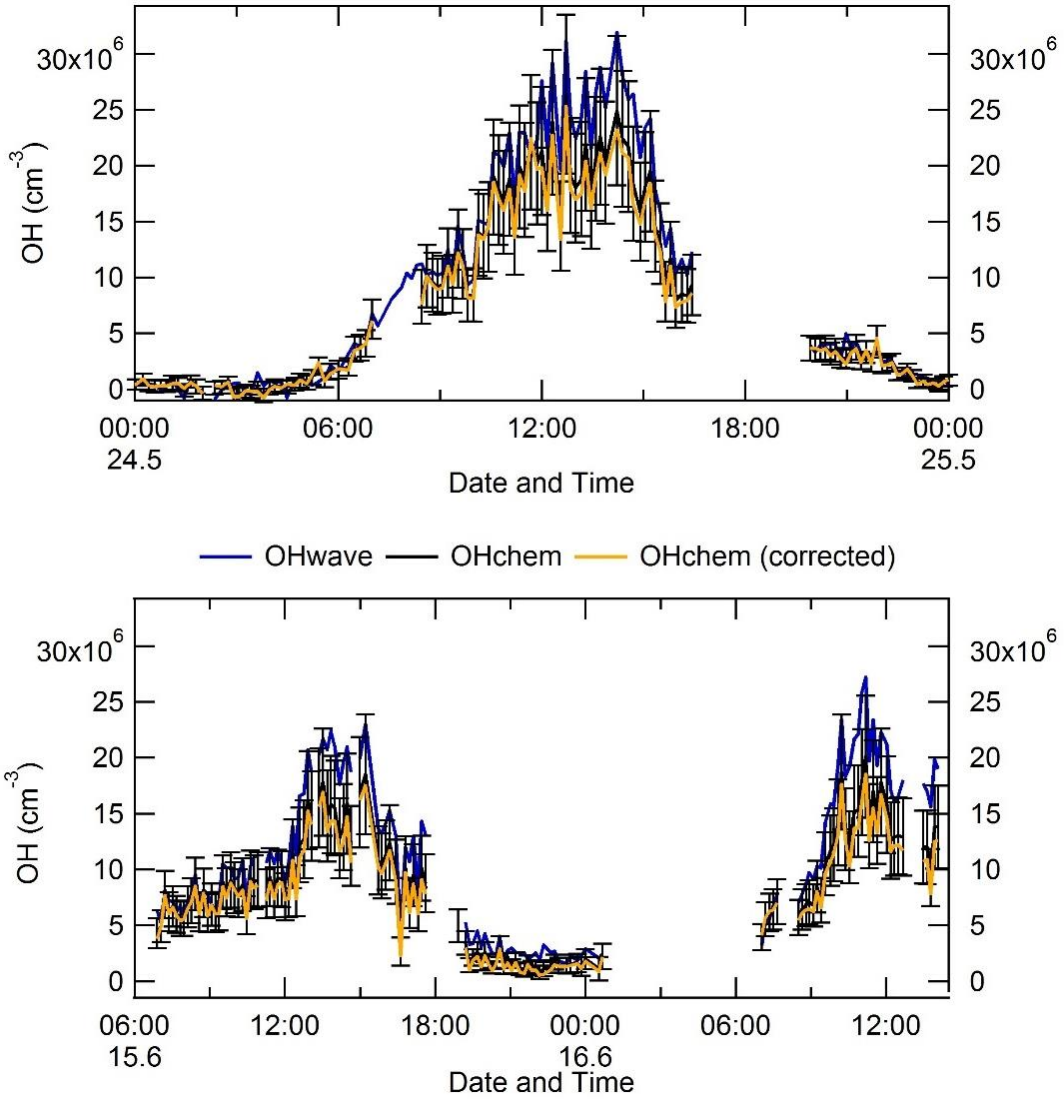

Figure 3.7 Top – Case study comparison of OHwave, Ohchem and OHchem(corrected) for the 24/05/2017. Bottom - Case study comparison of OHwave, Ohchem and OHchem(corrected) for the 15/06/2017 – 16/06/2017. For both the error bars on the OHchem represents 2σ, and OHchem(corrected) is the OHchem data corrected for internal removal.

Figure 3.8 shows a comparison between the error of the OHchem measurements and the difference between OHchem and OHchem corrected for internal removal plotted against OHcherm. Figure 3.8 shows that both the OHchem error and the

difference between the OHchem data sets increases with increasing OH concentration, it also shows that the correction for internal removal is much smaller than the OHchem error (~5 times smaller at 2.7 x 10^7 molecule cm^{-3}). Figure 3.7 and Figure 3.8 shows that in summertime Beijing where only small difference between OHwave and OHchem was observed, the internal removal is a small correction. Since the internal removal correction is very small and uncertain, the APHH summer campaign data has not been corrected for internal removal, hence all the data presented in Chapter.5 is OHchem and not OHchem(corrected).

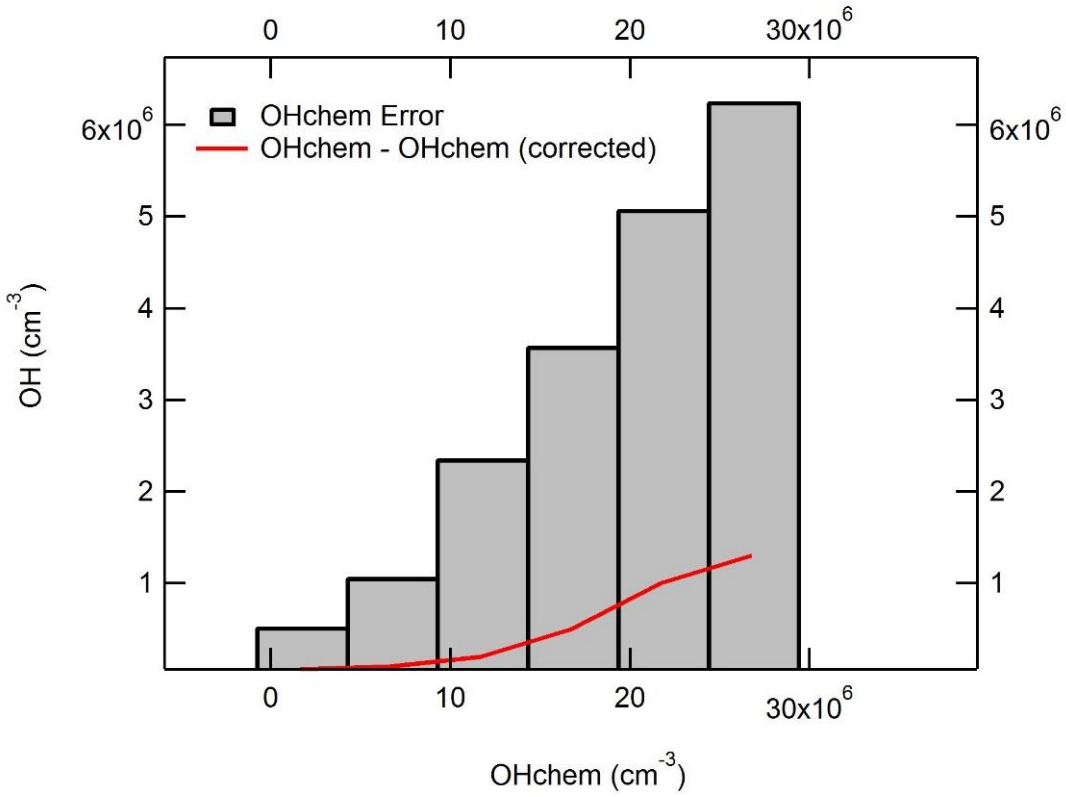

Figure 3.8 Comparison of the OHchem errors and the difference between OHchem and OHchem corrected for internal removal.

3.3.3.2 Tibet Campaign

The Tibet data has been corrected using the steps shown in section.3.3.2. The comparison between OHwave, OHchem and OHchem(corrected) for the Tibet campaign is shown in Figure 3.9. It should be noted that the Tibet data has not been finalised, and the data shown in Figure 3.9 is subject to change. As discussed in section.3.3.1 the step change in the data between 11/05/2019 to 13/05/2019 is suspected to be caused by NO leaking into the HO_x cell during the

OH measurement period converting HO_2 into OH. The high OHchem signal observed during this period is suspected to be caused by internal removal of OH by the propane used to remove the ambient OH, decreasing the internally generated OH background signal. The comparison in Figure 3.9 for OHwave/OHchem (01/05/2019 to 11/05/2019) and OHchem(corrected, 1305/2019 to 205/2019) shows a consistent OH concentration between the two time-periods, rather than the previous large step-change. The good agreement between the two time-period suggests the internal removal correction of 38% is correct. Although the internal removal needs to be determined quantitatively in the laboratory, as discussed previously this could not be achieved in the time-frame of this project.

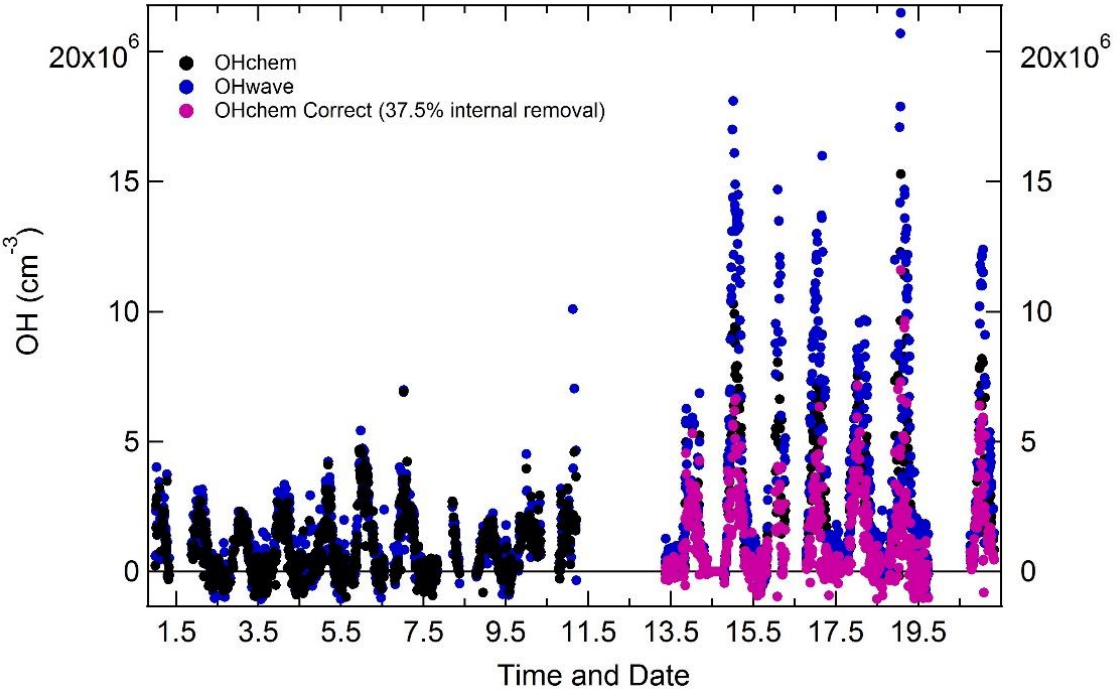

Figure 3.9 Time-series comparison of OHwave, OHchem and OHchem(corrected). The OHchem(corrected) data has had the correction applied for internal removal.

3.4 Ozone Interference Testing

3.4.1 Experimental

In FAGE instruments there is a known interference from laser generated OH from ozone photolysis in the presence of water-vapour (Griffith et al., 2016, Fuchs et al., 2016, Tan et al., 2016). The ozone interference has been explored for the

Leeds ground-based FAGE instrument, the experimental set-up is shown in Figure 3.10. Ozone was generated from the 184.9 nm photolysis of oxygen in a flow of zero air (BOC, BTCA 178) using a Hg(Ar) pen-ray lamp (LOT LSP035), the ozone concentration was varied during the experiment by changing the flow past the mercury lamp between 12 – 20 slm. Another flow of zero air was used to humidify the flow by passing the air through a water (HPLC grade) bubble, the H_2O concentration was varied between 0.1 – 1% by changing the zero airflow past the bubbler or removing the bubbler from the system. A further 5 slm dilution flow of zero air was used to allow for more variability in changing the flow past the lamp and bubbler whilst keeping a total flow of 32 slm. The water vapour was detected using a hygrometer (General Eastern 1311DR sensor and 4x4 Optica, range -65-20 ^oC). The inlet pre-injector was used during this experiment to measure both OHwave and OHchem background (see section.2.1.2 for more details), OHchem – OHwave (background) measured the interference generated within the cells from the O_3 + H_2O interference.

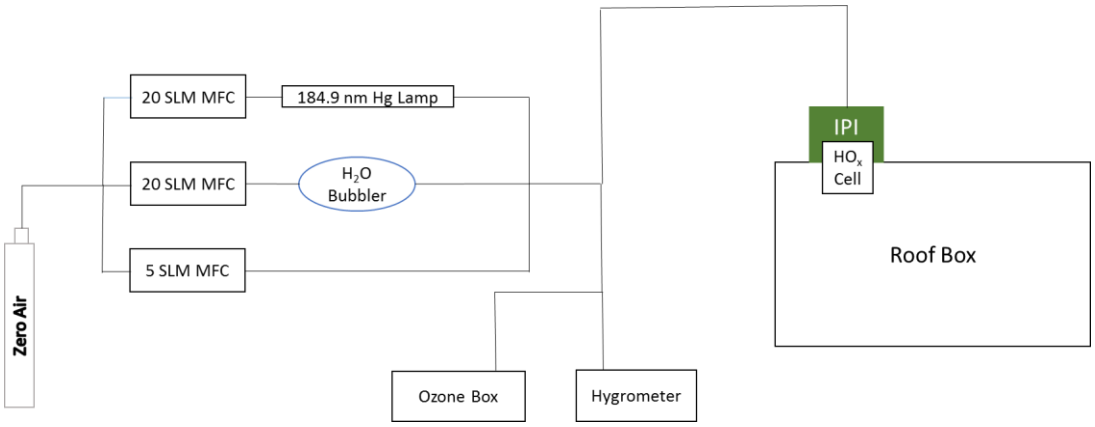

Figure 3.10 Experimental set-up for testing the ozone interference in the Leeds ground-based FAGE instrument.

Three separate experiments were performed to measure the OH interference dependence upon ozone concentration, H_2O vapour mixing ratio and laser power. For the ozone experiment, the ozone was changed between 0 – 2.5 ppmv, whilst water vapour and laser power were kept constant at 0.71% and 9.1 mW, respectively. For the H_2O vapour experiments, the H_2O vapour concentration was varied between 0.1 – 1%, whilst ozone and laser power were kept constant at 2390 ppbv and 8.25 mW, respectively. For the laser power experiment the laser power was varied between 3 – 17 mW by varying the ratio of acetone:water in a cuvette placed before the fibre launcher that is used to send the laser light to the

detection cells, and hence attenuating the 308 nm laser power. During the laser power experiments, the ozone and H_2O concentration was kept constant at 2450 ppbv and 0.07%, respectively.

3.4.1 Results

The results from the O_3 interference test is shown in Figure 3.11. It can be seen that the interference signal is linear with both ozone (a) and H_2O vapour (b) mixing ratio, and that the interference in terms of raw counts has a quadratic dependence with laser power. The quadratic dependence on laser power indicates the interference originates from a two-photon process. Once the data was normalised to laser power, the equivalent OH concentrations have a linear dependence with respect to laser power. The overall interference is linear with ozone, H_2O vapour and laser power and can be calculated by normalising the slope in Figure 3.11a to O_3 = 1 ppbv, H_2O = 1% and laser power = 1 mW yields E3.7:

$$[\mathrm{OH_{int}}] = (520 \pm 140)\mathrm{molecule\ cm^{-3}ppbv^{-1}mW^{-1}x}\,[\mathrm{O_3}] * [\mathrm{H_2O}] * \mathrm{LP} \qquad \text{E3.7}$$

where LP represents laser power. The ozone interference has been characterised for the Indiana University FAGE (IU-FAGE) to be given by E3.8 (Griffith et al., 2016):

$$[\mathrm{OH_{int}}] = (7500 \pm 1000)\mathrm{molecule\ cm^{-3}ppbv^{-1}mW^{-1}x}\,[\mathrm{O_3}] * [\mathrm{H_2O}] * \mathrm{LP} \qquad \text{E3.8}$$

which shows a 14.4 times higher ozone interference in the IU-FAGE compared to the Leeds ground-based FAGE instrument. However, the IU-FAGE uses a multipass system and in general a lower laser power. The differences between the observed ozone interference between FAGE instruments highlights the importance of each FAGE group investigating the potential interferences separately.

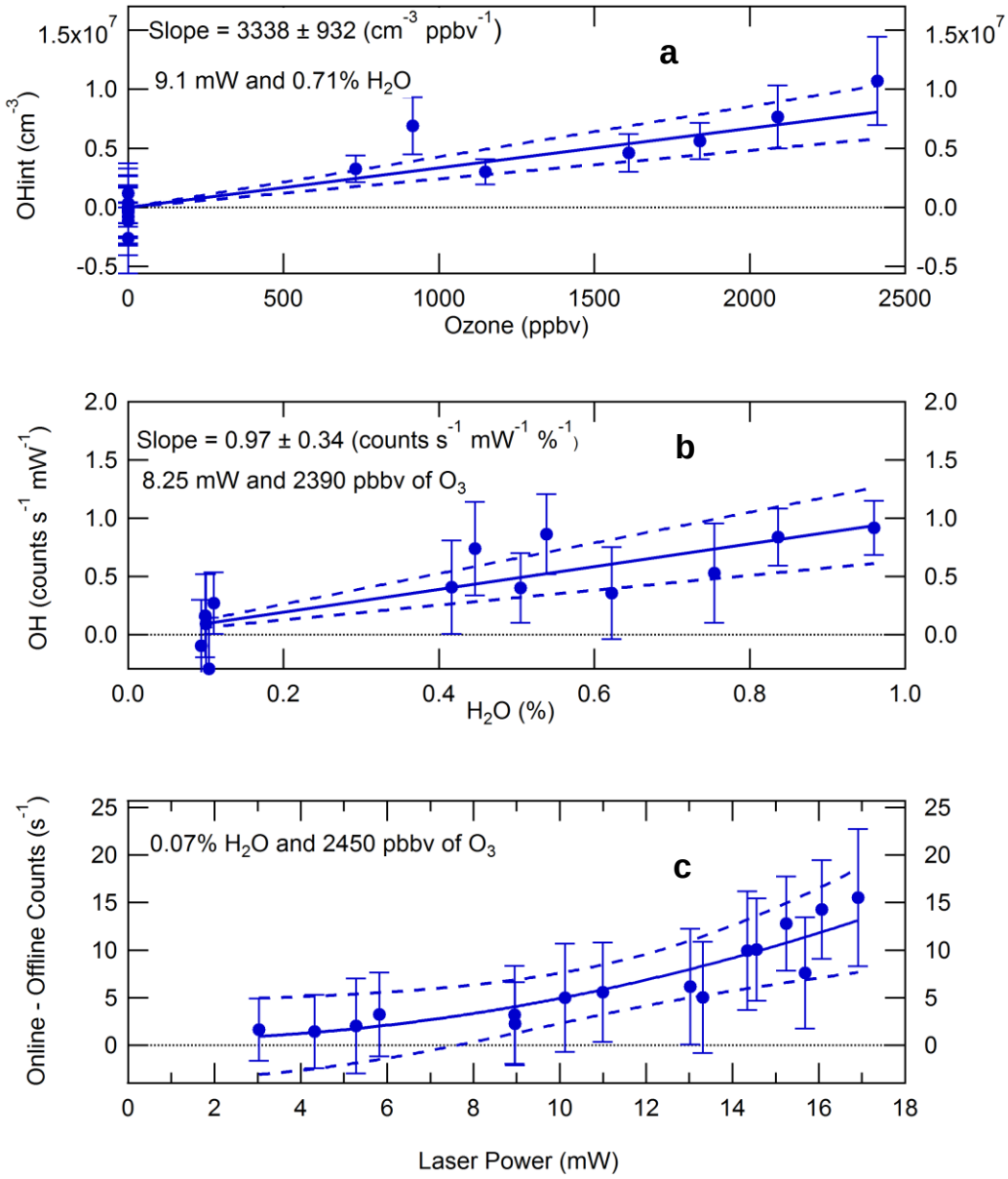

Figure 3.11 OH interference (±2σ) from O_3 + H_2O as a function of (a) O_3, (b) H_2O vapour, and (c) laser power. The interference signal is linear in O_3 and H_2O vapour mixing ratios and quadratic in laser power, confirming the two-photon nature of the process. Normalising the slope in panel (a) to O_3 = 1 ppbv, H_2O = 1%, and laser power = 1 mW yields an OH interference equivalent to a concentration of 520 ± 140 molecule cm^{-3}.

Figure 3.12 shows the comparison between OHwave and OHwave corrected for the experimentally determined O_3 interference using E3.7 for the APHH summer campaign in Beijing where O_3 concentrations were very high. The results show that the O_3 interference constitutes ~9% of the OHwave signal, with the average O_3 interference for the campaign 0.65 x 10^6 molecule cm^{-3}, at an average laser power of ~ 11mW. These results show the importance of determining different

interferences in individual FAGE set-ups, as the signal from an interference could become significant in different environments.

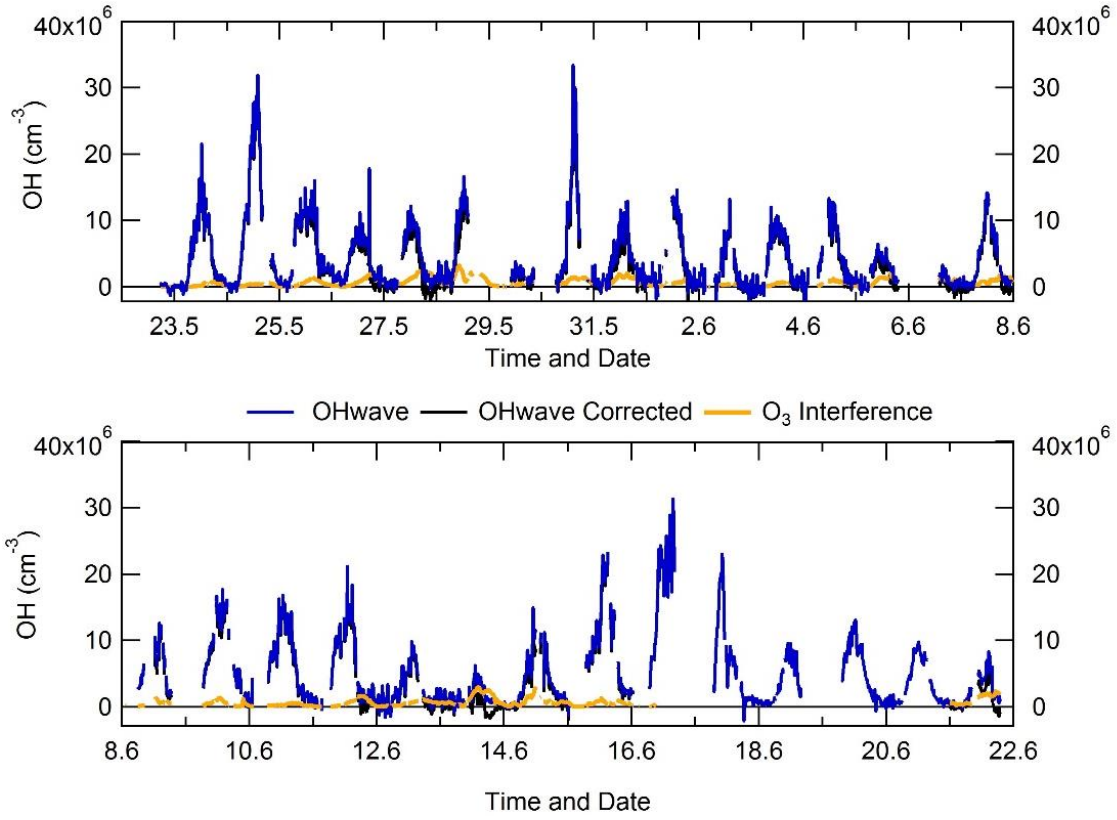

Figure 3.12 Time-series comparison of OHwave and OHwave corrected for ozone interference, alongside the calculated O_3 interference. Top – represents the time-series comparison between 22/05/2017 to 08/06/2017. Bottom – represents the time-series comparison between 08/06/2017 – 22/06/2017. The gap between 16/06/2017 to 21/06/2017 is caused by missing data not allowing for the O_3 interference to be calculated.

3.6 NO_3 Interference Testing

3.6.1 Experimental

Previously a NO_3 interference has been observed in the Juelich FAGE instrument (Fuchs et al., 2016) which has a similar set-up and design to the Leeds ground-based FAGE instrument (single pass and a relatively short distance between pinhole to laser excitation axis). An OH interference from NO_3, despite the absence of a hydrogen was observed and was equivalent to 1.1 x 10^5 molecule cm^{-3} per 10 pptv of NO_3 (Fuchs et al., 2016). The OH interference signal observed in the Juelich instrument showed a linear dependence with NO_3, and no dependence on inlet length, cell pressure, laser power or humidity. It was

postulated that a heterogeneous process involving NO_3 and H_2O vapour adsorbed onto the cell walls was the source of the interference.

The NO_3 interference was tested for the Leeds ground-based FAGE instrument, the experimental set-up is shown in Figure 3.13.

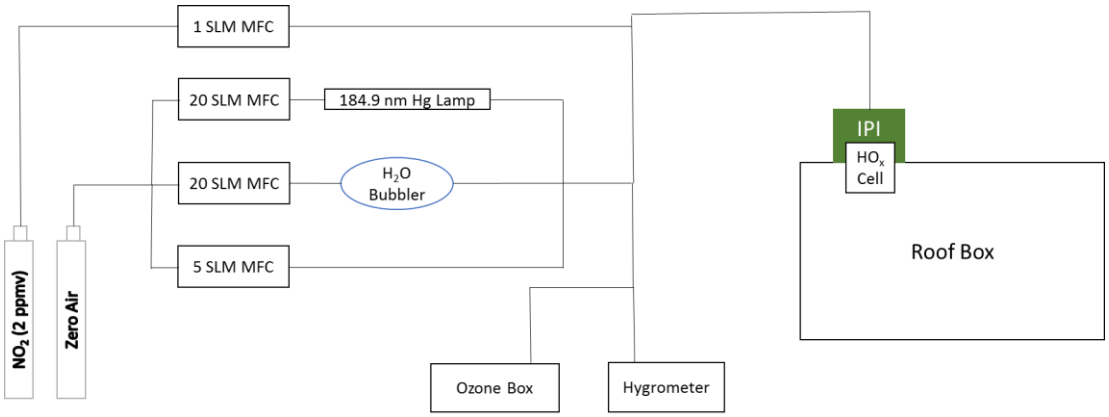

Figure 3.13 The experimental set-up for the NO_3 interference testing

The NO_3 was generated from the reaction of ozone with NO_2:

$$O_3 + NO_2 \rightarrow NO_3 + O_2 \qquad \text{R3.1}$$

$$NO_3 + NO_2 + M \rightarrow N_2O_5 + M \qquad \text{R3.2}$$

$$N_2O_5 + M \rightarrow NO_3 + NO_2 + M \qquad \text{R3.3}$$

The ozone was generated by flowing zero air (BOC, BTCA 178) past a Hg(Ar) penray lamp (LOT LSP035) at 15 slm, the ozone concentration was changed between 0 – 3000 ppbv during the experiment by changing the lamp current between 0 – 21 A. A constant 0.5 slm of NO_2 (BOC, 2ppmv) was diluted in the 25 slm flow of zero air/ozone mixture yielding a final concentration of 40 ppbv of NO_2, the additional 10 slm for the dilution flow was provided by 20 slm MFC (25% - 5 slm) and 5 slm MFC (100% - 5 slm). The gas was delivered to the system using the calibration wand with a total residence time of ~3.7 s for the O_3 + NO_2 reaction. The NO_3 mixing ratios during the experiment range between 0 – 90 pptv and was calculated using a zero-dimensional box model with rate constants taken from the Master Chemical Mechanism shown in Table 3.1. The results from the box model calculation of NO_3 at three different O_3 concentration is shown in Figure 3.1b, which was been used to calculate the NO_3 concentration vs O_3 at a residence time of 3.7 s which is shown in Figure 3.14a. The slope from

Figure 3.14a was used to calculate the NO_3 concentration for the interference experiment. It should be noted that NO_3 was not measured during the experiment so the experimental concentration is uncertain. The experiment was performed under dry conditions (H_2O(v) ~0.07%) to reduce the signal from the O_3 + H_2O interference, the water was measured using a hygrometer (General Eastern 1311DR sensor and 4x4 Optica, range -65-20 ^oC). The interference from O_3 + H_2O was corrected using the equation that was presented in section.3.4.

Reaction	Rate Constant	Reference
$O_3 + NO_2 \rightarrow NO_3$	3.52×10^{-17} cm^3 molecule^{-1} s^{-1}	http://mcm.leeds.ac.uk/MCM
$NO_3 + NO_2 \rightarrow N_2O_5$	1.24×10^{-12} cm^3 molecule^{-1} s^{-1}	http://mcm.leeds.ac.uk/MCM
$N_2O_5 \rightarrow NO_3 + NO_2$	0.045 s^{-1}	http://mcm.leeds.ac.uk/MCM

Table 3.1 The reactions and rate constants used in a box model to calculate the NO_3 concentration for the interference experiment.

The inlet pre-injector was used during this experiment to measure both OHwave and OHchem background (see section.2.1.2 for more details), E3.9-E3.10 shows how the NO_3 interference was calculated:

$$OH'_{int} = OHchem - OHwave(offline) \quad \text{E3.9}$$

$$OH_{int,NO3} = OH'_{int} - OH_{int,O3} \quad \text{E3.10}$$

where OH'int is the difference between OHchem and OHwave(offline) and is the sum of the interference from both NO_3 and O_3 + H_2O. As shown in E3.10 the NO_3 interference can be calculated by subtracting the known O_3 + H_2O interference away from the OH'int.

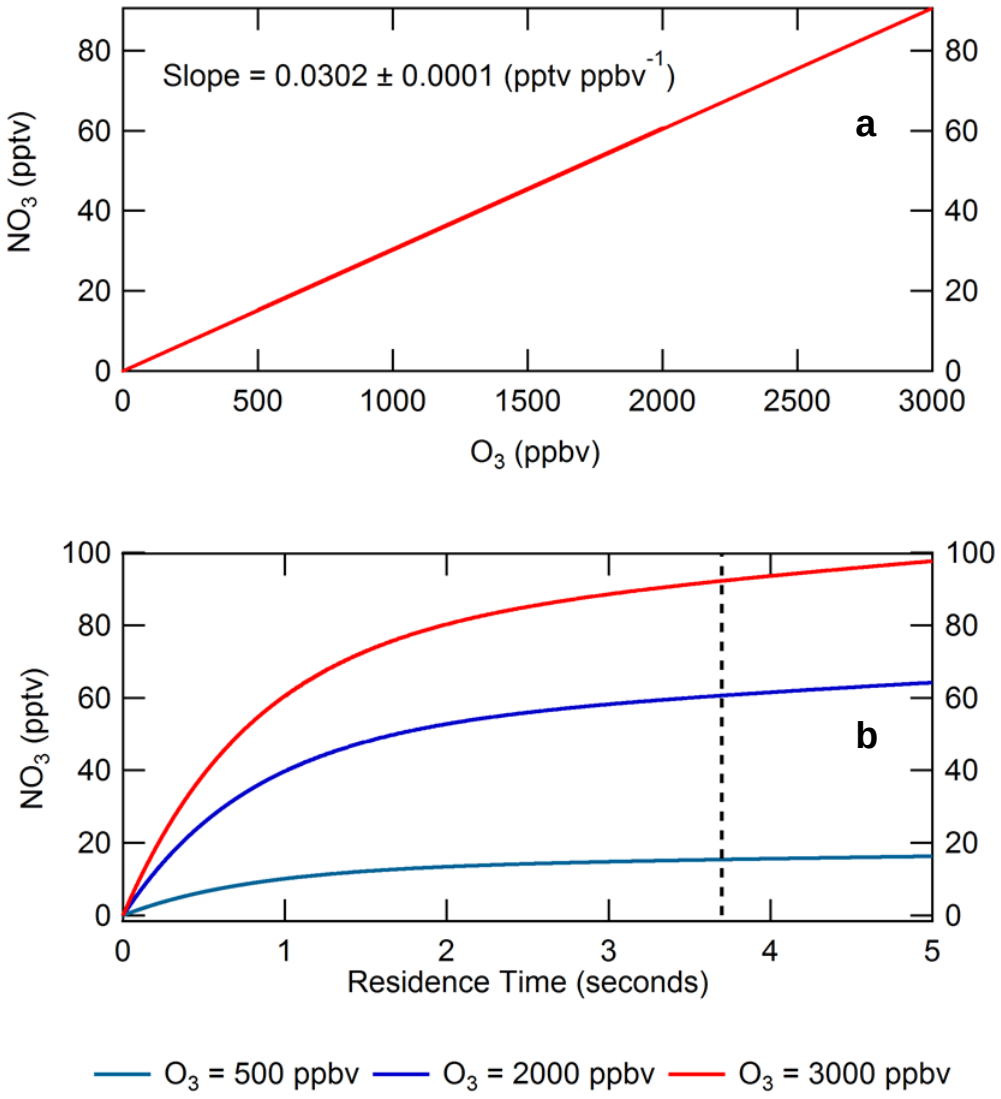

Figure 3.14 a) The linear dependence of NO_3 vs O_3 for a residence time of 3.7 s, the NO_2 concentration was kept constant at 40 ppbv. The slope has been used to calculate the NO_3 concentration during the NO_3 interference experiment. b) NO_3 concentration as a function of time at 500, 2000 and 3000 ppbv of O_3, the vertical dashed line represents a residence time of 3.7 s.

3.6.2 Results

The results from the NO_3 interference testing is shown in Figure 3.15 and shows that whilst there was an observed interference during the experiment, the interference signal observed was from OH internally generated from $O_3 + H_2O$ (see section.3.4) and not from NO_3. The OH signals from NO_3 interference were all $<8 \times 10^5$ molecule cm^{-3}, and almost always below the instrument LOD of 6.3×10^5 molecule cm^{-3} (SNR = 2).

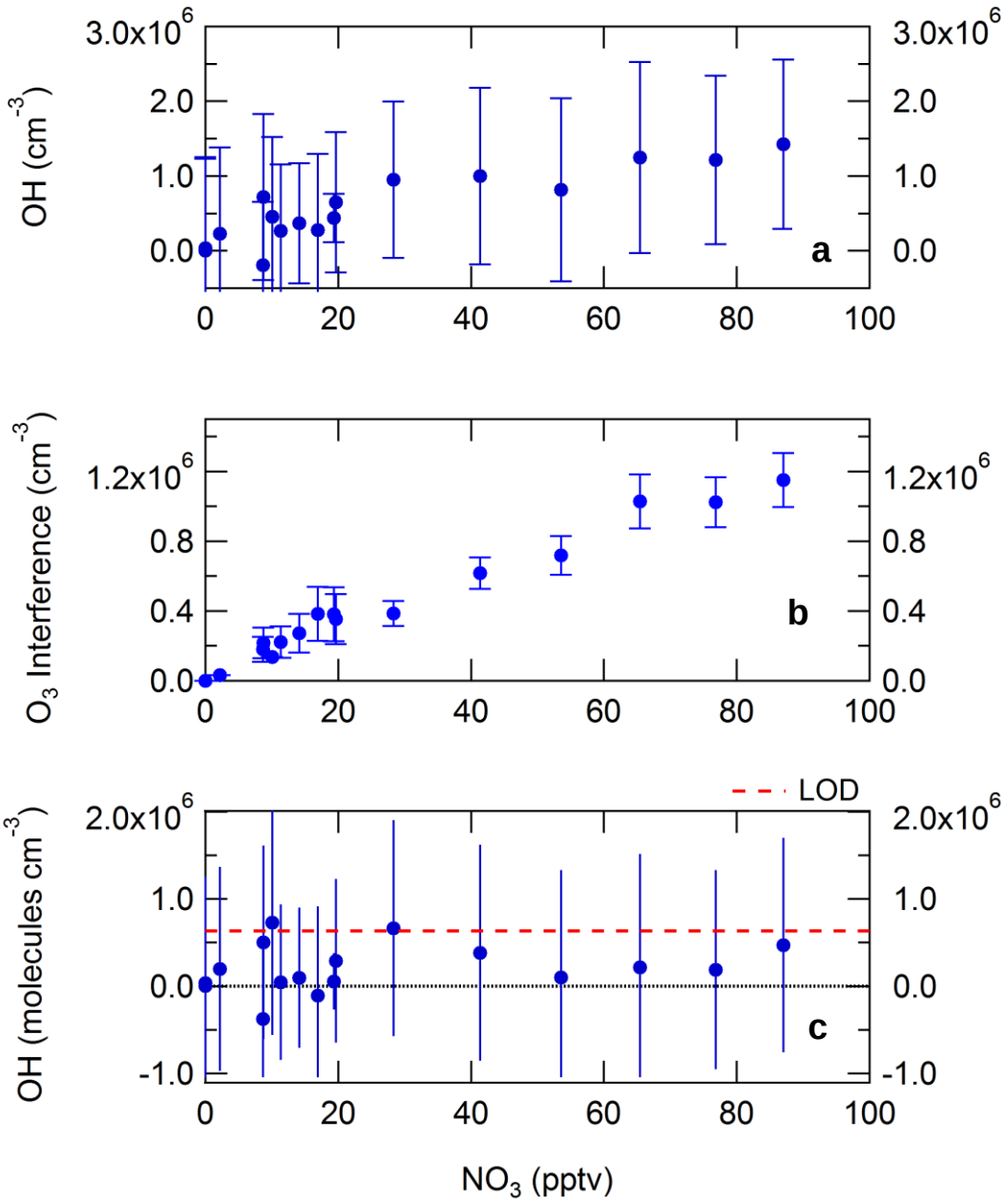

Figure 3.15 a) The total OH concentration of internally generated OH as a function of NO_3 during the NO_3 interference experiments, the error bars represents 2σ errors. b) The internally generated OH as a function of NO_3 from the known O_3 + H_2O interference using E3.7 (section.3.4) with 2σ error bars. c) The internally generated OH from the NO_3 interference as a function of NO_3 obtained by subtracting (b) from (a), with 2σ error bars. The red dashed line represents the LOD during the experiment.

Unlike the results from Fuchs et al. (2016), the interference does not increase linearly with the NO_3 mixing ratio. However, using the point taken at 90 pptv, the interference is equivalent to ~ 6 x 10^4 molecule cm^{-3} at 10 pptv, which is approximately half that was observed by Fuchs et al. (2016) at 10 pptv. These experiments suggest that an interference from NO_3 is not significant for the detection of OH inside the Leeds ground-based FAGE instrument. These results

are also supported by no observed interference during the APHH summer campaign at night-time, where NO_3 reached up to 100 pptv.

3.7 Summary

This chapter has described experiments that have been used to determine: the reduction in sensitivity from the introduction of the IPI; the qualitative analysis for internal removal; ozone interference in the FAGE instrument and experiments to test for a NO_3 interference. The determination of the reduction in sensitivity due to radical wall losses proved to be a challenge. Previous experiments performed in Leeds showed ~40% loss in sensitivity using the turbulent calibration method, whilst further experiments in the field in Beijing and analogous laboratory measurements in Leeds mimicking ambient sampling but with higher concentrations of OH gave consistent results and showed a loss closer to ~0%. This work highlights the importance of performing experiments under conditions similar to ambient sampling methods, as the turbulent flow can perturb the flow within the IPI compared to ambient sampling. The impact of performing experiments using a turbulent flow is highlighted for determining the internal removal. Whereas previous turbulent flow experiments showed ~0% internal removal, measurements during the Tibet field campaign following a suspected leak of NO into the fluorescence cell showed that using 2020 ppmv of propane as the scavenger resulted in ~38 ± 26% internal removal. However, the Tibet campaign estimation of internal removal is only qualitative and is based on an assumption that a there was a leak of NO between the HO_x and RO_x cell during the latter part of the campaign, causing ambient HO_2 to convert to OH *via* reaction with NO. Also, the Tibet campaign estimations of internal removal is very sensitive to real-time differences in ambient OH concentration due to different ambient conditions. Also, the internal removal calculated for the APHH summer campaign was reduced to ~20 ± 14 as the propane mixing ratio was ~1.82 times smaller than the Tibet campaign. The internal removal value of ~20 ± 14 is similar to the theoretically calculated values of ~12% by Woodward-Massey et al. (2020). Since the difference between OHwave and OHchem was small in the APHH summer campaign, hence internal removal was less important the APHH summer data presented in Chapter.5 has not been corrected for internal removal. The internal removal experiment will have to be repeated under laboratory conditions,

using conditions that would not perturb the flow and analogous to ambient sampling conditions. Alternatively, a mercury lamp could be placed within the cell to generate OH inside the cell, which was the method used by Mao et al. (2012) in the Penn. State University instrument. Also, in future campaigns, the propane concentration used will be reduced to reduce the internal removal of internally generated OH.

Interference testing was also conducted for ozone photolysis in the presence of water vapour and the interference from NO_3. The O_3 interference test showed a linear relation with ozone and H_2O mixing ratios and a quadratic relationship with laser power (linear once normalised to laser power).[1] The interference is smaller than the one determine by Griffith et al. (2016), although as discussed previously as the FAGE instrument is a home-built with large variations from instrument-to-instrument this was to be expected, especially since the Pasadena State University (PSU) instrument uses a multi-pass cell whilst the Leeds instrument is a single pass cell. The NO_3 interference testing showed no interference up to 90 pptv of NO_3, the NO_3 concentration made during the experiment was limited by O_3 mixing ratio and the residence time. The NO_3 experiment results were also supported by the comparison between OHwave and OHchem during the summer campaign, where NO_3 could reach up to 100 pptv at night, but no differences between OHwave and OHchem was observed at night-time (see section.5.4.2 for details).

Going forward, the internal removal experiment needs to be determined using experimental conditions analogous to ambient sampling. Quantitative determination of internal removal will allow for the Tibet data to be finalised and should be determined before any future campaigns. Also, in future campaigns, a lower propane flow will be used (most likely 110 ppmv mixing ratio as used in the Beijing winter campaign) so that internal removal does not occur. Also, further laboratory investigation to different interferences that may be present in the FAGE instrument, such as reaction O_3 with different biogenic VOCs.

---

[1] Raw counts(counts s^{-1}) is quadratic in nature as it is a two-photon process, but becomes linear once normalised to laser power (counts s^{-1} mW^{-1})

3.8 References

Faloona, I., Tan, D., Brune, W., Hurst, J., Barket Jr, D., Couch, T. L., Shepson, P., Apel, E., Riemer, D. and Thornberry, T. (2001) 'Nighttime observations of anomalously high levels of hydroxyl radicals above a deciduous forest canopy', *Geophysical Research: Atmospheres*, 106(D20), pp. 24315-24333.

Fuchs, H., Tan, Z., Hofzumahaus, A., Broch, S., Dorn, H.-P., Holland, F., Künstler, C., Gomm, S., Rohrer, F. and Schrade, S. (2016) 'Investigation of potential interferences in the detection of atmospheric RO_x radicals by laserinduced fluorescence under dark conditions', *Atmospheric Measurement Techniques*, 9, pp. 1431-1447.

Griffith, S., Hansen, R., Dusanter, S., Michoud, V., Gilman, J., Kuster, W., Veres, P., Graus, M., Gouw, J. and Roberts, J. (2016) 'Measurements of hydroxyl and hydroperoxy radicals during CalNex-LA: Model comparisons and radical budgets', *Journal of Geophysical Research: Atmospheres,* 121(8), pp. 4211-4232.

Hofzumahaus, A. and Heard, D. (2015) 'Assessment of local HOx and ROx Measurement Techniques: Achievements, Challenges, and Future Directions'.

Lelieveld, J., Butler, T., Crowley, J., Dillon, T., Fischer, H., Ganzeveld, L., Harder, H., Lawrence, M., Martinez, M. and Taraborrelli, D. (2008) 'Atmospheric oxidation capacity sustained by a tropical forest', *Nature,* 452(7188), pp. 737-740.

Mao, J., Ren, X., Zhang, L., Van Duin, D., Cohen, R., Park, J.-H., Goldstein, A., Paulot, F., Beaver, M. and Crounse, J. (2012) 'Insights into hydroxyl measurements and atmospheric oxidation in a California forest', *Atmospheric Chemistry and Physics,* 12(17), pp. 8009-8020.

Novelli, A., Hens, K., Ernest, C. T., Kubistin, D., Regelin, E., Elste, T., Plass-Dulmer, C., Martinez, M., Lelieveld, J. and Harder, H. (2014a) 'Characterisation of an inlet pre-injector laser-induced fluorescence instrument for the measurement of atmospheric hydroxyl radicals', *Atmospheric Measurement Techniques*, 7(10), pp. 3413-3430

Novelli, A., Vereecken, L., Lelieveld, J. and Harder, H. (2014b) 'Direct observation of OH formation from stabilised Criegee intermediates', *Physical Chemistry Chemical Physics,* 16(37), pp. 19941-19951.

Rickly, P. J. A. M. T. (2018) 'Measurements of a potential interference with laser-induced fluorescence measurements of ambient OH from the ozonolysis of biogenic alkenes', *Atmospheric Measurement Techniques*,11(1), pp. 1-16.

Stevens, P., Mather, J. and Brune, W. H. (1994) 'Measurement of tropospheric OH and HO_2 by laser-induced fluorescence at low pressure', *Geophysical Research: Atmospheres,* 99(D2), pp. 3543-3557.

Tan, Z., Fuchs, H., Lu, K., Bohn, B., Broch, S., Dong, H., Gomm, S., Haeseler, R., He, L. and Hofzumahaus, A. (2016) 'Radical chemistry at a rural site (Wangdu) in the North China Plain: Observation and model calculations of OH, HO_2 and RO_2 radicals', *Atmospheric Chemistry and Physic*, 17, pp. 663 - 690.

Tan, Z., Fuchs, H., Lu, K., Hofzumahaus, A., Bohn, B., Broch, S., Dong, H., Gomm, S., Häseler, R. and He, L. (2017) 'Radical chemistry at a rural site (Wangdu) in the North China Plain: observation and model calculations of OH, HO_2 and RO_2 radicals', *Atmospheric Chemistry and Physics,* 17(1), pp. 663-690.

Whalley, L., Edwards, P., Furneaux, K., Goddard, A., Ingham, T., Evans, M., Stone, D., Hopkins, J., Jones, C. E. and Karunaharan, A. (2011) 'Quantifying the magnitude of a missing hydroxyl radical source in a tropical rainforest', *Atmospheric Chemistry and Physics,* 11(14), pp. 7223-7233.

Wolfe, G., Thornton, J., Bouvier-Brown, N., Goldstein, A., Park, J.-H., McKay, M., Matross, D., Mao, J., Brune, W. H., LaFranchi, B. (2011) 'The Chemistry of Atmosphere-Forest Exchange (CAFE) model–part 2: application to BEARPEX-2007 observations', *Atmospheric Chemistry Physics*, 11(3), pp. 1269-1294.

Woodward-Massey, R. (2018) 'Observations of radicals in the atmosphere: measurement validation and model comparisons', *Thesis*.

Woodward-Massey, R., Slater, E., Alen, J., Ingham, T., Cryer, D., Stimpson, L., Ye, C., Seakins, P., Whalley, L. and Heard, D. J. A. M. T. D. (2020) 'Implementation of a chemical background method for atmospheric OH measurements by laser-induced fluorescence: characterisation and observations from the UK and China', *Atmospheric Measurement Techniques Discussions*

4. Measurements of OH, HO_2, RO_2 and OH reactivity made in central Beijing and a comparison with the Master Chemical Mechanism during wintertime.

This chapter describes the measurement of OH, HO_2, RO_2 and k(OH) and their comparison with a box model incorporating the master chemical mechanism (MCM). The measurements were made in central Beijing at the Institute of Atmospheric Physics (IAP) in November and December 2016, as a part of “Air Pollution and Human Health in Chinese megacities” (APHH). A review of previous publications of radical measurements made in China and other urban environments has been described in Chapter 1.

The structure of this chapter is summarised in the following paragraph. First, an introduction to the APHH and AIPRO project (Shi et al., 2018) is provided including the: motivation for the project; details of the instrumentation; details about the measurement site; chemical and meteorological conditions encountered and description of various models used to compare to radical observations. The next section will explore the results from the APHH campaign which includes: a comparison of the measurements with previous Chinese campaigns; an investigation of potential interferences in the OH measurement by comparing OHwave and OHchem; a comparison of the measured OH to OH calculated using photostationary steady-state; a comparison of the measurements with the MCM-base model; a discussion of the major sources and sinks of radicals during the APHH campaign; an analysis of the NO-dependence of measured and modelled radical species which is followed by a discussion of missing chemistry/understanding in high NO environments; then a discussion of the impact of using modelled HONO to predict OH; followed by an investigation into the behaviour of radicals under haze conditions and the implications for gas-phase oxidation under these conditions, and, finally a comparison the models ability to predicts ozone production, especially in high NO environments.

4.1 Introduction to the Winter "An Integrated study of AIR Pollution PROcesses in Beijing"

Air Pollution and Human Health (APHH) in a Chinese Megacity is a joint UK-China programme which aims to: identify the concentrations and sources of urban air pollution in Beijing; identify how people are exposed; understand how it affects your health and determine future strategies to decrease air pollution. APHH has been broken into five different projects: AIRPOLL, AIRPRO, APIC-ESTEE, AIRLESS and INHANCE. The work undertaken by the University of Leeds and described below was under the AIRPRO section of the APHH campaign and was separated into two field campaigns: one in winter (Nov – Dec 2016) and one in summer (May – June 2017). The results from the winter campaign are described in this chapter, whilst the summer results are presented in Chapter 5.

AIRPRO (AIR Pollution PROcesses) is an integrated study of air pollution in Beijing. The project aimed to assess which pollutants are transformed or removed through transport, chemical reactions or photolysis. A further aim of the project is to compare the environment in Beijing with the understanding of environments that are fundamentally different from Beijing. Another key aim is to quantify detailed properties of PM and how this can influence its physical properties and behaviour within the atmosphere (e.g. for haze formation). The AIRPRO project has been separated into seven different sections including: oxidation chemistry; nitrogen budgets; physical and optical properties of aerosols; secondary aerosols; urban meteorology; feedback between haze, photochemistry and dynamics and integration through a multiscale modelling approach.

The APHH campaign took place in central Beijing at the Institute of Atmospheric Physics (IAP), the location of the site is shown in Figure 4.1 (coordinates: 39°58'N 116°22'41'' E). The site is typical of central Beijing with roads ~150 m away to the north, south and west. There is a small canal directly north of the site, and further west there is a park covered mainly by conifer pine trees (Yuan Dynasty Wall Heritage). Beijing is the capital city of China and is classified as a megacity, with a population of more than 20 million people. Beijing is located on the northwest border of the North China Plain (NCP), and is surrounded by the Yanshan Mountains in the west, north and northeast. The topography of Beijing allows for the accumulation of pollutants, especially under southerly winds

carrying emissions from the industrial regions. As shown by Figure 4.1, the measurement site was close to major roads. Thus, local anthropogenic activities might influence the site although no noticeable rush hour was observed (*k*(OH) diurnal in Figure 4.11). The site was also close to a few restaurants and a petrol station. More details of the measurement site can be found in the APHH overview paper (Shi et al., 2018).

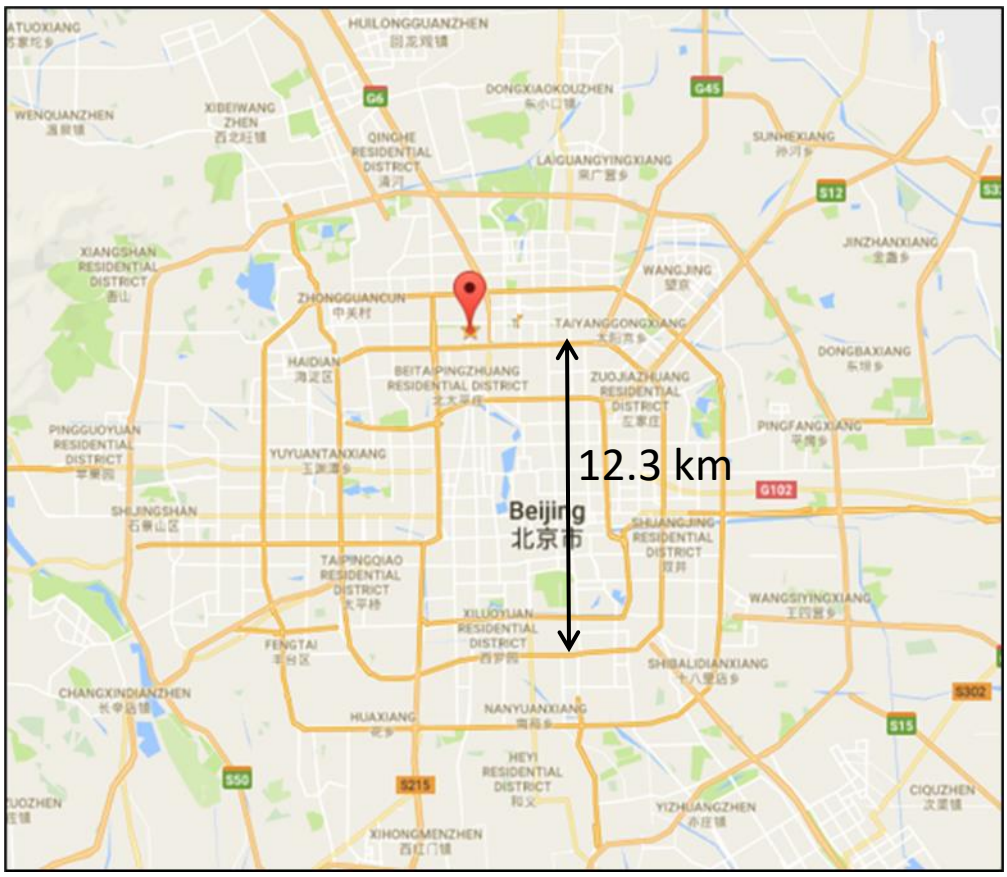

Figure 4.1 Location of the Institute of Atmospheric Physics, Chinese Academy of Sciences (source: Google Maps), the location (39˚58’33’’ N 116˚22’41’’ E) of the APHH campaign.

Alongside the Leeds observation of radicals ($OH/HO_2/RO_2$), OH reactivity, HCHO and photolysis rates; there were a variety of other supporting measurements operated by several universities. A full list of instrumentation present at the IAP site during the APHH winter campaign is shown in Table 4.1. The supporting measurements used in the work below were operated by collaborators from the Universities of Birmingham, York, Cambridge and IAP providing measurements of trace gases (e.g. CO, NO_x, O_3 SO_2, VOCs, $PM_{2.5}$, HONO) and aerosol surface area.

Instrument	Measurements	Institute	References
Container 1			
FAGE	OH (chem and wave), HO_2 and RO_2	Leeds	Whalley et al. (2010)
OH Reactivity	OH reactivity	Leeds	Stone et al. (2016)
Spectral Radiometer	Photolysis Rates	Leeds	Bohn et al. (2016)
Filter radiometer	$j(O^1D)$	Leeds	Bohn et al. (2016)
Dew point hygrometer	Water Vapour	Leeds	Whalley et al. (2010)
Davis met station	Wing speed, direction, temp, RH, pressure	Leeds	
Vaisala CL31 ALC ceilometer	Cloud-base height, mixing height, attenuated backscatter profiles	Reading	Kotthaus and Grimmond (2018)
Personal air monitors (PAMS)	CO, NO, NO_2, PM_1, PM_{10}, $PM_{2.5}$	Cambridge	Moore et al. (2016)
MicroPEMs	Personal PM exposure	IOM	Sloan et al. (2016)
Container 2			
DC-GC_FID	C_2–C_7 VOCs and oVOCs	York	Hopkins et al. (2011)
GCxGC-FID	C_6–C_{13} VOCs and oVOCs	York	Dunmore et al. (2015)
TEI 42i	NO	Birmingham	
Teledyne CAPS	NO_2	York	
TEI 42c	Total NO_y	York	
TEI 49i	O_3	York	
TEI 43i	SO_2	York	
Sensor box	CO	York	Smith et al. (2017)
BBCEAS	HONO, NO_3, N_2O_5	Cambridge	Le Breton et al. (2014)

Container 3			
LOPAP	HONO	Birmingham	Crilley et al. (2016)
LIF-HCHO	HCHO	Leeds	Cryer (2016)
LOPAP	HONO	IC-CAS	Zhang et al. (2019)
GC-MS	Organic nitrates	East Anglia	Mills et al. (2016)
ROS online analyser	Reactive organic species	Cambridge	Wragg et al. (2016)
Container 4			
FAGE	OH (wave), HO_2	Peking	Lu et al. (2012)
FAGE	OH (chem)	Peking	Tan et al. (2017)
TEI 42i	NO	Peking	Tan et al. (2017)
Teledyne CAPS	NO_2	Peking	
TEI 42c with Moly converter	NO_2	Peking	
TEI 49i	O_3	Peking	
TEI	CO	Peking	
Spectral radiometer	Photolysis rates	Peking	
GC-ECD	PAN	Peking	Zhang et al. (2011)
GC-MS	VOCs	Peking	Wang et al. (2015a)
Container 5			
H-TDMA/V-TDMA	Hygroscopicity/volatility	Peking	Wu et al. (2016)
SMPS+APS	Particle number size distribution	Peking	Wu et al. (2016)
Particle size magnifier	Size distribution of < 3 nm particles	Peking	Vanhanen et al. (2011)
IGAC-IC	Water-soluble ions	Peking	Yu et al. (2018)
Xact	Metal	Peking	Yu et al. (2018)
Sunset OC/EC	EC/OC	Peking	Zhang et al. (2017)

Container 6			
IBBCEAS	HONO, NO_2	AIOFM	Duan et al. (2018)
CRDS	NO_3 and N_2O_5	AIOFM	Li et al. (2018)
Nitrate Api-ToF-CIMS	Organics, clusters (HOMs)	Birmingham	Junninen et al. (2010)
SMPS	Particle size distribution	Birmingham	Shi et al. (1999)
Particle size magnifier	Size distribution of < 3 nm particles	Birmingham	Vanhanen et al. (2011)
Container 7			
Fast NOx	NO_x fluxes	York	Vaughan et al. (2016)
AL5002 CO analyser	CO fluxes	York	Gerbig et al. (1999)
HR-ToF-AMS	Fluxes of PM_1 non-refractory (NR) species	CEH	Nemitz et al. (2008)
SP2	BC fluxes	Manchester	Liu et al. (2017)
PTR-ToF-MS	VOC fluxes	GIG Lancaster	Huang et al. (2016)
SYFT-MS Voice 200 Ultra	VOC fluxes	York	Storer et al. (2014)
Container 8			
SMPS3968-APS3321	Particle number size distribution	BNU	Du et al. (2017)
H/V TDMA	Particle hygroscopicity	BNU	Wang et al. (2017b)
CCNC-100	CCN	BNU	Wang et al. (2017b)
PAX (870 nm)	Extinction and absorption coefficients	IAP	Xie et al. (2019)
Ammonia analyser	NH_3	IAP	Meng et al. (2018)
Sunset OC/EC analyser	Online OC/EC	IAP	Zhang et al. (2017)

Container 9			
Iodide FIGAERO-ToF-CIMS	Particle- and gas-phase molar molecule	Manchester	Breton et al. (2018)
CPMA-SP2	Black carbon mass and mixing state	Manchester	Liu et al. (2017)
Micro-reactor	oVOCs	York	Pang et al. (2014)
Tower ~ 100 m			
QCL NH_3	Ammonia fluxes	CEH	McManus et al. (2010)
IRGA LiCOR-7500	CO_2/H_2O flux	CEH	McDermitt et al. (2011)
DMT UHSAS	Size-resolved particle flux (0.06–1 µm)	CEH	Deventer et al. (2015)
TSI APS3021	Size-resolved particle flux (0.5–25 µm)	CEH	Nemitz et al. (2002)
TSI CPC3785	Total particle number flux	CEH	Petäjä et al. (2006)
ROFI	O_3 flux	CEH	Coyle et al. (2009)
Sonic anemometer R3-50	Turbulence, sensible heat flux	CEH	Högström and Smedman (2004)
WXT530 weather station	T , P, RH, wind speed and direction, precipitation	CEH	
2B O_3 analyser	O_3 concentration	CEH	Johnson et al. (2014)
Tower ~ 120 m			
High-volume sampler	$PM_{2.5}$ filter samples	IAP	
Anderson sampler	Size-resolved PM samples	IAP	
Tower ~ 260 m			
High-volume sampler	$PM_{2.5}$ filter samples	IAP	
Anderson sampler	Size-resolved PM samples	IAP	
ACSM	NR PM_1 species	IAP	Sun et al. (2012)

CAPS-PM-Ext (630 nm)	Extinction	IAP	Wang et al. (2015b)
SMPS 3938	Particle number size distribution	IAP	Du et al. (2017)
Gas analyser	CO, O_3 and SO_2	IAP	Zhou et al. (2018)
Aethalometer AE33	Black carbon	IAP	Xie et al. (2019)
Single particle sampler	Individual particles	CUMTB	Wang et al. (2018)
Tower and Tower Basket Measurement			
SNAQ boxes (×6 at different heights)	CO, NO, NO_2, SO_2, PM_1, PM_{10}, $PM_{2.5}$	Cambridge	Popoola et al. (2018)
LOPAP	HONO (3 min average)	Birmingham	Crilley et al.(2016)
Spectral radiometer[c]	Photolysis rates	Leeds	Bohn et al.(2016)
SNAQ	CO, NO, NO_2, SO_2, PM_1, PM_{10}, $PM_{2.5}$	Cambridge	Popoola et al.(2018)
WIBS	Fluorescent biological aerosol particles (FBAPs)	IAP	Yue et al.(2016)
AE33	BC	IAP	Xie et al.(2019)
Los Gatos NH_3 analyser	NH_3	IAP	Meng et al.(2018)
PAX	Light scattering/absorption	IAP	Xie et al.(2019
IAP Ground			
High-volume sampler	$PM_{2.5}$ filter samples	Peking	
Four-channel sampler	$PM_{2.5}$ filter samples	Peking	
High-volume sampler	High-time-resolution $PM_{2.5}$ filter samples	York	
FDMS+Thermo Scientific 1405-DF	Online $PM_{2.5}$ mass concentration	IAP	
IAP Roof/Lab			

Partisol sampler	$PM_{2.5}$ + $PM_{2.5-10}$	Birmingham	Taiwo et al.(2014)
Streaker sampler	Hourly elements in $PM_{2.5}$ and $PM_{2.5-10}$	Birmingham	Taiwo et al.(2014)
Digitel high-volume	$PM_{2.5}$ daily	IAP	
Digitel high-volume	PM_1 – 3-hourly	IAP	
Andersen sampler	Size-resolved PM	IAP	
WIBS	Fluorescent biological particles	IAP	Yue et al.(2016)
CAPS-NO	NO_2	IAP	Ge et al.(2013)
Aethalometer AE33	Black carbon	IAP	Xie et al.(2019)
CAPS-PMSSA	Extinction, scattering	IAP	Han et al.(2017)
HR-ToF-AMS	NR-PM species	IAP	Sun et al.(2016)
SP-AMS	Refractory BC and coated aerosol composition	IAP	Wang et al.(2017a)
Iodide FIGAERO-ToF-CIMS	Particle- and gas-phase molar molecule	IAP	Zhou et al.(2018
Single particle sampler	Individual particles	CUMTB	Wang et al.(2018)

Table 4.1 Table showing the measurements made at the Institute of Atmospheric Physics (IAP) during the winter APHH campaign. AIOFM is Anhui Institute of Fine Optics and Mechanics; BNU is Beijing Normal University; CEH is Centre for Ecology and Hydrology; CUMTB is China University of Mining and Technology (Beijing); GIG is Guangzhou Institute of Geochemistry, Chinese Academy of Sciences; NUIST is Nanjing University of Information Science and Technology; IC-CAS is Institute of Chemistry, Chinese Academy of Sciences. a - Deployment of instrument from 10 November 2016 to 25 June 2017. b - Winter campaign only. c – summer campaign only. Table taken from Shi et al.(2019)

The APHH winter campaign official campaign dates were from the 10th of November to the 10th of December 2016, but radical measurements commenced on the 8th of November. The last radical observations were made on the 10th of December in the early morning followed by a final calibration. The coverage of radical data shown in section.4.4.1 is patchy due to several logistical and instrumental issues that arose during the winter campaign, including: delays in gas delivery which meant OH measurements were only available between

08/11/2019 – 17/11/2019; failure of the roots blower (Leybold RUVAC WAU 1001) on the 9th of November and replacement on 16th of November and laser alignment problems from the 24th of November to the 2nd of December. The OH reactivity measurements were also dependant on the roots blower and the laser, so the OH reactivity and radical data coverage is very similar. The photolysis frequency, filter radiometer and HCHO measurements were consistently made from 08th November to 10th December. The measurements of OH made from 08th November to 24th November were OHwave only, whilst the measurements from 2nd December to 10th December utilised the inlet pre-injector (IPI) allowing measurements of both OHwave and OHchem.

As shown in Figure 4.3, throughout the campaign various chemical and meteorological conditions were observed, including several haze periods. According to the meteorological standards (QX/T113-2010), haze is defined as either visibility < 10 km at a relative humidity (RH) < 80% or if RH is between 80 - 95%, visibility < 10 km and $PM_{2.5}$ > 75 μg m^{-3}. For this work the periods defined as haze events are when $PM_{2.5}$ exceeds 75 μg m^{-3}, the date and time of the measured haze events is shown in Table 4.2. The windrose diagram shown Figure 4.2a shows the 30-year climatology between 5 November – 10 December, this climatology shows that during this winter period the dominant wind direction is from the northwest which coincides with higher wind speeds. The wind roses for the winter 2016 campaign (Figure 4.2b) is noisier but shows a similar trend to the 30-year climatology, although southwesterly winds were more frequent during the winter of 2016. The south-westerly winds observed in Beijing during the winter 2016 campaign potentially brought an increased amount of more polluted air from the upwind Hebei province.

The variation, during the campaign, of $j(O^1D)$, relative humidity (RH), temperature, CO, SO_2, O_3, NO, NO_2, HONO and $PM_{2.5}$ is shown in Figure 4.3. There were several co-located measurements of HONO made during the APHH campaign. The HONO mixing ratios shown in Figure 4.3 and used in the models were values taken from a combination of all measurements taken at the IAP site, as recommended in Crilley et al. (2019) where further details of the methodology for selecting the HONO data is provided. For a given time of day, large variations in $j(O^1D)$ were observed during the campaign, with the reductions in $j(O^1D)$ driven by enhanced $PM_{2.5}$ (see Figure 4.3). The temperature during the campaign varied

between -10°C and +15°C. The relative humidity during the campaign varied between 20% and 80% RH; generally higher RH coincided with haze events. The time-series for trace gas species showed high mole fractions for CO (1000-4000 ppbv), SO_2 (5 – 25 pbbv), NO (20 – 250 ppbv) but relatively low O_3 (1 – 30 ppbv). During the campaign HONO was generally quite high, reaching up to 10 ppbv (Crilley et al., 2019). Frequent haze events were also observed during the winter campaign, with $PM_{2.5}$ mass concentration reaching up 530 µg m^{-3}.

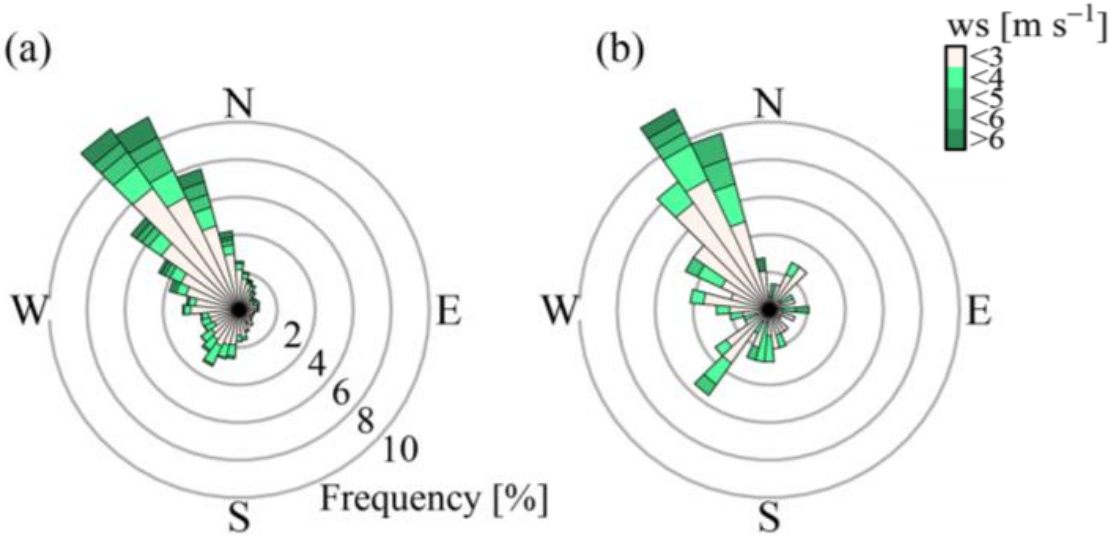

Figure 4.2 Beijing wind roses from ERA-Interim 10 m horizontal wind (40° N, 116°E) for a) 5 November – 10 December 1988 – 2017 and b) 5 November – 10 December 2016. Diagram modified from Shi et al. (2019)

The median diurnal variation for $j(O^1D)$, NO, NO_2, O_3, O_x (O_3 + NO_2), HONO, SO_2 and CO separated into haze and non-haze is shown in Figure 4.4; the periods defined as haze are shown in Table 4.2. During the haze events $j(O^1D)$ decreased by ~50% at midday on average. The photo-activity of j(HONO) and $j(NO_2)$ extends further into the visible region of the solar spectrum and so they exhibit lower reductions in their photolysis rates during haze; ~40% reduction for j(HONO) and ~35% for $j(NO_2)$ (see Hollaway et al. (2019)). On average, during haze periods NO concentrations reached 100 ppbv at 8 am, although on some days NO was close to 250 ppbv. On clearer days, peak NO was ~ 40 ppbv at 8 am. A distinct increase in CO, NO_2 and SO_2 was also observed during haze periods, however, no distinct diurnal pattern inside and outside of haze for these

species was observed. On average, the O_3 during the haze periods was reduced by a factor of 3, this is due to the high NO observed during haze periods titrating the O_3. As shown in Figure 4.4, NO and O_3 shows an anti-correlation during the cleaner periods due to inter-conversion. O_x is the sum of NO_2 and O_3; during haze periods O_x increased from 40 ppbv to a maximum of 53 ppbv on average. HONO in both clean and haze periods showed a distinct diurnal pattern, with a large decrease in the morning due to loss through photolysis and a minimum in the afternoon. A large increase in HONO concentration overnight probably originates from heterogeneous sources (i.e. NO_2 converting to HONO on humid surfaces) (Lu et al., 2018, Li et al., 2012, Zhang et al., 2016, Lee et al., 2015, Finlayson-Pitts et al., 2003, Zhou et al., 2003). On average, the HONO concentration was larger by a factor of 3 at midday during haze periods compared with during the clearer periods.

Event	Time (LT)	$PM_{2.5}$ (μg m^{-3})	Visibility (km)
Event 1	08/11 21:00 – 10/11	158 (79 – 229)	4.1 (2.3 – 8)
Event 2	15/11 21:00 – 19/11	143 (56 – 244)	4.2 (0.6- 8)
Event 3	24/11 12:00 – 27/11	210 (68 – 363)	4.2 (1.5 -8)
Event 4	02/12 16:00 – 05/12	239 (58 – 530)	3.9 (0.9 -8)
Event 5	06/12 09:00 – 08/12	144 (64 – 229)	4.6 (2.2 – 8)

Table 4.2 Table showing the haze periods observed during the winter campaign. Table recreated from Shi et al. (2018), from which further details can be found.

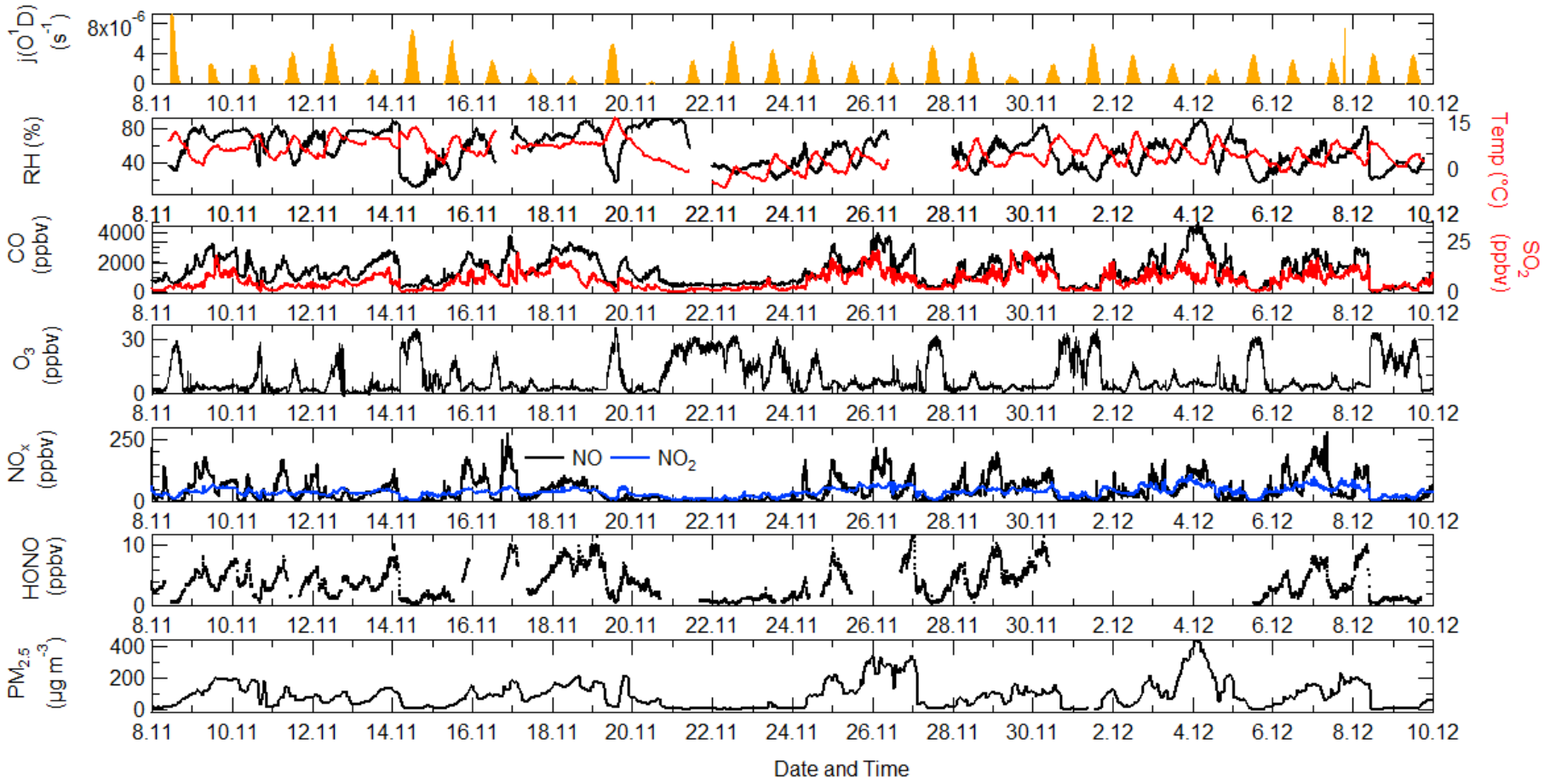

Figure 4.3 Time-series of *j*(O^1D), relative humidity (RH), temperature (Temp), CO, SO_2, O_3 NO_x HONO and $PM_{2.5}$ from the 8th of November to 10th December 2016 at Institute of Atmospheric Physics (IAP), Beijing.

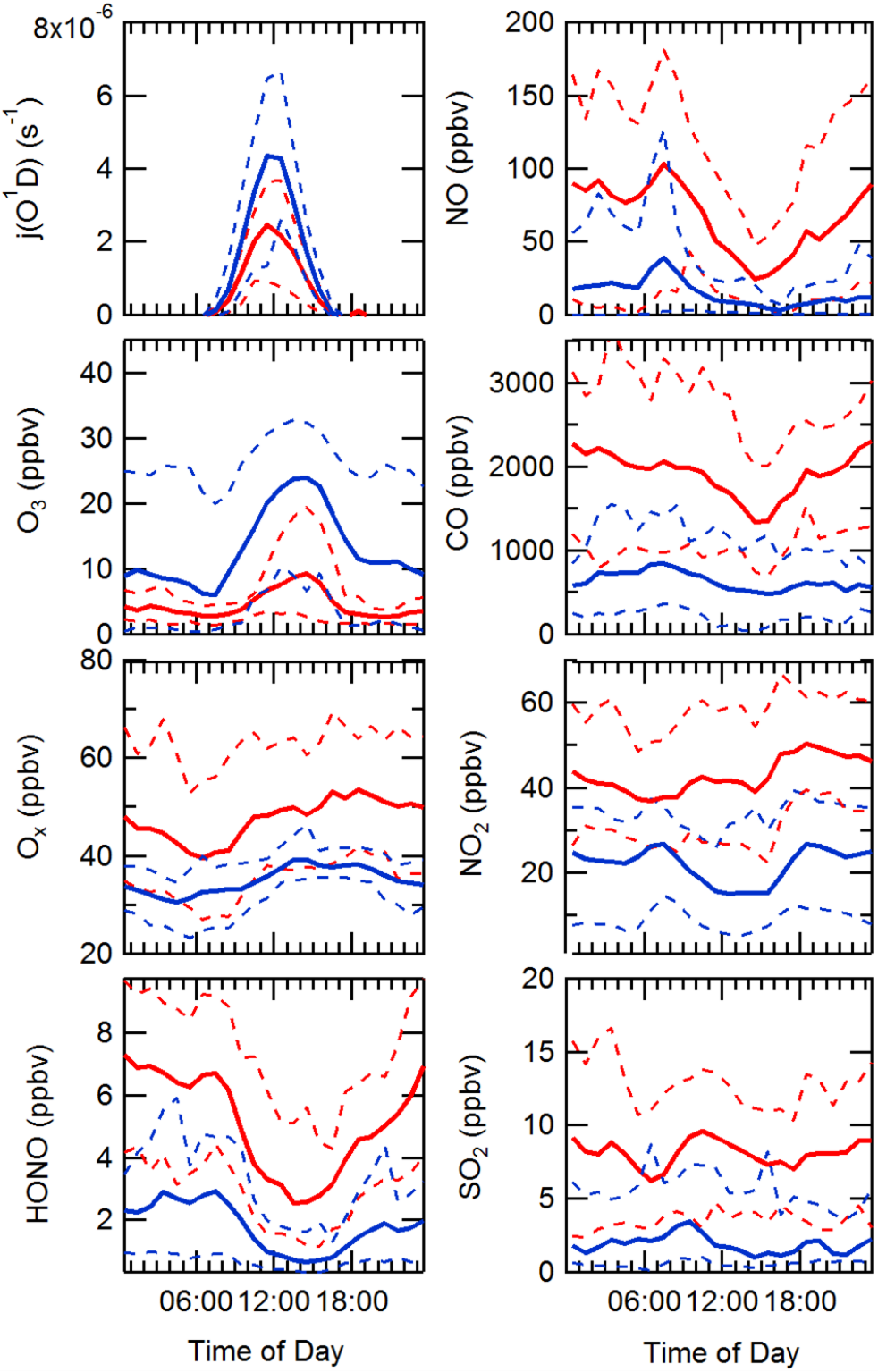

Figure 4.4 Comparison of $j(O^1D)$ (s^{-1}), NO (ppbv), O_3 (ppbv), CO (ppbv), O_x (ppbv), NO_2 (ppbv), HONO (ppbv) and SO_2 (ppbv) during and outside of haze events; red and blue respectively. The dashed lines represent the 25/75 percent confidence intervals for the respective species and pollution period. The data has been averaged over the entire campaign period.

4.2 FAGE operating parameters

The Leeds ground-based FAGE instrument was operated with and without the inlet pre-injector (IPI) which is mounted onto the HO_x fluorescence cell. The difference in sampling timings when operating with or without the IPI was described in section.2.41. Both the OHwave and OHchem data is presented in this chapter. The OHchem data has not been corrected for the known interference of O_3 photolysis within the cell by the laser in the presence of water vapour, as the large error on the O_3/H_2O interference may cause some night-time values for OH to become negative. The average O_3/H_2O correction for the campaign would be $(8.2 \pm 2.2) \times 10^3$ molecule cm^{-3}.

The general running conditions for the Leeds ground-based FAGE instrument has been described in Chapter 2, for the work described below the following gases and flows were used. The NO (Messer, 99.99%) flow was added to the HO_x cell (during HO_2 mode) and RO_x cell (continuously) at 5 and 100 sccm, respectively. CO (Messer, 10% in N_2) was added continuously to the RO_x flow tube at 125 sccm. In RO_x mode NO (Messer, 500 ppmv in N_2) was added to the flow tube at 30 sccm. For the determination of the OHchem background, 5 sccm of propane (110 ppmv - diluted in 500 sccm of N_2) was injected into the ambient air, see Chapter 2 for more details.

Calibrations for OH, HO_2, HO_2' (HO_2 calibration in RO_x cell) and RO_2 were performed at regular intervals throughout the campaign, approximately every four days. Figure 4.5 shows the calibrations factors for OH, HO_2, HO_2' and RO_2 taken during the APHH winter campaign, and the value of the calibration factors applied for each day. Figure 4.5 shows that changes in the C_{OH} is tracked by C_{HO2} whilst C_{HO2*} is tracked by C_{RO2}. The correlation of calibration factors shows that the differences are caused by changes in each respective cell. Figure 4.5 also shows that C_{RO2} and C_{HO2*} do not change significantly during the APHH winter campaign, whilst the C_{OH} and C_{HO2} show a decrease during the campaign, and this is reflected in the calibration factors applied to different days. The calibration factors C_{OH} and C_{HO2} drops significantly for the 08/12 and 09/12 due to a change in the PMT. The limits of detection (LOD) varied during the APHH campaign as it is dependent on several factors, with laser power fluctuating between performance

tune-ups. The campaign-median 5 min averaged LODs was 7.7 x 10^5 molecule cm^{-3}, 2.8 x 10^6 molecule cm^{-3} and 8.4 x 10^6 molecule cm^{-3} for OH, HO_2 and RO_2, respectively. The average laser power during the APHH campaign was 11 mW.

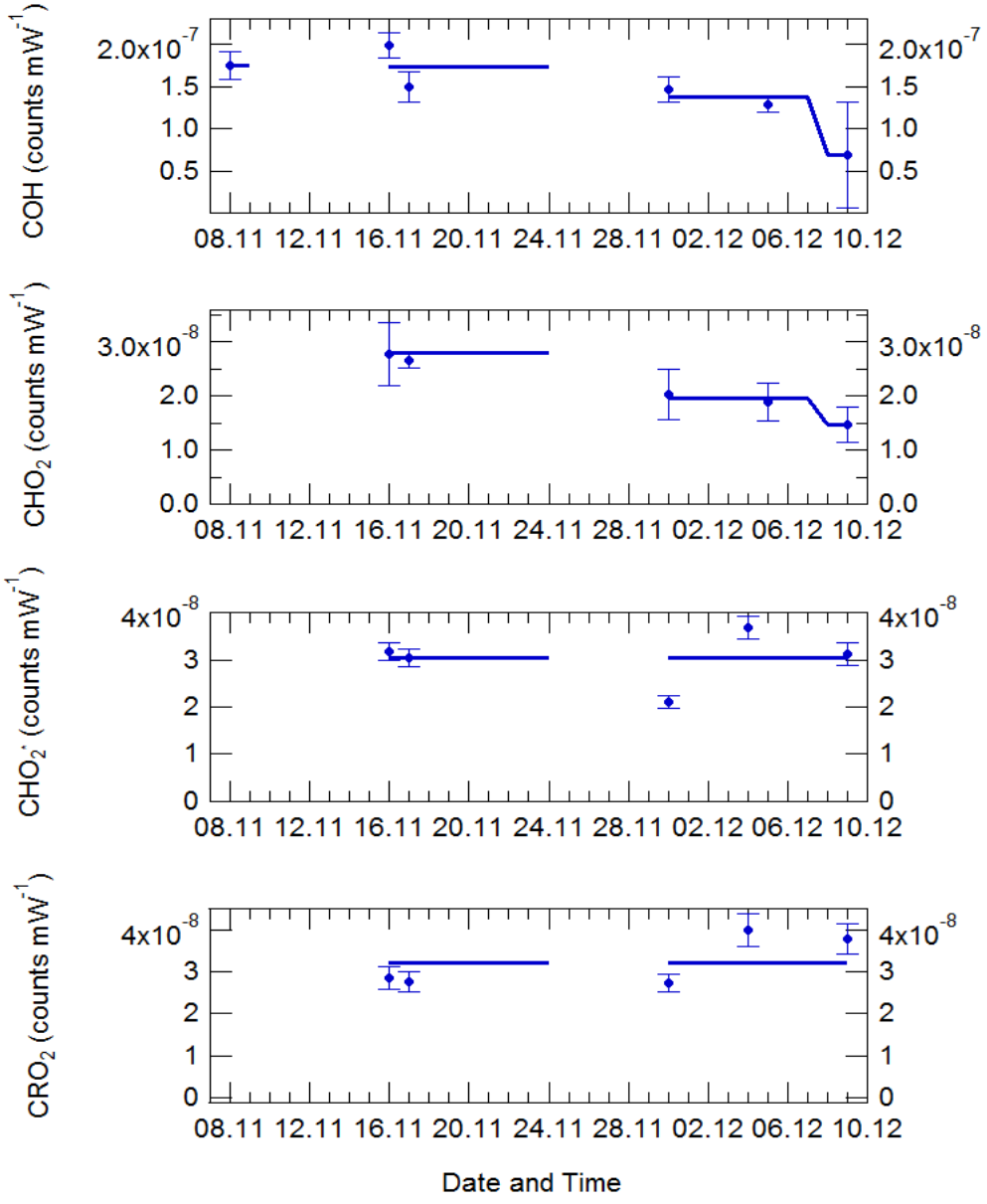

Figure 4.5 The calibration factors (circles) determined for OH, HO_2, HO_2^* and RO_2 throughout the APHH winter campaign and the calibration factors associated errors. The line through the data shows the calibration factors that have been applied to the data for different days.

4.3 Model Descriptions

4.3.1 Master Chemical Mechanism

The radical concentration has been compared to the predictions from a box model incorporating the Master Chemical Mechanism (MCM) using several different model scenarios, for this work MCM version 3.3.1 was used. The master chemical mechanism (http://mcm.leeds.ac.uk/MCM/home) was used in a zero-dimensional box model. The MCM is a near-explicit chemical mechanism representing the degradation of methane and 142 primary emitted VOCs. The mechanism has a total of ~17,000 reactions and ~6,700 species. As described below, the model was run with a sub-set of the MCM and treated the degradation of simultaneously measured trace VOCs, CH_4 and CO following oxidation by OH, O_3 and NO_3, and included 15333 reactions and 3800 species. The complete details of the kinetic and photochemical data used in the mechanism can be found on the MCM website. The model was constrained by measurements of NO, NO_2, O_3, CO, HCHO, HNO_3, HONO, water vapour, temperature, pressure and individual VOC species measured by GC-FID (gas chromatography with flame ionisation). Table 4.3 shows the different species measured by GC-FID. The model was constrained with measured $j(O^1D)$ (measured using filtered radiometer) and $j(NO_2)$, j(HONO) measured using a spectral radiometer. For other UV-active species, such as HCHO and CH_3CHO, photolysis rates were calculated by applying a scale factor of the ratio of clear-sky $j(O^1D)$ to observed $j(O^1D)$ to account for clouds. For species able to photolyse further into the visible, the ratio of clear-sky $j(NO_2)$ to observed $j(NO_2)$ was used. The variation of the clear-sky photolysis rates (j) with solar zenith angle (χ) was calculated within the model using the following expression E4.1:

$$j = l\cos(x)^m \mathrm{x}\, e^{-nsec(x)} \qquad \text{E4.1}$$

The parameters l, m and n were optimised for each photolysis frequency (see Table.2 in Saunders et al. (2003)).

A constant H_2 concentration of 500 ppbv was assumed (Forster et al., 2012). The model inputs were updated every 15 minutes, the species measured more frequently were averaged to 15 minutes whilst the measurements with lower time resolution were interpolated. The loss of all non-constrained, model generated species by deposition or mixing, was represented as a first-order deposition rate

equivalent to 0.1/MH, where MH represents the measured boundary layer – see section.4.4.5.1 for more details. The model was run for the entire campaign in overlapping 7-day segments. To allow the unmeasured, model generated intermediate species time to reach steady-state concentrations, the model was initialised with inputs from the first measurement day (16th November) and spun-up for 2 days before comparison to measurements were made. Since measurements of up-to C7 VOC were measured by the PTR-MS (Proton-transfer-reaction Mass Spectrometry), sensitivity analysis has been performed to observe the impact of including higher weight VOCs. The result of the sensitivity analysis shows that introducing a greater number of higher weight VOCs does not have a larger impact on the model results (see section.4.4.5.1 for more details).

Instrument	Species	Reference
DC-GC-FID	CH_4, C_2H_6, C_2H_4, C_3H_8, C_3H_6, isobutane, butane, C_2H_2, trans-but-2-ene, but-1ene, Isobutene, cis-but-2-ene, 2-Methylbutane, pentane, 1,3-butadiene, trans-2-pentene, cis-2-pentene, 2-methylpetane, 3-methypetane, hexane, isoprene, heptane, Benzene, Toluene, m-xylene, p-xylene, o-xylene, CH_3OH, CH_3OCH_3.	Hopkins et al., 2011

Table 4.3 Table showing the species measured by the DC-GC-FID that have been used to constrain the box model using the Master Chemical Mechanism.

The different model scenarios that are considered are described below:

1. **MCM-base**: The base model was run using the parameter described above.

2. **MCM-MH**: The base model was modified to have different deposition rates of model intermediates. The deposition rate was changed from 0.1/MH, 0.05/MH and 0.01/MH, where MH represents the measured boundary layer (Kotthaus and Grimmond, 2018)). It should be noted that this model was only run between 02/12/2016 – 05/12/2016, as the different models

are being used to represent how deposition rates affect the OH reactivity and radical concentration.

3. **MCM-fVOC**: The base model was modified to include higher weight VOCs including: ethylbenzene, isopropylbenzene, propylbenzene and trimethylbenzene. The higher weight VOCs were measured by PTR-MS (Huang et al.2016).

4. **MCM-cHO$_2$**: This scenario is the same as MCM-base but the model has been constrained to the measurements of HO$_2$.

5. **MCM-uHONO**: This model is the same as MCM-base but the model has been unconstrained to HONO.

6. **MCM-cOH-uHONO**: This model is the same as MCM-uHONO but the model has been constrained to cOH.

7. **MCM-PRO$_2$**: This model is the same as MCM-base but includes an extra primary source of RO$_2$ species. The additional primary source has been calculated using E4.2 (Tan et al., 2017):

$$P'(RO_x) = k_{HO2+NO}\,[HO_2][NO_2] + P(HO_2)_{prim} + P(RO_2)_{prim} - k_{VOC}[OH] - L(HO_2)_{term} - L(RO_2)_{term} \quad \text{E4.2}$$

The calculated additional RO$_2$ source was included in the model (model run MCM-PRO2) as a single species 'A-I' that formed several RO$_2$ species at the required RO$_2$ production rate (i.e. *k**[A-I] = missing primary production rate). The RO$_2$ species produced were, using their MCM name: HOCH2CH2O2, HYPROPO2, TM135BPRO2, STYRENO2, IBUTOLBO2, TM123BPRO2, BUTDBO2, OXYBIPERO2 and CH3O2 and the structures of these RO$_2$ species are shown in Table 4.4. The RO$_2$ species were chosen after a rate of production analysis (ROPA) analysis showed they were highest produced RO$_2$ species in the model.

MCM Name	Structure	MCM Name	Structure
HOCH2CH2O2	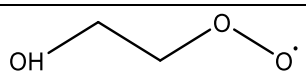	BUTDBO2	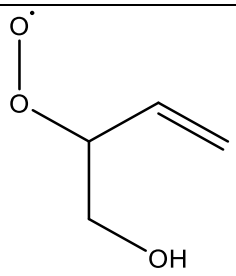
HYPROPO2	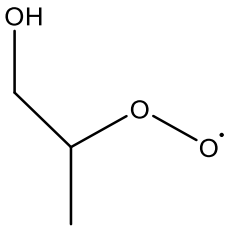	OXYBIPERO2	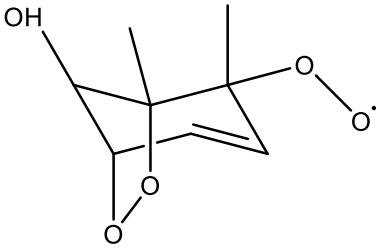
IBUTOLBO2	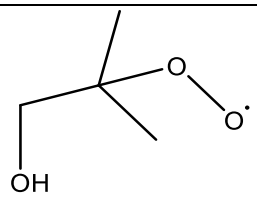	CH3O2	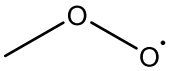
BUT2OLO2	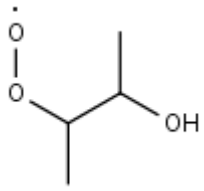	NBUTOLAO2	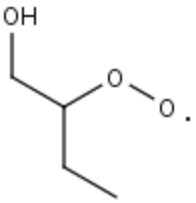

Table 4.4 The names and associated structures of the RO_2 species used to add additional primary production of RO_2 species into MCM-PRO2 and MCM-PRO2-SA. See http://mcm.leeds.ac.uk/MCMv3.3.1/home.htt for more details.

8. **MCM-PRO$_2$-SA**: This model is the same MCM-PRO$_2$ but includes the uptake of HO_2 with a coefficient of $\gamma = 0.2$.

9. **MCM-kRO2NO-2**: This model is the same as MCM-base, but the kRO2NO (rate of reaction for RO_2 + NO) and kAPNO (rate of reaction for acyl RO_2 species + NO) rate constant has been decreased by a factor of 2 by changing KRO2NO from 2.7E-12*EXP(360/Temp) to 1.35E-12*EXP(360/Temp) and KAPNO from 7.5E-12*EXP(290/Temp) to 3.75E-12*EXP(290/Temp).

10. **MCM-kRO2NO-10**: This model is the same as MCM-base, but the KRO2NO and KAPNO has been decreased by a factor of 10 by changing KRO2NO from 2.7E-12*EXP(360/Temp) to 2.7E-13*EXP(360/Temp) and KAPNO from 7.5E-12*EXP(290/Temp) to 7.55E-13*EXP(290/Temp).

4.3.2 Photostationary Steady-State (PSS)

Using field measured quantities, a steady-state approach has been used to calculate the OH concentrations for comparison with measurements, and to determine the major sources of OH measured during the campaign. The photostationary steady-state equation for OH, obtained from $d[OH]/dt = 0$, is given by a balance of the rate of production and the rate of destruction of OH:

$$[OH]_{pss} = \frac{p(OH) + j(HONO)[HONO] + k[HO_2][NO]}{k(OH)} \quad \text{E4.3}$$

where p(OH) is the measured rate of OH production from ozone photolysis and the subsequent reaction of $O(^1D)$ with water vapour, k is the rate coefficient for the reaction of HO_2 with NO at the relevant temperature, and k(OH) is the measured OH reactivity. E4.3 is a simplification, and only takes into account the production of OH from two photolysis sources (O_3 and HONO) and the reaction of HO_2 + NO. Owing to the generally low ozone experienced O_3+alkene reactions were not included as these reactions were found to contribute < 10% to the total OH production, as discussed in the MCM modelling section below. The pseudo first-order rate of loss of OH was constrained using the measured OH reactivity during the campaign, and hence includes all loss processes for OH. OH reactivity is discussed further in section.4.4.5.

4.4 Results

4.4.1 Time-series

Figure 4.6 shows the time-series for OH (wave and chem), HO_2, RO_2 (and the speciation into simple and complex RO_2 species, see section.2.1.8 for more details) and OH reactivity measurements from the 8th November to 10th December 2016.

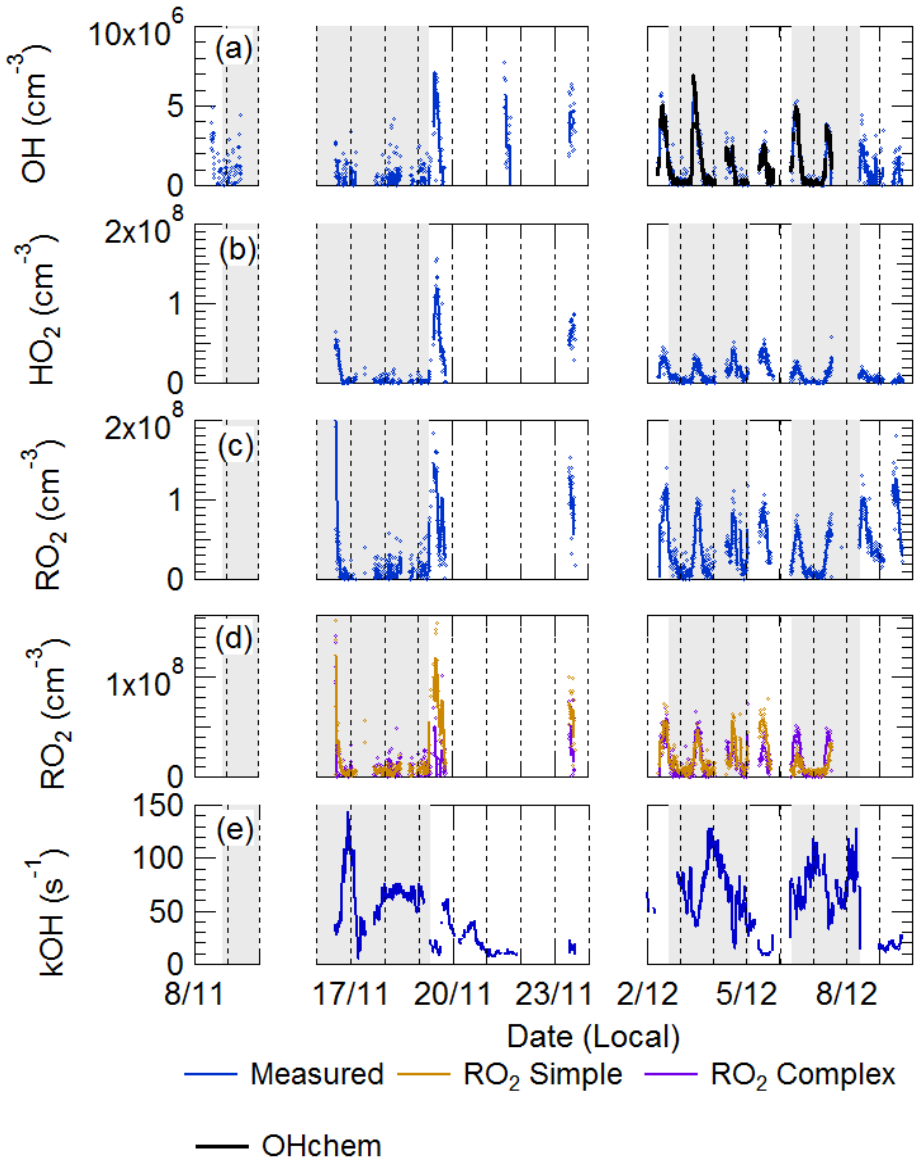

Figure 4.6 a) Time-series for OHwave (blue) and OHchem(black). b) time-series for HO_2. c) Time-series for total RO_2. d) Time-series for speciated RO_2 into simple(gold) and complex(purple) e) Time-series for measured *k*(OH). The shaded grey areas represent haze periods. A haze period is defined when $PM_{2.5}$ is greater than 75 µg m^{-3}.

The radical observations follow the expected diurnal profile with a maximum at midday and low night-time concentrations. Both the OH and HO_2 night-time values are scattered around zero and below their average limit of detection for the campaign; 7.7 x 10^5 and 5.6 x 10^6 for OH and HO_2, respectively. Whilst total RO_2 generally shows a non-zero value at night-time, the concentration measured is higher than the average LOD for the campaign (5 x 10^6 molecule cm^{-3}). The daily maximum for the radical species varied day-to-day by 1 to 8 x 10^6 cm^{-3}, 0.7 to 1.5 x 10^8 cm^{-3} and 1 to 2.5 x 10^8 cm^{-3} for OH, HO_2 and RO_2, respectively.

The general trend for the radical measurements can be seen more easily in Figure 4.7 which shows the average diurnal for OH, HO_2 and RO_2 (speciated into simple and complex). Both OH and RO_2 peak at 12:30 (solar noon (12:00)), whilst the peak in HO_2 concentration is slightly later at 13:30. The speciation into simple and complex RO_2 species (see section.2.1.8 for definition) shows almost a 1:1 ratio across the day, although simple RO_2 species become more dominant in the afternoon. The rise in OH coincides with sunrise (~06:15) and the OH concentration is almost zero (less than 2 x 10^5 molecule cm^{-3}) by sunset (~17:15). By comparison, both the HO_2 and RO_2 rise also coincide with sunrise but do not decrease to zero after sunset. Although the HO_2 concentration (~2 x 10^6 molecule cm^{-3}) past 21:00 is below the average LOD of 2.8 x 10^6 molecule cm^{-3}, the RO_2 concentration is generally above the LOD of 8.4 x 10^6 molecule cm^{-3}. The average diurnal in Figure 4.7 shows a double peak for OH and HO_2, the levelling of OH and HO_2 earlier in the day (~09:00) is caused by the depletion of HONO to form OH through photolysis, which has built up overnight, by photolysis (see section.1.2.5 for more details).

A comparison of previous winter urban campaigns is shown in Table 4.5. The OH concentration measured during the APHH winter campaign is relatively high for a winter urban campaign, on average the OH concentration peaked at 2.7 x 10^6 molecule cm^{-3}. The OH concentration is ~ 3, 2.3, 2, 1.65 and 1.5 times larger than winter measurements during the New York (Ren et al., 2006), Beijing (Ma et al., 2019), Tokyo (Kanaya et al., 2007), Birmingham (Emmerson et al., 2005) and BEST-ONE (Tan et al., 2018) campaigns, respectively, and similar to the campaign in Boulder (Kim et al., 2014). However, it should be noted that the Boulder campaign took place in late February/March in the northern hemisphere when there are higher light levels and water vapour (see Table 4.5 for details). As shown in Figure 4.6, the sustained OH concentration inside haze events, for example up to 6 x 10^6 molecule cm^{-3} of OH was observed on the 03/12/2016, suggests gas-phase oxidation is still active under these haze events despite the lower light levels and is discussed more in section.4.4.8

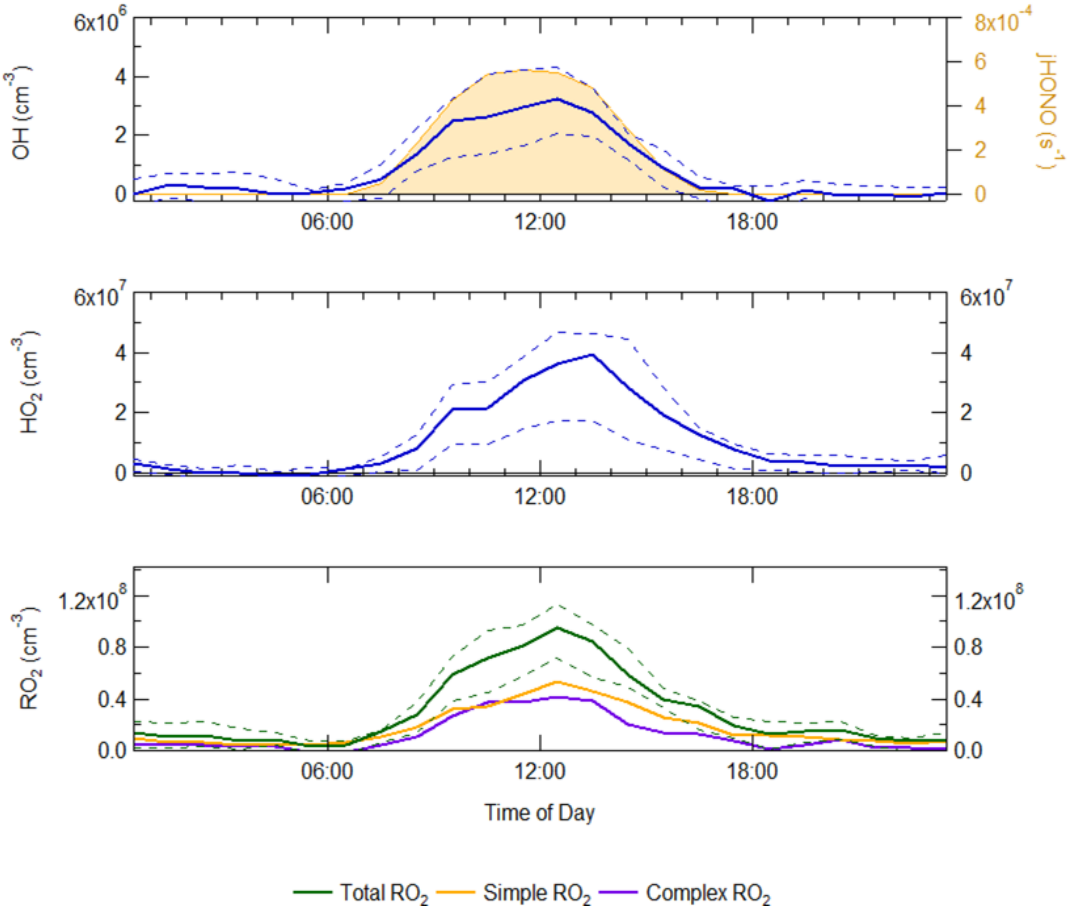

Figure 4.7 a) Average median diurnal of OH and *j*(HONO) b) Average median diurnal for HO_2 c) Average median diurnal for total RO_2 (green) and speciation into simple (yellow) and complex (purple). The dashed lines represent the 25/75th percentile.

Campaign	Months, Year	NO (ppbv)	O_3 (ppbv)	OH		HO_2		RO_2		Notes	References
				Measured (10^6 cm^{-3})	Model/ Obs	Measured (10^8 cm^{-3})	Model/ Obs	Measured (10^8 cm^{-3})	Model/ Obs		
APHH, Central Beijing, China	Nov – Dec, 2016	60	12	2.7	0.58	0.39	0.17	0.88	0.04	Average midday.	This work.
BEST-ONE Suburban Beijing, China	Jan – March, 2016	7	30	2.2	0.5	0.5	0.4	0.7	0.2	Campaign Median, midday, polluted period	Tan et al. 2018
NACHTT Boulder, USA	Late Feb, 2011	7	37	3	0.9	-	-	-	-	Average midday	Kim et al. (2014)
PUMA, Birmingham, UK	Jan-Feb, 2000	10	13	2	0.50	3	0.49	-	-	Average midday	Emmerson et al. (2005)
IMPACT Tokyo, Japan	Jan-Feb, 2004	8.1	35	1.5	0.93	0.27	0.88	-	-	Average midday	Kanaya et al. (2007)
PMTACS-NY2001 New York, US	Jan–Feb, 2004	25	20	1	0.83	0.17	0.17	-	-	Average midday	Ren et al. (2006)
PKU, Beijing, China	Nov – Dec, 2017	30	10	1.4	1.4	0.3	0.13	-	-	Average Midday, Polluted period	Ma et al. (2019)

Table 4.5 Previous field measurements of OH, HO_2 and (only for APHH and BEST-ONE) that have taken place during wintertime in urban areas, together with the typical midday average NO and O_3 levels and the average measured to modelled ratio. Modified from Kanaya et al., 2007.

4.4.3 Investigation of possible OH interferences by chemical modulation experiments

As discussed in section.2.1.4 the traditional way to measure the background signal (OHwave) in the LIF technique is to discriminate OH fluorescence signal from non-resonant signals by tuning the laser to off-resonance with respect to the OH radical $Q_1(1)$ transition of the $A^2\Sigma^+$, $v'=0 \leftarrow X^2\Pi_i$, $v''=0$ band. The OHwave method, however, cannot discriminate between ambient OH and OH radicals potentially artificially generated within the detection cells. A well characterised interference in FAGE systems is from the laser photolysis of O_3, which generates a small OH artefact signal. This artefact has been observed in FAGE systems (Griffith et al., 2013, Fuchs et al., 2010, Whalley et al., 2018), although the level of interference differs between different FAGE instruments. The ozone interference has been fully characterised in the Leeds FAGE ground-based field instrument (see section.3.4) and is represented by E4.4:

$$\mathrm{OH_{int}} = 520 * [\mathrm{O_3}](\mathrm{ppbv}) * \text{laser power (mW)} * \mathrm{H_2O}\ (\%) \qquad \text{E4.4}$$

Another recently reported OH interference is produced by NO_3 radicals and may cause a noticeable interference at night (Fuchs et al., 2016). The NO_3 interference has been investigated in the Leeds ground-based FAGE instrument, but no detectable interference has been discovered (see section.3.5 for more details). During the APHH campaign interference free OH were measured using the IPI *via* OHchem. The time-series for the comparison of OHwave vs OHchem is shown in Figure 4.6a and shows a very good agreement between the two measurements. Hence the OHwave data has not been corrected for the known O_3 interference as the error on the interference correction is large and would cause the OH night-time data to become negative. The O_3/H_2O interference correction for the APHH winter campaign is very small (median 8.5 x 10^3 molecules cm^{-3}) due to the low concentration of ozone and water. The overall agreement between OHwave and OHchem is shown in the correlation plot in Figure 4.8. The OHwave and OHchem data has been averaged to 15 minutes, and Figure 4.8a. shows a tight correlation with points scattered around the 1:1 agreement line. The correlation plot of

OHwave vs OHchem has been fitted with an ODR (orthogonal distance regression) fitting, to take into account the error in both the *x*- and *y*-axis and yields a slope of 1 within error (1.05 ± 0.7).

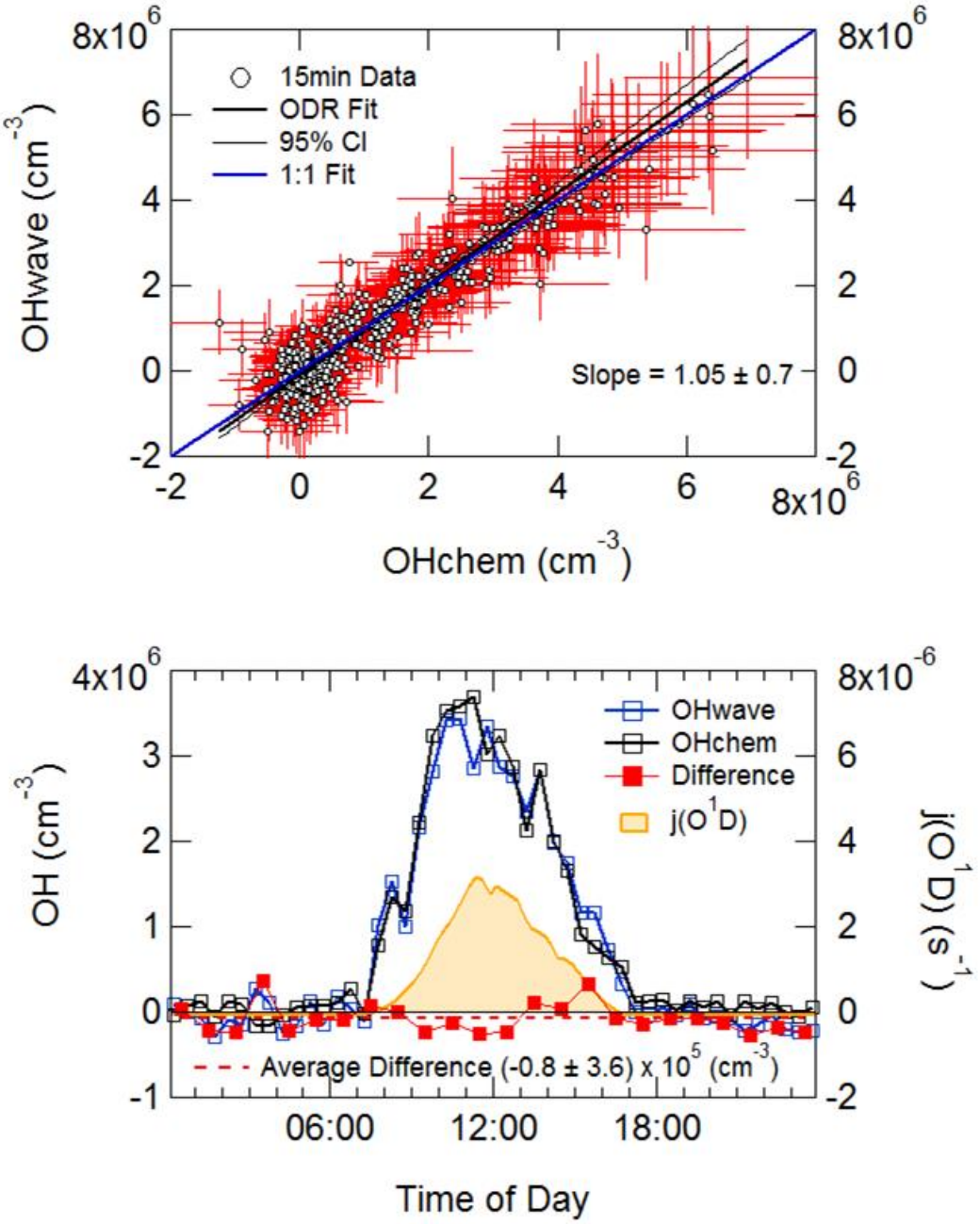

Figure 4.8 Top - Comparison of OHwave and OHchem during the winter APHH campaign. The white dots represent measured data averaged to 15 minutes. The red line is the line represents an ODR fit through the data, with its 95% CI. For comparison, the blue line denotes a 1:1 fit. Bottom – An hourly averaged diurnal profile of OHwave, OHchem, $j(O^1D)$ and the average difference (OHchem-OHwave) between OHwave and OHchem.

The hourly average diurnal profile for OHwave and OHchem is shown in Figure 4.8b, the two measurements exhibit the same diurnal profile with a peak just before noon. The average difference between OHwave and OHchem is shown in Figure 4.8b and shows that there is no distinct difference between the two data sets across the day, with a negative average difference of -0.8 x 10^5 molecule cm^{-3}. The agreement between the time-series shown in Figure 4.6 and the correlation plot in Figure 4.8 indicates there was no observable interference during the APHH winter campaign, this is consistent with the closure of the OH budget using a PSS (see section.4.4.4).

4.4.4 Photostationary Steady-State calculation of OH concentration

A PSS calculation was performed using measured O_3, H_2O, HONO, HO_2 and NO mixing ratios, alongside measured photolysis rates for $j(O^1D)$ and j(HONO) (see section.4.3.2 for more details). Figure 4.9 shows the comparison of calculated OH_{pss} and the measured values for OH between 17/11/2016 to 8/12/2016 (full data coverage of HONO, NO, photolysis rates, HO_2 and k(OH) measurements were available on these days). The agreement between the observed OH (blue line) and the OH produced from HO_2+NO and HONO photolysis highlights that the experimental budget is essentially closed, within 10% which is well within the 26% error on the OH measurements. However, the steady-state does over predict the OH concentration on the 04/12/2016, unlike the other days, and suggests that maybe there was a large point-source of NO picked up by the NO measurement resulting in large recycling of HO_2 into OH. The closure of the experimental budget suggests that measured OH and HO_2 are internally consistent and that just from measured quantities the rate of production and the rate of destruction for OH is the same. The reaction of HO_2 and NO (propagation reaction) is the dominant source of OH (~80 – 90%) for Beijing during the wintertime, owing to NO being such an abundant pollutant. The photolysis of HONO (initiation reaction) is the second most important source producing ~10 – 20% of OH. Due to such low concentrations of O_3 and H_2O in winter, the reaction of $O(^1D)$

with water vapour and H_2O vapour is not an important source, being < 1% of the rate of production. Also, the reaction of O_3 (concentration was low) with alkenes (whose concentrations were elevated in the winter) also contributed < 10% to the OH production.

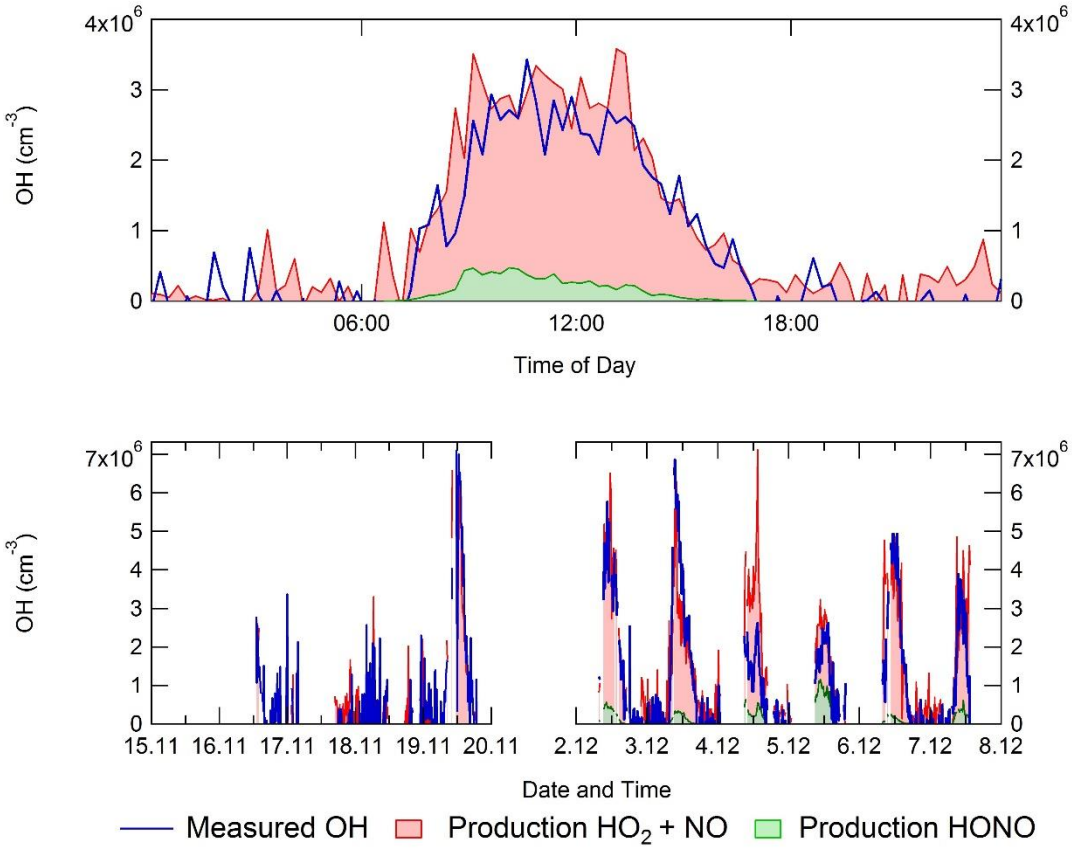

Figure 4.9 Top - Average diurnal for steady-state calculation of OH comparison with measured OH (blue). Bottom - Time series for the steady-state calculation of OH comparison with measured OH (blue). For both diagrams, the contribution from HONO photolysis and the reaction of HO_2 + NO is shown in green and red, respectively.

4.4.5 MCM base model

Figure 4.10 shows the time-series of OH (wave only), HO_2, RO_2 (speciated into simple and complex) and OH reactivity (k(OH)) compared with the results from the MCM-base (described in section.4.3.1). Figure 4.10 shows that in general, the MCM-base model under predicts OH, HO_2 and RO_2. On the days (19/11/2016 and 05/12/2016) when OH reactivity is relatively low (k(OH) < 30 s^{-1}) the model can reproduce OH and HO_2, although RO_2 is still under predicted by the MCM-base.

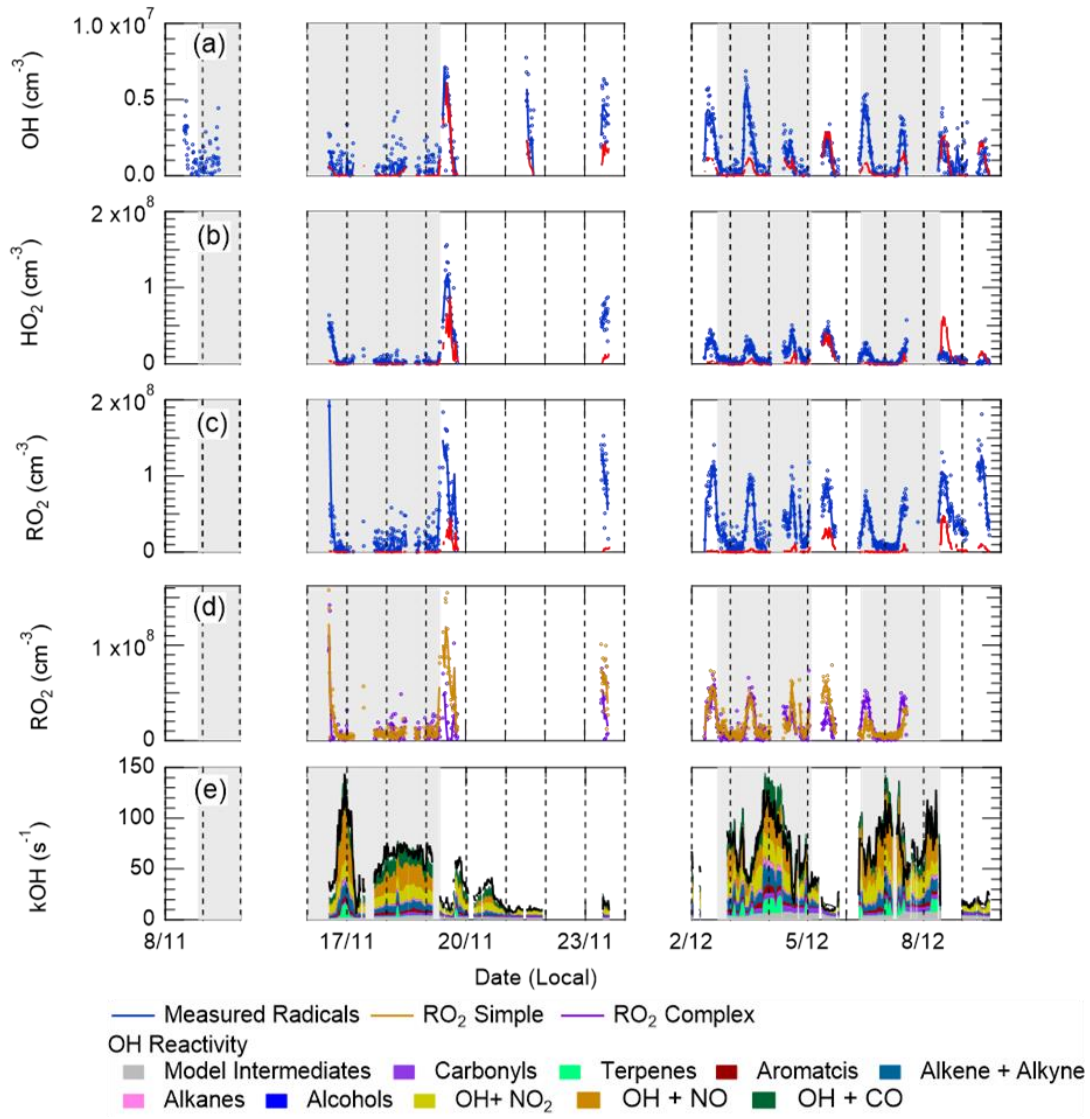

Figure 4.10 a) Time-series of OH, b) time-series of HO_2, c) time-series of total RO_2, d) time-series of RO_2 speciated and e) OH Reactivity. The measurements are in blue and model is in red for OH, HO_2 and total RO_2. The speciated RO_2 is separated into simple (gold) and complex (purple). The OH reactivity is broken down by the key on the key below the graph. The grey shaded areas show periods when $PM_{2.5}$ > 75 µg m^{-3}.

In general, the model underpredicts the OH, HO_2 and RO_2 concentrations by a factor of 1.7, 5.8 and 25, as shown in Figure 4.11. Although the underprediction by the model varies day-to-day: for OH, the underprediction varies from a factor of 5.9 to an overprediction of 1.05 (good agreement) between the model and measurements; for HO_2 the underprediction varies from a factor of 14 to an overprediction by a factor of 5.2 and for RO_2 the underprediction varies from a factor of 2.05 to an over prediction of 8. Figure

4.11 shows the diurnal profile of OH, HO_2 and RO_2 averaged over the campaign, with daily averaged maximum of 2.7 x 10^6 cm^{-3}, 0.39 x 10^8 cm^{-3} and 0.88 x 10^8 cm^{-3} for OH, HO_2 and total RO_2, respectively. The MCM-base model does a good job (modelled concentration less than LOD) of reproducing the night-time concentration of both OH and HO_2, although RO_2 is not replicated well.

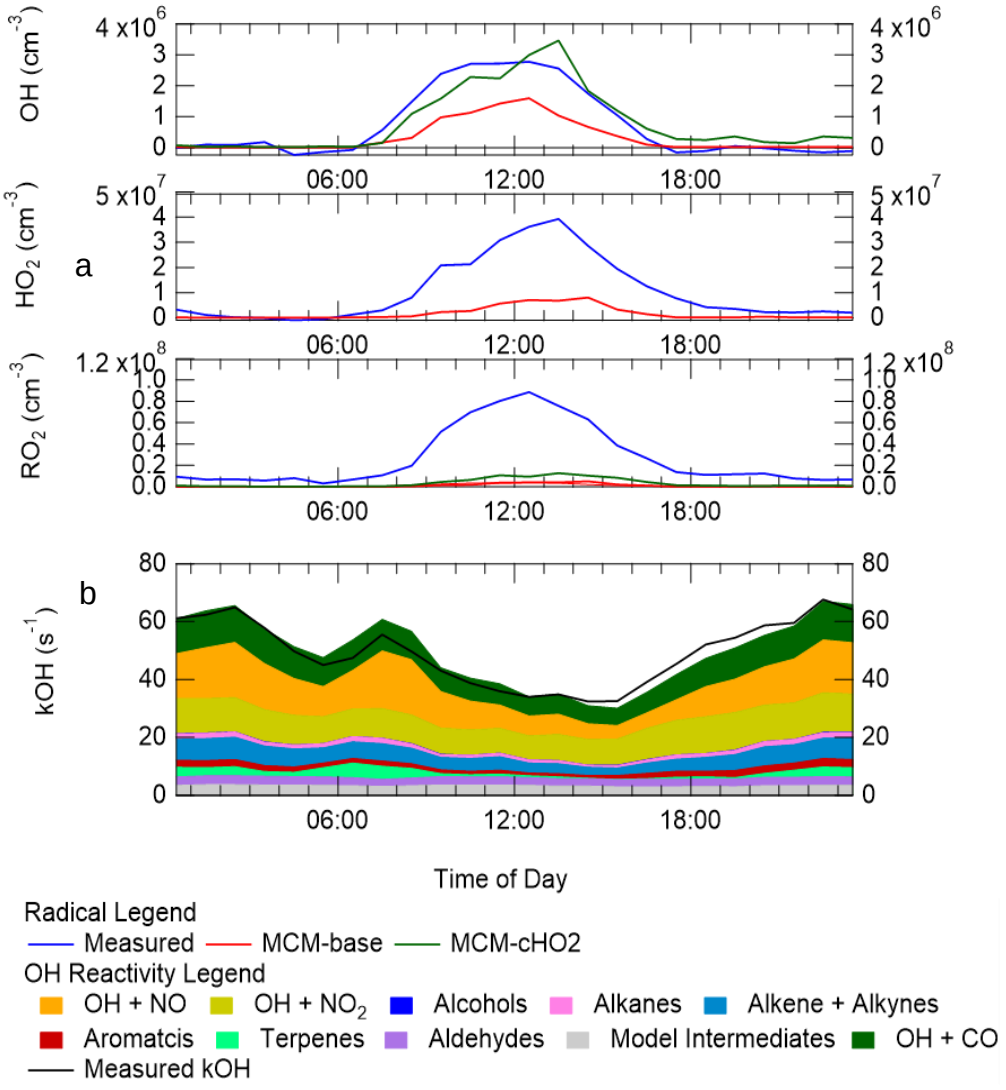

Figure 4.11 a) Campaign averaged diel profile of OH (top panel), HO_2 (middle panel) and the sum of RO_2 (lower panel) for measurements (blue) and box-model calculations: MCM-base (red) and MCM-cHO_2 (green) See text for descriptions of each model scenario. (b) OH reactivity (s^{-1}) for measurements (black line) and model (stacked plot) with the contribution to reactivity from different measured species and modelled intermediates shown in the key.

The measured RO_2 at night-time tends to have a non-zero value with an average of 0.8 x 10^7 molecule cm^{-3}, whilst the model predicts no RO_2 species at night-time. The OH loss is reproduced within 10% implying that the OH reactivity budget is captured well by the model. The modelled OH reactivity is the sum of all measured and modelled intermediate species multiplied by the respective rate coefficient for their reaction with OH. The average diurnal for both modelled and measured OH reactivity is shown in Figure 4.11. The total measured OH reactivity during the campaign was quite large and varied between 10 to 145 s^{-1}. Averaged over the full period the contributions to reactivity came from CO (17.3%), NO (24.9%), NO_2 (22.1%), alkanes (3.0%), alkynes and alkenes (10.8%), carbonyls (5.7%), terpenes (3.7%) and modelled intermediates (6.77%).

Previous radical measurements made during the wintertime are summarised in Table 4.5. The environments of these previous winter campaigns are generally dominated by NO, and a model-to-measurement comparison shows an under prediction of OH, HO_2 and RO_2 under the high NO conditions (Tan et al., 2017, Lu et al., 2013, Tan et al., 2018). For the BEST-ONE (Tan et al., 2018) campaign, which took place in suburban Beijing (~60 km from the centre) it was suggested that an additional source of RO_2 was required to reconcile the model with the measurements.

4.4.5.1 Sources and Sinks of RO_x

A rate of production analysis (ROPA) was performed on the MCM-base model. The ROPA calculates the contribution of the reactions and species involved in the production and destruction of a desired molecule, in this case, the ROPA was performed on OH, HO_2 and total RO_2. The output from the ROPA can be separated into reactions for primary production, termination and propagation. Primary production is the reaction of non-radicals to form radicals; termination is the reaction of radicals to form non-radicals and propagation is radical-radical recycling. Figure 4.12 shows the primary production and termination results from the ROPA for OH, HO_2 and RO_2 (RO_x). The primary production of new radicals (RO_x = OH + HO_2 + RO_2) during the campaign was dominated by the photolysis of: HONO (~83%),

HCHO (~1%); other carbonyl species (4.4%) and the ozonolysis of alkenes (~ 10%). When only ozonolysis products that form OH are considered the production of alkenes from ozonolysis contributed to <1%, this highlights the importance of considering the HO_2 and RO_2 products from ozonolysis.

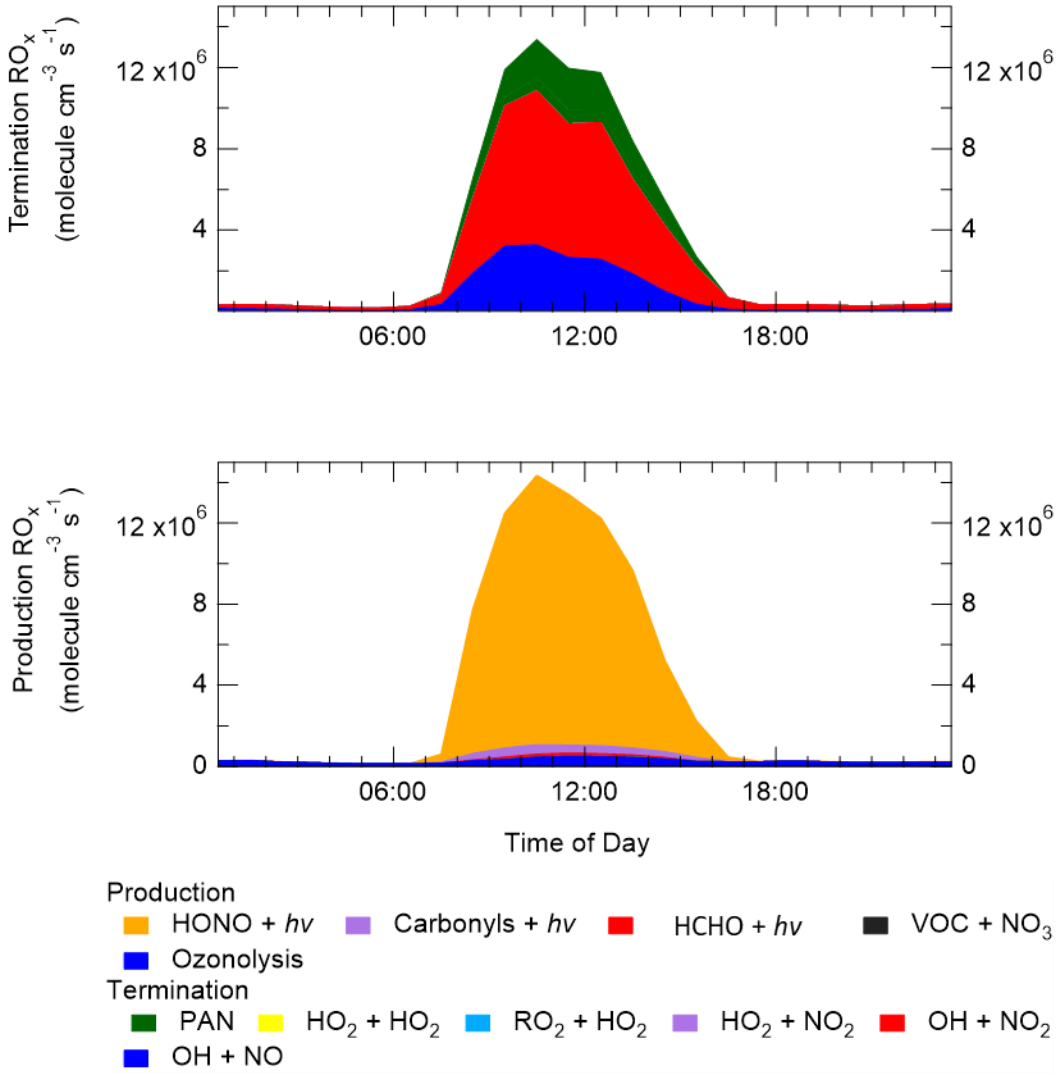

Figure 4.12 Top – ROPA for the primary production of RO_x radicals from ozonolysis, photolysis of ozone (O^1D), VOC + NO_3, photolysis of HCHO and photolysis of HONO. Bottom - ROPA for the termination of RO_x radical from: OH + NO; OH + NO_2, HO_2 + HO_2 and net-PAN formation. The ROPA was performed on the MCM-base model.

The photolysis of HONO, HCHO and carbonyl species are all daytime sources, whilst a small amount of radicals are produced between

17:00 - 19:00 from ozonolysis. At night (after 19:00) all primary sources of radicals reduce to ~zero. The termination of radicals (RO_x) is dominated by the reaction of OH + NO (~30%), OH + NO_2 (~55%) and net-formation of PAN (~15%). The net-formation of PAN is calculated from the production of PAN minus the destruction of PAN (back reaction). Ozone photolysis does not play an important role in the primary production of OH, due to the low observed values of O_3 during the campaign caused by titration via NO (Figure 4.3). Also, the low temperatures observed during winter causes low water vapour percentage (~0.5%).

The importance of HONO photolysis as a source of OH has been highlighted in several previous studies in both urban and suburban sites, as summarised in Table 4.6. The BEST-ONE campaign to the north of Beijing showed HONO produced ~ 46% of the RO_x during the campaign. In comparison to the APHH campaign, ozonolysis and carbonyl photolysis in BEST-ONE made a significant portion of primary production of radical at 28% and 9%, respectively. Both the APHH and BEST-ONE campaign showed that ozone photolysis is not an important source of radicals. Another campaign took place in central Beijing at PKU (Ma et al., 2019) and showed that HONO was responsible for ~86% of the primary production of radicals, similar to the measurements taken during the APHH winter campaign. Similar to APHH, the other sources of OH during the PKU campaign were ozonolysis (3%) and carbonyl photolysis (7%). Several other winter-time campaigns have highlighted the importance of HONO including the PUMA campaign in Birmingham (Emmerson et al., 2005); IMPACT campaign in Tokyo (Kanaya et al., 2007); NCITT campaign in Boulder (Kim et al., 2014) and the PMTACS-NY campaign in New York (Ren et al., 2006), these campaigns showed 36.2, 19, 80.4, and 46% contribution to primary production from HONO, respectively (Table 4.6). However, it should be noted that HONO was not measured during the PUMA campaign, so the percentage contribution to the primary production of radicals should be used as a lower limit as it is modelled HONO. Modelled HONO is normally underestimated.

	PUMA, Birminham, UK	IMPACT, Tokyo, Japan	NCITT, Boulder USA	PMTACS-NY, New York, USA	BEST-ONE, Suburban Beijing, China	APHH, Central Beijing, China	PKU, Central Beijing, China[3]
Date	Jan – Feb 2000	Jan – Feb, 2004	Late Feb 2011	Jan – Feb, 2001	Jan – March 2016	Nov -Dec, 2016	Jan-Feb, 2017
OH (cm^{-3})	~1.7 x 10^6	~1.6 x 10^6	~2.7 x 10^6	~1.4 x 10^6	3 x 10^6	2.7 x 10^6	1.4x 10^6
O_3 (ppbv)	37	20	40	20	30	15	10
***j*(O^1D) (s^{-1})**	~1 x 10^{-5}	~2.8 x 10^{-5}	~1 x 10^{-5}	~5 x 10^{-6}	7 x 10^{-6}	~3 x 10^{-6}	-
***j*(O_3) (%)**	0.6	<1	14.7	1.1	<1	<1	<1
***j*(HONO) (%)**	36.2[1]	19	80.4	65.5	46	83.3	86
Ozonolysis (%)	63.2	35	4.9	42.4	28	10.0	6
***j*(Carbonyls) (%)**	22	23	-	-	9	4.5	7%[2]
***j*(HCHO) (%)**	6	10	-	6	9	1.1	
Reference	Emmerson et al.(2005)	Kanaya et al.(2007)	(Kim et al., 2014)	Ren et al.(2006)	Tan et al.(2018)	This work.	Ma et al. (2019)

Table 4.6 Summary of previous winter measurements of OH, HO_2 and RO_2, and a summary of the major primary radical sources during these campaigns. All values are the noon average for each campaign. [1]This should be considered a lower limit due to no HONO measurements being made during the campaign. [2] Primary production from the sum of *j*(Carbonyls) and *j*(HCHO). [3] Values for polluted periods only *k*(OH) > 20 s^{-1}.

The Birmingham, Tokyo, New York and the suburban Beijing campaigns all showed a high contribution from ozonolysis, 63.2, 35, 42.4, 28% respectively, only the Boulder campaign (4.9%) showed a low contribution, which is similar to the observations made during APHH campaign. Only the Boulder campaign showed photolysis of O_3 to give a significant contribution (14.9%) to primary production, other winter campaigns show a contribution less than 1%. The higher contribution from photolysis of O_3 during the Boulder campaign is probably due to the campaign taking place in late February when higher photolysis rates, water vapour concentrations and temperature would be expected.

4.4.5.2 Radical concentration and OH Reactivity dependence on deposition rate

The MCM includes reactions that generate oxidised intermediates, without a deposition constraint the intermediates will build-up in the model. Unfortunately, the physical loss mechanisms for these oxidise intermediates are not well known and must be estimated in the models. Whilst the MCM-base replicates the measured OH reactivity very well, the impact of different deposition rates has been explored. The MCM-base model has a deposition of 0.1/MH (MH being the measured boundary layer in cm) and has been modified for several different deposition rates for the model generated intermediates. The effect of the different deposition on OH, HO_2, RO_2 and *k*(OH) is shown in Figure 4.13, which shows that the modelled radical concentration is insensitive to changes in the loss rate, with less than 5% change.

The reactivity budget was closed without a large contribution from model intermediates (6.77%) which shows that the reactivity was dominated by primary emissions that have been measured. It also shows that the deposition used in the base model is correct as the OH reactivity is replicated well by the model, and that changes in the deposition does not change the total radical concentration significantly.

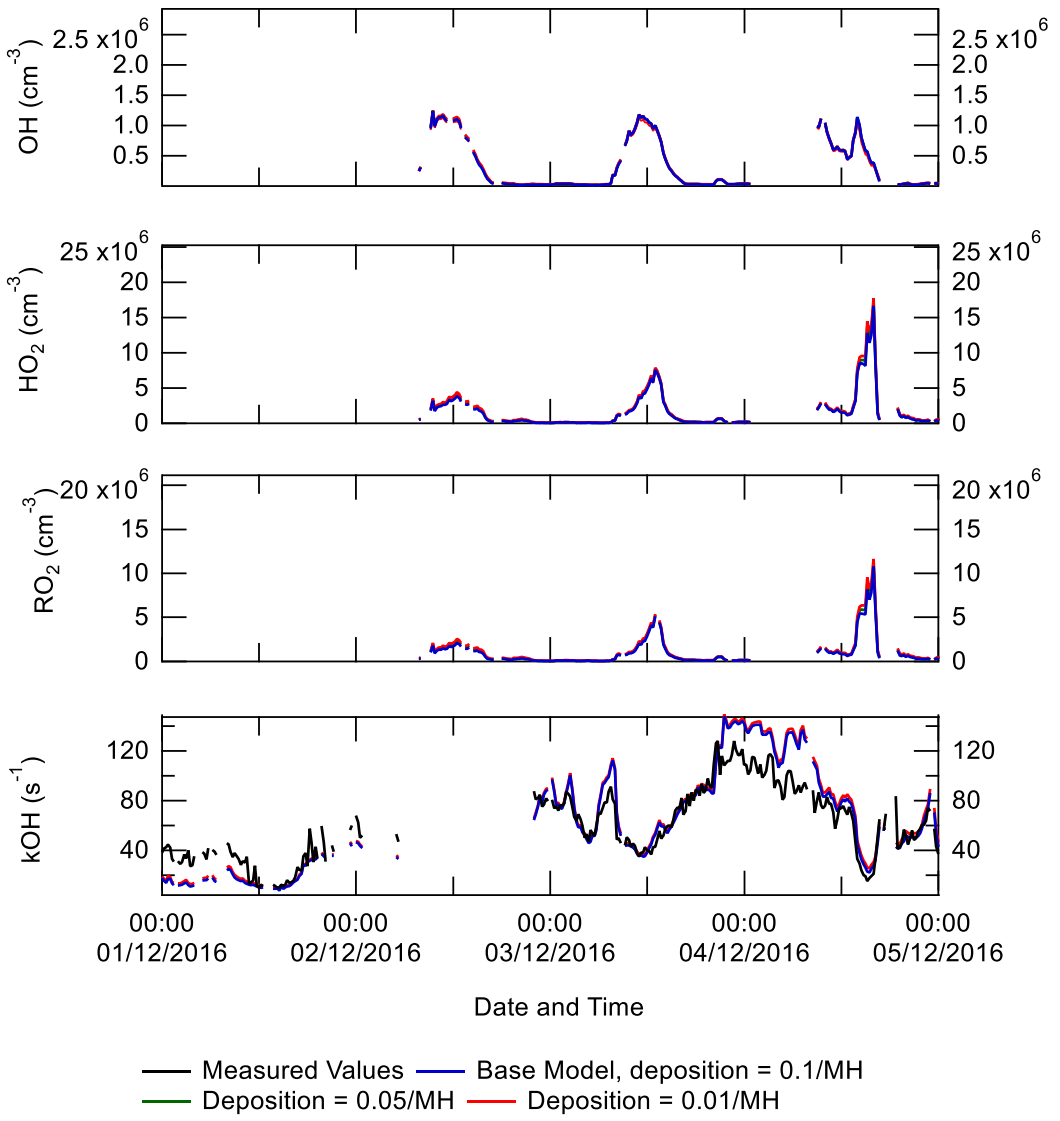

Figure 4.13 Effect of the deposition rate of the model generated intermediates on the reactivity of OH, HO_2, RO_2 and OH, and a comparison with the measurements.

4.4.5.3 Impact of higher weight VOCs

For this campaign only VOC species up to C7 were measured by the GC-FID, but to test the sensitivity of the model to higher weight VOCs, measurements from a PTR-MS were incorporated into the MCM-base model to include C2 and C3 aromatic species. C2 and C3 aromatics are compounds that have either two or three carbons that are not in the aromatic ring, respectively. The PTR-MS lumped measurements are split between ethylbenzene(C2), propyl benzene(C3), isopropyl benzene(C3), 2-Ethyltoluene(C3), 3-Ethyltoluene(C3), 4-Ethyltoluene(C3), 1,3,5-trimethylbenzene(C3),

1,2,4-trimethylbenzene(C3) and 1,2,3-trimethylbenzene (C3). Since the GC-FID measured three C2 aromatic species (o-xylene, m-xylene and p-xylene) but not the higher weight (> C7), the concentration of ethylbenzene was calculated through the difference between the PTR C2 (measured lower and higher weight) and the GC-FID C2 measurements. The model comparison between MCM-base and MCM-fVOC (see section.4.3.1 for model details) is shown in Figure 4.14, and shows that introducing higher weight VOCs does not affect the radical concentration significantly with the largest difference of ~7% observed on the 5/12/2016.

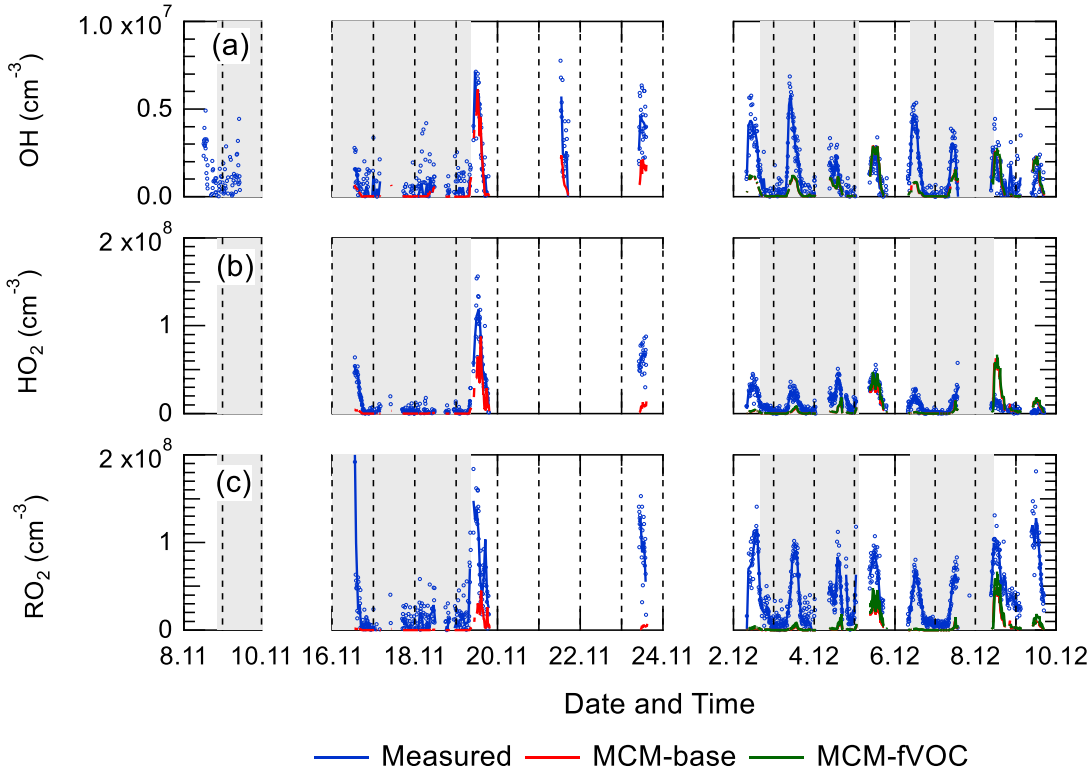

Figure 4.14 a) Comparison of measured OH with modelled OH from MCM-base and MCM-fVOC. b) Comparison of measured HO_2 with modelled HO_2 from MCM-base and MCM-fVOC. c) Comparison of measured total RO_2 with modelled total RO_2 from MCM-base and MCM-fVOC. It should be noted that PTR-MS data was only available from 24/11/2016 onwards, hence the data comparison is only between the 02/12 – 10/12.

The impact of the higher weight VOCs on OH reactivity in the model is shown in Figure 4.15. Introducing the higher weight VOCs has a very small impact

on modelled k(OH) from MCM-base and is in good agreement with measured k(OH). These results show that the MCM-base model does not have a large sensitivity to the introduction of higher weight aromatic species.

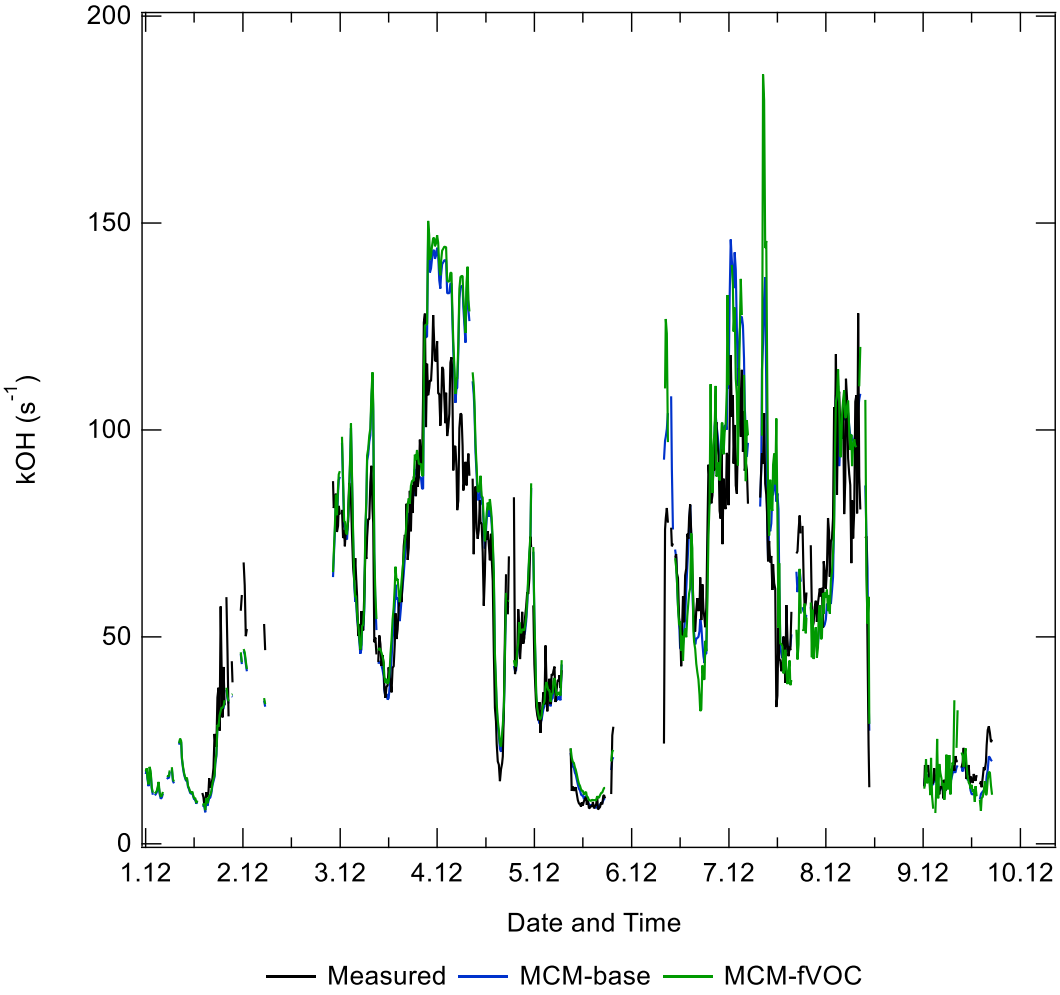

Figure 4.15 Comparison of measured OH reactivity (*k*(OH)) with modelled OH reactivity from MCM-base and MCM-fVOC.

4.4.5.4 Model constrained to HO_2

The MCM-base model was modified and constrained to the measurements of HO_2 (MCM-cHO_2), whilst everything else in the model was kept the same. Figure 4.16 shows the time-series comparison of MCM-base and MCM-cHO_2 with the measurements of OH, HO_2 and RO_2. The comparison of MCM-cHO_2 and measurement for OH shows very good agreement across the whole time-series and is consistent with the photostationary steady-state calculation (see section.4.4.4). The comparison also shows that the recycling chemistry

of HO_2 into OH *via* NO seems well understood in the model under different NO_x regimes throughout the campaign. However, it should be noted that the OH concentration is overpredicted on the 23/11 and 02/12, and underpredicted on the 08/12. Constraining to HO_2 improved the agreement between the measured RO_2 and the modelled RO_2 values (MCM-cHO_2), although in general the RO_2 values are still underestimated in the model especially on high NO days.

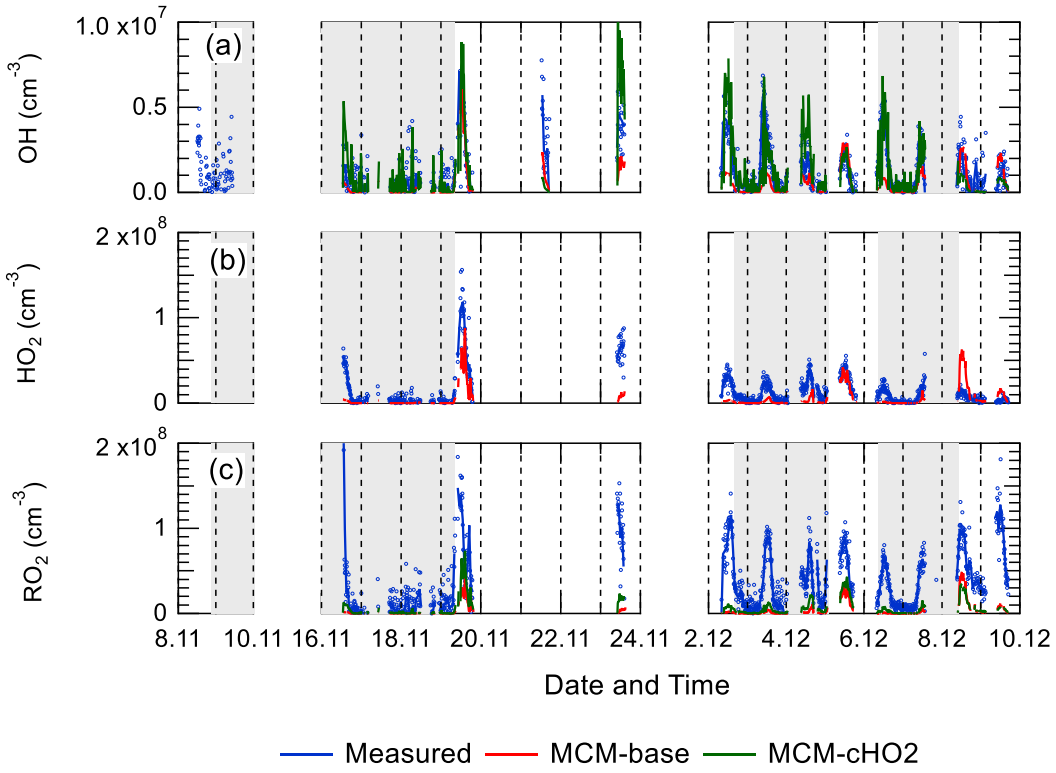

Figure 4.16 Comparison of measured (blue) OH, HO_2 and RO_2 with results from the MCM-base (red) model and MCM-cHO_2 (green). Note: the HO_2 from MCM-cHO_2 is included on the graph, but overlayed by the HO_2 measurements.

The good agreement between the measured values and the MCM-cHO_2 is clearer in the average diurnal for the whole campaign, which is shown in Figure 4.17. The comparison shows an underprediction between 06:30-12:30 by an average of 20%, and an overprediction between 12:30-14:30 by ~21% which are both within the ~26% error for the measured OH values. The MCM-cHO_2 overpredicts the OH values at night-time, the overprediction is caused by the non-zero values for HO_2 at night-time (0.3 x 10^7 molecule cm^{-3})

in the model. The significant night-time values of HO_2 allows for efficient recycling of HO_2 to OH *via* NO at night. The model was constrained to measurements of HO_2, and the measurements of HO_2 at night-time hover around the LOD for HO_2 (average 5.6 x 10^6 molecule cm^{-3}) and, hence there will be greater uncertainty than the daytime measurements. The RO_2 values on average have increased in the MCM-cHO_2 compared with the MCM-base, resulting in a better agreement with the measured values. However, the MCM-cHO_2 still severely underpredicts the RO_2 values by a factor of ~11 compared with the measured values.

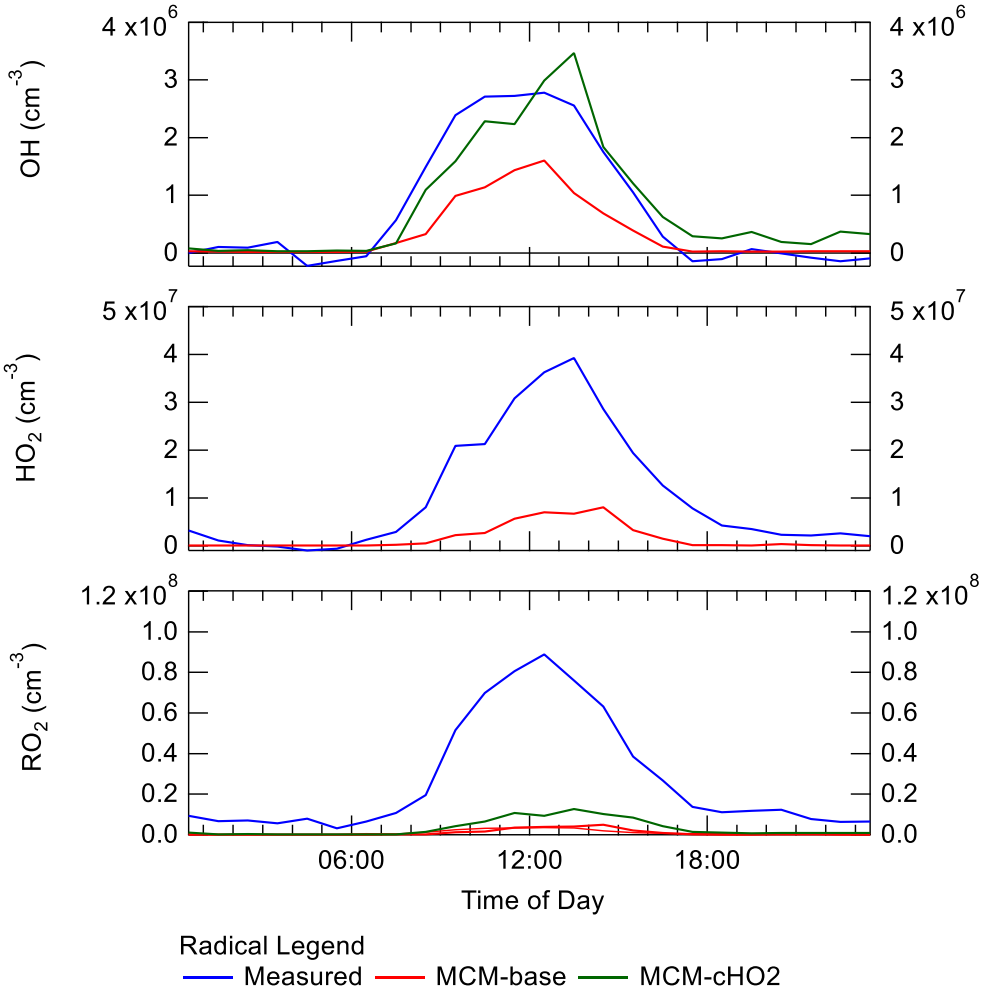

Figure 4.17 Average diurnal comparison of measured values (blue) with MCM-base (red) and MCM-cHO_2 (green) for OH, HO_2 and RO_2 across the whole winter campaign.

The results from MCM-cHO_2 are consistent with the steady-state (PSS) calculation when the box-model is constrained to the HO_2 measured using FAGE in the field. In the PSS, the measured and modelled OH concentrations agree within 10%, which is smaller than the 26% error on the OH measurements. When the MCM is constrained to the measurements of HO_2 (MCM-cHO_2), the model can replicate the OH measurements within 26% error, as shown in Figure 4.17. Also, the MCM-base model can replicate the OH reactivity within 10% (Figure 4.11), implying that almost all the major sources and sinks of OH are included. Therefore, the underestimation of HO_2 by the model is likely to be explained by the underestimation of RO_2 by the model, owing to an insufficient rate of recycling of RO_2 to HO_2. The ability to replicate OH when the model is constrained to HO_2, along with OH reactivity being captured well by the model, suggests the presence of unknown RO_2 chemistry; either additional sources of RO_2 radicals under high levels of NO_x or unknown chemistry/behaviour of RO_2 under high levels of NO_x. This has been explored further in section.4.4.6.

4.4.6 Radicals under different NO_x conditions

NO is central to the recycling of radicals through propagation ($RO_2 \rightarrow HO_2 \rightarrow OH$). Previous work has shown that measurement-to-model ratios can exhibit strong dependencies on the NO mixing ratio (Tan et al., 2017, Lu et al., 2012, Whalley et al., 2018, Dusanter et al., 2009, Griffith et al., 2013). The ratio of measured:modelled(MCM-base) for OH, HO_2 and RO_2 was binned against NO mixing ratios, and is shown in Figure 4.18. The analysis was confined to daytime measured ($j(O^1D) > 1 \times 10^{-6}$ s^{-1}). Since the NO mixing ratios during the campaign varied from 1 ppbv to 250 ppbv, the data here has been binned to the natural logarithm of NO concentration to give an even split of data points in each bin (less data available at the very high NO concentrations, i.e. above 100 ppbv).

As shown in Figure 4.18, the ratio of measured to modelled OH is close to 1 below 6 ppbv of NO, whilst HO_2 and RO_2 is close to 1 below 2.2 ppbv. With increasing NO the underprediction of OH, HO_2 and RO_2 increases. At 6 ppbv of NO; HO_2 and RO_2 are underpredicted by a factor of 5.4 and 18,

respectively; similar peroxy radical under-predictions were reported from the BEST-ONE campaign (Tan et al., 2017, Tan et al., 2018), with HO_2 and RO_2 being underpredicted by a factor of 5 and 10 at 6 ppbv.

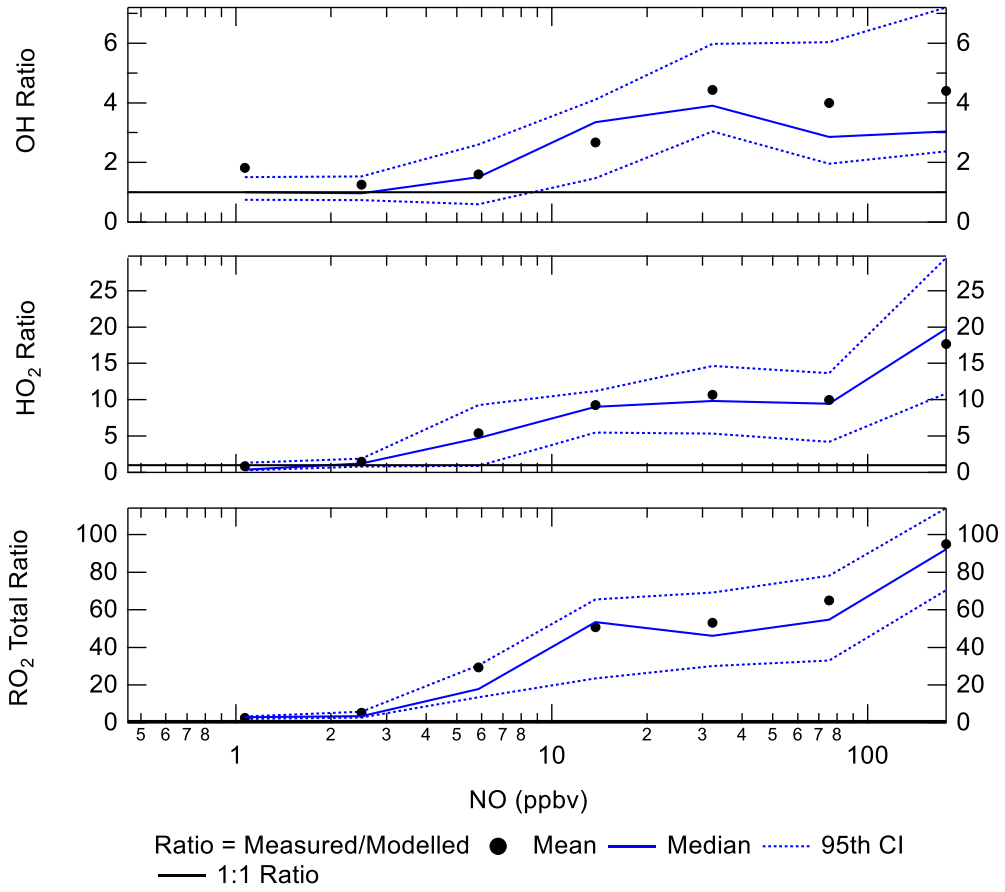

Figure 4.18 The ratio of measurement/model for OH (top), HO_2 (middle) and RO_2 (bottom) across various NO concentrations for daytime values only ($j(O^1D) > 1 \times 10^{-6}$ s^{-1}).

Many previous urban campaigns have more extensive data coverage at lower NO_x values; however, no other campaign with *in-situ* measurements of OH has experienced NO values up to 250 ppbv as seen during APHH. There have been some suggestions for the origin of the discrepancy between modelled and measured radical concentrations at high mixing ratios of NO. Dusanter et al., (2009) suggested that poor mixing of point source NO with peroxy radicals across a site may cause some of the observed discrepancies. Chapter 3 discusses why segregation across the site is not the reason for the discrepancy. Tan et al., (2017) suggested there may be a missing source of peroxy radicals under high-NO_x conditions. Alternatively, the discrepancy

could be driven by unknown or poorly understood oxidation pathways of the larger, more complex, RO_2 species that are present in these urban environments, whose laboratory kinetics are under-studied.

When the MCM is constrained to the measurement of HO_2, the model can accurately replicate the OH measurements and replicate the reactivity within 10%, implying that all major OH sources and sinks can be captured when an additional source of HO_2 is added to the model. The underestimation of modelled HO_2 could be explained by the underestimation of RO_2, causing insufficient recycling of RO_2 to HO_2. Both the replication of OH when the model is constrained to HO_2 along with OH reactivity being captured well by the model suggests there is unknown RO_2 chemistry; either additional sources of RO_2 radicals under high NO_x or unknown chemistry/behaviour of RO_2 under high levels of NO_x. Indeed, many rate coefficients in the MCM for the more complex RO_2 species are based on structure activity relationships (SARs) determined from studies of simpler RO_2 species (http://mcm.leeds.ac.uk/MCM/home, Jenkin et al. (2019)). During the APHH campaign, measurements of partially speciated RO_2 species were made in two categories: RO_2 simple (deriving from alkanes up to C3) and RO_2 complex (deriving from alkanes > C4, alkene and aromatics). Further details on RO_2 speciation can be found in the section.2.1.8 and Whalley et al. (2013). The dependence of speciated RO_2 measurements against [NO], as shown in Figure 4.19, highlights that the concentration of complex RO_2 species has a steady decrease across the NO range, whilst the concentration of simple RO_2 species starts to decrease rapidly above 2.5 ppbv, and can almost be reproduced by the model at NO concentrations above 100 ppbv. The chemistry of simpler RO_2 species with NO should be well understood, owing to a more extensive laboratory database of the rate coefficients and product branching. Therefore, the model discrepancy for RO_2 species may be due to inaccuracies within the MCM for the degradation of the more complex RO_2 species into these simple RO_2. There appears to be a limited understanding of the degradation pathways of complex RO_2 species, which may be the reason why the concentration of simple RO_2 species remain high even under

high NO_x conditions, whereas the modelled simple RO_2 concentration decreases at high NO.

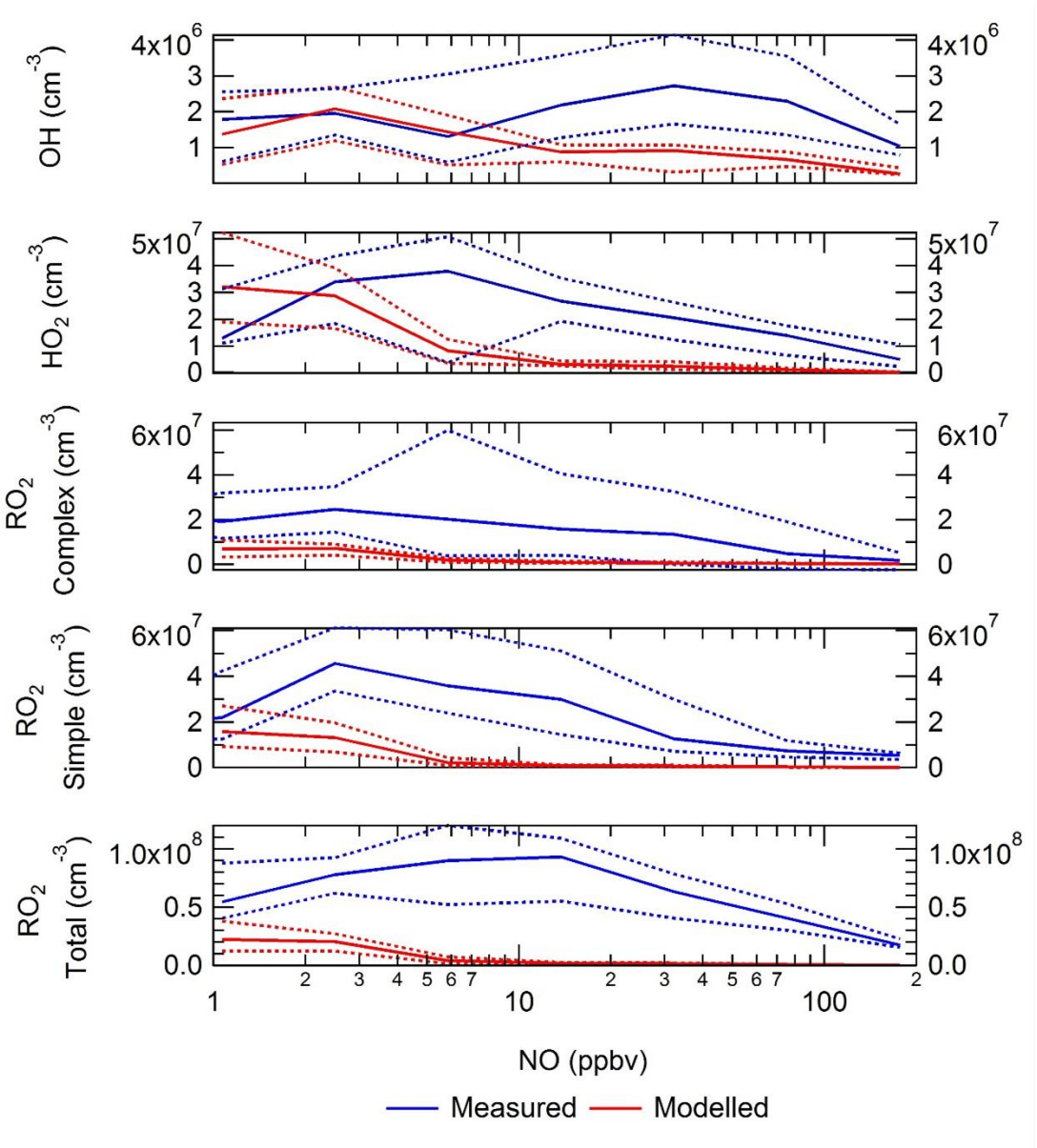

Figure 4.19 Comparison of RO_2 complex, RO_2 simple and total RO_2 measurements with the MCM-base model bin against NO mixing ratios.

4.4.6.1 Primary production of RO_2

As discussed above, the agreement between measured and modelled OH when the model is constrained to HO_2, as well as the closure of the OH reactivity budget, suggests there is unknown RO_2 chemistry. To investigate whether the 'missing chemistry' could be caused by an additional primary source of RO_2 radicals, the MCM-base modelled has been modified. The

MCM-PRO2 has an additional source of several RO_2 species (see section.4.3.1 for more detail) including both simple and complex. The extra primary production of RO_x ($P'RO_x$) radicals required to bridge the gap between measured and modelled was found to be 1.2 x 10^8 molecules cm^{-3} s^{-1} (17 pbbv hr^{-1}) on average as shown in Figure 4.20, calculated from E4.5:

$$P'(RO_x) = k_{HO2+NO}[HO_2][NO_2] - P(HO_2)_{prim} - P(RO_2)_{prim} - k_{VOC}[OH] + L(HO_2)_{term} + L(RO_2)_{term} \quad \text{E4.5}$$

In E4.5 $P(HO_2)_{prim}$, $P(RO_2)_{prim}$, $L(HO_2)_{term}$ and $L(RO_2)_{term}$ are the rate of primary production of HO_2, rate of primary production of RO_2, termination rate of HO_2 and termination rate of RO_2, respectively.

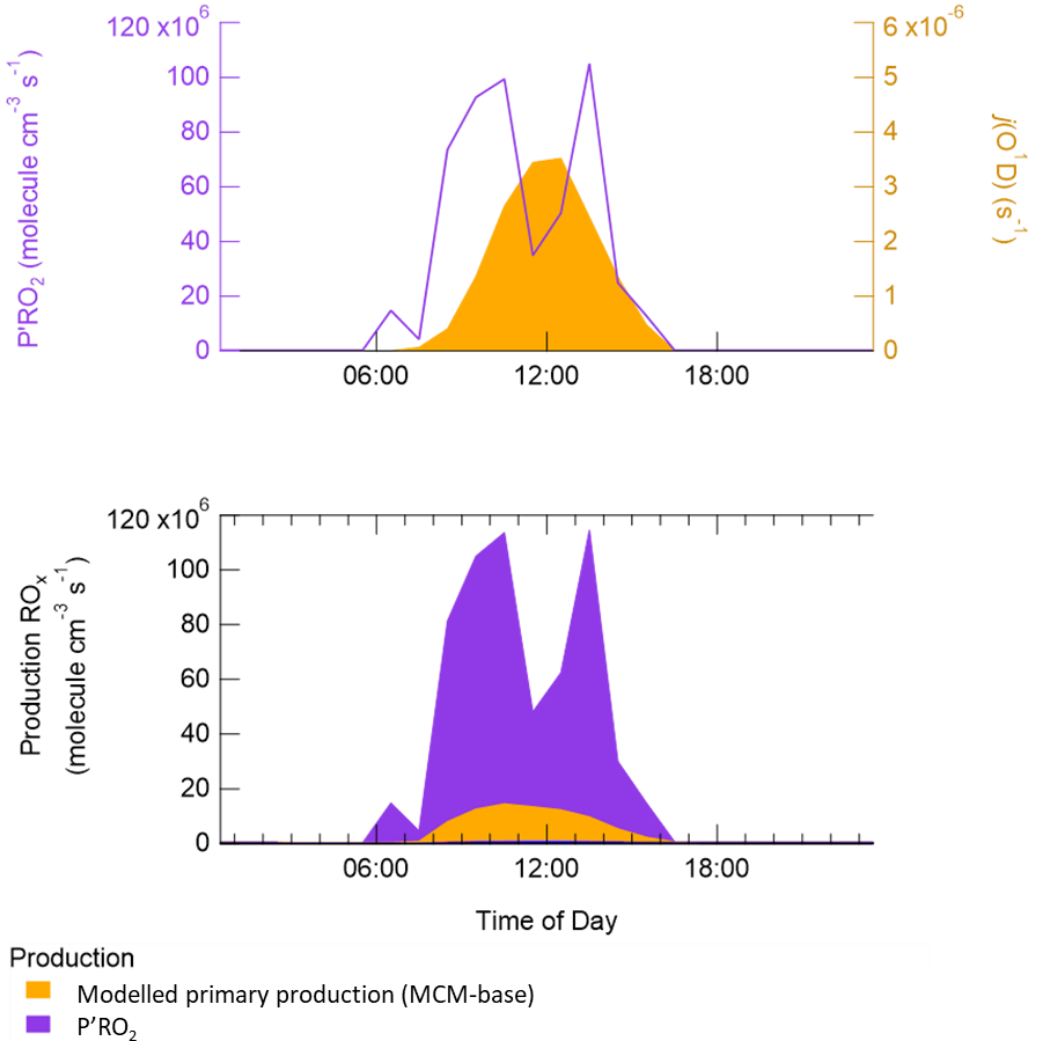

Figure 4.20 a) Average diurnal of the additional primary production ($P'RO_x$) required to reconcile measurements with the model (blue) and $j(O^1D)$ average (yellow). b) Total primary production of radicals with additional RO_2 source.

The additional primary source of RO_2 is almost four times larger than the additional RO_2 source that was required to resolve the measured and modelled RO_2 during the BEST-ONE campaign (5 ppbv h^{-1} during polluted periods, also calculated using E4.5), and is much larger compared to the noon-average modelled primary production of RO_x during the APHH campaign of 1.6 ppbv h^{-1}. It has been previously suggested (Tan et al., 2017) that the missing primary radical source originates from the photolysis of $ClNO_2$ and Cl_2 to generate Cl atoms, which can further oxidise VOCs to form peroxy radicals, but as no measurements of $ClNO_2$ or Cl_2 were made during the APHH winter campaign this cannot be quantified. However, Cl atom chemistry may only play a minor role, as the inclusion of $ClNO_2$ in a model during a summer campaign in Wangdu (60 km from Bejing) could only close 10 – 30% of the gap between the model and measurements for RO_2 (Tan et al., 2017).

E4.5 has been used to calculate an additional primary source $P'(RO_x))$ required to reconcile measured and modelled RO_2; on average this peaked at 1.05 x 10^8 molecule cm^{-3} s^{-1}. The calculated additional RO_2 source $P'(RO_x))$ was included in the model (model run titled: MCM-PRO2, see section.4.3.1 for more details). The comparison between observed RO_2 and modelled RO_2 from MCM-PRO_2 is in good agreement in general, although there is a slight overprediction of RO_2 in the afternoon and a slight underprediction in the morning. However, the MCM-PRO_2 model run overpredicts the observed OH and HO_2 by a factor of 1.6 and 2.4, respectively, with the large overprediction of HO_2 driving the overprediction of OH. To investigate whether the uptake of HO_2 onto the surface of aerosol could improve the agreement between measured and modelled HO_2, the MCM-PRO2 model was modified to include the uptake of HO_2 with an uptake coefficient of 0.2, as suggested by Jacob (2000), in the model run now called MCM-PRO2-SA. The measured average aerosol surface area peaked at an average of 6.4 x 10^{-6} cm^2 cm^{-3}. The comparison of MCM-PRO2-SA with both measurements and MCM-PRO2 (see section.4.3.1 for details) is shown in Figure 4.21 and shows that the uptake of HO_2 has a very small impact (< 8%) on the modelled OH, HO_2 and RO_2. The decrease in HO_2 in MCM-PRO2-SA is not enough to reconcile

measurements with the model and suggests that an additional primary source of RO_2 may not be the cause of the model underprediction of RO_2 species, as the inclusion of additional RO_2 production worsens the model's ability to predict OH and HO_2. However recent work from Li et al. (2019) has shown that using GEOS-Chem, the observed increasing ozone trend in North China Plain is caused by reduced uptake of HO_2 onto aerosol due to reduction in $PM_{2.5}$ by ~40% between 2013 – 2017. The impact of HO_2 uptake on O_3 formation has been discussed further in section.6.3.6.2. If there is missing RO_2 production, the rate of propagation of these species to HO_2 would need to be slower than currently assumed in the model to reconcile the observations of OH, HO_2 and RO_2.

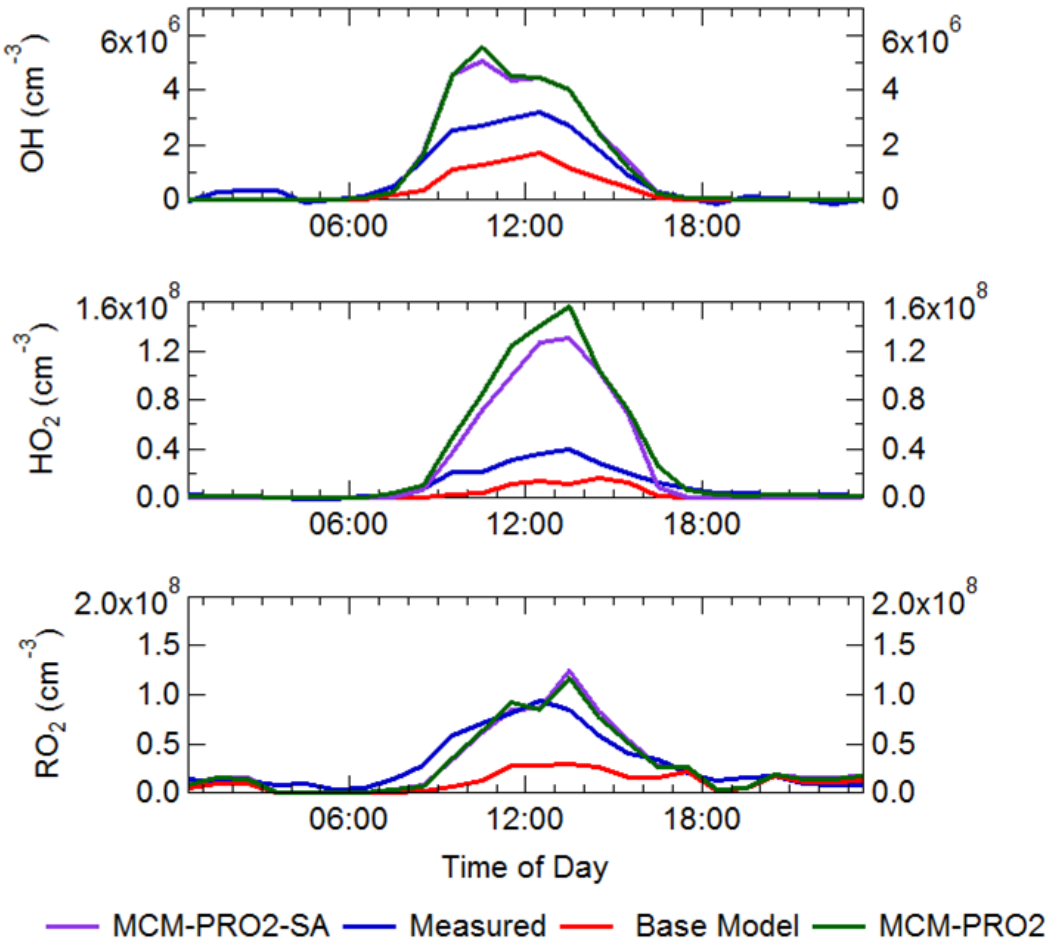

Figure 4.21 Average diurnal comparison of measurements of OH, HO2 and RO_2 with the MCM-base, MCM-PRO2 and MCM-PRO2-SA. The average diurnal is from the entire APHH winter campaign.

4.4.6.2 Dependence of modelled radicals with the RO_2 + NO rate constants

As discussed above, other than CH_3O_2 and $C_2H_5O_2$, the rate constants for the reaction of RO_2 + NO is based on structure activity relationships (SARs) in the MCM and is lumped to kRO2NO and kAPNO (http://mcm.leeds.ac.uk/MCM/). The lumped rate constants kRO2NO and kAPNO were decreased by a factor of 2 and 10 to investigate the effects on modelled OH, HO_2 and RO_2. The model where the rate constant for RO_2 + NO was decreased by a factor of 2 is titled MCM-kRO2-2, whilst the model where the rate constant was decreased by a factor of 10 is titled MCM-kRO2NO-10.

The comparison of measured values with modelled values (MCM-base, MCM-kRO2-2 and MCM-kRO2-10) is shown in Figure 4.22. Figure 4.22 shows that on the previous day when the model could reproduce the measured values of RO_2 (19/11, 5/12 and 9/12) the MCM-kRO2NO-10 now overpredicts the concentration. However, on the days when RO_2 could be reproduced by the MCM-base model, the MCM-kRO2NO-10 does not change the OH or HO_2 concentration too significantly. Whilst on the days when MCM-base underpredicts the RO_2 concentration, MCM-kRO2NO-10 does decrease the gap between measurements and modelled compared to MCM-base. MCM-kRO2NO-2 does not significantly increase the total RO_2 concentration on days when MCM-base underpredicts the concentration, unlike MCM-kRO2NO-10. Since changing the rates of RO_2 + NO will be very dependent on the NO concentration, the ratio of measured:modelled radical concentration has been binned against the log of NO for MCM-base, MCM-kRO2NO-2 and MCM-kRO2NO-10 in Figure 4.23. Figure 4.23 shows similar results to the timeseries where at the lower concentration of NO (19/11, 5/12 and 9/12) the MCM-base can reproduce the radical concentration, whilst decreasing the rate constant of RO_2 + NO causes the model to overpredict the total RO_2 concentration. The maximum overprediction for MCM-kRO2NO-2 and MCM-kRO2NO-10 is at 1 ppbv of NO, with the measured:modelled ratio for MCM-kRO2NO-2 and MCM-kRO2NO-10 of 0.15 and 0.44, respectively. The concentration of OH and HO_2 is only changed

significantly from MCM-base to MCM-kRO2NO-2 and MCM-kRO2NO-10 at lower NO concentrations (below 30 ppbv). MCM-kRO2NO-2 and MCM-kRO2NO-10 increase the concentration of both OH and HO_2 at lower [NO] compared with MCM-base, this means the increased RO_2 concentration is recycling through to HO_2 and OH. The results at higher [NO] show that decreasing the rate of RO_2 + NO improves the agreement between measured:modelled RO_2, especially for MCM-kRO2NO-10, but decreasing the rate does not change the OH and HO_2 concentration.

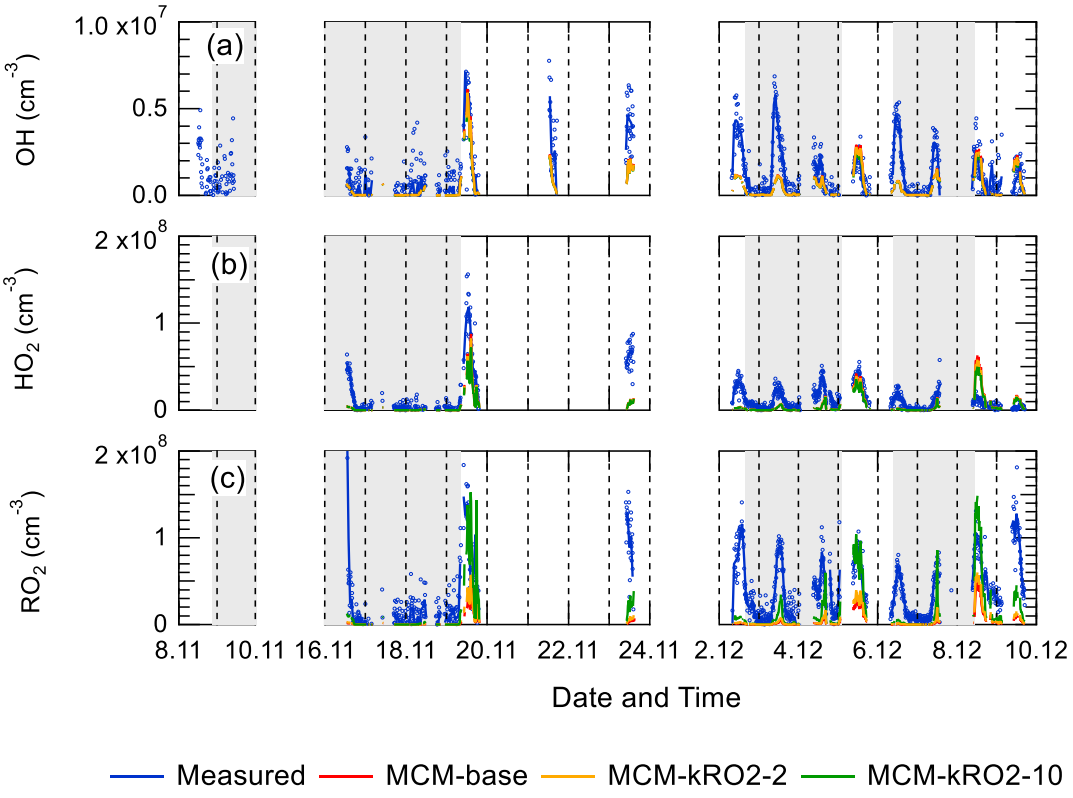

Figure 4.22 a) Time-series comparison of measured values of OH with modelled OH concentrations from MCM-base, MCM-kRO23NO-2 and MCM-kRO2-10. b) Time-series comparison of measured values of HO_2 with modelled HO_2 concentrations from MCM-base, MCM-kRO23NO-2 and MCM-kRO2-10. c) Time-series comparison of measured values of total RO_2 with modelled total RO_2 concentrations from MCM-base, MCM-kRO23NO-2 and MCM-kRO2-10. The data sets are 15-minutes averaged.

The fact that the OH and HO_2 modelled concentrations do not change at higher [NO] (above 30 ppbv) for the models with reduced RO_2 + NO rate constant highlights that the RO_2 radicals are not recycling into HO_2 or OH

under these higher NO concentrations, even though the RO_2 concentration is improved in these models (MCM-kRO2NO-2 and MCM-krO2NO-10). The lack of RO_2 recycling highlights that the RO_2 and RO radicals are terminating rather than propagating in the model.

This work highlights alternative chemistry and solutions must be applied for the two different NO regimes observed during the Beijing wintertime campaign. At lower [NO] (below 10 ppbv) the model starts to overpredict the RO_2 concentration, but recycling of RO_2 to both OH and HO_2 is observed. Whilst at higher [NO] (above 30 ppbv) the ratio of measured:modelled for total RO_2 is improved by decreasing the rate constant of RO_2 + NO, but the RO_2 species are not recycling into OH or HO_2.

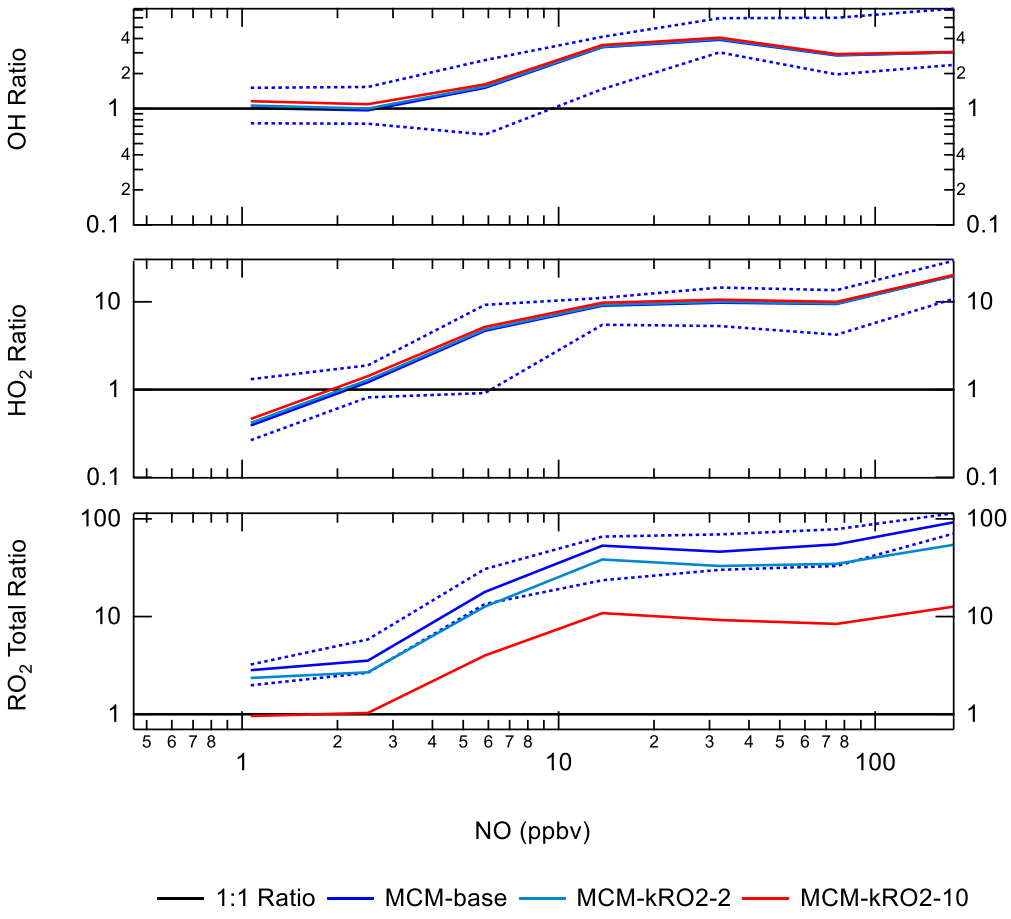

Figure 4.23 The ratio of measurement/model for OH (a), HO_2 (b) and RO_2 (c) across various NO concentrations for daytime values only ($j(O^1D) > 1 \times 10^{-6}$ s^{-1}). Light blue represents for results from MCM-kRO2NO-2, dark blue represents results from MCM-base and red represents results from MCM-kRO2NO-10.

4.4.7 Impact of HONO

HONO is the dominant primary source of OH during the APHH winter campaign (see section.4.4.5.1), but, in general, HONO is underpredicted in models. The disagreement between measured and modelled HONO is thought to be caused by additional heterogeneous sources of HONO, this has been discussed more in section.1.2.5. The MCM-base model is constrained to the measurements of HONO made during the APHH winter campaign, section.4.4.7.1 shows the impact on unconstraining the model to HONO on both the modelled HONO and OH mixing ratios. The reaction involved in the production and destruction of HONO in the MCM is shown in Table 4.7.

Reaction	Rate coefficient at 298 K and 1 atm
$OH + NO \xrightarrow{M} HONO$	9.76×10^{-12} (molecule^{-1} cm^3 s^{-1})
$HONO + h\nu \rightarrow OH + NO$	j(HONO) (s^{-1})
$HONO + OH \rightarrow NO_2 + H_2O$	5.98×10^{-12} (molecule^{-1} cm^3 s^{-1})

Table 4.7 The reactions in the MCM for the production and destruction of HONO.

4.4.7.1 Model unconstrained to HONO

The MCM-base model has been modified by unconstraining MCM-base to HONO (MCM-unHONO), and Figure 4.24 shows the average diurnal comparison of measurements with MCM-unHONO. The model MCM-unHONO captures the average diurnal of the HONO measurements very well, with MCM-unHONO peaking at night-time. The peak at night-time in the MCM-unHONO is caused by a combination of boundary layer effects and the reaction of OH + NO (Table 4.7) and the destruction process at night-time being very slow. The modelled and measured HONO concentration decreases rapidly after sunrise (~06:30) due to the photolysis of HONO to OH reaching a minimum at 14:30. After 14:30, the HONO concentration starts to rise with the reaction of OH + NO beginning to dominate over the decreasing photolysis rate.

Whilst the MCM-unHONO model replicates the shape of measured HONO well, the model underpredicts the measurements by at least factor of 10

across the entire day. The underprediction of HONO in MCM-unHONO has a large impact on the model's ability to predict OH concentration. Figure 4.24 also shows the average diurnal comparison of measured OH with the results from MCM-unHONO. MCM-unHONO underpredicts the OH concentration by a factor of 6.4, whilst the model constrained to HONO (MCM-base) only underpredicts the OH by a factor of 1.7. The large decrease in the model's ability to predict OH from MCM-base to MCM-unHONO is caused MCM-unHONO not replicating the HONO concentration, and since HONO is the dominant primary source of radicals during the APHH winter campaign the impact on OH is large. This highlights the importance of using measured HONO in models and that there is currently missing understanding of HONO production.

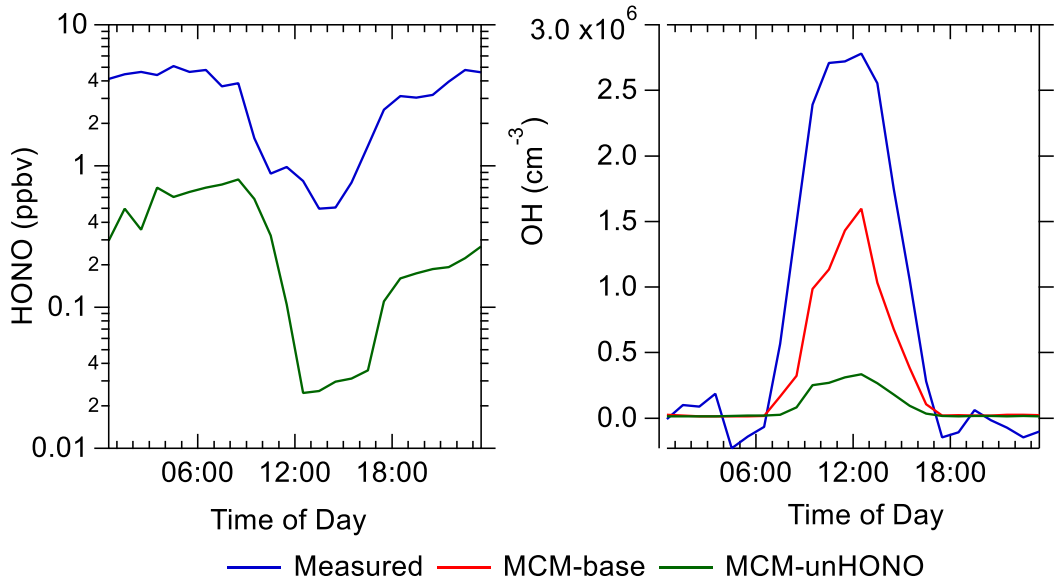

Figure 4.24 Average diurnal comparison of measurements(blue) with MCM-unHONO(green) for OH(right) and HONO(left), and MCM-base(red) for OH only. The average diurnal profiles were calculated from the entire winter APHH campaign period.

4.4.7.2 Model constrained to OH

The only source of HONO in the MCM is the reaction of OH + NO, even though OH + NO in previous studies cannot reconcile the measurements of HONO with the model. To investigate how much HONO was produced during the APHH winter campaign through the reaction of OH + NO the MCM-base model was modified. The MCM-base model was constrained to the

measurements of OH and unconstrained to HONO, the modified model was called MCM-cOH-unHONO. The average diurnal comparison of measured HONO and the results from MCM-cOH-unHONO is shown in Figure 4.25. MCM-cOH-unHONO underpredicts the HONO concentration from 02:30 to 19:30, although from 07:00 to 13:00 and 19:30 – 02:30 the model can replicate the concentration of HONO very well. The ability of MCM-cOH-unHONO to reproduce the HONO concentration between 07:00 to 13:00 and 19:30 to 02:30 shows that no additional heterogeneous sources to produce HONO are required. Between 02:30 to 11:30 the model overpredicts the HONO concentration, and this is probably caused by non-zero values of measured OH that was constrained in the model. Non-zero values of OH at night-time will lead to the efficient formation of HONO through OH + NO because there is no loss through photolysis. The underprediction of HONO by MCM-cOH-unHONO in the afternoon and evening suggests that the reaction of OH + NO is not an adequate source of HONO and additional heterogeneous sources of HONO are required to reconcile model with measurements. Additional heterogeneous sources of HONO have not been explored in this work (see section.1.2.5 for a discussion on different sources).

The 95 CI (confidence interval) on the average diurnal for MCM-cOH-unHONO is very large which implies that different chemical conditions experienced during the campaign may be influencing the results. The ratio of measured:modelled HONO binned against log(NO) is shown in Figure 4.25. It shows that at [NO] above 12 ppbv, MCM-cOH-unHONO can reproduce the measured HONO concentration very well, whilst at lower NO the model underpredicted the HONO concentration. Figure 4.25 implies that at higher [NO] the reaction of OH + NO can reproduce the HONO concentration and therefore no heterogeneous reactions are required to close the HONO budget. However, at lower NO heterogeneous sources are required to close the HONO budget.

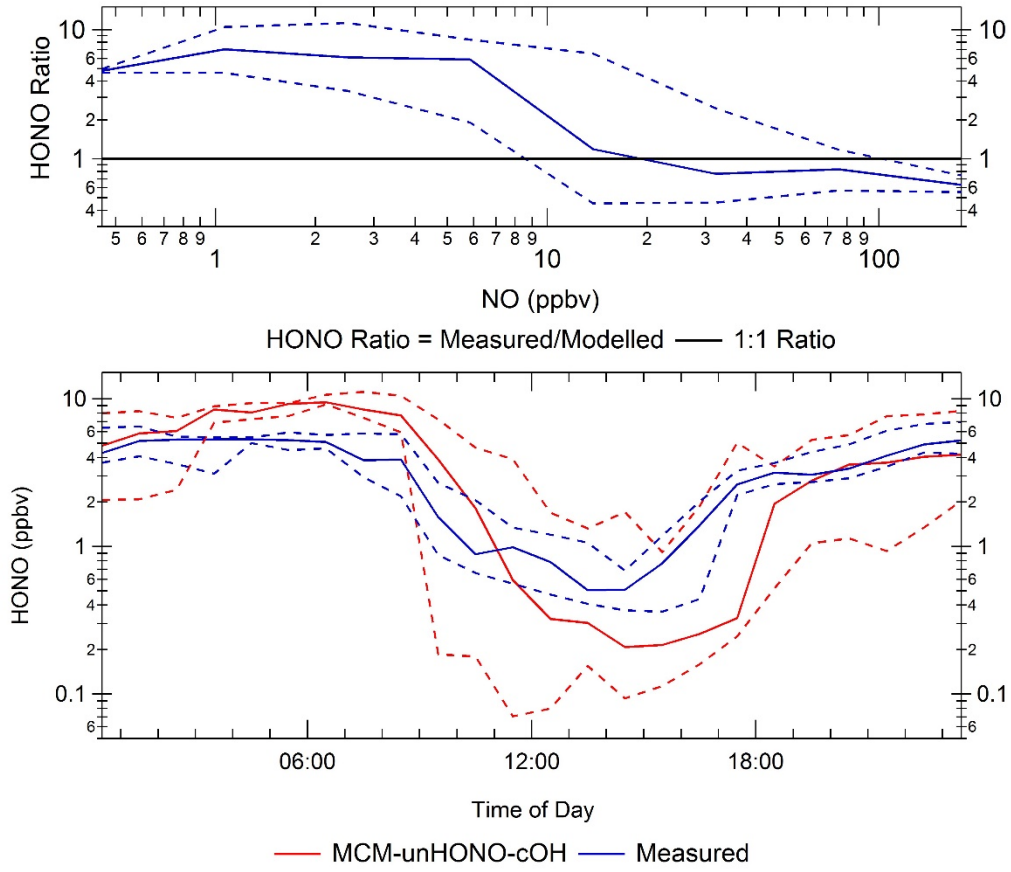

Figure 4.25 Top – Ratio of measured:modelled HONO binned to the logNO. Bottom - Average diurnal comparison of measured HONO with the results from MCM-cOH-unHONO. The average diurnal was averaged across the whole of the APHH winter campaign. The dashed lines in both graphs represents the 95 CI (confidence interval).

4.4.8 Radical concentration under haze conditions

4.4.8.1 Radical vs Model performance in haze

The observed OH concentrations during the APHH campaign are much higher than those predicted by global models (~4 x 10^4 cm^{-3}, for a 24 hr average during summertime) for the North China Plain (NCP) (Lelieveld et al., 2016). During the winter APHH campaign several haze events were observed, haze being defined when $PM_{2.5}$ > 75 µg m^{-3} (see Table 4.2 for more details). The campaign midday average for OH is higher than previous measurements of OH during wintertime, although comparable measurements of 2.7 x 10^6 molecule cm^{-3} and 3 x 10^6 molecule cm^{-3} have been made in Boulder and suburban Beijing respectively, as summarised in Table 4.6. It should be noted that both of these campaigns on average had larger photolysis rates

(see Table 4.6) by factors of 2.3 and 3.3 for BEST-ONE and NCITT, respectively. To investigate the impact haze conditions have on OH, HO_2 and RO_2 radicals measurements, the MCM-base model has been separated into the haze and non-haze periods (see Table 4.2 for more details) and is shown in Figure 4.26. The OH concentrations in- and outside of haze events are comparable despite the lower light levels during haze events (up to 50% less light on average, see Figure 4.4). The HO_2 and RO_2 concentration in- and outside of haze events show a slight decrease, especially in the morning hours (between 06:00 – 14:00).

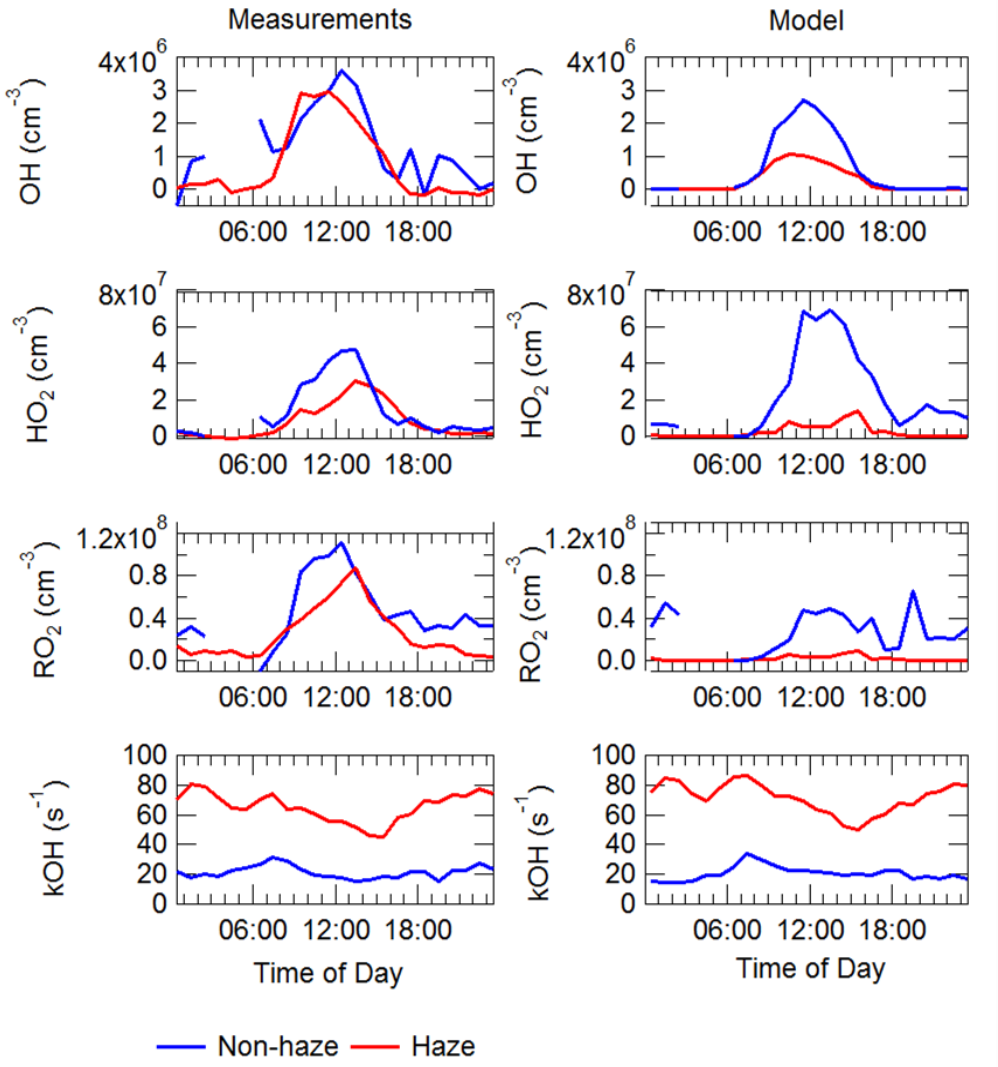

Figure 4.26 Average diurnal for OH, HO_2, RO_2 and *k*(OH) for measurements (left) and MCM-base (right) separated into haze (red) and non-haze (blue).

The average diurnal profiles of radical concentrations, both measured and calculated by the model, inside and outside of haze periods are presented in Figure 4.26. The maximum average OH concentration observed is almost the same in and out of haze (~3 x 10^6 molecule cm^{-3}) whilst the concentrations of the observed peroxy radicals decrease in haze. The model can replicate OH (within 20%) outside of haze but significantly underpredicts OH during haze events. The model also underpredicts HO_2 and RO_2 during haze events, but overpredicts HO_2 during non-haze conditions. The OH reactivity is replicated well by the model in both haze and non-haze conditions. The similar OH concentration observed in- and outside of haze events indicates that fast gas-phase oxidation is taking place, and hence the formation of secondary oxidation products, even within haze conditions. The impact of fast gas-phase oxidation on SO_2 and NO_2 production is discussed in section.4.4.8.2.

The average midday OH reactivity measured inside and outside of haze was 47 (s^{-1}) and 17 (s^{-1}), respectively. The comparable OH concentrations inside and outside of haze implies that within haze there is a larger turnover rate (defined as the product of [OH] and *k*(OH)) or a greater rate of chemical oxidation initiated by OH radicals. The radical chain length, ChL, is defined by the rate of radical propagation divided by the rate of radical production, and is given by:

$$\mathrm{ChL} = [\mathrm{OH}]\, k_{\mathrm{voc}} / \mathrm{P(RO_x)} \qquad \text{E4.1}$$

where in E4.1 k_{VOC} is the total OH reactivity with VOC and $P(RO_x)$ is the primary production of RO_x radical. As shown in Table 4.8, the average ChL calculated using E4.1 during the APHH campaign was ~5.9. This large value indicates that radical propagation during the APHH campaign is very efficient; this ChL is higher than calculated for previous winter campaigns that had OH radical and OH reactivity measurements available as summarised in Table 4.8. The large chain length comes from a combination of large OH concentrations and high OH reactivity measurements.

Campaign	OH 10^6 cm^{-3}	$P(RO_x)$ (ppbv h^{-1})	kOH (s^{-1})	NO_2 (ppbv)	Chainlength	Reference
Birmingham	1.7	2.8	30	9.3	2.1	Emmerson et al., 2005
NYC, US	1.4	1.4	27	15	3.3	Ren et al., 2006
Tokyo	1.5	1.4	23	12	3.1	Kanaya et al., 2007
Boulder	2.7	0.7	5	5	2.0	Kim et al., 2014
Suburban Beijing	2.8	0.9	12	6	4.7	Tan et al., 2017
Central Beijing	3	1.6	47	30	5.9	This work.

Table 4.8 Comparison of OH concentration, primary production of RO_x radicals ($P(RO_x)$), OH reactivity (k(OH)), NO_2 concentration and chainlength for various campaigns. The values presented here are for noon-time.

4.4.8.2 Gas-phase oxidation of SO_2 and NO_2

The high OH concentration observed in- and outside of haze events indicates a high rate of gas-phase oxidation (Figure 4.26), including the formation of secondary products that are believed to be major contributors to particles in haze events (Huang et al., 2014). Secondary oxidation products, such as nitric acid and sulphuric acid, which partition to the aerosol phase, are major contributors towards the formation of secondary particulate matter during haze events (Huang et al., 2014). The OH measurements enable calculation of the rate of SO_2 and NO_2 oxidation *via* reaction with OH to form gas-phase HNO_3 and H_2SO_4. Figure 4.28 shows that on average 1.5 ppbv/hr and 0.03 ppbv/hr of gas-phase NO_2 and SO_2 are oxidised to form their acidic species. The oxidation increase during these haze periods is caused by comparable OH concentration inside and outside of haze and, as shown in Figure 4.26, an increase in the NO_2 and SO_2 concentrations. The reaction of OH + SO_2 in the gas-phase is the rate-determining step in the formation of $SO_4^{2-}(aq)$, so the H_2SO_4 formed in the gas-phase will partition in the aerosol phase (Barth et al., 2000). H_2SO_4 is effectively a non-volatile gas at atmospheric temperatures, and H_2SO_4 condensation onto pre-existing

particles is an irreversible kinetic process (Zaveri et al., 2008). Whilst HNO_3 is semi-volatile species and the gas-particle partitioning is highly sensitive to meteorological conditions including: temperature, RH, particle size distribution, pH and particle composition. If the relative humidity is lower than the deliquescence relative humidity (RH_d), then the HNO_3 that is formed in the gas phase reacts with NH_3 to form ammonium nitrate aerosol (NH_4NO_3):

$$\mathrm{HNO_3(g) + NH_3(g) \leftrightarrow\ NH_4NO_3(s)} \qquad \text{R4.1}$$

If the ambient RH exceeds the RH_d then HNO_3 and NH_3 dissolve into the aqueous phase (aq):

$$\mathrm{HNO_3(g) + NH_3(g) \leftrightarrow NO_3^-(aq) +\ NH_4^+(aq)} \qquad \text{R4.2}$$

To consider the reversible process, knowledge of the RH_d that marks the transition between the solid and aqueous phases is required, in addition to the equilibrium constant, K_p, for the two phases (Ackermann et al., 1998). The MADE module (modal aerosol dynamics model for europe) uses the thermodynamic parameters as given by (Mozurkewich 1993), resulting in:

$$\mathrm{In}\left(\frac{\mathrm{RH_d}}{100}\right) = \frac{618.3}{\mathrm{T}} - 2.551 \qquad \text{E4.6}$$

for RH_d and:

$$\mathrm{In}\left(\mathrm{K_p}\right) = 118.87 - \frac{24084}{\mathrm{T}} - 6.025\ \mathrm{ln}\ (\mathrm{T}) \qquad \text{E4.7}$$

for K_p E4.6 and E4.7 show that nitrate formation is favoured thermodynamically at low temperatures and high relative humidity's (Ge et al., 2017). Previous measurements of SO_4^{-2} and NO_3^- in the aerosol phase made in Beijing in the wintertime suggests that photochemistry is important in the formation of nitrate aerosol, but not the formation of sulphate (Sun et al., 2013, Ge et al., 2017).

The average diurnal profiles for the measurements of NO_3^- (aq) and $SO_4^{2-}(aq)$, made during the APHH are shown in Figure 4.27 separated into haze and non-haze periods. As shown in Figure 4.27, the $SO_4^{2-}(aq)$, tracks the RH very well suggesting that the dominant path for sulphate formation during winter-time in Beijing is through the aqueous processing of SO_2. The shape of the average diurnal of NO_3^- and $SO_4^{2-}(aq)$, is consistent with studies made by Sun et al. (2013) and Ge et al. (2017). Figure 4.28 shows that the gas-phase

oxidation of NO_2 increases under haze conditions, showing that nitrate formation is driven by photochemistry in haze events despite the lower photolysis rates. Similar conclusions have been made in Lu et al. (2019) from measurements made during the BEST-ONE campaign; with SO_4^- aerosol predominantly driven by aqueous-phase chemistry whilst the production of NO_3^- aerosol from gas-phase oxidation of NO_2 with OH is important. The maximum production rate of HNO_3 observed during the BEST-ONE campaign is very similar to the production rate calculated for the APHH campaign (3 ppbv hr^{-1}). The BEST-ONE campaign assumed all the gas-phase HNO_3 partitioned into the aerosol-phase due to the high relative humidity observed during the campaign.

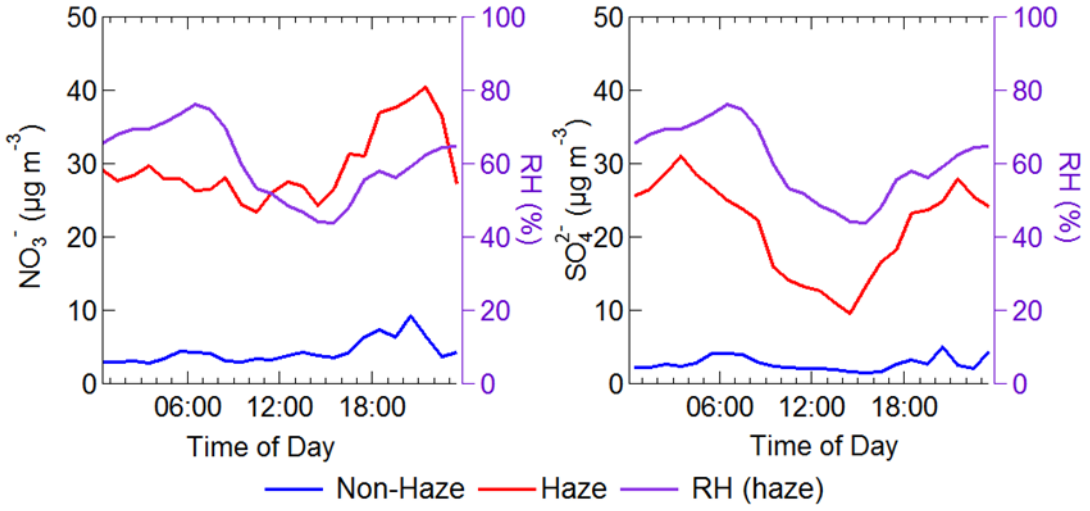

Figure 4.27 Average diurnal of NO_3^- and SO_4^- made during the APHH winter campaign separated into haze and non-haze conditions. And the relative humidity (RH) measured during haze periods. Haze = $PM_{2.5}$ > 75 µg m^{-3}. Measurements were made using AMS (see Table 4.1 for details).

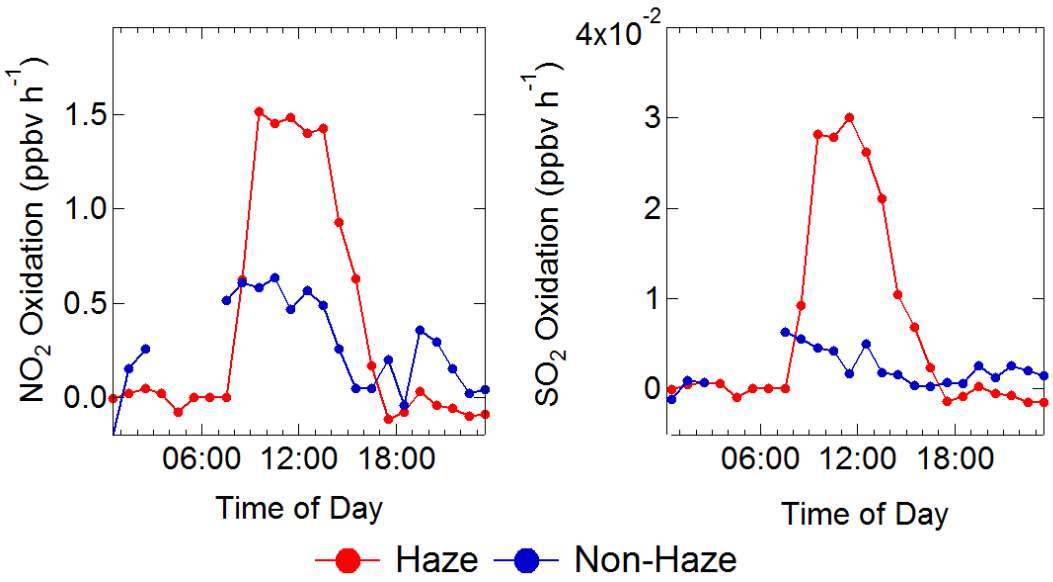

Figure 4.28 Average diel profiles of the rate of oxidation of NO_2 (left) and SO_2 (right) via reaction with OH in non-haze (blue) and haze (red) conditions. The gaps in the non-haze diurnal profile are caused by reduced data coverage during these periods as haze events were so frequent.

4.4.8.3 Sources and Sinks of Radicals in Haze

The average rates of initiation and termination of radicals (RO_x) for the entire APHH winter campaign is shown in section.4.4.5.1. To investigate the differences in initiation and termination in- and outside of haze the data has been separated by haze and non-haze conditions (see Table 4.2 for more details). Figure 4.29 shows the rate of primary production and termination of RO_x radicals inside and outside haze conditions, and shows that the rate of primary production of radical (RO_x) increases under haze conditions, despite the light levels and photolysis rate decreasing (see Figure 4.4 for details). The primary production of radicals in- and outside of haze events are both dominated by the photolysis of HONO, despite the decreasing photolysis rate. The decrease in photolysis rate is offset by an increase in HONO concentration by an average factor of 3.5 under haze conditions (see Figure 4.4). The termination of radicals in- and outside of haze conditions is dominated by the reaction of OH + NO, OH + NO_2 and net-PAN formation. Although under haze conditions net-PAN formation is significantly reduced,

contributing ~8% to the total termination of radicals compared with 30% under non-haze conditions.

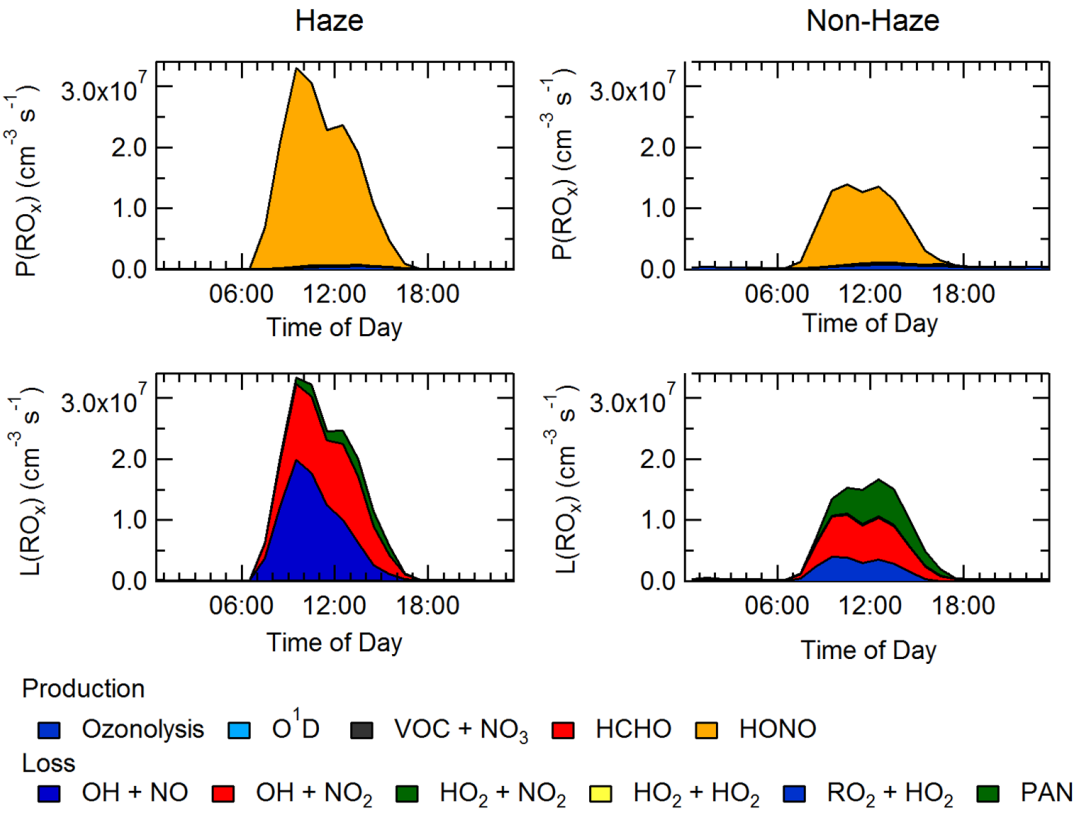

Figure 4.29 Left – A rate of production analysis (ROPA) for the primary production of RO_x radicals (top) and termination (bottom) in haze events. Left – ROPA for the primary production of RO_x radicals (top) and termination (bottom) in non-haze conditions. The contribution to production is from ozonolysis, photolysis of ozone (O^1D), VOC + NO_3, photolysis of HCHO and photolysis of HONO. The contribution to termination of RO_x radicals is from: OH + NO; OH + NO_2, HO_2 + HO_2 and net-PAN formation. The ROPA was performed on the MCM-base model.

In comparison to the BEST-ONE campaign during non-haze periods, the termination reaction of OH + NO_x, net-PAN and peroxy self-reaction contributed ~ 55%, 8%, 30%, respectively. During polluted periods in the BEST-ONE campaign the termination reaction of OH + NO_2 increases to 80%, and the net-PAN formation and peroxy self-reaction decrease to ~ 12% and 6% respectively. The BEST-ONE campaign shows very similar trends to the APHH campaign, except the APHH campaign shows a higher contribution to termination from OH + NO_x even under cleaner periods, this is probably due to the higher NO_x values observed during the APHH campaign compared to

the BEST-ONE campaign. The higher NO_x observed during the APHH campaign also resulted in limited termination of radicals through the peroxy self-reaction channel, due to the high NO_x out-competing the peroxy self-reaction channel compared with the BEST-ONE campaign.

4.4.9 Effect of underprediction of RO_2 radicals on ozone production

Although ozone pollution is generally not considered a wintertime phenomenon in Beijing, the elevated levels of RO_2 observed under high NO_x conditions suggests that ozone could be produced rapidly. Ozone may not be considered a significant factor because it is also rapidly titrated to NO_2 by reaction with NO, and therefore removed from the system.

The RO_2 radicals are under-predicted in the model, especially under higher NO_x conditions, as shown in Figure 4.30. The underprediction of RO_2 has implications for the model's ability to predict O_3 production. The net rate of O_3 production is to be equal to the net rate of NO_2 production:

$$\begin{aligned} \mathrm{P(O_3)} = {} & k_{\mathrm{HO_2+NO}}[\mathrm{HO_2}][\mathrm{NO}] + k_{\mathrm{RO_2+NO}}[\mathrm{RO_2}][\mathrm{NO}] \\ & - k_{\mathrm{OH+NO_2+M}}[\mathrm{OH}][\mathrm{NO_2}][\mathrm{M}] - k_{\mathrm{HO_2+O_3}}[\mathrm{HO_2}][\mathrm{O_3}] \\ & - P(\mathrm{RONO_2}) \end{aligned} \qquad \text{E4.8}$$

where the last three terms allow for the reduction of ozone production owing to reactions that remove NO_2. $P(RONO_2)$ represents the net formation of $RONO_2$ species.

When the rate of O_3 production is calculated using the measured values of HO_2 and RO_2, there is a positive trend with increasing NO. When the modelled concentrations of HO_2 and RO_2 are used, there is a general downward trend of $P(O_3)$ above [NO] = 3 ppbv, leading to a large underestimation of O_3 production by the model at higher values of NO. O_3 has a negative impact on both human health and crop yields (Lin et al., 2018), and in China leads to 74.2 thousand premature deaths and 7.6 billion US$ lost from the economy in 2016 (Maji et al., 2019). Figure 4.30 also shows that there is a large rate of *in-situ* ozone production in Beijing and the maximum observed ozone production is higher than the values observed during the summer-time

ClearfLo campaign, as shown in Table 4. 9. However, the very high NO concentrations seen during the campaign, resulting in very low levels of ozone due to the rapid titration of any O_3 formed, as shown in Figure 4.4. Table 4. **9** shows that the average observed ozone production between 08:00 and 17:00 during the APHH campaign (57 ppbv hr^{-1}, at 57 ppbv of NO) was higher than those observed during the BEST-ONE campaign (10 ppbv hr^{-1}, at 8 ppbv of NO) and the PKU campaign (43 ppbv hr^{-1}, at 39 ppbv of NO). The isopleth for ozone production as a function of NO_x and VOC for the BEST-ONE campaign (Lu et al., 2019) shows that a reduction in NO_x alone will lead to an increase in O_3 production and increase the amount of secondary organic aerosol produced. The higher ozone production observed during the APHH campaign is driven by higher NO concentration observed.

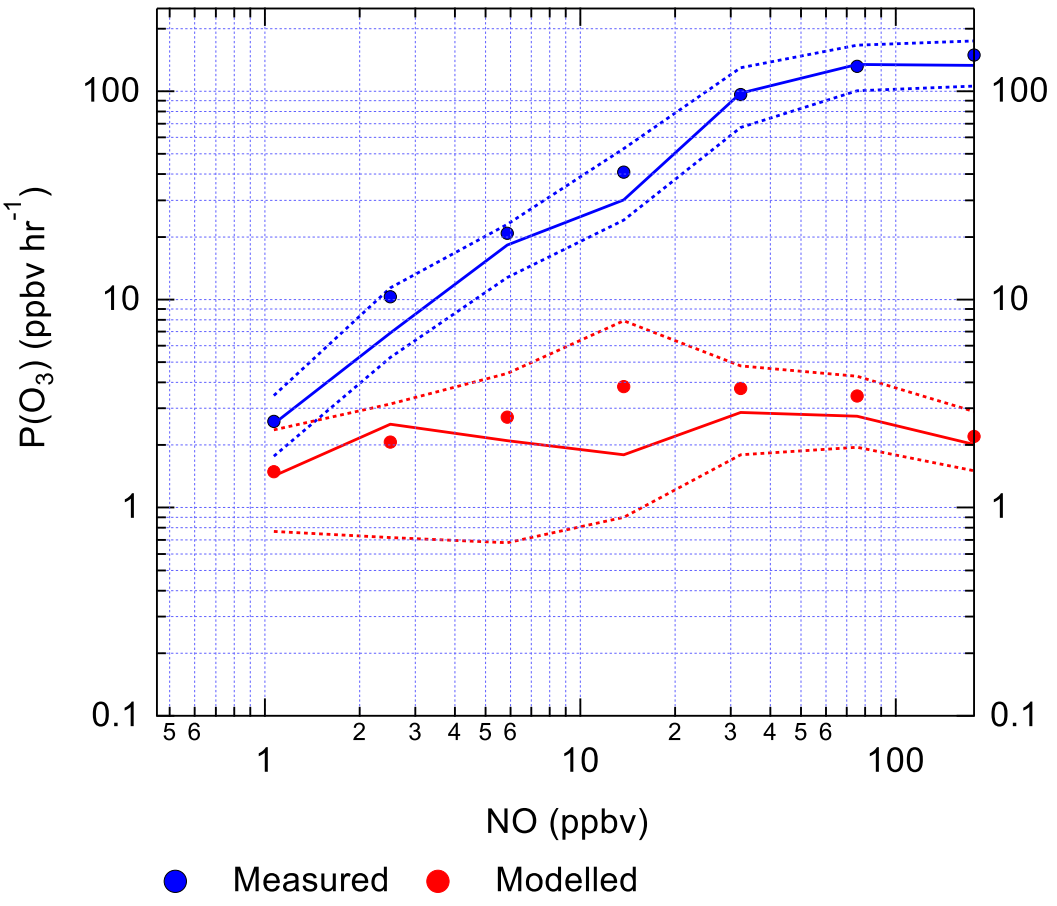

Figure 4.30 The calculated rate of ozone production as a function of [NO] using modelled (red) and measured (blue) values of HO_2 and RO_2 radicals. E4.8 was used to calculate the net ozone production.

Campaign	Dates	NO	$P(O_3)$ (ppbv hr^{-1})	Notes	Reference
APHH	Nov – Dec, 2016	40	71	Rate average for the daytime periods between 08:00 and 17:00	This work.
		180	132	Maximum ozone production.	
BEST-ONE	Jan – Feb, 2016	8.0	10	Rate average for the daytime periods between 08:00 and 17:00	Tan et al. (2018)
PKU	Nov – Dec 2017	43	39	Rate average for the daytime periods between 08:00 and 17:00	Ma et al. (2019)
ClearfLo	July – Aug 2012	52	41	Maximum ozone production.	Whalley et al. (2018)

Table 4. 9 Ozone production averaged between 08:00 – 17:00 for the APHH, BEST-ONE and PKU campaigns and the associated NO concentrations. Also shown is the maximum ozone production observed

4.5 Summary and Conclusions

OH, HO_2 and RO_2 radicals were measured using the FAGE technique in winter 2016 as a part of the APHH project, the project took place at the Institute of Atmospheric Physics in central Beijing, China. The whole APHH project had several aims, the radical measurements were part of a sub-project called Air Pollution and Human Health in Chinese Megacities (AIRPRO). The AIRPRO project aimed to assess which pollutants are transformed or removed through transport, chemical reactions and photolysis.

Measured OH peaked at 12:30 coinciding with solar noon, the average daily maxima was ~3.5 x 10^6 molecule cm^{-3} with daily maxima of OH varying between 1 – 8 x 10^6 molecule cm^{-3}. The OH diurnal profile tracks light levels very well, with measurements of OH scattered around before sunrise (~06:30) and after sunset (~17:15). The ratio of measured:modelled(MCM) shows a strong underprediction of OH at increasing mixing ratios of NO. There is a good modelled-to-measurement agreement between 3 – 9 ppbv of NO, the ratio of measured:modelled reaches a maximum of 7.2 at 170 ppbv of NO. The measured OH reactivity is replicated well in the model (within 10%). A photostationary steady-state (PSS) calculation was used to assess the

experimental budget of OH. The PSS showed the experimental budget agreed with the measurements within 10%, which is well within the 26% error on the measurements. The PSS also shows that HO_2 + NO was the dominant source of OH contributing ~85%, whilst HONO contributed almost all the remaining 15% of OH. From the 02/12/2016 to 09/12/2016 measurements of both OHwave and OHchem were taken and showed a very good agreement, with a slope of 1.05±0.07 for the correlation plot of OHwave and OHchem. The agreement of OHwave and OHchem shows that no interference was observed for the measurements of OH during the winter campaign.

Measured HO_2 peaked at 13:30, later than OH, the daily maxima average was 4.5×10^7 molecule cm^{-3}, coinciding with the daily trough in NO concentration (~43 ppbv, campaign average). The daily maxima of HO_2 varied between $0.7 – 1.5 \times 10^8$ molecule cm^{-3}. The MCM simulations predict a peak in HO_2 concentration at 11:30, rather than the peak of 13:30 that was observed. On average non-zero values of HO_2 were measured with a daily average of 5.6×10^6 molecule cm^{-3}, but the average LOD for the campaign was 2.8×10^6 molecule cm^{-3}. Like OH, the MCM generally underpredicts HO_2, especially under high NO conditions. The ratio of measured:modelled(MCM) peaks at 24 at 170 ppbv of NO. At 3 ppbv of NO the ratio of measured:modelled(MCM) is ~1, whilst below 3 ppbv of NO HO_2 starts to be overpredicted.

The RO_2 measurements (total, simple and complex) peaked at 12:30, the same time as OH peaked. The daily average maxima of total RO_2, simple RO_2 and complex RO_2 were 1×10^8, 0.6×10^8 and 0.57×10^8 molecule cm^{-3}, respectively. The daily maxima varied between $1 – 2.5 \times 10^8$ molecule cm^{-3} for total RO_2. The concentration for the speciated measurements of RO_2 showed almost a 50:50 contribution to total RO_2 between 20:00 to 10:00, whilst a greater number of simpler RO_2 species were measured than complex RO_2 species in the afternoon hours (between 10:00 – 20:00). Non-zero values of $\sim 5 \times 10^6$ molecule cm^{-3} for total RO_2 was measured, although the measured values were below the campaign average LOD for RO_2 ($\sim 8.4 \times 10^6$ molecule cm^{-3}). The MCM generally underpredicts the RO_2 radical

species especially under high NO conditions, like the results for both OH and HO_2. The ratio of measured(totalRO_2):modelled(MCM) has a peak of 35 at 60 ppbv of NO, unlike both OH and HO_2 the underprediction plateaus at a ratio of 35 above 60 ppbv of NO. Similar to the ratio of measured:modelled for OH and HO_2 at ~3 ppbv of NO the ratio is ~ 1, showing there is good understanding of OH, HO_2 and RO_2 chemistry at 3 ppbv of NO. Above 3 ppbv of NO the MCM starts to underpredict OH, HO_2 and RO_2. The speciated measurements of RO_2 into simple and complex also shows an underprediction of these species at higher NO. The simple RO_2 is underpredicted by the modelled across the whole observed NO range, the model also shows a decrease in the simple RO_2 with increasing NO. Whilst the measurements of simple RO_2 only start to decrease after 10 ppbv. The model overpredicts the concentration of complex RO_2 at the lower NO mixing ratios observed, and similar to the similar RO_2 the modelled complex RO_2 decreases with increasing NO. The measured complex RO_2 concentration stays almost constant throughout the different NO mixing ratios observed.

The MCM-base model was used to assess the primary source and termination of radicals during the campaign using rate of production analysis. The primary production of radicals was dominated by the photolysis of HONO (~94%), with 3% each from both ozonolysis and photolysis of HCHO. The termination of radicals was dominated by OH + NO (~37%) and OH + NO_2 (~43%), with 20% of the termination from net-formation of PAN. The sources and sinks in haze and non-haze conditions have been explored and it is shown that there is more primary production under haze conditions compared to non-haze conditions. The increase in primary production under haze conditions is caused by increased HONO concentration. The termination in non-haze conditions shows a larger contribution from the net-formation of PAN compared to haze conditions.

The underprediction of OH, HO_2 and RO_2, especially under higher NO conditions, represents missing understanding in either the sources of these radical species, or the chemistry of propagation between radical species. When the model is constrained to HO_2, the model can replicate OH within

10%, which is well within the error of the measurements (~26%). The replication of OH by the model when constrained to HO_2, and capturing the OH reactivity, provides evidence of good understanding of both the radical propagation between HO_2 to OH *via* NO and the losses of OH to other species. This implies there is missing understanding in the RO_2 either: additional primary source of these RO_2 species or missing understanding the recycling chemistry between RO_2 to HO_2. An additional RO_2 source was added into the base model at an average of 12 ppbv hr^{-1} to match the measurements and modelled concentration. With the inclusion of an additional RO_2 source, the model overpredicted both OH and HO_2 by a factor of 1.6 and 4, respectively. With HO_2 now overpredicted in the model, HO_2 uptake was considered using γ=0.2, the model with HO_2 uptake still overpredicted OH and HO_2 by a factor of 1.6 and 3.5. These results show that an additional primary source of RO_2 may not be the only solution to the underprediction of radicals at high NO concentration.

The impact on OH caused by not constraining the model to measured HONO was explored. The unconstrained model resulted in an underprediction of HONO and OH by a factor of ~10 and ~6.4 respectively, whilst in the base model (when constrained to HONO) the OH concentration is underpredicted by a factor of ~2. The amount of HONO from the reaction of OH + NO was explored by unconstraining the model to HONO whilst constraining the model to measured OH. This showed that the reaction of OH + NO could replicate the HONO concentration between 07:00 to 13:00 and 19:30 – 02:30 and additional heterogeneous sources are required. The HONO is underpredicted between after 13:30, suggesting that heterogeneous reactions are required to reconcile measured and modelled HONO.

During the APHH winter campaign, several haze events were observed. When the radical species are separated into haze and non-haze it showed that the OH concentration was similar inside and outside haze events. The impact of a consistent OH concentration inside and outside of haze events on the gas-phase oxidation of NO_2 and SO_2 was explored. The gas-phase oxidation

of NO_2 and SO_2 increased during haze events by a factor of 3 and 4.2, respectively.

As discussed earlier, the peroxy radicals (HO_2 and RO_2) were underpredicted by the model, and this impairs the models ability to predict ozone production. The maximum ozone production calculated using the measurements was 162 ppbv hr^{-1}, whilst the ozone production calculated using the modelled was 10 ppbv hr^{-1}. The underprediction of ozone production by the model shows how missing understanding of the radical chemistry can impact the calculation of secondary pollutants. Also, the production of O_3 during winter-time in Beijing is very high, but is currently being titrated out by the high concentration of NO. Current mitigation strategies in China aims at reducing NO_x emissions and PM, the reduction in NO may lead to an increase in O_3 during the winter-time in Beijing.

Further modelling could be undertaken to explore the underprediction of OH, HO_2 and RO_2 in the model. This may include decreasing the rate constant for specific complex RO_2 species reacting with NO which should increase the RO_2 lifetime and increase the amount of RO_2 recycling in HO_2 and thus recycling in OH.

4.6 References

Ackermann, I. J., Hass, H., Memmesheimer, M., Ebel, A., Binkowski, F. S. and Shankar, U. (1998) 'Modal aerosol dynamics model for Europe: Development and first applications', *Atmospheric environment,* 32(17), pp. 2981-2999.

Barth, M., Rasch, P., Kiehl, J., Benkovitz, C. and Schwartz, S. (2000) 'Sulfur chemistry in the National Center for Atmospheric Research Community Climate Model: Description, evaluation, features, and sensitivity to aqueous chemistry', *Journal of Geophysical Research: Atmospheres,* 105(D1), pp. 1387-1415.

Bohn, B., Heard, D. E., Mihalopoulos, N., Plass-Dülmer, C., Schmitt, R. and Whalley, L. K. (2016) 'Characterisation and improvement of j (O 1 D) filter radiometers', *Atmospheric Measurement Techniques,* 9(7), pp. 3455-3466.

Breton, M. L., Wang, Y., Hallquist, Å. M., Pathak, R. K., Zheng, J., Yang, Y., Shang, D., Glasius, M., Bannan, T. J. and Liu, Q. (2018) 'Online gas-

and particle-phase measurements of organosulfates, organosulfonates and nitrooxy organosulfates in Beijing utilizing a FIGAERO ToF-CIMS', *Atmospheric Chemistry and Physics,* 18(14), pp. 10355-10371.

Coyle, M., Nemitz, E., Storeton-West, R., Fowler, D. and Cape, J. N. (2009) 'Measurements of ozone deposition to a potato canopy', *Agricultural and Forest Meteorology,* 149(3-4), pp. 655-666.

Crilley, L. R., Karmer, L. J., Ouyang, B., Duan, J., Zhang, W., Tong, S., Ge, M., Ge, K. T., Qin, M., Xie, P., Shaw, M. D., Lewis, A. C., Mehra, A., Bannan, T. J., Worrall, S. D., Priestley, M., Bacak, A., Coe, H., Allan, J., Percival, C. J., Popoola, O. A. M., Jones, R. L. and Bloss, W. J. (2019) 'Intercomparison of nitrous acid (HONO) measurement techniques in a megacity (Beijing)', *AMT*.

Crilley, L. R., Kramer, L., Pope, F. D., Whalley, L. K., Cryer, D. R., Heard, D. E., Lee, J. D., Reed, C. and Bloss, W. J. (2016) 'On the interpretation of in situ HONO observations via photochemical steady state', *Faraday discussions,* 189, pp. 191-212.

Cryer, D. (2016) 'Measurements of hydroxyl radical reactivity and formaldehyde in the atmosphere', *PhD Thesis,* University of Leeds.

Deventer, M. J., El-Madany, T., Griessbaum, F. and Klemm, O. (2015) 'One-year measurement of size-resolved particle fluxes in an urban area', *Tellus B: Chemical and Physical Meteorology,* 67(1), pp. 25531.

Du, W., Zhao, J., Wang, Y., Zhang, Y., Wang, Q., Xu, W., Chen, C., Han, T., Zhang, F. and Li, Z. (2017) 'Simultaneous measurements of particle number size distributions at ground level and 260 m on a meteorological tower in urban Beijing, China', *Atmospheric Chemistry and Physics,* 17(11), pp. 6797-6811.

Duan, J., Ouyang, B., Fang, W., Li, X., Lu, K., Tang, K., Liang, S., Meng, F., Hu, Z. and Xie, P. (2018) 'Development of an incoherent broadband cavity-enhanced absorption spectrometer for in situ measurements of HONO and NO_2', *Atmospheric Measurement Techniques*, 11, pp. 4531 – 4543.

Dunmore, R., Hopkins, J., Lidster, R., Lee, J., Evans, M., Rickard, A., Lewis, A. and Hamilton, J. (2015) 'Diesel-related hydrocarbons can dominate gas phase reactive carbon in megacities', *Atmospheric Chemistry and Physics,* 15(17), pp. 9983-9996.

Dusanter, S., Vimal, D., Stevens, P., Volkamer, R., Molina, L., Baker, A., Meinardi, S., Blake, D., Sheehy, P. and Merten, A. (2009) 'Measurements of OH and HO_2 concentrations during the MCMA-2006 field campaign–Part 2: Model comparison and radical budget', *Atmospheric Chemistry and Physics,* 9(18), pp. 6655-6675.

Emmerson, K., Carslaw, N. and Pilling, M. (2005) 'Urban atmospheric chemistry during the PUMA campaign 2: Radical budgets for OH, HO_2 and RO_2', *Journal of atmospheric chemistry,* 52(2), pp. 165-183.

Finlayson-Pitts, B., Wingen, L., Sumner, A., Syomin, D. and Ramazan, K. (2003) 'The heterogeneous hydrolysis of NO_2 in laboratory systems and in outdoor and indoor atmospheres: An integrated mechanism', *Physical Chemistry Chemical Physics,* 5(2), pp. 223-242.

Fuchs, H., Brauers, T., Dorn, H.-P., Harder, H., Haseler, R., Hofzumahaus, A., Holland, F., Kanaya, Y., Kajii, Y. and Kubistin, D. (2010) 'Formal blind intercomparison of HO_2 measurements in the atmosphere simulation chamber SAPHIR during the HOxComp campaign', *Atmospheric Chemistry and Physics*, 10(24), 12233 – 12250.

Fuchs, H., Tan, Z., Hofzumahaus, A., Broch, S., Dorn, H.-P., Holland, F., Künstler, C., Gomm, S., Rohrer, F. and Schrade, S. (2016) 'Investigation of potential interferences in the detection of atmospheric RO_x radicals by laser-induced fluorescence under dark conditions', *Atmospheric measurement techniques,* 9(4), pp. 1431-1447.

Ge, B., Sun, Y., Liu, Y., Dong, H., Ji, D., Jiang, Q., Li, J. and Wang, Z. (2013) 'Nitrogen dioxide measurement by cavity attenuated phase shift spectroscopy (CAPS) and implications in ozone production efficiency and nitrate formation in Beijing, China', *Journal of Geophysical Research: Atmospheres,* 118(16), pp. 9499-9509.

Ge, X., He, Y., Sun, Y., Xu, J., Wang, J., Shen, Y. and Chen, M. (2017) 'Characteristics and formation mechanisms of fine particulate nitrate in typical urban areas in China', *Atmosphere,* 8(3), pp. 62.

Gerbig, C., Schmitgen, S., Kley, D., Volz-Thomas, A., Dewey, K. and Haaks, D. (1999) 'An improved fast-response vacuum-UV resonance fluorescence CO instrument', *Journal of Geophysical Research: Atmospheres,* 104(D1), pp. 1699-1704.

Griffith, S., Hansen, R., Dusanter, S., Stevens, P., Alaghmand, M., Bertman, S., Carroll, M., Erickson, M., Galloway, M. and Grossberg, N. (2013) 'OH and HO_2 radical chemistry during PROPHET 2008 and CABINEX 2009–Part 1: Measurements and model comparison', *Atmospheric Chemistry and Physics,* 13(11), pp. 5403-5423.

Han, T., Xu, W., Li, J., Freedman, A., Zhao, J., Wang, Q., Chen, C., Zhang, Y., Wang, Z. and Fu, P. (2017) 'Aerosol optical properties measurements by a CAPS single scattering albedo monitor: Comparisons between summer and winter in Beijing, China', *Journal of Geophysical Research: Atmospheres,* 122(4), pp. 2513-2526.

Högström, U. and Smedman, A.-S. (2004) 'Accuracy of sonic anemometers: laminar wind-tunnel calibrations compared to atmospheric in situ calibrations against a reference instrument', *Boundary-layer meteorology,* 111(1), pp. 33-54.

Hollaway, M., Wild, O., Yang, T., Sun, Y., Xu, W., Xie, C., Whalley, L., Slater, E., Heard, D. and Liu, D. (2019) 'Photochemical impacts of haze pollution in an urban environment', *Atmospheric Chemistry Physics*, 19(15), pp. 9699-9714.

Hopkins, J. R., Jones, C. E. and Lewis, A. C. (2011) 'A dual channel gas chromatograph for atmospheric analysis of volatile organic compounds including oxygenated and monoterpene compounds', *Journal of Environmental Monitoring,* 13(8), pp. 2268-2276.

Huang, R.-J., Zhang, Y., Bozzetti, C., Ho, K.-F., Cao, J.-J., Han, Y., Daellenbach, K. R., Slowik, J. G., Platt, S. M. and Canonaco, F. (2014) 'High secondary aerosol contribution to particulate pollution during haze events in China', *Nature,* 514(7521), pp. 218-222.

Huang, Z., Zhang, Y., Yan, Q., Zhang, Z. and Wang, X. (2016) 'Real-time monitoring of respiratory absorption factors of volatile organic compounds in ambient air by proton transfer reaction time-of-flight mass spectrometry', *Journal of hazardous materials,* 320, pp. 547-555.

Jacob, D. J. (2000) 'Heterogeneous chemistry and tropospheric ozone', *Atmospheric Environment,* 34(12-14), pp. 2131-2159.

Jenkin, M. E., Valorso, R., Aumont, B. and Rickard, A. R. (2019) 'Estimation of rate coefficients and branching ratios for reactions of organic peroxy radicals for use in automated mechanism construction', *Atmospheric Chemistry and Physics,* 19(11), pp. 7691-7717.

Johnson, T., Capel, J. and Ollison, W. (2014) 'Measurement of microenvironmental ozone concentrations in Durham, North Carolina, using a 2B Technologies 205 Federal Equivalent Method monitor and an interference-free 2B Technologies 211 monitor', *Journal of the Air & Waste Management Association,* 64(3), pp. 360-371.

Junninen, H., Ehn, M., Petäjä, T., Luosujärvi, L., Kotiaho, T., Kostiainen, R., Rohner, U., Gonin, M., Fuhrer, K. and Kulmala, M. (2010) 'A high-resolution mass spectrometer to measure atmospheric ion composition', *Atmospheric Measurement Techniques,* 3(4), pp. 1039-1053.

Kanaya, Y., Cao, R., Akimoto, H., Fukuda, M., Komazaki, Y., Yokouchi, Y., Koike, M., Tanimoto, H., Takegawa, N. and Kondo, Y. (2007) 'Urban photochemistry in central Tokyo: 1. Observed and modeled OH and HO_2 radical concentrations during the winter and summer of 2004', *Journal of Geophysical Research: Atmospheres,* 112(D21).

Kim, S., VandenBoer, T. C., Young, C. J., Riedel, T. P., Thornton, J. A., Swarthout, B., Sive, B., Lerner, B., Gilman, J. B. and Warneke, C. (2014) 'The primary and recycling sources of OH during the NACHTT-2011 campaign: HONO as an important OH primary source in the wintertime', *Journal of Geophysical Research: Atmospheres,* 119(11), pp. 6886-6896.

Kotthaus, S. and Grimmond, C. S. B. (2018) 'Atmospheric boundary-layer characteristics from ceilometer measurements. Part 1: A new method to track mixed layer height and classify clouds', *Quarterly Journal of the Royal Meteorological Society,* 144(714), pp. 1525-1538.

Le Breton, M., Bacak, A., Muller, J. B., Bannan, T. J., Kennedy, O., Ouyang, B., Xiao, P., Bauguitte, S. J.-B., Shallcross, D. E. and Jones, R. L. (2014) 'The first airborne comparison of N_2O_5 measurements over the UK using a CIMS and BBCEAS during the RONOCO campaign', *Analytical Methods,* 6(24), pp. 9731-9743.

Lee, J., Whalley, L., Heard, D., Stone, D., Dunmore, R., Hamilton, J., Young, D., Allan, J., Laufs, S. and Kleffmann, J. (2015) 'Detailed budget analysis of HONO in central London reveals a missing daytime source', *Atmospheric Chemistry and Physics Discussions,* 15(16), pp. 22097-22139.

Lelieveld, J., Gromov, S., Pozzer, A. and Taraborrelli, D. (2016) 'Global tropospheric hydroxyl distribution, budget and reactivity', *Atmospheric Chemistry and Physics,* 16(19), pp. 12477.

Li, K., Jacob, D. J., Liao, H., Shen, L., Zhang, Q. and Bates, K. H. (2019) 'Anthropogenic drivers of 2013–2017 trends in summer surface ozone in China', *Proceedings of the National Academy of Sciences,* 116(2), pp. 422-427.

Li, X., Brauers, T., Häseler, R., Bohn, B., Fuchs, H., Hofzumahaus, A., Holland, F., Lou, S., Lu, K. and Rohrer, F. (2012) 'Exploring the atmospheric chemistry of nitrous acid (HONO) at a rural site in Southern China', *Atmospheric Chemistry and Physics,* 12(3), pp. 1497-1513.

Li, Z., Hu, R., Xie, P., Chen, H., Wu, S., Wang, F., Wang, Y., Ling, L., Liu, J. and Liu, W. (2018) 'Development of a portable cavity ring down spectroscopy instrument for simultaneous, in situ measurement of NO_3 and N_2O_5', *Optics express,* 26(10), pp. A433-A449.

Lin, Y., Jiang, F., Zhao, J., Zhu, G., He, X., Ma, X., Li, S., Sabel, C. E. and Wang, H. (2018) 'Impacts of O_3 on premature mortality and crop yield loss across China', *Atmospheric environment,* 194, pp. 41-47.

Liu, D., Whitehead, J., Alfarra, M. R., Reyes-Villegas, E., Spracklen, D. V., Reddington, C. L., Kong, S., Williams, P. I., Ting, Y.-C. and Haslett, S. (2017) 'Black-carbon absorption enhancement in the atmosphere determined by particle mixing state', *Nature Geoscience,* 10(3), pp. 184.

Lu, K., Fuchs, H., Hofzumahaus, A., Tan, Z., Wang, H., Zhang, L., Schmitt, S., Rohrer, F., Bohn, B. and Broch, S. (2019) 'Fast photochemistry in wintertime haze: Consequences for pollution mitigation strategies', *Environmental science & technology*.

Lu, K., Hofzumahaus, A., Holland, F., Bohn, B., Brauers, T., Fuchs, H., Hu, M., Häseler, R., Kita, K. and Kondo, Y. (2013) 'Missing OH source in a suburban environment near Beijing: observed and modelled OH and HO_2 concentrations in summer 2006', *Atmospheric Chemistry and Physics,* 13(2), pp. 1057-1080.

Lu, K., Rohrer, F., Holland, F., Fuchs, H., Bohn, B., Brauers, T., Chang, C., Häseler, R., Hu, M. and Kita, K. (2012) 'Observation and modelling of OH and HO_2 concentrations in the Pearl River Delta 2006: a missing OH source in a VOC rich atmosphere', *Atmospheric chemistry and physics,* 12(3), pp. 1541-1569.

Lu, X., Wang, Y., Li, J., Shen, L. and Fung, J. C. (2018) 'Evidence of heterogeneous HONO formation from aerosols and the regional photochemical impact of this HONO source', *Environmental Research Letters,* 13(11), pp. 114002.

Ma, X., Tan, Z., Lu, K., Yang, X., Liu, Y., Li, S., Li, X., Chen, S., Novelli, A. and Cho, C. (2019) 'Winter photochemistry in Beijing: Observation and model simulation of OH and HO_2 radicals at an urban site', *Science of The Total Environment,* 685, pp. 85-95.

Maji, K. J., Ye, W.-F., Arora, M. and Nagendra, S. S. (2019) 'Ozone pollution in Chinese cities: Assessment of seasonal variation, health effects and economic burden', *Environmental pollution,* 247, pp. 792-801.

McDermitt, D., Burba, G., Xu, L., Anderson, T., Komissarov, A., Riensche, B., Schedlbauer, J., Starr, G., Zona, D. and Oechel, W. (2011) 'A new low-power, open-path instrument for measuring methane flux by eddy covariance', *Applied Physics B,* 102(2), pp. 391-405.

McManus, J. B., Zahniser, M. S., Nelson, D. D., Shorter, J. H., Herndon, S. C., Wood, E. C. and Wehr, R. (2010) 'Application of quantum cascade lasers to high-precision atmospheric trace gas measurements', *Optical Engineering,* 49(11), pp. 111124.

Meng, Z., Xu, X., Lin, W., Ge, B., Xie, Y., Song, B., Jia, S., Zhang, R., Peng, W. and Wang, Y. (2018) 'Role of ambient ammonia in particulate

ammonium formation at a rural site in the North China Plain', *Atmospheric Chemistry and Physics,* 18(1), pp. 167-184.

Mills, G. P., Hiatt-Gipson, G. D., Bew, S. P. and Reeves, C. E. (2016) 'Measurement of isoprene nitrates by GCMS', *Atmospheric Measurement Techniques,* 9(9), pp. 4533-4545.

Moore, E., Chatzidiakou, L., Jones, R. L., Smeeth, L., Beevers, S., Kelly, F. J., Quint, J. K. and Barratt, B. (2016) 'Linking e-health records, patient-reported symptoms and environmental exposure data to characterise and model COPD exacerbations: protocol for the COPE study', *BMJ open,* 6(7), pp. e011330.

Mozurkewich, M. (1993) 'The dissociation constant of ammonium nitrate and its dependence on temperature, relative humidity and particle size', *Atmospheric Environment. Part A. General Topics,* 27(2), pp. 261-270.

Nemitz, E., Hargreaves, K. J., McDonald, A. G., Dorsey, J. R. and Fowler, D. (2002) 'Micrometeorological measurements of the urban heat budget and CO_2 emissions on a city scale', *Environmental Science & Technology,* 36(14), pp. 3139-3146.

Nemitz, E., Jimenez, J. L., Huffman, J. A., Ulbrich, I. M., Canagaratna, M. R., Worsnop, D. R. and Guenther, A. B. (2008) 'An eddy-covariance system for the measurement of surface/atmosphere exchange fluxes of submicron aerosol chemical species—first application above an urban area', *Aerosol Science and Technology,* 42(8), pp. 636-657.

Pang, X., Lewis, A., Rickard, A., Baeza-Romero, M., Adams, T., Ball, S., Daniels, M., Goodall, I., Monks, P. S. and Peppe, S. (2014) 'A smog chamber comparison of a microfluidic derivatisation measurement of gas-phase glyoxal and methylglyoxal with other analytical techniques', *Atmospheric Measurement Techniques,* 7(2), pp. 373-389.

Petäjä, T., Mordas, G., Manninen, H., Aalto, P. P., Hämeri, K. and Kulmala, M. (2006) 'Detection efficiency of a water-based TSI condensation particle counter 3785', *Aerosol Science and Technology,* 40(12), pp. 1090-1097.

Popoola, O. A., Carruthers, D., Lad, C., Bright, V. B., Mead, M. I., Stettler, M. E., Saffell, J. R. and Jones, R. L. (2018) 'Use of networks of low cost air quality sensors to quantify air quality in urban settings', *Atmospheric environment,* 194, pp. 58-70.

Ren, X., Brune, W. H., Mao, J., Mitchell, M. J., Lesher, R. L., Simpas, J. B., Metcalf, A. R., Schwab, J. J., Cai, C. and Li, Y. (2006) 'Behavior of OH and HO_2 in the winter atmosphere in New York City', *Atmospheric Environment,* 40, pp. 252-263.

Saunders, S. M., Jenkin, M. E., Derwent, R. and Pilling, M. (2003) 'Protocol for the development of the Master Chemical Mechanism, MCMv3 (Part A): tropospheric degradation of non-aromatic volatile organic compounds', *Atmospheric Chemistry and Physics,* 3(1), pp. 161-180.

Shi, J. P., Harrison, R. M. and Brear, F. (1999) 'Particle size distribution from a modern heavy duty diesel engine', *Science of the Total Environment,* 235(1-3), pp. 305-317.

Shi, Z., Vu, T., Kotthaus, S., Grimmond, S., Harrison, R. M., Yue, S., Zhu, T., Lee, J., Han, Y. and Demuzere, M. (2018) 'Introduction to Special Issue-In-depth study of air pollution sources and processes within Beijing and its surrounding region (APHH-Beijing)', *Atmospheric Chemistry and Physics*, 11, 7519 – 7546.

Sloan, C. D., Philipp, T. J., Bradshaw, R. K., Chronister, S., Barber, W. B. and Johnston, J. D. (2016) 'Applications of GPS-tracked personal and fixed-location $PM_{2.5}$ continuous exposure monitoring', *Journal of the Air & Waste Management Association,* 66(1), pp. 53-65.

Smith, K. R., Edwards, P. M., Evans, M. J., Lee, J. D., Shaw, M. D., Squires, F., Wilde, S. and Lewis, A. C. (2017) 'Clustering approaches to improve the performance of low cost air pollution sensors', *Faraday discussions,* 200, pp. 621-637.

Stone, D., Whalley, L. K., Ingham, T., Edwards, P., Cryer, D. R., Brumby, C. A., Seakins, P. W. and Heard, D. E. (2016) 'Measurement of OH reactivity by laser flash photolysis coupled with laser-induced fluorescence spectroscopy', *Atmospheric Measurement Techniques*, pp. 2827-2844.

Storer, M., Salmond, J., Dirks, K. N., Kingham, S. and Epton, M. (2014) 'Mobile selected ion flow tube mass spectrometry (SIFT-MS) devices and their use for pollution exposure monitoring in breath and ambient air–pilot study', *Journal of breath research,* 8(3), pp. 037106.

Sun, Y., Du, W., Fu, P., Wang, Q., Li, J., Ge, X., Zhang, Q., Zhu, C., Ren, L. and Xu, W. (2016) 'Primary and secondary aerosols in Beijing in winter: sources, variations and processes', *Atmospheric Chemistry and Physics,* 16(13), pp. 8309-8329.

Sun, Y., Wang, Z., Dong, H., Yang, T., Li, J., Pan, X., Chen, P. and Jayne, J. T. (2012) 'Characterization of summer organic and inorganic aerosols in Beijing, China with an Aerosol Chemical Speciation Monitor', *Atmospheric Environment,* 51, pp. 250-259.

Sun, Y., Wang, Z., Fu, P., Yang, T., Jiang, Q., Dong, H., Li, J. and Jia, J. (2013) 'Aerosol composition, sources and processes during wintertime

in Beijing, China', *Atmospheric Chemistry and Physics,* 13(9), pp. 4577-4592.

Taiwo, A., Beddows, D., Calzolai, G., Harrison, R. M., Lucarelli, F., Nava, S., Shi, Z., Valli, G. and Vecchi, R. (2014) 'Receptor modelling of airborne particulate matter in the vicinity of a major steelworks site', *Science of the Total Environment,* 490, pp. 488-500.

Tan, Z., Fuchs, H., Lu, K., Hofzumahaus, A., Bohn, B., Broch, S., Dong, H., Gomm, S., Häseler, R. and He, L. (2017) 'Radical chemistry at a rural site (Wangdu) in the North China Plain: observation and model calculations of OH, HO_2 and RO_2 radicals', *Atmospheric Chemistry and Physics,* 17(1), pp. 663-690.

Tan, Z., Rohrer, F., Lu, K., Ma, X., Bohn, B., Broch, S., Dong, H., Fuchs, H., Gkatzelis, G. I. and Hofzumahaus, A. (2018) 'Wintertime photochemistry in Beijing: observations of RO_x radical concentrations in the North China Plain during the BEST-ONE campaign', *Atmospheric Chemistry and Physics,* 18(16), pp. 12391-12411.

Vanhanen, J., Mikkilä, J., Lehtipalo, K., Sipilä, M., Manninen, H., Siivola, E., Petäjä, T. and Kulmala, M. (2011) 'Particle size magnifier for nano-CN detection', *Aerosol Science and Technology,* 45(4), pp. 533-542.

Vaughan, A. R., Lee, J. D., Misztal, P. K., Metzger, S., Shaw, M. D., Lewis, A. C., Purvis, R. M., Carslaw, D. C., Goldstein, A. H. and Hewitt, C. N. (2016) 'Spatially resolved flux measurements of NO_x from London suggest significantly higher emissions than predicted by inventories', *Faraday discussions,* 189, pp. 455-472.

Wang, J., Zhang, Q., Chen, M., Collier, S., Zhou, S., Ge, X., Xu, J., Shi, J., Xie, C. and Hu, J. (2017a) 'First chemical characterization of refractory black carbon aerosols and associated coatings over the Tibetan Plateau (4730 m asl)', *Environmental science & technology,* 51(24), pp. 14072-14082.

Wang, M., Shao, M., Chen, W., Lu, S., Liu, Y., Yuan, B., Zhang, Q., Chang, C.-C., Wang, B. and Zeng, L. (2015a) 'Trends of non-methane hydrocarbons (NMHC) emissions in Beijing during 2002–2013', *Atmospheric Chemistry and Physics,* 15(3), pp. 1489-1502.

Wang, Q., Sun, Y., Jiang, Q., Du, W., Sun, C., Fu, P. and Wang, Z. (2015b) 'Chemical composition of aerosol particles and light extinction apportionment before and during the heating season in Beijing, China', *Journal of Geophysical Research: Atmospheres,* 120(24), pp. 12708-12722.

Wang, W., Shao, L., Xing, J., Li, J., Chang, L. and Li, W. (2018) 'Physicochemical characteristics of individual aerosol particles during

the 2015 China victory day parade in Beijing', *Atmosphere,* 9(2), pp. 40.

Wang, Y., Zhang, F., Li, Z., Tan, H., Xu, H., Ren, J., Zhao, J., Du, W. and Sun, Y. (2017b) 'Enhanced hydrophobicity and volatility of submicron aerosols under severe emission control conditions in Beijing', *Atmospheric Chemistry and Physics,* 17(8), pp. 5239-5251.

Whalley, L., Blitz, M., Desservettaz, M., Seakins, P. and Heard, D. (2013) 'Reporting the sensitivity of laser-induced fluorescence instruments used for HO_2 detection to an interference from RO_2 radicals and introducing a novel approach that enables HO_2 and certain RO_2 types to be selectively measured', *Atmospheric Measurement Techniques,* 6(12), pp. 3425-3440.

Whalley, L., Furneaux, K., Goddard, A., Lee, J., Mahajan, A., Oetjen, H., Read, K., Kaaden, N., Carpenter, L. and Lewis, A. (2010) 'The chemistry of OH and HO_2 radicals in the boundary layer over the tropical Atlantic Ocean', *Atmospheric Chemistry and Physics,* 10(4), pp. 1555-1576.

Whalley, L. K., Stone, D., Dunmore, R., Hamilton, J., Hopkins, J. R., Lee, J. D., Lewis, A. C., Williams, P., Kleffmann, J. and Laufs, S. (2018) 'Understanding in situ ozone production in the summertime through radical observations and modelling studies during the Clean air for London project (ClearfLo)', *Atmospheric Chemistry and Physics,* 18(4), pp. 2547-2571.

Wragg, F., Fuller, S. J., Freshwater, R., Green, D. C., Kelly, F. J. and Kalberer, M. (2016) 'An automated online instrument to quantify aerosol-bound reactive oxygen species (ROS) for ambient measurement and health-relevant aerosol studies', *Atmospheric Measurement Techniques*, 9(10), pp. 4891 – 4900.

Wu, Z., Zheng, J., Shang, D., Du, Z., Wu, Y., Zeng, L., Wiedensohler, A. and Hu, M. (2016) 'Particle hygroscopicity and its link to chemical composition in the urban atmosphere of Beijing, China, during summertime', *Atmospheric Chemistry and Physics,* 16(2), pp. 1123-1138.

Xie, C., Xu, W., Wang, J., Wang, Q., Liu, D., Tang, G., Chen, P., Du, W., Zhao, J. and Zhang, Y. (2019) 'Vertical characterization of aerosol optical properties and brown carbon in winter in urban Beijing, China', *Atmospheric Chemistry and Physics,* 19(1), pp. 165-179.

Yu, J., Yan, C., Liu, Y., Li, X., Zhou, T. and Zheng, M. (2018) 'Potassium: A Tracer for Biomass Burning in Beijing', *Aerosol Air Qual. Res,* 18, pp. 2447-2459.

Yue, S., Ren, H., Fan, S., Sun, Y., Wang, Z. and Fu, P. (2016) 'Springtime precipitation effects on the abundance of fluorescent biological aerosol particles and HULIS in Beijing', *Scientific reports,* 6, pp. 29618.

Zaveri, R. A., Easter, R. C., Fast, J. D. and Peters, L. K. (2008) 'Model for simulating aerosol interactions and chemistry (MOSAIC)', *Journal of Geophysical Research: Atmospheres,* 113(D13).

Zhang, J., Xu, Z., Yang, G. and Wang, B. (2011) 'Peroxyacetyl nitrate (PAN) and peroxypropionyl nitrate (PPN) in urban and suburban atmospheres of Beijing, China', *Atmospheric Chemistry and Physics Discussions,* 11(3), pp. 8173-8206.

Zhang, L., Wang, T., Zhang, Q., Zheng, J., Xu, Z. and Lv, M. (2016) 'Potential sources of nitrous acid (HONO) and their impacts on ozone: A WRF-Chem study in a polluted subtropical region', *Journal of Geophysical Research: Atmospheres,* 121(7), pp. 3645-3662.

Zhang, W., Tong, S., Ge, M., An, J., Shi, Z., Hou, S., Xia, K., Qu, Y., Zhang, H. and Chu, B. (2019) 'Variations and sources of nitrous acid (HONO) during a severe pollution episode in Beijing in winter 2016', *Science of the Total Environment,* 648, pp. 253-262.

Zhang, Y., Ren, H., Sun, Y., Cao, F., Chang, Y., Liu, S., Lee, X., Agrios, K., Kawamura, K. and Liu, D. (2017) 'High contribution of nonfossil sources to submicrometer organic aerosols in Beijing, China', *Environmental science & technology,* 51(14), pp. 7842-7852.

Zhou, W., Zhao, J., Ouyang, B., Mehra, A., Xu, W., Wang, Y., Bannan, T. J., Worrall, S. D., Priestley, M. and Bacak, A. (2018) 'Production of N_2O_5 and $ClNO_2$ in summer in urban Beijing, China', *Atmospheric Chemistry and Physics,* 18(16), pp. 11581-11597.

Zhou, X., Gao, H., He, Y., Huang, G., Bertman, S. B., Civerolo, K. and Schwab, J. (2003) 'Nitric acid photolysis on surfaces in low-NO_x environments: Significant atmospheric implications', *Geophysical Research Letters,* 30(23).

5. Measurements of OH, HO_2, RO_2 and OH reactivity made in central Beijing during summertime and a comparison with a model incorporating the Master Chemical Mechanism

This chapter describes the measurement of OH, HO_2, RO_2 and OH reactivity and their subsequent comparison with a zero-dimensional box model that incorporates the Master Chemical Mechanism. These measurements were made in central Beijing at the Institute of Atmospheric Physics (IAP) in May and June 2017, as a part of the “Air Pollution and Human Health in Chinese megacities” (APHH). Previous publications of radical measurements made in China and other urban environments have been described in section.1.5.2.

The structure of this chapter is as follows. First, a brief introduction to the APHH campaign, with a focus on the chemical and meteorological conditions encountered and description of various model scenarios used to compare to radical observations. A detailed introduction of the AIRPRO and APHH campaign can be found in Chapter 4. The next section will explore the results from the APHH summer campaign. First a comparison of the measurements with previous Chinese campaigns. Followed by an investigation into potential interference in the OH measurement by comparing OHwave and OHchem. Then a comparison between the measured OH to calculated OH using a photostationary steady-state (PSS) expression. Followed by a comparison of the MCM-base model with the measurement followed by a discussion on the major sources and sinks for radicals during the APHH campaign. Then a discussion on study the impact of HO_2 uptake onto aerosols on the model. The following section will explore the NO-dependence of measured and modelled radical species and use this to comment on where missing chemistry/understanding may be in low NO environments (below 1 ppbv). Then a study on the impact of using modelled HONO to predict OH, followed by an investigation into the missing OH reactivity and investigate the impact of filling the OH reactivity with different species. Finally, the impact of underprediction of peroxy radicals on the models ability to predict ozone production.

5.1 Introduction to the Summer "An Integrated study of AIR Pollution PROcesses in Beijing (AIRPRO)"

The summer project was the second campaign that took place as a part of the APHH programme, this campaign followed the winter project in May and June 2017. Details about the aims of the project can be found in section.4.1. The measurements were taken at the same site (IAP) as the winter campaign with the Leeds group measuring OH, HO_2, RO_2, k(OH), HCHO and photolysis rates. More details about the campaign site and the auxiliary measurements available can be found in the section.4.1 and Table.4.1, and also found in Shi et al. (2018).

The APHH summer campaign official science period was between the 23rd May and 22nd June 2017, with radical measurements taken consistently throughout this period. Gaps in the radical data generally came during rain[2] periods, laser alignment and calibration. OH reactivity, HCHO and spectral radiometry measurements were also made consistently made between 23rd May to 22nd June. Measurements of OHwave and OHchem were made consistently throughout the campaign (see section.2.1.2 for details), although it should be noted on the 13th of June measurements of OHwave were only available as tests for wall losses on the IPI were being conducted (see section.3.2 for more details).

Various meteorological conditions were observed during the summer campaign. Figure 5.1a shows the 30-year wind-rose diagrams between 15th May – 22nd June 1988 – 2017, this climatology shows that during the summertime in Beijing southerly winds are most common. The wind-rose diagram for the time-period of the summer campaign (15th May – 22nd June 2017) is noisier than the 30-year diagram but shows that the southerly wind direction was still the most common. Although in general stronger winds were observed during the campaign compared to the 30-year average.

[2] The FAGE instrument is turned off when it was raining due to the possibility of water reaching the detectors and causing damage.

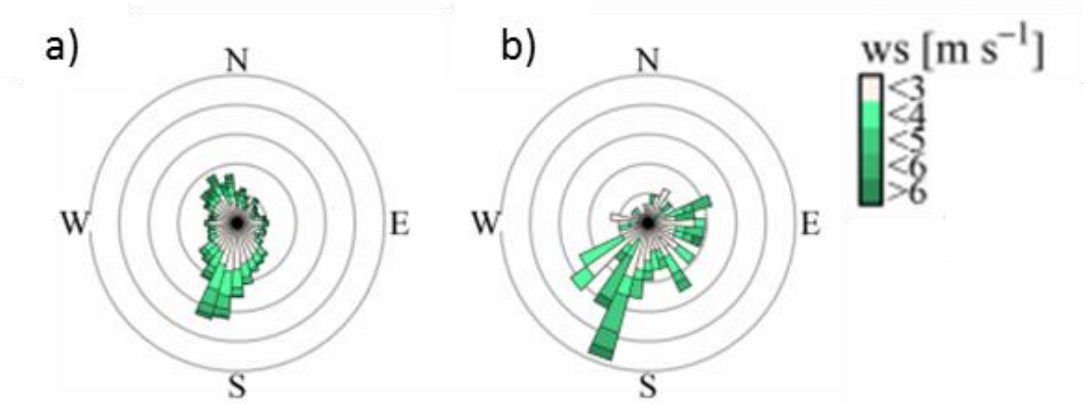

Figure 5.1 Beijing wind-roses from ERA-Interim 10 m horizontal wind (40° N, 116°E) for a) 15 May – 22 June 1988 – 2017 and b) 15 May – 22 June 2017. This diagram modified from Shi et al. (2018).

The variation for $j(O^1D)$, relative humidity (RH), temperature, CO, SO_2, O_3, NO, NO_2 and HONO across the entire campaign is shown in Figure 5.2. In general, the $j(O^1D)$ was quite constant in the summer campaign with values between 2.5 – 3.0 x 10^{-5} s^{-1}; although there were four days (22/05, 29/05, 06/06 and 17/06) when the $j(O^1D)$ was below this value and these low values were generally caused by cloud cover rather than haze. The peak in $j(O^1D)$ (noon) was observed at 12:00. $PM_{2.5}$ pollution is generally not considered a summertime phenomenon in Beijing, however, there were just two haze events observed during the campaign that are summarised in Table 5.1. According to the meteorological standards (QX/T113-2010) (Meteorology, 2010), haze is defined as (i) visibility < 10 km at relative humidity (RH) < 80% or (ii) if RH is between 80 and 95%, visibility < 10 km and PM2.5 > 75 μg m^{-3}. For this work, the periods defined as haze are when $PM_{2.5}$ exceeds 75 μg m^{-3}. In summer, the low $j(O^1D)$ values do not generally coincide with the haze events.

Event	Time (LT)	$PM_{2.5}$ (μg m^{-3})	Visibility (km)
Event 1	27/05 12:00 – 28/05 13:00	107 (62 – 163)	6.8 (4.5 – 9)
Event 2	17/06 09:00 – 18/06 17:00	90.5 (60 – 153.3)	9.3 (7 – 13)

Table 5.1 Table showing the haze periods observed during the summer campaign.

During the summer campaign, the conditions were warm with the noon temperature varying between 28 - 40°C. Figure 5.2 showed that CO and SO_2

tracked each other very well with variations between 200-1700 pbbv and 0.1 – 12 ppbv, respectively. High O_3 concentrations were observed throughout the campaign with values between 0 – 170 ppbv. The NO and NO_2 levels varied between 0.1 – 100 ppbv and 10 – 100 pbbv, respectively. The HONO concentration was high during the campaign with values varying between 1 – 8 ppbv.

The average diurnal variation for $j(O^1D)$, NO, NO_2, O_3, O_x, HONO, SO_2 and CO is shown in Figure 5.3. The dashed lines for the diurnal trends represent the $25^{th}/75^{th}$ percentile – or the general variation in the campaign. The $j(O^1D)$ values show an average peak at 2.9×10^{-5} s^{-1}, the larger variations from the average are observed between 09:00 – 14:00. The diurnal variation for NO is very distinct with a peak at rush-hour (~07:00), the median NO concentration decreases to very low values for a megacity in the afternoon with a median minimum at 18:30 of 0.22 ppbv. The low NO values observed during the afternoon are due to the very high values of O_3 observed during these periods which titrate the NO. O_3 shows a distinct diurnal trend with a median maximum observed at 15:30 of 95 ppbv, and a minimum observed at 06:30 of 17 ppbv. The $25^{th}/75^{th}$ variation of O_3 shows small changes away from the median O_3. CO does not have a distinct diurnal trend with an average of ~470 ppbv, there is a small dip in the median CO concentration in the afternoon to ~400 ppbv. Ox is the sum of NO_2 and O_3, the Ox shows a distinct diurnal profile that is very similar to the O_3 trend. NO_2 shows an anti-correlation with O_3 with a peak at 06:30 (when O_3 at its minimum) of 33 ppbv and a trough at 15:30 (O_3 at its maximum) of 9 ppbv. HONO shows an expected diurnal pattern with a maximum just before sunrise (~05:30) of 3.3 ppbv and a fast decrease after sunrise due to photolysis of HONO forming OH + NO. The minimum HONO concentration is observed during the afternoon period (between 14:00 - 18:00) of ~0.7 ppbv.

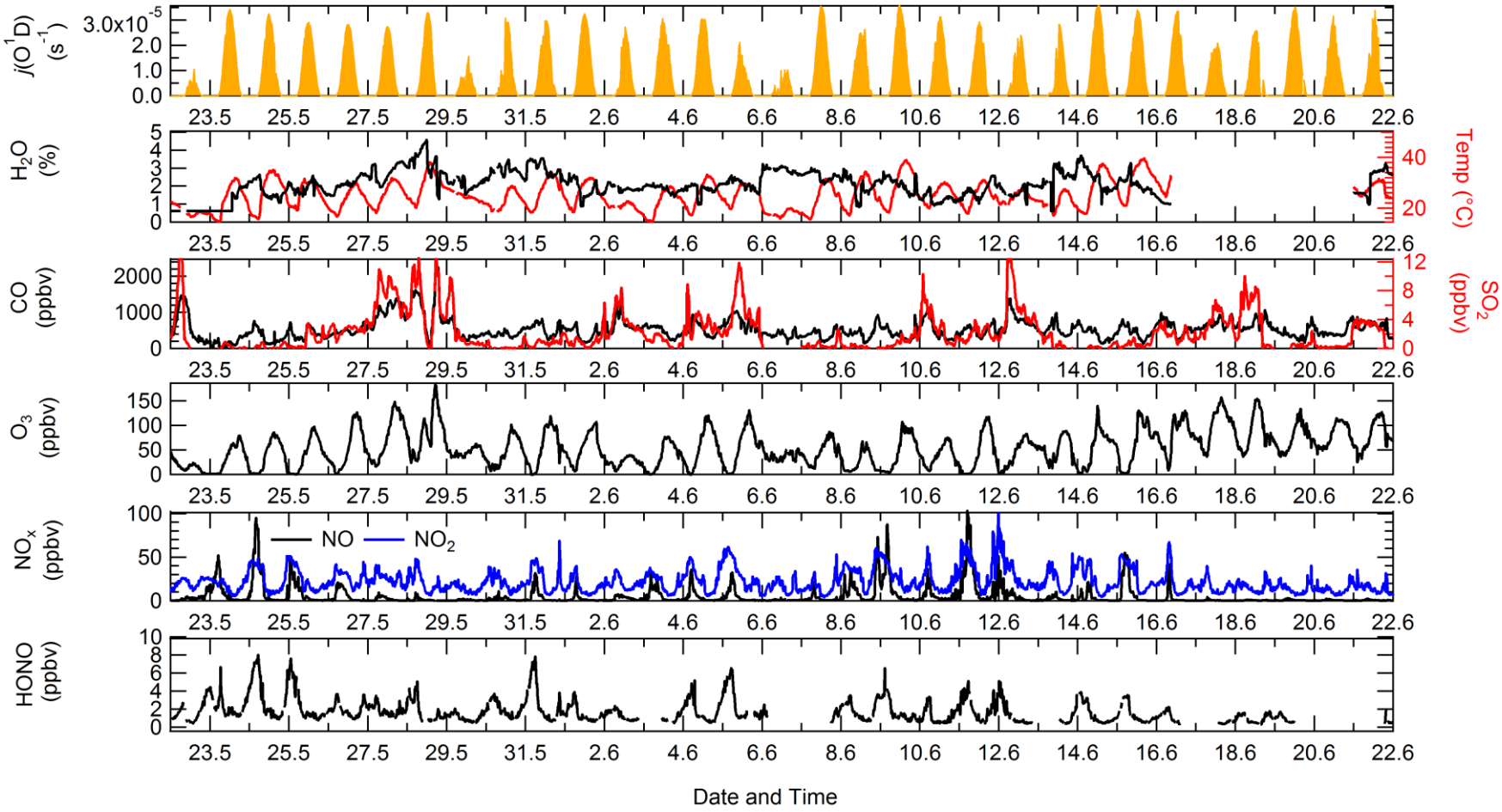

Figure 5.2 Time-series for measurements of j(O^1D), H_2O (%) temperature (Temp), CO, SO_2, O_3, NO, NO_2, HONO and from the 22nd of May to 22nd June at Institute of Atmospheric Physics (IAP).

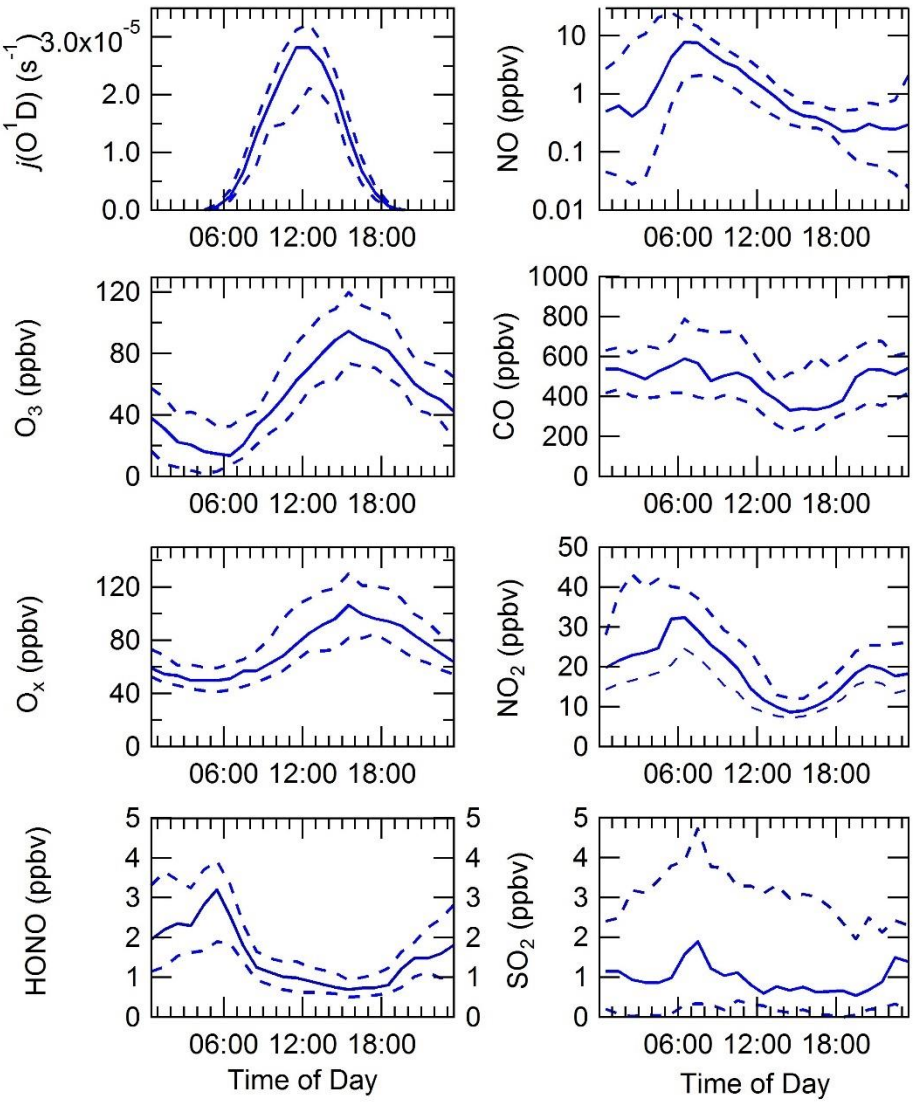

Figure 5.3 Median diurnal profile for measurements $j(O^1D)$ (s^{-1}), NO (ppbv), O_3 (ppbv), CO (ppbv), O_x (ppbv), NO_2 (ppbv), HONO (ppbv) and SO_2 (ppbv) at IAP between 22nd of May to 22nd of June. The dashed lines represent the 25/75th percent confidence interval.

The HONO concentration starts to increase after sunset as HONO is no longer lost through photolysis. Boundary layer effects and heterogeneous sources (i.e NO_2 converting to HONO on humid surfaces) (Lu et al., 2018, Li et al., 2012, Zhang et al., 2016, Lee et al., 2015, Finlayson-Pitts et al., 2003, Zhou et al., 2003) also serve to enhance the HONO concentration. SO_2 shows a small peak at rush hour (~07:00) of 1.88 ppbv and throughout the rest of the day has a constant value ~0.9 ppbv.

5.2 FAGE operating parameters

Throughout the campaign, the Leeds ground-based FAGE instrument was operated with the inlet pre-injector (IPI) which was mounted onto the HO_x fluorescence cell. The period with the IPI is called OHchem (more details in section.2.1.2 and (Woodward-Massey et al., 2020)). On the 13/06/2017 tests to qualitatively determine the losses of the OH radical onto the walls of the IPI was determined and on this day no measurements of OHchem were made. The difference in sampling timings when operating with or without the IPI is described in section.2.1.4. Both the OHwave and OHchem data are presented in section.5.4.3. The OHwave data has been correct for the known interference from O_3/H_2O (see section.3.4 for more details) as the O_3 concentration was very high during this campaign and the average interference correction for the campaign was 6.5 x 10^5 molecule cm^{-3}, whilst the average maximum for the interference correction was 1.02 x 10^6 molecule cm^{-3} at 17:30.

The general running conditions for the Leeds ground-based FAGE instrument was described in Chapter 2, for the work described below the following gases and flows were used. The NO (Messer, 99.0%) flow was added to the HO_x cell (during HO_2 mode) and RO_x cell (continuously) at 5 and 100 sccm, respectively. CO (Messer, 10% in N_2) was added continuously to the RO_x flow tube at 125 sccm. In RO_x mode NO (Messer, 500 ppmv in N_2) was added to the flow tube at 30 sccm. For the determination of the OHchem background 5 sccm of propane (110 ppmv) (diluted in 500 sccm of N_2) was injected into the ambient air; see section.2.1.2 for more detail.

Calibrations for OH, HO_2, HO_2^* (HO_2 in the RO_x cell) and RO_2 were performed at regular intervals throughout the campaign, approximately every 3 days. Figure 5.4 shows the calibration factors for OH, HO_2, HO_2^* and RO_2 taken during the APHH summer campaign, and the value of the calibration that has been applied to the data each day. Figure 5.4 shows that changes in C_{OH} is tracked well by C_{HO2} (determined in the HO_x cell), and C_{HO2*} is tracked well by C_{RO2} (determined in the HO_x cell); which shows that the calibrations differences are caused by changes in each cell. There is a large step-change

in the C_{HO2}^* and C_{RO2} on the 09/06/2017, which was caused by changing the MCP detector on the RO_x cell. Two calibrations for both C_{HO2}^* and C_{RO2} were taken on the 09/06/2019 to account for the change in sensitivity.

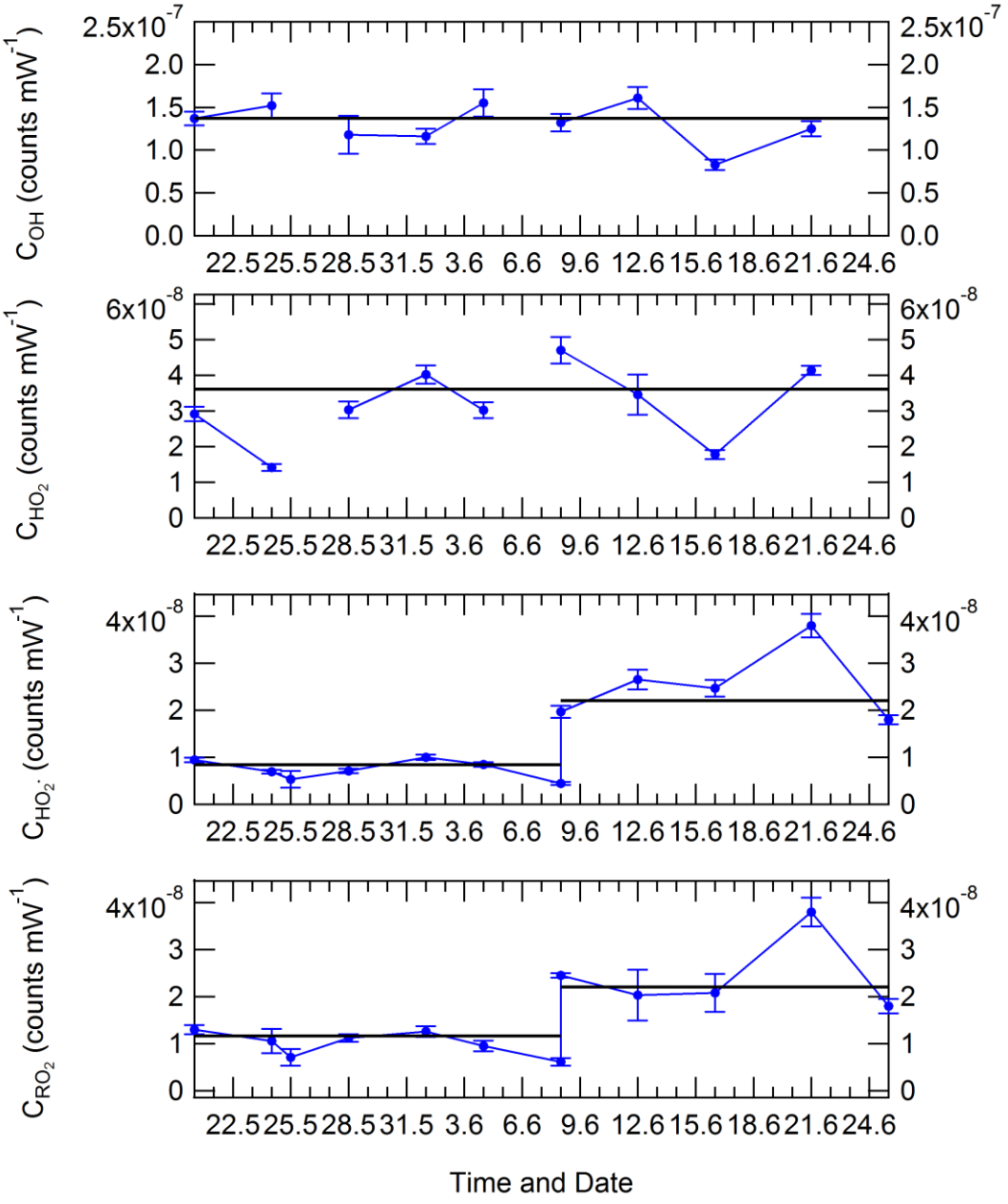

Figure 5.4 The calibration factors (blue circles) determined for OH, HO_2, HO_2^* and RO_2 throughout the APHH summer campaign, and the associated errors. The line (black) through the data shows the calibration factors that have been applied to the data for different days. The error on the individual calibration factor is determined from the slope of a multipoint calibration, the error represents 2σ.

The calibration factors pre- and post-change of the detectors are constant, and this is reflected in the values applied for the two-separate time-periods. The calibration factors for C_{OH} and C_{HO2} shows a fairly constant value across the campaign, and this is reflected in the same calibration factor applied for C_{OH} and C_{HO2} throughout the project. The limits of detection (LOD) varied during the APHH campaign as it is dependent on several factors, one being laser power which fluctuates between performance tune-ups. The campaign-median 5 min averaged LODs of 6.1 x 10^5 molecule cm^{-3}, 2.79 x 10^6 molecule cm^{-3} and 7.24 x 10^6 molecule cm^{-3} were determined for OH, HO_2 and RO_2, respectively. The average laser power during the summer APHH campaign was 11 mW.

5.3 Model Descriptions

5.3.1 Master Chemical Mechanism

In this work, the measured radical concentrations have been compared to model predictions from a zero-dimensional box model that incorporates the Master Chemical Mechanism using several different model scenarios, for this work version 3.3.1 of the MCM was used. The Master Chemical Mechanism (http://mcm.leeds.ac.uk/MCM/home) was coupled to a zero-dimensional box model. The MCM is a near-explicit chemical mechanism representing the degradation of methane and 142 primary emitted VOCs. The mechanism has a total of ~17,000 reactions and ~6700 species. For this work described below the model was run with a sub-set of the MCM, and included 15,333 reactions and ~3,800 species. The complete details of the kinetic and photochemical data used in the mechanism can be found at the MCM website (http://mcm.leeds.ac.uk/MCM/home).

The model was constrained to measurements of NO, NO_2, O_3, CO, HCHO, HNO_3, HONO, water vapour, temperature, pressure and individual VOC species measured by both GC-FID (gas chromatography with flame ionisation) and also PTR-ToF-MS (proton-transfer reaction time of flight mass spectrometry). Table 5.2 shows the different species measured by the GC-FID and PTR-ToF-MS. The photolysis rates for $j(O^1D)$, $j(NO_2)$ and j(HONO),

calculated from the measured actinic flux and published absorption cross-sections and quantum yields, were included as model inputs. Other photolysis frequencies used in the model were calculated. For UV-active species, such as HCHO and CH_3CHO, photolysis rates were calculated by scaling to the ratio of clear-sky $j(O^1D)$ to observed $j(O^1D)$ to account for clouds. For species able to photolyse further into the visible the ratio of clear-sky $j(NO_2)$ to observed $j(NO_2)$ was used. The variation of the clear-sky photolysis rates (j) with solar zenith angle (χ) was calculated within the model using the following expression:

$$j = l\ cos(x)^m * e^{-nsec(x)} \quad \text{E5.1}$$

with the parameters l, m and n optimised for each photolysis frequency (see Table.2 in Saunders et al. (2003)).

A constant H_2 concentration off 500 ppbv was assumed (Forster et al., 2012). The model was run for the entirety of the campaign period (21st May 2017 – 25th June 2017).

Instrument	Species	Reference
DC-GC_FID	CH_4, C_2H_6, C_2H_4, C_3H_8, C_3H_6, isobutane, butane, C_2H_2, trans-but-2-ene, but-1ene, Isobutene, cis-but-2-ene, 2-Methylbutane, pentane, 1,3-butadiene, trans-2-pentene, cis-2-pentene, 2-methylpetane, 3-methypetane, hexane, isoprene, heptane, Benzene, Toluene, o-xylene, CH_3OH, CH_3OCH_3, ethylbenzene, CH_3CHO, C_2H_5OH	Hopkins et al. (2011)
PTR-ToF-MS	α-pinene, limonene, isopropylbenzene, propylbenzene, xylene, trimethylbenzene.	Huang et al. (2016)

Table 5.2 Table showing the species measured by the DC-GC-FID and PTR-ToF-MS that have been constrained in the master chemical mechanism.

The model inputs were updated every 15 minutes, the species that were measured more frequently were averaged to 15 minutes whilst the measurements with lower time resolution were interpolated. The loss of all non-constrained, model generated, species by deposition or mixing was

parameterised and evaluated by comparing the model-predicted glyoxal concentration with the observed glyoxal concentration (see section.5.4.4.1 for more details). Glyoxal was used as it is a model generated intermediate that was measured during the campaign. The model was run for the entirety of the campaign in overlapping 7-day segments. To allow all the unmeasured model generated intermediate species time to reach steady-state concentrations, the model was initialised with inputs from the first measurement day (19th May) and spun-up for 2 days before comparison to the radical measurements were made.

Below are the different model scenarios that have been used in this work:

1. **MCM-base**: The base model was run using the parameters described above, see section.5.4.4.1 for how the deposition of oxidised intermediates was constrained.
2. **MCM-cHO$_2$**: This model scenario was the same as MCM-base but the model has been constrained to the measurements of HO_2.
3. **MCM-SA**: This model scenario was the same as MCM-base but includes HO_2 uptake using a coefficient of 0.2. The total aerosol surface area was calculated from an SMPS (scanning mobility particle sizer) and PSM (particle size magnifier) (Wu et al., 2016). The average surface area during the campaign was 4.3 x 10^6 cm^2 cm^{-3}.
4. **MCM-X**: This model scenario was the same as MCM-base but includes the reaction of HO_2 + X. The concentration of X varied with the concentration of NO, see section.5.4.6.2 for details.
5. **MCM-Cl**: This model scenario was the same as MCM-base but includes Chlorine (Cl) chemistry, the Cl chemistry inputted into the MCM is from Xue et al. (2015). The model was constrained to measurements of $ClNO_2$ that was measured by CIMS-ToF-MS.
6. **MCM-P'RO$_2$**: This model is the same as MCM-base but includes an extra primary source of RO_2 species. The additional primary source has been calculated using:

$$P'(RO_x) = k_{HO2+NO}\,[HO_2][NO_2] - P(HO_2)_{prim} - P(RO_2)_{prim} - k_{VOC}[OH] + L(HO_2)_{term} + L(RO_2)_{term} \quad \text{E5.2}$$

In E5.2 $P(HO_2)_{prim}$, $P(RO_2)_{prim}$, $L(HO_2)_{term}$ and $L(RO_2)_{term}$ are the rate of primary production of HO_2, rate of primary production of RO_2, termination rate of HO_2 and termination rate of RO_2, respectively. The calculated additional RO_2 source was included in the model (model run MCM-PRO2) as a single species 'A-I' that formed several RO_2 species at the required RO_2 production rate (i.e. k*[A-I] = missing primary production rate). The RO_2 species produced were $HOCH_2CH_2O_2$, HYPROPO2, TM135BPRO2, STYRENO2, IBUTOLBO2, TM123BPRO2, BUTDBO2, OXYBIPERO2 and CH3O2 and the structures of these RO_2 species are shown in Table 5.3. The RO_2 species were chosen after a ROPA analysis showed they were highest produced RO_2 species in the model. See http://mcm.leeds.ac.uk/MCMv3.3.1/home.htt for more details.

7. **MCM_kRO2NO-2**: This model scenario is the same as MCM-base, but the kRO2NO (rate of reaction for RO_2 + NO) and kAPNO (rate of reaction for acyl RO_2 species + NO) rate constants have been decreased by a factor of 2 from changing KRO2NO from 2.7E-12*EXP(360/Temp) to 1.35E-12*EXP(360/Temp) and KAPNO from 7.5E-12*EXP(290/Temp) to 3.75E-12*EXP(290/Temp).
8. **MCM_kRO2NO-10**: This model scenario is the same as MCM-base, but the KRO2NO and KAPNO has been decreased by a factor of 10 from changing KRO2NO from 2.7E-12*EXP(360/Temp) to 2.7E-13*EXP(360/Temp) and KAPNO from 7.5E-12*EXP(290/Temp) to 7.55E-13*EXP(290/Temp).
9. **MCM-uHONO**: This model scenario is the same as MCM-base but the model has been unconstrained to measured HONO.
10. **MCM-cHO$_2$-uHONO**: This model scenario is the same as MCM-cHO2 but the model has been unconstrained to HONO.

MCM Name	Structure	MCM Name	Structure
HOCH2CH2O2	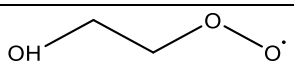	TM123BPRO2	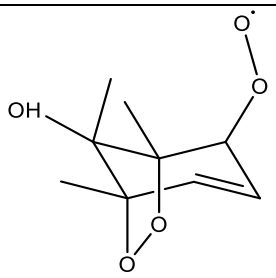
HYPROPO2	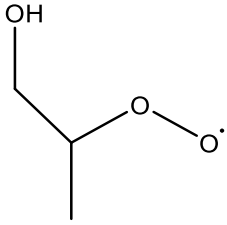	BUTDBO2	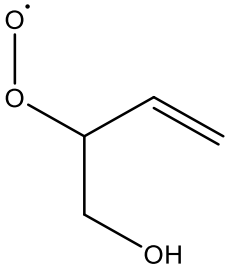
TM135BPRO2	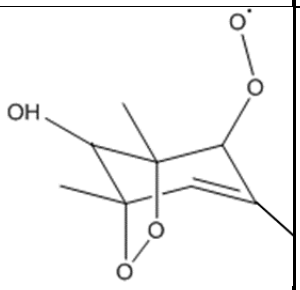	OXYBIPERO2	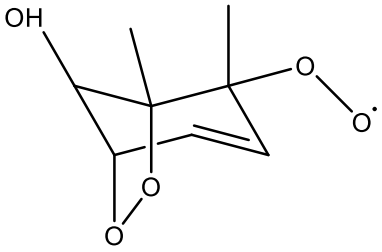
STYRENO2	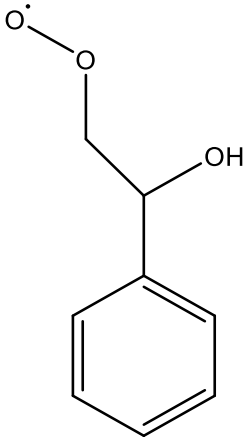	CH3O2	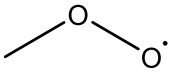
IBUTOLBO2	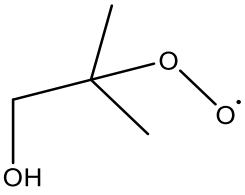		

Table 5.3 The names and associated structures of the RO_2 species used to add additional primary production of RO_2 species into model scenarios MCM-PRO2 and MCM-PRO2-SA.

11. **MCM-kOH-CH3O2**: During the campaign, the comparison between measured and modelled OH reactivity showed there was a missing reactivity. The missing reactivity was ~9.5 s^{-1} on average throughout the whole day (see section.5.4.4.3 for details). The model scenario is the same as MCM-base but the OH reactivity gap has been filled by species 'A' that reacts with OH to form CH_3O_2.
12. **MCM-kOH-CH3CO3**: The model is the same as MCM-base but the OH reactivity gap has been filled by species 'A' that reacts with OH to form CH_3CO_3.
13. **MCM-kOH-C6H5O2**: The model is the same as MCM-base but the OH reactivity gap has been filled by species 'A' that reacts with OH to form $C_6H_5O_2$.
14. **MCM-kOH-CH3O2-k**: The model scenario is the same as MCM-kOH-CH3O2 but the kRO2NO and kAPNO has been decreased by a factor of 10 by changing kRO2NO from 2.7E-12*EXP(360/Temp) to 2.7E-13*EXP(360/Temp) and kAPNO from 7.5E-12*EXP(290/Temp) to 7.55E-13*EXP(290/Temp).
15. **MCM-kOH-CH3CO3-k**: The model scenario is the same as MCM-kOH-CH3CO3 but the kRO2NO and kAPNO has been decreased by a factor of 10 by changing kRO2NO from 2.7E-12*EXP(360/Temp) to 2.7E-13*EXP(360/Temp) and kAPNO from 7.5E-12*EXP(290/Temp) to 7.55E-13*EXP(290/Temp).
16. **MCM-kOH-C6H5O2-k**: The model scenario is the same as MCM-kOH-C6H5O2 but the kRO2NO and kAPNO has been decreased by a factor of 10 by changing kRO2NO from 2.7E-12*EXP(360/Temp) to 2.7E-13*EXP(360/Temp) and kAPNO from 7.5E-12*EXP(290/Temp) to 7.55E-13*EXP(290/Temp).

5.4 Results

5.4.1 Time-series

Figure 5.5 shows the time-series for OH (wave and chem), HO_2, RO_2 and OH reactivity measurements from the 23rd May to 22nd June 2017. The radical

observations follow the expected diurnal profile with a maximum at midday and lower concentrations observed at night-time. It should be noted that all night-time measurements for OH, HO_2 and RO_2 were above the limit of detection. The average limit of detections for the summer APHH campaign was 6.9 x 10^5, 3.6 x 10^6 and 5 x 10^6 molecule cm^{-3} for OH, HO_2 and RO_2 respectively. The daily maximum of the radical species varied day-to-day by 0.6 – 1.7 x 10^7 cm^{-3}, 0.5 – 7.98 x 10^8 cm^{-3} and 0.7 – 3.8 x 10^9 cm^{-3} for OH, HO_2 and RO_2 respectively. The measured simple and complex RO_2 species (see section.2.1.8 for details) also tracked one another very well. The *k*(OH) had a day-to-day variation between 20 to 85 s^{-1}. The average diurnal trends for OH, HO_2, RO_2 (speciated into simple and complex) and *j*(HONO) is shown in Figure 5.6. OH peaks at 11:30 and follows the trend of *j*(HONO) very well, OH starts to increase at 04:30 which coincides with the increase *j*(HONO). OH peaks at 9.7 x 10^6 molecule cm^{-3} at 11:30. The OH concentration is still ~8 x 10^5 molecule cm^{-3} between 19:30 – 22:00 which is above the average LOD for the OH (8.6 x 10^5 molecule cm^{-3}). The OH values between 22:00 - 04:00 on average is ~3 x10^5 molecule cm^{-3} which is below the average LOD for the campaign. Both HO_2 and RO_2 peak later than *j*(HONO) at 14:30, the average peak value for HO_2 and total RO_2 was 2.3 x 10^8 and 1.15 x 10^9 molecule cm^{-3}, respectively. All the values for HO_2 and RO_2 at night-time are higher than the LOD, the total RO_2 75^{th} percentile shows a secondary peak in the values at ~20:30.

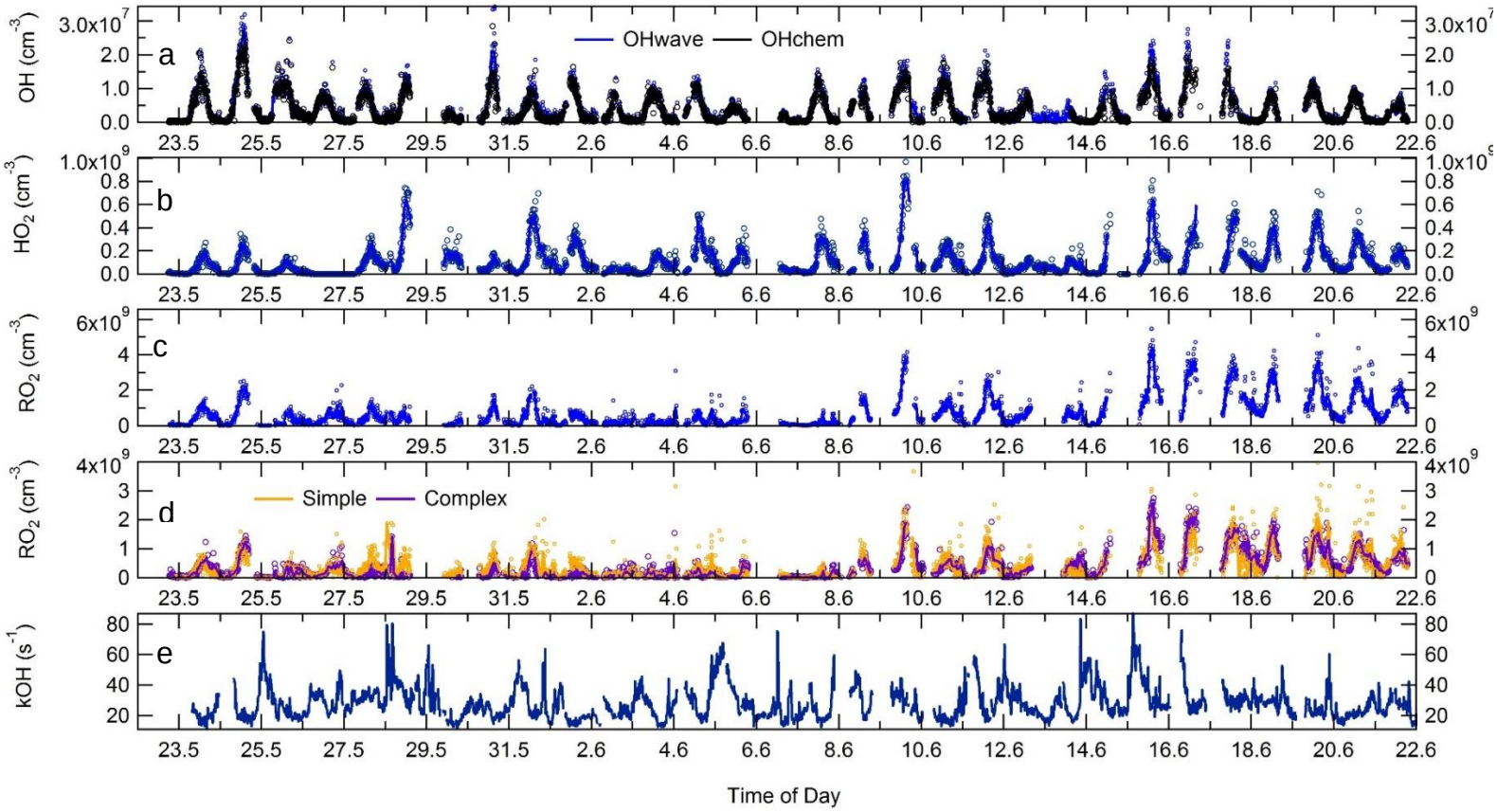

Figure 5.5 a) Time-series for OHwave (blue) and OHchem(black). b) Time-series for HO_2. c) Time-series for total RO_2. d) Time-series for speciated RO_2 separated into simple (gold) and complex (purple). e) Time-series for *k*(OH). For a-d graphs, the circles represent the raw data (7-min average), and the thick line represents the 15-minute average.

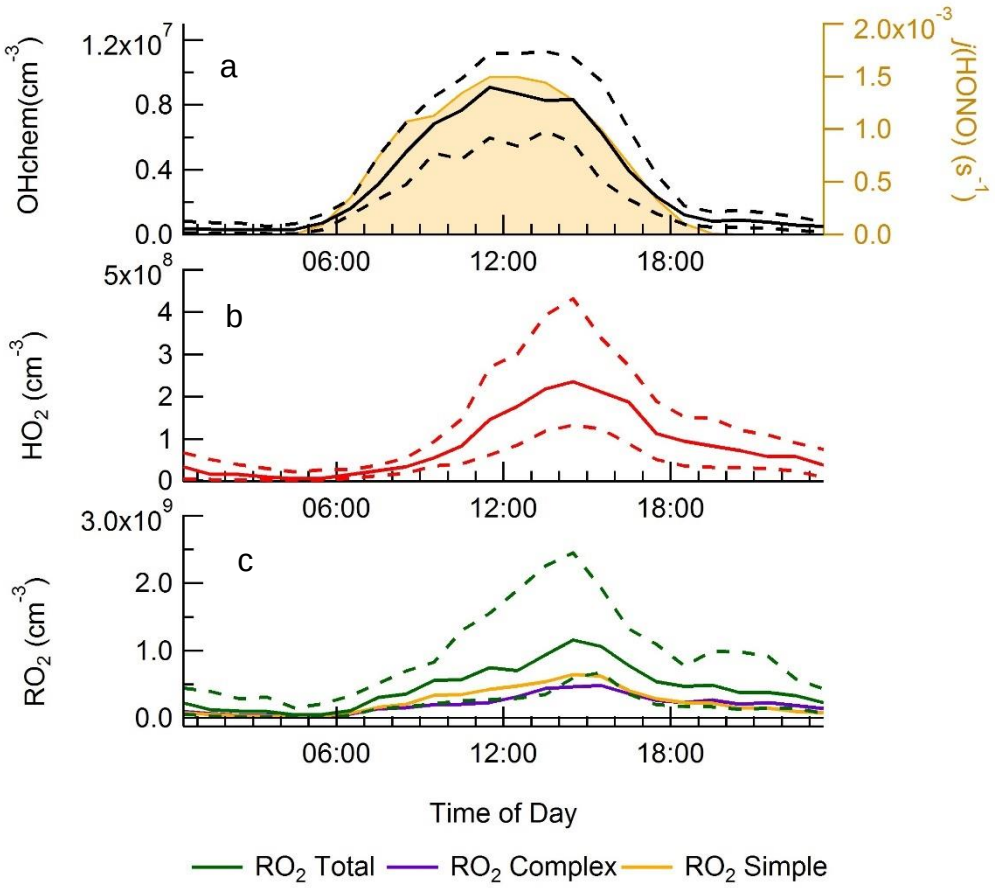

Figure 5.6 a) Average diurnal of OHchem and *j*(HONO) b) Average diurnal for HO_2 c) Average diurnal for total RO_2 (green) and speciation into simple (yellow) and complex (purple). The dashed lines represent the 25/75th percentile.

5.4.2 Investigation of possible OH interference by chemical modulation experiments

As discussed in both section.1.4.2.2, some FAGE instruments may be susceptible to interference (Mao et al., 2012, Fuchs et al., 2016) from internally generated OH, and to explore whether the Leeds ground-based FAGE instrument is susceptible to interference in Beijing during the summer both the OHwave and OHchem background method was used for the whole of the campaign period. The OHchem data has been corrected for the quantified and understood O_3/H_2O interference, see section.3.4.

The correlation of 15 minute average OHwave vs OHchem data is shown in Figure 5.7c and shows a tight correlation scattered around the 1:1 agreement line. The correlation plot has been fitted with an ODR fitting, to take into

account the error in both the *x*- and *y*-axis, and yields a slope of 1.10 ± 0.02. Since the slope is higher than 1 an observable interference was detected during the APHH summer campaign. The ODR (orthogonal distance regression) fit and 1:1 fit is shown in Figure 5.7c, and shows the correlation deviates at higher OH concentrations (above ~1 x 10^7 molecule cm^{-3}). The deviation away from the 1:1 fit at OH concentrations ~1 x 10^7 molecule cm^{-3} is also seen in the 15-minute average data.

Figure 5.7b shows the hourly-averaged diurnal for OHwave and OHchem for the campaign and shows a good agreement between 17:00 – 10:00. Between 10:00 to 17:00 the diurnals of OHwave and OHchem deviate from one another with a maximum average difference at 15:00 of 1.8 x 10^6 molecule cm^{-3}, although on average the difference is less than ~26% error on the OH measurements. Figure 5.7a shows the difference of OHwave minus OHchem binned against the concentration of OHwave, and shows that at higher OH concentrations the difference between the two measurements increase. The highest interference was 8.8 x 10^6 molecule cm^{-3} when the OHwave concentration is 3 x 10^7 molecule cm^{-3}. Figure 5.7b shows the plot of OHwave – OHchem and shows similar results to the average diurnal, that as the observed OH concentration increases a larger difference between OHwave and OHchem is observed, hence a larger observable interference. Figure 5.7a shows OHwave – OHchem binned against OHwave and that the interference is statistically significant above 3 x 10^7 molecule cm^{-3}, as the average error of OHwave is lower than the average difference of the two background methods. As shown in Figure 5.5 the interference was observed on certain days, with significant interference observed on 24/05, 29/05, 16/06 and 17/06.

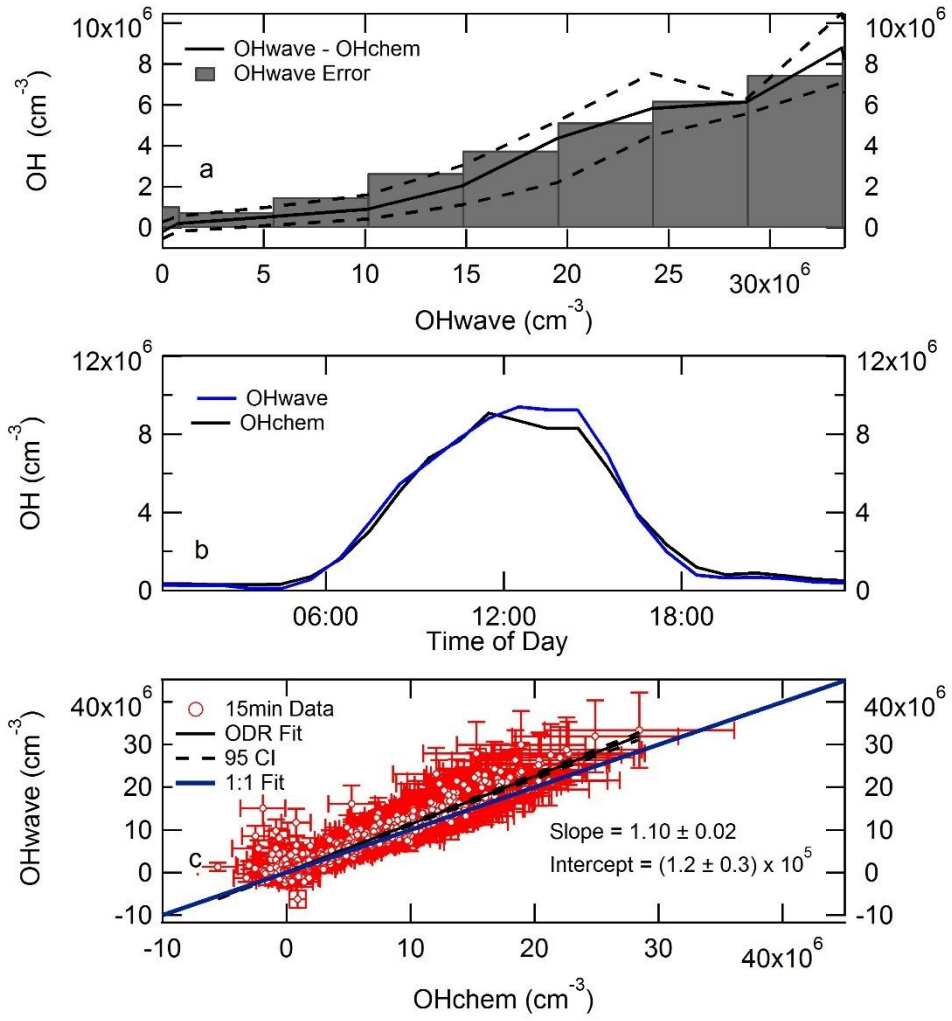

Figure 5.7 a) The difference between OHwave and OHchem binned against OHwave concentrations (black line, median with 25th/75th percentile). The grey bar charts represent the median 2σ error in the OHwave values for the different bins of OHwave. b) Average median diurnal of OHwave (blue) and OHchem (black). c) Correlation graph of the 15-min average data OHwave vs OHchem (white dots) with 2σ error, the black line represents an ODR fit for the data with the dashed black lines showing the 95% confidence interval. The blue line represents a 1:1 fit of OHwave vs OHchem.

To investigate possible interferences, the difference between OHwave – OHchem, from now on called OHint, was correlated with the measured VOCs (see Table 5.2 for details), OH, HO_2, RO_2, O_3, NO, NO_2, CO, HONO, temperature, photolysis rates and missing reactivity. The Pearson's correlation coefficient (r) is shown in Figure 5.8, the coefficient shown as a heatmap. Figure 5.8 shows that the strongest correlation with OH_{int} is from the variables temperature (r = 0.35), ozone (r = 0.20), OH (r = 0.40), RO_2 (r = 31),

HO_2 (0.27) and photolysis rates (0.30). Isoprene also shows a significant correlation (r = 0.21) and previous work has shown biogenic VOCs are a source of interference in forested environments (Mao et al., 2012). Also, previous laboratory experiment has been shown to produce interferences from isoprene and ozone (Fuchs et al., 2016).

To see whether the highest correlated species may correlate better with co-factors (factors that when combined may increase the correlation), the products (multiplication of the co-factors) of the best correlated species have been taken and are shown in Figure 5.9. Figure 5.9 also includes the correlation coefficient for the original variable for a comparison. From the original variables, it can be seen that a product improves the correlation when OH is multiplied by any other factor. The highest correlation coefficients come from the OH*O_3 (0.48) and OH*RO_2 species (0.47). The product of OH*RO_2 improved the correlation coefficient from 0.32 to 0.47; whilst the product of O_3*OH improves the correlation coefficient by 20 to 48. The heatmap in Figure 5.10 is to see if the correlation of the RO_2 species could be improved by taking the product with several variables (OH, temperature(T), *j*(HONO) (J)). Figure 5.10 shows that none of the correlation products increase the correlation coefficient. These results suggest that the OH interference may be from complex RO_2 species, previous work from Fittschen et al. (2019) has suggested that the reaction of RO_2 + OH may form ROOOH which can breakdown in the FAGE cell to form OH.

Even though the best correlations are from RO_2, O_3, OH, isoprene, temperature and photolysis rates, it should be noted that other than the photolysis rates all of these species peak in the afternoon which is when maximum OH_{int} is observed. The correlation of OH_{int} with RO_2, O_3 and temperature may be a spurious correlation from a third confounding factor (Aldrich, 1995). This third confounding factor may be from a species/process that has a similar diurnal pattern to the species that are correlating (i.e. peaking in the afternoon).

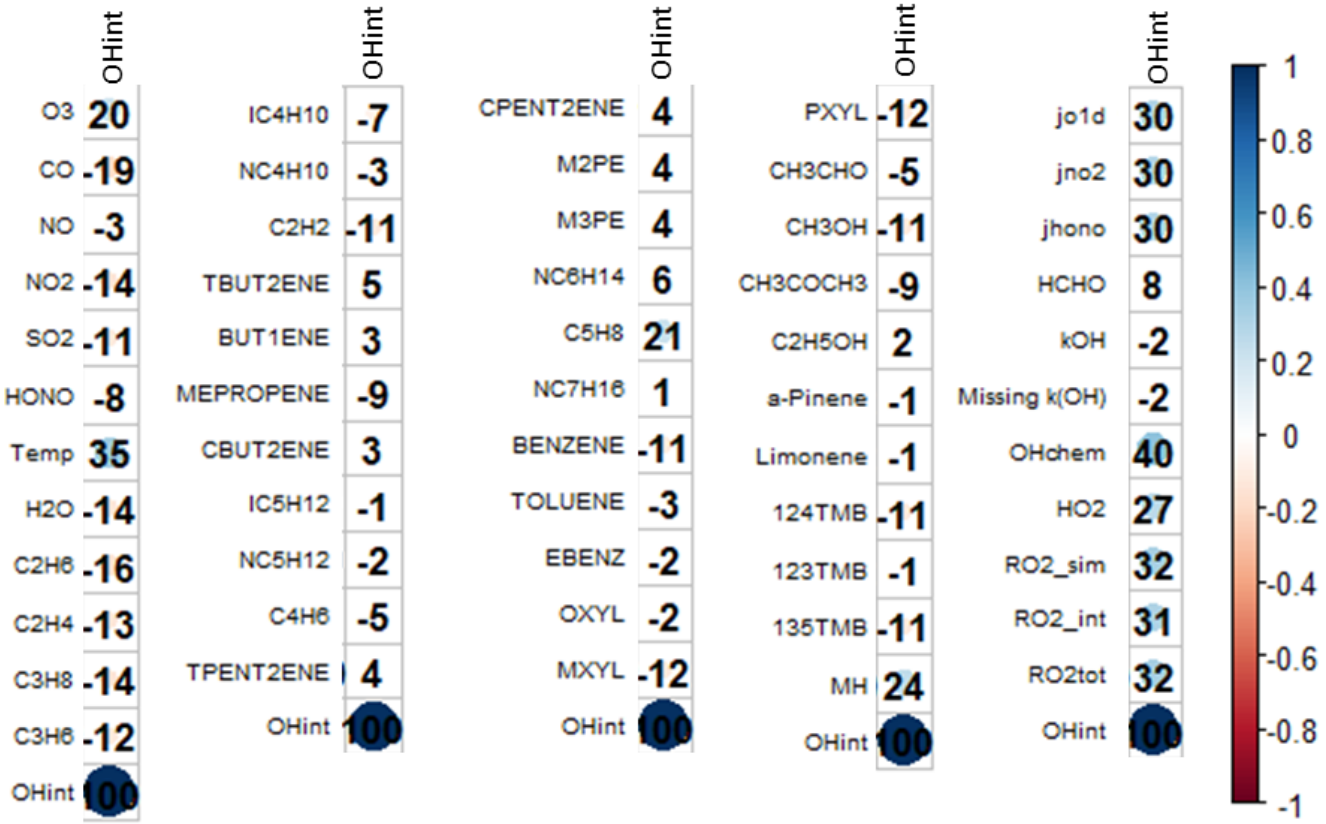

Figure 5.8 Heatmap showing the Pearson's correlation coefficient (r) of OHint correlated with measured VOCs, trace gas species, photolysis rates, radical species (OH, HO_2, RO_2) and missing reactivity. The size of the circle represents the magnitude of the correlation coefficient and the number is Pearson's r coefficient multiplied by 100.

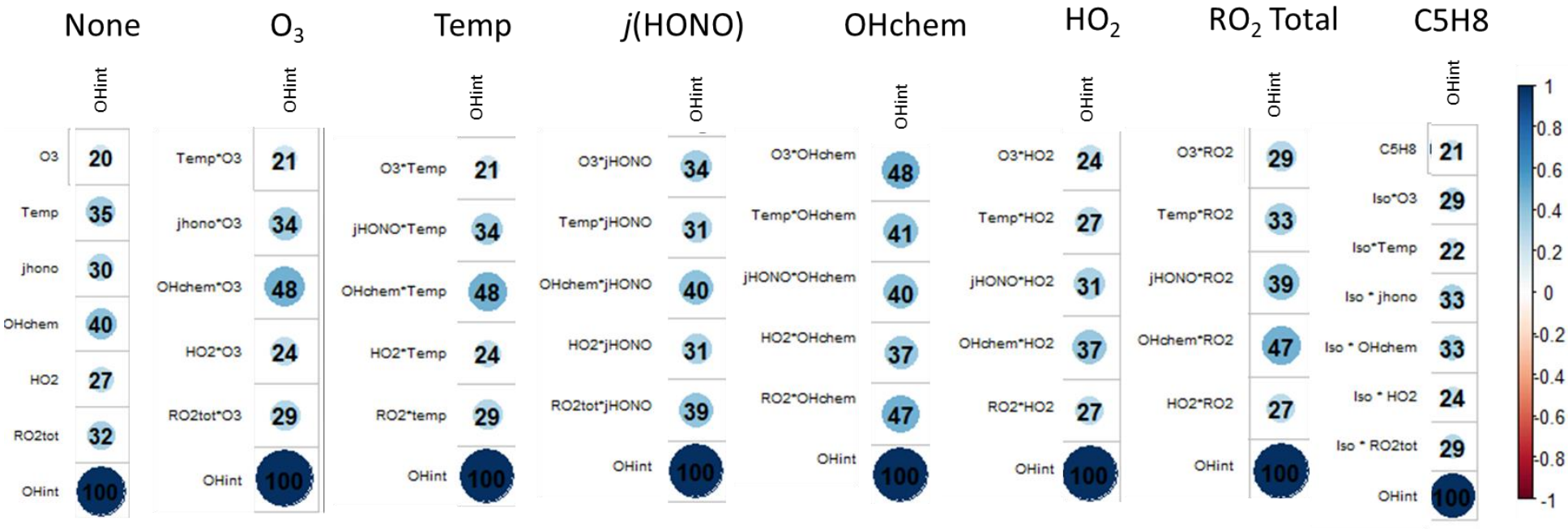

Figure 5.9 Heatmap of the Pearson's correlation coefficient (r) of OHint correlated with OH, RO_2 (simple, interfering and total), isoprene, *j*(HONO), HO_2, temperature and O_3 which is represented by the heading "none". The following headings represent what temperature, O_3, *j*(HONO), OH, HO_2 and RO_2 (simple, interfering and total) was multiplied by for each correlation matrix. The RO_2 values used for taking the product was total RO_2. The size of the circle represents the magnitude of the correlation coefficient and the number is Pearson's r coefficient multiplied by 100.

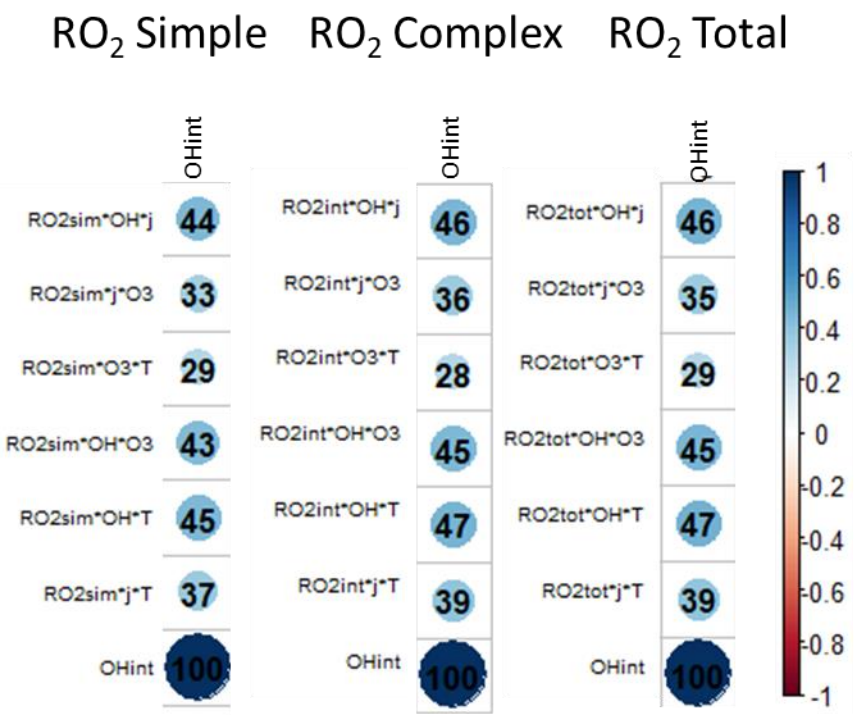

Figure 5.10 Heatmap of the Pearson's correlation coefficient (r) for simple RO_2, complex RO_2 and total RO_2 multiplied by several different combination of OH, temperature (T), *j*(HONO) (J) and O_3. The size of the circle represents the magnitude of the correlation coefficient and the number is Pearson's r coefficient multiplied by 100.

5.4.3 Photostationary Steady State calculation of OH

A PSS calculation was performed using O_3, H_2O, HONO, HO_2, NO, *k*(OH) and several VOCs mixing ratios, the latter for the production of OH from ozonolysis including: C_2H_4, C_3H_6, C_4H_6, isoprene, α-pinene, limonene, 1,2-dimethylethylene, but-1-ene, isobutene,cis-but-2-ene, cis-2-pentene, trans-2-pentene. Measured photolysis rates for both *j*(O^1D) and *j*(HONO). See section.4.3.2 for more details on the steady-state calculation. Figure 5.11 shows the time-series and average diurnal for the comparison of measured OHchem with OH calculated from a PSS between 23/05/2017 to 16/06/2017 (full data coverage – HONO, NO, *j*, radical, *k*(OH) and VOCs measurements available on these days). On average the PSS calculation underpredicts the OH by a factor of 2.1, and shows that the experimental budget is not closed.

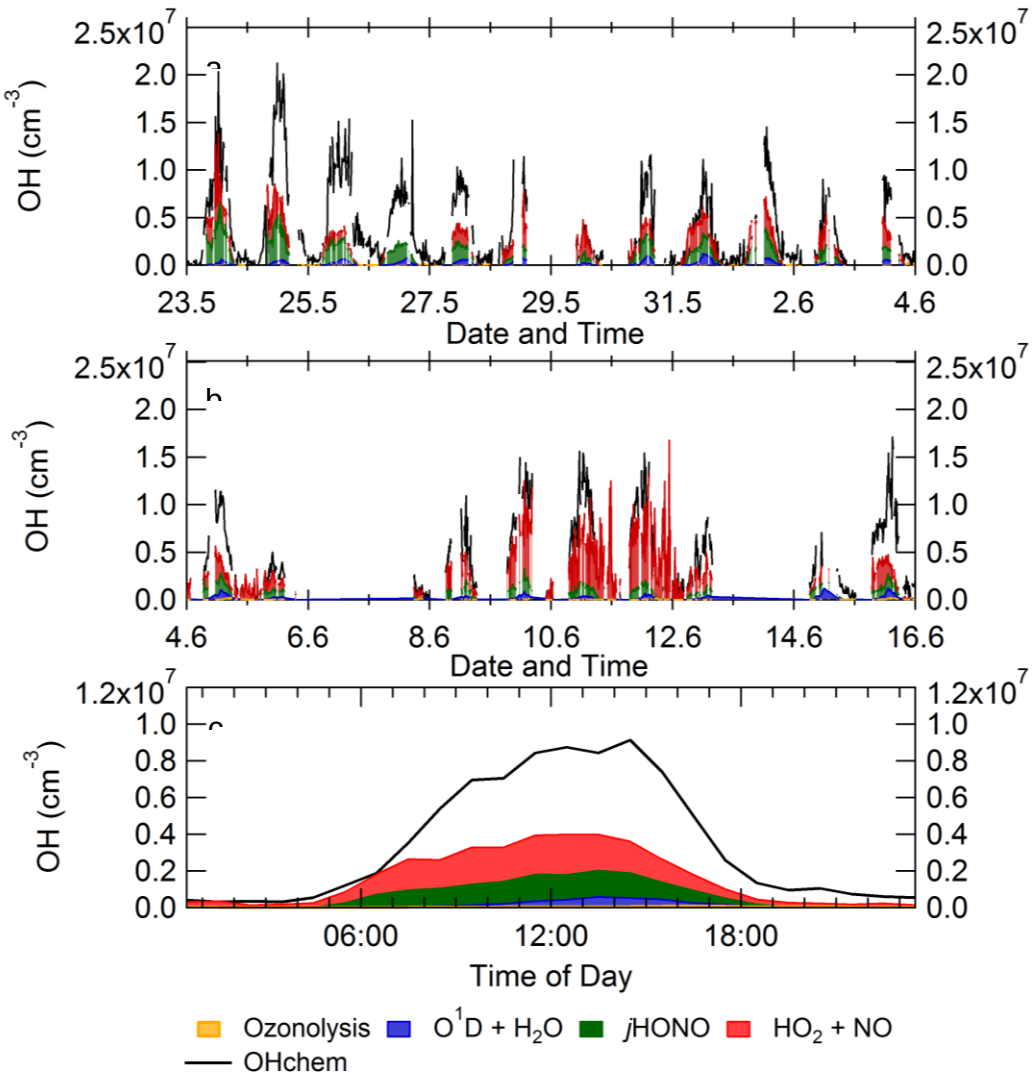

Figure 5.11 a) Time series for the steady-state calculation of OH, and a comparison with measured OHchem (black) between 23/05/2017 – 04/06/2017. B) Time series for the steady-state calculation of OH, and a comparison with measured OHchem (black) between 05/06/2017 – 16/06/2017 c) Average diurnal for steady-state calculation of OH, and a comparison with measured OHchem(black).

The average diurnal comparison between the steady-state and the OHchem measurements at midday shows that: HO_2 + NO contributes 22.3%; photolysis of HONO contributes 20%, production from O^1D + H_2O contributes 4.6% and finally, ozonolysis contributes <1% to OH production. The different production sources of OH varied day-to-day for: O^1D + H_2O by 5 – 28%; photolysis of HONO by 4.8 – 29% and HO_2 + NO by 7 – 31%. The steady-state calculation

shows there is a large missing source of OH radicals that are not measured, with the ratio of measured: calculated (PSS) is ~2.1.

5.4.4 MCM base model

5.4.4.1 Deposition Constraints for Oxidise Intermediates

The MCM includes reactions that generate oxidised intermediates that without a deposition term would build-up in the model to unrealistic levels. Unfortunately, the deposition for these oxidised intermediates are not well known and must be estimated in the model. In the case for the winter model, the deposition could be determined by matching measured and modelled OH reactivity (see section.4.4.5.2 for more details) as there was very little missing reactivity, and suggests the model intermediates do not build-up in winter. In the case for the summer model, there is on average ~ 9.5 s^{-1} missing reactivity throughout the entire day (see section.5.4.4.3 for more details) when oxidised intermediates are not considered. During the summer APHH, there were measurements of glyoxal (see Table.4.1 for instrument details), which is an oxidised intermediate, so the deposition of oxidised intermediates was constrained by reproducing the measured glyoxal in the model. The time-series and average diurnal comparison between measured and MCM-base glyoxal is shown in Figure 5.12, the comparison is only made between 02/06/2017 to 25/06/2017 due to availability of glyoxal data. As shown in Figure 5.12 the model was able to reproduce the observations of glyoxal reasonably well when a loss rate that increases with the measured boundary layer depth, was applied. As a result of this first-order loss process, the partial lifetime of the model generated species was ~2 hrs overnight, then decreased rapidly to a lifetime of <30 min in the morning as the boundary layer increased and mixed with air from aloft, effectively ventilating the model box. With the collapse of the boundary layer in the late afternoon, the model lifetime with respect to ventilation of glyoxal (and other model generated species) increased. However, the model tends to under-estimate glyoxal concentrations between 4 pm and midnight. This under-estimation suggests that either the lifetime with respect to ventilation should be even longer, or that

the model is underestimating oxidation processes that lead to glyoxal production at these times.

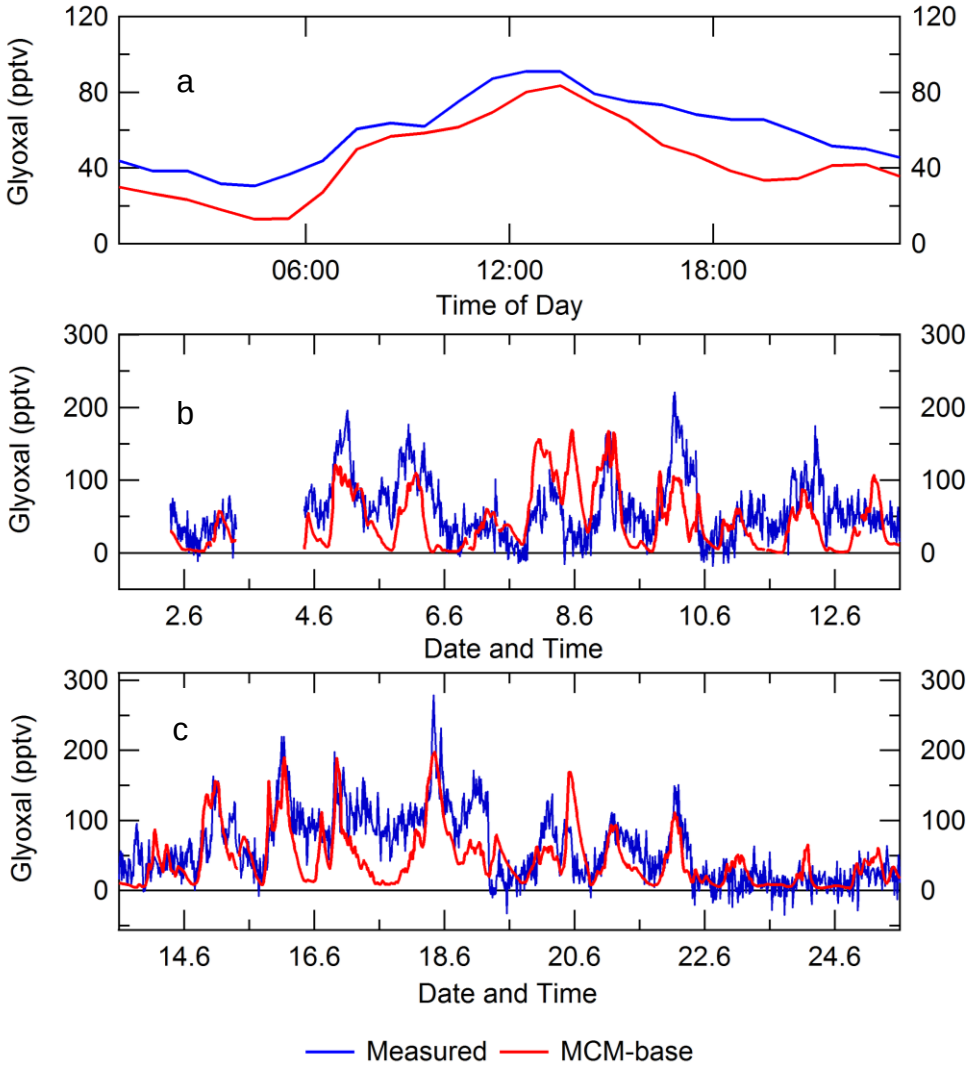

Figure 5.12. a) Average diurnal comparison of measured glyoxal and modelled glyoxal from MCM-base. b) Time-series comparison of measured glyoxal and modelled from MCM-base between 02/06/2017 – 13/06/2017 c) Time-series comparison of measured glyoxal and modelled from MCM-base between 13/06/2017 – 25/06/2017. For all graphs measured is shown in blue and modelled is shown in red. The glyoxal was measured by a cavity ring-down instrument (see Table.4.1 for details).

5.4.4.2 Model Results

Figure 5.13 shows the time-series of OH(chem only), HO_2, total RO_2, RO_2 (speciated into simple and complex) and OH reactivity (k(OH)) compared with the results from the MCM-base (described in Section.5.1.3). Figure 5.13

shows that in general the MCM-can predicted OH very well with an underprediction observed on 10/06 and 11/06, but overestimates HO_2 and underestimates RO_2. On several days (29/05, 08/06 and 12/06) the measured HO_2 values can be replicated by the MCM-base model, although these days still accompany underprediction of the total RO_2 radical concentration. The model underpredicts the measured *k*(OH) throughout the entire campaign.

An average diurnal comparison between modelled results and measured results for the entire campaign can be seen in Figure 5.14. The average diurnal shows that the model can replicate the trend of OH, HO_2 and RO_2 very well, the modelled peaks for OH, HO_2 and RO_2 coincide with the measurement peak at ~12:30, ~14:30 and ~14:30 respectively. The model can replicate the OH concentration within ~26% error, although on average there is a slightly underprediction between 08:00 – 11:00 coinciding with elevated NO concentration (see section.5.1). The OH concentration at night-time is underpredicted by a factor ~3. The HO_2 concentration at its peak (14:30) is overpredicted by a factor of ~2.3 by the model, the night-time concentration of HO_2 is predicted well by the model although the 75^{th} percentile for the model shows a higher night-time peak is observed in the model for some days.

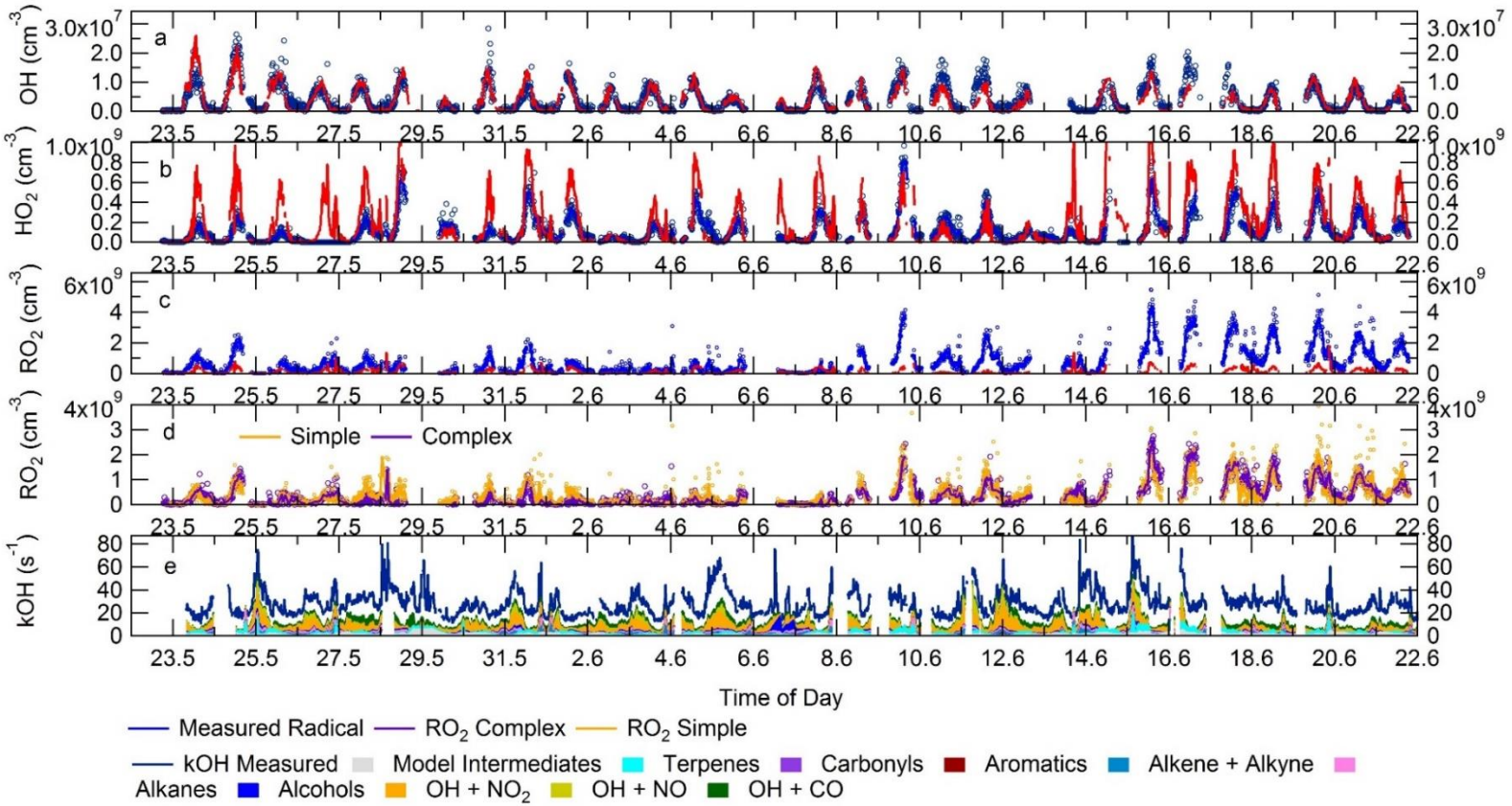

Figure 5.13. Time-series of a) OH, b) HO_2, c) total RO_2, d) speciated RO_2 and e) OH Reactivity. The measurements are in blue and model is in red for OH, HO_2 and RO_2. The speciated RO_2 is separated into simple (gold) and complex (purple). The OH reactivity is broken down by the key below the graph.

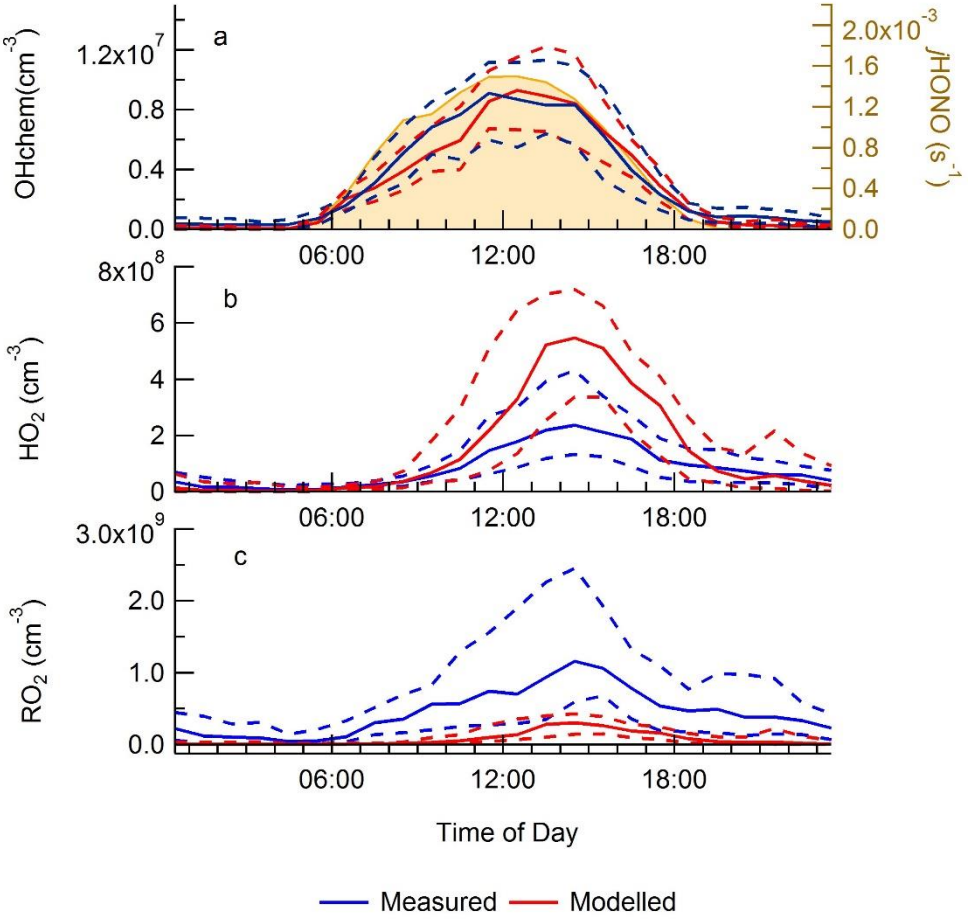

Figure 5.14 The average median diurnal comparison for measured and modelled for: a) OHchem (left axis) and OH (left axis) modelled and j(HONO) (gold, right axis); b) HO_2 and HO_2 modelled and c) total RO_2 and total RO_2 modelled. The model results are all for MCM base. The dashed line represents day-to-variability using the 25th/75th percentile.

The RO_2 concentration is underpredicted by the model across the whole campaign. The peak in the RO_2 measurements at ~14:30 is underpredicted by a factor of ~3.8, and whilst the measurements predict high night-time concentrations, the model is zero by 21:00. The model's 95 CI also predicts the secondary peak that is observed in the RO_2 measurements between 18:30 – 22:30, although the secondary peak is shifted later to 20:30 – 22:30.

5.4.4.3 OH Reactivity Model Output

OH reactivity measurements can be compared to calculated values using:

$$k_{OH} = \sum_{i} k_{OH+Xi}[X]_i \qquad \text{E5. 3}$$

where X is restricted to species that are measured during the field campaign, alongside knowledge of kinetic data. The OH reactivity for the APHH summer campaign has been calculated using a model which also includes unmeasured OH sinks which are often oxygenated VOCs (OVOCs). These OVOCs are generally formed from the oxidative degradation of directly emitted VOCs. The average diurnal comparison between the measured and model is shown in Figure 5.15, and shows that whilst the model captures the trend of the measured OH reactivity, the model tends to underpredict the measurements across the entire day. The underprediction shows that not all the VOCs were captured during the campaign and there is a missing source of reactivity in central Beijing, the missing reactivity shows a constant trend across the entire day with an average of 9.5 s^{-1}. The constant trend of missing reactivity across the day suggests the source is primary in nature. Discussion into the missing OH reactivity can be found in the section.5.4.8, alongside a comparison with other work.

The contribution to measured OH reactivity from model intermediates, terpenes, aromatics, carbonyls, alkenes + alkynes, alkanes, alcohols, NO_2, NO, CO and other are 1.5 s^{-1} (5.6%), 1.6 s^{-1} (5.8%), 0.61 s^{-1} (2.2%), 0.92 s^{-1} (3.4%), 1.5 s^{-1} (5.7%), 1.4 s^{-1} (5.1%), 0.91 s^{-1} (3.3%), 4.7 s^{-1} (17%), 0.78 s^{-1} (2.8%), 2.75 s^{-1} (10%) and 0.38 s^{-1} (1.4%), respectively. The remaining 9.5 s^{-1} (35%) is missing OH reactivity.

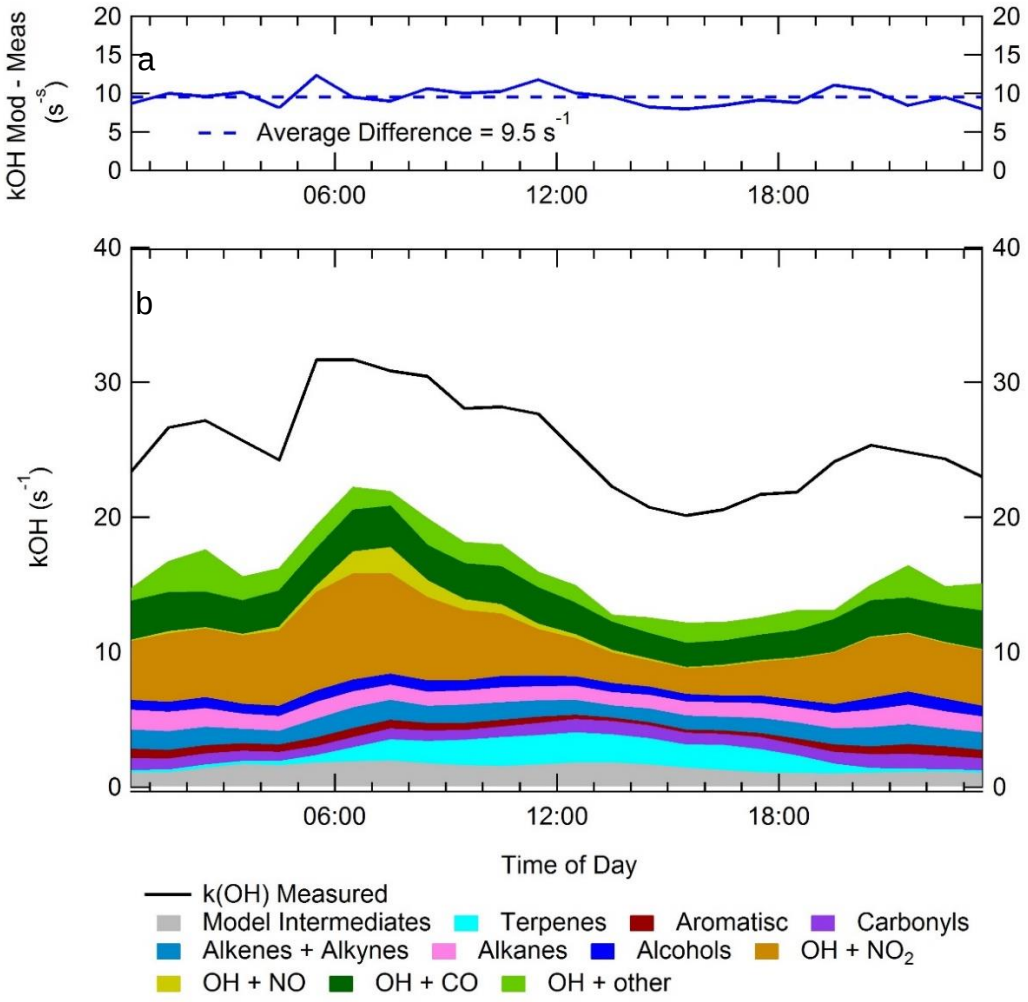

Figure 5.15 a) The difference between the average diurnal for total measured OH reactivity and modelled OH reactivity across a day. b) The average diurnal comparison for measured OH reactivity and modelled OH reactivity from MCM-base. The contribution to the OH reactivity from different species is shown in the stacked plot. The OH + Other in the reactivity key is the sum of the following reactions: OH + O_3, OH + H_2, OH + H_2O_2, OH + HO_2, OH + NO_3, OH + HO_2NO_2, OH + HONO, OH + HNO_3 and OH + SO_2.

Previous radical measurements made in urban environments during the summertime have been summarised in Table 5. 4. The measurements generally have NO concentrations varying between 0.14 to 35 ppbv of NO, and the O_3 varies between 17 – 90 ppbv for the different campaigns.

The OH concentration during the APHH campaign were quite high with an average peak of 8.5 x 10^6 molecule cm^{-3}, some days this value exceeded

2 x 10^7 molecule cm^{-3}. Campaigns in PRD (PRIDE-PRD2006), Yufa (CARE-Beijing), New York (PMTACS-NY), Mexico City (MCMA), Wangdu and both the campaigns in Texas (SHARP and TRAMP) observed average radical concentrations above 7 x 10^6 molecule cm^{-3}.

The model:measured agreement for the OH and HO_2 comparison between different campaigns cannot be discussed separately as the results are highly related, as an under or overprediction of one will change the result for the other. During the APHH campaign, the model was able to reproduce the OH very well with a model:measured ratio of 1.04, whilst HO_2 is overpredicted with a model:measured ratio of 1.85. The campaign in the PRD (PRIDE-PRD2006, Lu et al. (2012)) underpredicted OH with a model:measured of 0.33, but unlike the APHH campaign the model could replicate the HO_2 value with a ratio of 1.25. Many of the campaigns summarised in Table 5. 4 observed an overprediction of the HO_2, including campaigns that took place in Mexico City (MCMA, Dusanter et al. (2009)), Tokyo (IMPACT-L, Kanaya et al. (2007)), London (ClearfLo, Whalley et al. (2018)), Ren et al. (2006)) and Wangdu with a model:measured ratio of 1.27, 1.29, 3.3 and 1.1 respectively. The campaigns in Los Angeles (CalNex, Griffith et al. (2013)) and Mexico City showed an overprediction of OH with a ratio of 1.4 and 1.3, respectively. The Wangdu (Tan et al. (2017)) campaign showed an overprediction for both HO_2 and an underprediction for OH. Although it should be noted that the Wangdu campaign is a rural campaign and has only be used in this list as it occurred in China ~60 km away from Beijing. The Texas (TRAMP, Chen et al. (2010)), Birmingham (PUMA, Emmerson et al. (2005)) and New York (PMTACS-NY2001 campaigns underpredicts both the OH and HO_2. The campaigns Boston (CalNex, Griffith et al. (2013)) and Tokyo (IMPACT-L, Kanaya et al. (2007)) underpredicted OH and overpredicted HO_2, and finally, the campaigns in Paris (MEGAPOLI, Michoud et al. (2012)) and Texas (SHARP, Ren et al. (2013)) predicted both the OH and HO_2 concentration very well.

Overall, the measurement of OH and comparison between campaigns shown in the Table 5. 4 is only an averaged snapshot for all the summer urban

campaigns, and the difference between measurement and modelled agreement will be very sensitive to the NO_x regime where the measurements were taken. The difference between modelled and measurements under different NO_x conditions will be discussed in section.5.4.6.

Campaign	Months, Year	NO (ppbv)	O_3 (ppbv)	OH		HO_2		RO_2		Notes	References
				Measured (10^6 cm^{-3})	Calc/ Obs	Measured (10^6 cm-3)	Calc/ Obs	Measured (10^6 cm^{-3})	Calc/ Obs		
APHH, Beijing, China	May – June, 2016	2	65	9.7	1.04	1.77	1.85	7	0.2	Average midday.	This work.
PRIDE-PRD2006, China	July, 2006	0.141	62	132	0.33	132	1.25	-	-	[1] - mean between 12:00 – 16:00 [2] - average midday	Lu et al. (2012)
CAREBeijing Yufa, China	Aug - Sep, 2011	0.151	76	7.52	0.85	10	1.05	-	-	[1] - mean between 12:00 – 16:00 [2] - average midday	Lu et al. (2013)
PUMA, Birmingham, UK	Jun – Jul, 1999	2.7, 4.2	29, 41	3	0.58	3	0.56	-	-	[1] - mean between 11:00 – 15:00 for easterly and westerly [2] - average midday	Emmerson et al. (2005)
ClearfLo	Jul-Aug, 2012	33.4, 11.9	34.4, 87.8	2.1, 2.8	0.75, 0.67	1.3, 1.49	3.3, 3.3	0.97, 1.5	1.6, 0.97	Average midday – (south-westerly, easterly)	Whalley et al. (2018)
PMTACS-NY2001 New York, US	Jun-Aug, 2001	0.14	40	7	0.91	1	0.81	-	-	Average midday	Ren et al. (2006)
MCMA, Mexico City, Mexico	March, 2003	16.41	56.21	7	1.32	1.8	1.272	-	-	[1] - mean between 08:40 – 18:40 [2] - average midday	Dusanter et al. (2009)
IMPACT-L, Tokyo, Japan	Jul – Aug, 2004	2.6	17	6.3	0.86	2.31	1.29	-	-	Average midday	Kanaya et al. (2007)
Wangdu, China	Jun – Jul, 2014	0.5	90	9	0.67	9	1.1	1.1	1.2	Average midday	Tan et al. (2017)
CalNex, LA, US	May – Jun, 2010	4.8, 2.5	35, 53	4.0, 3.5	1.4, 1.0	5.0, 2.01	0.8, 0.3	-	-	Weekday, weekend. Midday average.	Griffith et al. (2013)
MEGAPOLI, Paris, France	July 2009	2	30	4.2	0.9	1.4	0.9	-	-	All points	Michoud et al. (2012)
SHARP, Texas, US	April-May, 2009		-	9.3	1.05	4.9	1.02	-	-	Midday average	Ren et al. (2013)
TRAMP, Texas, US	Aug – Oct, 2006	0.14	87	15	0.67	1.2	0.58	-	-	Value at 12:30	Chen et al. (2010)

Table 5. 4 Previous field measurements of OH, HO_2 and RO_2 that have taken place during summertime in urban areas, listing the average measured to modelled ratio, as well at the typical NO and O_3 mixing ratios. The NO and O_3 are the noontime average value for the campaigns.

5.4.4.4 Sources and Sink of RO_x radicals

A rate of production analysis (ROPA) was performed on the MCM-base model. The ROPA analysis calculates the reactions and species involved in the production and destruction of a desired molecule, in this case, the ROPA analysis was performed on OH, HO_2 and total RO_2. The output from the ROPA can be separated into reactions for primary production, termination and propagation. Primary production is the reaction of non-radicals that form radical species; termination is the reaction of radicals to form non-radicals and propagation is radical-radical recycling. Figure 5.16 shows the primary production and termination results from the ROPA analysis for RO_x ($OH + HO_2 + RO_2$).

The primary production during the campaign was dominated by the photolysis of HONO (77%), the other primary sources of OH during the APHH campaign was: $O^1D + H_2O$ (11%); ozonolysis of alkenes (5.5%); photolysis of HCHO (3.4%); photolysis of carbonyls (other than HCHO, 0.66%) and VOCs + NO_3 (2.2%). The photolysis of HONO, HCHO and carbonyls are all daytime source, whilst after 19:30 the only source of radicals is ozonolysis and VOCs + NO_3. During night-time ozonolysis contributed 52% of the radical formation, whilst VOC + NO_3 contributed the other 48%. The termination of radicals (RO_x) is dominated by the reaction of OH + NO_2 (63%). The other terminations reactions during the APHH campaign was: OH + NO (11.3%); net $HO_2 + NO_2$ (0.8%); $HO_2 + HO_2$ (1.5%); $RO_2 + HO_2$ (3.1%) and net formation PAN contribute (14%). The net-formation of PAN is calculated from the production of PAN minus the destruction of PAN (back reaction). The peroxy self-reactions do not play a large role in the termination but in the average diurnal shows an increasing contribution in the afternoon when the NO concentration is lower (see section.5.1).

The primary sources of radical species in summer urban campaigns are summarised in Figure 5.16. During the APHH campaign HONO photolysis (77%) was the dominant primary source RO_x, radicals, every other summer urban campaign showed that HONO photolysis was responsible for less than 40% of primary production. However, it should be noted that winter campaigns

tend to show a larger percentage contribution to primary production from HONO photolysis. The previous China campaigns in Yufa (CAREBeijing) and Wangdu showed that HONO photolysis was responsible for 24% and 34%, respectively.

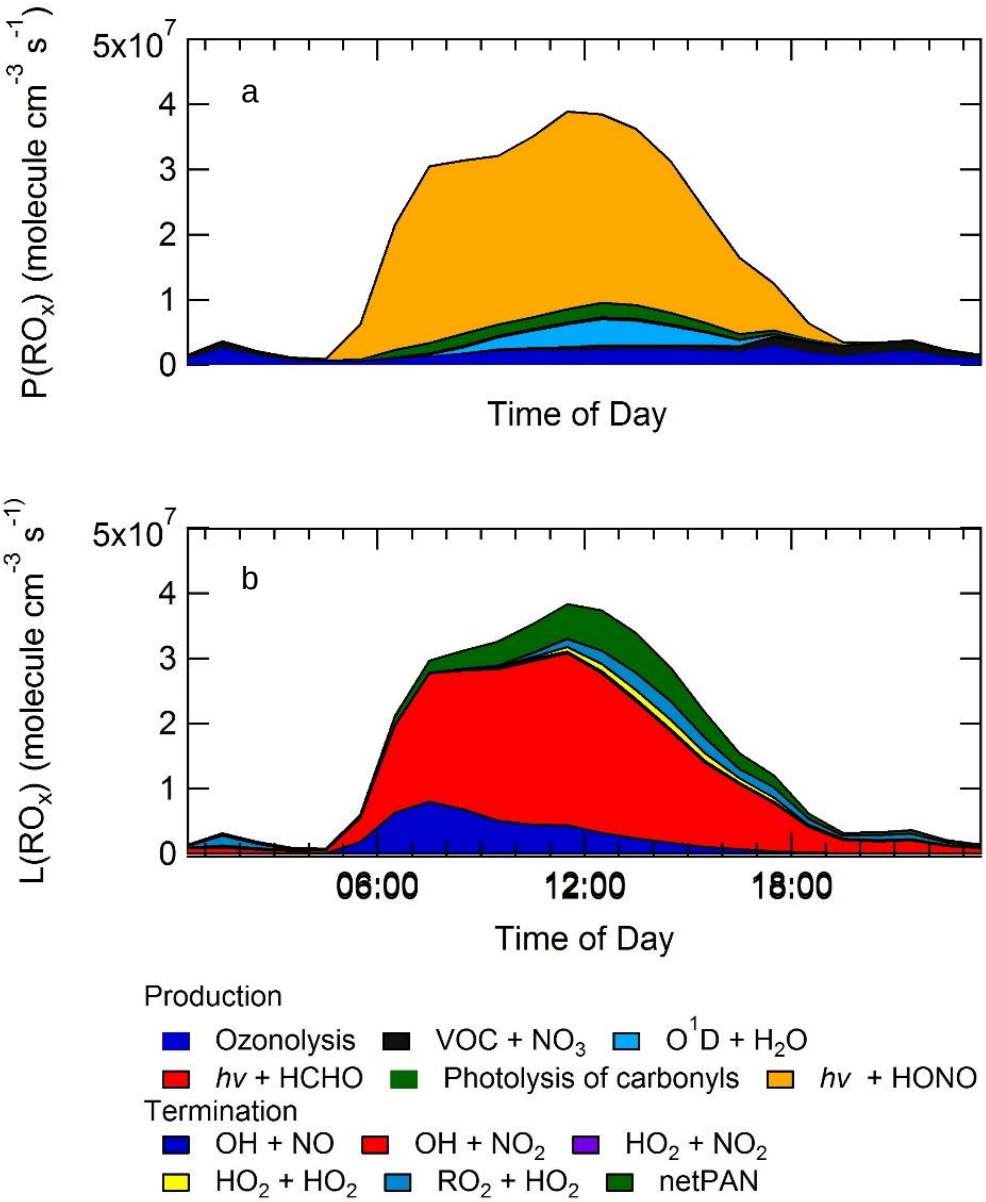

Figure 5.16 a) ROPA analysis for the termination of RO_x radicals from: OH + NO (blue); OH + NO_2 (red), HO_2 + HO_2 (purple), RO_2 + HO_2 (light blue) and net-PAN formation (green). Bottom – ROPA analysis for the primary production of RO_x radicals from ozonolysis (blue), photolysis of ozone (O^1D + H_2O, light blue), VOC + NO_3 (black), photolysis of HCHO (red), photolysis of carbonyls (green) and photolysis of HONO (yellow).

The highest RO_x radical production other than the APHH campaign, was during the London (ClearFlo) campaign, from HONO photolysis contributing 40%. The production from $O^1D + H_2O$ during the Wangdu and Yufa campaign was 15% and 15%, respectively, which is very similar to the APHH summer campaign (11%). There were larger contributions to the production of radicals from the photolysis of carbonyls (including HCHO) during the Wangdu and Yufa campaign contributing ~45% and 21% of the primary production, whilst in APHH campaign only 4% was formed this way. The only other campaigns to report significant contributions to primary production of RO_x radical through VOC + NO_3 reaction producing ~1.5% and ~7.7% were the campaigns in Tokyo (IMPACT-L) and London (ClearfLo), respectively. The contribution to primary radical production through ozonolysis varied significantly between 0 – 46% for the summer campaigns. The APHH campaign was the lower range of this at ~ 5.5%. The previous Chinese campaigns in Wangdu and Yufa showed a similar trend to APHH with ozonolysis producing <1% and 10% of the radicals, respectively. The production sources between different campaigns are seen to vary considerably and probably due to the high sensitivity on the O_3/NO_x/VOC regimes.

Campaign	Months, Year	OH (cm^{-3})	O_3 (ppbv)	$j(O^1D)/10^5$ (s^{-1})	$j(O^1D)$ (%)	j(HONO) (%)	Ozonolysis (%)	j(Carbonyls) (%)	j(HCHO) (%)	VOC + NO_3	Notes	References
APHH, Beijing, China	May – Jun, 2017	8.5	65	2.5	11	77	5.5	3.42	0.66	2.2	Midday average	This work.
CareBeijing, China	Aug - Sep, 2011	7.5	76	1.6	15	24	>1%	18	27	-	Midday average	Lu et al. (2013)
PUMA, Birmingham, UK	Jun – Jul, 1999	3	29, 41[1]	1.17, 1.28[1]	24	29	46	-	-	-	[1] - mean between 11:00 – 15:00 for easterly and westerly	Emmerson et al. (2005)
ClearFlo	Jul-Aug, 2012	2.1, 2.8	34.4, 87.8		12	40	9	17.5	20	7.7	Average between 11:00 - 15:00	Whalley et al. (2018)
PMTACS-NY2001 New York, US	Jun-Aug, 2001	7	40	2.5	30	34	27	-	9	-	Midday average	Ren et al. (2006)
MCMA, Mexico City, Mexico	March, 2003	7	56.2[1]	N/A	6	35	19	8	24	-	[1] - mean between 08:40 – 18:40 [2]-average midday	Dusanter et al. (2009)
IMPACT-L, Tokyo, Japan	Jul – Aug, 2004	6.3	36	2.7	30,13	9,7	3, 20	18,28	22,20	0,1.5	Midday value for 8th Aug, 12th Aug	Kanaya et al. (2007)
Wangdu, China	Jun – Jul	9	90	2	15	38	10	3	18	-	Midday average	Tan et al. (2017)
CalNex, LA, US	May – Jun	4.0, 3.5	35, 53	2, 2.5	11,14	29, 26	14, 14	32, 31	9, 10	-	Weekday, weekend. Midday average.	Griffith et al. (2013)
MEGAPOLI,Paris, France	July 2009	4.2	30	2	23.3	34.6	8.1	-	15.5	-	Average between 06:00 – 18:00	Michoud et al. (2012)
SHARP, Texas, Houston	April-May, 2009	9.3	-	-	30	22	13	15	14	-	Midday average	Ren et al. (2013)
TRAMP, Texas, US	Aug – Oct, 2006	15[1]	87[1]		24[2]	25[2]	10[2]	37[2]		-	[1] – Average at 12:20 [2] -Average between 06:00 – 18:00	Chen et al. (2010)

Table 5. 5 Summary of previous measurements of OH which have taken place during the summer urban campaigns, and a summary of the major primary radical sources during these campaigns. All values are the noon average for each campaign.

5.4.5 Impact of HO_2 uptake onto aerosol

The MCM-base model overpredicts the HO_2 concentration by a factor of 2.2 on average. It has been shown via modelling studies that HO_2 can be taken up onto aerosol, see section.1.2.6 for a discussion of previous HO_2 uptake work. The average diurnal of the aerosol surface area in summertime Bejing is shown in Figure 5.17, and shows that the surface area does not display a distinct diurnal pattern and was an average value of 4.3 x 10^6 cm^2 cm^{-3}. The variability in the surface area is shown in Figure 5.19a. The impact of HO_2 uptake onto aerosol has been assessed in MCM-SA (see section.5.3.1 for details) using an uptake coefficient of 0.2 (Jacob, 2000), see section.1.2.6 for justification for the uptake coefficient.

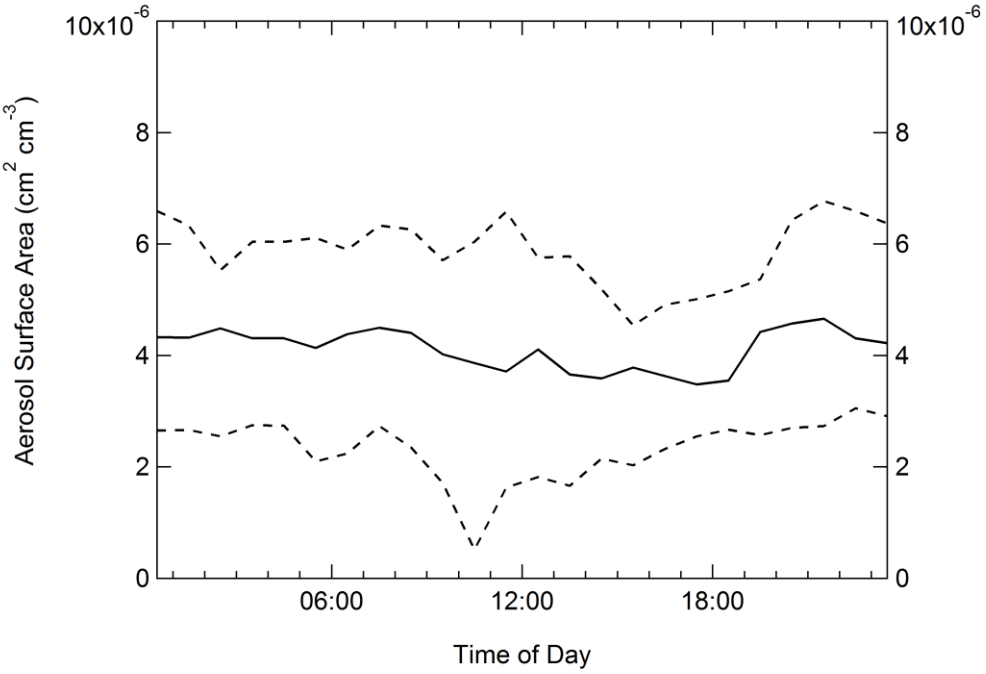

Figure 5.17 Average 60-min diurnal of aerosol surface area measured during the summer APHH campaign.

The time-series comparison of measured OH, HO_2 and RO_2 with results from MCM-base and MCM-SA is shown in Figure 5.19. It shows that uptake does impact both HO_2 and OH, using an uptake coefficient of 0.2, whilst having little impact on the total RO_2 concentration. The day-to-day impact from HO_2 uptake is variable with the biggest differences being observed on the 27/05, 28/05, 04/06 and 17/06 and highlights that it is important to take uptake into account, although the uptake is not enough to reconcile the measurements

with the model. Section.6.3.6.2 will include more discussion on HO_2 uptake and the impact on O_3 formation in haze events during summer and winter.

An average diurnal comparison of measured OH, HO_2 and RO_2 with results from MCM-base and MCM-SA is shown in Figure 5.18. The average diurnal comparison shows that on average the total RO_2 concentration is not affected by HO_2 uptake during the summer APHH campaign, whilst the ratio of MCM-base:MCM-SA decreased OH and HO_2 by 1.05 and 1.1 at the maximum, respectively.

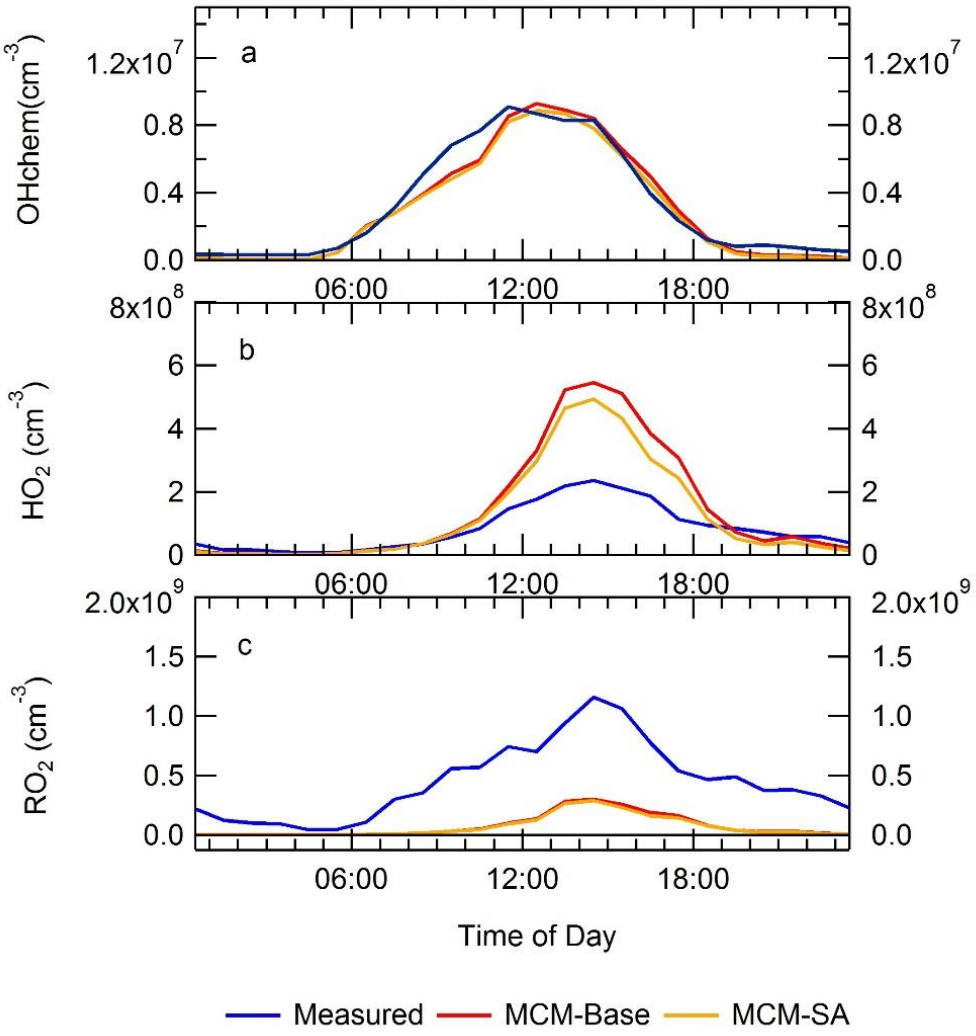

Figure 5.18 a) Average diurnal comparison between OHchem and the modelled OH from both the MCM-base and MCM-SA. b) Average diurnal comparison between measured HO_2 and MCM-base and MCM-SA c) Average diurnal comparison between measured total RO_2 and total RO_2 modelled from MCM-base and MCM-SA. The entire campaign period was averaged to make the diurnals, the diurnals are 1-hour averages.

The largest difference between the two models of ~21% is between 13:30 – 18:00, which coincides with lower NO concentrations. The increased uptake is observed in the afternoon when NO and HO_2 has a longer lifetime, so the impact of uptake is increased. To see whether the NO concentration is affecting the HO_2 uptake, the ratio of measured:model HO_2 is binned against the log of the NO concentration, and is shown in Figure 5.20. Figure 5.20 is consistent with the time-series and average diurnal as the RO_2 concentration is not affected by HO_2 uptake. As discussed earlier, Figure 5.20 shows that HO_2 uptake has a larger effect on the model at the lower NO concentrations. Also, HO_2 uptake only starts to impact the model below 6 ppbv of NO. The modelled OH concentration from MCM-SA starts to underpredict the OH concentration below 0.4 ppbv, and is caused by the reduction of HO_2 by uptake onto aerosols reducing the recycling from HO_2 + NO.

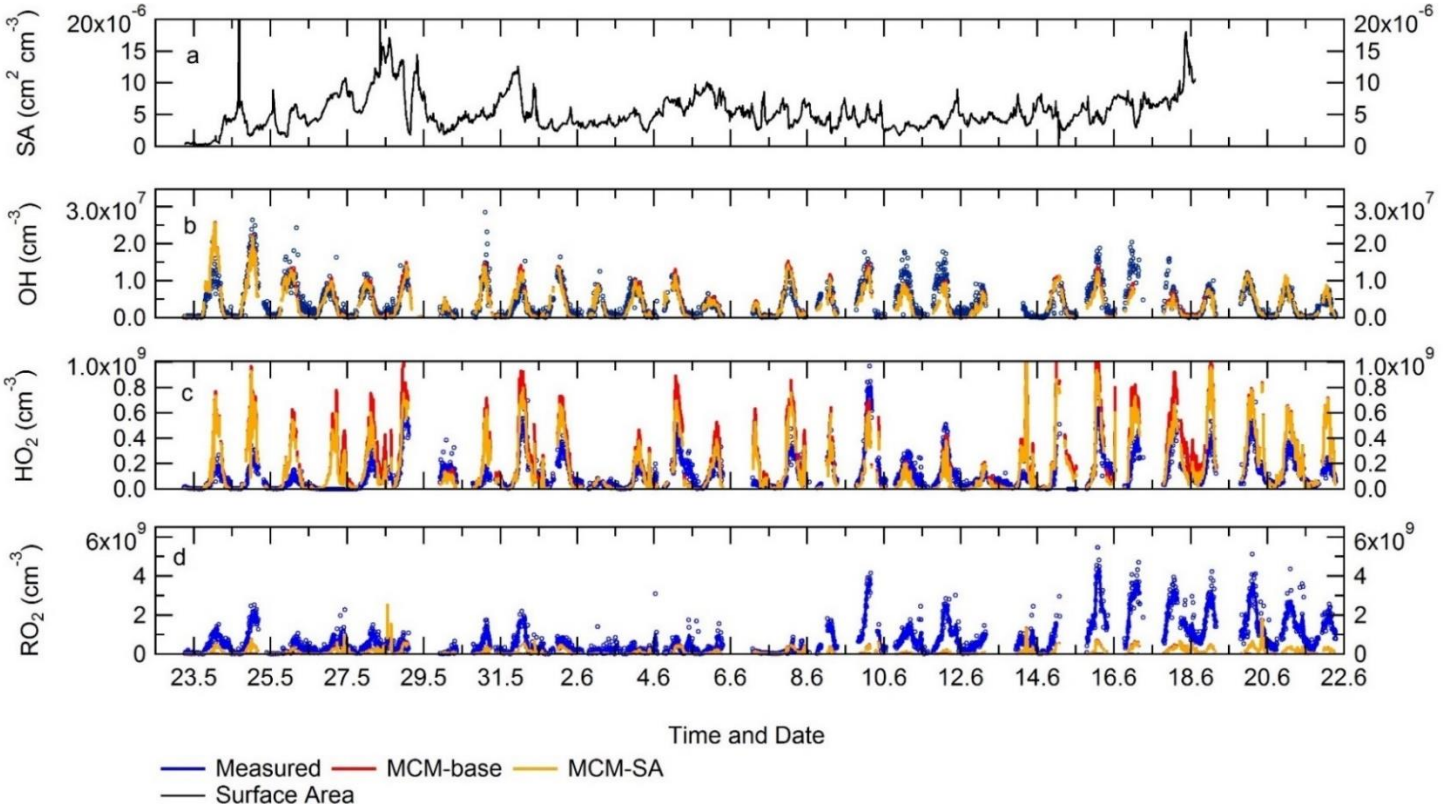

Figure 5.19 a) Timeseries for the measured surface area from a SMPS. b) Time-series comparison of measured OHchem with modelled OH from MCM-base and MCM-SA. c) Time-series comparison of modelled HO_2 with from MCM-base and MCM-SA - it should be noted that measured and modelled HO_2 from MCM-SA are the same. d) Time-series comparison of measured total RO_2 with modelled OH from MCM-base and MCM-SA. The solid line represent 15min average data, whilst the small circles represent the raw data (measurements only).

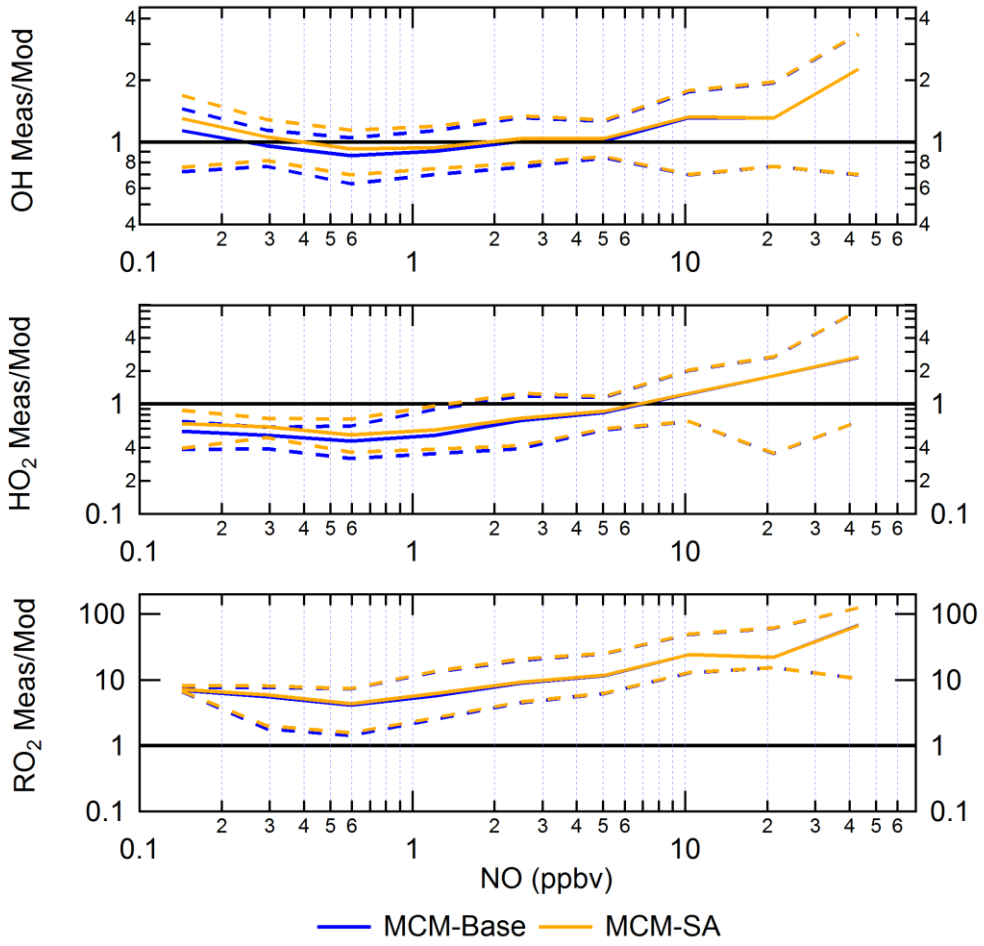

Figure 5.20 The ratio of measurement/model for OH (top), HO_2 (middle) and RO_2 (bottom) across various NO concentrations for daytime values only ($j(O^1D) > 1 \times 10^{-6}$ s^{-1}). Yellow represents for results from MCM-SA and blue represents results from MCM-base.

5.4.6 Radicals under high and low NO_x conditions

NO is central to the recycling of radicals through propagation ($RO_2 \rightarrow HO_2 \rightarrow OH$), and previous work has shown that measurement:model ratios can exhibit strong dependences on the NO mixing ratio ((Tan et al., 2017, Lu et al., 2012, Whalley et al., 2018, Dusanter et al., 2009, Griffith et al., 2013). The ratio of measured:modelled(MCM-base) for OH, HO_2 and RO_2 was binned against NO mixing ratios, and is shown in Figure 5.21. The analysis was confined to daytime measured ($j(O^1D) > 1 \times 10^{-6}$ s^{-1}). Since the NO mixing ratios during the campaign varied from 1 ppbv to 80 ppbv, the data was binned to the natural logarithm of NO concentration to give an even split of data points

in each bin (less data available at the very high NO concentrations, i.e. above 20 ppbv).

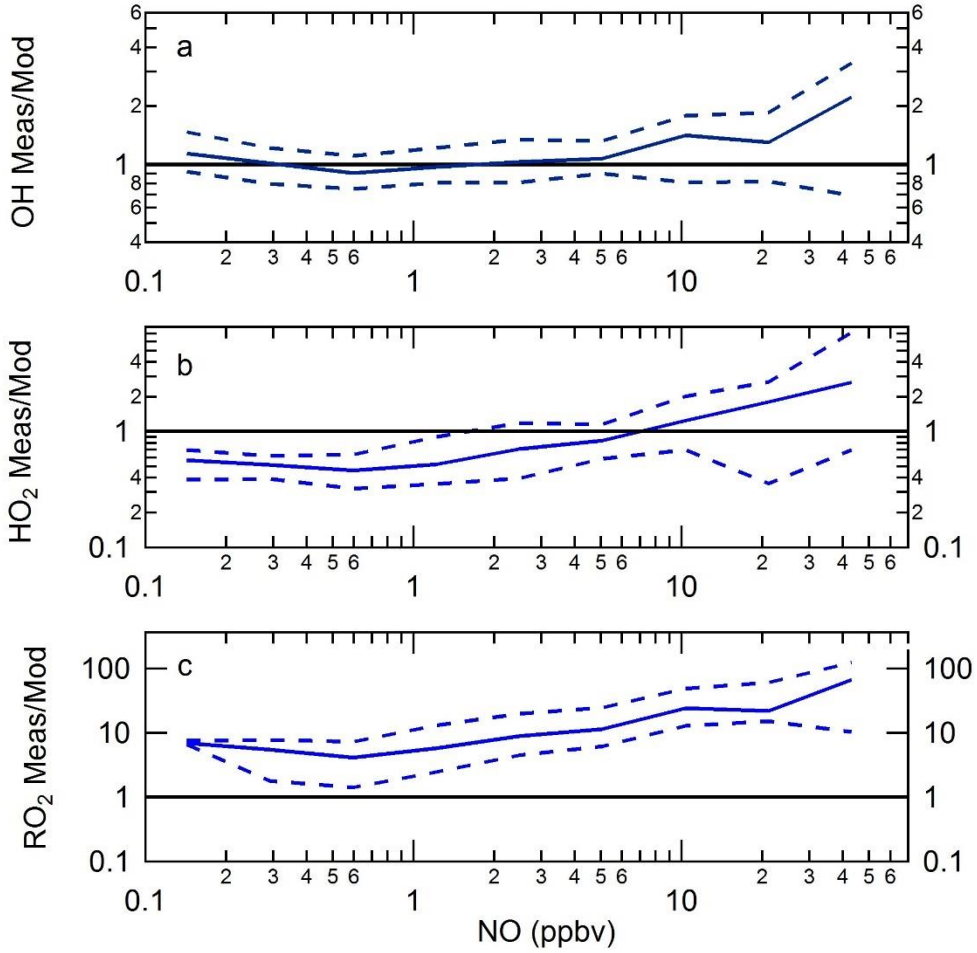

Figure 5.21 The ratio of measurement:model(MCM-base) for OH (a), HO_2 (b) and RO_2 (c) across various NO concentrations for daytime values only ($j(O^1D) > 1 \times 10^{-6}$ s^{-1}). The dashed lines represent the 95% confidence intervals.

As Figure 5.21 shows the measurement:modelled OH ratio is close to one between 0.1 – 5 ppbv of NO, although above 5 ppbv of NO the model starts to underpredict the OH concentration. The HO_2 measured:modelled ratio shows a similar underprediction as OH above 5 ppbv of NO. The HO_2 at NO concentrations below 5 ppbv starts to show an overprediction by the model, this overprediction settles at a factor of 2 between 0.1 – 1 ppbv of NO. The measured:modelled total RO_2 shows an underprediction across the whole NO

range, although the underprediction increases with increasing NO. The following section will explore reasons the MCM-base model is underpredicting OH and RO_2 and overpredicting HO_2 including: additional recycling of HO_2 into OH that is independent of NO (section.5.4.6.2); additional primary production from generic species (section.5.4.6.3.1) and Cl chemistry (section.5.4.6.3.2) and finally exploring the impact of autoxidation of RO_2 species.

5.4.6.1 Model constrained to HO_2

The MCM-base model overpredicts HO_2 by a factor ~2, but could reproduce the OH concentration within the 26% error on the measurements. The replication of OH by MCM-base suggests that high HO_2 might be leading to the reproduction of OH in the model through high HO_2 + NO recycling. To assess whether MCM-base is replicating the measurements due to the model overpredicting HO_2, the model was constrained to the measured HO_2, this model from now on is called MCM-cHO_2. Figure 5.22 shows the average diurnal comparison of MCM-base and MCM-cHO_2 with the measurements of OH, HO_2 and RO_2. The modelled OH from MCM-cHO_2 is smaller than that from MCM-base, caused by the lower HO_2 concentration in the model; hence less HO_2 + NO recycling. Whilst MCM-cHO_2 does show a good agreement between measured and modelled OH, the model does generally underpredict the OH concentration by ~15% which is within the 26% error on the OH measurements. Due to the decrease in the modelled OH concentration for MCM-cHO_2, the modelled total RO_2 concentration decreases compared to MCM-base. The total modelled RO_2 concentration by MCM-cHO_2 decreases by 33% compared with MCM-base and shows how sensitive the RO_2 concentration is to model OH.

Whilst the average diurnal does not show a large difference between measured and modelled (MCM-cHO_2) for OH, it may be more important on a day-to-day variation under different NO conditions. The time-series for the comparison of MCM-base and MCM-cHO_2 with measured OH, HO_2 and total RO_2 values is shown in Figure 5.23. The time-series shows that constraining the model to measurements of HO_2 can have larger impacts on different days,

the largest impact is seen on the 25/05, 27/05, 30/05 and 18/06. It is difficult to see the impact of constraining the model to HO_2 on the modelled total RO_2, as both MCM-cHO_2 and MCM-base underpredict the total RO_2 by at least a factor of ~6. To see whether the day-to-day variations are caused by different NO regimes on these days the ratio of measurement:modelled (MCM-base and MCM-cHO_2) are binned against the log of the NO concentration, and is shown in Figure 5.24. The ratios have been taken for daytime values only ($j(O^1D) > 1 \times 10^{-6}$ s^{-1}). Figure 5.24 shows that whilst the average diurnal, shown in Figure 5.22, of measured OH and modelled OH from MCM-cHO_2 show a good agreement, this is due to averaging across the whole campaign time-series. The time-series comparison shows a day-to-day variation with a few days (25/05, 27/05, 30/05 and 18/06) showing a large difference between modelled(MCM-cHO_2) and measured OH, whilst the ratio of measured:modelled shows that larger differences occur at lower NO.

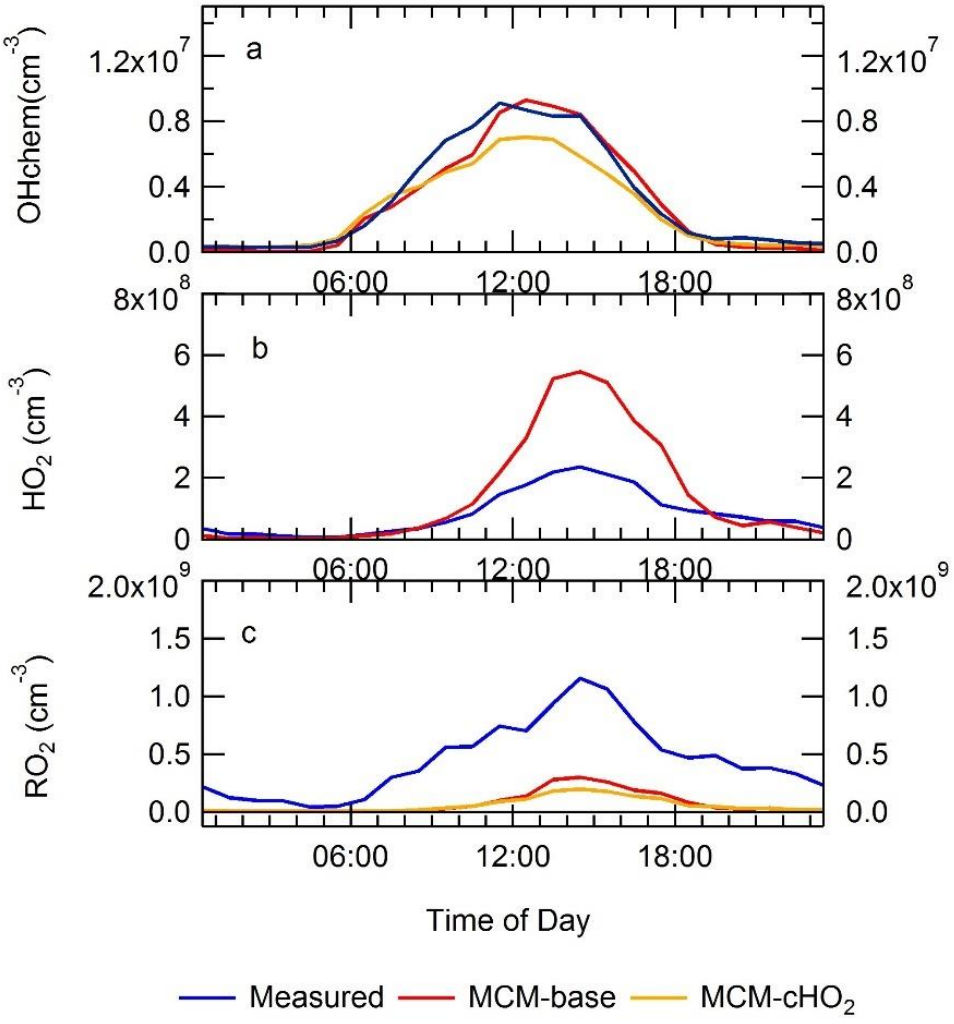

Figure 5.22 a) Average diurnal comparison between OHchem and the modelled OH from both the MCM-base and MCM-cHO_2. b) Average diurnal comparison between measured HO_2 and MCM-base, it should be noted that the modelled HO_2 from MCM-cHO_2 would be the same as measured. c) Average diurnal comparison between measured total RO_2 and total RO_2 modelled from MCM-base and MCM-cHO_2. The entire campaign period was averaged to make the diurnals, the diurnals are 1- hour averages.

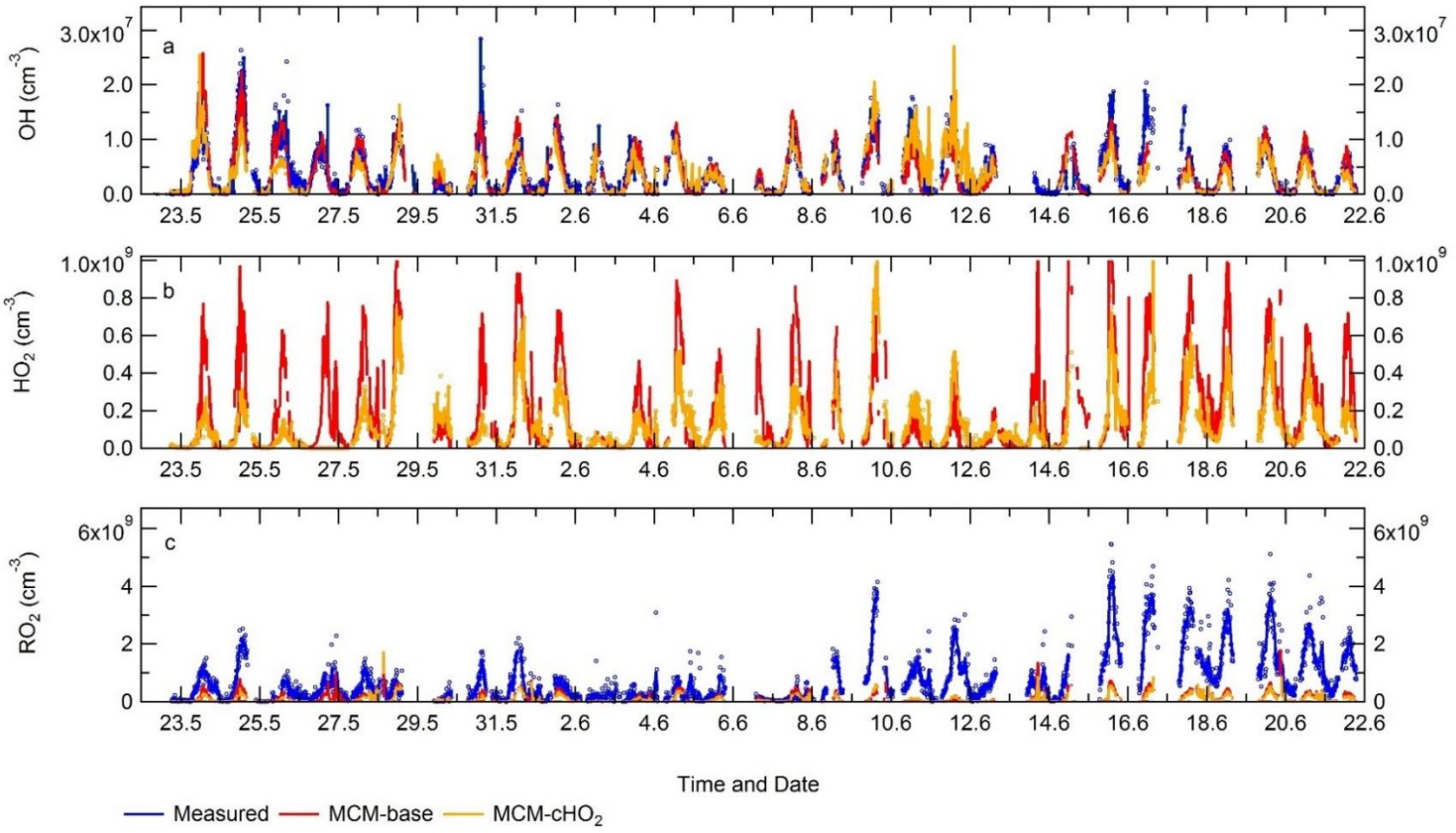

Figure 5.23 a) Time-series comparison of measured OHchem with modelled OH from MCM-base and MCM-cHO_2. b) Time-series comparison of modelled HO_2 with from MCM-base and MCM-cHO_2, it should be noted that measured and modelled HO_2 from MCM-cHO_2 are the same. c) Time-series comparison of measured total RO_2 with modelled OH from MCM-base and MCM-cHO_2. The solid line represents 15min average data, whilst the small circles represent the raw data (measurements only).

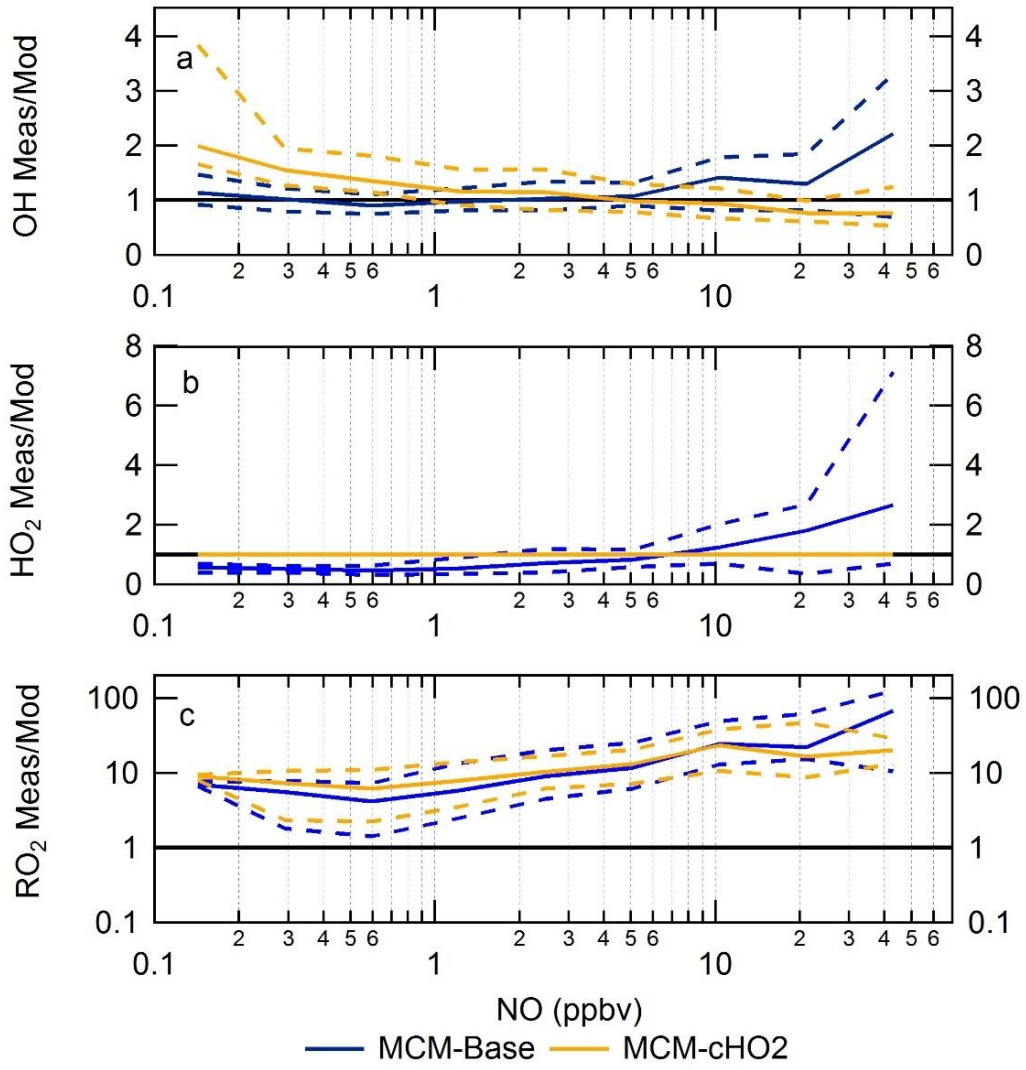

Figure 5.24 The ratio of measurement:model for OH (a), HO_2 (b) and RO_2 (c) across various NO concentrations for daytime values only ($j(O^1D) > 1 \times 10^{-6}$ s^{-1}). Yellow represents for results from MCM-cHO_2 and blue represents results from MCM-base. It should be noted that the ratio of measured HO_2 and modelled HO_2 (MCM-cHO_2) is 1 as the values are the same.

The comparison between the two ratios shows that at low NO (between 0.1 – 5 ppbv) the recycling of measured HO_2 + NO is not sufficient to replicate the measured OH, whilst above 5 ppbv the recycling of measured HO_2 + NO is sufficient. The impact of the MCM-cHO_2 undepredicting the OH concentration at low NO on the total RO_2 concentration can be seen in Figure

5.24. Figure 5.24 shows that the underprediction of OH does cause the underprediction of total RO_2 to increase between 0.1 – 5 ppbv of NO. The agreement between measured:modelled(MCM-cHO_2) total RO_2 improves at higher NO (5 – 60 ppbv), and this is caused by the increase in modelled OH between measured and model OH at these NO concentrations.

The underprediction of OH (MCM-HO_2) at low NO concentration suggests that additional recycling HO_2 to OH (*via* an unknown species) may play an important role. Section.5.4.6.2 explores the addition of HO_2 + X into the MCM, and how it impacts the models ability to predict the radical species.

5.4.6.2 HO_2 + X radical recycling

The reaction of HO_2 + X, with X being an unknown species that recycles HO_2 to OH was first proposed in Hofzumahaus et al. (2009). The study compared the experimental OH loss rate (*k*(OH) x [OH]), calculated from measured concentration and reactivities with OH, with major known sources of OH ($O^1D + H_2O$, photolysis of HONO and recycling from HO_2 + NO) for the PRIDE-PRD2006 campaign. The study found that OH loss and production rate were balanced in the morning, whilst in the afternoon when NO was low a significant OH source was missing. The reaction (HO_2 + X) was proposed to reconcile measurements in the PRD with the model, and found that a strong source of X was required in the noon and afternoon hours with [X] ~ 0.85 ppbv, and the assumption that the HO_2 + NO and HO_2 + X rate constant were the same (Hofzumahaus et al., 2009). It should be noted that during the PRIDE-PRD2006 campaign HO_2^* was measured rather than HO_2.

Similar work has been carried out in Tan et al. (2017) and showed that the concentration of X on average to reconcile measurement with the model was ~5 ppbv, although it should be noted for this work it was HO_2^* measured rather than HO_2. In this study, Tan et al. (2017) discussed whether halogen chemistry could be the missing source, but since the concentration of the required X exceeds all tropospheric observations of halogens, this was discounted. The reaction of HO_2 + X in the model represents either the reaction with the one unknown species X or a more complex mechanism.

As discussed in section.5.4.4 the MCM-base model overpredicts HO_2, and to see whether the recycling of HO_2 into OH is able to reconcile measurements with the model the MCM-base model has been modified to include the reaction of HO_2 + X. The model with the reaction of HO_2 + X is called MCM-X from now on. The rate constant for the reaction is the same as the rate constant for HO_2 + NO, and the concentration of X has been optimised. As Figure 5.25 shows the concentration of X used into the model is dependent on the concentration of NO, species [X] is only above zero when the [NO] is below 6 ppbv. Below 6 ppbv and above 0.4 ppbv of NO there is a linear relationship between X and NO that has the equation [X] = -0.118[NO] + 1.084. Then when [NO] is between 0.4 – 0.2 ppbv the [X] is set at 0.75 ppbv, and when [NO] is between 0 – 0.2 ppbv the [X] is set at 0.25. The relationship between [X] and [NO] shows that only additional loss of HO_2 is required to reconcile measurement and model below 6 ppbv of NO. Then [X] increasing with decreasing [NO] peaking at 1.03 ppbv of X when NO is 0.4 ppbv. Once the NO drops below 0.4 ppbv the amount of additional loss of HO_2 rapidly decreases. It should be noted that the model has been optimised for HO_2 loss rather than optimise the measured and model comparison of OH. Figure 5.25 shows that the concentration of species X has a similar diurnal profile to an oxidised intermediate, and if this process is occurring it may be an oxidised intermediate that recycles HO_2 to OH independent of NO.

The time-series of measured OH, HO_2 and total RO_2 with modelled results from MCM-base and MCM-X is shown in Figure 5.27. The results show that HO_2 is modelled well in MCM-X, especially compared to MCM-base, which means the concentration of X inputted into the model has been optimised well. Although the HO_2 concentration is now underpredicted on days (29/05, 10/06, 11/06) when MCM-base replicated the measurements well. The 10/06 and 11/06 are high NO days (see Figure 5.2), and could be the reason for the overprediction, as in general under high NO conditions, HO_2 is underpredicted (see section.1.5.2 for details). While HO_2 is replicated well in the MCM-X model, the OH concentration is overpredicted compared to the measurements. However, OH reactivity is still underpredicted by the model, and if measured OH reactivity was used the OH concentration would

decrease. The RO_2 concentration is increased in MCM-X compared to MCM-base, which is caused by the increased OH concentration in MCM-X.

The change in the average diurnal and trend throughout the day from MCM-base to MCM-X, including a comparison with the measurements, is shown in Figure 5.26. The average diurnal shows a good agreement between measured HO_2 and modelled HO_2 from MCM-X, although a slight overprediction during between 08:30 - 15:30.

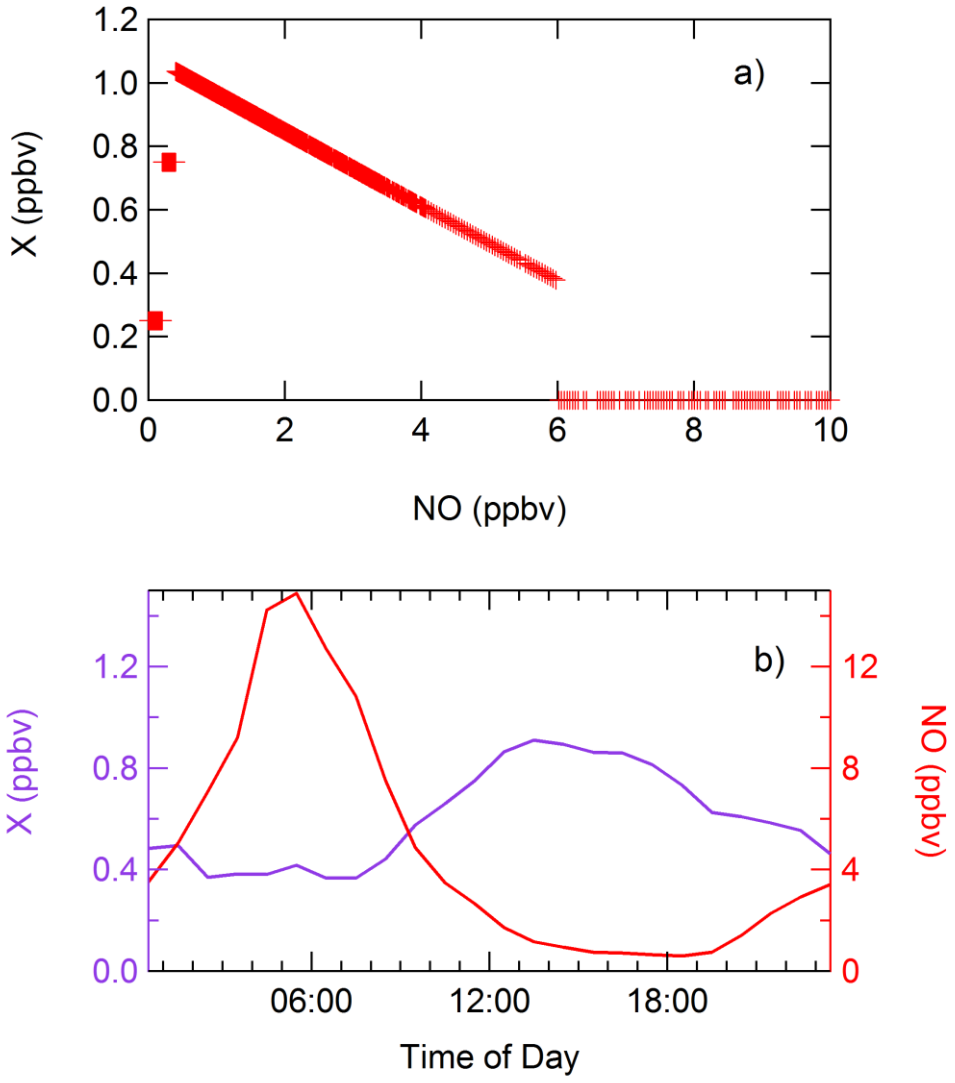

Figure 5.25 a) Concentration of species X as a function of NO, the NO concentration has been shown in only between 0 – 10 ppbv as the concentration of X above 6 ppbv is set to zero. b) The average diurnal for the concentration of X and NO across the whole campaign, it shows they have an inverse relationship.

The OH concentration peak in MCM-X has been shifted from 12:30 (both measured and MCM-base) to 13:30 (MCM-X) and highlights the extra production from HO_2 + X. MCM-X also start to overpredict OH in the afternoon period between 11:30 – 17:30, which highlights that too much OH is being produced from the reaction of HO_2 + X. The modelled total RO_2 concentration is improved for the whole day showing that increased OH concentration is producing more RO_2 radicals, also, a decreased loss from the RO_2 + HO_2 cross-reaction since the HO_2 concentration is significantly smaller in HO_2 + X. Since the concentration, and hence the reaction of HO_2 + X is dependent on the [NO] the ratio of measurement:modelled has been binned as a function of NO, as shown in Figure 5.28.

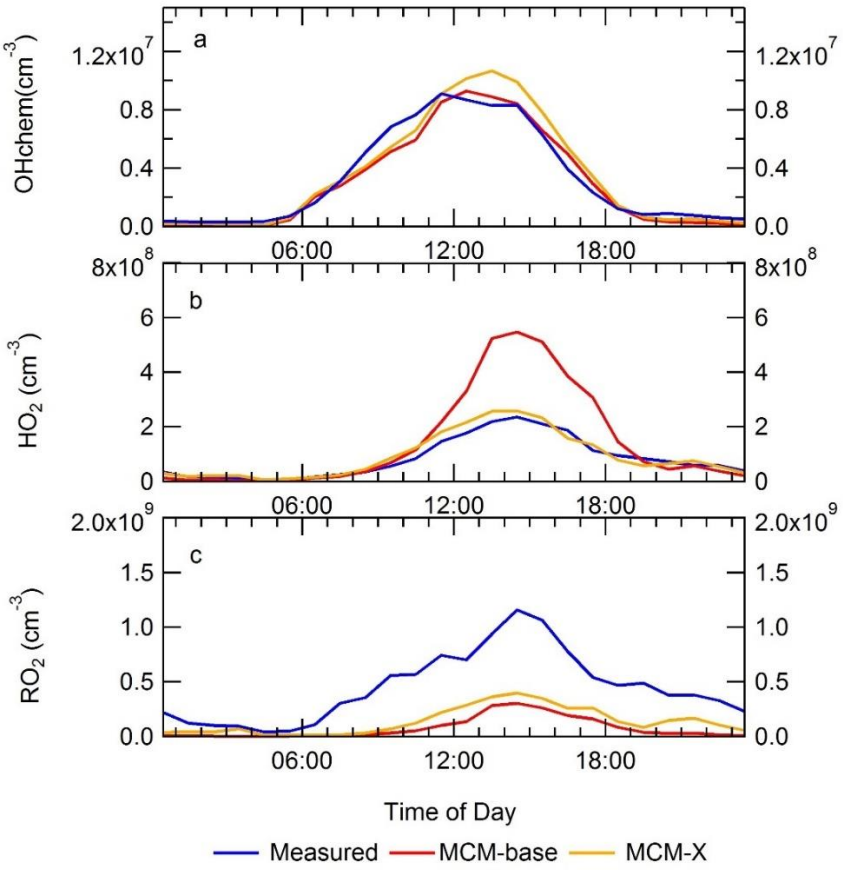

Figure 5.26 a) Average diurnal comparison between OHchem and the modelled OH from both the MCM-base and MCM-X. b) Average diurnal comparison between measured HO_2, MCM-base and MCM-X. c) Average diurnal comparison between measured total RO_2 and total RO_2 modelled from MCM-base and MCM-X. The entire campaign period was averaged to make the diurnals, the diurnals are 1-hour averages.

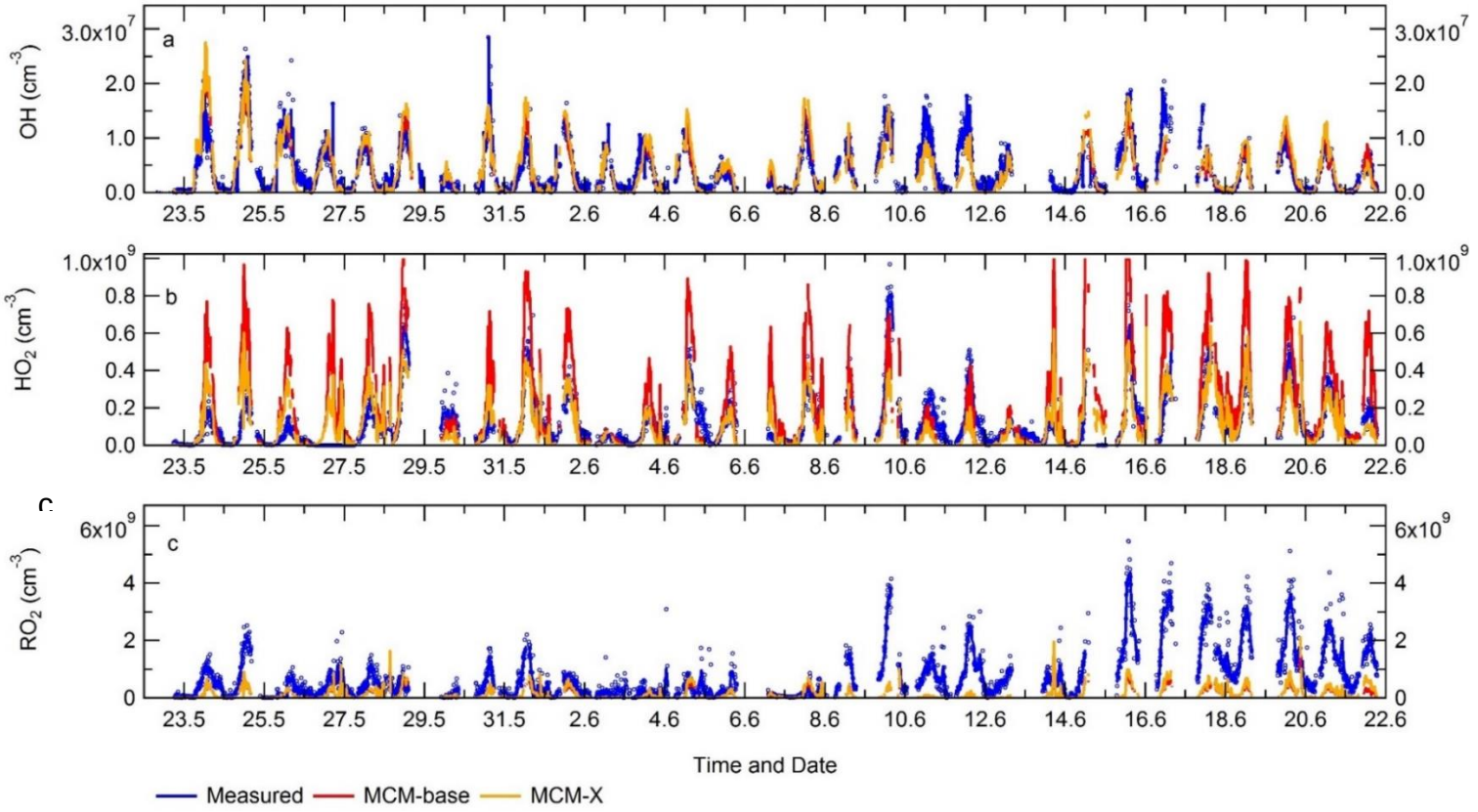

Figure 5.27 a) Time-series comparison of measured OHchem with modelled OH from MCM-base and MCM-X. b) Time-series comparison of modelled HO_2 with from MCM-base and MCM-X, it should be noted that measured and modelled HO_2 from MCM-X are the same. c) Time-series comparison of measured total RO_2 with modelled OH from MCM-base and MCM-X. The solid line represents 15-min average data, whilst the small circles represent the raw data (measurements only).

The measurement:model ratio shows that the HO_2 ratio from MCM-X is ~1 for [NO] less than 6 ppbv, the effect of introducing the reaction of HO_2 + X can be seen in the ratio of measurement:model for OH. The measurement:model ratio shows that the OH concentration is starting to be overpredicted by the model, and the overprediction peaks at a ratio of 0.7 at 0.3 ppbv of NO. The total RO_2 measurement:modelled ratio is improved by the introduction of HO_2 + X, and is for the reason discussed above, i.e. the OH concentration is increased and the peroxy self-reaction RO_2 + HO_2 is reduced. The results are shown in Figure 5.27 - Figure 5.28 shows that whilst HO_2 + X does improve the modelled HO_2 and RO_2 when [NO] is below 6 ppbv, the model's ability to reproduce OH is decreased. Although if modelled OH reactivity matched the measured this would reduce the OH concentration.

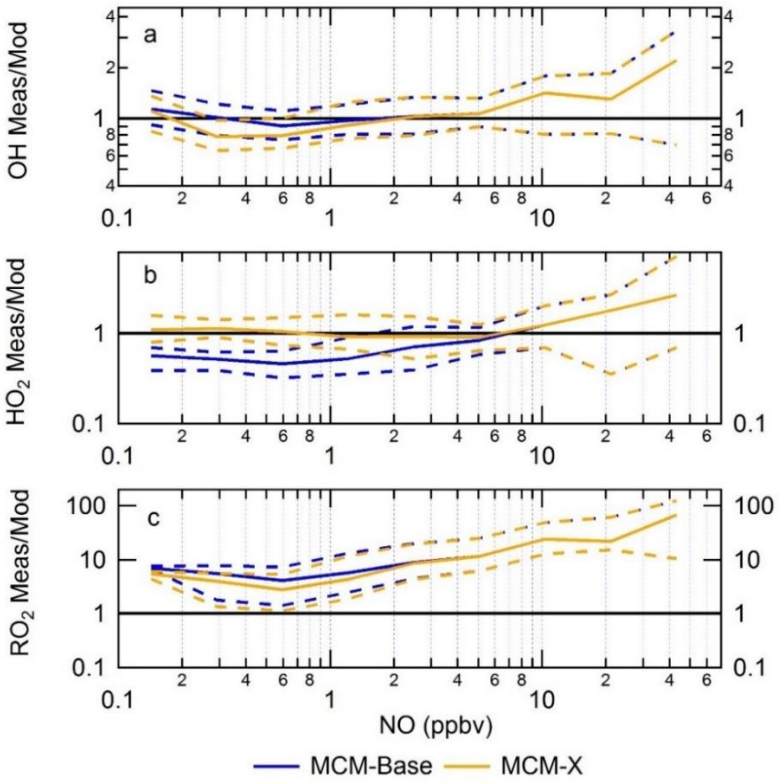

Figure 5.28 The ratio of measurement/model for OH (a), HO_2 (b) and RO_2 (c) across various NO concentrations for daytime values only ($j(O^1D)$ > 1 x 10^{-6} s^{-1}). Yellow represents for results from MCM-X and blue represents results from MCM-base. The ratio above [NO] of 6 ppbv is the same for MCM-base and MCM-X and the model has not been changed between these points.

5.4.6.3 Primary production of the RO_2 Radical

5.4.6.3.1 Additional primary source

As discussed above, the ratio of measured:modelled(MCM-base) shows that the total RO_2 radicals tend to be underpredicted by the model, and suggests there is unknown RO_2 chemistry. To investigate whether the 'missing chemistry' could be caused by an additional primary source of RO_2 radicals the MCM-base has been modified, now called MCM-P'RO2. The MCM-P'RO2 has an additional source of several RO_2 species (see section.5.3.1 for more detail) including both simple and complex. The average maximum extra primary production of RO_x ($P'RO_x$) radicals required to bridge the gap between measured and modelled was found to be 0.47 x 10^8 molecules cm^{-3} s^{-1} (6.88 ppbv h^{-1}) at 11:30 as shown in Figure 5.29.

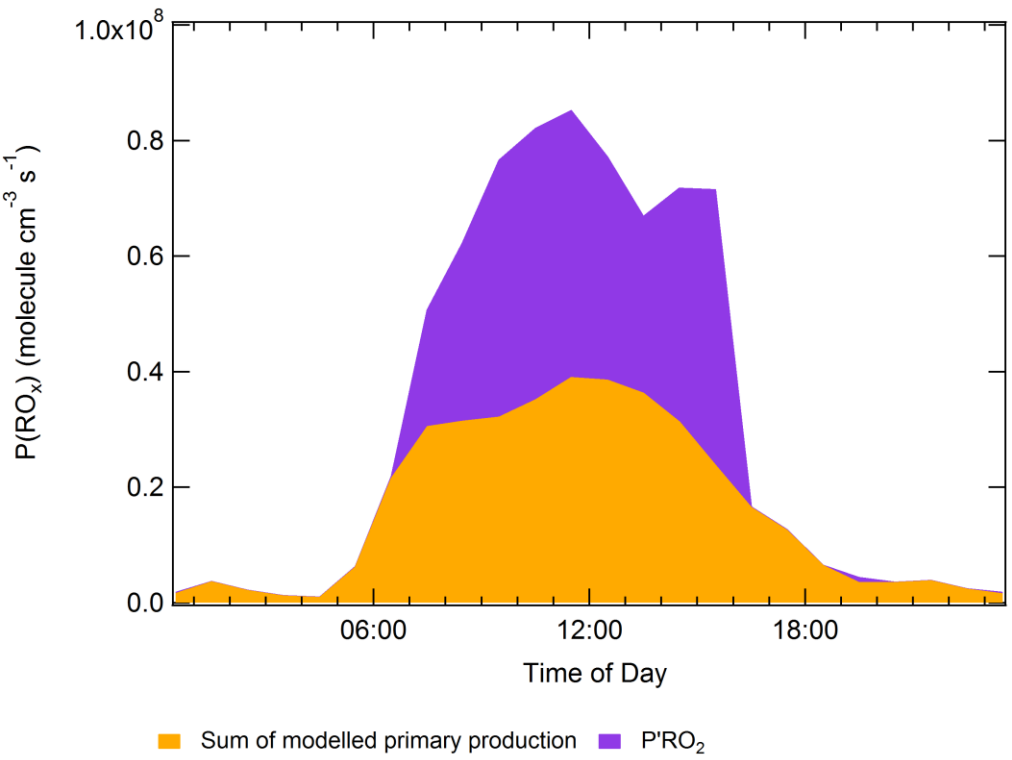

Figure 5.29 Total primary production of radicals (shown in yellow) with additional RO_2 source (purple). The yellow represents the sum of primary production from HONO, $O^1D + H_2O$, ozonolysis, HCHO, VOC + NO_3 and photolysis of carbonyls.

The additional primary source of RO_2 is similar to the additional RO_2 source that was required to resolve the measured and modelled RO_2 during the BEST-ONE campaign (5 ppbv hr^{-1} during polluted periods) and is also similar to the noon-average modelled(MCM-base) primary production of RO_x during the APHH campaign of 5.56 ppbv h^{-1}. However, the BEST-ONE campaign was a winter-time campaign and under high NO regimes, the RO_2 underprediction tends to increase (see section.1.5.2 for details). It has been previously suggested (Tan et al., 2017) that the missing primary radical source originates from the photolysis of $ClNO_2$ and Cl_2 to generate Cl atoms, which can further oxidise VOCs to form peroxy radicals, this has been explored in section.5.4.6.3.2.

The time-series comparison between measured, MCM-base and MCM-P'RO_2 is shown in Figure 5.31. The comparison between modelled total RO_2 from MCM-P'RO_2 and measured values shows a good agreement across the timeseries, although there is an underprediction between 08/06 – 12/06 and an overprediction between 16/06 – 17/06. The underprediction highlights that there is not enough primary RO_2 used into the modelled, whilst when there is an overprediction it highlights that too much primary RO_2 is being used into the model. The introduction of additional RO_2 now causes an overprediction of both HO_2 and OH across the entire time-series. The overprediction of measured HO_2 by MCM-P'RO_2 is much higher than the overprediction by MCM-base. Also, whilst before the MCM-base could replicate the OH measurement within the 26% error, the MCM-P'RO_2 now overpredicts the OH radicals outside of the instrumental error range.

The ratio of measured:modelled for both MCM-base and MCM-P'RO_2 has been binned against the log of the [NO], and is shown in Figure 5.30 - please note that only day-time values have been used. It shows that even with the additional primary source for RO_2 there is still an underprediction at NO concentration above 1 ppbv. For MCM-base the model overpredicts HO_2 below 6 ppbv of NO, but in MCM-P'RO_2 the model overpredicts HO_2 across the whole NO range. The OH in MCM-P'RO_2 is now overpredicted below 20 ppbv of NO, whilst the MCM-base only overpredicted OH below 5 ppbv.

MCM-P'RO_2 model run shows that processes other than additional primary RO_2 must be important to reconcile measurement with the model for OH, HO_2 and RO_2, as just adding more RO_2 into the model leads to large overpredictions of OH and HO_2. Futhermore whilst HO_2 uptake has not been taken into account for the MCM-P'RO_2 model, it has been shown in MCM-SA that it can't reconcile measurements with modelled when the λ = 0.2. For MCM-P'RO_2 where the modelled HO_2 is higher than MCM-base it would not be expected to resolve the HO_2 overprediction, so this model has not been run.

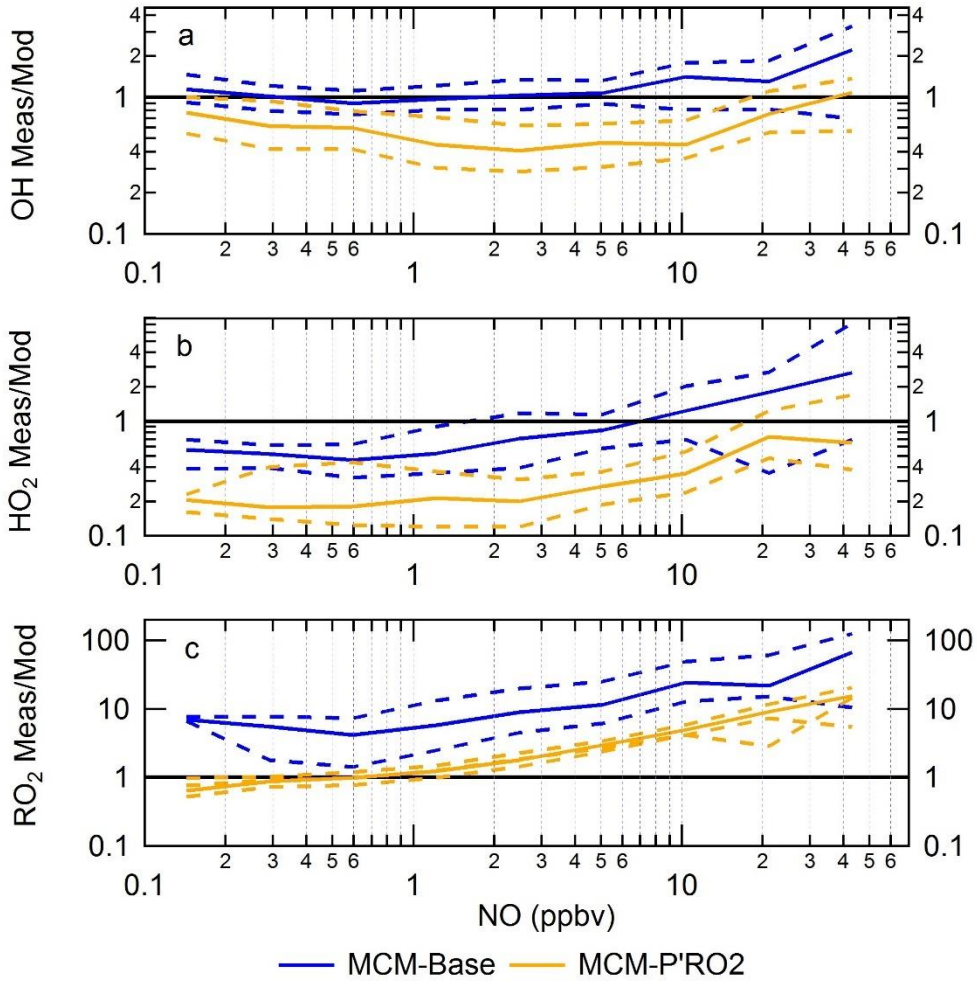

Figure 5.30 The ratio of measurement/model for both MCM-base(blue) and MCM-P'RO_2 (yellow) OH (a), HO_2 (b) and RO_2 (c) across various NO concentrations for daytime values only ($j(O^1D) > 1 \times 10^{-6}$ s^{-1}). The dashed lines represent the 95% confidence intervals. All y-axis is on a log scale.

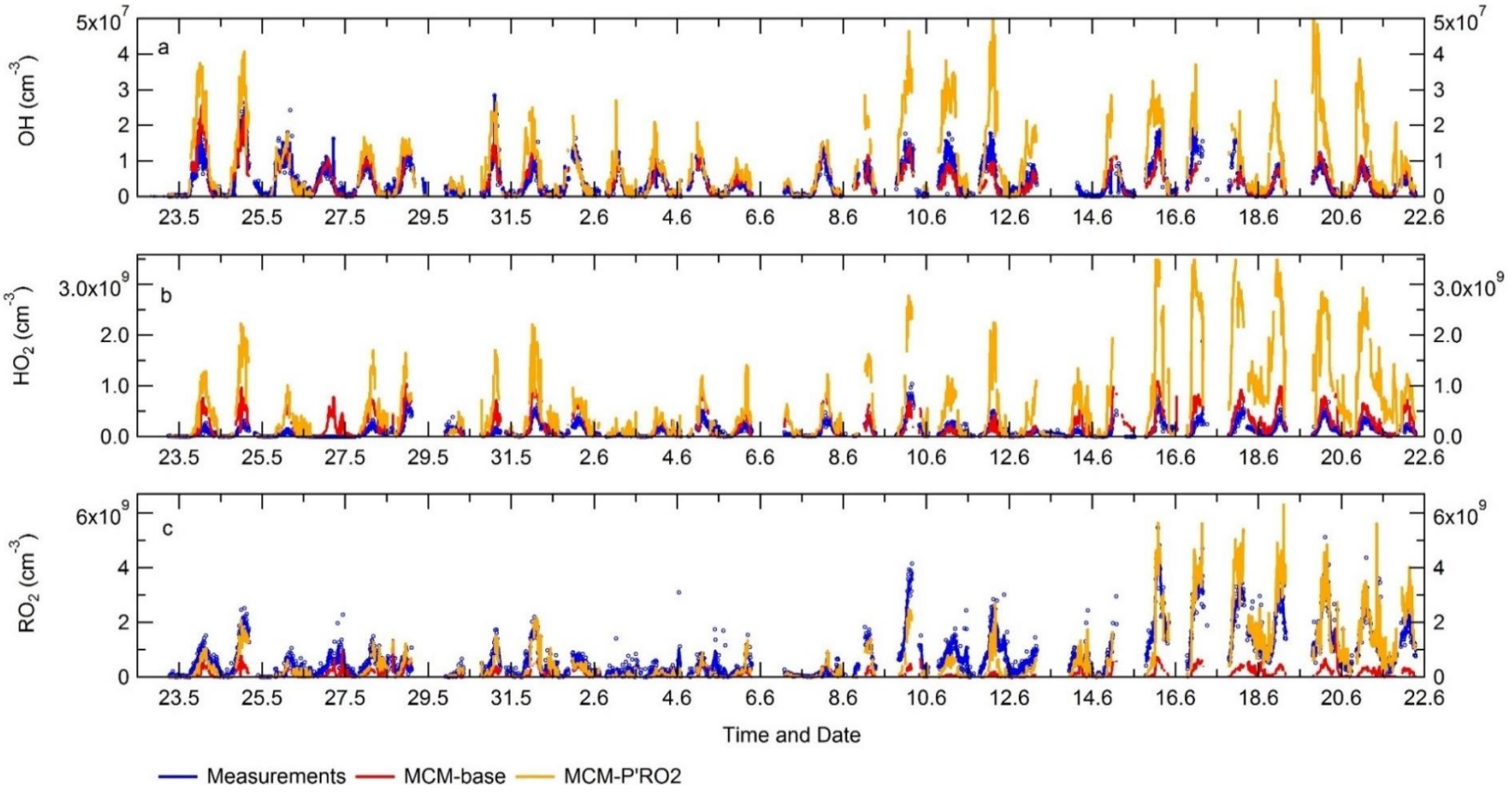

Figure 5.31 a) Time-series of measured OH and OH modelled from MCM-base and MCM-P'RO_2. b) Time-series of measured HO_2 and HO_2 modelled from MCM-base and MCM-P'RO_2. c) Time-series of measured total RO_2 and total RO_2 modelled from MCM-base and MCM-P'RO_2. All of the average diurnals are taken from the entire APHH campaign. The solid lines represent the median whilst the dashed lines represent the mean, only used for MCM-P'RO_2 as the data was not even distributed

5.4.6.3.2 Cl Radical Chemistry

The chlorine atom can act as a major oxidant in the atmosphere (Finlayson-Pitts, 1993), and can oxidise VOCs in a similar fashion to the OH radical but with reaction rates that are up to 2 orders of magnitude faster (Tanaka et al., 2003, Atkinson et al., 1999), and can lead to fast removal of VOCs and formation of O_3. Although it should be noted that Cl atom concentration is generally low (between ~10^3 – 10^4 molecule cm^{-3}). The Cl radicals can originate from several sources including: HCl + OH; photolysis of Cl_2; photolysis of HOCl; photolysis of $ClNO_2$ and finally the photolysis of $ClONO_2$. In an urban environment, such as Beijing, the major sources of Cl atoms are from the photolysis of $ClNO_2$, with $ClNO_2$ being produced by the hydrolysis of N_2O_5 on Cl-containing aerosols (Thornton et al., 2010).

During the APHH summer campaign an iodide CIMS-ToF-MS instrument was used to measure $ClNO_2$ between 03/06/2017 – 19/06/2017. The Master Chemical Mechanism only considers the reactions of Cl with alkanes for which oxidation by Cl may play an important role (see http://mcm.leeds.ac.uk/MCM/ for more details). For this work a more explicit Cl chemistry mechanism was employed alongside the master chemical mechanism, details on the mechanism used can be found in Xue et al. (2015). The model with the additional Cl chemistry is called MCM-Cl from now on. The average diurnal for the measured $ClNO_2$ is shown in Figure 5.32, and shows an expected diurnal trend with the concentration peaking at night-time and a minimum in the afternoon (between 11:00 – 17:00). The median $ClNO_2$ concentration peaks at 250 pptv, and the maximum concentration observed during the summer APHH campaign was 2180 pptv. In the comparison with previous $ClNO_2$ measurements in urban environments: the median concentration measured in central London was 150 pptv with a maximum value of 720 pptv (Bannan et al., 2015); in Houston, Texas the maximum was of $ClNO_2$ measured was 719 pptv (Simon et al., 2009); the maximum concentration in Calgary was 2500 pptv (Mielke et al., 2011); and in Wangdu, China the maximum $ClNO_2$ was 2070 pptv (Tham et al., 2016). The comparison shows that the $ClNO_2$ measurements were similar to other measurements in urban, non-costal environments.

The modelled Cl atoms shows an average maximum mixing ratio just after sunrise at 06:30 of 980 molecule cm^{-3}, with a slow decrease throughout the day with the concentration decreasing to zero at night-time (between 19:00 – 05:30). The influence of introducing Cl chemistry into the model is shown in Figure 5.34, with the time-series of the ratio of MCM-Cl:MCM-base with the Cl concentration overlaid. It shows that the ratio between MCM-Cl:MCM-base increases when the Cl chemistry increases with a maximum difference just after sunrise. Although it also shows that Cl chemistry does not increase the radical concentration significantly from the base model, with a maximum ratio of 1.04 (4% increase), 1.079 (7.9% increase) and 1.19 (19% increase) for OH, HO_2 and total RO_2, respectively. Even though a 19% increase in the total RO_2 is large, the largest impact is occurring at 06:30 when the median total RO_2 from the base model is 3×10^6 molecule cm^{-3} compared with the measured median total RO_2 concentration at 06:30 is 1×10^8 molecules cm^{-3}. The 20% increase from the base model results in a total RO_2 concentration of 3.6×10^6 molecule cm^{-3}, a factor of ~28 smaller than the measured.

Previous modelling studies have found that the production of RO_2 during the CalNex campaign from Cl-oxidation and OH-oxidation was ~25% and ~75% (Riedel et al., 2012), respectively. Work by Le Breton et al. (2018) also showed that in Hong Kong during Mt. Tai Mo Shan (TMS) the campaign Cl chemistry contributed ~22% of the total radical production. Also, for work in CalNex (LA, Riedel et al. (2012)), Houston (Osthoff et al., 2008) and Hong Kong (Le Breton et al., 2018) showed enhancements in ozone by 12 ppbv, 9 ppbv and 10 ppbv when $ClNO_2$ chemistry was used. In comparison, this work showed a maximum increased in ozone production of 0.64 ppbv hr^{-1}, as shown in Figure 5.33, and very little enhancement in the RO_2 radical concentration.

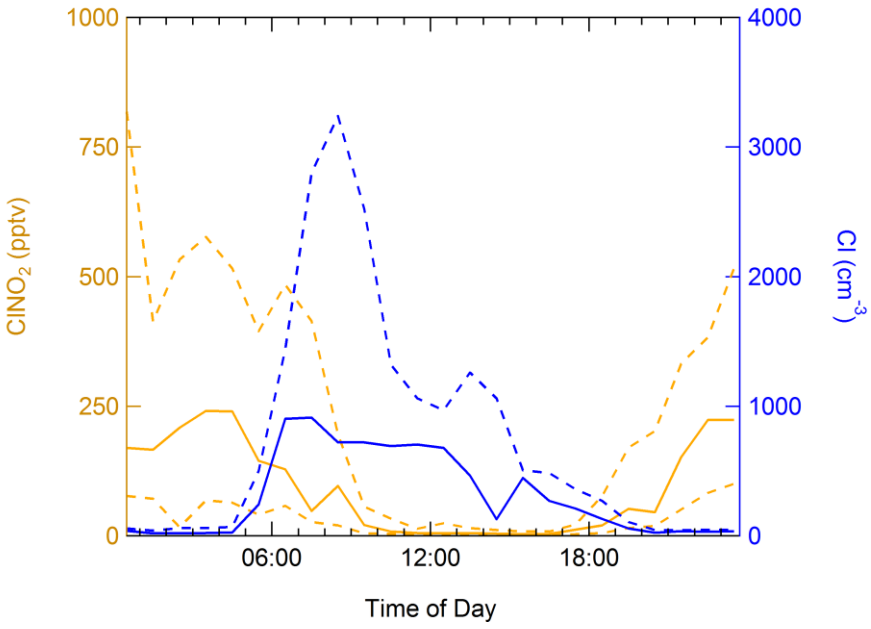

Figure 5.32 Average diurnal of the measured $ClNO_2$ (yellow) from the iodide ToF-CIMS-MS and the modelled Cl atom (blue) concentration. The dashed line denotes the 95th Cl (confidence interval). The data has been average between 03/06/2017 to 19/06/2017 as this was when $ClNO_2$ was available.

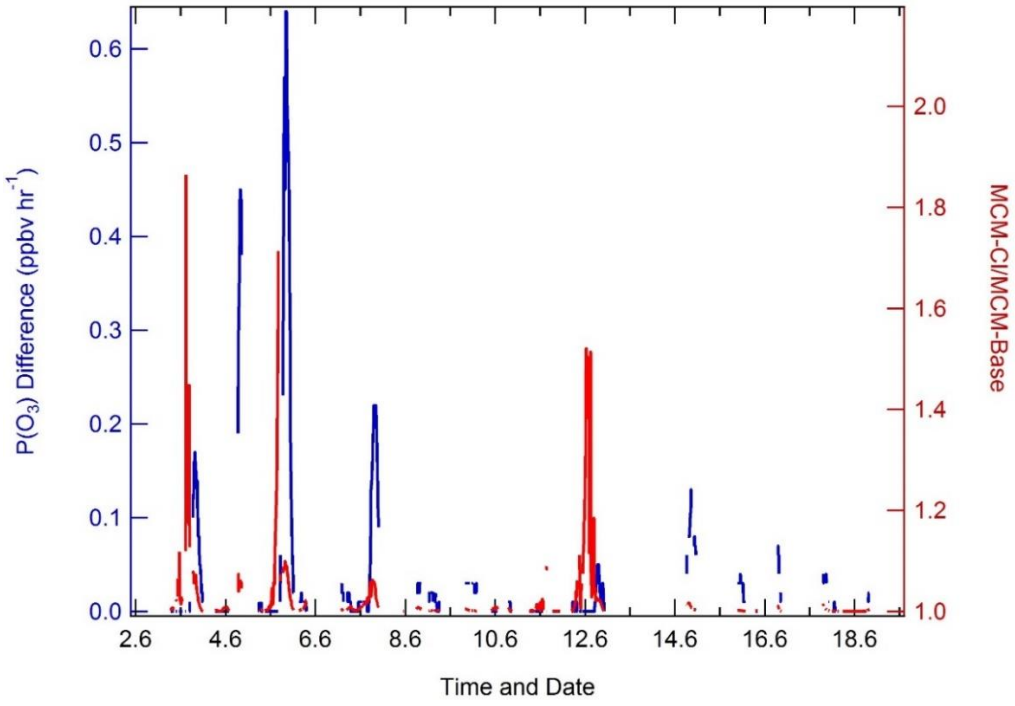

Figure 5.33 Left – The impact of ozone formation from introducing Cl chemistry into the model, the O_3 difference was calculated from subtracting $P(O_3)$ from MCM-base from MCM-Cl. Right – Ratio of MCM-Cl:MCM-Base to show when Cl chemistry has the largest impact on the model.

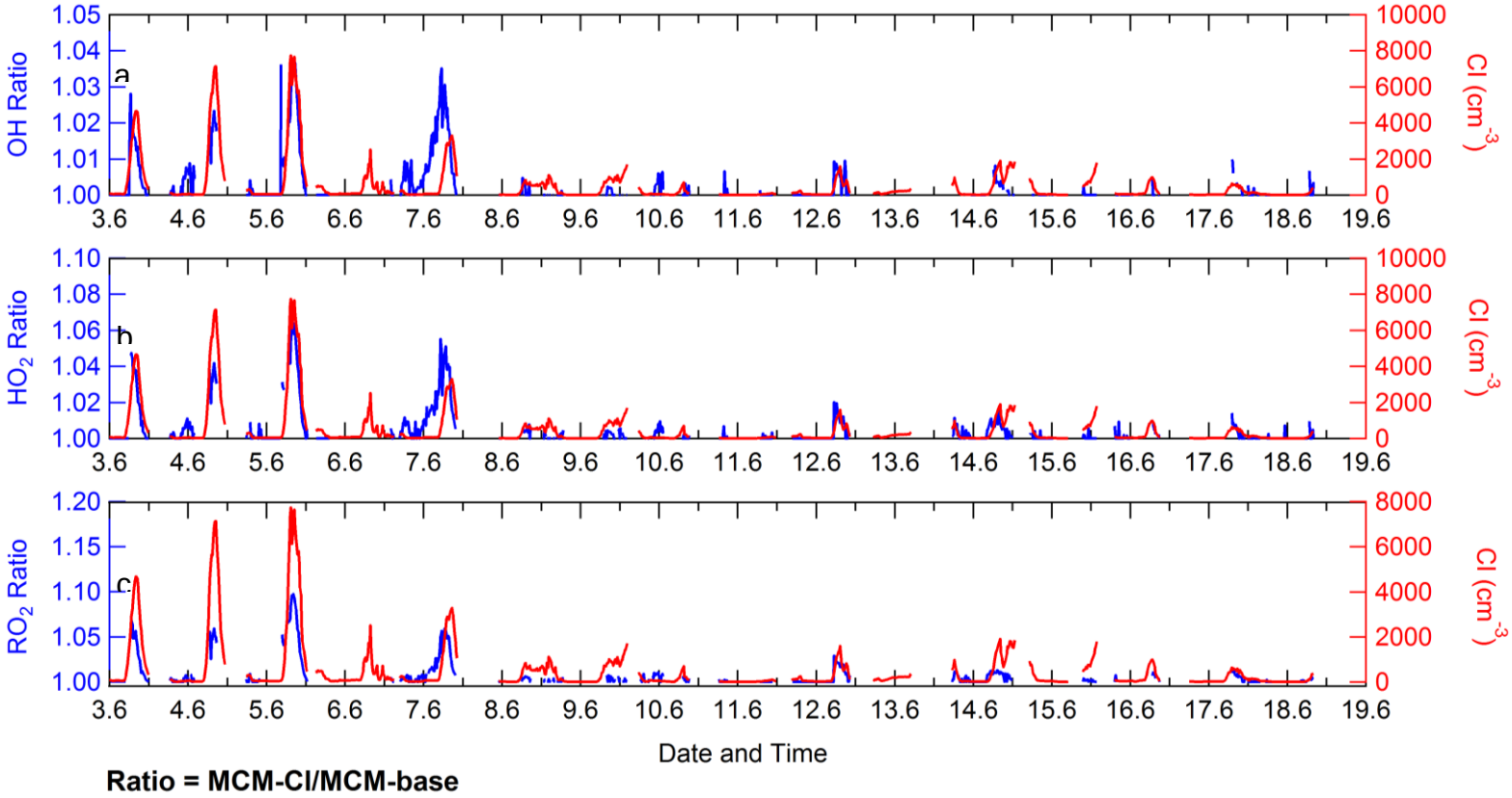

Figure 5.34 a) Time-series of ratio of MCM-Cl:MCM-base for OH(blue|), with the modelled Cl atom concentration shown in red. b) Time-series of ratio of MCM-Cl:MCM-base for HO_2 (blue), with the modelled Cl atom concentration shown in red. b) Time-series of ratio of MCM-Cl:MCM-base for total RO_2 (blue), with the modelled Cl atom concentration shown in red. For all the plots the data is 15-min averaged. The time-series dates are between 03/06/2017 to 19/06/2017 as this was when $ClNO_2$ was available.

5.4.6.4 Dependence on RO_2 + NO rate constants and autoxidation of RO_2

To explore whether autoxidation could be an important process, especially under the lower NO conditions observed in the summer campaign the rate constant of RO_2 + NO was slowed down. Autoxidation is where an RO_2 radical can undergo an inter- or intramolecular H-abstraction. For unsaturated RO_2 radicals, autoxidation can also proceed *via* endocyclization (Jokinen et al., 2014). Functionalised and complex RO_2 groups have weaker C-H bonds compared to pure hydrocarbons, making these molecules more prone to intramolecular H-abstraction. Section.1.2.4 goes into further details of the process of autoxidation.

For most VOCs in the MCM, no autoxidation pathways are included, so there are no competing reactions for RO_2 with NO, HO_2 and RO_2. A rudimentary way to see if the autoxidation pathway may be important is to use a smaller rate constant of RO_2 + NO, and compare the output of the model with both the base model and the measurements. As a part of this work, two models have been run with a decreased rate of kRO2NO and kAPNO by a factor of 2 and 10. In the following the output from these models will be called MCM-kRO2-2 and MCM-kRO2-10 for when the rate constant was changed by a factor of 2 and 10, respectively.

The average diurnal comparison between measurements of OH, HO_2 and total RO_2 with modelled values from MCM-base, MCM-kRO2-2 and MCM-kRO2-10 is shown in Figure 5.35. The comparison for OH shows little variation between measurement and the models, although currently all the models underpredict OH between 08:30 – 11:00. The results from the base model and MCM-kRO2-2 show an overprediction of OH between 12:00 – 18:00 with the maximum overprediction of a factor ~1.12 at 13:00. The MCM-kRO2-10 shows a good agreement for OH after 13:30 with the measurements. All of the models overpredict the measured HO_2, although MCM-base has the largest difference followed by MCM-kRO2-2 then MCM-kRO2-10 with a measured:modelled (at 14:30) ratio of 2.3, 1.96 and

1.41, respectively. This shows that as the rate constant for RO_2 + NO is decreased in the model, the agreement with measured HO_2 is improved. Both the MCM-base and MCM-kRO2-2 shows an underprediction of total RO_2 with a measured:modelled (at 14:30) ratio of 0.27 and 0.4. Whilst the MCM-kRO2-10 shows a good agreement between measured and modelled values with a ratio of 0.91 at 14:30, which is well within the 26% error for the RO_2 measurement. The MCM-kRO2-10 does show an underprediction of RO_2 radicals between 06:30 – 10:30.

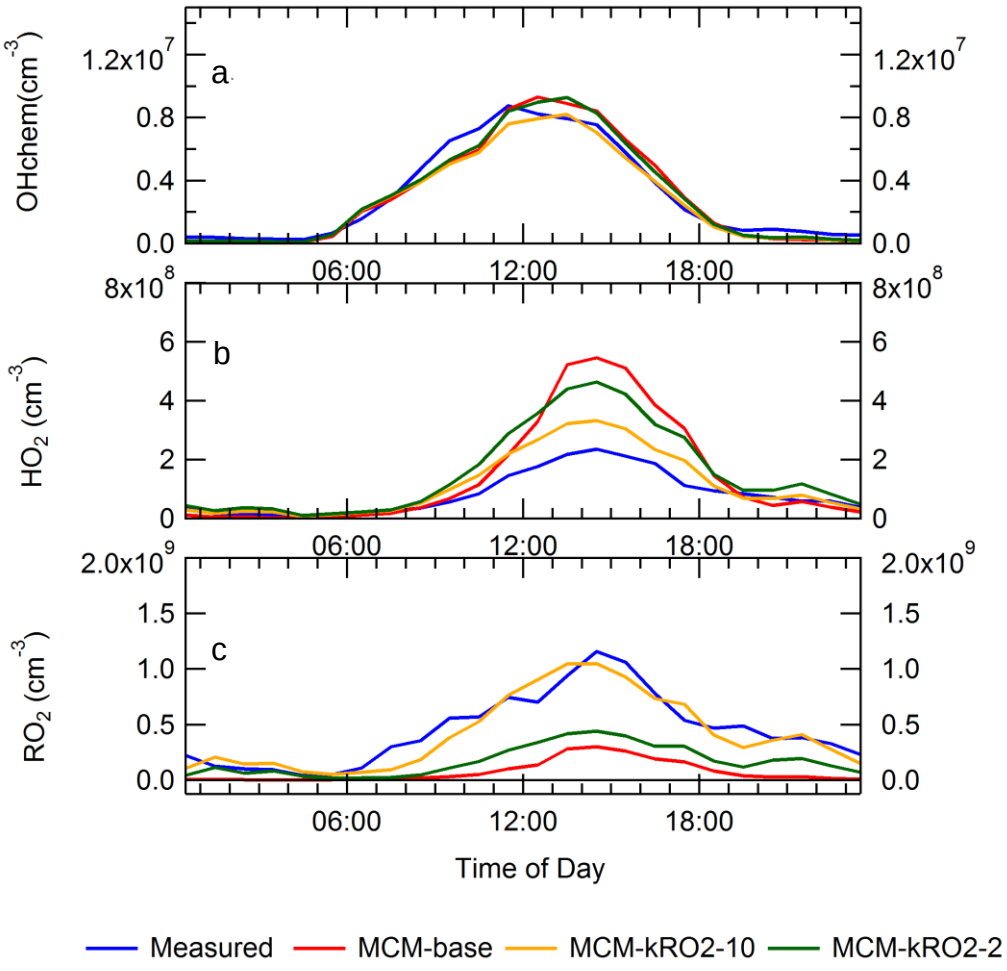

Figure 5.35 a) Average diurnal comparison for measured OH with modelled OH from MCM-base, MCM-kRO2-2 and MCM-kRO2-10. b) Average diurnal comparison for measured HO_2 with modelled HO_2 from MCM-base, MCM-kRO2-2 and MCM-kRO2-10.c) Average diurnal comparison for measured total RO_2 with modelled total RO_2 from MCM-base, MCM-kRO2-2 and MCM-kRO2-10. The average diurnal was averaged across the whole APHH campaign.

The average diurnal comparisons give a general idea of how well the models are doing, and the general trend across the day. To see the day-to-day variation for the comparison between measured values with MCM-base, MCM-kRO2-2 and MCM-kRO2-10, the time-series has been plotted and shown in Figure 5. 36. It shows that the OH modelled concentration is similar between the models, with not much difference between measured:modelled ratio in day-to-day variation. The HO_2 also shows a similar trend to what is observed in the average diurnal, with all the models overpredicitng HO_2 on most days, although HO_2 is underpredicted on 29/05 and between 09/06-13/06. The 09/06 and 13/06 the NO was higher (see section.5.1 for details), suggesting this may be the reason the HO_2 is underpredicted on these days. The overprediction HO_2 trend for the models is MCM-base>MCM-kRO2-2>MCM-kRO2-10.

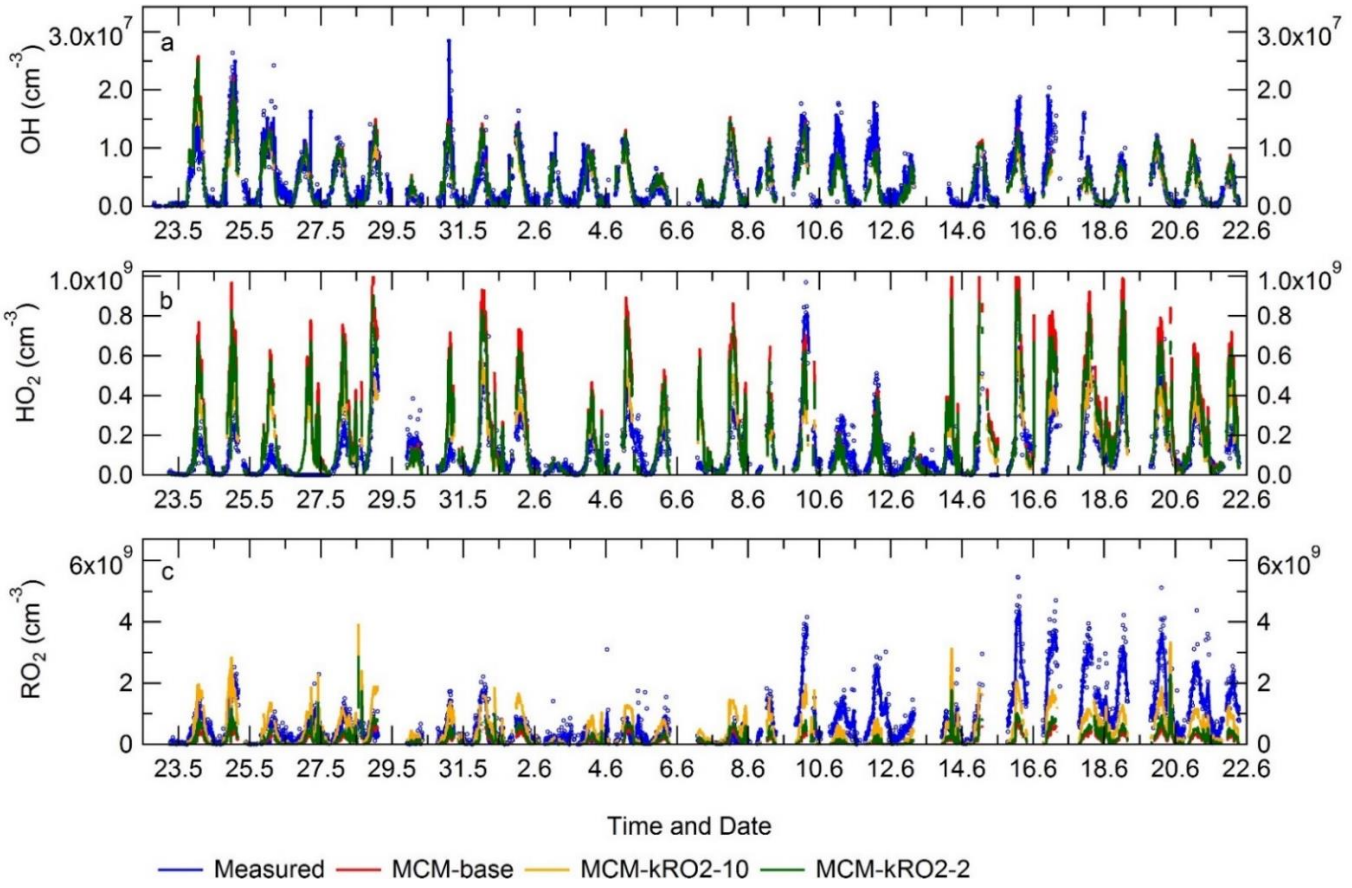

Figure 5. 36 a) Time-series comparison for measured OH with modelled OH from MCM-base, MCM-kRO2-2 and MCM-kRO2-10. b) Time-series comparison for measured HO_2 with modelled HO_2 from MCM-base, MCM-kRO2-2 and MCM-kRO2-10.c) Time-series comparison for measured total RO_2 with modelled total RO_2 from MCM-base, MCM-kRO2-2 and MCM-kRO2-10.

The comparison between the models and measured RO_2 shows a greater day-to-day variation compared to OH and HO_2, with the MCM-kRO2-10 showing a good agreement during the earlier half of the campaign (23/05 – 09/06) and then underprediction towards the end (10/06 – 22/06). The measured RO_2 concentrations are best represented by MCM-kRO2-10, with the trend as follows: MCM-kRO2-10>MCM-kRO2NO-2>MCM-base.

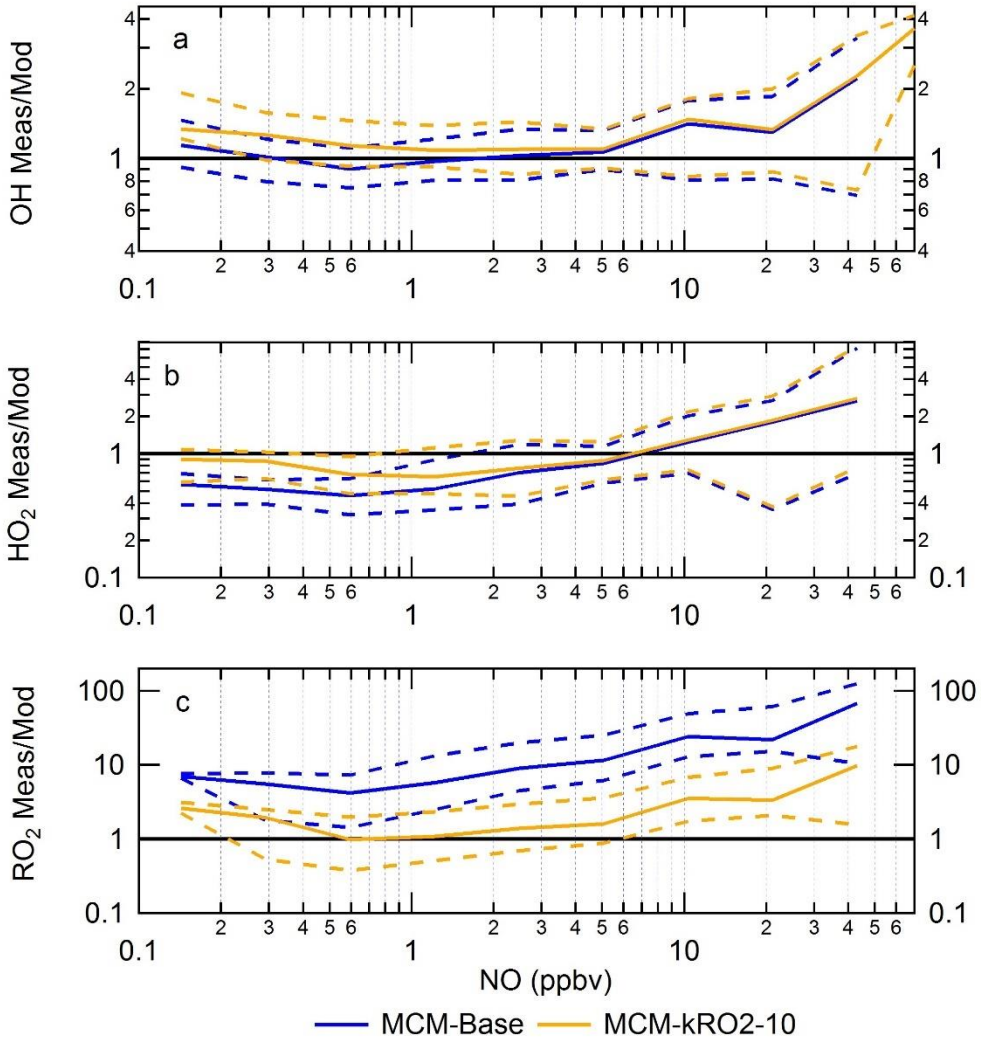

Figure 5.37. The ratio of measurement/model for OH (a), HO_2 (b) and RO_2 (c) across various NO concentrations for daytime values only ($j(O^1D) > 1 \times 10^{-6}$ s^{-1}). Yellow represents for results from MCM-kRO2NO-10, and blue represents results from MCM-base. The dashed line represents the 95% CI.

To see how well the MCM-kRO2-10 model preforms across different NO ranges compared to MCM-base, the measured:modelled ratio had been binned to the

log of the [NO], as shown in Figure 5.37. The x-axis is logNO to evenly distribute the data points between the bins as there is less data at the higher NO concentrations. It shows that at higher NO concentrations (above 2 ppbv) both MCM-base and MCM-kRO2-10 underpredict OH and HO_2 at similar ratios. Below 2 ppbv of NO the ratios for MCM-base and MCM-kRO2-10 start to diverge, with a ratio of 1 for MCM-kRO2-10 between 0.6 – 2 ppbv of NO and with the model starting to underpredict the OH below 0.6 ppbv of NO. The HO_2 measured:modelled ratio is closer to 1 below 2 ppbv of NO compared to MCM-base, and starts to have a ratio of ~1 below 0.3 ppbv of NO. The RO_2 modelled:measured ratio is improved across the whole range of NO, although MCM-kRO2-10 still underpredicts total RO_2 above 1.5 ppbv and below 0.5 ppbv.

HOMs were measured during the APHH campaign in both the gas-phase and particle-phase using an iodide-anion chemical ionisation mass spectrometer equipped with a filter inlet for gases and aerosols (FIGAERO-I-CIMS) (Lopez-Hilfiker et al., 2014) deployed by the University of Manchester (Zhou et al., 2018). It should be noted that the gas-phase HOMs data is preliminary while the particle-phase HOMs data is finalised. The HOMs measured in the gas-phase compared with the measured total RO_2 is shown in Figure 5.38. Figure 5.38 shows that in general the measured gas-phase HOMs and measured total RO_2 have the same trend across the time-series. However, the measurements do deviate at the start of the comparison period between 05/06/2017 – 06/06/2017 when the gas-phase HOMs increase significantly, but the RO_2 concentration does not. The general trend for the gas-phase HOMs is more easily seen in the average diurnal shown in Figure 5.38. The average diurnal for total RO_2 and gas-phase HOMs both start to increase just after sunrise (~05:00), but the gas-phase HOMs peak earlier (~11:30) compared to total RO_2 concentration (peaks at ~13:30). The decrease in both the HOMs and total RO_2 track each other well between 14:30 – 18:30, and then both species also show a secondary night-time peak between 18:30 – 23:30. The Pearson's correlation coefficient for the gas-phase HOMs correlated with radical species and O_3, NO and temperature is shown in Figure 5.39 as a heatmap. Figure 5.39 shows that strong correlation with gas-phase HOMs is observed for O_3 ($r = 0.66$), temperature ($r = 0.67$), OH ($r = 0.57$), HO_2 ($r = 0.56$), total RO_2 ($r = 0.57$), simple RO_2 ($r = 0.58$) and complex

RO_2 (r = 0.53). The relatively strong correlation for gas-phase HOMs with measured RO_2 highlights the relationship between RO_2 species and the process of autoxidation for HOM formation. This is the first time that measured RO_2 and HOM species have been compared side-by-side in an ambient field campaign.

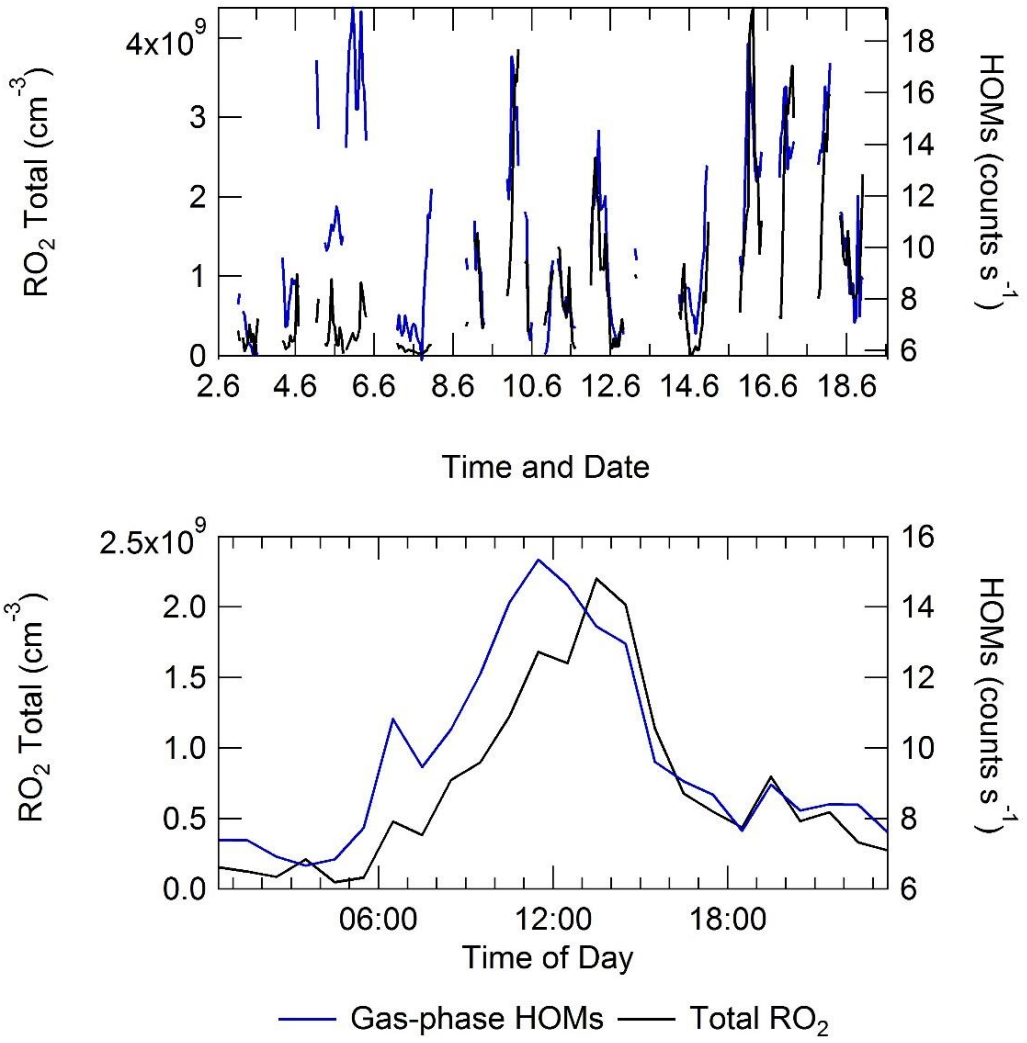

Figure 5.38 Top – Timeseries comparison of measured total RO_2 and measured gas-phase HOMs. The resolution of the HOMs data is 1h whilst the radical data has been averaged to 1h. Bottom – 60-minute average comparison of measured total RO_2 and gas-phase HOMs.

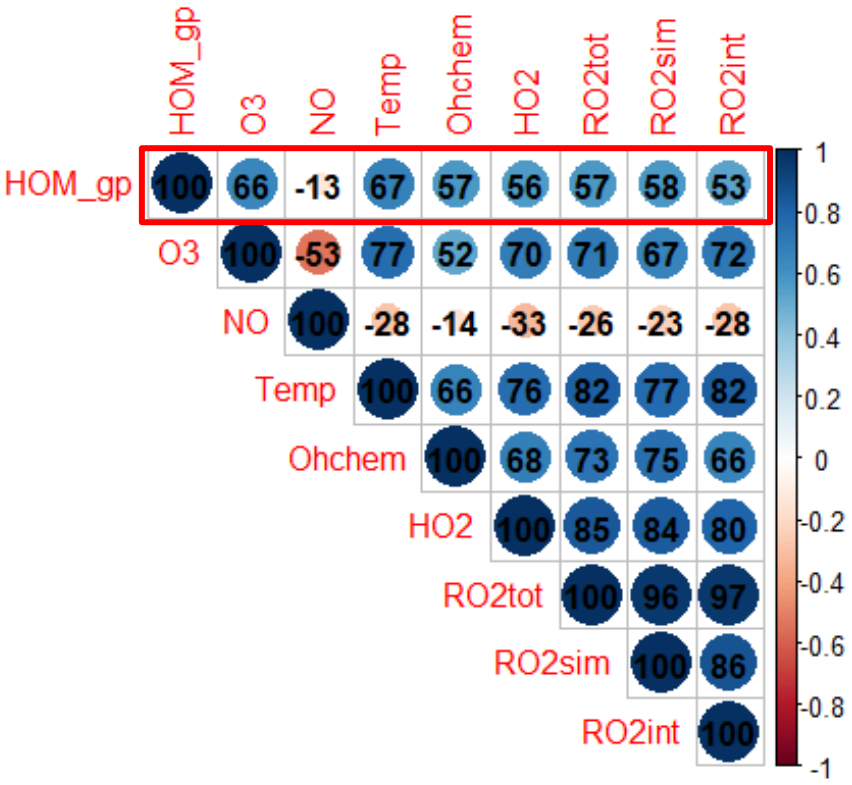

Figure 5.39 Pearson' correlation coefficient for gas-phase HOMs (HOM_gp) with O_3, NO, temperature (Temp) and radical species. The Pearson's correlation coefficient has been multiplied by 100.

Autoxidation results in formation of lower volatility compounds and thus some of the gas-phase HOMs may partition into the aerosol phase. During the APHH summer campaign, the FIGAERO-CIMS also measured HOMs in the aerosol-phase and a positive matrix factorization (PMF) approach (Paatero and Tapper, 1994, Zhang et al., 2011) was utilised to gain more insight into the sources and chemistry of SOA. PMF is a well-established technique used in atmospheric sciences to identify the sources of trace gases and aerosol particles (Massoli et al., 2018, Ulbrich et al., 2009, Yan et al.,2016). The PMF analysis was performed by Archit Mehra at the University of Manchester; of the factors identified, three factors related with the afternoon time: F4 which is related to high NO_x periods; F5 which is related low NO_x periods, high temperatures and south-westerlies and F7 which is related to low NO_x periods (Mehra et al., in prep). These factors are made up of many ions which show similar temporal variability including both HOM and non-HOM ions. F4, F5 and F7 contain between 20 –

27% contribution from HOMs to the signal of these factors, detailed composition analysis will be presented in Mehra et al. (in prep). F5 and F7 also shows strong diurnal profile, whilst F4 does not. This is consistent with previous observations which have that though some HOM species show distinct diurnal patterns, total HOMs often do not (Bianchi et al.,2019). The Pearson's correlation coefficient of the total particle-phase HOMs, F4, F5 and F7 with O_3, NO, temperature and radicals (OH, HO_2 and RO_2) is shown in Figure 5.40 as a heatmap. The particle-phase HOMs, F4 and F7 do not show a strong correlation with the trace gases or radical species ($r < 0.25$). Whilst F5 shows a strong correlation with OH ($r = 0.47$), HO_2 ($r = 0.51$), total RO_2 ($r = 0.62$), simple RO_2 ($r = 0.56$), complex RO_2 ($r = 0.64$), O_3 ($r = 0.57$) and temperature ($r = 0.69$) and may suggest that the gas-phase HOMs produced from autoxidation of RO_2 species are partitioning into particle-phase HOMs in summertime Beijing when the NO is low.

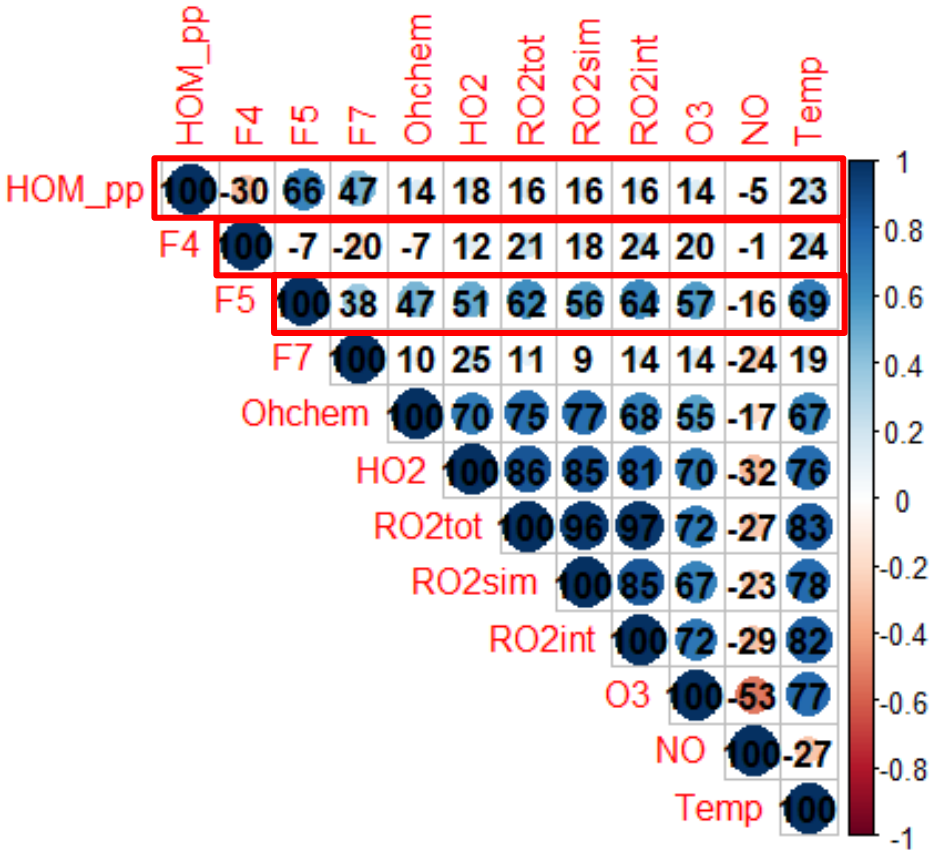

Figure 5.40 Pearson' correlation coefficient for particle-phase HOMs (HOM_pp), F4, F5 and F7 with O_3, NO, temperature (Temp) and radical species. F4, F5 and F7 represent the results from the PMF analysis for factor relating to afternoon periods. The Pearson's correlation coefficient has been multiplied by 100.

The strongest correlation for peroxy radicals with F5 is from complex RO_2 species (0.64) and in Mehra et al. (in prep) ions associated this factor have been related to aromatic oxidation in observed in laboratory experiments (Mehra et al., 2019). Overall, these three factors contribute 43% of the total particle-phase signal. F5 and F7 shows a strong correlation with total particle-phase HOM signal, whilst F4 shows a weak negative correlation (r=0.3). F5 and F7 together contain more of the HOM variability; F4 contains less HOMs and thus show a poor correlation with total HOM particularly because F4 is a more dominant component of the particle-phase when total HOMs are low. The stronger correlation with complex RO_2 species also reiterates this statement as the measured complex RO_2 will contain species derived from aromatic VOC oxidation (see section.2.1.8 for details). This work suggests that the autoxidation of aromatic species maybe resulting in the formation of particle-phase HOMs and contributing to SOA.

5.4.7 Impact of HONO

HONO was found to be an important primary source of OH during the APHH summer campaign (see section.5.4.4.4), and as discussed in section.1.2.5 in general measurements of HONO disagree with the model (MCM-base). The disagreement between measurements and model for HONO is thought to be caused by additional heterogeneous sources of HONO, this has been discussed more in section.1.2.5. The MCM-base model has been constrained to the measurements of HONO made during the APHH winter campaign, section.5.4.7.1 shows the impact of unconstraining the model to HONO on both the modelled HONO and OH mixing ratios. The reaction involved in the production and destruction of HONO in the MCM is shown in Table 5.6.

Reaction	Rate coefficient at 298 K
$OH + NO \rightarrow HONO$	9.76×10^{12} cm^3 molecule^{-1} s^{-1}
$HONO + hv \rightarrow OH + NO$	6×10^{-4} s^{-1}
$HONO + OH \rightarrow NO_2$	5.98×10^{-12} cm^3 molecule^{-1} s^{-1}

Table 5.6 Table showing the reaction in the MCM for the production and destruction of HONO.

5.4.7.1 Model unconstrained to HONO

The MCM-base model has been modified by unconstraining MCM-base to HONO (MCM-unHONO), and Figure 5.41 shows the average diurnal comparison of measurements of OH and HONO with MCM-unHONO. MCM-unHONO average diurnal does not capture the trend of the HONO measurement, with the modelled HONO concentration increasing throughout the day between 08:30 – 22:30. Also MCM-unHONO underpredicts the HONO concentration throughout the day, with the largest underprediction at 05:30 by a factor of ~9.2. The average underprediction across the entire day is by a factor ~3.1. The smallest underprediction is observed at 16:30 by a factor of 1.5, as the measured HONO concentration is at a minimum through loss from photolysis.

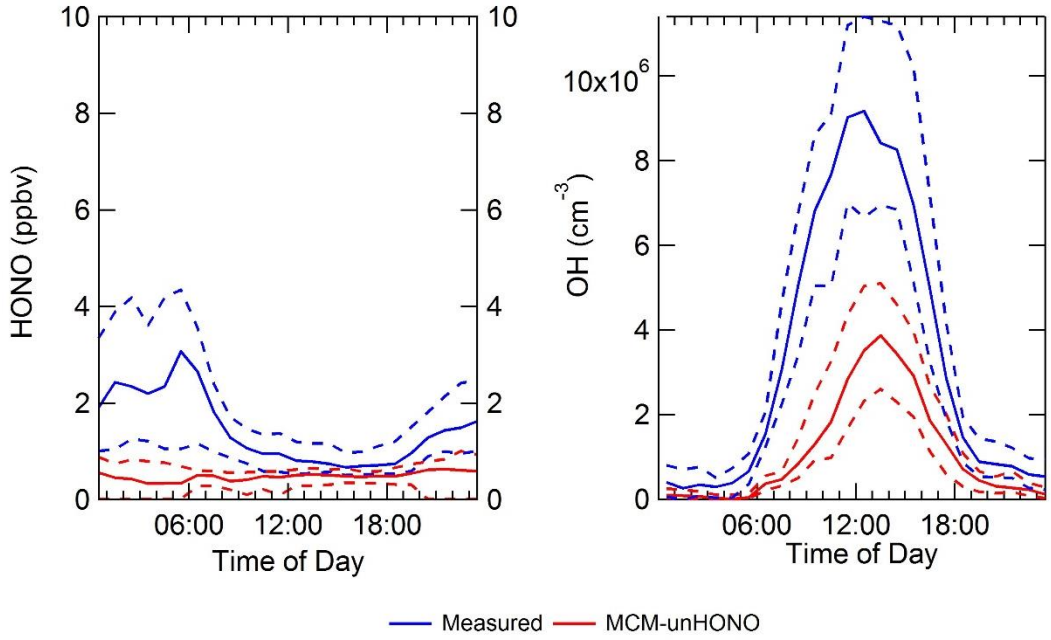

Figure 5.41 Average diurnal comparison of measurements (blue) with MCM-unHONO(red) for OH(right) and HONO (left). The average diurnals were calculated from the entire summer APHH campaign period. The dashed lines represents the 95 CI (confidence interval).

Figure 5.41 also shows the comparison of measured OH and modelled OH from MCM-unHONO. MCM-unHONO underpredicts the OH concentration by a factor of 2.2, whilst the model constrained to HONO (MCM-base) replicates the OH concentration very well. The decrease in the model's ability to predict OH from MCM-base to MCM-unHONO is caused by MCM-unHONO not replicating the

HONO concentration, and since HONO is an important primary source of radicals during the APHH summer campaign, the impact on the MCM-unHONO to predict OH is large. This work highlights the importance of using measured HONO in models, and that there is currently missing understanding for the production of HONO.

5.4.7.2 Model constrained to OH

The only source of HONO in the MCM is the reaction of OH + NO, although OH + NO in previous studies cannot reconcile the measurements of HONO with the model. To investigate how much HONO during the APHH summer campaign was produced through OH + NO, the MCM-base model was modified. The MCM-base model was constrained to the measurements of OH and unconstrained to HONO; the modified model was called MCM-cOH-unHONO. The average diurnal comparison of measured HONO and the results from MCM-cOH-unHONO is shown in Figure 5.42, and shows that the HONO predicted by MCM-cOH-unHONO does not show a distinct diurnal pattern for HONO, whilst the measurements show a large decrease after sunrise with a minimum at 16:30.

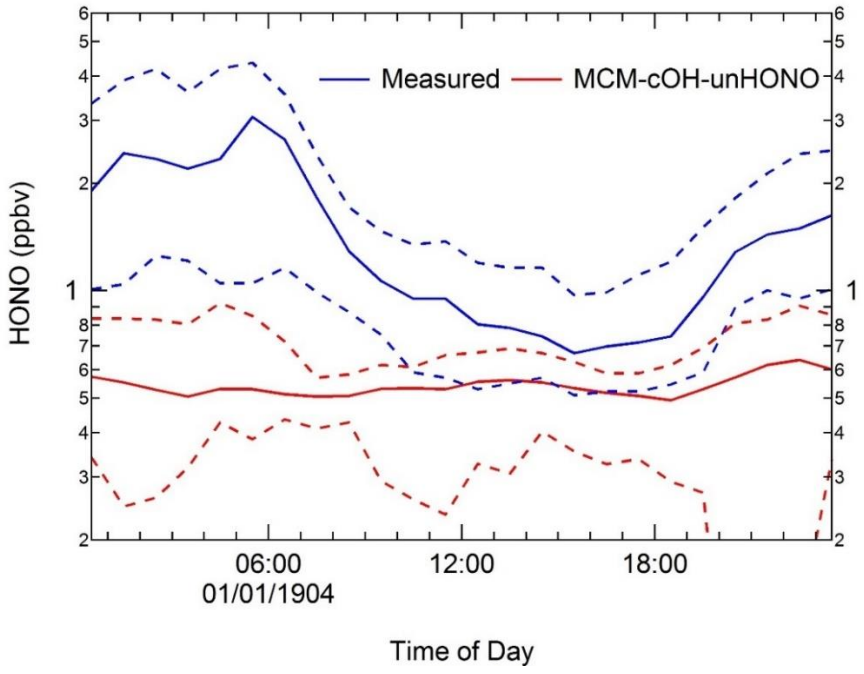

Figure 5.42 Average diurnal comparison of measured HONO with the results from MCM-cOH-unHONO. The average diurnal was averaged across the whole of the APHH winter campaign. 95 CI (confidence interval).

The average underprediction across the entire day is by a factor ~3.4, and shows a small improvement from MCM-unHONO (underpredicted measured HONO by ~3.1). MCM-cOH-unHONO underpredicts the HONO concentration throughout the day, with the largest underprediction at 05:30 by a factor of ~6. The smallest underprediction is observed at 16:30 by a factor of 1.3, as the measured HONO concentration is at a minimum through loss from photolysis. The comparison with the underprediction throughout the entire day suggests that the reaction of OH + NO is not a sufficient source of HONO and additional heterogeneous sources of HONO are required to reconcile the model with measurements. Additional heterogeneous sources of HONO has not been explored in this work.

5.4.8 Missing OH reactivity

5.4.8.1 OH Reactivity Comparison

For many campaigns, the measurements of OH reactivity are typically higher than those predicted (Yang et al., 2016), with the differences between measured and modelled OH reactivity often referred to as missing reactivity. Missing reactivity is generally largest in forested environments (Nakashima et al., 2014, Sinha et al., 2010, Di Carlo et al., 2004, Edwards et al., 2013, Nölscher et al., 2012) with both missing primary emissions and their oxidised intermediates (OVOCs) considered as sources. In contrast to forested environments, many urban campaigns have a closed OH reactivity budget when only considering OH reactivity from calculated rather than modelled sources. This shows that model intermediates do not contribute significantly to the OH reactivity in certain cities. Also, when comparing measured OH reactivity and missing OH reactivity, it is important to consider whether the missing reactivity is statistically significant. Measurement uncertainties can be assessed for each measurement technique. It is not straightforward to estimate the uncertainties in the calculated OH reactivities, as it should consider the errors in the OH rate constant and the trace gas measurement. For the trace gas species errors from precision, accuracy and difference in timescales for different measurement techniques need to be taken into account. The uncertainty using the sources of error mention above has previously been estimated between 25 – 30% (Barker et al., 2017).

A comparison of OH reactivity and its percentage contribution from NO_x, CO, hydrocarbons (HC), OVOCs and missing reactivity for different cities is shown in Figure 5. 43. Figure 5. 43 shows that averaged between different campaigns, the contribution to total reactivity from various source as follows: NO_x is between 20 – 50%; hydrocarbons is between 20 – 55%; OVOCs between 10 – 25% and CO between 7 – 15%. Also, the contribution from other inorganic species is negligible. The comparison for different campaigns shows that no missing OH reactivity was observed for PMTAC-NY (Mao et al., 2012), MCMA2003 (Mao et al., 2010), TRAMP2003 (Mao et al., 2010), LILLE2012 (Hansen et al., 2015) and TEXAQS2000 (Mao et al., 2010). Whilst missing reactivity was observed during the APHH campaign (35%), CLearFLo (Whalley et al., 2016) (15%), TOKYO2003 (Yoshino et al., 2006) (14%), TOKYO2007 (Chatani et al., 2009) (30%) and MEGAPOLI (Dolgorouky et al., 2012) (56%). Although as discussed above only missing reactivity above ~25% may be statistically significant with both CLearfLo and TOKYO2003 below this threshold. The MEGAPOLI campaign in Paris saw a missing OH reactivity of 70 – 80 s^{-1} when the airmass sampled was continental.

For the MEGAPOLI campaign, Dolgorouky et al.(2012) highlighted that the airmasses that exhibited larger missing OH reactivity were characterised by large emissions from photochemical processing, and suggested that the missing reactivity was likely due to unmeasured oxidation species that are currently not measured by conventional techniques. The closure of the OH reactivity budget in New York (PMTACS-NY) and Lille may reflect the dominance of NO_x, with NO_x contributing ~51% and 45%, respectively to total OH reactivity. Also, different cities will have a different suite of VOCs such as the Houston campaign having 15% of the reactivity from aromatic species due to its location close to petrochemical industries, whilst in places like Tokyo, aromatics only accounted for 5% of the total OH reactivity. However, care is needed when comparing different VOCs as different projects will have a different suite of measurements. Whilst oxygenated VOCs or biogenic species (in addition to isoprene) are often measured this is not always the case especially for urban campaigns (Barker et al., 2017).

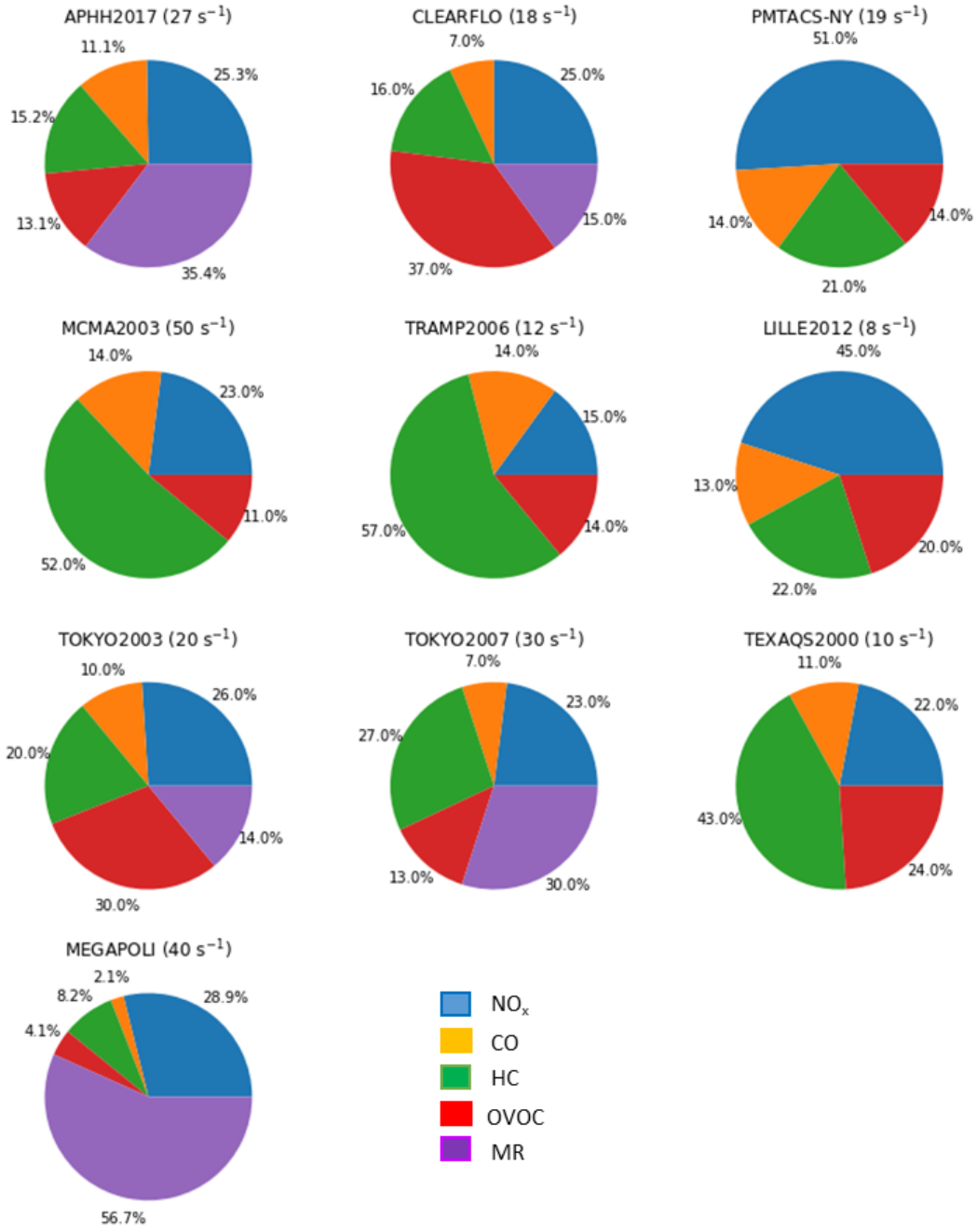

Figure 5. 43 Contributions of atmospheric compounds to total OH reactivity for a variety of urban field campaigns. Only the summer period is shown for TOKYO2003, and OH reactivity for TEXASAQS2000 are only for ambient NO conditions below 1 ppbv. HC, OVOC and MR represent the OH reactivity from hydrocarbons, oxidised volatile organic compounds and missing reactivity, respectively.

5.4.8.2 Filling the missing OH reactivity gap

As discussed in section.5.4.4.3, missing reactivity was observed for the summer APHH campaign. This section will explore filling the reactivity gap with different species, and the results will be compared with measured and modelled(MCM-base). The missing reactivity gap was filled throughout the time-series with species 'A' to form different peroxy radical species (CH_3O_2, CH_3CO_3 and $C_6H_5O_2$). For the MCM-kOH-CH3O2 the methyl peroxy radical was chosen product to represent a simple peroxy radical whose chemistry has been previously studied. For the MCM-kOH-CH3CO3, the CH_3CO_3 radical was the chosen product as currently PAN is underpredicted in the model, and CH_3CO_3 is a major source of PAN. For the MCM-kOH-C6H5O2 the $C_6H_5O_2$ was chosen as the major product as the $C_6H_5O_2$ peroxy radical does not recycle into HO_2.

The average diurnal comparison between measurements of OH, HO_2 and total RO_2 with results from MCM-base, MCM-kOH-CH3O2, MCM-kOH-CH3CO3 and MCM-kOH-C6H5O2 are shown in Figure 5.44. Figure 5.44 shows that the radical concentration is highly dependent upon the VOCs/peroxy radical that is formed. The OH concentration in all the models (relative to MCM-base) has been reduced as OH reactivity has been increased. Whilst MCM-kOH-CH3O2 reproduces the OH well in the afternoon hours (after 13:00) the OH is underpredicted in the morning hours (07:00 – 13:00). MCM-kOH-CH3O2 also increases the overprediction of HO_2 and on average at midday HO_2 is overpredicted by ~3.6. Although MCM-base overpredicts the HO_2 by a factor of ~2.3. Also, whilst RO_2 agreement between measured:modelled ratio is improved in MCM-kOH-CH3O2, the RO_2 species are still underpredicted in the model by a factor of 1.6. The impact of filling the reactivity gap with CH_3CO_3 shows that it reduces the OH predicted in the model compared with MCM-base. The model (MCM-kOH-CH3CO3) underpredicts OH by a factor ~2.1. Whilst the OH in MCM-kOH-CH3CO3 is underpredicted, the agreement between measured:modelled HO_2 is improved compared to MCM-base, with an average overprediction of factor ~2. The HO_2 is improved as the model concentration is decreased because the OH concentration has decreased. The RO_2 concentration modelled from MCM-kOH-CH3CO3 is very similar to that from MCM-base. Finally, filling the missing OH reactivity gap with $C_6H_5O_2$ leads to the largest

underprediction for OH from the models with extra OH reactivity, with an underprediction of ~2.7. Whilst the HO_2 is predicted well by MCM-kOH-C6H5O2, with a ratio of 0.95 at peak HO_2 (14:30). MCM-kOH-C6H5O2 underpredicts RO_2; the largest underprediction between the all the models with extra OH reactivity. These three models show that it is important which species is used to fill in the OH reactivity gap, as it can affect the model OH, HO_2 and RO_2 concentration in varying ways. It also shows that none of these species can completely reconcile the model with the measurements for OH, HO_2 and RO_2.

To assess the effect of filling the OH reactivity gap with different RO_2 species across different NO ranges, the ratio of measured:modelled OH, HO_2 and total RO_2 has been binned against NO and is shown in Figure 5.45. For MCM-kOH-CH3O2, the ratio of measured:modelled OH is not changed from MCM-base above 2 ppbv of NO, whilst below 2 ppbv the ratio starts to show a larger underprediction of OH. Whilst the ratio of measured:modelled OH in MCM-kOH-CH3O2 is not affected above 2 ppbv of NO, the ratio for HO_2 and RO_2 is changed. HO_2 has a larger overprediction and whilst in the MCM-base case the underprediction occurs at NO concentration below ~7 ppbv, for MCM-kOH-CH3O2 the underprediction starts at NO ~20 ppbv.

Compared with MCM-base, the RO_2 measured:modelled ratio is improved through the whole NO range. Both MCM-kOH-CH3CO3 and MCM-kOH-C6H5O2 ability to predict OH is reduced for the whole NO range compared to MCM-base, with the models underpredicting OH concentration. The MCM-kOH-CH3CO3 improved the agreement between measured:modelled HO_2, compared with MCM-base, through the whole range by decreasing the underprediciton and overprediction above and below 7 ppbv, respectively. Whilst MCM-kOH-C6H5O2 underpredicts the HO_2 concentration throughout the whole NO range, the ratio (~1.1) is close to 1 below 1 ppbv, whilst MCM-base shows a large underprediction with a ratio ~ 0.6 below 1 ppbv of NO. At low NO (below 1 ppbv) concentrations, the MCM-kOH-CH3CO3 ratio of measured:modelled RO_2 concentration is the same as MCM-base, whilst at higher NO concentration (above 1 ppbv) MCM-kOH-CH3CO3 improves the agreement with measurements. Finally, the MCM-C6H5O2 has the largest undeprediction of OH throughout the whole NO

range, and increases the measured:modelled ratio compared with MCM-base throughout the whole NO range.

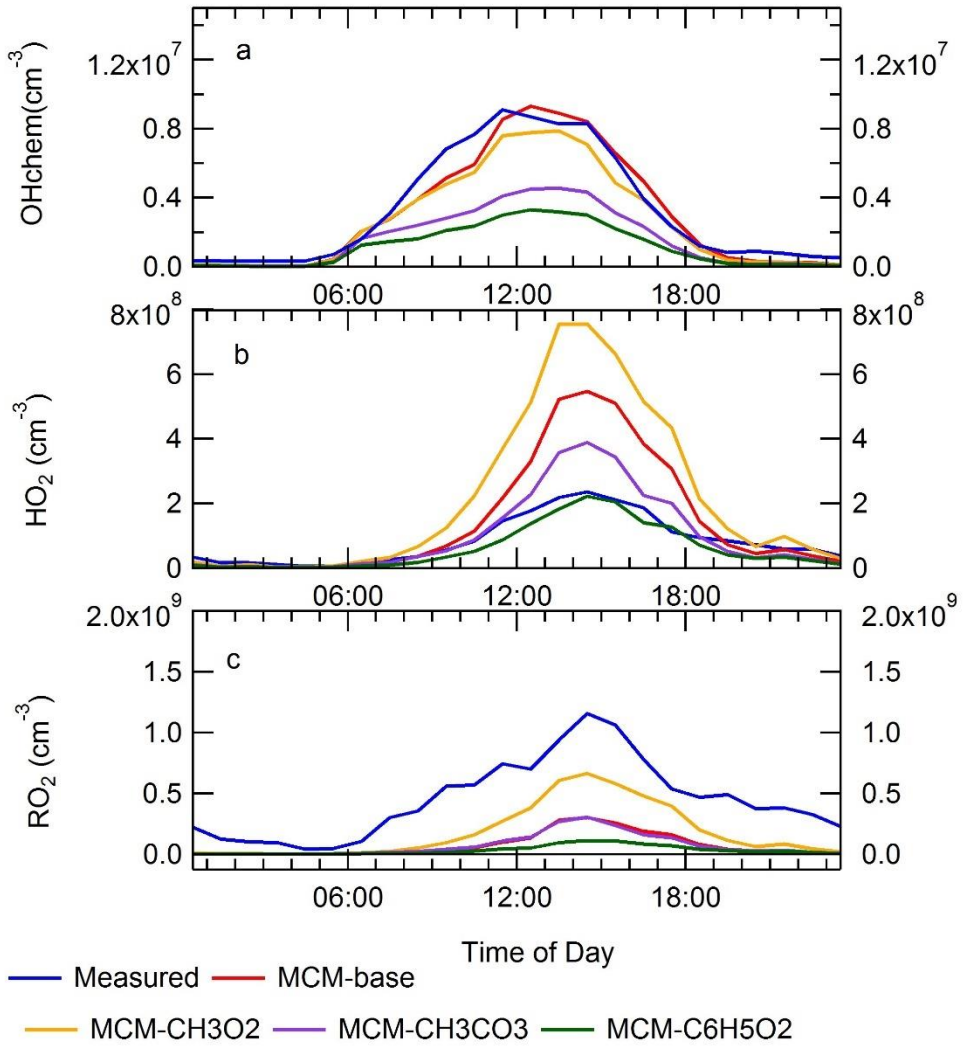

Figure 5.44 a) Average diurnal comparison between OHchem and the modelled OH from both the MCM-base, MCM-kOH-CH3O2, MCM-kOH-CH3CO3 and MCM-kOH-C6H5O2. b) Average diurnal comparison between measured HO2 and MCM-base, MCM-kOH-CH3O2, MCM-kOH-CH3CO3 and MCM-kOH-C6H5O2. c) Average diurnal comparison between measured total RO2 and total RO2 modelled from MCM-base, MCM-kOH-CH3O2, MCM-kOH-CH3CO3 and MCM-kOH-C6H5O2. The entire campaign period was average to make the diurnals, the diurnals are 1-hour averages.

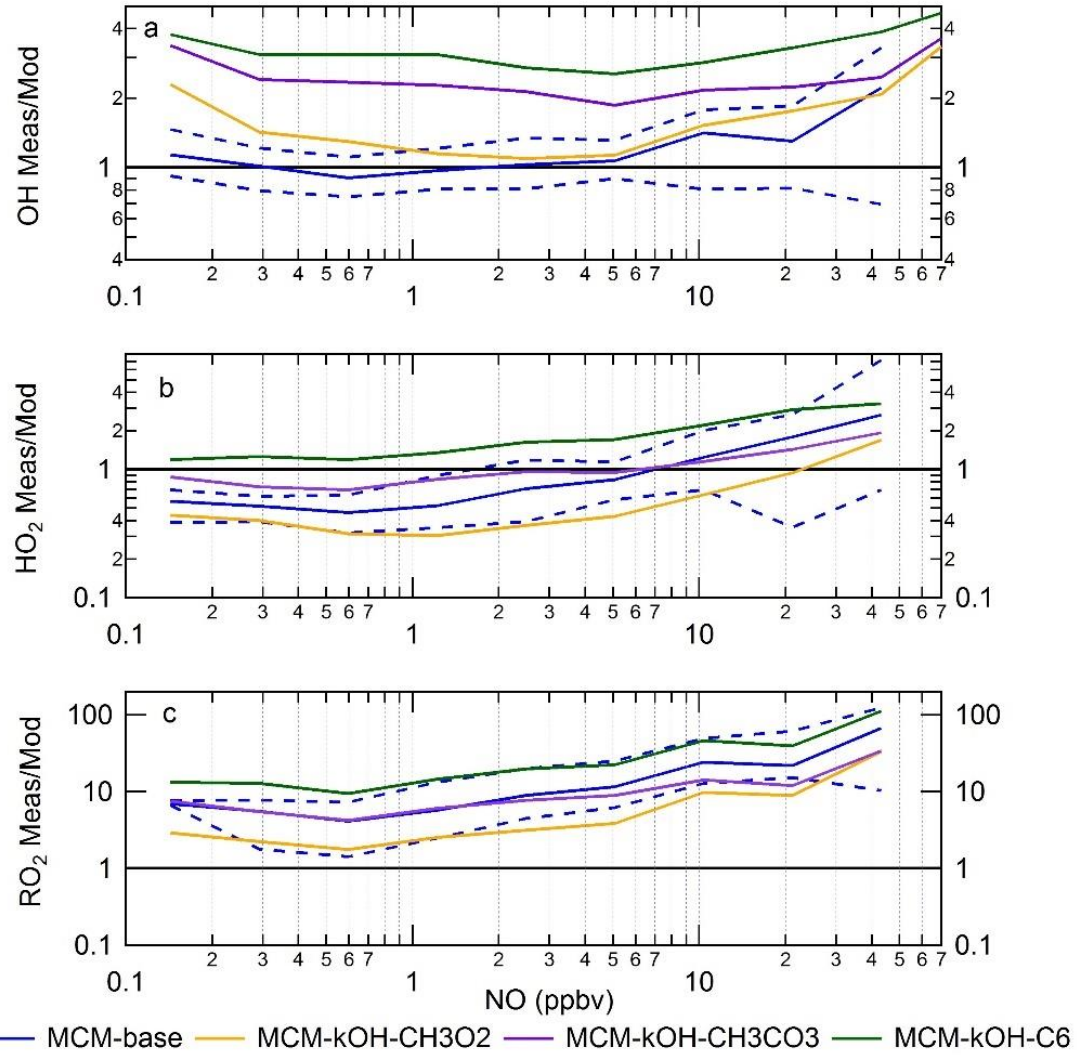

Figure 5.45 The ratio of measurement/model for OH (a), HO_2 (b) and RO_2 (c) across various NO concentrations for daytime values only ($j(O^1D) > 1 \times 10^{-6}$ s^{-1}). Yellow represents for results from MCM-kOH-CH3O2, blue represents results from MCM-base, purple represents results from MCM-kOH-CH3CO3 and green represents results from MCM-kOH-C6H5O2.

As discussed earlier the modelled PAN was underpredicted by the MCM-base model, whilst the deposition rate for oxidised intermediates was optimised to match measurement and modelled values of glyoxal (see section.5.4.4.1 for more details). The species CH_3CO_3 was chosen to fill the OH reactivity gap for one of the models (MCM-kOH-CH3CO3) and to assess if this could reconcile the PAN observed. This section will explore the effect of filling the OH reactivity gap with CH_3O_2, CH_3CO_3 and $C_6H_5O_2$ on modelled PAN and glyoxal, and a comparison with the measurements is shown in Figure 5.46. The glyoxal is predicted best by MCM-base with a measured:modelled ratio of 1.3, with the order shown as the

following: MCM-base > MCM-kOH-CH3O2 > MCM-kOH-CH3CO3 > MCM-C6H5O2. The trend for the underprediction of glyoxal is the same as the underprediction of OH, and the underprediction of OH will cause less glyoxal to be formed. Whilst PAN is underpredicted by all the model scenarios the MCM-kOH-CH3CO3 is the best agreement between measurement and model (due to increased PAN production from more CH_3CO_3 in the model). The measurement:model(MCM-kOH-CH3CO3) is 43. The order of best measurement to modelled agreement for PAN is: MCN-kOH-CH3CO3 > MCM-base > MCM-kOH-CH3O2 > MCM-kOH-C6H5O2. The order, other than MCM-CH3CO3, is the same as glyoxal and shows that the underprediction of PAN follows the underprediction of OH.

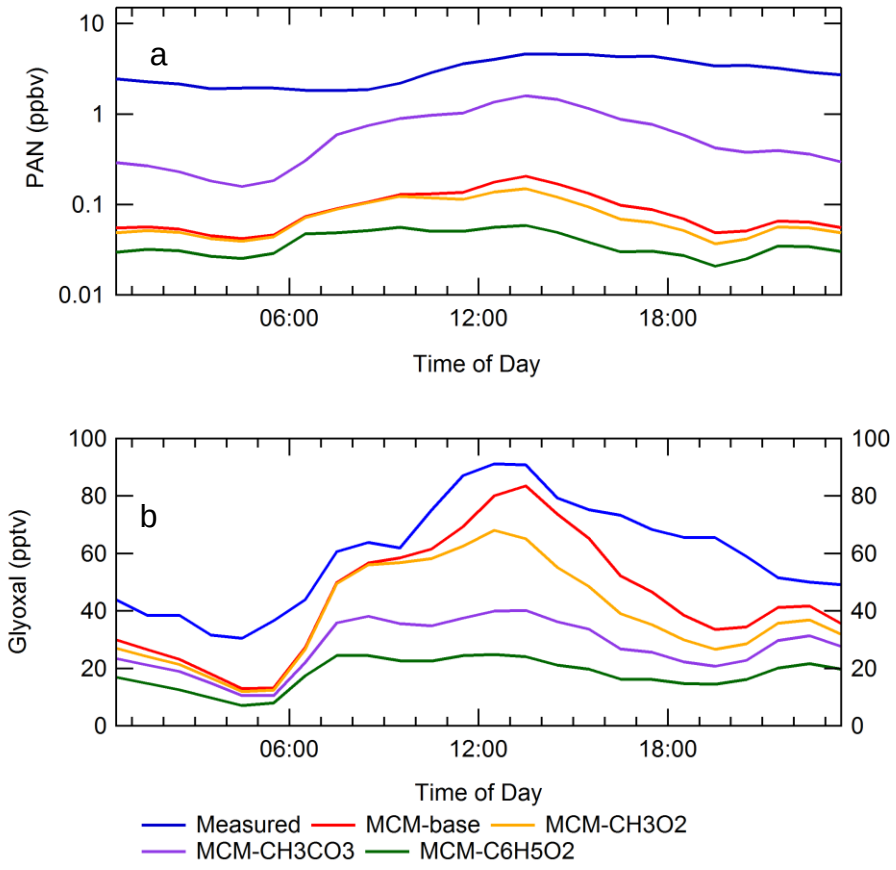

Figure 5.46 a) Average diurnal comparison of measured PAN with modelled PAN from MCN-kOH-CH3O2, MCM-kOH-CH3CO3 and MCM-C6H5O2. b) Average diurnal comparison of measured glyoxal with modelled glyoxal from MCN-kOH-CH3O2, MCM-kOH-CH3CO3 and MCM-C6H5O2.

These results show that the model loss rate of different species should occur at different rates, as PAN is still underpredicted in the model when the missing OH reactivity (on average 9.5 s^{-1}) was filled with a species that forms PAN (CH_3CO_3). Or either: ventilation of the model, or mixing of long-lived species into the model need to be considered. It also shows how dependant both PAN and glyoxal modelled concentrations are on the OH concentration.

5.4.8.3 Missing reactivity and autoxidation

In section.5.4.6.4 when the rate constant for kRO2NO and kAPNO was decreased by a factor of 10 there was a good agreement between measured and model values for OH, HO_2 and RO_2, but the model still had missing OH reactivity. This section also explores whether filling the OH reactivity gap with CH_3O_2, CH_3CO_3 and $C_6H_5O_2$, whilst also reducing the rate constant of RO_2 + NO can reconcile the model with the measurements.

Figure 5.47 shows an average diurnal comparison for the measurements of OH, HO_2 and total RO_2 with modelled values from MCM-base, MCM-kOH-CH3O3 and MCM-kOH-CH3O2-k. It shows that reducing the rate constant of RO_2 + NO by a factor of 10 gives a good agreement between measured and modelled RO_2, similar to the results from MCM-kRO2NO-10 (see section.5.4.6.4). Although, unlike MCM-kRO2NO-10, MCM-kOH-CH3O2-k overpredicts HO_2 and underpredicts OH. These results show that autoxidation cannot reconcile measurement and model concentration of OH, HO_2 and RO_2 when CH_3O_2 was used to fill the missing reactivity. Although in this modelled scenario autoxidation is only represented by a reduce rate constant, but in reality, it will be a much more complicated process.

Figure 5.48 shows an average diurnal comparison for the measurements of OH, HO_2 and total RO_2 with modelled values from MCM-base, MCM-kOH-C6H5O2 and MCM-kOH-C6H5O2-k. It shows that reducing the rate constant of RO_2 + NO by a factor of 10, does not give a good agreement between measured and modelled RO_2, but the modelled RO_2 is improved compared to MCM-base. Both the modelled OH and HO_2 concentration is underpredicted by MCM-kOH-C6H5O2-k by a factor of ~2.1 and ~2.33, respectively. The modelled OH concentration from MCM-kOH-C6H5O2-k is similar to that modelled from

MCM-kOH-C6H5O2, whilst the HO_2 concentration is decreased from MCM-kOH-C6H5O2 to MCM-kOH-C6H5O2-k. This again shows that when both the OH reactivity gap is filled by C6H5O2 and autoxidation is considered, the measurement of OH, HO_2 and RO_2 cannot be reconciled with the modelled values.

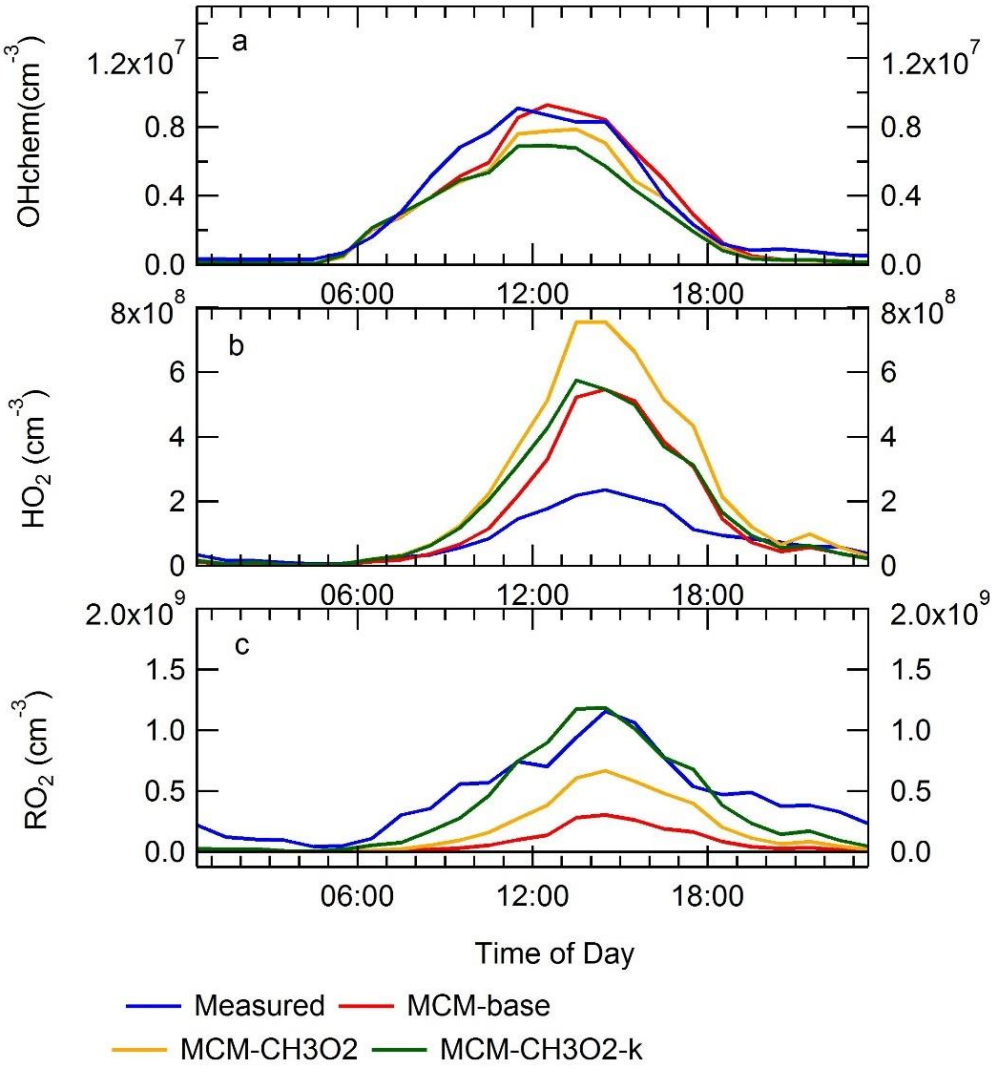

Figure 5.47 a) Average diurnal comparison between OHchem and the modelled OH from both the MCM-base, MCM-kOH-CH3O2 and MCM-kOH-CH3O2-k. b) Average diurnal comparison between measured HO_2 and MCM-base, MCM-kOH-CH3O2 and MCM-kOH-CH3O2-k. c) Average diurnal comparison between measured total RO_2 and total RO_2 modelled from MCM-base, MCM-kOH-CH3O2 and MCM-kOH-CH3O2-k. The entire campaign period was averaged to make the diurnals, the diurnals are 1-hour averages.

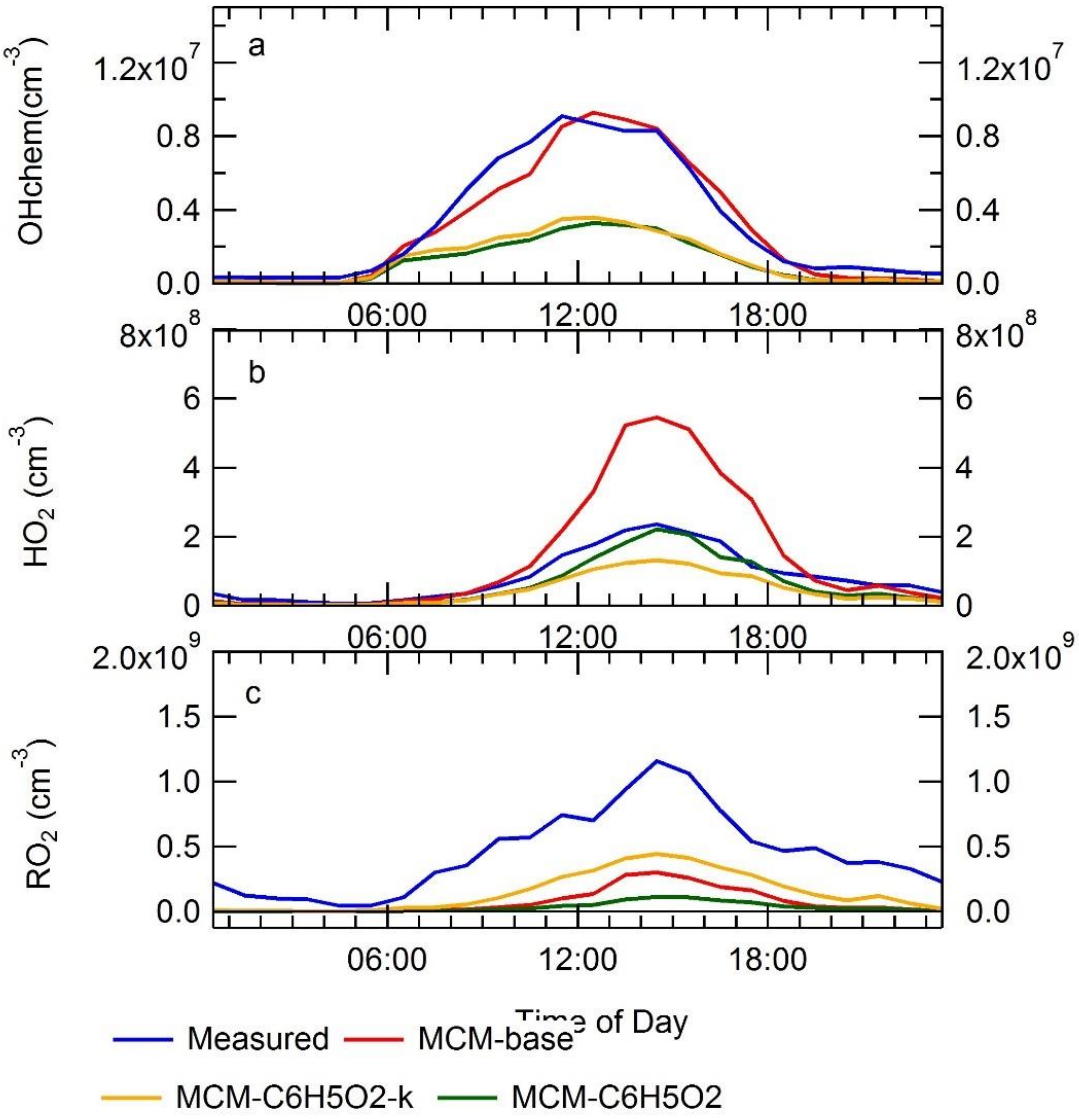

Figure 5.48 a) Average diurnal comparison between OHchem and the modelled OH from both the MCM-base, MCM-kOH-C6H5O2 and MCM-kOH-C6H5O2-k. b) Average diurnal comparison between measured HO_2 and MCM-base, MCM-kOH- C6H5O2 and MCM-kOH-C6H5O2-k. c) Average diurnal comparison between measured total RO_2 and total RO_2 modelled from MCM-base, MCM-kOH-C6H5O2 and MCM-kOH-C6H5O2-k. The entire campaign period was averaged to make the diurnals, the diurnals are 1-hour averages.

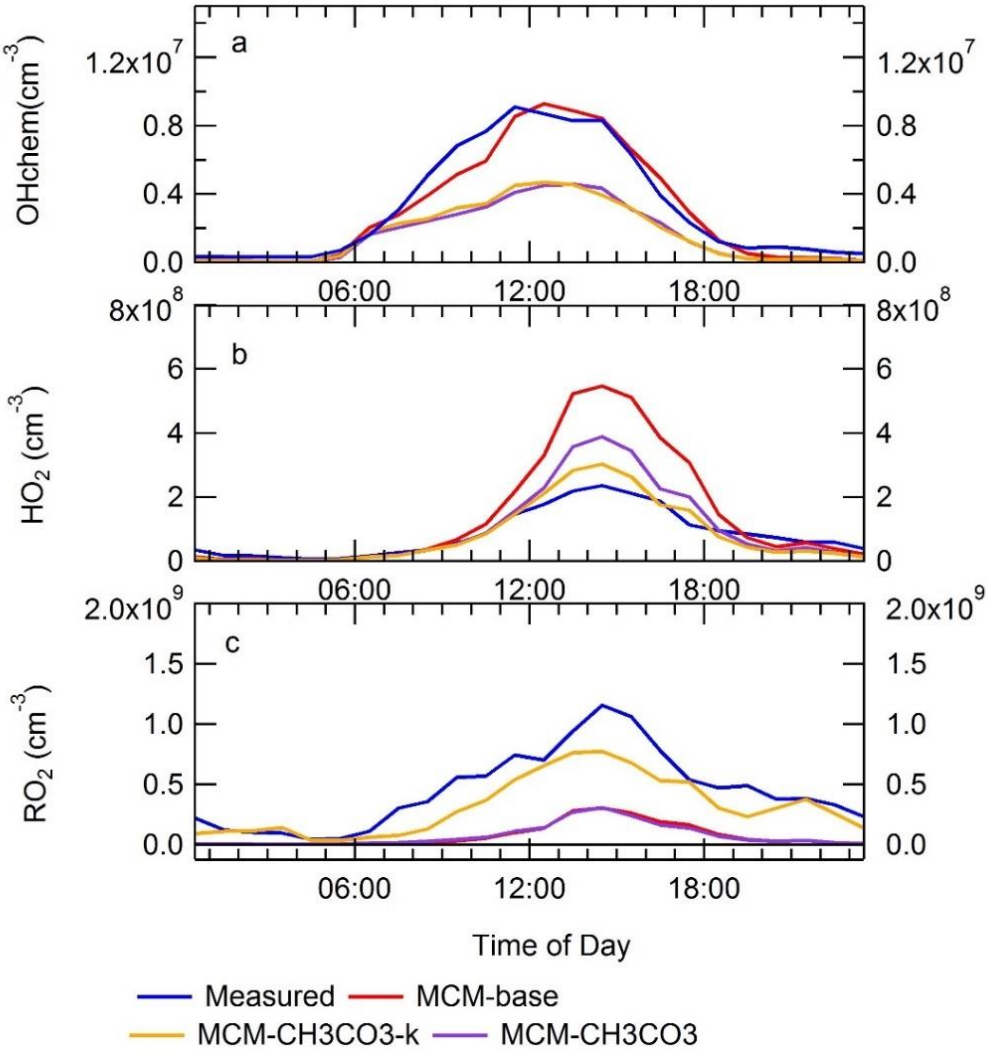

Figure 5.49 a) Average diurnal comparison between OHchem and the modelled OH from both the MCM-base, MCM-kOH-CH3CO3 and MCM-kOH-CH3CO3-k. b) Average diurnal comparison between measured HO_2 and MCM-base, MCM-kOH-CH3CO3 and MCM-kOH-CH3CO3-k. c) Average diurnal comparison between measured total RO_2 and total RO_2 modelled from MCM-base, MCM-kOH-CH3CO3 and MCM-kOH-CH3CO3-k. The entire campaign period was average up to make the diurnals, the diurnals are 1-hour averages.

Figure 5.49 shows an average diurnal comparison for the measurements of OH, HO_2 and total RO_2 with modelled values from MCM-base, MCM-kOH-CH3CO3 and MCM-kOH-CH3CO3-k. It shows that reducing the rate constant of RO_2 + NO by a factor of 10 the modelled RO_2 concentration is underpredicted by ~1.6 at 14:30. Whilst the HO_2 concentration is slightly overpredicted by ~1.2 at 14:30 by MCM-kOH-CH3CO3-k, in general, the measurement and modelled comparison

is greatly improved. The OH concentration is also underpredicted by MCM-kOH-CH3CO3-k Although unlike MCM-kRO2NO-10, which could replicate the radical concentration very well (see section.5.4.6.4 for more details), MCM-kOH-CH3O2-k overpredicts HO_2 and underpredicts OH. This works highlights how variable the results for the radical concentration can be when introducing different RO_2 species to fill the missing OH reactivity gap. This work also shows that filling the OH reactivity with CH_3O_2, CH_3CO_3 and $C_6H_5O_2$, and reducing the rate constant of RO_2 + NO cannot reconcile measurements with the model.

5.4.9 The effect of underprediction of RO_2 radicals on ozone production

Ozone concentration during summertime Beijing exceeded the WHO 8-hour limit of 80 ppbv often during the APHH summer campaign, on some days the ozone concentration exceeds 160 ppbv (see section.5.1). O_3 has a negative impact on both human health and crop yields (Lin et al., 2018), and in China led to 74.2 thousand premature deaths and a loss of 7.6 billion US$ in 2016 (Maji et al., 2019) to the economy. Also, whilst $PM_{2.5}$ has been decreasing in Beijing the ozone concentration has been increasing. The RO_2 radicals during summertime are underpredicted, with the underprediction increasing with increasing NO, as discussed in section.5.4.4. The HO_2 concentration is overpredicted when the NO concentration is below 6 ppbv of NO and underpredicted above 6 ppbv of NO, as discussed in section.5.4.6. The difference between the measurements and model values for HO_2 and RO_2 has an implication for the model's ability to predict the rate of *in-situ* O_3 production. The rate of O_3 production is assumed to be equal to the net rate of NO_2 production:

$$\begin{aligned} \mathrm{P}(\mathrm{O_3}) = {} & k_{\mathrm{HO_2+NO}}[\mathrm{HO_2}][\mathrm{NO}] + k_{\mathrm{RO_2+NO}}[\mathrm{RO_2}][\mathrm{NO}] \\ & - k_{\mathrm{OH+NO_2+M}}[\mathrm{OH}][\mathrm{NO_2}][\mathrm{M}] - k_{\mathrm{HO_2+O_3}}[\mathrm{HO_2}][\mathrm{O_3}] \\ & - \mathrm{P}(\mathrm{RONO_2}) \end{aligned} \qquad \text{E5.4}$$

where RO_2 represents the sum of RO_2, and the last three terms allow for the reduction of ozone production owing to reactions that remove NO_2 or its precursors (e.g. organic nitrates). The $P(RONO_2)$ term is the net rate of formation of organic nitrate, for example, the formation of peroxy acetylnitrates (PANs).

As shown in Figure 5.50, when the rate of O_3 production is calculated using the measured values of HO_2 and RO_2, there is a positive trend with increasing NO, and the trend is followed well by the modelled O_3 production (from MCM-base). However, the MCM-base starts to underpredict ozone formation above 1 ppbv of NO, whilst at lower NO (below 1 ppbv) concentrations the MCM-base overpredicts ozone formation. The overprediction by the model of O_3 formation is controlled by the overprediction of HO_2 that increases with decreasing NO (below 1 ppbv), whilst the underprediction is controlled by the underprediction of HO_2 and RO_2 in MCM-base.

The main RO_2 species that contribute to ozone formation are shown in Figure 5.51. Two of the major sources of ozone formation during the summer campaign were from isoprene derived RO_2 with ISOPBO2 and ISOPDO2 contributing to 13.95% and 6.86%, respectively. Ozone formation coming from isoprene derived RO_2 species in a major urban city like Beijing shows how even in polluted environments isoprene chemistry is important. The second highest species contributing to O_3 formation is CH_3O_2, contributing 12.38%, which is the most abundant RO_2 species in the troposphere (Copan et al., 2015). In general, the ozone is formed from a mixture of simple and complex RO_2 species.

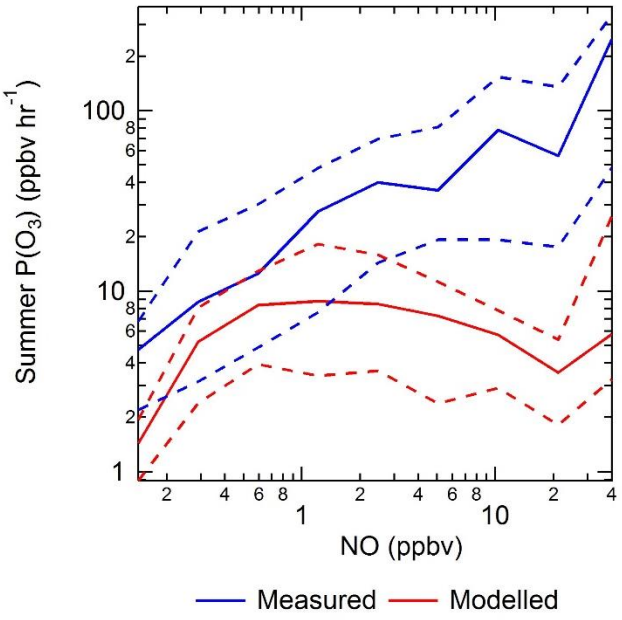

Figure 5.50 The calculated rate of ozone production as a function of [NO] using modelled (red) and measured (blue) values of HO_2 and RO_2 radicals. The ozone production was calculated using E5.4.

Comparison of calculated O_3 formation for summer urban campaigns is shown in Table 5.7. It shows that the maximum ozone formation for the APHH (310 ppbv hr^{-1}, at 80 ppbv of NO) was higher than that observed for the ClearfLo campaign (41 ppbv hr^{-1}, at 52 ppbv of NO). The higher ozone formation observed during the APHH campaign may be due to several factors including higher NO concentration and VOC concentration. The average maximum O_3 formation for the APHH campaign (44 ppbv hr^{-1}, at 3.4ppbv of NO) was higher than that observed for the rural campaign in Wangdu (60 km from Beijing) (20 ppbv hr^{-1}, at 1 ppbv of NO). Again, the difference can be due to the lower NO concentration observed at the Wangdu site compared to the APHH site, or a different mix/concentration of VOCs.

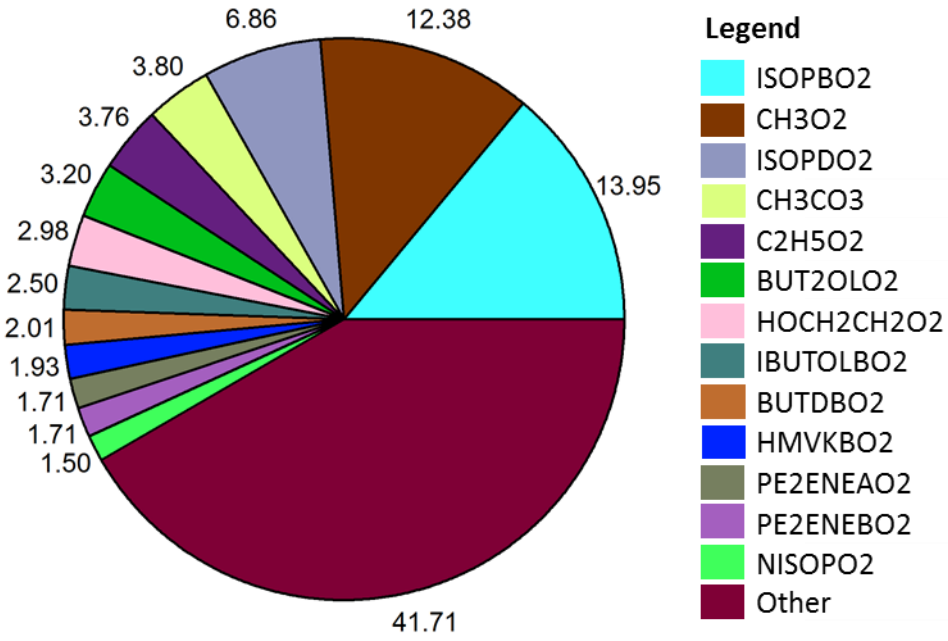

Figure 5.51 Pie chart showing the different RO_2 species that form O_3, the species that contribute above 1.5% of the total O_3 formation is shown. The 41.71% is from RO_2 species that contribute less than 1.5% to the ozone formation. The structure of the RO_2 species can be found at http://mcm.leeds.ac.uk/MCMv3.3.1/home.htt. The difference contributors were calculated from $k_{RO2+NO}[RO_2][NO]$.

Campaign	Dates	NO (ppbv)	$P(O_3)$ (ppbv hr^{-1})	Notes	Reference
APHH	May - Jun, 2016	3.4	44	Average maximum of $P(O_3)$ at 12:30	This work.
		80	310	Maximum ozone production.	
Wangdu	Jun- July, 2014	1	20	Maximum diurnal average at 11:00.	Tan et al. (2017)
ClearfLo	July – Aug 2012	52	41	Maximum ozone production.	Whalley et al. (2018)

Table 5.7 O_3 formation calculated from measured values of RO_2 and HO_2 for selected summer urban campaigns. The NO is either mean average for when the O_3 was calculated, or the NO concentration when the maximum ozone production was calculated.

5.5 Summary and Conclusion

OH, HO_2 and RO_2 radicals were measured using the FAGE technique in summer 2017 as part of the APHH project, which took place in the Institute of Atmospheric Physics in central Beijing, China. The whole APHH project had several aims, the radical measurements were a part of a sub-project called AIR PROcesses (AIRPRO). The AIRPRO project aimed to assess which pollutants are transformed or removed through transport, chemical reactions and photolysis.

Measured OH peaked at 11:30 coinciding with solar noon, the average daily maxima was ~ 8.5 $x10^6$ molecule cm^{-3} with the daily maxima of OH varying between 0.6 – 1.7 x 10^7 cm^{-3} day-to-day. The OH diurnal profile track light levels very well, especially *j*(HONO). The ratio of measured:modelled(MCM-base) shows a good agreement for OH below 5 ppbv of NO, whilst above 5 ppbv the underprediction of OH increases with NO. The ratio of measured:modelled reaches a maximum of 2.3 at 43 ppbv of NO. The comparison between measured and modelled OH reactivity highlights a missing OH reactivity throughout the entire day and that on average for the whole campaign, the missing OH reactivity was ~9.5 s^{-1}. The missing reactivity throughout the whole day suggests the

missing source is of primary nature. A photostationary steady-state (PSS) calculation for OH showed that during summer the experimental budget could not be closed, with a missing source of OH radicals. The ratio of measured:calculated(PSS) was ~2.08. On average, the steady-state shows that HO_2 + NO and HONO were the major OH sources during the APHH campaign each contributing ~47% and ~42%, respectively. $O^1D + H_2O$ also contributes 9.8%, whilst ozonolysis contributed ~1%.

The correlation of OHwave vs OHchem yielded a slope of 1.10 ± 0.02, highlighting there was a difference outside of the uncertainty and that an observable interference in the OHwave measurement was detected. The difference between OHwave and OHchem becomes pronounced at higher OH concentrations (above 1.0 x 10^7 molecule cm^{-3}). The possible source of the OH interference and the largest correlation with the difference between OHchem and OHwave was the product of RO_2*O_3 and $OH*O_3$. Even though the best correlations are from RO_2, O_3, temperature and photolysis rates, it should be noted that, other than the photolysis rates, all of these species peak in the afternoon which is when maximum interference is observed. The correlation of OHint with RO_2, O_3 and temperature may be a spurious correlation from a third confounding factor (Aldrich, 1995).

Measured HO_2 peaked later than OH at 14:30, the daily maxima average was 2.3 x 10^8 molecule cm^{-3} coinciding with the trough in the NO concentration (~240 pptv campaign average, at 14:30). The daily maxima of HO_2 varied between 0.7 – 3.8 x 10^8 molecule cm^{-3}. HO_2 concentration at night was also non-zero (average of 3.47 x 10^7 molecule cm^{-3}) with the HO_2 concentration in general being higher than the LOD (2.8 x 10^6 molecule cm^{-3}). The HO_2 measured:modelled ratio shows a similar underprediction as OH above 5 ppbv of NO. The HO_2 at NO concentrations below 5 ppbv starts to show an overprediction by the model, this overprediction settles at a factor of 2 between 0.1 – 1 ppbv of NO.

The RO_2 measurements (total, simple and complex) peaked at 14:30, the same time as HO_2. The daily average maxima for total RO_2, simple RO_2 and complex RO_2 was 1.15 x 10^9, 5.92 x 10^8 and 4.59 x 10^8 molecule cm^{-3}, respectively. The contribution of simple and complex RO_2 to total RO_2 was 1:1 between

16:30 – 06:30, whilst between these times there was more simple RO_2 species than complex RO_2 species. A non-zero value of total RO_2 was measured at night, the average night-time value was 2.8 x 10^8 molecule cm^{-3}. Also, a distinct secondary peak is observed in the 75th percentile for total RO_2 at 20:30 showing that RO_2 species are being generated at night-time. The MCM underpredicts the RO_2 species throughout different NO levels, with an increasing underprediction with NO. The ratio of measured:modelled of total RO_2 shows a minimum of 6.9 and a maximum of 67.4 at NO mixing ratios of 0.5 and 46 ppbv, respectively.

The MCM-base model was used to assess the primary sources and termination routes of radicals during the summer campaign using rate of production analysis (ROPA). The primary production of radicals was dominated by the photolysis of HONO (77%), the other primary sources of OH during the APHH campaign was: O^1D + H_2O (11%); ozonolysis of alkenes (5.5%); photolysis of HCHO (3.42%); photolysis of carbonyls (0.66%, other than HCHO) and VOCs + NO3 (2.2%). The termination of radicals (RO_x) is dominated by the reaction of OH + NO_2 (63%). The other termination reactions during the APHH summer campaign were: OH + NO (11.3%); HO_2 + NO_2 (0.8%); HO_2 + HO_2 (1.47%); RO_2 + HO_2 (3.12%) and net formation PAN (14%).

The MCM-base model was modified to assess the difference between measured and modelled values for OH, HO_2 and RO_2. First, as HO_2 is overpredicted by MCM-base, the impact of HO_2 taken onto aerosol was assessed using an uptake coefficient of 0.2. Whilst HO_2 uptake in the model did impact the HO_2 concentration by decreasing it ~8% at the maximum value of HO_2, and could not reconcile the model with the measurements. It also showed that the largest impact of HO_2 uptake was at lower NO concentrations, as at higher NO concentrations the reaction of HO_2 + NO dominates. To reconcile the modelled value of HO_2 with the measured value, the reaction of HO_2 + X was included in the model. The reaction HO_2 + X recycles HO_2 to OH independent of NO. The results showed that ~0.75 ppbv of X was required to reconcile measurements of HO_2 with the model when the same rate coefficient as HO_2 + NO was assumed. The concentration of X inputted into the model was dependent on the concentration of NO. The results from MCM-X showed that at lower NO

concentrations the model started to overpredict the OH concentration, and the model like the MCM-base model underpredicts the RO_2 concentration.

An additional source of primary RO_2 was added to the model to investigate whether this could improve the measurements and model agreement. First, several different sources of RO_2 species were added into the model to match RO_2 concentration from the model with the total RO_2 measurement. The results showed a large overprediction of both HO_2 and OH across different NO ranges. This work shows that just adding another primary source of RO_2 will not reconcile measurement with modelled values under the NO regimes observed during the summer Beijing campaign. To investigate whether chlorine chemistry could be important in central Beijing the model was constrained to measurements of $ClNO_2$. The Cl atom chemistry did improve the radical concentration, with a maximum ratio for MCM-Cl:MCM-base of 1.04 (4% increase), 1.079 (7.9% increase) and 1.19 (19% increase) for OH, HO_2 and total RO_2, respectively.

To see if autoxidation of the RO_2 radicals could be an important process in central Beijing, the rate constant of RO_2 + NO was decreased by factors of 2 and 10. Once the rate constant was decreased by a factor of 10, the model could replicate the measured values for OH, HO_2 and RO_2 well, highlighting that autoxidation could be an important process in Beijing. Autoxidation products (HOMs) were also observed by a CIMS instrument in both the gas and aerosol phase. However, decreasing the rate constant by a factor of 10 does not help with the missing OH reactivity, which is still ~9.5 s^{-1} throughout the entire day. To see the effect of filling the missing reactivity with different species the reactivity was filled with CH_3O_2, CH_3CO_3 and $C_6H_5O_2$, and after this, the rate constant for RO_2 + NO was decreased by a factor of 10 in another model for comparison. It showed that none of these models could reconcile measurements and modelled concentrations of OH, HO_2 and RO_2. This work highlights the impact of filling missing reactivity with different species, and also that if the missing reactivity was filled with CH_3O_2 CH_3CO_3 or $C_6H_5O_2$ autoxidation is not able to explain the differences between measured and modelled values.

The impact of not constraining the model to measured HONO on OH concentration was explored and showed the model underpredicts the HONO concentration throughout the day. With the largest underprediction at 05:30 with

a factor of ~11. The smallest underprediction is observed at 16:30 with a factor of 1.2, as the measured HONO concentration is at a minimum through loss from photolysis. The model underpredicts the OH concentration by a factor of 2.2, whilst the model constrained to HONO (MCM-base) replicate the OH concentration very well.

As discussed earlier, the peroxy radicals (HO_2 and RO_2) are underpredicted by the model at high NO, and HO_2 is overpredicted at low NO. The models ability not to reconcile measured and modelled peroxy radicals impacts the models ability to predicts ozone production. The peak ozone production calculated using the measurement values for HO_2 and RO_2 was 318 ppbv hr^{-1} when [NO] = 48 ppbv, whilst the ozone production calculated using the modelled values was 64 ppbv hr^{-1}. When the [NO] is less than 1 ppbv the model overpredicts the O_3 production. At 150 pptv of NO, the model predicts 11 ppbv hr^{-1} production of ozone, whilst the measurements show 6.1 ppbv hr^{-1} The underprediction of ozone production by the model shows the implications on missing understanding of the radical chemistry can impact the calculation of secondary pollutants.

Further modelling work can be used to explore whether autoxidation is important in central Beijing, but also chamber studies to investigate how different RO_2 species behave under different NO regimes. Further work is also needed to investigate the OH interference that has been observed at large values of OH in central Beijing and also forested environments (Mao et al., 2012).

5.6 References

Aldrich, J. (1995) 'Correlations genuine and spurious in Pearson and Yule', *Statistical science,* 10(4), pp. 364-376.

Atkinson, R., Baulch, D., Cox, R., Hampson Jr, R., Kerr, J., Rossi, M. and Troe, J. (1999) 'Evaluated kinetic and photochemical data for atmospheric chemistry, organic species: Supplement VII', *Journal of Physical and chemical reference Data,* 28(2), pp. 191-393.

Bannan, T. J., Booth, A. M., Bacak, A., Muller, J. B., Leather, K. E., Le Breton, M., Jones, B., Young, D., Coe, H. and Allan, J. (2015) 'The first UK measurements of nitryl chloride using a chemical ionization mass

spectrometer in central London in the summer of 2012, and an investigation of the role of Cl atom oxidation', *Journal of Geophysical Research: Atmospheres,* 120(11), pp. 5638-5657.

Barker, J. R., Steiner, A. L. and Wallington, T. J. (2017) 'Advances in atmospheric chemistry'.

Bianchi, F., Kurtén, T., Riva, M., Mohr, C., Rissanen, M. P., Roldin, P., Berndt, T., Crounse, J. D., Wennberg, P. O., Mentel, T. F., Wildt, J., Junninen, H., Jokinen, T., Kulmala, M., Worsnop, D. R., Thornton, J. A., Donahue, N., Kjaergaard, H. G. and Ehn, M.: Highly Oxygenated Organic Molecules (HOM) from Gas-Phase Autoxidation Involving Peroxy Radicals: A Key Contributor to *Atmospheric Aerosol, Chem. Rev*., 119, 3472–3509, doi:10.1021/acs.chemrev.8b00395, 2019.

Chatani, S., Shimo, N., Matsunaga, S., Kajii, Y., Kato, S., Nakashima, Y., Miyazaki, K., Ishii, K. and Ueno, H. (2009) 'Sensitivity analyses of OH missing sinks over Tokyo metropolitan area in the summer of 2007', *Atmospheric Chemistry and Physics,* 9(22), pp. 8975-8986.

Chen, S., Ren, X., Mao, J., Chen, Z., Brune, W. H., Lefer, B., Rappenglück, B., Flynn, J., Olson, J. and Crawford, J. H. (2010) 'A comparison of chemical mechanisms based on TRAMP-2006 field data', *Atmospheric Environment,* 44(33), pp. 4116-4125.

Copan, A. V., Schaefer III, H. F. and Agarwal, J. (2015) 'Examining the ground and first excited states of methyl peroxy radical with high-level coupled-cluster theory', *Molecular Physics,* 113(19-20), pp. 2992-2998.

Di Carlo, P., Brune, W. H., Martinez, M., Harder, H., Lesher, R., Ren, X., Thornberry, T., Carroll, M. A., Young, V. and Shepson, P. B. J. S. (2004) 'Missing OH reactivity in a forest: Evidence for unknown reactive biogenic VOCs', *Science*, 304(5671), pp. 722-725.

Dolgorouky, C., Gros, V., Sarda-Esteve, R., Sinha, V., Williams, J., Marchand, N., Sauvage, S., Poulain, L., Sciare, J. and Bonsang, B. (2012) 'Total OH reactivity measurements in Paris during the 2010 MEGAPOLI winter campaign', *Atmospheric Chemistry and Physics,* 12(20), pp. 9593-9612.

Dusanter, S., Vimal, D., Stevens, P., Volkamer, R., Molina, L., Baker, A., Meinardi, S., Blake, D., Sheehy, P. and Merten, A. (2009) 'Measurements of OH and HO_2 concentrations during the MCMA-2006 field campaign–Part 2: Model comparison and radical budget', *Atmospheric Chemistry and Physics,* 9(18), pp. 6655-6675.

Edwards, P., Evans, M., Furneaux, K., Hopkins, J., Ingham, T., Jones, C., Lee, J., Lewis, A., Moller, S., Stone, D. J. A. C. and Discussions, P. (2013) 'OH reactivity in a South East Asian tropical rainforest during the Oxidant and Particle Photochemical Processes (OP3) project', 13(2), pp. 5233-5278.

Emmerson, K., Carslaw, N. and Pilling, M. (2005) 'Urban atmospheric chemistry during the PUMA campaign 2: Radical budgets for OH, HO_2 and RO_2', *Journal of atmospheric chemistry,* 52(2), pp. 165-183.

Finlayson-Pitts, B. (1993) 'Chlorine atoms as a potential tropospheric oxidant in the marine boundary layer', *Research on Chemical Intermediates,* 19(3), pp. 235-249.

Finlayson-Pitts, B., Wingen, L., Sumner, A., Syomin, D. and Ramazan, K. (2003) 'The heterogeneous hydrolysis of NO 2 in laboratory systems and in outdoor and indoor atmospheres: An integrated mechanism', *Physical Chemistry Chemical Physics,* 5(2), pp. 223-242.

Fittschen, C., Ajami, M. A., Batut, S., Ferracci, V., Archer-Nicholls, S., Archibald, A. T. and Schoemaecker, C. (2019) 'ROOOH: a missing piece of the puzzle for OH measurements in low-NO environments?', *Atmospheric Chemistry and Physics,* 19(1), pp. 349-362.

Forster, G. L., Sturges, W. T., Fleming, Z. L., Bandy, B. J. and Emeis, S. (2012) 'A year of H_2 measurements at Weybourne Atmospheric Observatory, UK', *Tellus B: Chemical and Physical Meteorology,* 64(1), pp. 17771.

Fuchs, H., Tan, Z., Hofzumahaus, A., Broch, S., Dorn, H.-P., Holland, F., Künstler, C., Gomm, S., Rohrer, F. and Schrade, S. (2016) 'Investigation of potential interferences in the detection of atmospheric RO_x radicals by laser-induced fluorescence under dark conditions', *Atmospheric measurement techniques,* 9(4), pp. 1431-1447.

Griffith, S., Hansen, R., Dusanter, S., Stevens, P., Alaghmand, M., Bertman, S., Carroll, M., Erickson, M., Galloway, M. and Grossberg, N. (2013) 'OH and HO_2 radical chemistry during PROPHET 2008 and CABINEX 2009–Part 1: Measurements and model comparison', *Atmospheric Chemistry and Physics,* 13(11), pp. 5403-5423.

Hansen, R., Griffith, S., Dusanter, S., Rickly, P., Stevens, P., Bertman, S., Carroll, M., Erickson, M., Flynn, J., Grossberg, N. J. A. C. and Discussions, P. (2013) 'Measurements of total hydroxyl radical reactivity during CABINEX 2009–Part 1: field measurements', 13(6), pp. 17159-17195.

Hansen, R. F., Blocquet, M., Schoemaecker, C., Léonardis, T., Locoge, N., Fittschen, C., Hanoune, B., Stevens, P., Sinha, V. and Dusanter, S. (2015) 'Intercomparison of the comparative reactivity method (CRM) and pump-probe technique for measuring total OH reactivity in an urban environment', *Atmospheric Measurement Techniques,* 8(10), pp. 4243-4264.

Hofzumahaus, A., Rohrer, F., Lu, K., Bohn, B., Brauers, T., Chang, C.-C., Fuchs, H., Holland, F., Kita, K. and Kondo, Y. (2009) 'Amplified trace gas removal in the troposphere', *science,* 324(5935), pp. 1702-1704.

Hopkins, J. R., Jones, C. E. and Lewis, A. C. (2011) 'A dual channel gas chromatograph for atmospheric analysis of volatile organic compounds including oxygenated and monoterpene compounds', *Journal of Environmental Monitoring,* 13(8), pp. 2268-2276.

Huang, Z., Zhang, Y., Yan, Q., Zhang, Z. and Wang, X. (2016) 'Real-time monitoring of respiratory absorption factors of volatile organic compounds in ambient air by proton transfer reaction time-of-flight mass spectrometry', *Journal of hazardous materials,* 320, pp. 547-555.

Jacob, D. J. (2000) 'Heterogeneous chemistry and tropospheric ozone', *Atmospheric Environment,* 34(12-14), pp. 2131-2159.

Jokinen, T., Sipilä, M., Richters, S., Kerminen, V. M., Paasonen, P., Stratmann, F., Worsnop, D., Kulmala, M., Ehn, M. and Herrmann, H. (2014) 'Rapid autoxidation forms highly oxidized RO_2 radicals in the atmosphere', *Angewandte Chemie International Edition,* 53(52), pp. 14596-14600.

Kanaya, Y., Cao, R., Akimoto, H., Fukuda, M., Komazaki, Y., Yokouchi, Y., Koike, M., Tanimoto, H., Takegawa, N. and Kondo, Y. (2007) 'Urban photochemistry in central Tokyo: 1. Observed and modeled OH and HO_2 radical concentrations during the winter and summer of 2004', *Journal of Geophysical Research: Atmospheres,* 112(D21).

Le Breton, M., Hallquist, Å. M., Pathak, R. K., Simpson, D., Wang, Y., Johansson, J., Zheng, J., Yang, Y., Shang, D., Wang, H. J. A. C. and Physics (2018) 'Chlorine oxidation of VOCs at a semi-rural site in Beijing: Significant chlorine liberation from $ClNO_2$ and subsequent gas-A nd particle-phase Cl-VOC production', 18(17), pp. 13013-13030.

Lee, J., Whalley, L., Heard, D., Stone, D., Dunmore, R., Hamilton, J., Young, D., Allan, J., Laufs, S. and Kleffmann, J. (2015) 'Detailed budget analysis of HONO in central London reveals a missing daytime source', *Atmospheric Chemistry and Physics Discussions,* 15(16), pp. 22097-22139.

Li, X., Brauers, T., Häseler, R., Bohn, B., Fuchs, H., Hofzumahaus, A., Holland, F., Lou, S., Lu, K. and Rohrer, F. (2012) 'Exploring the atmospheric chemistry of nitrous acid (HONO) at a rural site in Southern China', *Atmospheric Chemistry and Physics,* 12(3), pp. 1497-1513.

Lin, Y., Jiang, F., Zhao, J., Zhu, G., He, X., Ma, X., Li, S., Sabel, C. E. and Wang, H. (2018) 'Impacts of O_3 on premature mortality and crop yield loss across China', *Atmospheric environment,* 194, pp. 41-47.

Lopez-Hilfiker, F. D., Mohr, C., Ehn, M., Rubach, F., Kleist, E., Wildt, J., Mentel, T. F., Lutz, A., Hallquist, M., Worsnop, D. and Thornton, J. A.: A novel method for online analysis of gas and particle composition: Description and evaluation of a filter inlet for gases and AEROsols (FIGAERO), Atmos. Meas. Tech., 7, 983–1001, doi:10.5194/amt-7-983-2014, 2014.

Lu, K., Hofzumahaus, A., Holland, F., Bohn, B., Brauers, T., Fuchs, H., Hu, M., Häseler, R., Kita, K. and Kondo, Y. (2013) 'Missing OH source in a suburban environment near Beijing: observed and modelled OH and HO_2 concentrations in summer 2006', *Atmospheric Chemistry and Physics,* 13(2), pp. 1057-1080.

Lu, K., Rohrer, F., Holland, F., Fuchs, H., Bohn, B., Brauers, T., Chang, C., Häseler, R., Hu, M. and Kita, K. (2012) 'Observation and modelling of OH and HO_2 concentrations in the Pearl River Delta 2006: a missing OH

source in a VOC rich atmosphere', *Atmospheric chemistry and physics,* 12(3), pp. 1541-1569.

Lu, X., Wang, Y., Li, J., Shen, L. and Fung, J. C. (2018) 'Evidence of heterogeneous HONO formation from aerosols and the regional photochemical impact of this HONO source', *Environmental Research Letters,* 13(11), pp. 114002.

Maji, K. J., Ye, W.-F., Arora, M. and Nagendra, S. S. (2019) 'Ozone pollution in Chinese cities: Assessment of seasonal variation, health effects and economic burden', *Environmental pollution,* 247, pp. 792-801.

Mao, J., Ren, X., Chen, S., Brune, W. H., Chen, Z., Martinez, M., Harder, H., Lefer, B., Rappenglueck, B. and Flynn, J. (2010) 'Atmospheric oxidation capacity in the summer of Houston 2006: Comparison with summer measurements in other metropolitan studies', *Atmospheric Environment,* 44(33), pp. 4107-4115.

Mao, J., Ren, X., Zhang, L., Van Duin, D., Cohen, R., Park, J.-H., Goldstein, A., Paulot, F., Beaver, M. and Crounse, J. (2012) 'Insights into hydroxyl measurements and atmospheric oxidation in a California forest', *Atmospheric Chemistry and Physics,* 12(17), pp. 8009-8020.

Massoli, P., Stark, H., Canagaratna, M. R., Krechmer, J. E., Xu, L., Ng, N. L., Mauldin, R. L., Yan, C., Kimmel, J., Misztal, P. K., Jimenez, J. L., Jayne, J. T. and Worsnop, D. R.: Ambient Measurements of Highly Oxidized Gas-Phase Molecules during the Southern Oxidant and Aerosol Study (SOAS) 2013, ACS Earth Sp. Chem., 2(7), 653–672, doi:10.1021/acsearthspacechem.8b00028, 2018.

Mehra, A., Wang, Y., Krechmer, J., Lambe, A., Majluf, F., Morris, M., Priestley, M., Bannan, T., Hamilton, J. and Croteau, P. 'Evaluation of the chemical composition of gas and particle phase products of aromatic oxidation–implications for ambient measurements and modelling studies'. *Geophysical Research Abstracts*.

Meteorology. (2010) *Observation and forecasting levels of haze*. Available at: https://www.chinesestandard.net/PDF/English.aspx/QXT113-2010 (Accessed: 31/03/2020 2020).

Michoud, V., Kukui, A., Camredon, M., Colomb, A., Borbon, A., Miet, K., Aumont, B., Beekmann, M., Durand-Jolibois, R. and Perrier, S. (2012) 'Radical budget analysis in a suburban European site during the MEGAPOLI summer field campaign', *Atmospheric Chemistry and Physics,* 12(24), pp. 11951-11974.

Mielke, L. H., Furgeson, A. and Osthoff, H. D. (2011) 'Observation of $ClNO_2$ in a mid-continental urban environment', *Environmental science & technology,* 45(20), pp. 8889-8896.

Nakashima, Y., Kato, S., Greenberg, J., Harley, P., Karl, T., Turnipseed, A., Apel, E., Guenther, A., Smith, J. and Kajii, Y. (2014) 'Total OH reactivity measurements in ambient air in a southern Rocky mountain ponderosa pine forest during BEACHON-SRM08 summer campaign', *Atmospheric Environment,* 85, pp. 1-8.

Nölscher, A., Williams, J., Sinha, V., Custer, T., Song, W., Johnson, A., Axinte, R., Bozem, H., Fischer, H., Pouvesle, N. (2012) 'Summertime total OH reactivity measurements from boreal forest during HUMPPA-COPEC 2010', *Atmospheric Chemistry Physics*, 12(3).

Osthoff, H. D., Roberts, J. M., Ravishankara, A., Williams, E. J., Lerner, B. M., Sommariva, R., Bates, T. S., Coffman, D., Quinn, P. K. and Dibb, J. E. J. N. G. (2008) 'High levels of nitryl chloride in the polluted subtropical marine boundary layer', *Nature Geoscience*, 1(5), pp. 324.

Paatero, P. and Tapper, U. J. E. (1994) 'Positive matrix factorization: A non-negative factor model with optimal utilization of error estimates of data values', *Environmetrics*, 5(2), pp. 111-126.

Ren, X., Brune, W. H., Oliger, A., Metcalf, A. R., Simpas, J. B., Shirley, T., Schwab, J. J., Bai, C., Roychowdhury, U. and Li, Y. (2006) 'OH, HO_2, and OH reactivity during the PMTACS–NY Whiteface Mountain 2002 campaign: Observations and model comparison', *Journal of Geophysical Research: Atmospheres,* 111(D10).

Ren, X., Van Duin, D., Cazorla, M., Chen, S., Mao, J., Zhang, L., Brune, W. H., Flynn, J. H., Grossberg, N. and Lefer, B. L. (2013) 'Atmospheric oxidation

chemistry and ozone production: Results from SHARP 2009 in Houston, Texas', *Journal of Geophysical Research: Atmospheres,* 118(11), pp. 5770-5780.

Riedel, T. P., Bertram, T. H., Crisp, T. A., Williams, E. J., Lerner, B. M., Vlasenko, A., Li, S.-M., Gilman, J., De Gouw, J., Bon, D. M. J. E. S. and Technology (2012) 'Nitryl chloride and molecular chlorine in the coastal marine boundary layer', *Environmental Science Technology*, 46(19), pp. 10463-10470.

Saunders, S. M., Jenkin, M. E., Derwent, R. and Pilling, M. (2003) 'Protocol for the development of the Master Chemical Mechanism, MCM v3 (Part A): tropospheric degradation of non-aromatic volatile organic compounds', *Atmospheric Chemistry and Physics,* 3(1), pp. 161-180.

Shi, Z., Vu, T., Kotthaus, S., Grimmond, S., Harrison, R. M., Yue, S., Zhu, T., Lee, J., Han, Y. and Demuzere, M. (2018) 'Introduction to Special Issue-In-depth study of air pollution sources and processes within Beijing and its surrounding region (APHH-Beijing)', *Atmospheric Chemistry and Physics*, 11, pp. 7519 - 7546

Simon, H., Kimura, Y., McGaughey, G., Allen, D. T., Brown, S., Osthoff, H., Roberts, J., Byun, D. and Lee, D. (2009) 'Modeling the impact of $ClNO_2$ on ozone formation in the Houston area', *Journal of Geophysical Research: Atmospheres,* 114(D7).

Sinha, V., Williams, J., Lelieveld, J., Ruuskanen, T., Kajos, M., Patokoski, J., Hellen, H., Hakola, H., Mogensen, D., Boy, M. J. E. s. and technology (2010) 'OH reactivity measurements within a boreal forest: evidence for unknown reactive emissions', *Environmental science technology*, 44(17), pp. 6614-6620.

Tan, Z., Fuchs, H., Lu, K., Hofzumahaus, A., Bohn, B., Broch, S., Dong, H., Gomm, S., Häseler, R. and He, L. (2017) 'Radical chemistry at a rural site (Wangdu) in the North China Plain: observation and model calculations of OH, HO_2 and RO_2 radicals', *Atmospheric Chemistry and Physics,* 17(1), pp. 663-690.

Tanaka, P. L., Allen, D. T., McDonald-Buller, E. C., Chang, S., Kimura, Y., Mullins, C. B., Yarwood, G. and Neece, J. D. (2003) 'Development of a

chlorine mechanism for use in the carbon bond IV chemistry model', *Journal of Geophysical Research: Atmospheres,* 108(D4).

Tham, Y. J., Wang, Z., Li, Q., Yun, H., Wang, W., Wang, X., Xue, L., Lu, K., Ma, N. and Bohn, B. (2016) 'Significant concentrations of nitryl chloride sustained in the morning: investigations of the causes and impacts on ozone production in a polluted region of northern China', *Atmospheric chemistry and physics*.

Thornton, J. A., Kercher, J. P., Riedel, T. P., Wagner, N. L., Cozic, J., Holloway, J. S., Dubé, W. P., Wolfe, G. M., Quinn, P. K. and Middlebrook, A. M. (2010) 'A large atomic chlorine source inferred from mid-continental reactive nitrogen chemistry', *Nature,* 464(7286), pp. 271.

Ulbrich, I. M., Canagaratna, M. R., Zhang, Q., Worsnop, D. R. and Jimenez, J. L.: Interpretation of Organic Components from Positive Matrix Factorization of Aerosol Mass Spectrometric Data., *Atmos. Chem. Phys*., 9, 2891, doi:10.5194/acp-9-2891-2009, 2009.

Whalley, L. K., Stone, D., Bandy, B., Dunmore, R., Hamilton, J. F., Hopkins, J., Lee, J. D., Lewis, A. C. and Heard, D. E. (2016) 'Atmospheric OH reactivity in central London: observations, model predictions and estimates of in situ ozone production', *Atmospheric Chemistry and Physics,* 16, pp. 2109-2122.

Whalley, L. K., Stone, D., Dunmore, R., Hamilton, J., Hopkins, J. R., Lee, J. D., Lewis, A. C., Williams, P., Kleffmann, J. and Laufs, S. (2018) 'Understanding in situ ozone production in the summertime through radical observations and modelling studies during the Clean air for London project (ClearfLo)', *Atmospheric Chemistry and Physics,* 18(4), pp. 2547-2571.

Woodward-Massey, R., Slater, E., Alen, J., Ingham, T., Cryer, D., Stimpson, L., Ye, C., Seakins, P., Whalley, L. and Heard, D. (2020) 'Implementation of a chemical background method for atmospheric OH measurements by laser-induced fluorescence: characterisation and observations from the UK and China', *Atmospheric Measurement Techniques Discussion*,*in review*

Wu, Z., Zheng, J., Shang, D., Du, Z., Wu, Y., Zeng, L., Wiedensohler, A. and Hu, M. (2016) 'Particle hygroscopicity and its link to chemical composition in

the urban atmosphere of Beijing, China, during summertime', *Atmospheric Chemistry and Physics,* 16(2), pp. 1123-1138.

Xue, L., Saunders, S., Wang, T., Gao, R., Wang, X., Zhang, Q. and Wang, W. (2015) 'Development of a chlorine chemistry module for the Master Chemical Mechanism', *Geoscientific model development*.

Yan, C., Nie, W., Äijälä, M., Rissanen, M. P., Canagaratna, M. R., Massoli, P., Junninen, H., Jokinen, T., Sarnela, N., Häme, S. A. K., Schobesberger, S., Canonaco, F., Yao, L., Prévôt, A. S. H., Petäjä, T., Kulmala, M., Sipilä, M., Worsnop, D. R. and Ehn, M.: Source characterization of highly oxidized multifunctional compounds in a boreal forest environment using positive matrix factorization, *Atmos. Chem. Phys*, 16, 12715–12731, doi:10.5194/acp-16-12715-2016, 2016.

Yang, Y., Shao, M., Wang, X., Nölscher, A. C., Kessel, S., Guenther, A. and Williams, J. J. A. E. (2016) 'Towards a quantitative understanding of total OH reactivity: A review', *Atmospheric Environment*, 134, pp. 147-161.

Yoshino, A., Sadanaga, Y., Watanabe, K., Kato, S., Miyakawa, Y., Matsumoto, J. and Kajii, Y. (2006) 'Measurement of total OH reactivity by laser-induced pump and probe technique—comprehensive observations in the urban atmosphere of Tokyo', *Atmospheric Environment,* 40(40), pp. 7869-7881.

Zhang, L., Wang, T., Zhang, Q., Zheng, J., Xu, Z. and Lv, M. (2016) 'Potential sources of nitrous acid (HONO) and their impacts on ozone: A WRF-Chem study in a polluted subtropical region', *Journal of Geophysical Research: Atmospheres,* 121(7), pp. 3645-3662.

Zhang, Q., Jimenez, J. L., Canagaratna, M. R., Ulbrich, I. M., Ng, N. L., Worsnop, D. R., Sun, Y. J. A. and chemistry, b. (2011) 'Understanding atmospheric organic aerosols via factor analysis of aerosol mass spectrometry: a review', 401(10), *Analytical bioanalytical chemistry*, pp. 3045-3067.

Zhou, X., Gao, H., He, Y., Huang, G., Bertman, S. B., Civerolo, K. and Schwab, J. (2003) 'Nitric acid photolysis on surfaces in low-NOx environments: Significant atmospheric implications', *Geophysical Research Letters,* 30(23).

6. Winter and Summer Beijing Comparison

6.1 Introduction

In Chapter 4 and Chapter 5 the major results from the APHH summer- and winter-time campaign was discussed. This chapter will focus on a comparison between the measurements of OH, HO_2, RO_2 and OH reactivity made during the summer and winter campaigns, and also a comparison of model runs where similar analysis has been performed.

The structure of this chapter is as follows: first, a comparison of the chemical and meteorological conditions between both summer and winter will be given. Then a comparison of OHwave and OHchem, with a discussion on potential sources of interferences. Then a comparison of measured OH, HO_2, RO_2 (speciated into total, complex and simple RO_2 species) and k(OH) will be presented and a discussion on differences of the observed values between the two campaigns. After this there is a steady-state comparison of OH, followed by a discussion on the major OH sources in both summer and winter and whether the experimental budget can be closed. Following this, a comparison between the measured radicals (OH, HO_2 and RO_2) with the results from the master chemical mechanism will be given, this is followed by a comparison between measured and modelled OH reactivity showing the major sinks of OH during both the campaigns. Next, the major primary production and termination pathways for both campaigns will be explored. Following this is a discussion on the differences between measured and modelled radical (OH, HO_2 and RO_2) concentrations under different NO_x regimes. This is followed by a discussion on where missing understanding/chemistry is under different NO_x regimes including: additional primary source of RO_2 and increasing/decreasing the rate constant of RO_2 + NO. Then the sensitivity of the model to HONO is discussed, looking at the impact of unconstraining the model to HONO on modelled OH, and how much of the measured HONO is from the gas-phase reaction of OH + NO. And finally, the impact of the missing understanding of the ozone production under different NO_x regimes and a discussion of the major RO_2 species that contributes to O_3 formation.

6.2 Chemical and Physical Conditions

The winter project took place in November and December 2016, whist the summer project took place in May and June 2017. More details about the aims of the project can be found in section.4.1. The summer and winter measurements were taken at the same IAP (Institute of Atmospheric Physics) site, the measurements that are compared in this chapter (OH, HO_2, RO_2, k(OH)) were taken by the same instruments in each campaign. More details about the campaign site and the auxiliary measurements available can be found in the section.4.1 and Table.4.1, and in (Shi et al., 2019). It should be noted that, other than the OHchem and OHwave comparison in section.6.3.1, all the OH data presented here from the summer campaign are OHchem.

Comparison of the meteorological conditions that were observed during the summer and winter campaign in Beijing is shown in Figure 6.1.

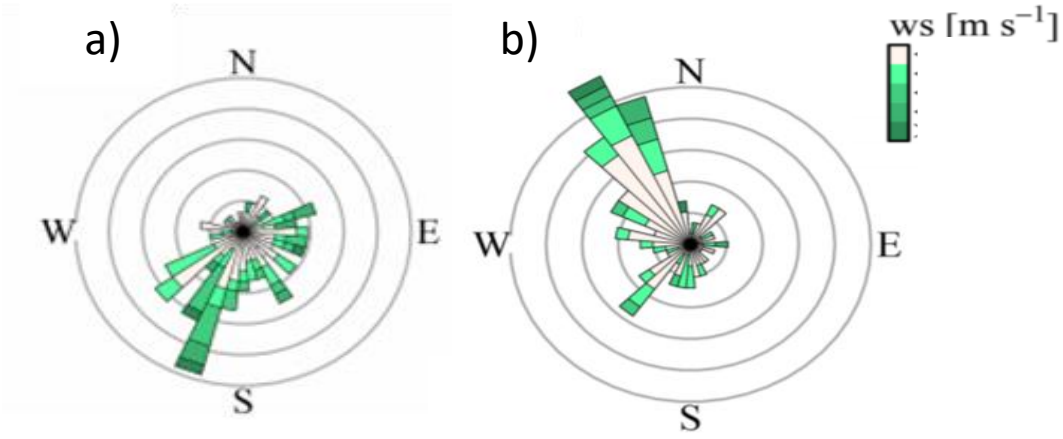

Figure 6.1 Beijing wind roses from ERA-Interim 10 m horizontal wind (40° N, 116°E) for a) 15 May – 22 June 2017 and b)) 5 November – 10 December 2016. This diagram modified from (Shi et al., 2019).

Various meteorological conditions were observed during the summer campaign. The wind-rose diagram for the period summer campaign (15 May – 22 June 2017) shows that south-westerlies were the most common wind direction, whilst during the winter campaign (5 November – 10 December 2016) northwest was the dominant wind direction. The wind rose in Figure 6.1 also shows that in general the summer campaign had stronger winds, whilst in winter slower winds speeds were observed.

The south-westerly wind direction observed in the summer 2017 campaign had the potential to bring more polluted air from the upwind Hebei province to the observations made in Beijing, although the southwesterly wind direction during the summer campaign generally coincided with higher wind speeds. The winter campaign wind rose showed that the northwest wind direction coincided with the higher wind speeds, whilst when the wind direction was observed from the southwest this generally coincided with low winds speeds which would bring stagnant polluted winds from the Hebei province.

The comparison between $j(O^1D)$ (s^{-1}), NO (ppbv), O_3 (ppbv), CO (ppbv), O_x (ppbv), NO_2 (ppbv), HONO (ppbv) and SO_2 (ppbv) for the summer and winter campaign is shown in Figure 6.2. The comparison shows that on average the $j(O^1D)$ observed during the summer peaked a factor ~4.3 larger than winter. The observed summer diurnal for $j(O^1D)$ is much broader than winter, with the $j(O^1D)$ photolysis rate starting to increase at 04:30 and returns to zero at 19:30; whilst in winter the $j(O^1D)$ starts to increase at 06:30 and returns to zero at 17:30. The comparison between the average NO diurnal in summer and winter shows very contrasting conditions between the campaigns, with the winter campaign observing an average maximum of NO of 39 ppbv at 07:30 am, whilst the maxima in the NO in summer was 16 ppbv at 06:30. The NO shows a similar diurnal pattern with [NO] peaking in the morning hours (rush hour) with a steady decline into the afternoon, although the winter campaign shows an increase after 16:30 whilst the summer campaign does not. Also, it should be noted that very low [NO] was observed during the summer campaign in the afternoon, with the lowest NO measured ~100 pptv. The opposite trend of NO was observed for O_3 for the summer and winter campaign, with high measurements of ozone in summer (average maximum peak of 88 ppbv at 15:30) and low concentration in the winter (average maximum peak of 17 ppbv at 14:30). The low ozone trend observed in winter is due to the high [NO] titrating the ozone, whilst the low [NO] observed in the summer campaign is due to high O_3 titrating the NO. Similar diurnals profile for [CO] was observed for both the summer and winter campaign with an almost constant concentration throughout the day, but the concentration in winter (2100 ppbv) was roughly ~2.1 times higher on average compared with summer (1000 ppbv). The O_x (O_3 + NO_2) concentration for both summer and winter shows

a similar distinct diurnal shape with a peak in the afternoon, the O_x in summer peaks earlier (at 15:30) compared to winter (17:30). The earlier peak in summer is caused by a large contribution from O_3 which also peaks at 15:30, whilst the later peak in O_x during winter is dominated by NO_2 which also peaks at 17:30.

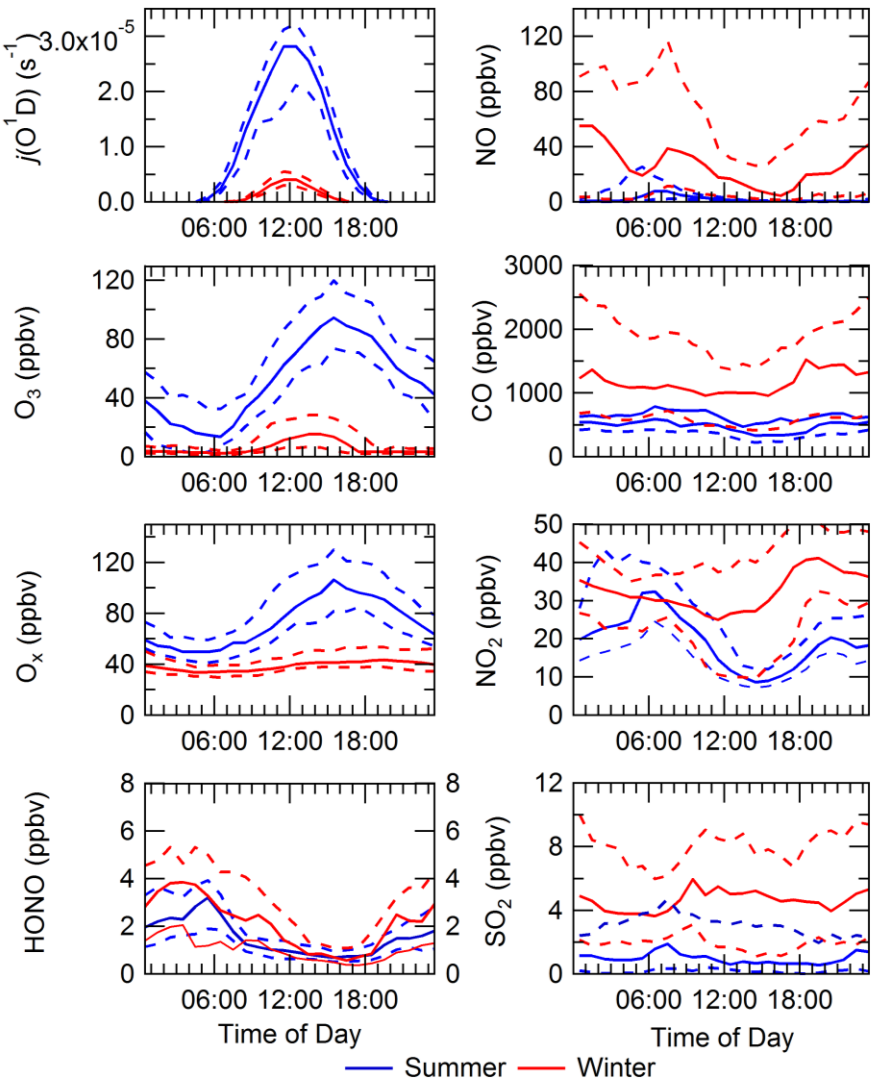

Figure 6.2 Median diurnal profile for measurements j(O^1D) (s^{-1}), NO (ppbv), O_3 (ppbv), CO (ppbv), O_x (ppbv), NO_2 (ppbv), HONO (ppbv) and SO_2 (ppbv) at for the winter(red) and summer (blue) campaign. The dashed lines represent the 25/75th percent confidence interval.

The HONO concentration shows the same distinct diurnal pattern in both summer and winter, with a plateau observed between 13:30 – 16:30. The HONO concentration in both summer and winter decreases rapidly after sunrise (loss through photolysis) and increases after sunset. The HONO concentration

increases at night through both boundary layer effects and heterogeneous sources (Harrison et al., 1996, Alicke et al., 2003, Stemmler et al.,2006, Dupart et al., 2014). Finally, the SO_2 concentration in summer and winter shows a very similar, constant diurnal pattern throughout the day with a slight bump at rush-hour. The SO_2 concentration is much higher in winter (average 4.8 ppbv) compared with summer (average 1.2 ppbv) and is due to increased energy use in winter for heating (Chen et al., 2015).

6.3 Results

6.3.1 Investigating Interferences in the OHwave measurements

As discussed in section.2.1.2, OHwave is the traditional way to measure the background but cannot discriminate against artificially generate OH within the cells. OHchem provides a second background method that allows for an interference free measurement of OH, see section.2.1.2 for more details on both OHwave and OHchem. Figure 6.3 shows the comparison of OHwave[3] vs OHchem for both summer and winter. The winter data shows a very close correlation between OHwave vs OHchem that is scattered around the 1:1 fit, and shows that no significant interference was detected during the winter campaign in Beijing. The ODR fit for the winter data of OHwave vs OHchem shows a slope of 1.05 ± 0.07, which is 1 within error reiterating that during the winter campaign no artificially generated OH was observed.

However, the summer comparison of OHwave vs OHchem shows a deviation away from a 1:1 fit, especially at higher concentrations of OH. The deviation of OHwave away from OHchem at high [OH] shows that an interference was detected during the summer campaign. The interference detected during the summer campaign and not the winter campaign is not a surprising result as previous results suggest that interferences are more likely to be present under higher O_3 and higher temperature conditions (Mao et al., 2012, Feiner et al, 2016,

[3] OHwave for summer is corrected for interference generated from laser photolysis of O_3, whilst winter data has not been corrected as ozone levels were so low and so this interference is very small.

Ren et al, 2013, Novelli et al, 2014). The Wangdu campaign that took place in China also measured an interference between 9 – 35% in the afternoon/early evening (Tan et al., 2017).

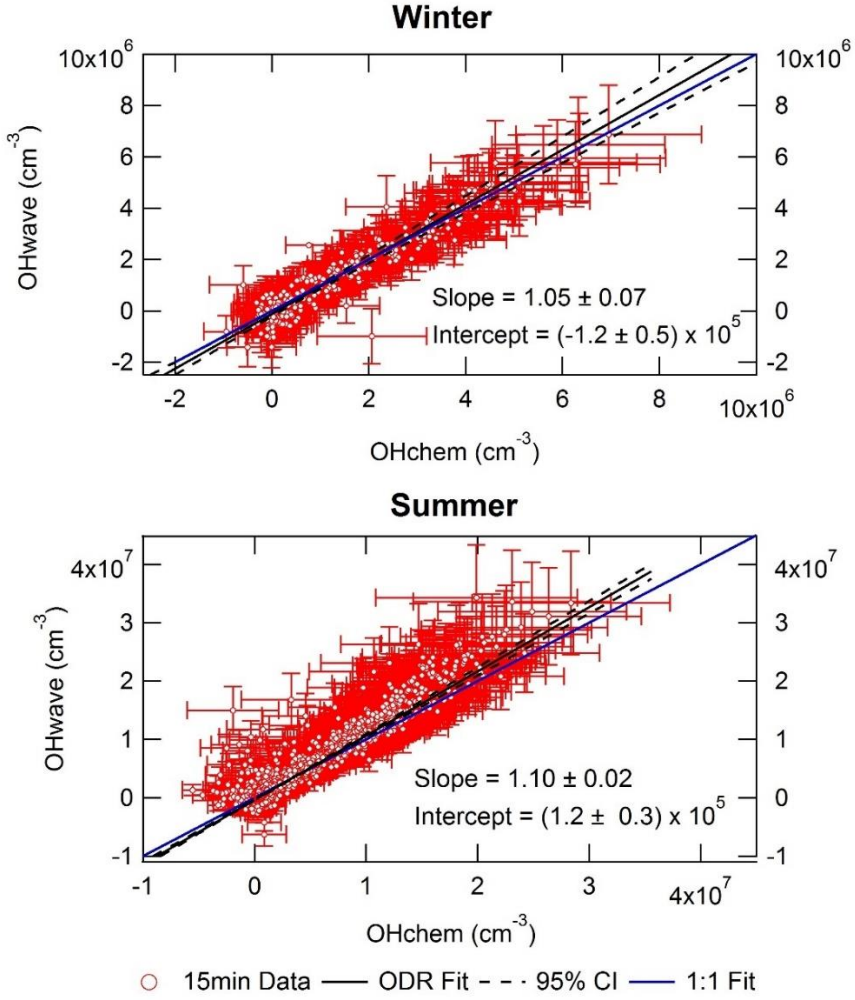

Figure 6.3 Top – Winter comparison of OHwave vs OHchem. Bottom – Summer comparison of OHwave vs OHchem. The white dots represent measured data averaged to 15 minutes, with 2σ error bars. The black line is the line represents an ODR fit through the data, with the dashed black lines representing the 95% CI. For comparison, the blue line denotes a 1:1 fit.

The summer campaign in Beijing had ~6.1 and ~1.3 times higher O_3 and isoprene, respectively. To the west of the APHH campaign site, there was a park that was covered mainly by conifer pine trees (Yuan Dynasty Wall Heritage). Also the interference during the summer campaign only presented itself when the OHchem concentration reached above 1 x 10^7 molecule cm^{-3}, whilst the winter campaign only observed concentrations up to 8 x 10^6 molecule cm^{-3}.

Section.5.4.2 discussed the possible sources of the interference observed during the summer campaign, with the strongest correlation from complex RO_2*Temperature*O_3. Previous work by Fittschen et al.(2019) has discussed the possibility of ROOOH (from reaction of RO_2 + OH) as a potential source of OH interference, and this work shows an increased Pearson's (R) coefficient when the product of RO_2 and OH is taken from 0.31 to 0.47. Also, the comparison between the concentration of measured RO_2 between the summer and winter shows the RO_2 (which derives from species including alkene-type VOCs) was ~22 times larger in summer, so if the OH interference does stem from RO_2 species it would be much more pronounced during the summer campaign. Although the highest correlation coefficient was 0.48 for OH*O3, it should be noted, as discussed in section.5.4.2, RO_2, temperature and O_3 all peak during the afternoon and the correlation may be masking another source of the interference that observes a maxima at the same point.

6.3.2 Radical measurement comparison

The comparison of measured OH, HO_2, RO_2 (total, simple and complex) and OH reactivity for the summer and winter campaign is shown in Figure 6.5. Figure 6.5 shows that for all the measured values, other than OH reactivity, the summer values are higher than the winter values. First, it is unsurprising that the summer radical concentrations are higher than those measured during the winter campaign as the light levels/photolysis rates were much higher during summer (e.g. $j(O^1D)$ was 4.3 times larger in summer compared to winter). The OH, HO_2 and total RO_2 concentrations are 3.5, 7.9 and 19 times larger, respectively, in summer compared to winter. These results are reflected in Figure 6.4 where: the OH concentration in winter is higher at similar $j(O^1D)$ levels and the HO_2 and RO_2 concentration in winter is smaller at similar $j(O^1D)$ levels.

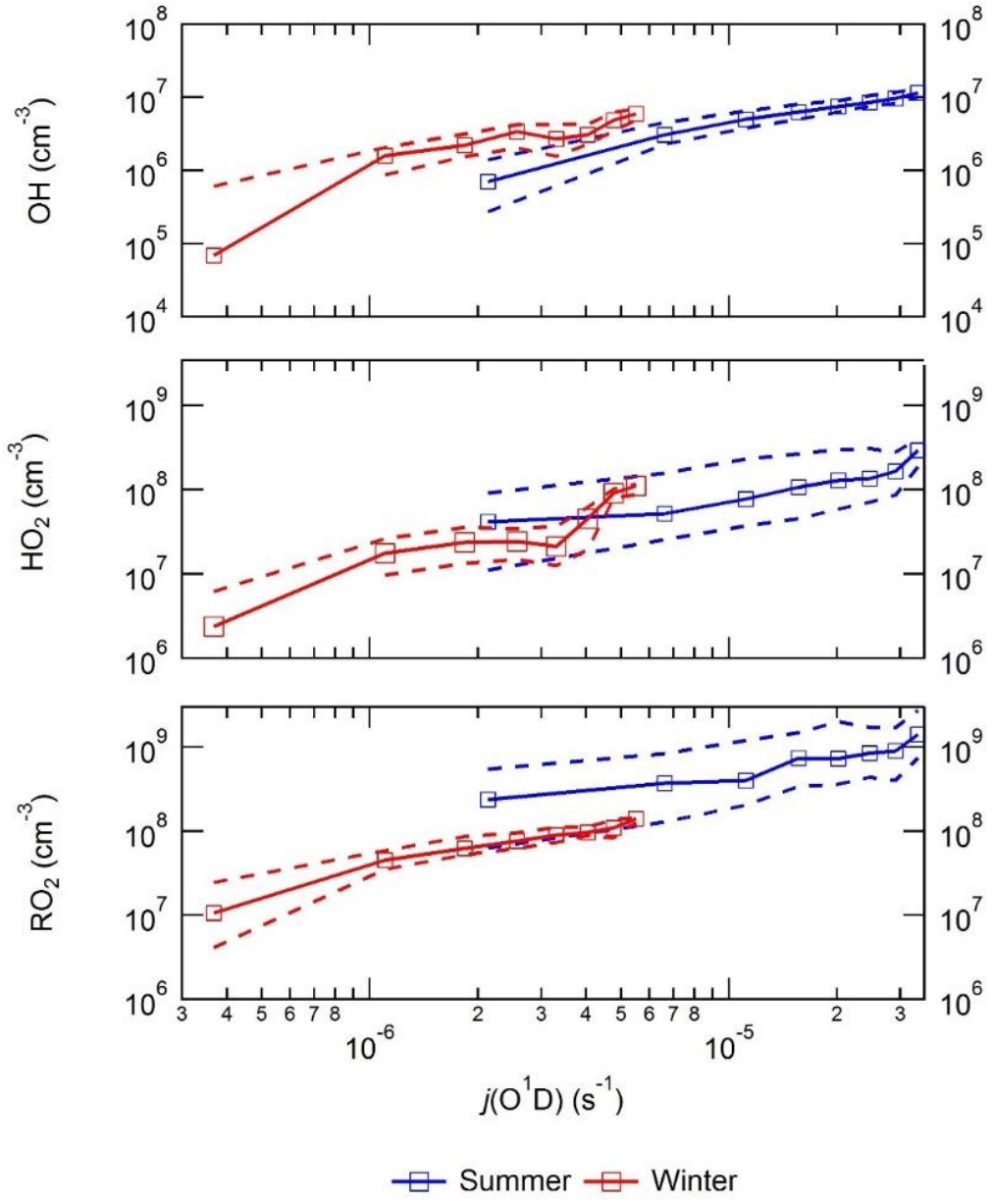

Figure 6.4 a) Comparison of summer and winter OH concentration binned against $j(O^1D)$. b) Comparison of summer and winter HO_2 concentration binned against $j(O^1D)$. c) Comparison of summer and winter RO_2 concentration binned against $j(O^1D)$. The dashed lines represent the 95 CI (confidence interval).

Whilst the difference between HO_2 and RO_2 for the two campaigns scales well with the difference in $j(O^1D)$, the differences in OH do not and this highlights how different chemical conditions are important to the formation of radical species. The discussion of different sources and sinks of radical species in summer and winter can be found in section.6.3.3.3. All the radical species in both summer and winter show a similar diurnal pattern, but with the species peaking at different

times and the summer, diurnals are broader due to the longer days. The OH concentration peaks at 11:30 and 12:30 in summer (OH average peak 9.7 x 10^6 molecule cm^{-3}) and winter (OH average peak 2.8 x 10^6 molecule cm^{-3}), respectively. Solar-noon for summer and winter was 12:30 in both campaigns. The HO_2 concentration peaks at 14:30 and 13:30 in summer (HO_2 average peak 2.3 x 10^6 molecule cm^{-3}) and winter (HO_2 average peak 2.95 x 10^6 molecule cm^{-3}), respectively.

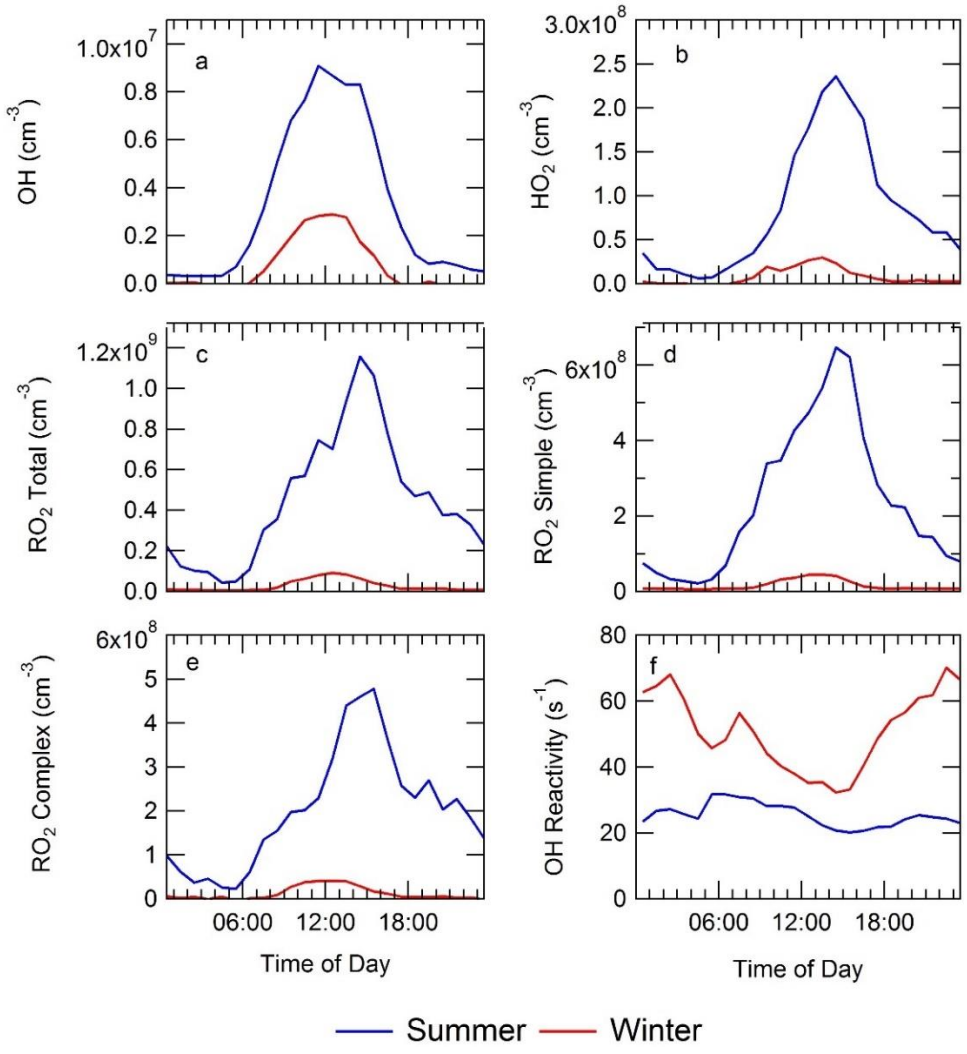

Figure 6.5 Comparison of measured species for both the summer(blue) and winter(red) campaign, the species compared are: a – OH, b – HO_2, c- Total RO_2, d – Simple RO_2, e – complex RO_2 and f - OH reactivity. The diurnals are median 1h averages.

All the peroxy radical measurements in summer peak at 14:30, whilst in winter complex and total RO_2 peak at 12:30 and simple RO_2 peaks at 13:30. The total

RO_2 median maximum concentration was 1.15 x 10^9 molecule cm^{-3} and 8.27 x 10^7 molecule cm^{-3}, for summer and winter, respectively. The simple RO_2 median maximum concentration was 6.5 x 10^8 molecule cm^{-3} and 4.4 x 10^7 molecule cm^{-3}, for summer and winter, respectively. The complex RO_2 median maximum concentration was 4.47 x 10^8 molecule cm^{-3} and 3.9 x 10^7 molecule cm^{-3}, for summer and winter, respectively. The largest shift in diurnal peak is observed for the peroxy radicals and this is probably caused by the shift in [O_3] peak from 14:30 in winter to 15:30 in summer. Also, unlike the winter campaign, the measured summer radical species (OH, HO_2 and RO_2) show significant night-time concentrations. The sources of the night-time radical are discussed in section.6.3.3.3. The OH reactivity is ~1.9 times larger during the winter (average k(OH) ~51 s^{-1}) campaign compared with the summer (average k(OH) ~ 27 s^{-1}) campaign, the major OH sinks for the summer and winter campaign is discussed in section.6.3.3.3.

A comparison of urban campaigns that took place in both the winter and summer is shown in Table 6.1. Table 6.1 shows that APHH campaign has the largest increase (factor of ~4.3) in $j(O^1D)$ between the campaign; the New York (Ren et al., 2006), Tokyo (Kanaya et al., 2007) and (Emmerson et al., 2005) campaigns have an increase by a factor of 1.7, 1.7 and 1.28, respectively. All the winter campaigns showed a higher NO concentration than the summer; whilst the O_3 concentration was higher for the summer campaigns. The increase in ozone between the summer and winter was highest for the APHH campaign; the O_3 increased by a factor of 5.41, 2, 1.02 and 2.2 for the APHH, New York, Tokyo and PUMA campaigns. The OH concentration increased by a factor of 3.5 for the APHH campaign; both the New York and Tokyo campaigns observed a higher increase by a factor of 7 and 4.2, respectively. However, the PUMA campaign had a lower increase between the winter to the summer campaign of ~1.5. The HO_2 concentration increased by a factor of 7.9, 5.88, 8.5 and 1 for the APHH, New York, Tokyo and PUMA campaigns, respectively.

Campaign	Ratio of summer/winter					Reference
	$j(O^1D)$	NO	O_3	OH	HO_2	
APHH, Beijing	4.3	0.03	5.41	3.5	7.9	This work
New York	1.7	0.0056	2	7	5.88	Kanaya et al. (2007)
IMPACT, Tokyo	1.7	0.32	1.02	4.2	8.5	Ren et al. (2006)
PUMA, Birmingham	1.28	0.27	2.2	1.5	1	Emmerson et al. (2005)

Table 6.1 Ratio of summer/winter for $j(O^1D)$, NO, O_3, OH and HO_2, the values are the ratio taken for noon-time average for each campaign. The HO_2, other than APHH, is HO_2^*.

6.3.3 Photostationary Steady-state expression for OH concentration

Using field-measured quantities, a steady-state approach has been used to calculate the OH concentrations for comparison with measurements for both summer and winter, and also to determine the major sources of OH measured during the campaigns. The photostationary steady-state equation for OH, obtained from the solution to $d[OH]/dt = 0$, is given by a balance of the rate of production and the rate of destruction of OH:

$$[OH]_{pss} = \frac{p(OH) + j(HONO)[HONO] + k[HO_2][NO]}{k_{OH}} \qquad \text{E6.1}$$

where p(OH) is the measured rate of OH production from ozone photolysis and the subsequent reaction of $O(^1D)$ with water vapour, k is the rate coefficient for the reaction of HO_2 with NO at the relevant temperature, and k(OH) is the measured OH reactivity. E6.1 is a simplification, and for winter only takes into account the production of OH from two photolysis sources (O_3 and HONO) and the reaction of HO_2 + NO. The summer steady-state also takes into account O_3+alkene reactions due to the high ozone concentration. The pseudo first-order rate of loss of OH was constrained using the measured OH reactivity during the campaign, and hence includes all loss processes for OH.

The comparison for measured OH with the results from the steady-state for both summer and winter is shown in Figure 6.6. It shows that whilst the experimental budget can be closed during the winter-time, it cannot be closed in the summer-time and highlights there is a missing source of OH. On average the steady-state calculation in summer underpredicts the OH concentration by ~2.2.

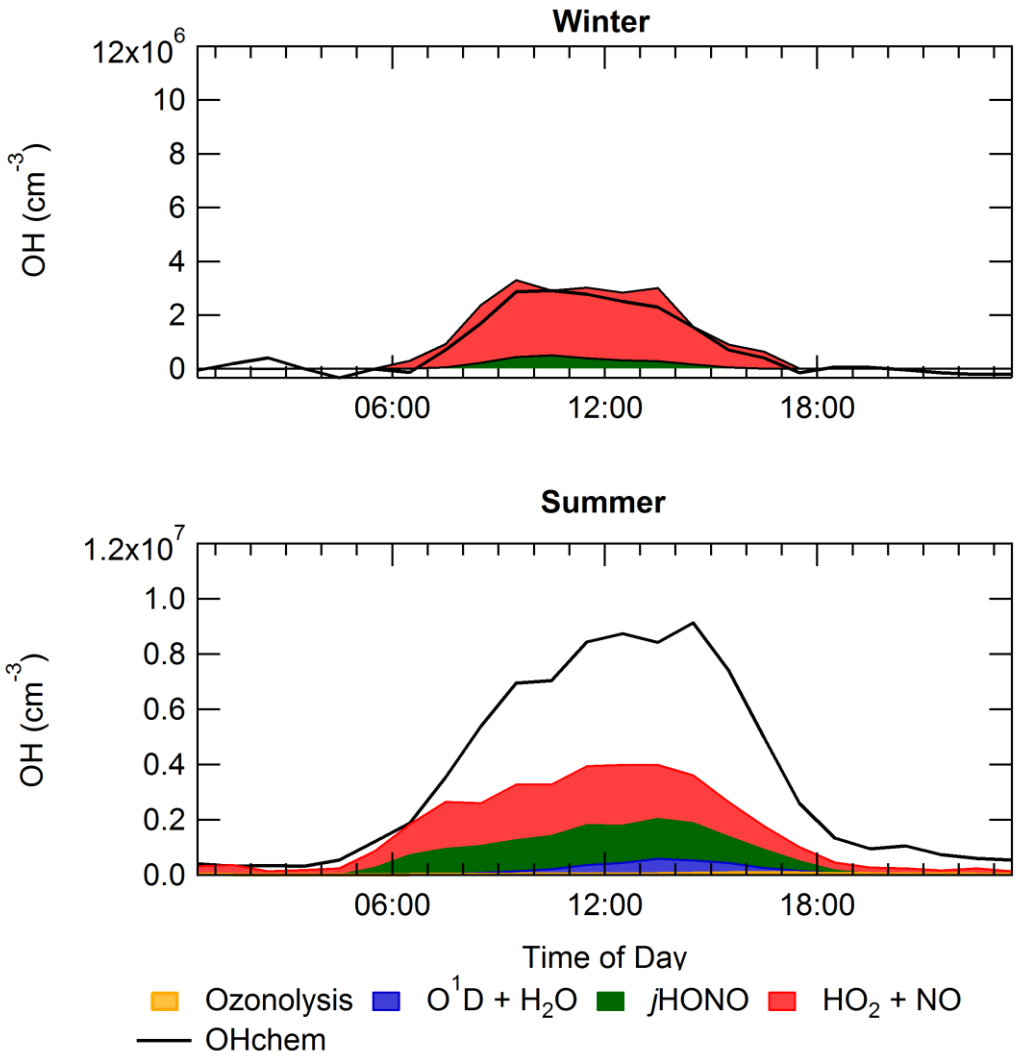

Figure 6.6 Top – Comparison of measured average median diurnal of OH with OH calculated from a photostationary steady-state for winter. Bottom - Comparison average median diurnal of OH with OH calculated from a photostationary steady-state for summer. The measured OH is shown in black, and the steady-state calculation shows the different sources in the stacked plot. The average diurnal is shown for 1-hr averages.

It also highlights different sources of OH in both summer and winter, with winter dominated by the reaction of HO_2 + NO (87%) whilst in summer this reaction only

contributes to 47% of OH production. The other source of OH radicals during the winter campaign is the photolysis of HONO contributing the remaining 13% whilst in summer it contributes ~42%. The winter campaign shows that the reaction of O^1D with water vapour is not a significant source of OH, whilst in summer it contributes ~9.8%. The comparison between measured and calculated OH for summer shows an agreement between 00:30 – 06:30, coinciding with the NO peak in the summer campaign. This highlights that the missing source of OH is required under low NO conditions, which is experienced in the afternoon in summer, and therefore the experimental budget can be closed in winter but not in summer. Figure 6.6 shows the average OH calculated for OH are 1.44×10^6 molecule cm^{-3} and 2.64×10^6 molecule cm^{-3}, and highlights that the magnitude of known sources in winter and summer is similar.

6.3.3 MCM base model

6.3.3.1 Model Results

For both the winter and the summer campaign, the measurements of OH, HO_2, RO_2 and k(OH) were compared with the results from Master Chemical Mechanism v 3.3.1. A side-by-side average diurnal comparison of measurements with the MCM-base model for both summer and winter is shown in Figure 6.7. It shows that in summer OH is reproduced well by the MCM-base model (within ~26% error), whilst in winter the OH concentration is underpredicted by ~1.7. Whilst OH is reproduced well by the MCM-base model in summer, the comparison between measured and modelled HO_2 for summer shows that it is due to the overprediction of HO_2. Alongside the underprediction of OH in winter the MCM-base model underpredicts both HO_2 and RO_2 by 5.9 and 25 at the peak values, respectively. Whilst the MCM-base model overpredicts the HO_2 concentration in summer, it underpredicts the RO_2 concentration by a factor of 5.2. For all the radical species in both summer and winter, the MCM-base model can reproduce the same diurnal trend that is observed in the measurements, in summer the model can reproduce the night-time HO_2 concentration within ~26% error but underpredicts both night-time OH and RO_2. The MCM-base for winter reproduces the observation of little to no OH at night-time, whilst it underpredicts the night-time concentration of HO_2 and RO_2. This work shows that under

different chemical conditions the MCM, representing our current understanding of tropospheric oxidative chemistry, cannot reproduce the measured radical concentration with different responses to different NO_x/O_3 regimes that were observed during the winter and summer campaign.

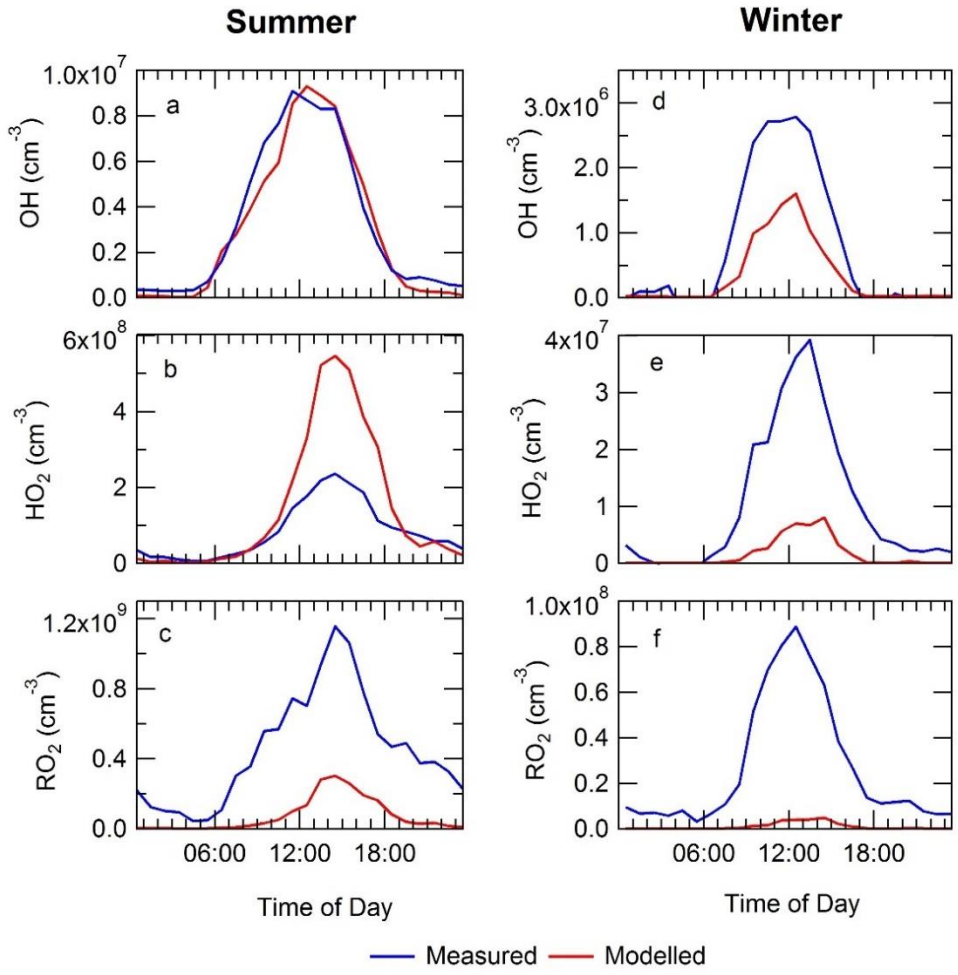

Figure 6.7 Plots a – c shows the comparison median average diurnal comparison of measured with modelled values for summer: a – OH, b – HO_2 and c – total RO_2. Plots d – f shows the comparison median average diurnal comparison of measured with modelled values for winter: d – OH, e – HO_2 and f – total RO_2.

6.3.3.2 OH Reactivity

The comparison of measured OH reactivity with modelled shows whether all OH sinks have been captured by the model, as OH reactivity is the measure of the total rate of removal by the sinks of OH, and in general if there is a difference it is from unmeasured VOCs. The comparison of measured OH reactivity with modelled OH reactivity for both summer and winter is shown in Figure 6.8. Figure

6.8 highlights that the OH reactivity budget can be closed in winter, whilst summer there is an average difference between measured and modelled of ~9.5 s^{-1} across the entire day. The missing OH reactivity in summer highlights that there is a missing source of OH reactivity, and since the source is present across the entire day suggests it is primary in nature as it doesn't display a peak when oxidants processes dominate or secondary OVOCs (e.g. glyoxal and HCHO) peak. In section.5.4.8 there is a discussion on missing sources of reactivity and comparison with previous OH reactivity measurements in summer urban environments, and the literature suggests that a missing primary source has been observed when NO is low (Whalley et al., 2016, Yoshino et al., 2006, Chatani et al., 2009, Dolgorouky et al., 2012).

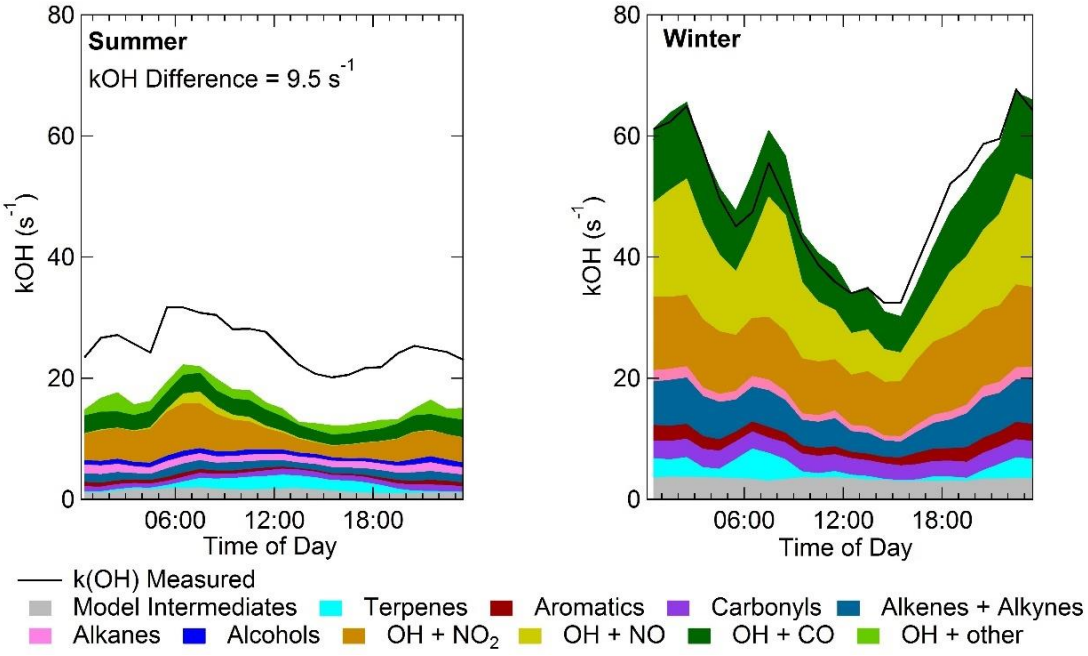

Figure 6.8 Left – Average median diurnal OH reactivity comparison between measured (black line) and modelled stacked plot for summer. Right - Average median diurnal OH reactivity comparison between measured (black line) and modelled stacked plot for winter. The OH + other represents contributions from OH + O_3, OH + H_2, OH + H_2O_2, OH + HO_2, OH + NO_3, OH + HO_2NO_2, OH + HONO, OH + HNO_3 and OH + SO_2.

The OH reactivity in winter is 1.9 times larger compared with summer, with 64.3% from the sum of OH + NO, OH + NO_2 and OH + CO., whilst in summer only 36.4% of the reactivity comes from the sum of OH + NO, OH + NO_2 and OH + CO. The rest of the reactivity in summer and winter is derived from VOCs with a similar

contribution of 23.2% and 25.2%, respectively. Also, the model intermediates have a similar contribution to total reactivity in summer and winter; 6.8% and 5.0%, respectively. This work shows that under lower NO_x conditions there is missing reactivity, whilst during winter the reactivity is dominated by the reaction of OH with NO, NO_2 and CO.

6.3.3.3 Sources and Sink of radicals

6.3.3.3.1 Production

Rate of production analysis (ROPA) has been performed to analyse which species/reactions were contributing to the primary production and termination of the radical species. Primary production is when a non-radical species forms a radicals species; whilst termination is when a radical species forms a non-radical species ending the chain reaction. The comparison of the average primary production of radicals in summer and winter is shown in Figure 6.9. Figure 6.9 shows that the primary production is ~3.6 times higher in summer compared to winter, the higher production in summer is driven by the higher light level observed with the $j(O^1D)$ ~6.3 times larger.

The comparison also shows that in summer there is a significant contribution from both ozonolysis and VOC + NO_3 at night-time contributing ~11% and 2.2%, respectively, to the total primary production. Whilst ozonolysis in winter does contribute ~10% of the total primary radical production, the formation of radical falls to almost zero at night-time and this is reflected in the measurements of OH reduced to ~zero at night. The small contribution from ozonolysis at night is due to the small O_3 concentration, see section.6.2. In both summer and winter, the primary production is dominated by the photolysis of HONO, with HONO contributing ~83% and 77% of the total primary radical formation. In summer significant primary production from $O^1D + H_2O$ (5.5%) is observed, whilst in winter <1% of radicals are from $O^1D + H_2O$. The photolysis of carbonyls species in winter and summer contributes 4.08% and 5.4%, respectively, and shows a similar percentage contribution. The comparison between percentage contribution from different primary sources shows that they are very similar in both summer and winter, although summer shows larger contribution from O^1D and VOC + NO_3

which is compensated by the decrease in contribution from the photolysis of HONO.

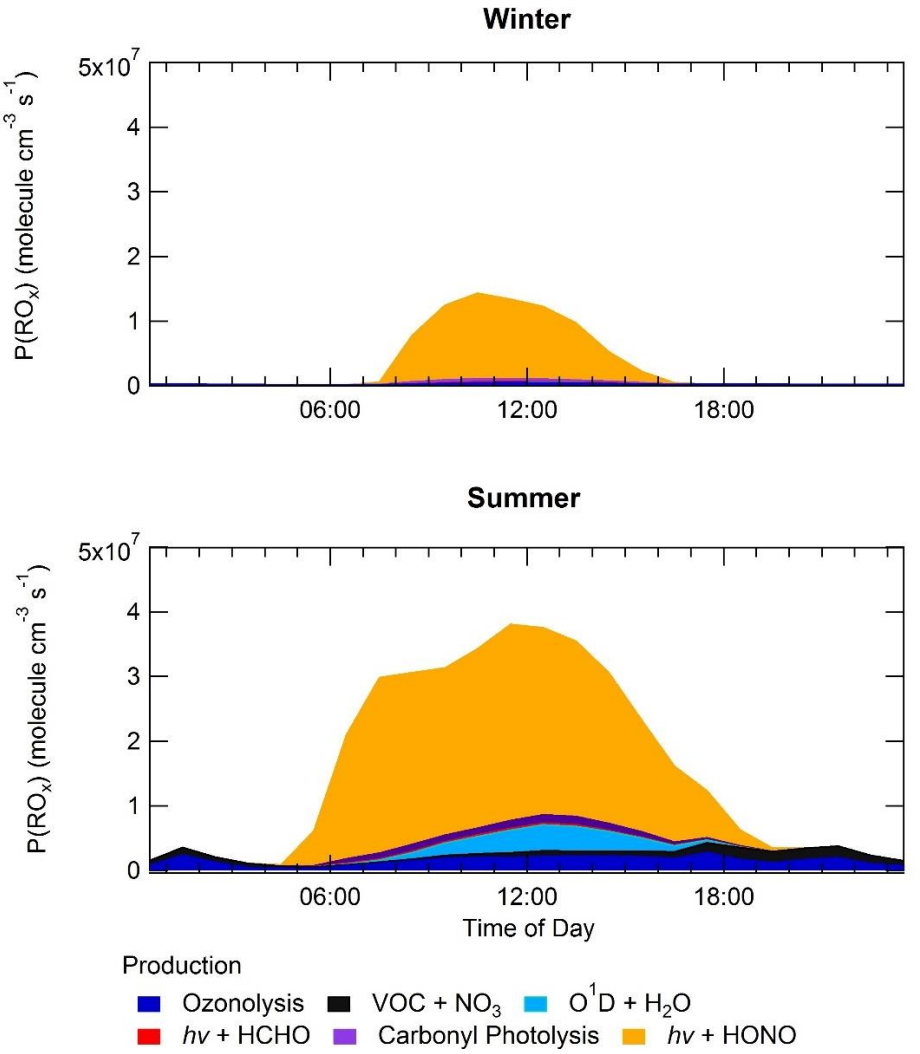

Figure 6.9 Top – Average median diurnal of primary production from a ROPA analysis perform on the MCM-base model for winter. Bottom - Average median diurnal of primary production from a ROPA analysis perform on the MCM-base model for summer.

6.3.3.3.2 Termination

The comparison of the average rate of termination of radicals in summer and winter is shown in Figure 6.10. Figure 6.10 shows that, like the primary production, the termination ~3.6 times higher in summer compared to winter. The comparison shows that the significant contributors to the termination in both summer and winter are OH + NO, OH + NO_2 and net-PAN formation; although in summer contributions from HO_2 + HO_2 (1.47%) and RO_2 + HO_2 (3.12%) are also observed. The dominant termination reaction in both summer and winter is

$OH + NO_2$ with total percentage contribution of 63% and 43%, respectively. The total percentage contribution from OH + NO in summer and winter is 11.3% and 37%, respectively. Finally, the contribution from the net formation of PAN is 14% and 20% in summer and winter, respectively. The major difference between the termination reactions in summer and winter is that much higher termination from OH + NO is observed in winter, and in summer when the NO is lower (especially in the afternoon) termination through the peroxy self-reaction pathways are observed.

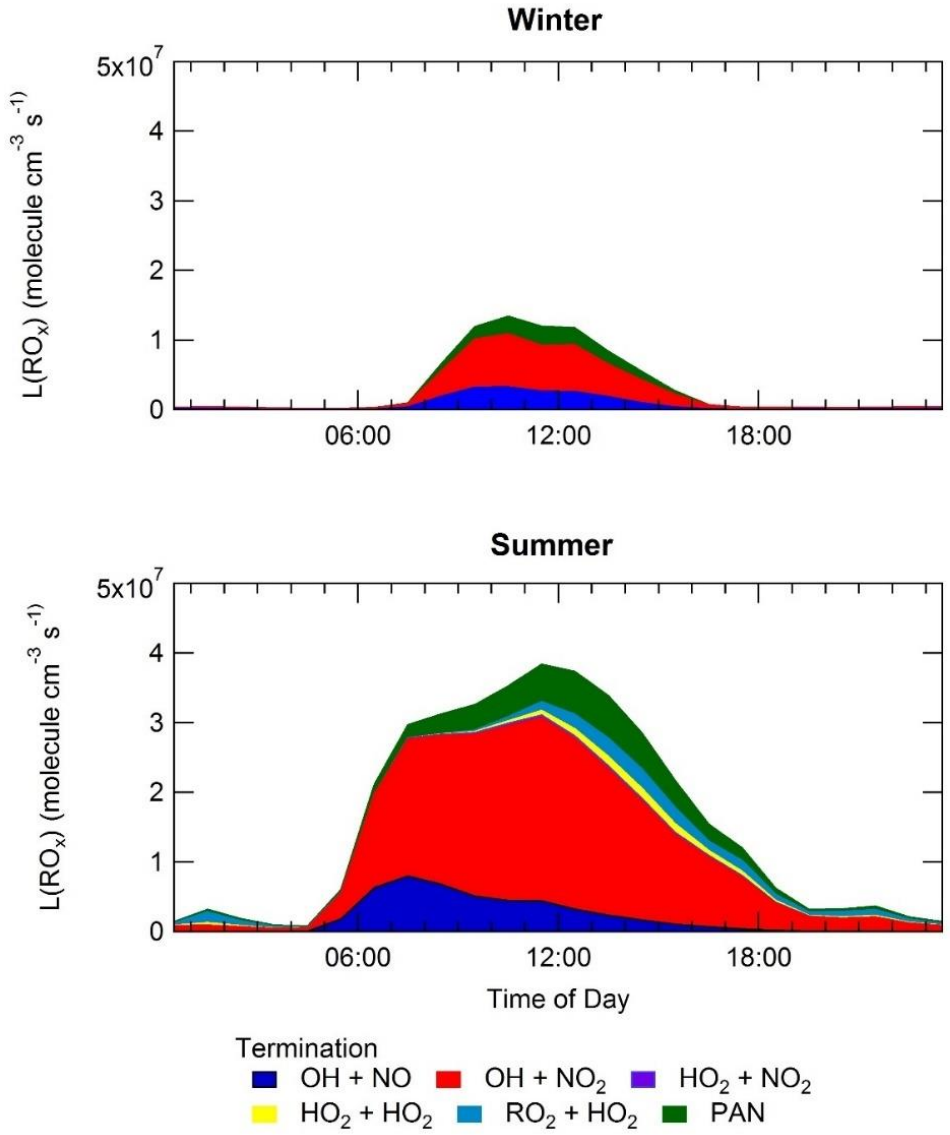

Figure 6.10 Top – Average median diurnal of termination of radicals from a ROPA analysis perform on the MCM-base model for winter. Bottom - Average median diurnal of termination of radicals from a ROPA analysis perform on the MCM-base model for summer.

6.3.4 Radicals under different NO_x Regimes

As discussed earlier in section.6.3.3, the MCM does not reproduce the measured radical concentrations very well, and Figure 6.11 shows how well the MCM does at different NO concentrations for both summer and winter. The winter campaign goes to a considerably higher NO range as more NO was observed during the campaign, and the converse is observed for summer with the bin/range lower than the winter. Figure 6.11 shows that the MCM has a similar trend as the measurements for OH across the whole NO range to that of the measurements, with the OH concentration reproduced well by the MCM between 0.15 - 2.2 ppbv. Above 2.2 ppbv and 5 ppbv of NO for winter and summer, respectively, the MCM starts to underpredict the OH concentration, although the underprediction increases more rapidly during the winter campaign compared to the summer campaign with increasing NO. The ratio of measured:modelled HO_2 also shows a similar trend across different NO ranges for both the summer and winter campaign, although similar to OH, the HO_2 underprediction for the winter increases more rapidly at higher NO concentration compared to summer. The underprediction of HO_2 starts at [NO] (same as OH) of 2.2 and 5 ppbv for winter and summer, respectively. The overprediction of HO_2 in summer shows a steady increase below 5 ppbv of NO for summer, whilst the overprediction in winter increases more rapidly below 2.2 ppbv of NO. The RO_2 concentration is underpredicted by the MCM-base model in both summer and winter. The winter underprediction shows an increasing underprediction with increasing NO above 2.2 ppbv, whilst the summer shows a minimum at 0.6 ppbv and the underprediction increasing above and below 0.6 ppbv. The order of magnitude of the underprediction for RO_2 in both summer and winter is very similar within the 95 CI (confidence interval). This work shows that different chemistry is required to resolve the differences between measurement and model for the different NO regimes. The work also highlights that the order of magnitude for the under- or overprediction of radicals in different NO regimes is different for both summer and winter, highlighting that NO is not the only factor that contributes to the differences in measurements and modelled values, suggesting that different chemical conditions (e.g. VOC mixes, light levels and RH) and meteorological conditions are important.

The average VOC mixing ratio measured by the GC-FID during both the summer and the winter campaign is shown in Table 6.2. Table 6.2 shows that the VOCs measured during the winter campaign were, in general, higher than those in the summer campaign, and this is reflected in the OH reactivity comparison in Figure 6.8.

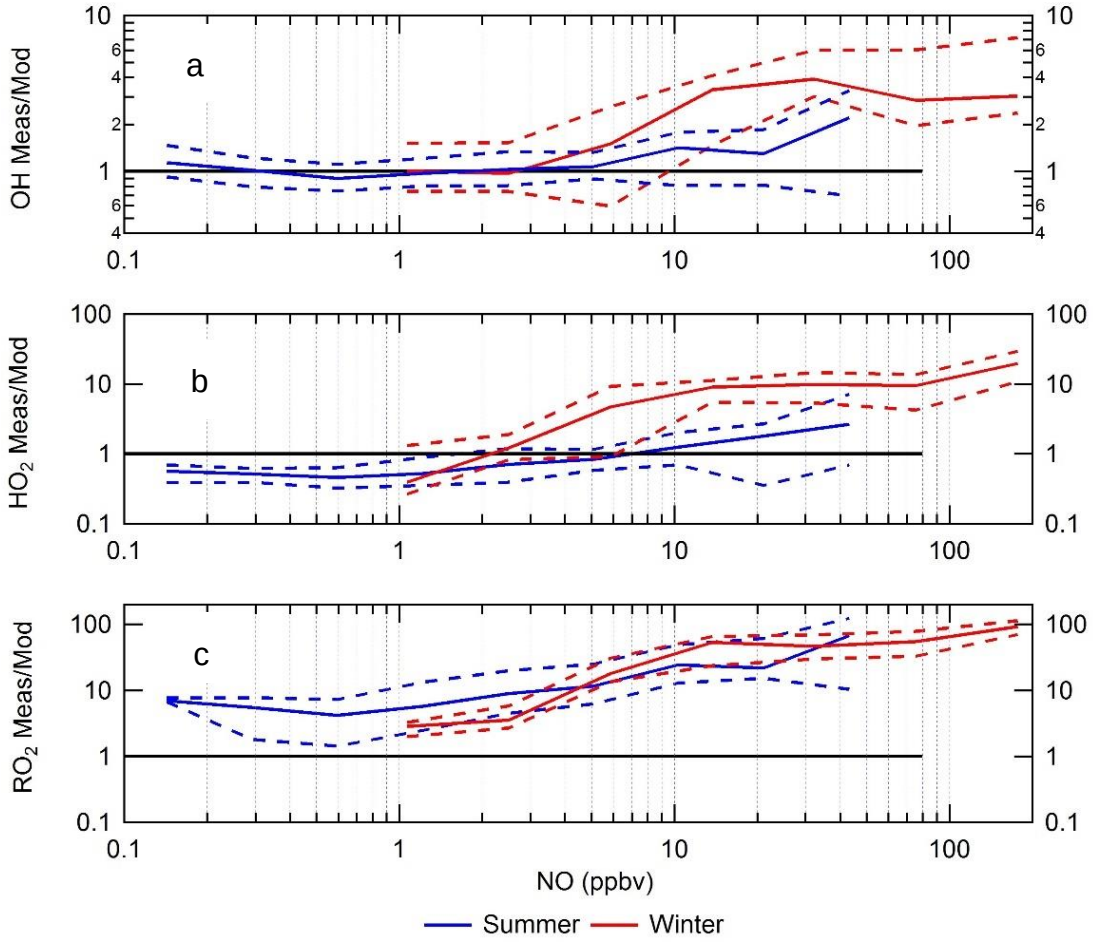

Figure 6.11 a) Ratio of measured:modelled OH binned against the log of NO. b) Ratio of measured:modelled HO_2 binned against the log of NO. c) Ratio of measured:modelled RO_2 binned against the log of NO. It should be noted that the ratio was only taken for daytime conditions ($j(O^1D) > 1 \times 10^{-6}$ s^{-1}).

The C_2H_6 and C_2H_4 is much higher in winter (9.56 abd 8.09 ppbv, respectively) compared with summer (3.47 and 1.37, respectively). The other alkane VOCs are comparative in summer and winter.

VOC	Winter Mixing Ratio (ppbv)	Summer Mixing Ratio (ppbv)
Alkanes		
C_2H_6	9.56	3.47
C_2H_4	8.09	1.37
C_3H_8	7.2	6.22
C_3H_6	1.4	0.3
isobutane	1.42	0.3
butane	2.91	4.01
hexane	1.04	0.77
heptane	0.23	0.21
pentane	1.19	1.07
2-methylpentane	0.82	0.79
2-methylbutane	2.17	2.66
3-methylpentane	0.82	0.79
Alkenes		
trans-but-2-ene	0.27	0.13
but-1-ene	0.38	0.15
isobutene	0.46	0.2
cis-but-2-ene	0.21	0.12
1,3 - butadiene	0.41	0.19
trans-2-pentene	0.21	0.13
cis-2-pentene	0.17	0.1
isoprene	0.51	0.64
Aromatics		
Benzene	1.74	0.58
Toluene	1.97	1.61
Ethyl benzene	0.96	0.56
o- xylene	0.96	0.24
Carbonyls		
CH_3CHO	1.97	0.88
CH_3OH	2.71	2.1
CH_3COCH_3	0.78	3.6
Alkynes		
C_2H_2	6.05	1.14

Table 6.2 Average mixing ratios of the VOCs measured by the GC-FID.

Other than isoprene (winter 0.51 ppbv and summer 0.64 ppbv) all the alkenes are higher in summer compared to winter. Benzene, ethyl benzene and o-xylene are ~3, 1.7 and 5 time higher in winter compared with summer, respectively, although toluene has a similar concentration in winter (1.97 ppbv) compared with summer (1.61 ppbv). CH_3OH and CH_3CHO is ~1.2 and 2.2 times higher in winter compared with summer, respectively, although the CH_3COCH_3 is ~4.6 times higher in summer. The higher VOC loading in winter will increase the OH reactivity (as seen in Figure 6.8) and lead to RO_2 formation. The rate constant also changes at different temperatures, the average temperature in the winter and summer campaign was 5°C and 26°C, respectively. The HO_2+ NO and RO_2 + NO rate constant was 7% and 9% faster in winter. The higher HO_2 + NO and RO_2 + NO rate constant in winter may drive the faster rise for the underprediction of the radicals under high NO conditions.

6.3.4.1 Additional primary production

In this section, the impact of adding additional RO_2 source into the model for both summer and winter will be explored. Previously it has been suggested that introducing an additional primary radical source into the model, such as Cl atom chemistry, can help reconcile measurements with the model (Tan et al., 2017). The impact of Cl chemistry in the summer model has been explored in chapter.5.4.6.3, but has not be explored for winter as no measurement of $ClNO_2$ was made. An additional primary source of RO_2 radicals was inputted into the MCM-base so measured and modelled values in both summer and winter for RO_2 were reconciled. Details about the RO_2 species and the rate for the summer and winter model can be found in section.4.3.1 and section.5.3.1. From now on, the winter model with the additional primary source of RO_2 radical is called MCM-PRO2-W, and the summer is called MCM-PRO2-S. The additional primary source of RO_2 radical required to reconcile measured total RO_2 with modelled total RO_2 was calculated using E6.2:

$$P'(RO_x) = k_{HO2+NO}\,[HO_2]\,[NO_2] - P(HO_2)_{prim} - P(RO_2)_{prim} - k_{VOC}\,[OH] + L(HO_2)_{term} + L(RO_2)_{term} \quad \text{E6.2}$$

Figure 6.12 shows a comparison modelled primary production (from HONO, O^1D + H_2O, ozonolysis, HCHO, VOC + NO_3 and photolysis of carbonyls) compared to

the additional source of RO_2 required to reconcile measured of RO_2 with modelled. The results show that the average additional primary production for summer is ~1.8 times larger than winter. Although the additional production for winter is ~6.3 times larger compared to the modelled primary production, the additional primary production is ~0.9 of the modelled primary production for summer. These results show that more primary production is required to be inputted into the model when the NO is higher (winter campaign) to reconcile the model with the measurements.

The average diurnal comparison between measured and modelled values from both MCM-base and the model with the additional RO_2 for OH, HO_2 and RO_2 can be found in Figure 6.13.

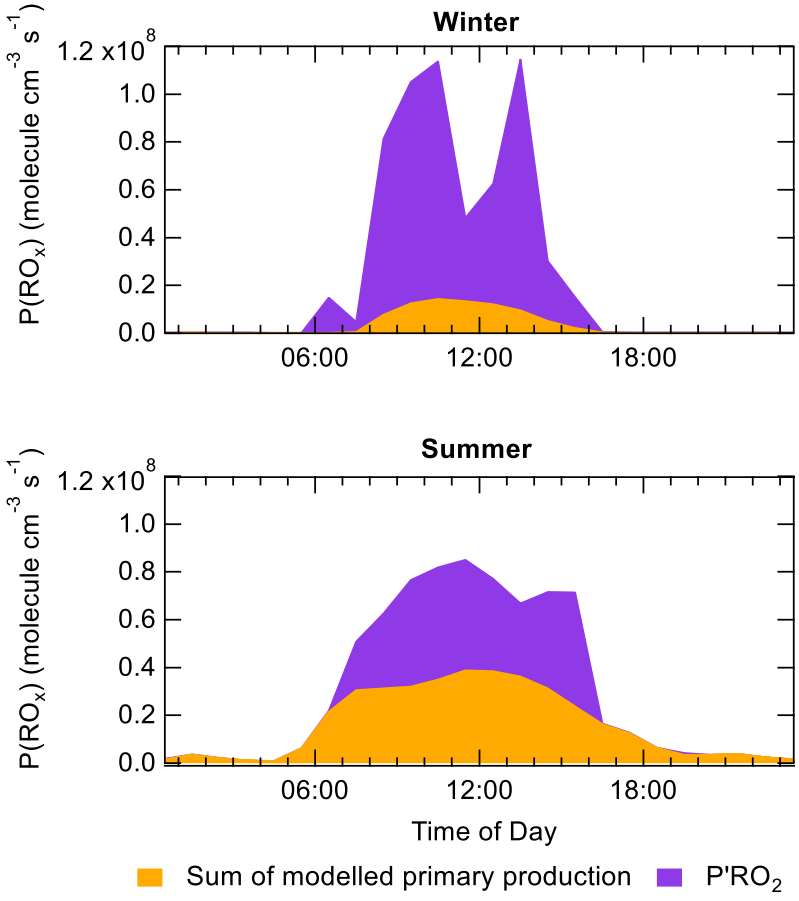

Figure 6.12 Top – Total primary production of RO_x (OH + HO_2 + RO_2) in the MCM-PRO2-W. Bottom - Total primary production of RO_x (OH + HO_2 + RO_2) in the MCM-PRO2-S. The yellow represents the sum of primary production from HONO, O^1D + H_2O, ozonolysis, HCHO, VOC + NO_3 and photolysis of carbonyls.

It shows that the introduction of additional RO_2 in the model causes an overprediction of OH and HO_2 in both summer and winter. Before, the winter model underpredicted both OH and HO_2 and shows that the additional RO_2 is efficiently recycling into HO_2 and OH once inside the model. Previously the MCM-base model could reproduce OH very well and overpredicted HO_2, and therefore introducing additional RO_2 is leading to a further overprediction of HO_2 leading to an overprediction of OH. For winter, the MCM-PRO2-W, compared with the base model, has increased the OH, HO_2 and total RO_2 concentration by 4.1, 12.3 and 22, respectively.

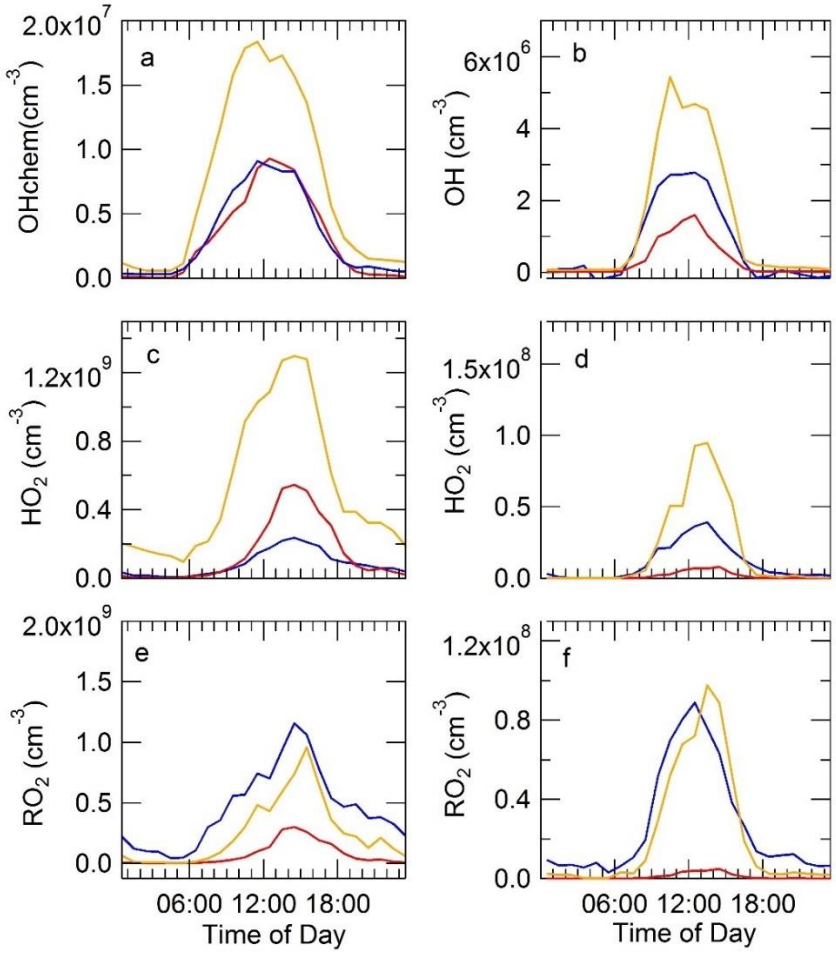

Figure 6.13 Plots a, c, and show the comparison median average diurnal comparison of measured (blue) with modelled (MCM-base - red and MCM-PRO2-S - yellow) values for summer: a – OH, c – HO_2 and e – total RO_2. Plots b, d, and f shows the comparison median average diurnal comparison of measured (blue) with modelled (MCM-base - red and MCM-PRO2-W - yellow) for winter: b – OH, d – HO_2 and f – total RO_2.

For summer, the MCM-PRO2-S, compared with the base model, has increased the OH, HO_2 and total RO_2 concentration by 2.2, 3.18 and 6.11. Normalising the ratio MCM-PRO2:MCM-base to the ratio of MCM-PRO2:MCM-base for total RO_2 for winter shows that for the increase in RO_2 in the model to match measurements increases the HO_2 and OH by 55% and 18% compared to the base, respectively. Doing a similar analysis for summer shows that matching model to measurement of RO_2 increases the OH and HO_2 concentration by 52% and 36% compared to the base model, respectively. Once the total RO_2 concentration in the model matches measurements there is a similar increase (~50%) in the HO_2 in both summer and winter, whilst the OH recycling from HO_2 into OH is more efficient in summer (36%) compared to winter (18%). These results show that for different chemical/meteorological conditions that were observed during the two campaigns, an additional source of RO_2 cannot reconcile the model with measurement, and leads to an overprediction for OH and HO_2 in both summer and winter. The overprediction of HO_2 and OH when the RO_2 agrees insinuates that not all the 'missing' chemistry is related to a missing additional source of RO_2 radicals in Beijing in contrast with the conclusion drawn by Tan et al.(2018).

6.3.4.2 Dependence on the RO_2 + NO rate constant

As discussed previously in chapter.4.4.6 and chapter.5.1.6.4, other than for CH_3O_2 and $C_2H_5O_2$, the rate constants for the reaction of RO_2 + NO in the MCM just take values kRO2NO and kAPNO. kRO2NO is the rate constant for RO_2 species + NO; whilst kAPNO is the rate constant for acyl RO_2 species + NO. The previous chapters explored whether more complex/larger RO_2 species may have a different rate constant and hypothesised if this could be why the MCM-base does not reproduce the radical concentration in both summer and winter. This section will explore the impact of reducing the RO_2 + NO rate constant in the winter and summer, with the rate constant of kRO2NO and KAPNO was decreasing by a factor of 2 and 10 in model runs named MCM-kRO2-2 and MCM-kRO2-10. The average median diurnal comparison for between measured OH, HO_2 and total RO_2 with results from MCM-base, MCM-kRO2-2 and MCM-kRO2-10 is shown in Figure 6.14. For winter, decreasing the rate constant of RO_2 + NO increases the RO_2 concentration but does not impact HO_2 or OH.

Whilst in summer decreasing the rate constant by a factor of 10 leads to the model reproducing the RO_2 concentration very well; also, the agreement between measured and modelled HO_2 is improved and OH is reproduced well. These results show that decreasing the rate constant for RO_2 + NO increases the RO_2 concentration in the model and decreases the HO_2 and OH.

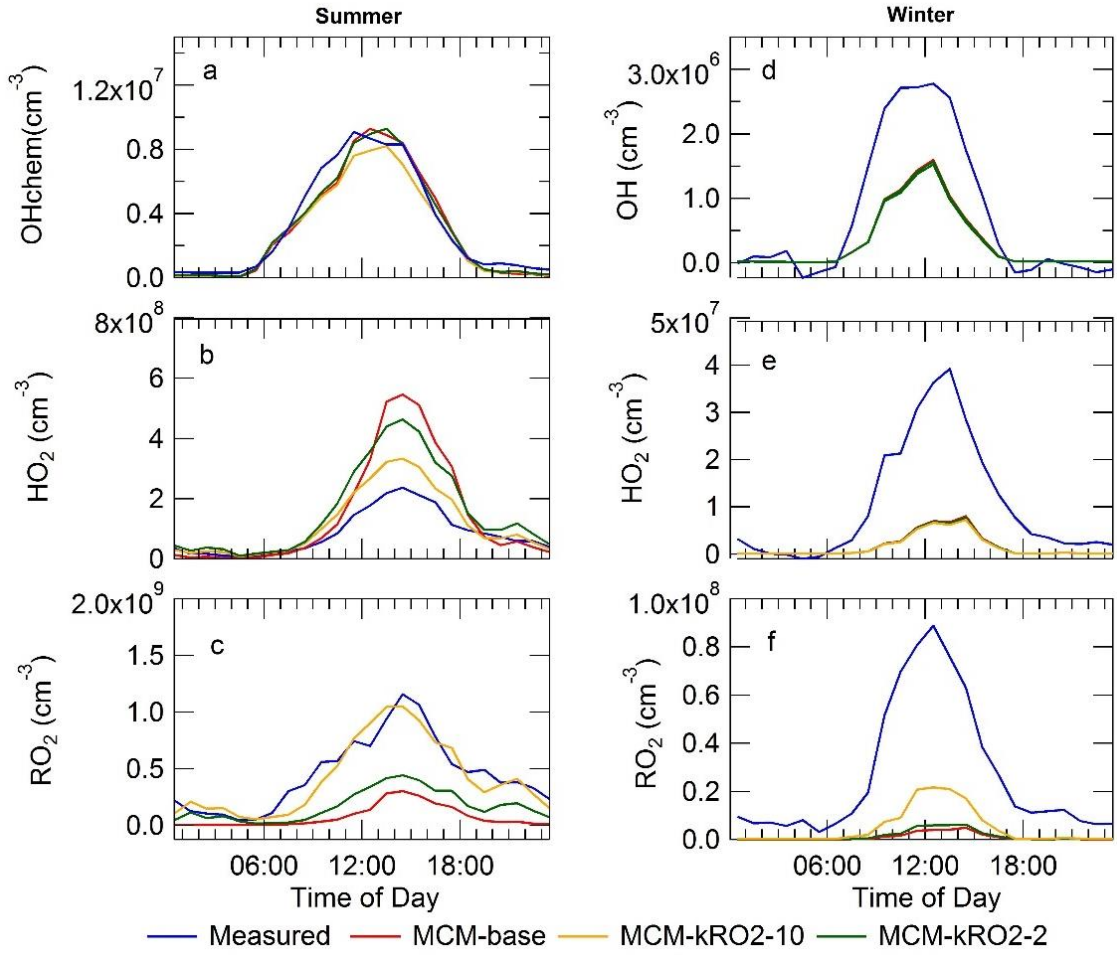

Figure 6.14 Plots a – c shows the comparison median average diurnal comparison of measured (blue) with modelled(MCM-base – red, MCM-kRO2-10 - yellow and MCM-kRO2-2 - green) values for summer: a – OH, b – HO_2 and c – total RO_2. Plots d – f shows the comparison median average diurnal comparison of measured (blue) with modelled (MCM-base – red, MCM-kRO2-10 - yellow and MCM-kRO2-2 - green) for winter: d – OH, e – HO_2 and f – total RO_2.

The effect of decreasing the OH and HO_2 is not effective in winter when the original model scenarios already underpredict their concentrations, such behaviour is seen in most urban studies in high NO environments (see Chapter.4, table.4.5) (Ma et al., 2019, Kanaya et al., 2007, Ren et al., 2013, Tan et al., 2018).

On the other hand, decreasing the rate constant of RO_2 + NO for an urban environment with lower NO improves the agreement between the measured and model values for all radicals.

The comparison of the ratio of measured:modelled(MCM-base) and measured:modelled(MCM-kRO2-10) for winter and summer is shown in Figure 6.15.

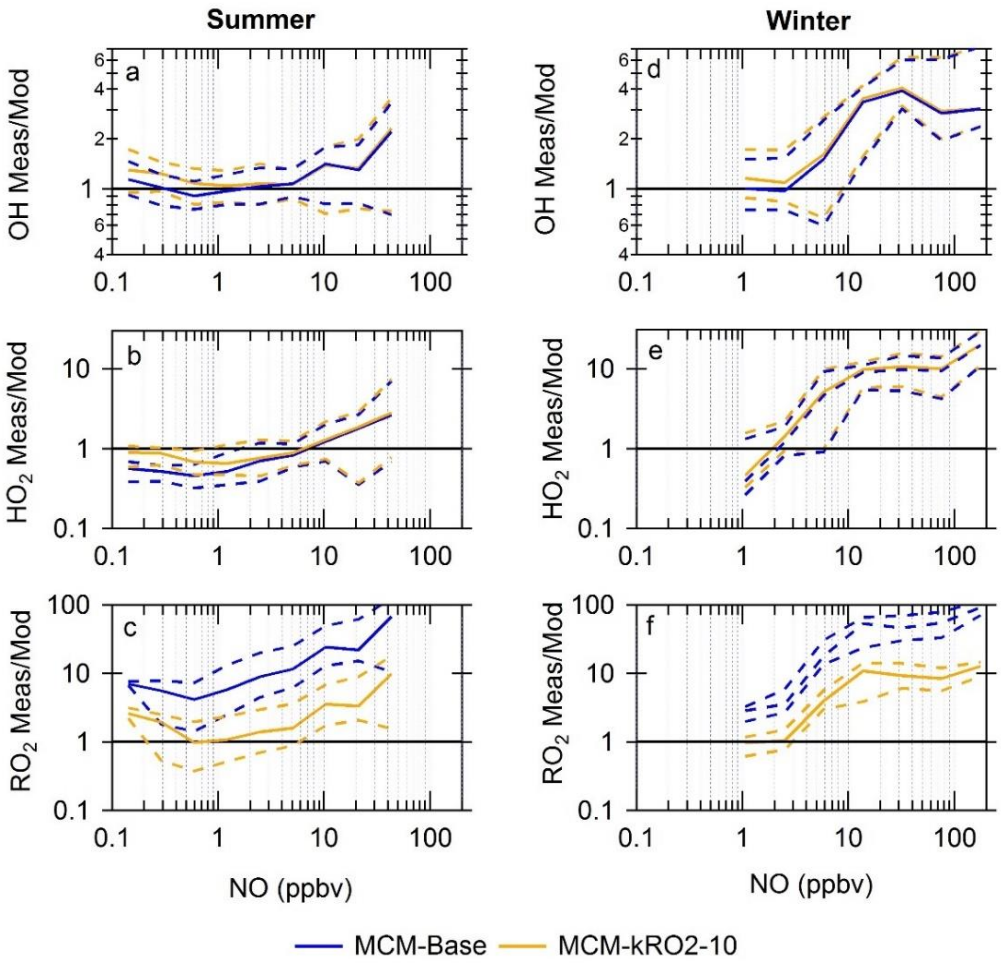

Figure 6.15 Plots a – c shows the ratio of measured:modelled(MCM-base) and measured:modelled(MCM-kRO2-10) binned against the log of NO for summer: a – OH, b – HO_2 and c – total RO_2. Plots d – f shows the ratio of measured:modelled(MCM-base) and measured:modelled(MCM-kRO2-10) binned against the log of NO for winter: d – OH, e – HO_2 and f – total RO_2. It should be noted the ratio was only taken for daytime values ($j(O^1D) > 1 \times 10^{-6}$ s^{-1}).

The results in Figure 6.15 show similar results to the average diurnal comparison in Figure 6.14 where the RO_2 concentration is increased throughout the NO_x range, whilst OH and HO_2 are only impacted at the lower NO values (less than 5 ppbv). The deviation of the ratio of measured:modelled(MCM-kRO2-10) from measured:modelled(MCM-base) for OH and HO_2 occurs at the same NO concentration (below 5 ppbv) for both the summer and the winter models. The deviation of OH and HO_2 at the same NO for winter and summer suggests that above 5 ppbv of NO the radical recycling through NO is still the dominant reaction. Whilst at lower NO (below 5 ppbv) the increase in RO_2 decreases the OH and HO_2 concentration suggesting that termination of the radical chain reaction increases and competes against the recycling reaction with NO.

Figure 6.15 also shows that for both summer and winter the model agreement with the measurements is improved at the lower range of NO (below 2 ppbv) and suggest autoxidation is occurring at low NO (below 5 ppbv) competing with RO_2 + NO. See section.5.1.6.4 for a wider discussion into autoxidation.

6.3.5 Impact of HONO

6.3.5.1 Model unconstrained to HONO

HONO is the dominant source of primary radical formation in both the summer and winter-time with photolysis of HONO contributing to 73% and 86%, respectively, as shown in section.6.3.3.3. However, HONO measurements are difficult to make and there can be large variability between different instruments and techniques. The MCM-base model in both winter and summer was been constrained to the measurement of HONO, the final HONO measurement has been determined from the several different HONO instruments present for both the APHH campaigns and details from this process can be found in (Crilley et al.). This section will explore the importance of using measurements of HONO in the model in both the winter- and summer-time, rather than modelled HONO which is solely formed and lost through the reactions shown in Table 6.3, for the model used in this work.

Reaction	Rate at 298 K
OH + NO → HONO	9.76 x 10^{-12} cm^3 $molecule^{-1}$ s^{-1}
HONO + hv → OH + NO	*j*(HONO) (s^{-1})
HONO + OH → NO_2	5.98 x 10^{-12} cm^3 $molecule^{-1}$ s^{-1}

Table 6.3 Table showing the reaction in the MCM for the production and destruction of HONO. The rate constant from: http://mcm.leeds.ac.uk/MCM/.

Exploring the impact of using modelled HONO rather than measured HONO is important as generally models significantly underpredict the HONO concentration (Lee et al., 2016, Acker et al., 2006, Kleffmann, 2007, Li et al., 2012), and this is thought to be caused by additional heterogeneous sources of HONO which are not in the model, and which has been discussed more in section.1.2.5. To explore the impact of using modelled HONO the MCM-base model was unconstrained to measured HONO, and this model scenario from now on is called MCM-unHONO. The comparison of the measured OH and HONO with the modelled OH and HONO from the MCM-unHONO is shown in Figure 6.16.

First, it shows that in both summer and winter the HONO concentration is underpredicted by ~3.2 and ~10 by the MCM-unHONO model. MCM-unHONO underpredicts the OH concentration by 2.7 and 8.5 in summer and winter, respectively. The underprediction of HONO and OH by MCM-unHONO is very similar. In contrast, previously the MCM-base underpredicted the OH concentration by ~1.7 and in summer the model could replicate the OH concentration very well. These results show the importance of constraining the model to HONO, as without measured HONO the models ability to predict the OH concentration decreases significantly. It also highlights the importance of measuring HONO well and accurately as shown in this work it can have a larger impact on modelling results.

6.3.5.2 Model constrained to OH

As discussed earlier, HONO is important to the primary formation of radical species. The only source of HONO in the MCM is the reaction of OH + NO, although OH + NO in previous studies cannot reconcile the measurements of HONO with the model (Lee et al., 2016, Acker et al., 2006, Kleffmann, 2007, Li

et al., 2012) To investigate how much HONO during the APHH winter campaign was produced through OH + NO, the MCM-base model was modified. The MCM-base model was constrained to the measurements of OH and unconstrained to HONO, the modified model was called MCM-cOH-unHONO. The average diurnal comparison of measured HONO and the modelled HONO from MCM-cOH_unHONO for summer and winter is shown in Figure 6.16.

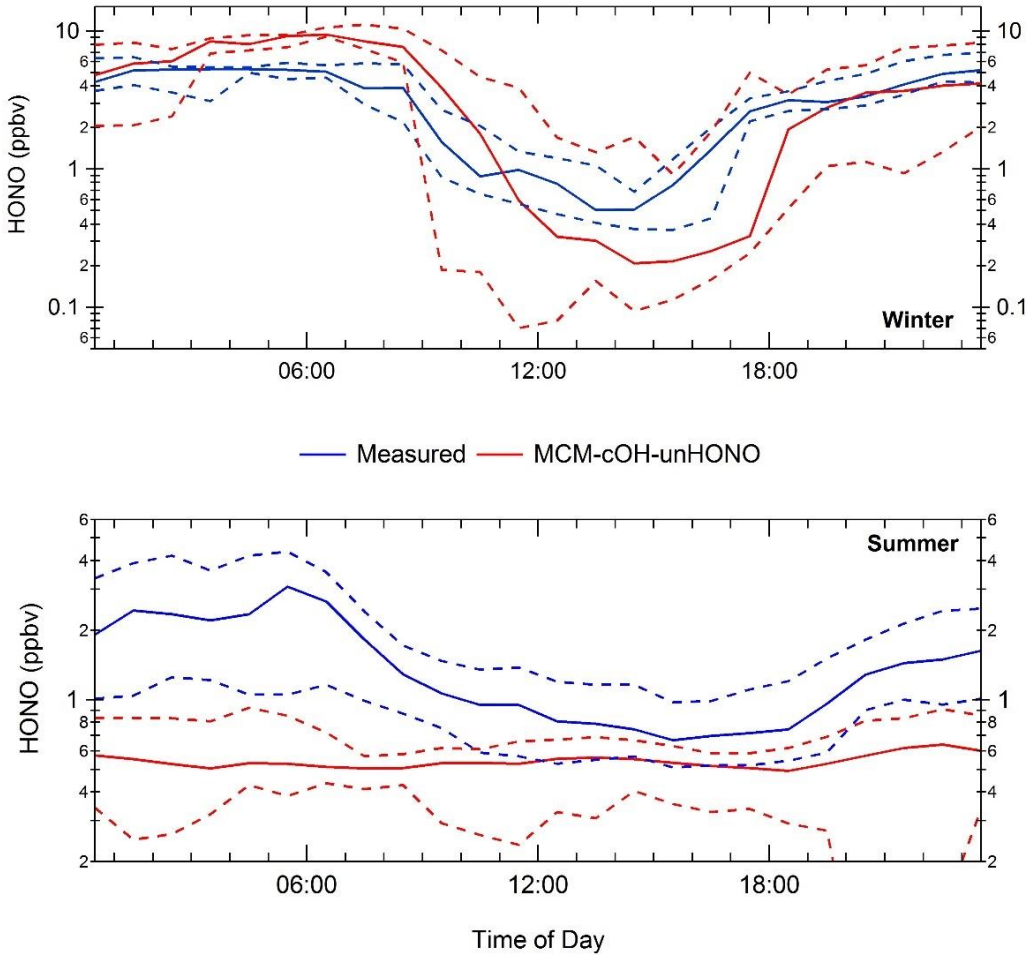

Figure 6.16 Top – Average median diurnal comparison of measured HONO and modelled HONO from MCM-cOH-unHONO for the winter campaign. Bottom - Average median diurnal comparison of measured HONO and modelled HONO from MCM-cOH-unHONO for the summer campaign. The dashed lines for all graphs represent the 95 CI.

Figure 6.16 shows very different results for summer and winter campaign, with the OH + NO contributing to most of the HONO observed during the winter campaign, whilst in summer the HONO is underpredicted by a factor of ~2.9. Although in winter the measurement and model does not fully match the

measured HONO concentration throughout the day with an underprediction between 11:30 to 19:30 and an overprediction between 02:30 to 11:30. However, Figure 6.16 also shows that for winter within the 95 CI throughout the day the measured and modelled HONO agrees. These results show that for summer the reaction of OH + NO is not enough to reconcile measurement with the model; whilst in winter especially under high NO conditions it is. This highlights that under lower NO conditions in Beijing that additional heterogeneous sources of HONO is required in the model.

6.3.6 Ozone production

6.3.6.1 Calculated ozone production comparison

As discussed in section.6.3.3 the MCM-base model generally undepredicts HO_2 and RO_2 during winter; whilst in summer MCM-base model underpredicts RO_2 whilst overpredicting HO_2. Peroxy radicals are important in the formation of tropospheric ozone, and the difference between measured peroxy radicals and modelled peroxy radicals impact the ability of models to predict ozone formation. The rate of O_3 production is assumed to be equal to the net rate of NO_2 production E6.3 :

$$\begin{aligned} \mathrm{P}(\mathrm{O_3}) = {} & k_{\mathrm{HO_2+NO}}[\mathrm{HO_2}][\mathrm{NO}] + k_{\mathrm{RO_2+NO}}[\mathrm{RO_2}][\mathrm{NO}] \\ & - k_{\mathrm{OH+NO_2+M}}[\mathrm{OH}][\mathrm{NO_2}][\mathrm{M}] - k_{\mathrm{HO_2+O_3}}[\mathrm{HO_2}][\mathrm{O_3}] \\ & - \mathrm{P}(\mathrm{RONO_2}) \end{aligned} \qquad \text{E6.3}$$

where RO_2 represents the sum of RO_2, and the last three terms allow for the reduction of ozone production owing to reactions that remove NO_2 or its precursors. The $P(RONO_2)$ term is the net rate of formation of organic nitrate, $RONO_2$, species, for example, peroxy acetyl nitrates (PANs). The comparison of the calculated O_3 production using measured and modelled values for summer and winter is shown in Figure 6.17. Figure 6.17 shows that in winter the model always underpredicts the ozone production, with the underprediction increasing with NO. Whilst in summer there is an overprediction of ozone at low NO (below 1 ppbv), this is from the overprediction of HO_2 by the model under low NO conditions. At higher NO (above 1 ppbv) the model underpredicts the ozone production, similar to the winter results, with the underprediction increasing with

NO. The O_3 production peaks at ~132 ppbv hr^{-1} at 177 pbbv of NO in winter, whilst summer the production peaks at 316 ppbv hr^{-1} at 68 ppbv of NO. The O_3 production is higher in summer compared to winter as there was much higher light levels, hence faster production of radicals. But, there is very high ozone production observed during winter showing that currently, titration of O_3 by NO is dominant, as low levels of ozone were observed. The winter results also imply that that ozone may start to increase as NO decreases.

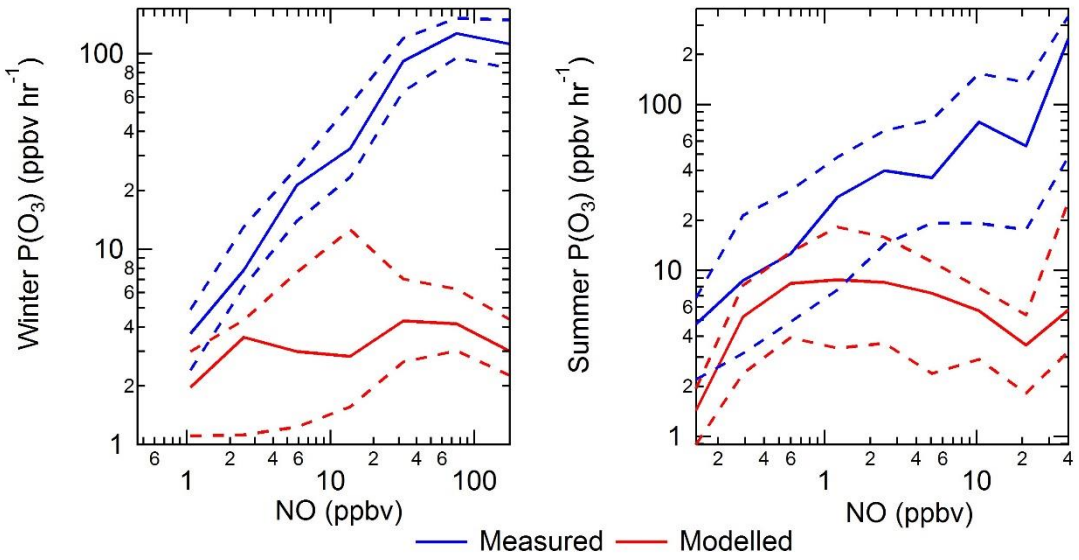

Figure 6.17 Left - The calculated rate of in situ ozone production as a function of [NO] using modelled (red) and measured (blue) values of HO_2 and the sum of RO_2 radicals for summer. Right - The calculated rate of in situ ozone production as a function of [NO] using modelled (red) and measured (blue) values of HO_2 and the sum of RO_2 radicals for winter.

The comparison of major RO_2 species that react with NO to form NO_2 for summer and winter is shown in Figure 6.18, and shows that CH_3O_2 is the 1st and 2nd most important RO_2 species for O_3 formation in winter and summer, respectively. Also CH_3CO_3, $C_2H_5O_2$, $BUTDBO_2$, $IBUTOLBO_2$, $HOCH_2CH_2O_2$ and $HYPOPO_2$ are found in both the lists for the highest contributing VOCs. The largest difference between winter and summer is that in summer there are two isoprene derived RO_2 species ($ISOPBO_2$ and $ISOPDO_2$ contributing 13.8% and 6.9%, respectively), which is not surprising as summer is the season when more plant emissions are expected. This work highlights that in Beijing, under the low NO_x conditions the emissions of isoprene/monoterpenes are important in the

formation of RO_2; which in turn is important to the formation of O_3 which is a major pollutant in summertime (Li et al., 2019).

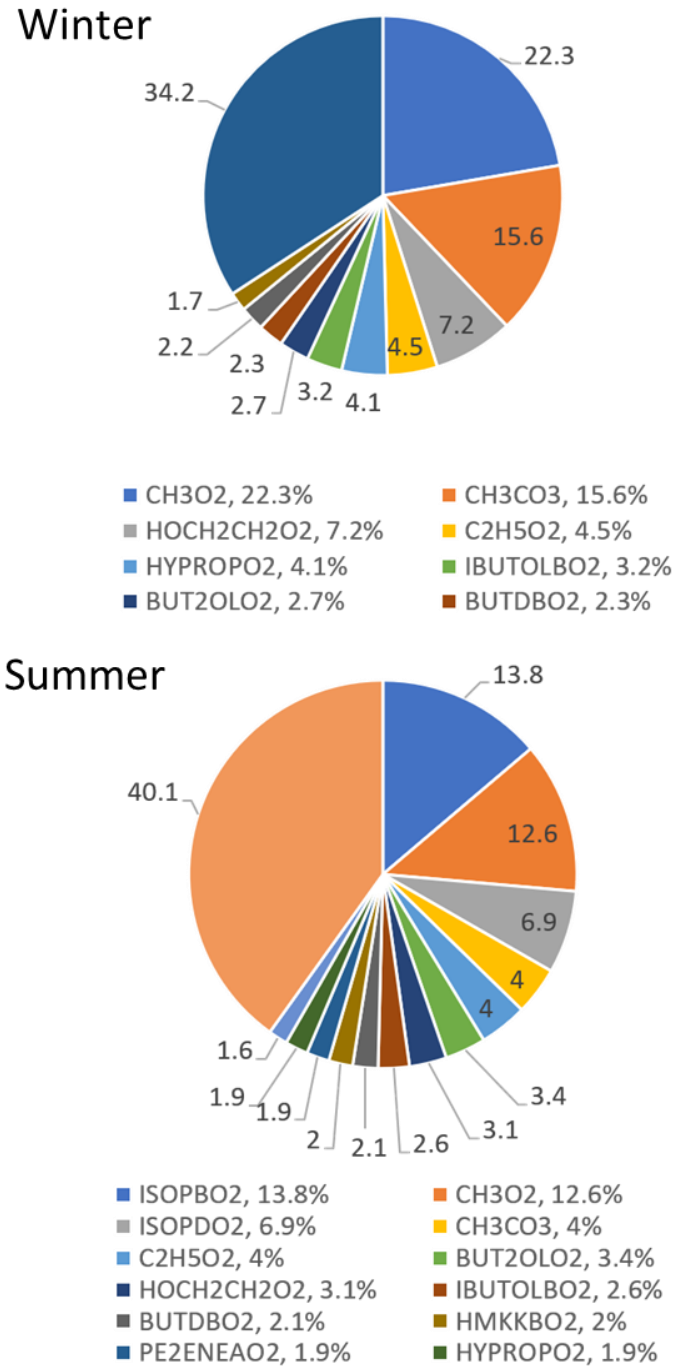

Figure 6.18 Pie charts representing the RO_2 species that contributing >1.5% ozone formation in the MCM-base model. Top –Results for the winter campaign, with the top ten RO_2 contributing 59.8% of total O_3 formation. Bottom - Results for the winter campaign, with the top ten RO_2 contributing 65.8% of total O_3 formation. The names for the RO_2 species are from the MCM, the related structures can be found http://mcm.leeds.ac.uk/MCM/.

6.3.6.2 Impact of HO_2 Uptake onto aerosols on Ozone Production

Previously, in section.5.4.5, the impact of HO_2 uptake for summer was discussed and showed that uptake of HO_2 onto aerosols could not reconcile the model with the measurements. For winter, the impact of HO_2 uptake onto aerosols was not discussed, as HO_2 was underpredicted in the model and uptake would not improve the measured:model comparison. This section will focus on the comparison between the MCM-base models for summer and winter with the base model modified to include HO_2 uptake onto aerosols (MCM-SA) using an uptake coefficient of 0.2 (see section.5.3.1 for details). The uptake coefficient is hypothetical as it was not measured during the campaign. It should be noted that the higher size bins for the aerosol size distribution are missing from the 18/06/2017 at 09:15 onwards, so any data for HO_2 uptake should be classed as a lower limit.

The importance of HO_2 uptake onto aerosols on the HO_2 concentration is dependant on both the NO concentration and the aerosol surface area, as the reaction of HO_2 + NO will compete against HO_2 uptake onto aerosol. The relationship between surface area and NO for the winter and summer campaign is shown in Figure 6.19, and is coloured by the difference between modelled HO_2 from MCM-base and MCM-SA. Figure 6.19 shows two very different relationships between SA (surface area) and NO for the summer and winter season. The winter campaign shows a positive correlation between SA and NO; whilst the summer campaign shows a negative correlation between SA and NO. However, during the winter campaign, the HO_2 concentration is not changed significantly except during the period when SA is high but the NO is lower (<1.5 ppbv).

A similar plot to Figure 6.19 is shown in Figure 6.20, except the plot has now been coloured by the difference between the calculated O_3 production between MCM-base and MCM-SA. The O_3 production was calculated using E6.3. A comparison between the modelled HO_2 difference and the difference in O_3 production between MCM-base and MCM-SA for summer shows that the difference in $P(O_3)$ is shifted to higher NO concentration compared to the HO_2 difference. The difference in $P(O_3)$ shifting to higher NO concentration compared to the modelled HO_2 difference is not surprising as NO is required to drive O_3 formation. Figure 6.20 also shows that the conditions observed in summer (high

surface area and low NO) can reduce the $P(O_3)$ up to 6 ppbv hr^{-1}. This work contrasts to work by (Li et al., 2019) who suggested the reduction in PM in China is driving the increase in O_3 through reduction of HO_2 uptake, as this work shows HO_2 uptake is important under the conditions observed during summer. In contrast to the summer, winter shows $P(O_3)$ is not significantly affected by HO_2 uptake. The HO_2 uptake is not as effective in winter as it is in summer at suppressing O_3 formation as the NO is much higher, thus leading to HO_2 + NO outcompeting the uptake of HO_2 onto aerosol. Although the correlation plot in Figure 6.20 does show on some days $P(O_3)$ difference between the model of ~3 ppbv hr^{-1}.

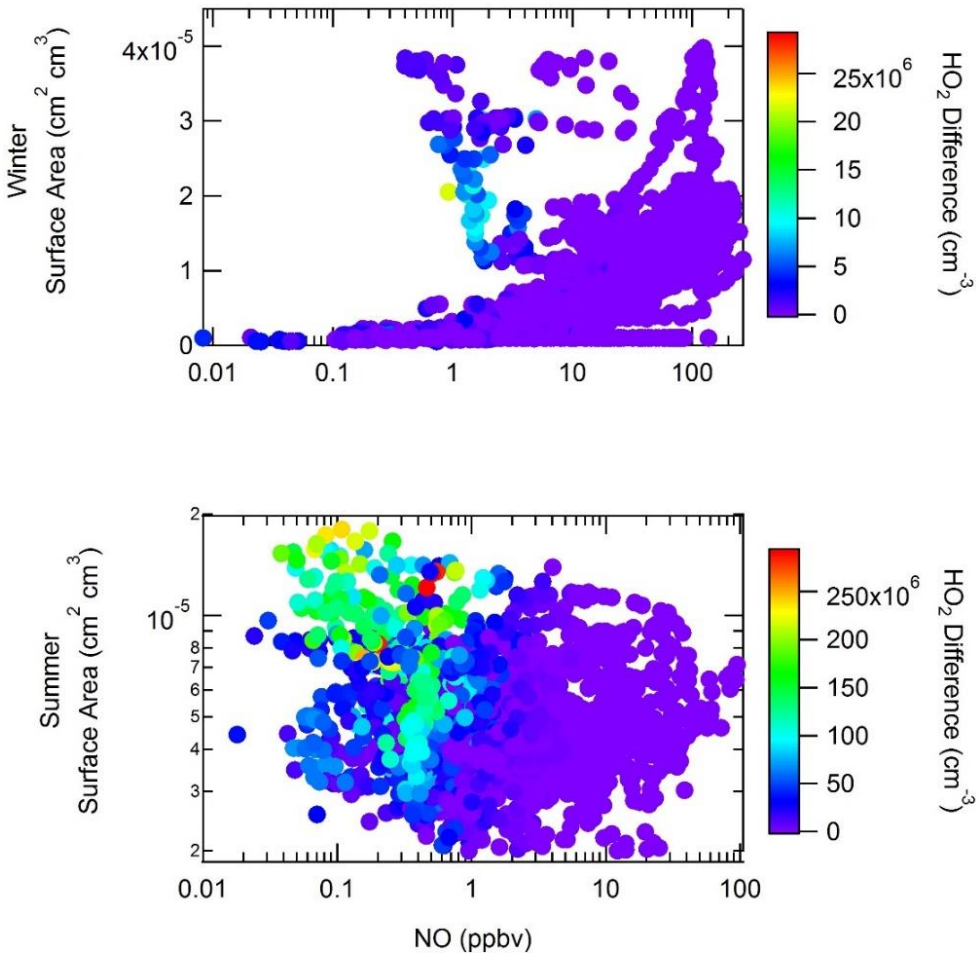

Figure 6.19 Relation between measured aerosol surface area (cm^2 cm^{-3}) and NO (ppbv) coloured by the difference in modelled HO_2 from MCM-base and MCM-SA. Winter is shown in the top panel and summer in the bottom panel. The surface area was measured using an SMPS (scanning mobility particle sizer) and PSM (particle size magnifier). The data from after the 18/06/2017 09:15:00 has been removed to not skew the data.

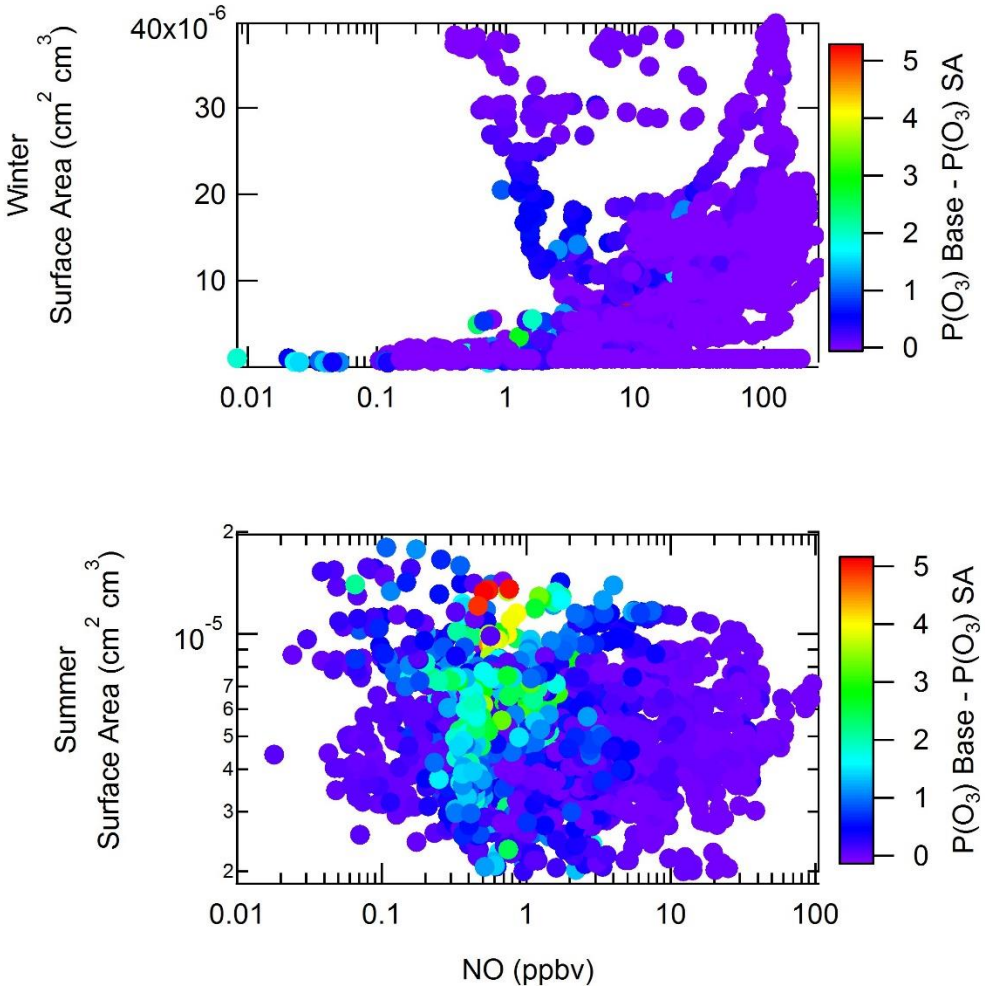

Figure 6.20 Relation between measured surface area (cm^2 cm^{-3}) and NO (ppbv) coloured by the difference in $P(O_3)$ calculated from MCM-base and MCM-SA. Winter is shown in the top panel and summer in the bottom panel. The surface area was measured using an SMPS and PSM (particle size magnifier). The data from after the 18/06/2017 09:15:00 has been removed to not skew the data.

Figure 6.21 shows the percentage difference between MCM-SA and MCM-base for modelled HO_2 and calculated $P(O_3)$. Figure 6.21 shows that for both the summer and winter campaign with increasing NO there is a larger impact on both O_3 production and HO_2. For summer it shows that at ~0.25 ppbv of NO the HO_2 concentration is reduced by 38% in the model, whilst the O_3 production is reduced by ~17%. The smaller impact on ozone production compared to HO_2 in summer at the lower [NO] is caused by the lower NO not driving O_3 formation. However, in winter when [NO] ~1 ppbv the HO_2 is reduced by ~5% in MCM-SA but, unlike summer, has a larger impact on the difference in ozone formation which is reduced by ~10%. The larger reduction in winter is caused by both higher [NO]

driving the O_3 formation and the low calculated ozone production from MCM-base (small perturbation can lead to larger difference in the ozone production ratio).

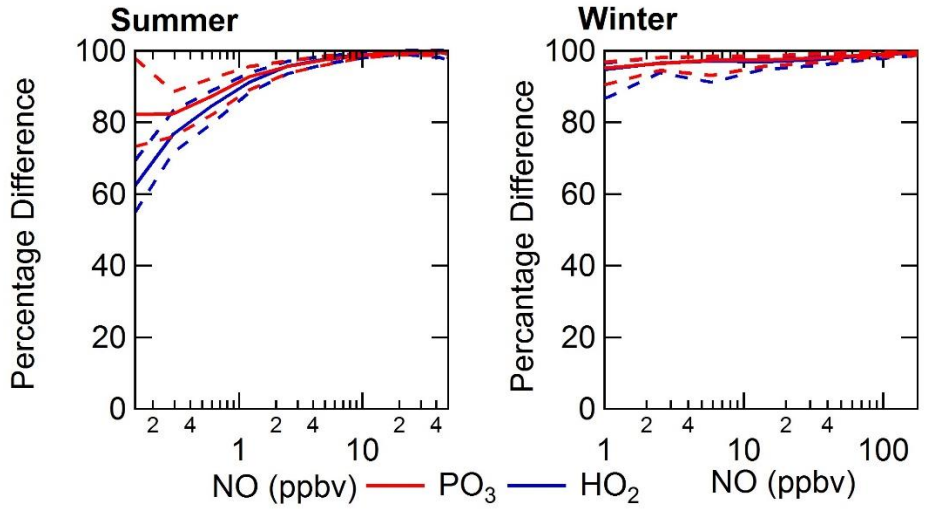

Figure 6.21 Percentage median difference (MCM-SA/MCM-base * 100) for modelled PO_3 and HO_2 for summer and winter. The dashed lines represent the 95th CI (confidence interval).

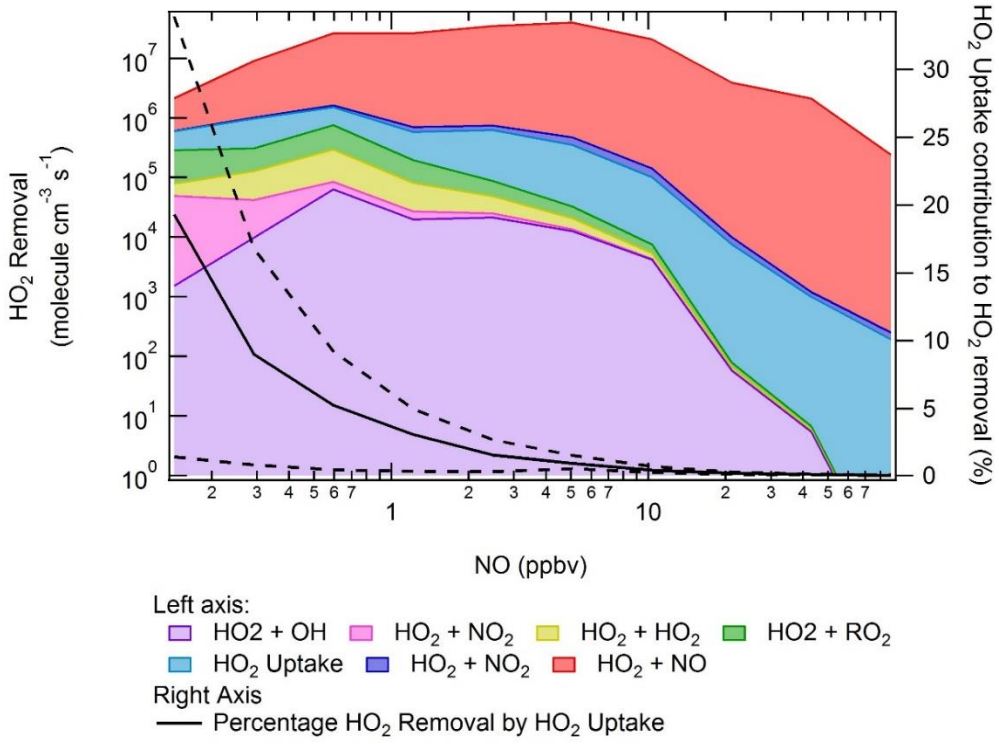

Figure 6.22 Results from the rate of production analysis (ROPA) for the removal of HO_2 for MCM-SA and the percentage contribution of HO_2 uptake to the total HO_2 removal plotted against logNO.

The impact of HO_2 uptake onto aerosol compared to the other reactions/processes is shown in Figure 6.22. Figure 6.22 shows that in general the reaction of HO_2 + NO is the dominant removal pathway for HO_2, although with decreasing [NO] the importance of HO_2 uptake increases. At 0.15 ppbv of NO the HO_2 uptake is ~18% of the total HO_2 removal.

During both of the campaigns haze events were observed, as discussed earlier the haze events in summer and winter are very different, with high aerosol surface area coinciding with high NO in winter whilst summer high aerosol surface area coincides with low NO. A time-series comparison between the HO_2 from MCM-base and MCM-SA, alongside the impact on the ozone formation for one haze event in winter (between 02/12/2016 – 06/12/2016) and two haze events in summer (first haze event between 27/05/20147 – 29/05/2017 and second haze event between 17/06/2017 – 19/06/2017) is shown in Figure 6.23. Figure 6.23 shows that during the haze events in summer, HO_2 uptake significantly affects the HO_2 concentration and hence the O_3 formation (up to 5.8 ppbv hr^{-1} difference). Figure 6.23 also shows that the HO_2 uptake can reconcile the measurements with the model on 17/06/2017 and 28/05/2017. The impact on O_3 formation during the summer haze events is observed across the whole day, although the highest impact coincides with the highest HO_2 concentration. Whilst for the winter haze event HO_2 uptake is shown to be important and decreases the O_3 formation by up to 2.8 ppbv hr^{-1}. However, the effect is only observed for small time-periods during the day (< 2 hr), and tends to coincide when HO_2 concentration peaks in the afternoon when the NO is lower. The results from summer highlights that HO_2 uptake is important for O_3 formation, although as the haze events in summer are not related to decrease in pollution observed in China, this contrasts with the work by (Li et al., 2019). However, the haze events in winter do show that HO_2 uptake does have a small impact on O_3 formation for small time-periods during the day, and agrees with work by (Li et al., 2019) that decreasing pollutants will lead to an increase in O_3 formation.

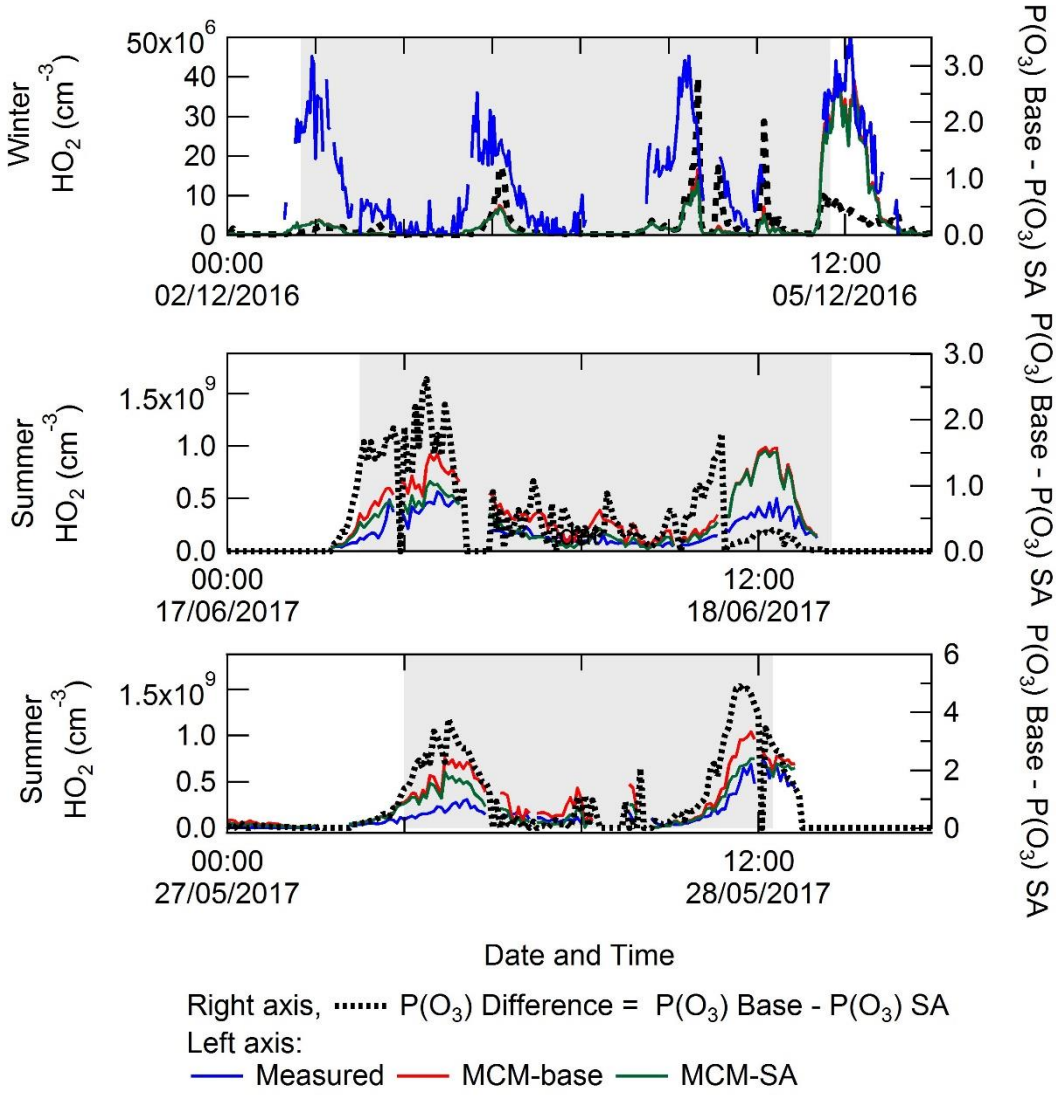

Figure 6.23 Comparison of measured HO_2, together with modelled HO_2 from MCM-base and MCM-SA, alongside the difference in calculated O_3 production from the two models for haze events in summer (b and c) and winter (a). The large drop on the 18/06/2017 for the impact on O_3 production is caused by the larger size aerosol data not being available.

Figure 6.24 shows the impact of windspeed and wind direction on NO, surface area and the difference in ozone formation between MCM-base and MCM-SA for winter and summer. In winter, high NO concentrations occurs when slower stagnant winds are observed; whilst lower NO concentration is observed for strong northerly winds from the mountains. Higher surface area in winter is observed when the wind direction is predominantly from the south, where there is a lot of industry, and also coincides with higher wind speeds. As discussed earlier, the reaction of HO_2 + NO competes with HO_2 uptake, and this can be seen in the polar plot for the impact of HO_2 uptake on ozone formation in winter.

The highest difference in O_3 production between MCM-base and MCM-SA is observed for strong winds from the northwest in winter, coinciding with low NO.

Similar to winter, high NO concentration in summer are observed at slow wind speeds, although higher NO concentrations also coincide with north westerlies. High surface area in summer occurs for most windspeeds and wind direction, although the highest surface area is observed for strong north easterlies. As discussed earlier, for HO_2 uptake to impact O_3 production during the summer campaign the NO concentrations need to be below ~ 1 ppbv. Concentrations of NO above ~ 1 ppbv are required to drive the ozone formation because HO_2 uptake has the largest difference on O_3 production at the highest SA and lowest NO for modelled HO_2. Figure 6.24 shows that the highest O_3 formation, similar to the case for surface area, is not dependant on meteorological conditions, but high O_3 formation does coincide with high NO concentrations as well. These results show that HO_2 uptake onto aerosols impact on O_3 formation in summer, but this is not largely dependant on meteorological conditions; whilst in winter HO_2 uptake only impacts O_3 formation when northwesterlies were observed that brought cleaner air from the mountain ranges.

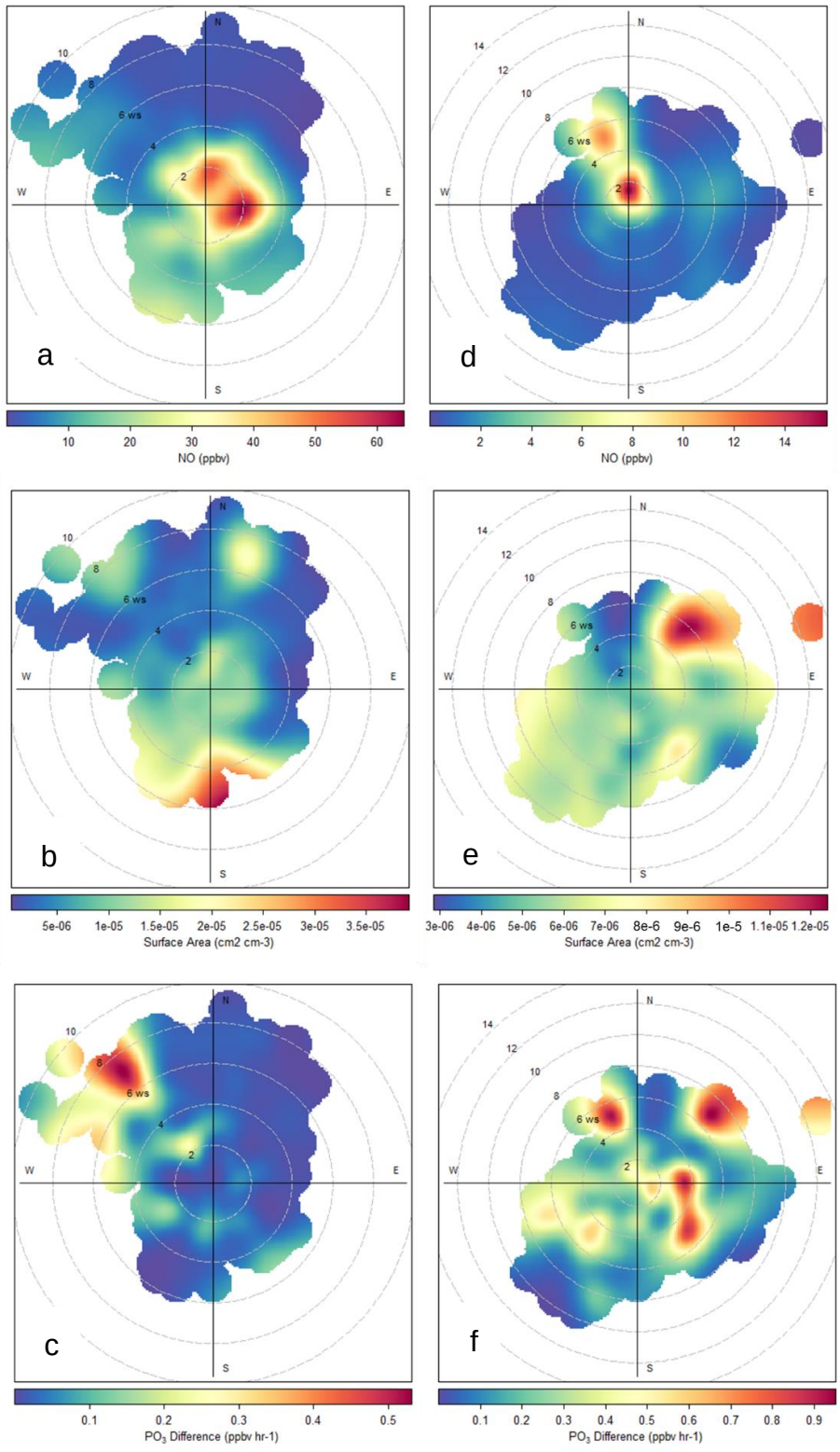

Figure 6.24 Polar plot showing wind direction and windspeed coloured by different variables (NO, surface area and ozone production difference between MCM-base and MCM-SA). a – NO during winter, b – surface area during winter, c – O_3 production difference in winter, d – NO during summer, e – surface area during summer and f– O_3 production difference in summer.

6.4 Summary and Conclusions

OH, HO_2, RO_2 and OH reactivity was measured in both the winter- and summertime in Beijing as a part of the APHH project. The measurements took place at the same site, located at the Institute of Atmospheric Physics in central Beijing, the instrument/container stayed in Beijing in-between the two campaigns.

The two seasons in Beijing exhibited very different chemical and physical conditions. During the wintertime the dominant wind direction is from the north-west; whilst in summer the wind is from the south-west. The wind direction is important in Beijing as towards the south there is a lot of air pollution and slow stagnant winds can bring aged air pollution into Beijing. Whilst towards the north-west and north-east are the Yanshan mountains meaning that strong winds bring clean air. The O_3/NO_x regimes during the winter and summer campaigns were very different. The O_3 during the summer campaign was very high reaching above 160 ppbv, and on average peaking at 88 ppbv. Whilst in winter the average maximum ozone observed was 17 ppbv. The NO showed an opposite trend to the O_3 for the summer and winter campaigns, with the NO reaching above 250 ppbv during winter and peaking at a maximum average of 39 ppbv. Whilst in summer the NO concentration was much lower and on some afternoons the NO was below 100 pptv. The average maxima of NO during summer was 16 ppbv. Also, the summer campaign had much higher light levels compared with the winter campaign, on average the $j(O^1D)$ was ~4.3 times higher during summer.

The OH, HO_2 and total RO_2 concentration was 3.5, 7.9 and 19 times larger, respectively, in summer campaign compared to winter. Also, during the summer campaign, the OH, HO_2 and RO_2 concentrations were above the limit of detection (LOD) at night-time, whilst in winter only RO_2 was higher than the LOD (5×10^6 molecule cm^{-3}). OH, HO_2 and RO_2 and OH reactivity were modelled using the MCM(v3.3.1) using several different scenarios. The MCM-base model in winter underpredicted the OH, HO_2 and RO_2 concentration by 1.7, 5.9 and 25, respectively. Whilst in summer the OH concentration was predicted well by the base model; HO_2 was overpredicted by 2.3 and the RO_2 concentration was underpredicted by 5.2. The ratio of the measured:modelled(MCM-base) for summer and winter was plotted as a function of log NO and shows that at higher

NO, above 2.5 ppbv of NO for winter and 5 ppbv in summer, all the measured radical species (OH, HO_2 and RO_2) are underpredicted by the model. The best agreement between measurement and model is found to be at ~2 ppbv of NO in both summer and winter, although the RO_2 species are still underpredicted in the model by a factor of ~3 and ~7 in winter and summer, respectively. At low NO (below 5 ppbv) in summer the HO_2 starts to be overpredicted and OH is reproduced well by the model. At the lower NO in summer, the RO_2 concentration is underpredicted. Whilst the same trend of under- and overprediction is observed over different NO ranges in summer and winter the magnitude is different highlighting that NO is not the only factor that contributes to the differences in the measured and modelled values, suggesting that different chemical conditions (e.g. VOC mixes, light levels and RH) and meteorological conditions are important.

During the summer and winter campaign, both OHwave and OHchem was measured, with OHchem being the interference free method. The comparison of OHwave and OHchem in summer and winter showed very little difference (1.05 ± 0.07) observed between the OHwave and OHchem highlighting that no interference was observed during the winter campaign. Although in summer an interference when the OHwave concentration reached above 1.5×10^7 molecule cm^{-3} was observed, and coincided with high temperature; elevated RO_2 and O_3 concentration. This work shows that species/processes that causes the unknown interference in the Leeds ground-based FAGE instrument for conditions promoting very high levels of OH and is more prominent in the afternoon when the NO is low.

The comparison of measured and modelled(MCM-base) OH reactivity shows that k(OH) is replicated within 10% of the model in winter; whilst in summer there is on average ~9.5 s^{-1} missing reactivity (35% of the measured OH reactivity). The measured OH reactivity in winter is ~1.8 times larger compared to summer. The contribution to the total OH reactivity from OH + NO, OH + NO_2 and OH + CO is 64.3% in winter whilst these reactions only contribute to 36.4% in summer. In both summer and winter, the contribution is similar for VOCs and model intermediates. The VOCs contribute 23.2% and 25.2% in summer and winter, respectively. The model intermediates contribute 6.8% and 5.0% to the total

reactivity in summer and winter, respectively. This work shows that in lower NO_x conditions there is missing reactivity that is related to a primary source and is emitted through the entire day.

The difference between the major sources and sinks of RO_x radical was assessed for summer and winter. The major source of RO_x was HONO is summer and winter contributing to 83% and 77%. In contrast to winter, significant primary production from $O^1D + H_2O$ (5.5%) was observed in summer, in winter $O^1D + H_2O$ contributed <1%. The photolysis of carbonyl species contributed a similar amount to the primary production: 4.1% and 5.4% in winter and summer, respectively. During summer a significant contribution to primary production from ozonolysis and VOC + NO_3 was observed contributing ~11% and 2.2%, respectively. The high production of radical species from ozonolysis and VOC + NO_3 is reflected in the significant night-time radical concentrations that are observed during summer. However, the model does still underpredict the OH radical concentration at night-time. Whilst in winter ozonolysis does contribute 10% to primary production, very little is produced through ozonolysis at night- which is reflected in the near-zero radical measurements. The comparison of the species that are terminating the radicals shows that in summer and winter the main contributors are OH + NO and OH + NO_2. OH + NO_2 contribute 63% and 43% to the total termination reaction in summer and winter, respectively. The reaction OH + NO contributes 11.3% and 37% to the total termination in summer and winter, respectively. The net formation of PAN contributes 14% and 20% to total termination in summer and winter, respectively. Also in summer, unlike winter, contributions from HO_2 + HO_2 (1.47%) and RO_2 + HO_2 (3.12%) are observed. This work shows that in winter there is a large contribution from OH + NO to radical termination; whilst in summer termination through peroxy radical self-reactions was observed.

To try and reconcile measurements and model in both summer and winter an additional primary source of RO_2 was inputted to match measurements of RO_2 with the model. The amount of additional source for summer was ~1.8 times larger than that required to bridge the gap in winter. Although the additional production for winter was ~6.3 times larger compared to the modelled primary production, whilst the additional primary production in summer is ~0.9 times

smaller than the modelled primary production. The results showed that once an additional primary source of RO_2 was added into the model, the OH and HO_2 are overpredicted in the model. The OH concentration is overpredicted by a factor of 1.9 and 1.8 in summer and winter, respectively. The HO_2 concentration is overpredicted by a factor of 6.3 and 2.5 in summer and winter, respectively. These results show that for the different chemical/meteorological conditions that were observed during the two campaigns an additional source of RO_2 cannot reconcile measurement with model and leads to an overprediction in both summer and winter.

As discussed earlier, HONO is the dominant primary source of OH in both the summertime and wintertime in Beijing. The model was unconstrained to measured HONO in summer and winter to assess the impact on modelled OH and HONO. When the model is unconstrained to HONO in both the summer and winter an underprediction of both HONO and OH is observed. In summer and winter the HONO concentration is underpredicted by a factor of ~3.2 and 10, respectively, and since HONO is the major primary source of OH it has a large impact on the modelled OH. Now the model underpredicts the OH concentration by a factor of 2.7 and 8.5 in summer and winter, respectively. This work highlights the importance of constraining the model to measured HONO, or the models ability to predict the OH radical is impaired. The contribution of OH + NO to the formation of HONO has been assessed for both summer and winter. These results show that in winter the reaction of OH + NO contributes significantly to the HONO formation and can almost reconcile the HONO measurement across the whole day within 95 CI (confidence interval). Whilst in summer the HONO concentration is underpredicted by a factor of~2.9 across the whole day. These results show that OH + NO is a dominant pathway to the formation of HONO in winter, whilst extra heterogeneous sources are required in summer.

O_3 production has been calculated from measured and modelled(MCM-base) values for both summer and winter production peaks at ~132 ppbv hr^{-1} at 177 pbbv of NO in winter, whilst in summer the production peaks at ~ 316 ppbv hr^{-1} at 68 ppbv of NO. The O_3 production is higher in summer compared to winter as there are much higher light levels, hence the production of radicals. Although there is very high ozone production observed during winter, the titration of O_3 by

NO is dominant as low levels of ozone were observed. In winter, the model underpredicts the ozone production across the whole NO range which is caused by the underprediction of HO_2 and RO_2. However, in summer an overprediction is observed at higher NO (above 1 ppbv), whilst at lower NO the model overpredicts O_3 production which is caused by the overprediction of HO_2 by the model. These results highlight how the model's ability to predict O_3 production is impaired in varying ways under different NO conditions.

The impact of HO_2 uptake on modelled HO_2 and O_3 formation has been investigated. The results show that high aerosol surface area in summer coincides with low NO, whilst in winter the high surface area coincides with high NO showing an anthropogenic trend. The results show that in general HO_2 uptake is not important in winter as the reaction of HO_2 + NO outcompetes HO_2 uptake, although HO_2 uptake did decrease the calculated O_3 formation by ~ 3 ppbv hr^{-1} on some days. In comparison, in summer the high surface area coincided with low NO and caused a large impact on modelled HO_2 when uptake was considered. The decrease in modelled HO_2 in MCM-SA only translates to a decrease in O_3 formation when the NO is >0.8 ppbv, as NO is required to drive the O_3 formation. The meteorological conditions that favour decreased O_3 formation in Beijing from HO_2 uptake was investigated for summer and winter. Winter showed that HO_2 uptake is only important when cleaner air from the northwest led to lower NO. Whilst in summer no distinctive correlation between meteorological conditions and decreased O_3 formation from HO_2 uptake was observed.

Future work should focus understanding the reasons behind the measured:modelled deviations at high and low NO including autoxidation, additional radical sources and whether the RO_2 + NO rate constant is different for more complex RO_2 species. Future work should also investigate the sources of haze events in summer that leads to significant uptake, as the higher aerosol surface area does not correlate with NO, unlike in winter.

6.5 References

Acker, K., Möller, D., Wieprecht, W., Meixner, F. X., Bohn, B., Gilge, S., Plass-Dülmer, C. and Berresheim, H. (2006) 'Strong daytime production of OH

from HNO_2 at a rural mountain site', *Journal of Geophysical Research*, 33(2).

Chatani, S., Shimo, N., Matsunaga, S., Kajii, Y., Kato, S., Nakashima, Y., Miyazaki, K., Ishii, K., Ueno, H.(2009) 'Sensitivity analyses of OH missing sinks over Tokyo metropolitan area in the summer of 2007', *Atmospheric Chemistry Physics*, 9(22).

Chen, W., Tang, H. and Zhao, H. (2015) 'Diurnal, weekly and monthly spatial variations of air pollutants and air quality of Beijing', *Atmospheric Environment* ,119, pp. 21-34.

Crilley, L. R., Karmer, L. J., Ouyang, B., Duan, J., Zhang, W., Tong, S., Ge, K. T., Qin, M., Xie, P., Shaw, M. D., Lewis, A. C., Mehra, A., Bannan, T. J., Worrall, S. D., Priestley, M. and Bacak, A. (2019) 'Intercomparison of nitrous acid (HONO) measurement techniques in a megacity (Beijing)', *AMT*.

Dolgorouky, C., Gros, V., Sarda-Esteve, R., Sinha, V., Williams, J., Marchand, N., Sauvage, S., Poulain, L., Sciare, J. and Bonsang, B. (2012) 'Total OH reactivity measurements in Paris during the 2010 MEGAPOLI winter campaign', *Atmospheric Chemistry and Physics*, 12(20), pp. 9593 - 9612.

Emmerson, K., Carslaw, N., Carpenter, L., Heard, D., Lee, J. and Pilling, M. (2005) 'Urban atmospheric chemistry during the PUMA campaign 1: Comparison of modelled OH and HO_2 concentrations with measurements', *Journal of Atmospheric Chemistry*, 52(2), pp. 143-164.

Fittschen, C., Al Ajami, M., Batut, S., Ferracci, V., Archer-Nicholls, S., Archibald, A. T. and Schoemaecker, C. (2019) 'ROOOH: the Missing Piece of the Puzzle for OH measurements in low NO Environments', *Atmos. Chem. Phys*, 19, 349 - 362.

Harrison, R. M., Peak, J. D. and Collins, G. M (1996) 'Tropospheric cycle of nitrous acid', *Journal of Geophysical Research: Atmospheres*, 101(D9), pp. 14429-14439.

Kanaya, Y., Cao, R., Akimoto, H., Fukuda, M., Komazaki, Y., Yokouchi, Y., Koike, M., Tanimoto, H., Takegawa, N. and Kondo, Y. (2007) 'Urban photochemistry in central Tokyo: 1. Observed and modeled OH and HO_2 radical concentrations during the winter and summer of 2004', 112(D21).

Kleffmann, J. J. C. (2007) 'Daytime sources of nitrous acid (HONO) in the atmospheric boundary layer', *ChemPhysChem*, 8(8), pp. 1137-1144.

Lee, J., Whalley, L., Heard, D., Stone, D., Dunmore, R., Hamilton, J., Young, D., Allan, J., Laufs, S., Kleffmann, J. (2016) 'Detailed budget analysis of HONO in central London reveals a missing daytime source', *Atmospheric Chemistry Physics*, 16, pp. 2747-2764.

Li, K., Jacob, D. J., Liao, H., Shen, L., Zhang, Q. and Bates, K. H. J. P. o. t. N. A. o. S. (2019) 'Anthropogenic drivers of 2013–2017 trends in summer surface ozone in China', *Proceedings of the National Academy of Sciences,* 116(2), pp. 422-427.

Li, X., Brauers, T., Häseler, R., Bohn, B., Fuchs, H., Hofzumahaus, A., Holland, F., Lou, S., Lu, K. and Rohrer, F. (2012) 'Exploring the atmospheric chemistry of nitrous acid (HONO) at a rural site in Southern China'. *Atmos. Chem. Phys*, 12, pp. 1497 - 1513.

Ma, X., Tan, Z., Lu, K., Yang, X., Liu, Y., Li, S., Li, X., Chen, S., Novelli, A. and Cho, C. J. S. o. T. T. E. (2019) 'Winter photochemistry in Beijing: Observation and model simulation of OH and HO_2 radicals at an urban site', *Science of The Total Environment,* 685, pp. 85-95.

Mao, J., Ren, X., Zhang, L., Van Duin, D., Cohen, R., Park, J.-H., Goldstein, A., Paulot, F., Beaver, M. and Crounse, J. (2012) 'Insights into hydroxyl measurements and atmospheric oxidation in a California forest', *Atmospheric Chemistry and Physics,* 12(17), pp. 8009-8020.

Ren, X., Brune, W. H., Oliger, A., Metcalf, A. R., Simpas, J. B., Shirley, T., Schwab, J. J., Bai, C., Roychowdhury, U. and Li, Y. (2006) 'OH, HO_2, and OH reactivity during the PMTACS–NY Whiteface Mountain 2002 campaign: Observations and model comparison', *Journal of Geophysical Research: Atmospheres,* 111(D10).

Ren, X., Van Duin, D., Cazorla, M., Chen, S., Mao, J., Zhang, L., Brune, W. H., Flynn, J. H., Grossberg, N. and Lefer, B. (2013) 'Atmospheric oxidation chemistry and ozone production: Results from SHARP 2009 in Houston, Texas', *Journal of Geophysical Research: Atmospheres,* 118(11), pp. 5770-5780.

Shi, Z., Vu, T., Kotthaus, S., Harrison, R. M., Grimmond, S., Yue, S., Zhu, T., Lee, J., Han, Y., Demuzere, M. (2019) 'In-depth study of air pollution sources and processes within Beijing and its surrounding region (APHH-Beijing)', *Atmospheric Chemistry Physics* ,(11), pp. 7519-7546.

Tan, Z., Fuchs, H., Lu, K., Hofzumahaus, A., Bohn, B., Broch, S., Dong, H., Gomm, S., Häseler, R., He, L. (2017) 'Radical chemistry at a rural site (Wangdu) in the North China Plain: observation and model calculations of OH, HO_2 and RO_2 radicals', *Atmospheric Chemistry Physics*, 17(1), pp. 663-690.

Tan, Z., Rohrer, F., Lu, K., Ma, X., Bohn, B., Broch, S., Dong, H., Fuchs, H., Gkatzelis, G. I., Hofzumahaus, A. (2018) 'Wintertime photochemistry in Beijing: observations of RO_x radical concentrations in the North China Plain during the BEST-ONE campaign', *Atmospheric Chemistry Physics*, 18(16), pp. 12391-12411.

Whalley, L. K., Edwards, P. M., Cryer, D. R., Brumby, C. A., Seakins, P. W. and Heard, D. E. (2016) 'Measurement of OH reactivity by laser flash photolysis coupled with laser-induced fluorescence spectroscopy', *Atmospheric Measurement Techniques,* 9(7), pp. 2827.

Yoshino, A., Sadanaga, Y., Watanabe, K., Kato, S., Miyakawa, Y., Matsumoto, J. and Kajii, Y. (2006) 'Measurement of total OH reactivity by laser-induced pump and probe technique—comprehensive observations in the urban atmosphere of Tokyo', *Atmospheric Environment* , 40(40), pp. 7869-7881.

7. HO_x Measurement comparison made during wintertime in Beijing

7.1 Introduction

This chapter compares measurements of OH (OHchem) and HO_2 made by two different FAGE instruments. The measurements were made in central Beijing at the Institute of Atmospheric Physics (IAP) in November and December 2016, as a part of “Air Pollution and Human Health in Chinese megacities” (APHH). The OH and HO_2 measurements were made by the Leeds ground-based FAGE instrument and the Peking University (PKU) FAGE instrument.

The structure of the chapter is as follows. First, a time-series comparison of the OH (OHchem) and HO_2 measured by the Leeds and PKU FAGE instrument. Followed by an average diurnal comparison of both OH and HO_2, then correlation plots of the two different OH and HO2. Following this a comparison of the measured OH from both the Leeds and PKU instruments with OH calculated using a photostationary steady-state (PSS) will be presented. The following section will discuss reasons for possible differences between the measurements including: NO segregation; calibration differences and correlation with other measured species (chemical conditions – i.e. VOCs, trace gas species and photolysis rates).

7.2 FAGE Instrument Comparison and Set-up

Due to the home-built nature of FAGE instruments, the design can vary significantly between groups. A brief comparison between the Leeds and PKU design set-ups are shown in Table 7.1. The FAGE set-up between the Leeds and PKU instrument is very similar, both instruments: have single-pass cell; use MCPs (micro-channel plate) as the detector; same sampling rate and similar cell pressure. In contrast, the two instruments differ by: Leeds instrument measuring sequentially for OH and HO_2 in the same cell (HO_x cell) whilst PKU have separate cells for OH and HO_2; Leeds has a taller inlet (Leeds and PKU turret height 5 cm and 2.6 cm, respectively.) that also has a larger diameter (Leeds and PKU pinhole 1 mm and 0.4 mm, respectively). The Leeds instrument has been characterised

for the conversion of different RO_2 species at different NO flows to minimise the interference in the HO_2 measurement (Whalley et al., 2013); whilst PKU uses different flows of NO on a campaign to assess the RO_2 interference. The details of the Leeds instrument can be found in Whalley et al. (2013) and Chapter 2; whilst details of the PKU instrument can be found in Tan et al. (2016).

Type	Leeds	PKU
Laser Pass	Single-pass fluorescence cell.	Single-pass fluorescence cell.
Measurement cells	HO_x cell that measured OH and HO2 sequentially.	Separate OH and HO_2 cell.
Detectors	Micro-channel plate detectors (Photek PMT 135)	Micro-channel plate detectors, (Photek GM10-50B)
Sampling flow rate (SML)	7	7
Inlet	5 cm tall and 2.54 cm wide turret	2.6 cm tall, 3.9 cm wide turret
Orifice diameter (mm)	1 mm	0.4 mm
Cell Pressure (mbar)	1.6	1.3
HO_2 conversion	5 sccm (Messer 99.99%), 8% conversion of HO_2 to OH.	0.5 to 2 sccm of NO resulting in HO_2 4% and 18% conversion, respectively.
Errors (2σ)	~26% error on OH and HO_2 measurements	OH – 20% and HO_2 – 26%.

Table 7.1 Comparison of different FAGE designs for the Leeds ground-based FAGE and the PKU FAGE instrument.

The two instruments are calibrated the same way through photolysis of water at 184.9 nm using a mercury lamp (see Chapter 2 for details), which, is similar to the Leeds instruments where the error in the measurements are largely from the determination of the actinometry value (see section 2.1.6 and section.2.1.7). However, the determination of the actinic flux of the mercury lamp between the two instruments is different as Leeds uses N_2O actinometry and PKU uses O_3 actinometry. The two instruments during the winter campaign were co-located, as shown in Figure 7.1. The instruments were sampling very close together and in section.7.3.3 there is a discussion on whether segregation across the site might

have affected the radical measurements/comparison between the two instruments.

Figure 7.1 Picture of the Institute of Atmospheric Physics (IAP) showing the layout of the shipping containers housing different instruments. The container 1 housed the trace gas measurement (O_3, NO, NO_2, CO) as well as the VOC measurements. Container 2 housed the Leeds ground-based FAGE instrument used to measure OH, HO_2, RO_2 and OH reactivity. Container 3 housed the PKU FAGE instrument that measured OH and HO_2 as well as trace gas measurements (O_3, NO, NO_2, CO). See Table 4.1 for detail on the instruments housed in each container.

7.3 Results

7.3.1 Time-series comparison

The time-series comparison of the OH and HO_2 measured by the Leeds and PKU FAGE instrument is shown in Figure 7.2. It shows that between 16/11/2016 to 20/11/2016 there is a very good agreement between the two datasets for Leeds and PKU. Between 02/12/2016 to 08/12/2016, there is a good agreement for OH on 02/12/2016 and 04/12/2016; whilst for HO_2 the trend between the two

measurements is similar, however, the PKU instrument consistently measured higher than the Leeds instrument. Unlike HO_2, where the PKU instrument consistently measures higher, neither the Leeds nor PKU instruments measured OH is consistently higher or lower than the other instrument across the time series. The Leeds instrument measures higher than the PKU instrument on 03/04/2016, 06/12/2016 and 07/12/2016 by ~2.3, 1.6 and 2.1, respectively. Whilst the PKU instrument measured higher on the 05/12/2016 by 1.7. In general, the same trend is observed for the OH measurements, but with the Leeds and PKU measurements differing on some days. Also, there is more noise observed for the OH and HO_2 measurements from PKU at night-time, although the measurements are similar to Leeds, the measurements scattered around zero.

Diurnal comparison of OH and HO_2 measured by the Leeds and PKU FAGE instruments is shown in Figure 7.3. Figure 7.3 shows a good agreement for OH at night-time with the values for both instruments ~ zero. For both instruments HO_2 was ~zero between 21:30 to 05:30; but between 17:30 to 21:30 the PKU instrument measured non-zero values whilst the Leeds instrument measured ~zero. The Leeds instrument on average measured ~1.25 times higher OH than the PKU instrument across the campaign, although this difference is within the ~26% error on the Leeds instrument and ~20% error on the PKU instrument. The average difference between the OH measurements was 0.56×10^6 molecule cm^{-3}. On average, the PKU instrument measured ~2.2 times higher HO_2 than the Leeds instrument across the campaign. The largest difference between the Leeds and PKU measurements is observed during the morning between 09:30 to 13:30 where the maximum differences reaches 0.48×10^8 molecules cm^{-3}.

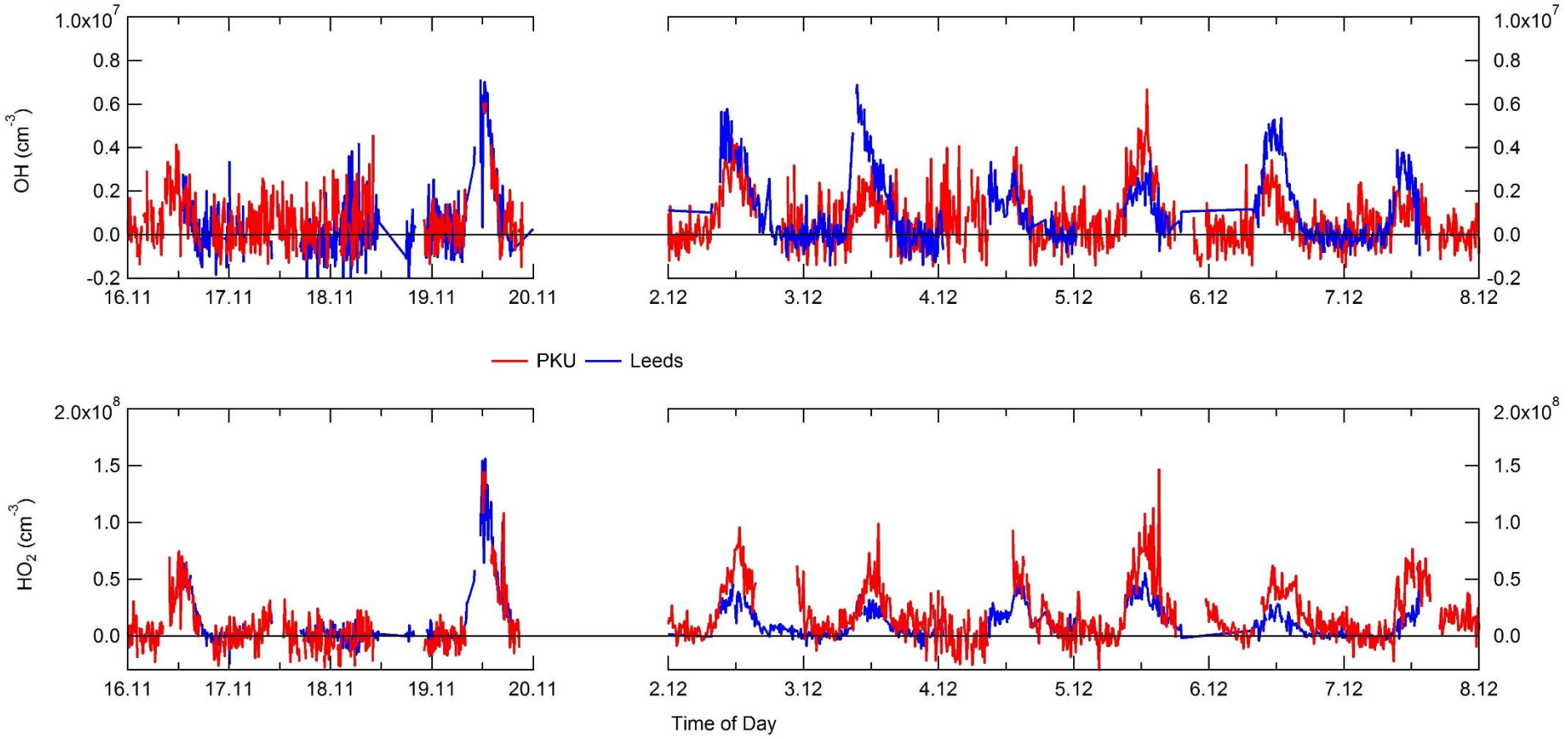

Figure 7.2 Time-series comparison of OH (top) and HO_2 (bottom) measured by the Leeds (blue) and PKU (red) FAGE instruments. The data shown above is only for periods when measurements overlapped.

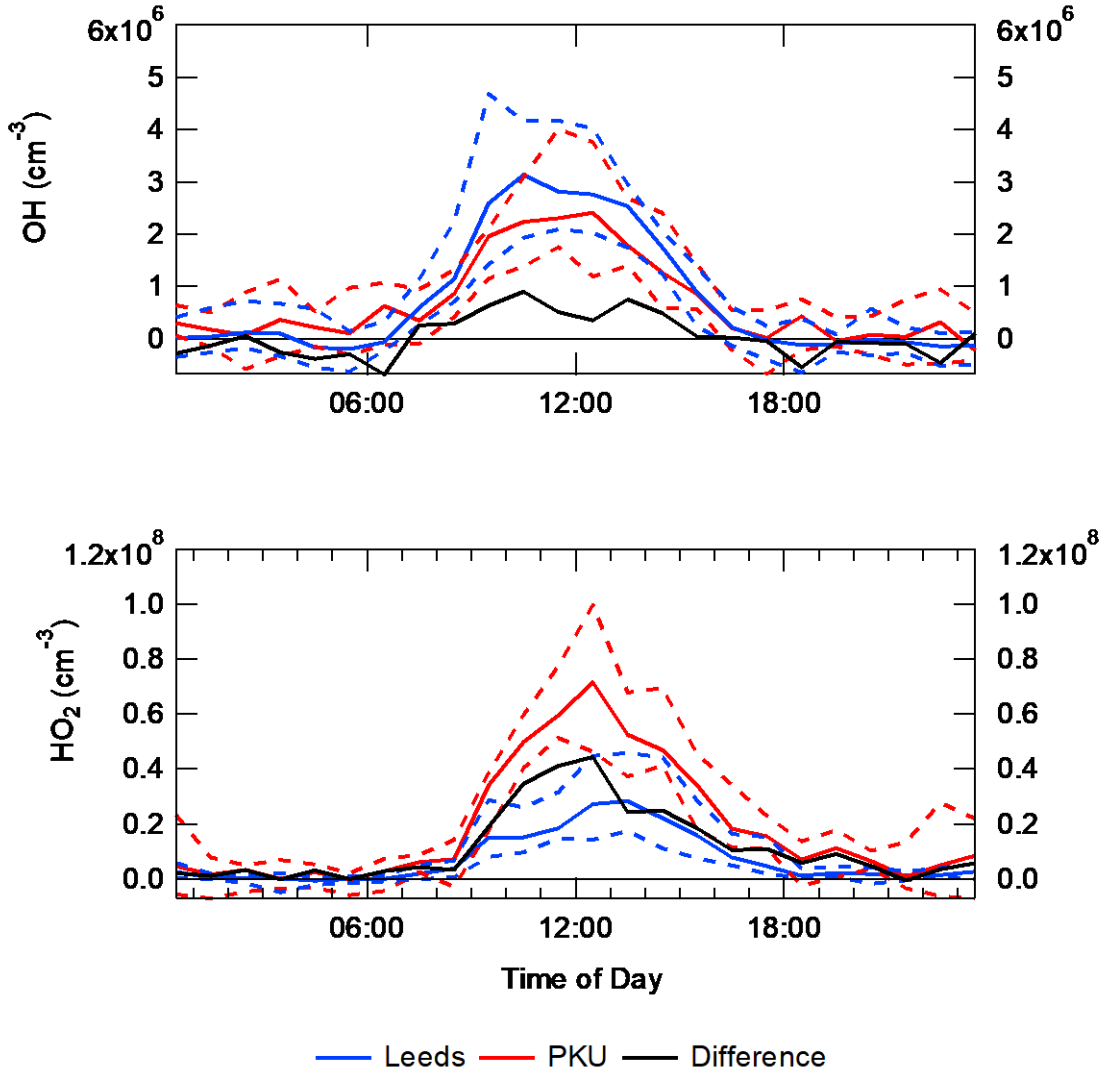

Figure 7.3 Top – Average diurnal comparison of OH measured by the Leeds (blue) and PKU (red) FAGE instruments, with black representing the difference between the two instruments. Bottom - Average diurnal comparison of HO_2 measured by the Leeds (blue) and PKU (red) FAGE instruments, with black representing the difference between the two instruments.

Correlation plots of OH and HO_2 measured by Leeds and PKU are shown in Figure 7.4. Figure 7.4 shows the slope for OH and HO_2 is 0.74 and 0.56, respectively. The correlation slope between the Leeds and PKU for OH contrasts with the average diurnal, as the diurnal shows Leeds in general measures higher whilst the correlation shows PKU measuring higher. The correlation plot is most likely influenced by night-time data, and as shown in the time-series and diurnal the PKU instrument tends to measure higher and have more noise at night. Even though the slope for OH is higher than HO_2 the R^2 value for OH is only 0.32 whilst for HO_2 it is 0.57. The low R^2 value for OH is caused by neither the Leeds or PKU

instrument consistently measuring higher or lower, which causes a much more scattered plot observed. Whilst for HO_2 the PKU instrument consistently measured higher than the Leeds instrument, hence the low slope, but the higher correlation coefficient.

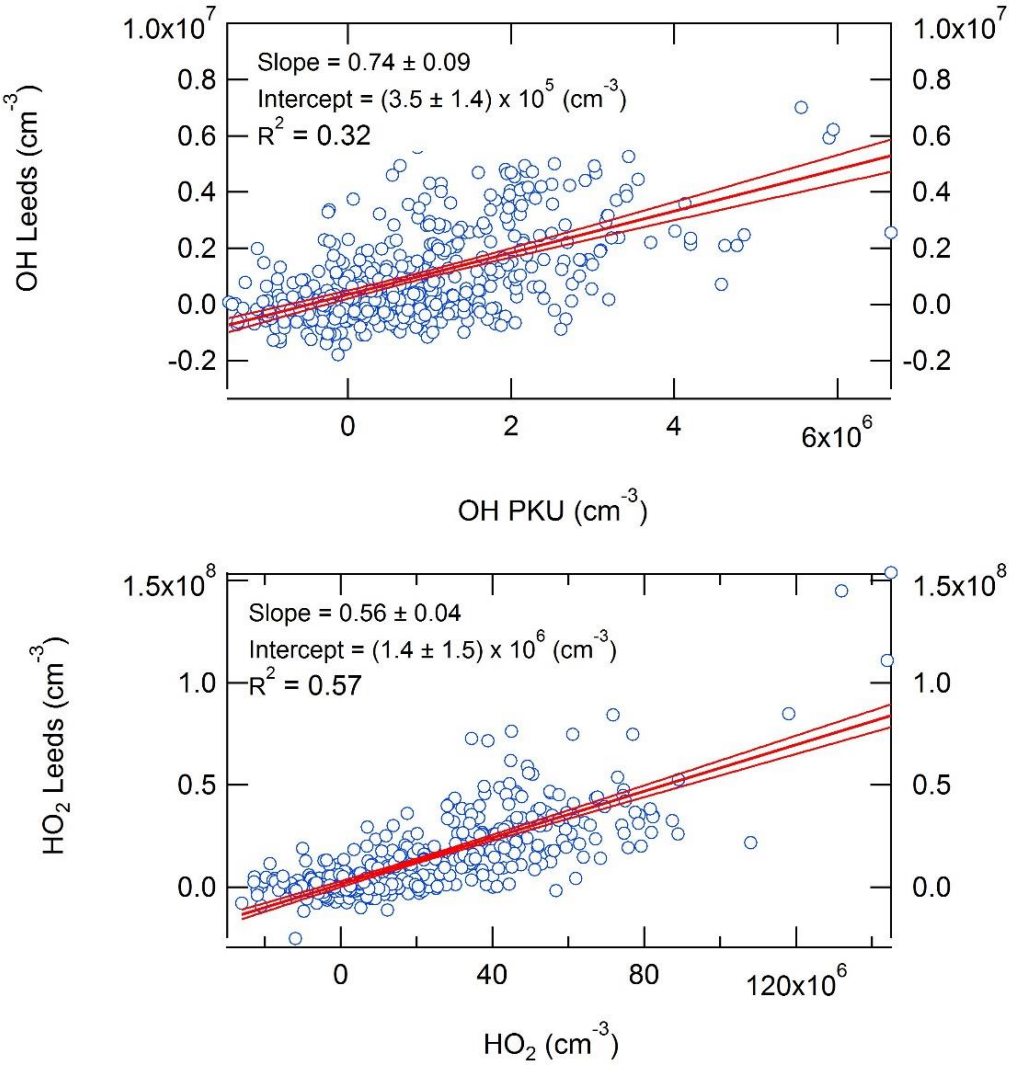

Figure 7.4 Top – Correlation plot of OH measured from the Leeds and PKU FAGE instrument. Bottom - Correlation plot of HO_2 measured from the Leeds and PKU FAGE instrument. The red line represents the slope with the 95% CI. The data are averaged to 15 minutes. The errors have not been considered due to the errors from PKU not being available.

In a previous study (Schlosser et al., 2009, Fuchs et al., 2010, Kanaya et al., 2012) HO_x measurements were made by different FAGE instruments (neither Leeds or PKU were involved) as a part of a formal blind intercomparison, with 3 days ambient HO_x observations and 6 days of measurement in the SAPHIR chamber. For OH the R^2 value varied between 0.75 – 0.96 which is much higher

than the R^2 during APHH campaign; although the intercomparison slopes for ambient data varied between 1.06 – 1.69 showing similar variability in the OH measurements during HO_xComp and APHH campaigns. For HO_2 during HO_xComp the R^2 varied between 0.82 – 0.98 which is higher than the APHH campaign. The intercomparison slope for HO_2 for ambient data during the HO_xComp varied between 0.46 – 2.95 showing a large variability in the magnitude of HO_2 measured during HO_xComp. Although since HO_xComp, interferences from RO_2 (Whalley et al., 2013, Fuchs et al., 2011) and NO_3 (Fuchs et al., 2016) radicals in the HO_2 measurement have been recognised and may contribute to the disparities observed during HO_xCOMP. The suggested reason for differences between the OH and HO_2 measurements during HO_xComp was caused by inhomogeneous sampling and calibration issues and RO_2 interferences. The inhomogeneity of the site will be discussed in section.7.3.3 and calibration issues will be discussed briefly in section.7.3.4.

7.3.2 Photostationary Steady-state comparison

As seen in section.4.4.4 the PSS used to calculate OH and compared to Leeds OH data was able to close the experimental budget, showing that all major sources and sinks of OH were captured using the Leeds measurements for HO_2 and supporting measurements from other groups. A comparison between PSS calculation using the measured HO_2 from both the Leeds and PKU is shown in Figure 7.5. The PSS was performed using measured O_3, H_2O, HONO, HO_2 (Leeds and PKU) and NO mixing ratios, alongside measured photolysis rates for $j(O^1D)$ and j(HONO). The PSS using Leeds and PKU HO_2 values has been compared to measured OH from Leeds and PKU, respectively. The total sink, OH reactivity, used in both cases was measured from the Leeds OH reactivity instrument (the only k(OH) measurement at the IAP site).

Figure 7.5 shows, that as discussed in section.4.4.4, the comparison between the PSS using Leeds measured HO_2 with Leeds measured OH closes the experimental budget. Although on the 04/12/2016 the PSS (Leeds) does overpredict the OH (Leeds) concentration by a factor of ~2.5, on the same day the PSS (PKU) overpredicts the OH (PKU) by ~ 3.2 showing that perhaps NO segregation was observed across the site. Figure 7.5 also shows that the PSS

(PKU) overpredicts the OH (PKU) concentration on average by ~3.6, the overprediction is caused by the ~2.2 higher HO_2 measured by PKU which quickly propagates to OH *via* NO. However, when there was good agreement between Leeds and PKU for both OH and HO_2 (16/11/2016 – 20/11/2016) the steady-state can predict the OH concentration for both Leeds and PKU. The difference in agreement between Leeds and PKU for the two time-periods may highlight at calibration issue occurring after 02/12/2016.

The PSS calculation for both Leeds and PKU is calculated using the Leeds OH reactivity measurement. The PSS calculation is very sensitive to the measured OH reactivity. To bring the PSS (PKU) calculation to agree with the measured OH (PKU) would require the OH reactivity to be increased by a factor of ~3.6. The Leeds OH reactivity instrument was involved in an intercomparison campaign at the SAPHIR campaign in Juelich (Fuchs et al., 2017) and the instrument response under high NO_x is well understood, and the measurements at Juelich were in good agreement with other instruments. Also, as seen in Chapter 4 the measured OH reactivity compared well with modelled OH reactivity (with ~15%) from the APHH campaign. The combination of a good comparison between measured and modelled OH reactivity alongside a well understood instrument response under different NOx environments suggests that the OH reactivity measured during the APHH campaign is accurate.

Figure 7.6 shows the correlation comparison of the Leeds and PKU PSS calculations with the measured Leeds and PKU OH values, respectively. Figure 7.6 reiterates that the Leeds PSS OH compares very well with the Leeds measured OH values yielding a slope of 0.77 and R^2 of 0.57. However, the PKU PSS OH does not compare well with the PKU measured OH value yielding a slope of 0.14 and R^2 of 0.12. The Leeds and PKU HO_2 values do not compare very well, and this may point to an inhomogeneous site, thus causing segregation of NO. As peroxy radical chemistry is driven by NO (the budgets shown in section.4.4.5.1 are dominated by reactions with NO_x), segregation of NO across the site may cause the difference observed in the radical concentrations.

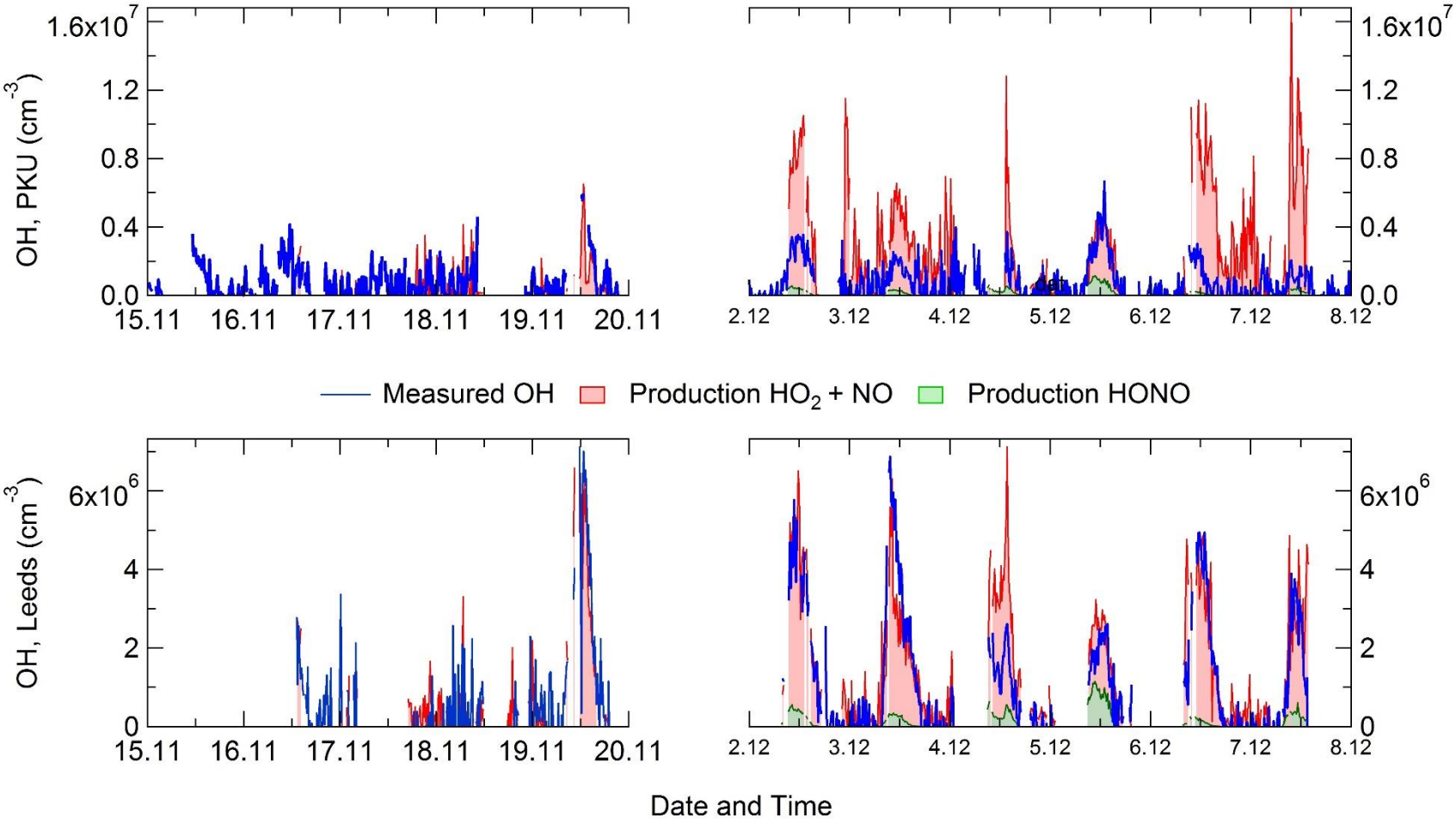

Figure 7.5 Top - Time series for the steady-state calculation of OH compared with measured OH (blue, PKU) using the measured HO_2 from PKU. Bottom - Time series for the steady-state calculation of OH compared with measured OH (blue, Leeds) using the measured HO_2 from Leeds.

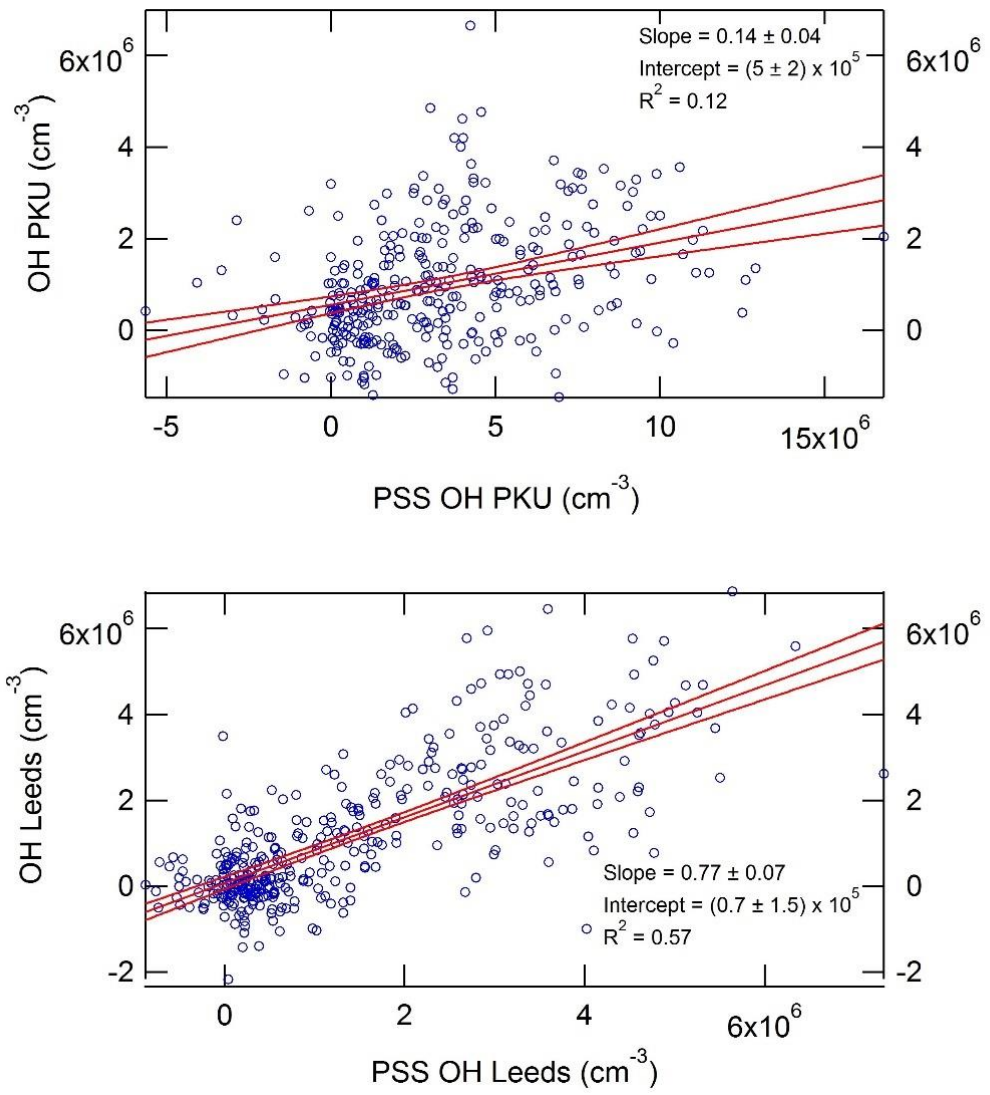

Figure 7.6 Correlation of the measured OH vs OH calculated from the PSS. Top – PSS uses the measured HO_2 value from PKU and is compared with measured PKU OH values. Bottom – PSS uses the measured HO_2 value from Leeds and is compared with measured Leeds OH values. The red line represents the linear slope with the 95% CI.

7.3.3 NO Segregation

During the campaign York and PKU both measured NO, the York and PKU containers sandwiched the Leeds container (see Figure 7.1). The comparison of both measurements would show if segregation across the site would be significant enough to affect the radical measurements. The correlation and time-series comparison of the York and PKU measured NO is shown in Figure 7.7. Figure 7.7 shows that the NO measured by PKU was slightly higher than the

NO measured by York across the comparison period. On average the NO measured by York was ~13% lower than that measured by PKU. The NO data between both York and PKU correlated very well with a Pearson's R^2 coefficient of 0.99.

The difference between the OH and HO_2 measurements has been correlated with the difference in NO, as shown in Figure 7.8, to assess whether NO segregation is the reason behind the measurement differences.

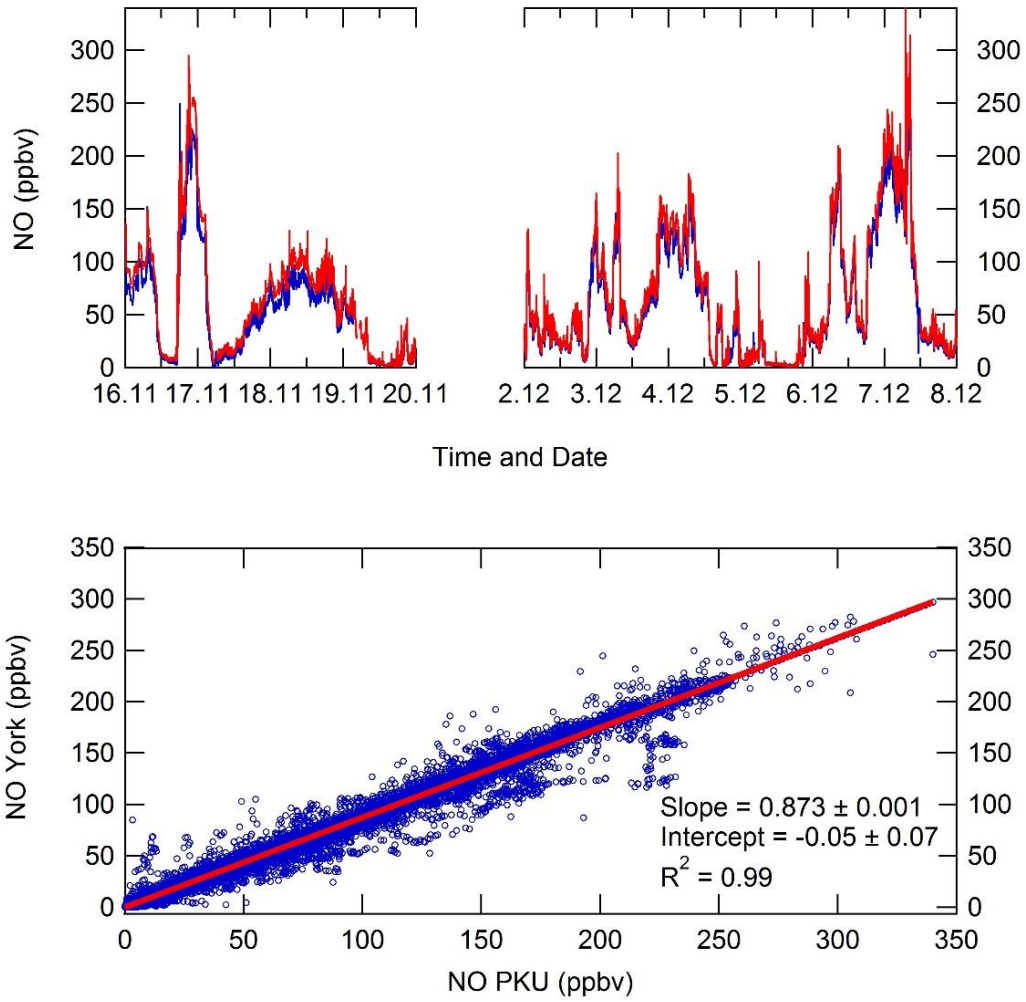

Figure 7.7 Top – Time series comparison of NO measurements by York (blue) and PKU (red). The period shown is the same as the OH and HO_2 comparison period between Leeds and PKU. The data are 1-minute averages. Bottom – Correlation plot comparing NO measured by York and PKU, the data are 1-minute averages.

Figure 7.8 shows that the difference in the OH measurements do not correlate well (R^2 = 0.0002) with the difference in the NO measurements, the slope for OH correlation plot is -2.9 x 10^3 cm^{-3} $ppbv^{-1}$. However, HO_2 shows a small negative correlation (R^2 = 0.05) with the difference in the NO measurements, the slope of the HO_2 correlation plot is and -7.5 x 10^5 cm^{-3} $ppbv^{-1}$. The small correlation of the difference in HO_2 measurements with the difference in NO measurements suggests that the biggest difference in the HO_2 measurements occurs when the NO measurements are homogeneous. The negative slope and low correlation coefficient suggest that NO segregation across the site is not the source of the difference in OH and HO_2 measured between the two instruments.

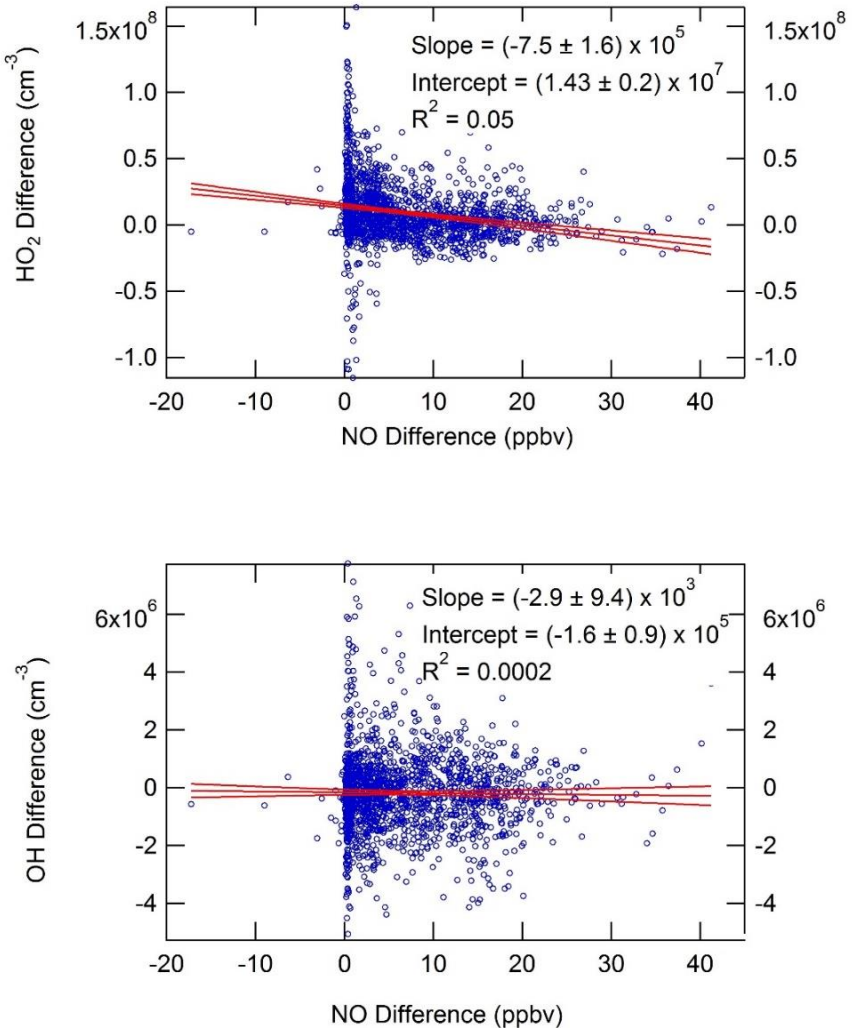

Figure 7.8 Top – Correlation of the HO_2 difference (HO_2 PKU – HO_2 Leeds) with the difference in NO (NO PKU – NO York). The data are 15-minute averages. Bottom – Correlation of the OH difference (OH Leeds – OH PKU) with the difference in NO (NO PKU – NO York). The data are 15-minute average.

7.3.4 Correlations

To investigate whether the difference in the OH or HO_2 measurements increased under different chemical conditions, the difference in the OH and HO_2 measurements were correlated with the measured VOCs, OH, HO_2, RO_2, O_3, NO, NO_2, CO, HONO, temperature, photolysis rates (see Table 4.1 for instrument detail). The Pearson's correlation coefficient (r) is shown in Figure 7.9 for correlation with VOCs, O_3 NO, NO_2 CO, HONO, PM with the OH difference; whilst the correlation with radical species is shown in Figure 7.10. The correlations shown in Figure 7.9 are quite small ($r<0.3$), the strongest correlation is from HO_2 with a correlation coefficient of $r = 0.29$. Figure 7.10 shows the correlation graph of the difference in OH with different radical species, and shows that all radical species have a larger coefficient than those in Figure 7.9.

The larger coefficient suggests that maybe the difference is related to different peroxy radical concentrations; and may suggest that one of the instrument suffers from an interference related to RO_2 (i.e. ROOOH decomposition into OH (Fittschen et al., 2019)) although both measurements were OHchem and would have been interference free. The correlation coefficient of the difference in OH measurements with radical species are all less than 0.45, suggesting that there is not a large correlation. The correlation with peroxy radical may be a spurious correlation where the largest difference is observed at the same time as when peroxy radicals peak, but not related to the peroxy radical just another species/process that occurs at this time. The difference between the OH measurements were not large, and most days within the error range of one another (~26% for Leeds and ~20% for PKU).

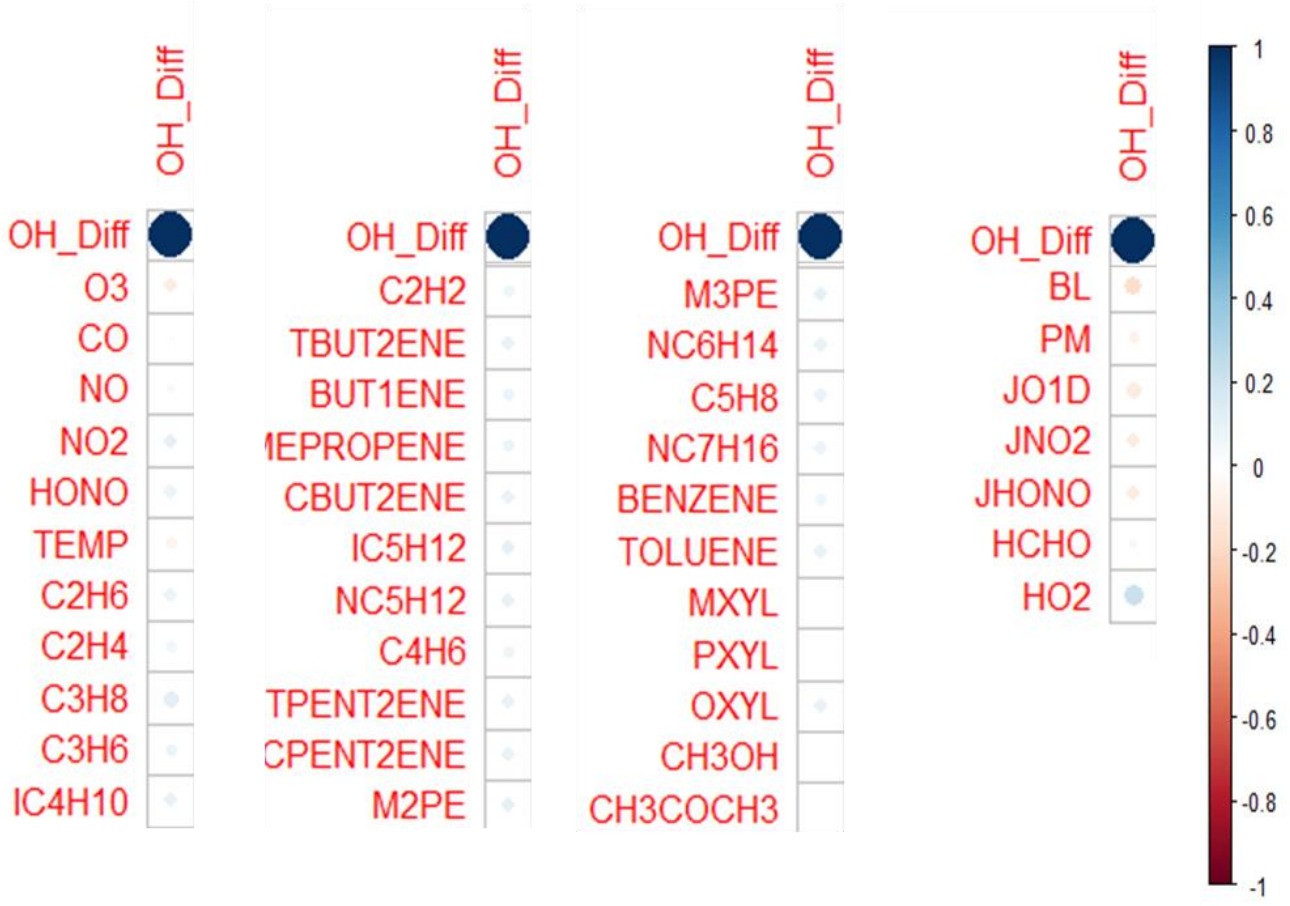

Figure 7.9 Heatmap showing the Pearson's correlation coefficient (r) of the difference in OH measurements (OH Leeds – OH PKU) correlated with measured VOCs, trace gas species and photolysis rates.

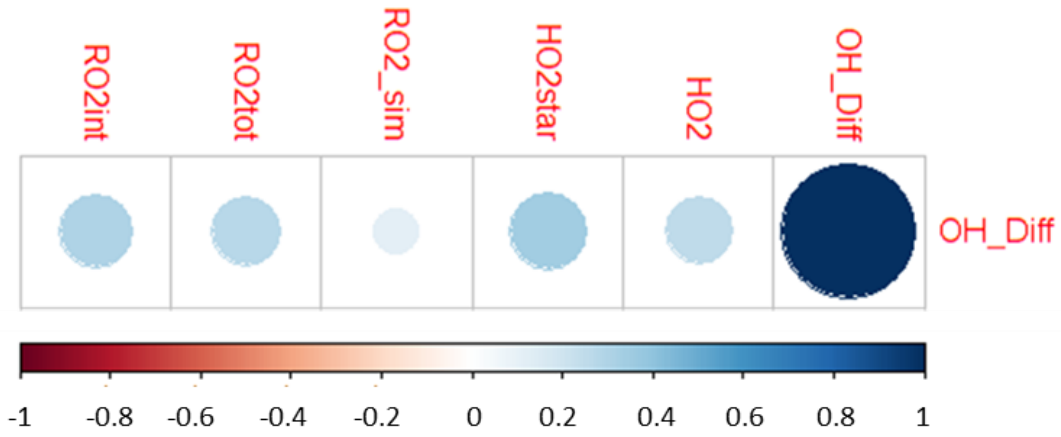

Figure 7.10 Heatmap showing the Pearson correlation coefficient (r) of the difference in OH measurements (OH Leeds – OH PKU) correlated with measured radical species.

The Pearson's correlation coefficient (r) is shown in Figure 7.11 for correlation with VOCs, O_3 NO, NO_2 CO, HONO, PM with the HO_2 difference; whilst the correlation with radical species is shown in Figure 7.12. The correlation shown in Figure 7.11 are much stronger than those for the OH difference. The positive correlations are observed for O_3, BL (boundary layer) and photolysis rates ($j(O^1D)$, $j(NO_2)$ and j(HONO). The positive correlations with photolysis rates may suggest that shading of the pinholes of one instrument, which would have a larger impact on the higher photolysis rates, could be reason for the differences observed. However, the difference in OH measurements did not correlate strongly with photolysis rates, but this may suggest that shading might have occurred upwind of the instruments and would have affected HO_2 more since it is a longer-lived species than OH. Figure 7.12 shows the correlation graph of the HO_2 difference with different radical species and shows that there is large correlation coefficient with RO_2int (complex RO_2 species, see section.2.1.8 for details) and RO_2tot (total RO_2 concentration).

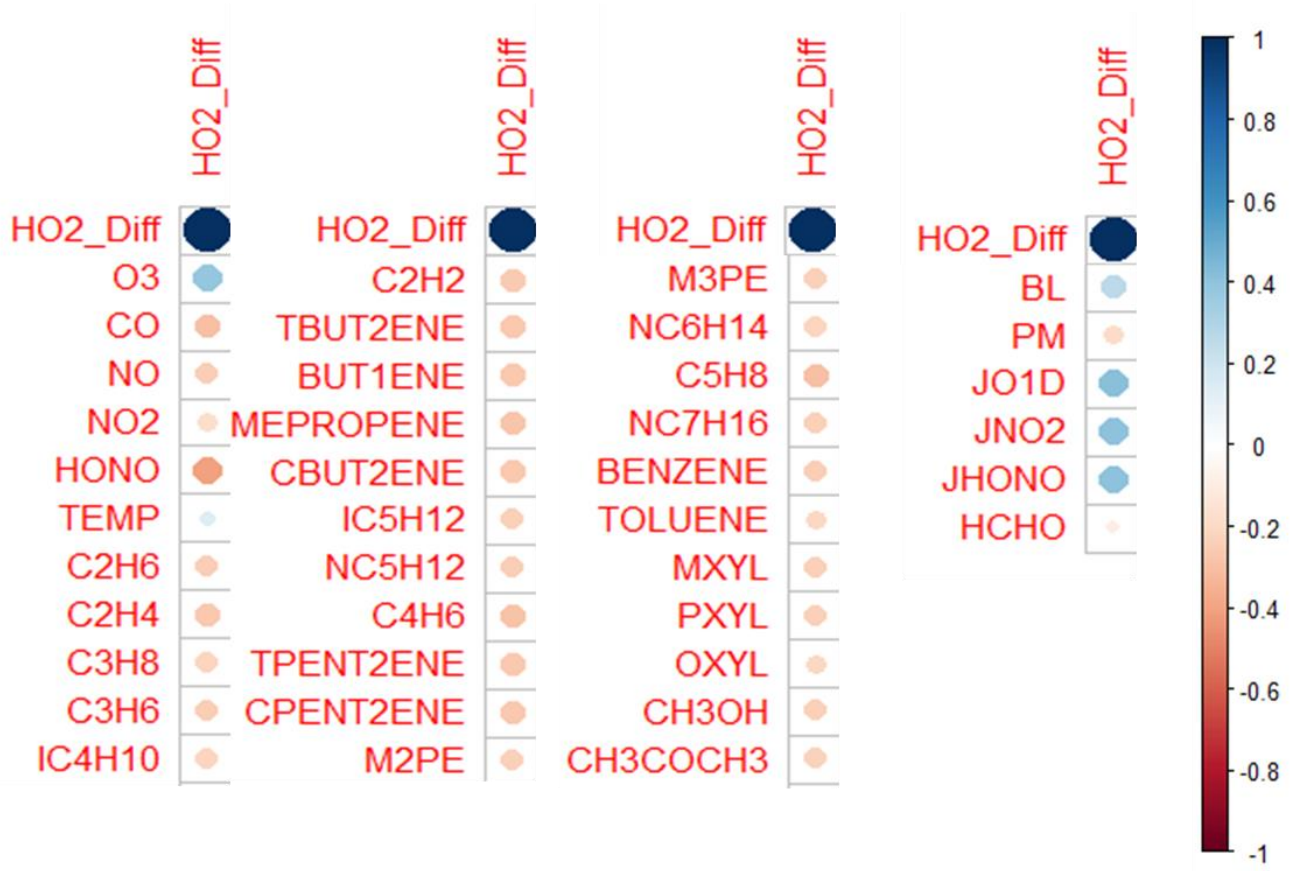

Figure 7.11 Heatmap showing the Pearson's correlation coefficient (r) of the difference in HO_2 measurements (HO_2 PKU – HO_2 Leeds) correlated with measured VOCs, trace gas species and photolysis rates.

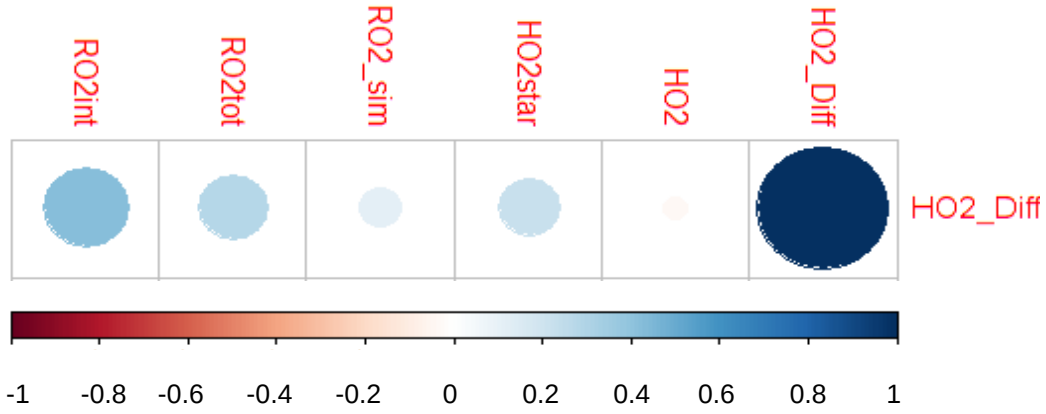

Figure 7.12 Heatmap showing the Pearson correlation coefficient (r) of the difference in HO_2 measurements (HO_2 PKU – HO_2 Leeds) correlated with measured radical species.

Fuchs et al. (2011) reported that more complex RO_2 species (alkenes and aromatics) could be converted into HO_2 via NO within a FAGE cell on a timescale fast enough to cause an interference in the HO_2 measurements. Since then, FAGE groups have decreased the amount of NO injected to convert HO_2 to OH to minimise the conversion of complex RO_2 into HO_2 (Fuchs et al., 2011, Whalley et al., 2013), whilst accepting any concomitant reduction in sensitivity towards HO_2 detection. The correlation with RO_2int may suggest that some complex RO_2 are converted into HO_2 in the PKU FAGE, causing the larger HO_2 that is observed. Although the difference between the measurements could also be caused by a calibration issue as the HO_2 calibration is more complex that the OH calibration. In the Leeds HO_2 calibration, an intercept is observed (HO_2 signal is observed when NO OH is generated in the calibration, see section.2.1.5 for details) which is caused by impurities in the NO/NO gas lines forming OH within the FAGE detection axis. The intercept tends to decrease across a campaign as the cylinder/gas lines get cleaner. across the campaign the intercept decreases. The difference observed may be caused by inaccurate determination of the intercept, which also may cause the higher HO_2 signal observed by PKU.

7.4 Summary and Conclusion

Measurements of OH and HO_2 were made by two separate FAGE instruments during the APHH winter campaign. The co-located FAGE instrument allowed for an opportunity for measurements of OH and HO_2 to be compared across a field campaign in a complex, highly complicate urban environment.

The time-series comparison of OH shows a very good agreement between 16/11/2016 to 20/11/2016, but afterwards the two measurements start to deviate. However, neither the Leeds nor PKU measurement consistently measured higher/lower than the other instrument for OH. On average the Leeds instrument measured 1.25 times higher than the PKU instrument, but this average difference is within the ~26% error on the Leeds measurements and ~20% on the PKU measurements. Like OH, between 16/11/2016 to 20/11/2016 the HO_2 measurements agreed well, but after this PKU consistently measured higher than the Leeds HO_2 value. On average the PKU instrument measured ~2.2 times higher than the Leeds instrument, and this difference cannot be accounted for within ~26% on both the HO_2 values.

Two separate photostationary steady-state (PSS) calculations were used to calculate OH and compared to the measured OH value from Leeds and PKU. Both PSS used the same measured O_3, H_2O, HONO, NO, j(HONO), $j(O^1D)$ and k(OH) but different measured HO_2 values (either from Leeds or PKU). The PSS calculations showed that when using the Leeds HO_2 measurements the experimental budget for OH could be closed with all sources and sink captured, showing a very good agreement between PSS OH and measured OH within 26% error (expect on 04/12/2016). In comparison, the PSS calculation using PKU HO_2 measurements overpredicts the measured OH (PKU) by a factor of 3.2, and suggests the higher measured HO_2 value is leading to faster propagation of HO_2 into OH *via* NO. Other than the HO_2 value in the PSS for PKU being too high, it may be that the k(OH) (which is the denominator in the PSS, see section.4.3.2) is too low. However, the behaviour of Leeds OH reactivity instrument under high NO is well understood (Fuchs et al., 2017), and when the measured k(OH) was

compared to modelled kOH (using MCM, see section.4.4.5 for details) the model could reconcile the measurements within 15%.

NO segregation across the field site has been investigated as a potential reason the OH and HO_2 measurements differing between the two instruments. Two different NO measurements were compared from two different measurement containers, the results show that in general PKU measured higher than the York NO by 13%. The two NO measurements also tracked each other very well. To investigate whether the difference in the measurements was caused by the difference in the NO measurement, hence the segregation of air mass across the site, could be the reason the measurements are different the difference in the measurements were correlated against the difference in the NO. The R^2 for the OH and HO_2 plots correlation plots the difference in the NO measurement (York and PKU) was 0.05 and 0.0002 with negative slopes for both, suggesting that the NO measurement difference was not related to the difference in the OH and HO_2 measurements.

To investigate whether the difference between the radical measurements increases under different chemical conditions, the difference in OH and HO_2 measurements were plotted against various VOCs, traces gases and meteorological factors. The difference in OH correlated best with the peroxy radical measurements, although the R^2 value was less than 0.45 for all peroxy species. The correlation was much stronger for the difference in HO_2, the strong correlation are derived from O_3, photolysis rates and RO_2 measurements. O_3, photolysis rates and RO_2 (largest R^2 from complex RO_2) all peak in the afternoon so the correlation may be spurious rather than real. *However,* unlike OH, HO_2 is not a direct measurement and needs to be converted into OH via NO. Also, previous work by Fuchs et al. (2011) has shown that complex RO_2 can interfere in the HO_2 measurements if too much NO is added. The correlation with RO_2int may suggest that some complex RO_2 are converted into HO_2 in the PKU FAGE, causing the larger HO_2 that is observed. However, PKU during the campaign did use two different flows to determine the HO_2 concentration and no differences were observed *and* so no correction was made for interfering RO_2's in the HO_2 measurement. Also, the difference between the measurements could also be

caused by a calibration issue as the HO_2 calibration is more complex that the OH calibration and needs to be corrected for artefact signals that arise from the NO injection which can vary with time. In the Leeds calibration, an intercept is observed (see section.2.1.5 for details) which is caused by NO that is injected, across the campaign the intercept decreases. The difference observed may be caused by the inaccurate determination of the intercept, which also may cause the higher HO_2 signal observed by PKU.

Future work should investigate whether the calibration coefficients changed between the first periods (16/11/2016 to 20/11/2016) and the second period (02/11/2016 – 08/11/2016) for the two instruments as during the first time-period there was good agreement between both OH and HO_2 measurements and the second time-period is where they start to deviate (~2.5 for HO_2). Also, future work should consider the errors on both the Leeds and PKU measurements to assess the true error in the correlation plots.

7.5 References

Fittschen, C., Al Ajami, M., Batut, S., Ferracci, V., Archer-Nicholls, S., Archibald, A. T. and Schoemaecker, C. (2019) 'ROOOH: the Missing Piece of the Puzzle for OH measurements in low NO Environments', Atmos. Chem. Phys, 19, pp. 349–362

Fuchs, H., Bohn, B., Hofzumahaus, A., Holland, F., Lu, K., Nehr, S., Rohrer, F. and Wahner, A. (2011) 'Detection of HO_2 by laser-induced fluorescence: calibration and interferences from RO_2 radicals', *Atmospheric Measurement Techniques,* 4(6), pp. 1209-1225.

Fuchs, H., Brauers, T., Dorn, H.-P., Harder, H., Haseler, R., Hofzumahaus, A., Holland, F., Kanaya, Y., Kajii, Y. and Kubistin, D. (2010) 'Formal blind intercomparison of HO_2 measurements in the atmosphere simulation chamber SAPHIR during the HOxComp campaign', Atmospheric Chemistry and Physics, 10(24), pp. 12233 - 12250

Fuchs, H., Novelli, A., Rolletter, M., Hofzumahaus, A., Pfannerstill, E. Y., Kessel, S., Edtbauer, A., Williams, J., Michoud, V. and Dusanter, S. (2017) 'Comparison of OH reactivity measurements in the atmospheric simulation chamber SAPHIR', *Atmospheric Measurement Techniques,* 10(10), pp. 4023-4053.

Fuchs, H., Tan, Z., Hofzumahaus, A., Broch, S., Dorn, H.-P., Holland, F., Künstler, C., Gomm, S., Rohrer, F. and Schrade, S. (2016) 'Investigation of potential interferences in the detection of atmospheric RO_x radicals by laserinduced fluorescence under dark conditions', *Atmospheric Measurement Techniques,* 9, pp. 1431-1447.

Kanaya, Y., Hofzumahaus, A., Dorn, H., Brauers, T., Fuchs, H., Holland, F., Rohrer, F., Bohn, B., Tillmann, R. and Wegener, R. (2012) 'Comparisons of observed and modeled OH and HO_2 concentrations during the ambient measurement period of the HO_xComp field campaign', Atmospheric Chemistry and Physics, 12(5), 2567-2585

Schlosser, E., Brauers, T., Dorn, H.-P., Fuchs, H., Haseler, R., Hofzumahaus, A., Holland, F., Wahner, A., Kanaya, Y. and Kajii, Y. (2009) 'Formal blind intercomparison of OH measurements: results from the international campaign HO_xComp', *Atmospheric Chemistry and Physics,* 9(20), pp. 7923-7948.

Tan, Z., Fuchs, H., Lu, K., Bohn, B., Broch, S., Dong, H., Gomm, S., Haeseler, R., He, L. and Hofzumahaus, A. (2016) 'Radical chemistry at a rural site (Wangdu) in the North China Plain: Observation and model calculations of OH, HO_2 and RO_2 radicals', *Atmos. Chem. Phys*, 17, 663–690

Whalley, L., Blitz, M., Desservettaz, M., Seakins, P. and Heard, D. (2013) 'Reporting the sensitivity of laser-induced fluorescence instruments used for HO2 detection to an interference from RO_2 radicals and introducing a novel approach that enables HO_2 and certain RO_2 types to be selectively measured', *Atmospheric Measurement Techniques,* 6(12), pp. 3425-3440.

8. Conclusions and Future Work

Chapter 1 outlined the tropospheric oxidation chemistry involving OH, HO_2 and RO_2 radicals, collectively known as RO_x, followed by an overview of Chinese air quality including trends of PM, NO_2, NO, SO_2 and O_3. Then an overview of measurement techniques for OH, HO_2 and RO_2 was presented, with a focus on the FAGE (fluorescence assay by gas expansion) technique, including a section on interference in the OH and HO_2 measurements. Finally, Chapter 1 also outlines the results from previous urban field campaigns that have taken place in summer and winter and comparisons with detailed chemical box models. Previous campaigns show that the most severe measurement-model discrepancies occurs when [NO] < 1 ppbv) and [NO]> 3 ppbv. Chapter 2 describes the details of the Leeds ground-based FAGE instrument and the methods used to calibrate the instrument's response to radical concentrations. Chapter 2 covers in detail the operation of FAGE in the field and the procedures used to workup ambient data to obtain the OH, HO_2 and RO_2 (speciated into simple and complex) radical concentration.

Chapter 3 covers the experimental work on the inlet pre-injector system and determination of interference in the Leeds-ground based FAGE from NO_3 and O_3. The inlet pre-injector (IPI) system allows for an interference free background method called OHchem, unlike the traditional background method called (OHwave) OHchem can distinguish between real, atmospheric OH or OH generated internally within the cells. The IPI works by injecting a scavenger (propane) into the ambient air so during the OHchem period only internally generated OH is measured. Chapter 3 shows that the sensitivity loss from use of the IPI is minimal (< 5%) for OH, and also highlights the importance of conducting experiments analogous to ambient sampling conditions, as using a turbulent flow (as used in normal calibration procedure) results in a ~40% sensitivity decrease for OH which is not representative of ambient sampling. Following this results are presented from a campaign that took place in Namco, Tibet (~4800 m, pressure = 0.55 bar), the results showing that during the campaign there was a step-change in the OH data in both the OHwave and OHchem measurements.

The step-change is thought to be from a leak between the HO_x and RO_x cell causing NO to leak into the HO_x cell during the OH measurement period, a NO leak would have resulted in HO_2 converting to OH and thus increasing the OH concentration. However, if only the NO leak occurred, the OHchem measurements should not be affected. Still, the OHchem measurements were affected and may suggest a 2200 ppmv mixing ratio of the scavenger propane removes internally generated OH and thus the internally generated interference is underestimated. Theoretical calculations suggest that ~ 38 ± 26% of the OH is internally removed, and under normal ambient sampling conditions used during the APHH summer campaign (1110 ppmv of propane) ~20 ± 13% is internally removed. The APHH summer campaign has been corrected for internal removal and showed that at the highest measured OHchem concentrations, the difference between OHchem – Ohchem(corrected) is ~ 5 times smaller than the error of the OHchem value, so is not significant. Finally, Chapter 3 covers the interference testing for O_3 and NO_3, and shows that the O_3 interference is equivalent to [OH] = 520 molecule cm^{-3} $ppbv^{-1}$ mW^{-1} $\%^{-1}$ and the NO_3 interference was found to be negligible up to ~90 pptv of NO_3.

Chapter 4 covers the measurements of OH, HO_2 and RO_2 radicals, and OH reactivity measurements from the APHH winter campaign that took place in November and December 2016 in central Beijing, and the comparison with a detailed chemical box model. The aim of the project was to assess which pollutants are transformed or removed through transport, chemical reactions and photolysis. On a diel basis, the OH, HO_2 and RO_2 concentration peaked at 2.8×10^6 molecule cm^{-3}, 4.5×10^7 molecule cm^{-3} and 1×10^8 molecule cm^{-3}, respectively. A photostationary steady-state (PSS) calculation for OH showed that the experimental budget was closed (all sources and sinks captured), and that the OH and PSS calculation agreed within 10% on a diurnal basis. During the APHH winter campaign, very little interference was observed in the OH measurement, with the correlation of OHwave and OHchem yielding a slope of 1.05 ± 0.07. The radical (OH, HO_2 and RO_2) measurements were compared to several model scenarios from a box model constrained to the Master Chemical Mechanism (MCM, v3.3.1). The MCM-base model generally underpredicted the

radical species, and on average at midday the model:measured ratio was ~0.58, ~0.17 and ~0.04 for OH, HO_2 and RO_2, respectively. The underprediction of the radical species increased with increasing NO, with a maximum underprediction of OH, HO_2 and RO_2 at ~170 ppbv of [NO] by a factor of 4.3, 19, 95, respectively. However, the MCM base model was able to replicate the OH reactivity within 10% showing the major OH sinks were captured during the campaign. The major primary source of RO_x was assessed in the MCM base model. It showed that it was dominated by the photolysis of HONO (~83%), with the remaining primary production from ozonolysis (~10%), photolysis of HCHO (1%) and photolysis of carbonyl species (4.4%). The termination of radicals was controlled by the reaction of OH + NO (~30%), OH + NO_2 (~55%) and net formation of PAN (~15%).

The MCM base model was constrained to HO_2 and showed the model was now able to replicate OH well, which combined with the closure OH reactivity budget suggests that missing understanding under high NO conditions stems from unknown RO_2 chemistry. Additional RO_2 was added into the MCM-base model such that the measured and modelled total RO_2 agreed. The additional RO_2 resulted in both OH and HO_2 being overpredicted by the model by ~1.6 and ~4, respectively, and even when HO_2 uptake onto aerosol was considered (using γ=0.2), the model could not reconcile the measured HO_2. The MCM base model was unconstrained to measured HONO and resulted in OH and HONO underpredicted by ~6.4 and ~10, respectively, and highlights the importance of using measured HONO. The MCM base model was also unconstrained to HONO and constrained to OH and highlighted to model could reproduce HONO between 07:00 – 13:00, suggesting gas-phase chemistry was able to close to the HONO budget and did not need additional heterogeneous chemistry on average. During the APHH winter campaign several haze events were observed, and the measurement showed the OH concentration was similar inside and outside haze events. The gas-phase oxidation of NO_2 and SO_2 increased by ~3 and ~4.2 during haze events, respectively. The contribution to aerosol from NO_3^- and SO_4^{-2} was measured during the APHH campaign, the NO_3 shows a peak at midday suggesting gas-phase formation of nitrate is important. By contrast, the

formation of sulphate correlates well with the RH (relative humidity) suggesting that sulphate is formed through the aqueous pathway. Finally, the impact of the underprediction of peroxy radicals on O_3 formation was assessed. The maximum in situ ozone production calculated using the measurements of HO_2 and RO_2 was 162 ppbv hr^{-1} at ~180 ppbv of NO, whilst the ozone production calculated using the modelled HO_2 and RO_2 was 10 ppbv hr^{-1}. The O_3 production in Beijing is very high but currently is being titrated out by the high concentration of NO. Current mitigation strategies in China aims at reducing NO_x emissions and PM, so the reduction in NO may lead to an increase in O_3 during the winter-time in Beijing. Further modelling could be undertaken to explore the underprediction of OH, HO_2 and RO_2 in the model. This may include decreasing the rate constant for specific complex RO_2 species reacting with NO, this may increase the RO_2 lifetime and increase the amount of RO_2 recycling to HO_2, thus recycling in OH.

Chapter 5 covers the measurements of OH, HO_2, RO_2 and OH reactivity measurements from the APHH summer campaign that took place in May and June 2017 in central Beijing, and the comparison with a detailed chemical box model. On a diurnal basis the OH, HO_2 and RO_2 concentration peaked at ~8.5 x 10^6 molecule cm^{-3}, 2.3 x 10^8 molecule cm^{-3} and 1.15 x 10^9 molecule cm^{-3}, respectively. A photostationary steady-state calculation of OH underpredicted the OH concentration by ~2, showing the experimental budget could not be closed, and there is an additional source of OH during the summer APHH campaign. During the summer campaign a small interference in the OH measurement was observed, with the slope of OHwave and OHchem yielding 1.10 ± 0.02. The difference in OHwave and OHchem increased with increasing OH concentration. The source of the interference was investigated, and the interference correlated well with most species that peak in the afternoon (O_3, temperature and peroxy radicals). The highest correlation was observed for the products $RO_2 \times O_3$ and $OH \times O_3$ with a Pearson's correlation coefficient of 0.47 and 0.48, respectively. The correlation of OHint (difference between OHwave and OHchem) with RO_2, O_3 and temperature may be a spurious correlation from a third confounding factor (an unknown species/process that has the same diurnal pattern as O_3/Temp that causes the O_3 interference) (Aldrich, 1995).The MCM base model replicates the

OH concentration well, but underpredicts and overpredicts RO_2 and HO_2, respectively. The OH and HO_2 start to be underpredicted by the MCM base model above 5 ppbv of NO, and the RO_2 underprediction increases wth increasing NO. The comparison between measured and modelled OH reactivity highlights missing OH reactivity throughout the entire day, and on average for the missing OH reactivity was 9.5 s^{-1}. The primary production of radicals was dominated by the photolysis of HONO (77%), the other primary sources of OH during the APHH summer campaign was: $O^1D + H_2O$ (11%); ozonolysis of alkenes (5.5%), photolysis of HCHO (3.42%), photolysis of carbonyls (0.66%, other than HCHO) and VOCs + NO_3 (2.2%). The termination of radicals (RO_x) is dominated by the reaction of OH + NO_2 (63%). The other termination reactions during the APHH summer campaign were: OH + NO (11.3%), HO_2 + NO_2 (0.8%), HO_2 + HO_2 (1.47%), RO_2 + HO_2 (3.12%) and net formation PAN (14%).

HO_2 uptake onto aerosol using an uptake coefficient of 0.2 reduced the HO_2 compared to the MCM base model by ~8%, but was not able to reconcile the model with the measurements. The reaction of HO_2 + X was added to the MCM base model, where X recycles HO_2 into OH independent of NO. The results showed that ~0.75 ppbv of X was required to reconcile measurements of HO_2 with the model when the same rate coefficient as HO_2 + NO was used. However, the introduction of additional recycling resulted in OH being overpredicted at lower NO concentrations (<0.5 ppbv). Additional RO_2 was added into the MCM-base model so that the measured and modelled total RO_2 agreed. The additional RO_2 lead to both OH and HO_2 being overpredicted by the model and showed that just adding another primary source of RO_2 will not reconcile measurement with modelled values under the NO regimes observed during the summer Beijing campaign. Cl atom chemistry was added to the model. It did improve the model-measurement comparison, with a maximum ratio for MCM-Cl:MCM-base of 1.04 (4% increase), 1.08 (7.9% increase) and 1.19 (19% increase) for OH, HO_2 and total RO_2, respectively. Autoxidation chemistry was explored in the model by reducing the RO_2 + NO rate constant. Once the rate constant was decreased by a factor of 10, the model could replicate the measured values for OH, HO_2 and RO_2 well, highlighting that autoxidation could be an

important process in Beijing. Autoxidation products (HOMs) were also observed by a CIMS instrument in both the gas and aerosol phase. The MCM base model was unconstrained to measured HONO and resulted in OH being underpredicted by ~2.2 and highlights the importance of using measured HONO. The MCM base model was also unconstrained to HONO and constrained to OH, and the HONO concentration was underpredicted by the model by a factor ~11 and suggests additional heterogeneous sources of HONO was required in summer in Beijing. Finally, the impact of the underprediction of peroxy radicals on O_3 formation was assessed. The peak ozone production calculated using the measured values for HO_2 and RO_2 was 318 ppbv hr^{-1} when [NO] = 48 ppbv, while the ozone production calculated using the modelled radical concentrations was 64 ppbv hr^{-1}. When the [NO] is less than 1 ppbv the model overpredicts the O_3 production. The underprediction of ozone production by the model shows missing understanding of the radical chemistry can impact the calculation of secondary pollutants. Further modelling work can be used to explore whether autoxidation is important in central Beijing, but also chamber studies to investigate how different RO_2 species behave under different NO regimes. Further work is also needed to investigate the OH interference that has been observed at large values of OH in central Beijing and also forested environments (Mao et al., 2012).

Chapter 6 compares the results from both the winter and summer APHH campaigns that took place in Beijing. The O_3/NO_x regimes during the winter and summer campaigns were very different. The O_3 during the summer campaign was very high reaching above 160 ppbv, and on average peaking at 88 ppbv. Whilst in winter the average maximum ozone observed was 17 ppbv. The NO showed an opposite trend to the O_3 for the summer and winter campaigns, with the NO reaching above 250 ppbv during winter and peaking at a maximum average of 39 ppbv. Also, the summer campaign had significantly higher light levels compared with the winter campaign; on average, the $j(O^1D)$ was ~4.3 times higher during summer.

The OH, HO_2 and total RO_2 concentration was 3.5, 7.9 and 19 times larger, respectively, in the summer campaign compared to winter. Also, in summer, night-time measurements of OH, HO_2 and RO_2 were all above the limit of

detection (LOD), whilst in winter only RO_2 was above the LOD. The ratio of measured:modelled(base) showed that OH, HO_2 and RO_2 were underpredicted by the model at ~2.5 ppbv and ~ 5 ppbv of NO for winter and summer, respectively. The model for summer and winter agrees with the measurements at ~2 ppbv of NO for OH and HO_2, although the RO_2 species are still underpredicted in the model by factor of ~3 and ~7 in winter and summer, respectively. In the summer campaign there was ~9.5 s^{-1} missing OH reactivity. The combined contribution to the total OH reactivity from OH + NO, OH + NO_2 and OH + CO is 64.3% in winter whilst these reactions only contribute to 36.4% in summer. In both summer and winter the contribution is similar for VOCs and model intermediates. The VOCs contribute 23.2% and 25.2% in summer and winter, respectively. The model intermediates contribute 6.8% and 5.0% to the total reactivity in summer and winter, respectively. The major source of RO_x radicals was HONO in summer and winter contributing to 83% and 77% of primary radical formation, respectively. In summer, unlike winter, significant primary production of radicals from VOC + NO_3 reactions (2.2%). The comparison of the species that are terminating the radicals shows that in summer and winter the main contributors are OH + NO and OH + NO_2. OH + NO_2 contribute 63% and 43% to the total termination reaction in summer and winter, respectively. However, in summer, unlike winter, peroxy self-reactions also became an important termination pathway. In winter when the model was unconstrained to HONO and constrained to OH, the model could replicate the HONO concentration, but this is not the case in the summer campaign where the HONO concentration was underpredicted and highlights the need for additional heterogeneous sources in summer for HONO. O_3 production has been calculated from measured and modelled (MCM-base) values for both summer and winter and production peaks at ~132 ppbv hr^{-1} at 177 pbbv of NO in winter, whilst in summer the production peaks at ~ 316 ppbv hr^{-1} at 68 ppbv of NO. The O_3 production is higher in summer compared to winter as there is much higher light levels, hence production of radicals. Although there is very high ozone

production observed during winter, the titration of O_3 by NO is dominant as low levels of ozone was observed.

The impact of HO_2 uptake on modelled HO_2 and O_3 formation has been investigated. The results show that in general HO_2 uptake is not important in winter as the reaction of HO_2 + NO outcompetes HO_2 uptake, although HO_2 uptake did decrease the calculated O_3 formation by ~ 3 ppbv hr^{-1} on some days. By contrast, in summer the high surface area coincided with low NO and caused a large impact on modelled HO_2 (decreased HO_2 by up to ~40% at 0.15 ppbv of NO) when uptake was considered. The decrease in modelled HO_2 only translates to a decrease in O_3 formation in summer when the NO is >0.8 ppbv, as NO is required to drive the O_3 formation. Future work should focus on understanding the reasons behind the measured:modelled deviations at high and low NO including autoxidation, additional radical sources and whether the RO_2 + NO rate constant is different for more complex RO_2 species. Future work should also investigate the sources of haze events in summer that leads to significant uptake, as the higher aerosol surface area does not correlate with NO, unlike in winter.

Chapter 7 covers the comparison between the Leeds and PKU OH and HO_2 measurements during the APHH winter campaign. Time-series comparison of OH shows an excellent agreement at the start of the campaign, but after 20/11/2016, the measurements start to deviate. However, neither the Leeds nor PKU consistently measured higher/lower than the other instrument, but on average the Leeds instrument measured ~1.25 times higher than PKU for OH. Like OH, at the start of the campaign, the HO_2 measurements agreed well, but after this PKU consistently measured higher than the Leeds HO_2 value. On average, the PKU instrument measured ~2.2 times higher than the Leeds instrument. A photostationary steady-state was used to calculated the OH concentration using both the Leeds and PKU data. The PSS using Leeds HO_2 showed a good agreement of PSS calculated OH and Leeds measured OH, and they agree within 26% error for the OH measurements. However, the PSS using the PKU HO_2 data does not show a good agreement between PSS OH and measured PKU OH and results in measure OH (PKU) being overpredicted by ~3.2, and suggests the higher measured HO_2 value is leading to faster

propagation of HO_2 into OH *via* NO. NO segregation across the measurements site was investigated by comparing NO measured by the University of York and PKU, and the results showed that in general, PKU measured higher than York by 13%. However, the difference between the NO measurements and the difference between the radical measurements (OH and HO_2) did not correlate well, and the R^2 for the OH and HO_2 correlation plots was 0.05 and 0.0002, respectively, suggesting NO segregation was not the source of the differences in radical measurements. The difference in the HO_2 measurements correlated well with O_3, photolysis rates and RO_2. The correlation with RO_2, especially complex RO_2, may suggest that some complex RO_2 species are converted into HO_2 in the PKU FAGE instrument, causing the larger HO_2 that is observed. However, PKU during the campaign did use two different flows of NO to determine the HO_2 concentration, and no differences were observed, so no corrections were made for interfering RO_2's in the HO_2 measurement. Also, the difference between the measurements could be caused by a calibration issue as the HO_2 calibration is more complex that the OH calibration and needs to be corrected for artefact signals that arise from the NO injection, which can vary with time.

Future work should investigate whether the calibration coefficients changed between the first time-periods (16/11/2016 to 20/11/2016) and the second time-period (02/11/2016 – 08/11/2016) for the two instruments; as during the first time-period there was good agreement between both OH and HO_2 measurements and the second time-period is where they start to deviate (~2.5 for HO_2).